

Improved Quantification in Small Animal PET/MR



**This dissertation is submitted for the degree of
Doctor of Philosophy**

Eleanor Evans

Gonville and Caius College, University of Cambridge

June 2015

All components of this thesis were carried out in accordance with the UK Animals (Scientific Procedures) Act 1986, and with the approval of the University of Cambridge Ethical Review Panel, in line with the University of Cambridge Policy on the Use of Animals in Scientific Research. All animal experiments discussed in this thesis were approved by the UK Home Office Animals Scientific Procedures Department (ASPD).

This thesis is the result of my own work and includes nothing which is the outcome of work done in collaboration except where specifically indicated in the text. No part of this thesis has previously been submitted for examination of any other diploma or degree at any institution. This thesis does not exceed 60,000 words in length (excluding the bibliography, photographs, figures, tables and appendices).

Abstract

In translational medicine, complementary functional and morphological imaging techniques are used extensively to observe physiological processes *in vivo* and to assess structural changes as a result of disease progression. The combination of magnetic resonance imaging (MRI) and positron emission tomography (PET) provides excellent soft tissue contrast from MRI with exceptional sensitivity and specificity from PET. This thesis explores the use of sequentially acquired PET and MR images to improve the quantification of small animal PET data.

The primary focus was to improve image-based estimates of the arterial input function (AIF), which defines the amount of PET tracer within blood plasma over time. The AIF is required to produce physiological parameters quantifying key processes such as metabolism or perfusion from dynamic PET images. The gold standard for AIF measurement, however, requires serial blood sampling over the course of a PET scan, which is invasive in rat studies but prohibitive in mice due to small total blood volumes.

To address this issue, the geometric transfer matrix (GTM) and recovery coefficient (RC) techniques were applied using anatomical MR images to enable the extraction of partial volume corrected image-based AIFs from mouse PET images.

A non-invasive AIF extraction method was also developed for rats, beginning with the optimization of an automated voxel selection algorithm to assist in extracting MR contrast agent signal time courses from dynamic susceptibility contrast (DSC) MRI data. This procedure was then combined with dynamic contrast enhanced (DCE) MRI to track a combined injection of Gadolinium-based contrast agent and PET tracer through the rat brain. By comparison with gold standard tracer blood sample data, it was found that normalized MRI-based AIFs could be successfully converted into PET tracer AIFs in the first pass phase when fitted with gamma variate functions.

Finally, a MR image segmentation method used to provide PET attenuation correction in mice was validated using the Cambridge split magnet PET/MR scanner's transmission scanning capabilities. This work recommends that contributions from MR hardware in the PET field of view must be accounted for to gain accurate estimates of tracer uptake and standard uptake values (SUVs).

This thesis concludes that small animal MR data taken in the same imaging session can provide non-invasive methods to improve PET image quantification, giving added value to combined PET/MR studies over those conducted using PET alone.

Acknowledgements

I would like to thank Dr Guy Williams, Dr Stephen Sawiak, and Dr Adrian Carpenter for their kind supervision of this PhD project. The completion of this work would not have been possible without their enthusiasm for scientific research and dedication to the project. In particular I would like to thank Dr Guy Williams for his encouragement and advice when writing up this thesis, Dr Stephen Sawiak for his help and instruction in the practical aspects of MRI scanning and image analysis, as well as training in the use of his SPMmouse software, and Dr Adrian Carpenter for the construction of a data processing cluster to perform dynamic PET reconstruction. I am particularly grateful to Dr Roie Manavaki for her feedback on PET analysis techniques and for her proofreading of this thesis. I would also like to thank Dr Rob Hawkes for his valued instruction on the operation and calibration of the split magnet PET/MR scanner and Dr Richard Ansorge for his help troubleshooting the transmission scan mechanism, as well as feedback on my writing. I am also thankful to Dr Ian Cullum for his suggestions on how to validate the performance of the transmission scanning mechanism, to Dr Rob Smith and his team for providing PET tracer for use in phantom studies and to Dr Fraser Robb and Dr Floris Jansen from GE Healthcare, for their useful discussions and advice on this PhD project.

Mouse imaging data analysed in Chapters 4 and 8 were used with the kind permission of Dr Thomas Krieg and Dr Carmen Methner, who also performed the surgical procedures and tail vein cannulations on the mice involved. The imaging data in these Chapters was acquired by Dr Guido Buonincontri, who I am indebted to for his patience in teaching me how to perform PET and MRI experimental protocols effectively, and for the numerous discussions we engaged in over the course of my PhD. These conversations spanned a huge variety of subjects, from the subtleties of preclinical MRI image acquisition to Italian cuisine. I would also like to express my appreciation of both his and Asad Shabir's assistance in attaining the rat blood sampling results reported in Chapter 7, to Jason Day for his technical assistance in the processing of the blood samples using ICP-MS and to Dr David Williamson for performing the artery and vein cannulations on the rats for that study. Further mouse imaging data presented in Chapter 5 was acquired in collaboration with Agnese Irtle, Dr Janet Maguire, Dr Joe Bird and Dr Anthony Davenport, with mouse tail vein cannulations performed by Victoria Pell and blood samples taken via cardiac punc-

ture by Dr David Williamson. The rat imaging data analysed in Chapter 6 were used with the permission of Prof. Jean-Claude Baron and Dr Ulf Jensen-Kondering, with the surgical operations performed by Dr Sohail Ejaz and the DSC MRI protocol conducted by Alex Ward.

Finally, I would also like to thank all my friends and family, with special mention to my fellow Cambridge PhD students, Kate, Katie, Dimitra and my partner Eoin, as well as my parents Deirdre and John and my brother Eric, for their ongoing support throughout the duration of this PhD project.

The experiments outlined in Chapters 4, 6 and 8 have been presented at international conferences and are published as follows:

- Chapter 4: E. Evans, G. Buonincontri, D. Izquierdo, C. Methner, R. C. Hawkes, R. E. Ansorge, T. Krieg, T. A. Carpenter and S. J. Sawiak, “Combining MRI with PET for partial volume correction improves image derived input functions in mice”, presented at BC-ISMRM 2013 (York, UK) as an oral presentation and at ISMRM 2014 (Milan, Italy) and PSMR 2014 (Kos, Greece) as a poster presentation. This paper has been accepted for publication in a special edition of *IEEE Transactions on Nuclear Science*, which details the proceedings of the PSMR 2014 conference and an abstract of this work is published in *EJNMMI Physics*, July 2014, vol. 1, p A84.
- Chapter 6: E. Evans, S. J. Sawiak and T. A. Carpenter, “MRI-derived Arterial Input Functions for PET Kinetic Modelling in Rats”, was presented at BC-ISMRM 2012 (Cambridge, UK) and is published in a special edition of *Nuclear Instruments and Methods in Physics Research A (NIMA A): Accelerators, Spectrometers, Detectors and Associated Equipment*, Feb 2013, vol. 702, p. 126-128, which details the peer-reviewed proceedings of PSMR 2012 (Isola d’Elba, Italy)
- Chapter 8: E. Evans, G. Buonincontri, D. Izquierdo, C. Methner, R. C. Hawkes, R. E. Ansorge, T. Krieg, T. A. Carpenter and S. J. Sawiak, “Direct evaluation of MR-derived attenuation correction maps for PET/MR of the mouse myocardium”, presented as an poster presentation at ISMRM 2014 (Milan, Italy) and an oral presentation at PSMR 2014 (Kos, Greece). This paper is also currently under peer review for publication in a special edition of *IEEE Transactions on Nuclear Science*, which details the proceedings of the PSMR 2014 conference and an abstract of this work is also published in *EJNMMI Physics*, July 2014, vol. 1, p A85.

This PhD project was supported by an Medical Research Council (MRC) studentship, with grant code SRAG/038.

Contents

1	Introduction	12
1.1	Motivation behind PET/MR scanning	12
1.2	Small animal PET/MR scanner design	13
1.3	Applications for small animal PET/MR	16
1.4	Improving parameter quantification in small animal PET/MR	18
1.5	Thesis structure	19
2	Background theory to PET and MR imaging	20
2.1	PET scanning	20
2.1.1	Positron emission and annihilation	20
2.1.2	Count detection	22
2.1.3	Types of events	23
2.1.4	Basic PET image reconstruction	25
2.1.5	Further PET image reconstruction	31
2.1.6	Maintaining image quantification accuracy	38
2.1.7	Attenuation correction	40
2.1.8	Dynamic PET acquisition	48
2.1.9	Motion correction of dynamic PET data	49
2.2	MRI scanning	50
2.2.1	Background MRI physics	50
2.2.2	Scanner hardware	51
2.2.3	Creation of images	52
2.2.4	Relaxation rates and image contrast	60
2.2.5	Structural MRI pulse sequences - FISP MRI	63
2.2.6	Structural MRI pulse sequences - FLASH MRI	65
2.2.7	Structural MRI pulse sequences - RARE MRI	67
2.2.8	Vascular MRI pulse sequences - Time of flight MR angiography	68

2.2.9	Dynamic MRI pulse sequences - DSC MRI	72
2.2.10	Dynamic MRI pulse sequences - DCE MRI	74
2.2.11	Perfusion MRI pulse sequences - Arterial spin labelling	77
2.2.12	Summary of MR pulse sequences	80
2.3	Chapter summary	80
3	Current quantitative methods in small animal PET and MR	81
3.1	Quantification in PET	81
3.1.1	Standard uptake values (SUVs)	82
3.1.2	Compartmental modelling of tracer kinetics	83
3.1.3	Arterial input function derivation methods	88
3.1.4	Challenges of using image derived AIFs	90
3.2	Quantification in dynamic MR using contrast agents	92
3.2.1	Compartmental modelling of contrast agent kinetics in DCE MRI	93
3.2.2	Analysis of cerebral perfusion using DSC MRI	94
3.3	Chapter Summary	99
4	Comparison of image-derived input functions for use in ^{18}F-FDG murine studies	100
4.1	Introduction	101
4.1.1	ROI selection for IDIF extraction	101
4.1.2	Complications arising from partial volume effects and spillover	102
4.1.3	Use of geometric transfer matrix (GTM) method to provide partial volume correction	105
4.1.4	Alternative PVC approach - MAP reconstruction	107
4.2	Materials and Methods	108
4.2.1	Animal models	108
4.2.2	Sequential PET/MR imaging	109
4.2.3	IDIF extraction	111
4.2.4	Application of GTM method to LVBP ROI IDIFs	113
4.2.5	Conversion of IDIFs from whole blood to plasma	115
4.2.6	Kinetic modelling	115
4.3	Results	116
4.3.1	3DRP and MAP image comparison	116
4.3.2	Differences in SUV between control and drug treated mouse groups	120
4.3.3	IDIFs extracted from LVBP ROI	121
4.3.4	Comparison of LVBP IDIFs and VC IDIFs	123

4.3.5	Comparison of LVBP IDIFs with GTM correction to VC IDIFs	124
4.3.6	IDIFs generated for all mice - LVBP ROI	126
4.3.7	IDIFs generated for all mice - VC ROI	132
4.3.8	Kinetic modelling results (K_i values)	136
4.4	Discussion	138
4.4.1	Influence of reconstruction algorithm and cardiac gating on IDIFs	138
4.4.2	IDIFs derived from the VC ROI	139
4.4.3	Evaluation of GTM method for IDIF PVC	141
4.4.4	Observed differences between treated and control groups after kinetic analysis	142
4.5	Conclusions	142
4.6	Chapter Summary	143
5	Evaluation of image-derived input function techniques for use in ^{18}F-NaF murine studies	144
5.1	Introduction	144
5.1.1	^{18}F -NaF tracer kinetics in mice	145
5.1.2	^{18}F -NaF IDIF and TAC extraction	147
5.1.3	Use of recovery co-efficient method to provide PVC	149
5.2	Materials and Methods	151
5.2.1	Phantom scans used to calculate recovery co-efficients (RC)	151
5.2.2	Animal models	153
5.2.3	Sequential PET/MR imaging	153
5.2.4	IDIF and TAC extraction	154
5.2.5	Implementation of RC PVC method in IDIF extraction	156
5.2.6	Conversion of IDIFs from whole blood to plasma	157
5.2.7	Kinetic modelling	157
5.3	Results	158
5.3.1	NEMA phantom RC calibration	158
5.3.2	Influence of reconstruction algorithm and ROI location on IDIFs	160
5.3.3	Application of RC method for IDIF PVC	166
5.3.4	Kinetic modelling results (K_i values)	168
5.4	Discussion	170
5.4.1	IDIF accuracy compared to plasma samples	170
5.4.2	IDIFs derived from the VC ROI	172
5.4.3	Effect of IDIF on K_i parameter	172
5.4.4	Evaluation of RC PVC method	173

5.4.5	Improvements to experimental protocol	173
5.5	Conclusions	174
5.6	Chapter Summary	175
6	Automatic AIF detection using DSC MRI in rats	176
6.1	Introduction	176
6.1.1	Quantitative analysis of cerebral perfusion from MRI	176
6.1.2	Development of an automatic AIF selection method	177
6.1.3	Use of cerebral vasculature atlases for improved arterial voxel determination	178
6.2	Materials and Methods	178
6.2.1	Animal preparation	178
6.2.2	MRI imaging protocol	179
6.2.3	Construction of angiography atlas	181
6.2.4	AIF extraction using an automatic voxel selection algorithm	184
6.2.5	Addition of angiographic information to voxel selection algorithm	187
6.2.6	Gamma variate fitting to AIFs	188
6.2.7	Calculation of perfusion parameters	188
6.3	Results	190
6.3.1	Vasculature probability atlas	190
6.3.2	Comparison of AIFs computed using automatic and manual voxel selection	191
6.3.3	Perfusion parameter results - “Control” group	200
6.3.4	Perfusion parameter results - “Stroke” group	203
6.4	Discussion	206
6.4.1	Use of cerebral vasculature probability atlases in arterial voxel selection	206
6.4.2	Comparison of automatically and manually determined first pass AIFs	207
6.4.3	Perfusion parameter analysis	207
6.4.4	Improvements to voxel selection algorithm	209
6.5	Conclusions	210
6.6	Chapter summary	211
7	Comparison of AIFs derived from dual injections of Gd-based MRI contrast agent and ¹⁸F-FDG in rats	212
7.1	Introduction	213
7.1.1	Previous attempts to use dynamic MRI to estimate PET AIFs	214
7.1.2	Overview of experimental AIF conversion protocol	216
7.2	Materials and Methods	220

7.2.1	Animal preparation	220
7.2.2	MRI imaging and blood sampling, pre-injection	221
7.2.3	MRI imaging and blood sampling, post-injection	222
7.2.4	ICP-MS analysis of plasma to determine contrast agent concentrations	224
7.2.5	AIF extraction from dynamic MRI images	226
7.2.6	AIF conversion method testing	229
7.3	Results	231
7.3.1	^{18}F -FDG readings in blood and plasma samples	231
7.3.2	Repeatability of ICP-MS results for plasma samples	232
7.3.3	Comparison between gold standard ^{18}F -FDG and Gd-based contrast agent AIFs .	233
7.3.4	Scaling of DSC MRI data to create combined DSC and DCE MRI AIFs	238
7.3.5	Comparison between image-derived MR AIFs and Gd-based contrast agent AIFs	239
7.3.6	Conversion between MR image-derived AIFs, Gd-based contrast agent AIFs and ^{18}F -FDG AIFs	244
7.4	Discussion	268
7.4.1	Experimental challenges	268
7.4.2	Contrast agent concentration results from ICP-MS	270
7.4.3	Comparison with previously reported AIF conversion results	270
7.4.4	Evaluation of gamma variate AIF conversion and scaling method in first pass . .	273
7.5	Conclusions	275
7.6	Chapter summary	275
8	Direct evaluation of MR-based attenuation correction for mice	276
8.1	Introduction	276
8.2	Materials and Methods	279
8.2.1	Sequential PET/MR acquisition - <i>in vivo</i> imaging	279
8.2.2	Sequential PET/MR acquisition - phantom imaging	279
8.2.3	Reconstruction of images using different AC methods	280
8.2.4	SUV map calculation	283
8.3	Results	284
8.3.1	Phantom results	284
8.3.2	Mouse myocardial line profiles	286
8.3.3	ROI SUV comparison between AC methods <i>in vivo</i>	286
8.3.4	Whole-body SUV map comparison between AC methods	292
8.3.5	Cause of disparities between TXAC and other AC methods	296

8.4	Discussion	297
8.4.1	Evaluation of tested AC methods	297
8.4.2	Improvements to MRAC method	299
8.5	Conclusion	300
8.6	Chapter summary	300
9	Conclusions	301
9.1	Importance of partial volume correction in murine IDIF extraction	301
9.1.1	^{18}F -FDG	301
9.1.2	^{18}F -NaF	302
9.2	Relationship and conversion between PET tracer and MR contrast agent AIFs	303
9.3	Attenuation correction approaches for murine PET/MR	305
9.4	Further Work	306
A	Spilt magnet simultaneous PET/MR	308
B	Time of flight PET	311
C	Mathematics of MAP reconstruction	313
D	Segmentation-based MR attenuation correction techniques for PET	315
D.1	2 point DIXON	315
D.2	Ultra shot echo time (UTE) MR	316
E	Mathematics of singular value decomposition (SVD)	317
F	Dependence of GTM PVC method on ROI delineation in ^{18}F-FDG murine studies	320
F.1	Comparison of GTM IDIFs from “PET” or “MR” LVBP ROIs	321
F.2	Comparison of K_i values calculated using GTM IDIFs from “PET” or “MR” ROIs	322
G	Motion correction in ^{18}F-NaF murine studies	323
H	Additional TAC and IDIF parameter data from ^{18}F-NaF murine studies	324
I	DCE MRI	327
I.1	Validation of DCE MRI sequence <i>in vitro</i>	327
I.2	Relaxivity calculation	329
I.3	Arterial input function extraction for DCE MRI in small animals	330
I.4	Extraction of DCE MRI parameters from compartmental model	331

List of Abbreviations

- ^{18}F -FDG** - Fluorodeoxyglucose (^{18}F)
- ^{18}F FDG AIF** - Arterial Input Function derived from PET tracer plasma samples
- ^{18}F -NaF** - Sodium Fluoride (^{18}F)
- 3DRP** - Three-dimensional Reprojection
- AC** - Attenuation Correction
- AIF** - Arterial Input Function
- APD** - Avalanche Photodiode
- ApoE** - Apolipoprotein E
- ASL** - Arterial Spin Labelling
- AUC** - Area Under the Curve
- BAT** - Bolus Arrival Time
- BBB** - Blood Brain Barrier
- BOLD fMRI** - Blood-Oxygenation Level Dependent Functional Magnetic Resonance Imaging
- CASL** - Continuous Arterial Spin Labelling
- CBF** - Cerebral Blood Flow
- CBV** - Cerebral Blood Volume
- CSF** - Cerebrospinal Fluid
- CT** - Computerized Tomography
- CTAC** - Computerized Tomography-based Attenuation Correction
- DCE MRI** - Dynamic Contrast Enhanced Magnetic Resonance Imaging
- DPC** - Data Processing Cluster
- DSC MRI** - Dynamic Susceptibility Contrast Magnetic Resonance Imaging
- ECG** - Electrocardiogram
- EES** - Extracellular Extravascular Space
- EL-ICA** - Ensemble Learning Independent Component Analysis
- EM** - Expectation Maximization
- EPI** - Echo Planar Imaging
- FA** - Flip Angle
- FAIR** - Flow-sensitive Alternating Inversion Recovery
- FBP** - Filtered Backprojection
- FID** - Free Induction Decay
- FISP** - Fast Imaging with Steady-state Precession
- FLASH** - Fast Low Angle SHot

fMRI - Functional Magnetic Resonance Imaging

FOV - Field of View

FWHM - Full Width Half Maximum

Gd AIF - Arterial Input Function derived from MR contrast agent plasma samples

Gd-DTPA - Gadopentetic Acid

GE - Gradient Echo

GE-EPI - Gradient Echo-based Echo Planar Imaging

GM - Grey Matter

GTM - Geometric Transfer Matrix

HDPE - High Density Polyethylene

ICP-MS - Inductively Coupled Plasma Mass Spectrometry

IDIF - Image-Derived Input Function

LGE MRI - Late Gadolinium Enhancement Magnetic Resonance Imaging

LOR - Line Of Response

LSO - Lutetium Oxyorthosilicate

LVBP - Left Ventricular Blood Pool

MAP - Maximum A Posteriori

MAP TR - Maximum A Posteriori reconstruction for Transmission scan data

MCA - Middle Cerebral Artery

MGE - Multi Gradient Echo

ML - Maximum Likelihood

MMRGlc - Myocardial Metabolic Rate of Glucose

MOBY - 4D Mouse Whole Body Phantom

MR - Magnetic Resonance

MR AIF - Arterial Input Function derived from MR images

MRA - Magnetic Resonance Angiography

MRAC - Magnetic Resonance-based Attenuation Correction

MRI - Magnetic Resonance Imaging

MTT - Mean Transit Time

NEMA - National Electrical Manufacturers Association

NEX - Number of Excitations

NMR - Nuclear Magnetic Resonance

OSEM - Ordered Subsets Expectation Maximization

PASL - Pulsed Arterial Spin Labelling

PET - Positron Emission Tomography

PET AIF - Arterial Input Function derived from PET images
PET/CT - Combined Positron Emission Tomography and Computerized Tomography
PET/MR - Combined Positron Emission Tomography and Magnetic Resonance Imaging
PMMA - Poly(methyl methacrylate) plastic
PMT - Photomultiplier Tube
PSF - Point Spread Function
PVC - Partial Volume Correction
PVE - Partial Volume Effect
RARE - Rapid Acquisition with Relaxation Enhancement
RC - Recovery Co-efficient
RF - Radiofrequency
RMSD - Root Mean Square Deviation
ROI - Region Of Interest
RSF - Regional Spread Function
SE - Spin Echo
SHR - Spontaneously Hypertensive Rat
SNR - Signal to Noise Ratio
SPM - Statistical Parametric Mapping
SUV - Standardized Uptake Value
SVD - Singular Value Decomposition
TAC - Time Activity Curve
TE - Echo Time
TI - Inversion Time
TMRGlc - Tumour Metabolic Rate of Glucose
TOF - Time Of Flight
TOF-MRA - Time Of Flight Magnetic Resonance Angiography
TR - Repetition Time
TRX - Transmission Scan
TTP - Time To Peak
TXAC - Transmission-based Attenuation Correction
VC - Vena Cava
VFA - Variable Flip Angle
VOR - Volume Of Response
WM - White Matter

Chapter 1

Introduction

1.1 Motivation behind PET/MR scanning

The goal of combining functional and structural imaging information has given rise to the field of multimodality imaging. Positron Emission Tomography (PET) is an extremely sensitive and specific molecular imaging technique, but suffers from limited spatial resolution. PET therefore benefits from co-registered anatomical information to assist in localizing radiotracer distributions *in vivo*. This has driven the rapid assimilation of combined PET and Computed Tomography (PET/CT) into mainstream medicine [1], [2].

PET/CT scanners comprise a PET scanner in tandem with a multislice spiral CT scanner which provides attenuation maps of X-ray photons through patients. Each modality operates physically independent of the other, with the data linked via image registration algorithms. Due to the advantages of combining functional and structural imaging in oncologic diagnosis and treatment monitoring [1], since late 2006 PET/CT scanner sales have completely replaced those of PET scanners in the US [2].

The main advantage of dual modality scanners lies in the improved image registration and decreased time taken compared to separate scans, which leads to better treatment planning with reduced risk of misdiagnosis [1]. Structural imaging provided by Magnetic Resonance Imaging (MRI) has proved an excellent diagnostic tool for detecting pathological changes using high resolution images with exquisite soft tissue contrast provided by non-ionising radiation. Altered function, however, often precedes structural change [3] and therefore the functional information which PET provides can be an excellent complement to morphological MRI data. Combined PET and MRI (PET/MR) imaging retains the benefits of combining high resolution anatomical information with quantitative molecular imaging, as championed by PET/CT, and also possesses additional desirable qualities [4]. It is hoped that PET/MR may thus be harnessed in preclinical imaging to gain new insights into the mechanics of disease.

The main advantages of PET/MR compared to PET/CT in preclinical imaging are summarized below:

- MRI provides high resolution anatomical information with excellent soft tissue contrast, which can also be tailored for specific applications by adjusting the weighting of the MR imaging sequence or by injecting an MR contrast agent [5], [6], [7], [8].
- MRI images can be produced in any orientation using orthogonal gradient fields and retain similar (sub-millimetre) resolution to CT [7].
- MRI has many functional imaging sequences available including: Blood oxygen level dependent functional MRI (BOLD fMRI) to assess blood flow changes in line with brain activation, diffusion MRI to assess *in vivo* water diffusion and MR spectroscopy to assess metabolite changes [4], [9], [10], [11].
- MRI uses non-ionizing radiation, which is preferable to CT in pediatric and longitudinal studies where multiple imaging scans are required¹ [2], [9], [11]. Preclinical CT studies also require a large radiation dose to provide good spatial resolution and therefore, except in the cases of bone and lung imaging, PET/MR would be preferred over PET/CT [4], [12], [13].
- MRI can be conducted simultaneously with PET in a specially designed combined scanner, thus reducing costs and increasing subject throughput. This also ensures the datasets are co-registered both spatially and temporally, reducing motion errors [4]. Due to the inherently sequential nature of PET/CT acquisition, if the subject orientation changes due to involuntary movements in areas such as the abdomen there are no sufficiently identifiable “landmarks” for optimal image-based registration, leading to reduced accuracy of tracer activity quantification [5], [10].
- Truly simultaneous imaging also ensures that the subject remains in the same physiological state in both examinations. This is highly desirable in studies where changes in BOLD signal and metabolic rates with time may be significant [14], [15].

1.2 Small animal PET/MR scanner design

There are two variations of preclinical PET/MR scanner design, enabling either sequential or simultaneous PET/MR acquisition. The contrast in approaches is shown in Figure 1.1. Sequential systems can comprise either two separate scanners within close proximity with compatible animal beds, such as a PET scanner and a benchtop 1T MRI scanner [16] or can be both contained within the same dual modality scanner, with overlapping Fields of View (FOVs) [17].

¹For a typical 70kg human, a whole body CT results in a $\approx 8\text{mSv}$ effective dose. The average annual dose is 2.4mSv .

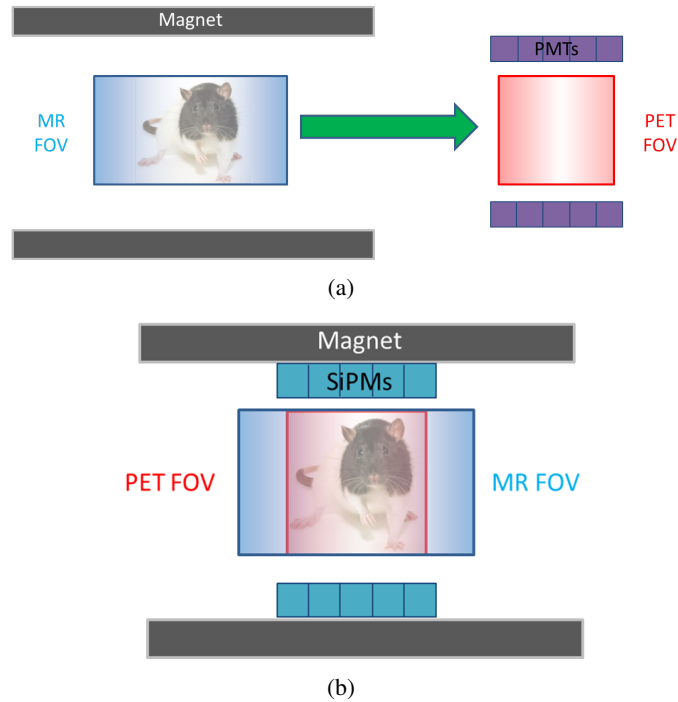


Figure 1.1: Approaches to PET/MR scanner design: (a) Sequential PET and MR acquisition, (b) Simultaneous PET/MR acquisition. PMTs = Photomultiplier tubes, traditional PET detectors based on a cathode/anode ray tube. SiPMs = Silicon photomultipliers, solid state PET detectors which can operate in a high magnetic field with similar performance to PMTs. Adapted from [18].

The vast majority of simultaneous small animal PET/MR scanner designs use a PET ring insert which is placed into the MR FOV. As the high magnetic field required to perform MRI interferes with traditional photomultiplier tube (PMT) PET detectors, the PMT detectors within the PET ring insert are replaced with avalanche photodiodes (APDs) [9], [13], [19], [20], [21], [22]. APDs are solid state photodetectors, in which electron hole pairs are created when photons are absorbed. A high reverse bias voltage is applied to the p-n junction of the APD, creating a strong internal electric field which accelerates the electrons through the semiconductor and produces an avalanche of secondary electrons by impact ionization. APDs are hence able to function in the high magnetic fields required for MRI as the path travelled by the electrons is very short. The drawback of APDs is that at typical operating voltages they produce an internal gain between 100-1000, compared to the PMT gain of 10^6 [12] and this gain is very susceptible to changes in temperature ($>3\%/C^\circ$) and voltage ($>10\%V^{-1}$) [23]. In more recent simultaneous PET/MR scanner designs, APDs have been superseded by silicon photomultipliers (SiPMs) [12], [20], [23], [24]. SiPMs are each composed of an array of micro-cell APDs working in Geiger mode². This allows SiPMs to create a larger gain than APDs, similar in magnitude to that produced by traditional PMTs [23].

²Geiger mode is reached when operating at a reverse bias voltage well above the breakdown voltage. This produces a very large signal, although it is no longer proportional to the energy deposited by the incident photon. As long as the number of incident photons is less than the total number of cells, the summed output from all cells is proportional to the energy deposited in the scintillator.

The Wolfson Brain Imaging Centre at the University of Cambridge, however, has developed an alternative solution - a 1T split magnet small animal simultaneous PET/MR scanner design [25], shown in Figure 1.2. This design utilizes a Focus 120 MicroPET scanner placed halfway along the MRI bore, with light guides used to convey scintillation signals in a radial direction to PMT-based detectors located in the fringe field of the magnet [26]. The scanner performance and design details can be found in Appendix A.

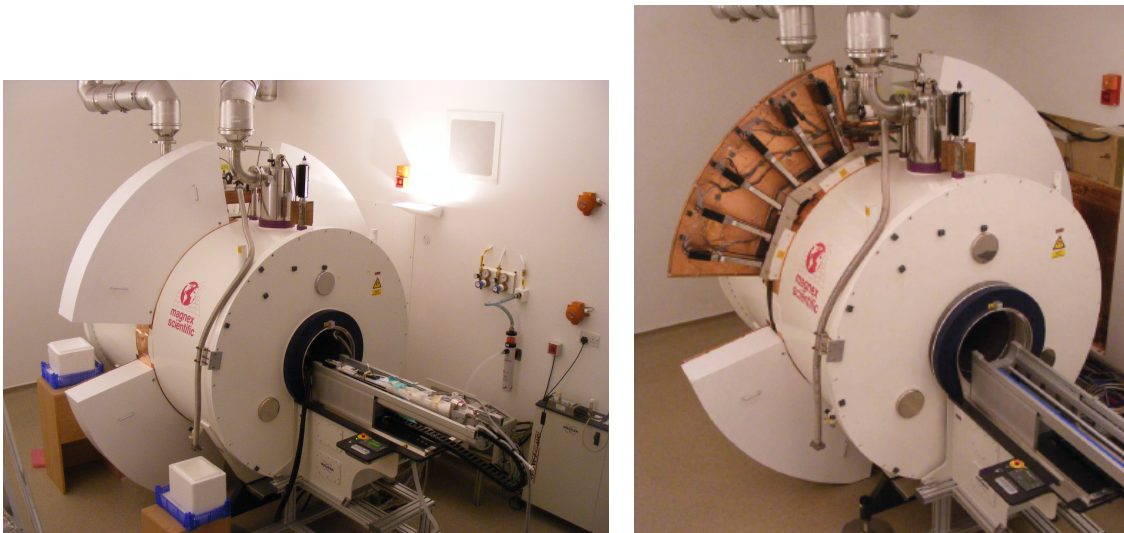


Figure 1.2: Preclinical 1T split magnet simultaneous PET/MR scanner. (a) Fully shielded and (b) PMT modules and light guides visible when Faraday screen removed.

Although the scanner was designed to perform simultaneous PET/MR imaging, the gradient coils required for MR imaging were broken during the first few months of this PhD project. As a consequence, all results reported in this thesis use sequentially acquired MR and PET data which were taken during the same imaging session. A separate MR scanner (4.7T, Bruker 47/40 model) in an adjacent room, in conjunction with a mutually compatible animal bed, was employed to provide the complementary MR for the PET images produced using the Focus 120 MicroPET scanner within the split magnet design.

Sample cardiac images taken using the Cambridge split magnet scanner using the PET tracer ^{18}F -Fluorodeoxyglucose (^{18}F -FDG) are shown in Figure 1.3 to illustrate the enhancement of PET functional information with spatial localization provided by MR.

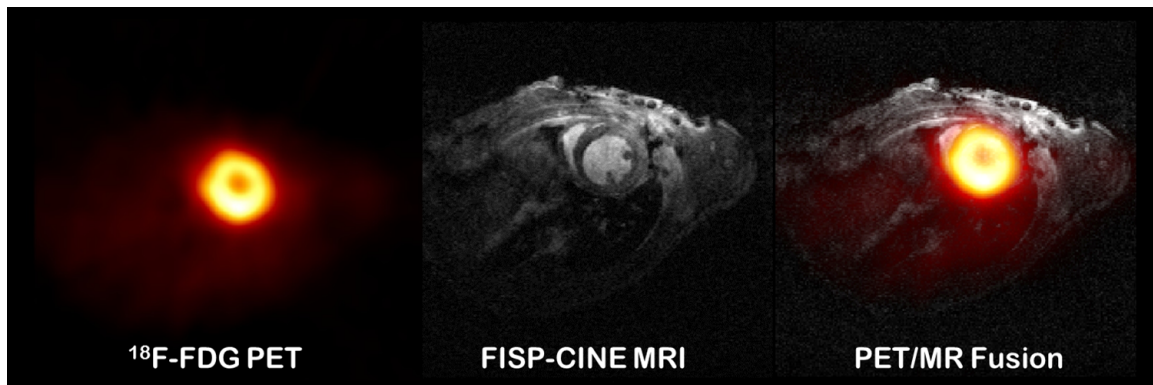


Figure 1.3: PET and MR images from mouse heart region in diastole, transverse view. Images were co-registered using the SPMMouse toolbox [27]. (Left) ^{18}F -FDG PET, (Centre) FISP MRI, (Right) Overlay of PET and MR images, localising tracer uptake to myocardium.

1.3 Applications for small animal PET/MR

Mice and rats are often the model of choice in preclinical imaging studies due to their low cost and the wide availability of a large range of transgenic and interventional disease models. Compared to conventional, invasive techniques such as dissection, small animal PET provides a 3D model of radiopharmaceutical distribution non-invasively. This allows for both earlier detection of disease through functional change, treatment evaluation and a more fundamental understanding of the exact molecular processes at work in disease [28].

PET can be used to analyze a range of disease models, such as evaluating myocardial infarction [29], [30] or the effect of radiotherapy/chemotherapy on a tumour type [31], [32]. Additionally radioactive PET tracers can be tracked dynamically over the course of the scan to provide pharmacokinetic data [33], [34], [35], [36], [37], to assess drug performance [28], [38], or to quantify binding to specific receptors [32], [39], [40]. Each of these applications can be repeated as part of a longitudinal study, giving insights into the disease progression at multiple time points [32], [41], [42].

With the advent of PET/MR, the wide variety of PET tracers available means that specific molecular targets can be identified and this information complemented with a range of high-resolution structural and functional MR techniques. Small animal PET/MR imaging has already been used to great effect in the fields of oncology [4], [16], [19], [43], cardiology [15], [44], [45], neurology [4], [42], [46], [47] and even infectious disease [15]. Figure 1.4 shows the benefits of small animal PET/MR in action, with Figure 1.4 illustrating its superiority in identifying tumour heterogeneity over PET/CT in preclinical oncological studies.

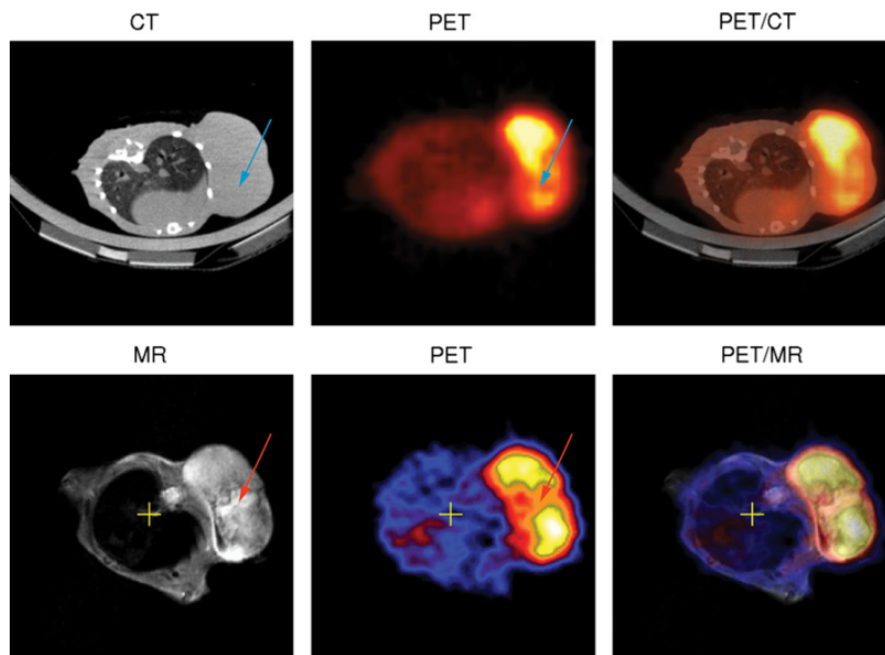


Figure 1.4: 2 BALB/c mice bearing CT26 tumour, images reproduced with permission from [12]. In PET/CT (top row) the tumour appears homogeneous (blue arrow), whereas T2-weighted MRI (bottom row) shows the inhomogeneous nature of the tumour, coinciding with an area of low PET tracer uptake.

The ability of preclinical PET/MR to highlight tumour heterogeneity has been expanded further in recent years through comparison of ^{11}C -choline uptake and MR spectroscopy in mice [48] or through the use of parametric MRI maps calculated from DCE MRI overlaid on PET uptake images to gain further insight into the tumour microenvironment [46]. Cross validation studies between PET and MRI techniques for perfusion [42], [49], and the analysis of functional brain networks [14] have also been performed using simultaneous preclinical PET/MR. As the data was spatially and temporally co-registered, mismatches discovered between PET and fMRI perfusion techniques could then be used to develop a fuller understanding of the specific physiological mechanisms measured by each technique [15], [49]. Finally, comparisons between β amyloid deposition derived from ^{11}C -PIB PET and cerebral blood flow determined using arterial spin labelling MR in a mouse model of Alzheimer's disease [42] have provided further evidence of the power of combining complementary preclinical PET and MR functional information together in specific neurological disease models, rather than simply using the MR information as an anatomical landmark for PET.

1.4 Improving parameter quantification in small animal PET/MR

To gain a deeper insight into physiological processes *in vivo*, attention has shifted towards quantification of physiological parameter maps rather than qualitative imaging over the last decade in small animal PET [41]. For preclinical PET/MR, the goal is to provide not only PET parametric data, but multi-parametric datasets comprising complementary PET and MRI physiological information to provide an even deeper understanding of pathologies than can be achieved using either technique alone [15], [46]. The aim of this thesis was to assess how MRI could be used to improve PET parameter quantification for future small animal PET/MR studies.

In order to produce quantitative estimates of PET tracer kinetic parameters, compartmental models must be applied to dynamic PET data and each kinetic model requires knowledge of the arterial input function (AIF), which defines the tracer concentration in arterial blood plasma over time. The gold standard for AIF evaluation is serial blood sampling over the course of the scan. The plasma from each arterial blood sample is extracted and then its tracer activity concentration measured using a well counter, providing readings at well-defined intervals to characterise the AIF curve. This procedure is highly invasive and difficult to perform preclinically due to the small spatial dimensions and fragile nature of rodent arteries [50], particularly in mice due to their low total blood volumes [28]. Non-invasive methods are therefore highly desirable, and two approaches which employ MR information to assist in the PET AIF extraction process are explored over the course of this thesis.

The first approach used high resolution structural MR images to provide anatomical priors to assist in ROI delineation and in image-based input function (IDIF) determination. IDIFs use PET activity concentration readings extracted from arterial regions of interest (ROIs) to approximate the AIF, but are complicated by the small size of the rodent arteries. Due to the limited spatial resolution of PET, the arterial concentration measurements taken from PET images deviate from their true value as a consequence of partial volume effects (PVE) and spillover from tissue regions into arterial ROIs [29], [33], [37], [41], [51], [52], [53]. MR-based techniques which provide corrections for PVE and spillover effects were tested in this thesis to see if they could improve IDIFs and hence refine kinetic parameter estimates in murine sequential PET/MR.

The second approach tested the hypothesis that dynamic MR images could be used to provide non-invasive AIF estimates if a combined bolus of MR contrast agent and PET tracer was administered [54]. In this application, the MR AIF (i.e. the MR contrast agent concentration in arterial plasma over time) is used to estimate the PET AIF for kinetic analysis. The validity of PET AIFs produced using this approach was assessed to ascertain if this hypothesis was true and to establish how the AIF conversion process between modalities could be performed.

1.5 Thesis structure

An introduction to preclinical PET/MR imaging has been presented in this Chapter, whilst the next Chapter comprises an introduction to PET and MR physics. Chapter 3 provides an overview of the mathematical methods and models used in the quantification of dynamic PET and MRI data.

The first aim of this thesis was to establish if sequentially acquired static MR images could improve PET IDIF determination in mice by providing partial volume correction (PVC). Chapter 4 explores how MR-based IDIF extraction methods performed compared to those which used PET data alone on a ^{18}F -FDG mouse PET/MR dataset. In addition, as the vena cava (VC) ROI is easily identified on MR images, its use in place of the left ventricular blood pool (LVBP) ROI for IDIF extraction was investigated to see if it could offer a viable alternative. It was hypothesized that as the cardiac output of mice is high, arterial and venous tracer concentrations may equilibrate very quickly and therefore the VC may produce IDIFs which were less susceptible to spillover and motion effects than the LVBP. Chapter 5 further evaluates MR and PET-based IDIF extraction methods, in both the LVBP and VC ROIs, by comparing their respective IDIFs against plasma sample readings, which were provided as part of a ^{18}F -NaF mouse dynamic PET dataset.

The second aim of this thesis was to ascertain if an MR AIF (measured using dynamic MR) could be used as a non-invasive estimate of the PET AIF. The development of an automated DSC MRI analysis method to produce consistent estimates of first pass bolus MR AIFs from the rat brain is outlined in Chapter 6. Chapter 7 assesses the relation between measured AIFs for ^{18}F -FDG and the MRI contrast agent Gadovist when these compounds are injected together as a single, combined bolus into a rat. The automated AIF detection method of Chapter 6 is used in Chapter 7 to extract MR AIFs from DSC and DCE MRI images for comparison to gold standard PET tracer and Gd-based contrast agent AIFs measured via blood sampling. Two different MR to PET AIF conversion methods are also tested in Chapter 7, the first to assess the validity of the bi-exponential conversion method proposed by Poulin et al. [54] and the second, a novel method based on the conversion of gamma variate functions which describe the first pass of the MR and PET AIFs in the brain.

Finally, Chapter 8 outlines the testing of an MR-based segmentation approach to attenuation correction (AC), which is compared to gold standard transmission scanning using the Cambridge split magnet PET/MR design. This was done as image quantification is vital to performing accurate kinetic modelling in small animal PET/MR, but due to the small size of PET/MR scanner bores, traditional methods of AC are unavailable and alternative AC methods must be considered.

The conclusions of this thesis are detailed in Chapter 9, which also explores avenues for future work in the area of preclinical PET quantification.

Chapter 2

Background theory to PET and MR imaging

This Chapter provides an overview of the physics and hardware which drive the imaging modalities of PET and MR, including the PET reconstruction algorithms and MR pulse sequences used in this thesis.

2.1 PET scanning

PET scanning provides uptake readings of radiolabelled, biologically significant molecular compounds, known as tracers. The radioactive isotopes are produced in a cyclotron by nuclear reaction and then incorporated into physiological molecules of interest. The radioactive part of the tracer undergoes β^+ decay, emitting positrons in proportion to the amount of tracer at the location, shown in Figure 2.1.

The most commonly used PET tracer, fluorodeoxyglucose (^{18}F -FDG), is a glucose analogue in which the hydroxyl group on the 2-carbon of glucose is replaced by fluoride. ^{18}F -FDG can therefore be taken up by cells and phosphorylated but the next step in glucose metabolism is prevented and the tracer will remain in the cell until it decays. This results in the study of tissues with high glucose metabolism and is therefore useful in staging cancers, due to their increased rate of glucose consumption compared to healthy tissue [3].

2.1.1 Positron emission and annihilation

The process of β^+ decay requires the binding energy difference between the mother and daughter nucleus to convert a proton (p^+) to a neutron (n), giving off a positron (e^+) and a neutrino (ν_e) in the process, shown in Figure 2.1.

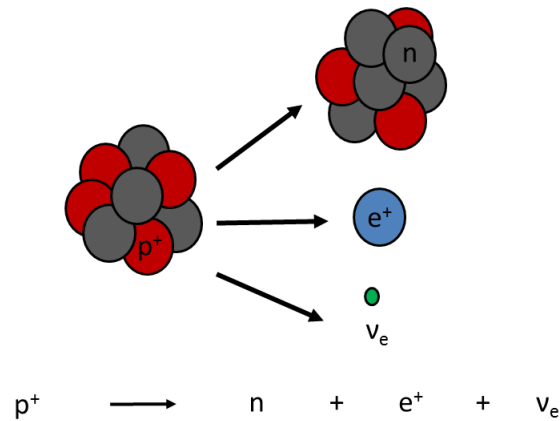


Figure 2.1: Diagram of β^+ decay, harnessed in PET tracers.

The positrons travel a finite distance and then annihilate on contact with electrons, releasing energy equivalent to the rest mass of the particles by conservation of energy, expressed mathematically in equation (2.1). This is emitted in the form of two simultaneous 511keV gamma photon emissions per annihilation at $180 \pm 0.25^\circ$ to each other by conservation of momentum, along a Line Of Response (LOR) as seen in Figure 2.2. These gamma rays are detected via a ring of scintillating crystal detectors and are used to analyse the tracer distribution within the patient.



The deviation from collinearity seen in Figure 2.2 occurs as positrons are emitted with non-zero kinetic energy and are slowed down in tissue by Coulomb interactions until they reach thermal equilibrium, travelling a typical range of 1–2mm in tissue, depending on the isotope used [20], [55]. Thus annihilation does not occur at rest, resulting in a small angular deviation which (combined with the positron range) limits the best possible PET spatial resolution to ~ 1 mm Full Width Half Maximum (FWHM) [20], [55].

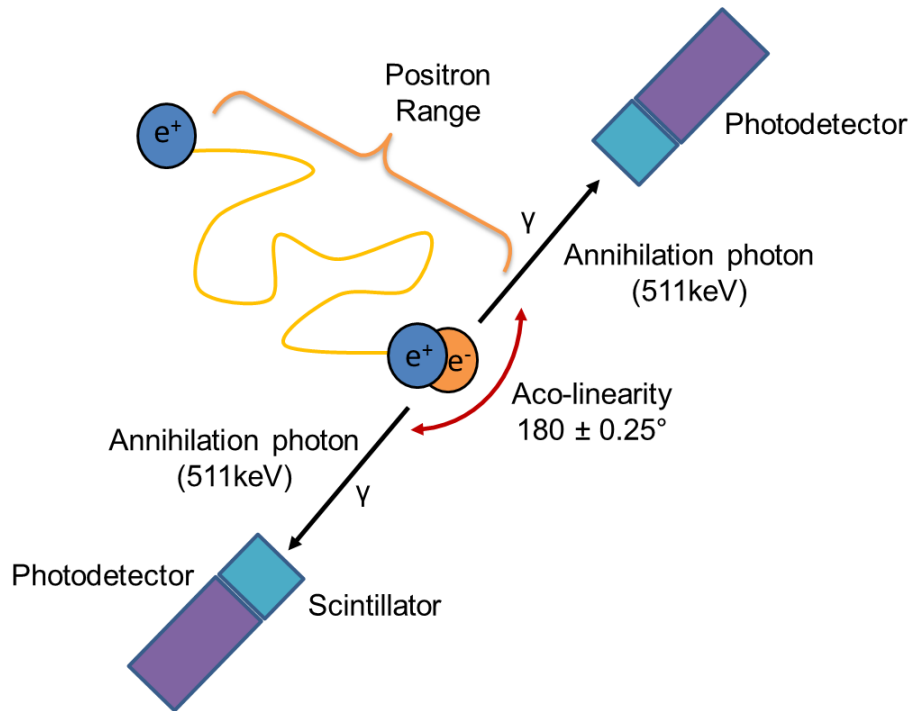


Figure 2.2: Positron emission and annihilation photon coincidence detection in PET. Adapted from [56].

2.1.2 Count detection

A PET scanner is composed of multiple cylindrical detector rings, with the greatest sensitivity at the centre of the FOV, where angular coverage is greatest. Incident gamma rays impact on inorganic scintillator crystals such as lutetium oxyorthosilicate (LSO) and their energy is converted into a characteristic wavelength photon shower (e.g. 420nm for LSO). Scintillators are chosen for their high light yields, large stopping power and short decay times, such that as many events are detected as possible. The re-emitted visible light is relayed via light guides and converted into an electrical signal by a photodetector, typically a photomultiplier tube (PMT), shown in Figure 2.3. PMTs consist of glass vacuum tubes with an exposed photocathode at one end and an anode with output pins at the other. Light passes through the input window and excites the photocathode, releasing photoelectrons which are accelerated towards the first dynode by the focusing electrode, and are multiplied via secondary electron emission. The subsequent dynodes are kept at increasingly higher potentials to repeat the process until the electrons reach the anode, creating fast electronic signals with a typical gain of $\sim 10^6$ and a rise time of several nanoseconds.

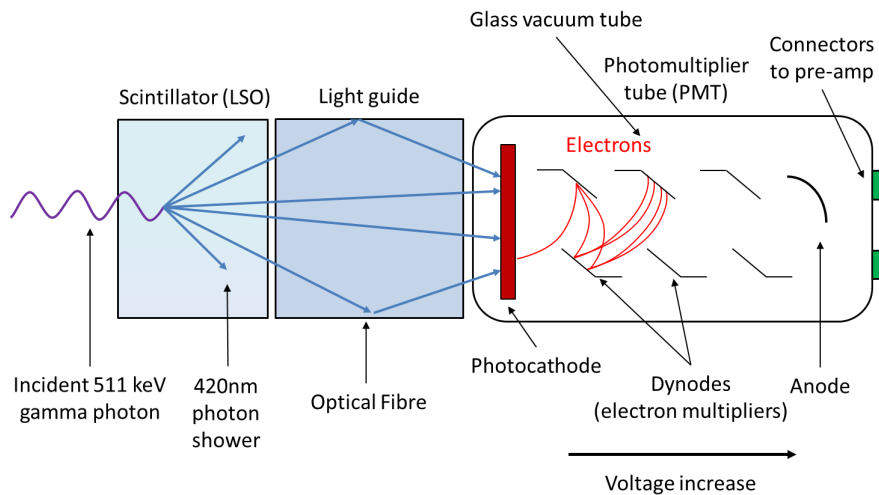


Figure 2.3: PET detector schematic showing scintillator, light guide and photomultiplier tube, with event triggering electron cascade.

Each scintillation photon shower is shared among multiple position sensitive PMTs which employ centroiding algorithms and Anger Logic to determine the origin of the shower and thus construct the LOR with its partner detector. PMTs are disrupted when high magnetic fields are applied, as strong magnetic fields deflect the electrons' path between the dynodes and end the electron cascade [12], [21], [24]. The split magnet PET/MR scanner used in this thesis therefore places its PMTs outside the 10 Gauss¹ level of the magnetic field, at which the deflections become significant [25]. This produces comparable performance to a Focus 120 PET scanner [26]. The full parameters of the split magnet design are contained in Appendix A.

2.1.3 Types of events

Detectors register a true, coincidence event (and record an LOR) when two gamma rays from an annihilation event are detected by two diametrically opposite detectors within a suitable time window, usually 6–10ns [20], depicted in Figure 2.4. This depends on the length of the coincidence window (τ), the timing resolution of the detectors, the pulse processing time of the electronics and the different transit times for each photon of the pair. Each LOR assumes a positron event occurred at some point along its length and incorrect assignment of LORs reduces the contrast present within the image. The volume of response (VOR) describes the 3D region between the two detectors in which the positron annihilation event must have occurred and is illustrated in Figure 2.5. The three types of recorded coincidence events in PET scanning are true events, scattered events and random events. These are depicted in Figure 2.6.

¹1T is equivalent to 10 000 Gauss.

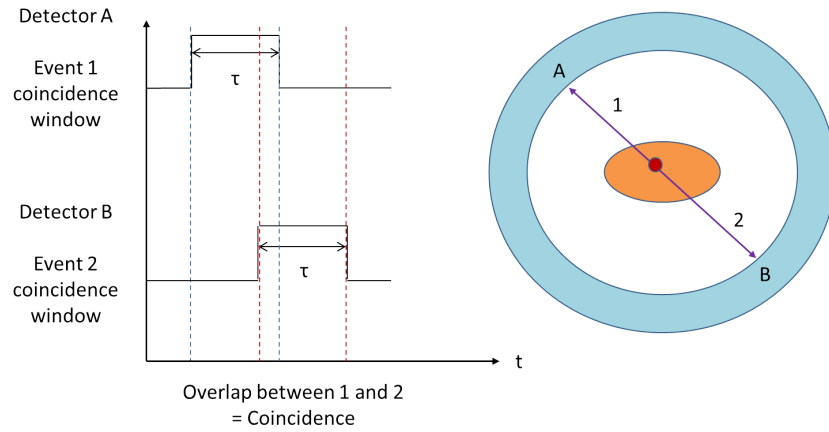


Figure 2.4: Events 1 and 2 are detected at A and B on the detector ring, creating time stamped electrical signals. The trigger pulse from event 1 marks the start of the first coincidence time window (duration τ) and event 2 generates the second coincidence window. LOR is recorded by the coincidence circuitry if both coincidence windows overlap, as shown by the overlapping blue and red lines.

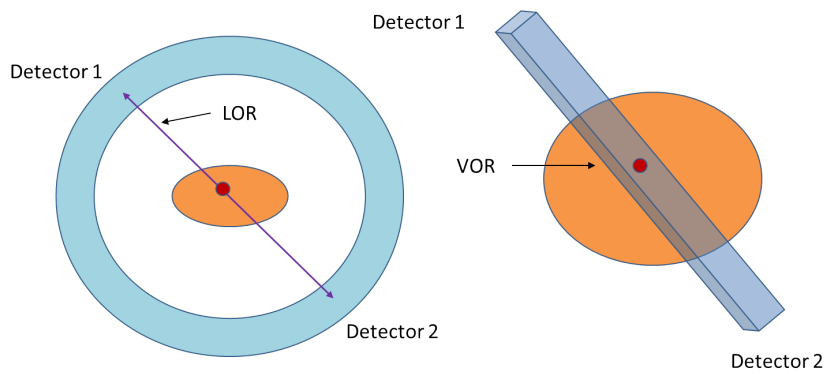


Figure 2.5: LOR and VOR definition. Adapted from [57].

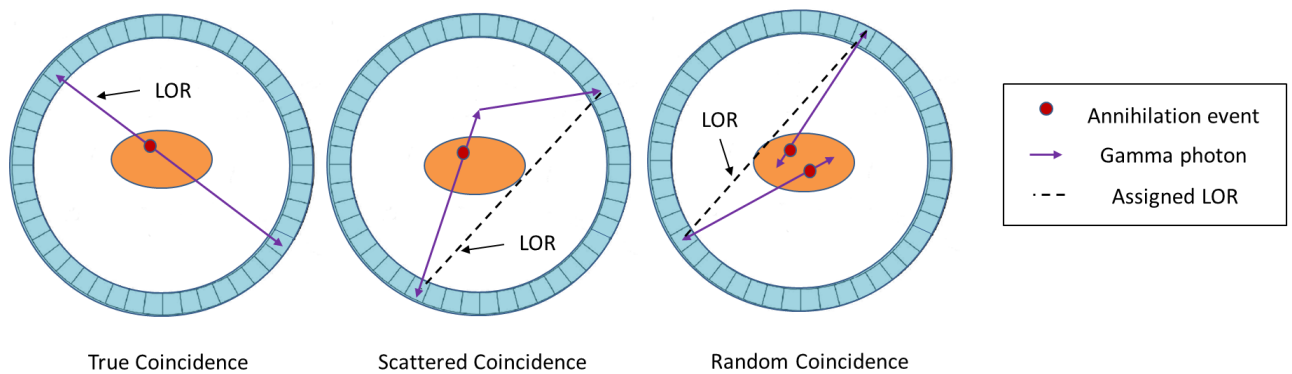


Figure 2.6: Different LORs generated by true counts, scattered counts and random counts.

- **True events** - Both photons are recorded with appropriate energies at opposite detectors within the coincidence time window. The number of true counts will increase linearly with the activity of the source, making PET an intrinsically quantitative molecular imaging technique.

- **Scatter events** - Compton scattering is dominant in PET and occurs when a gamma ray collides inelastically with a loosely bound orbital electron, ejecting the electron and altering the energy and trajectory of the incident photon. At least one photon of the gamma photon pair is removed from its original LOR trajectory and is assigned an incorrect LOR.
- **Random events** - Two uncorrelated gammas are detected within the coincidence time window, recording an incorrect LOR. This often occurs if photons experience significant interaction with materials in the FOV and one photon from the pair is attenuated.

In the absence of photon attenuation, scatter, randoms, detector efficiency variations and count-rate dependent effects, the total number of coincidences registered by the scanner will be proportional to the amount of tracer contained in the VOR. As scattering reduces the energy of incident photons, the scatter effect is minimised via an energy threshold window around the 511keV photopeak, ensuring only events within a suitable energy range (typically 350–650keV) are counted, as illustrated in Figure 2.7. A reduction in random counts can be achieved by using a shorter coincidence timing window (i.e. shortening the duration τ in Figure 2.4), with further reductions possible by using detectors with greater timing resolution and scintillators with faster decay times. In systems with fast enough timing resolution, the time of flight (TOF) reconstruction technique can be employed, as illustrated in Appendix B.

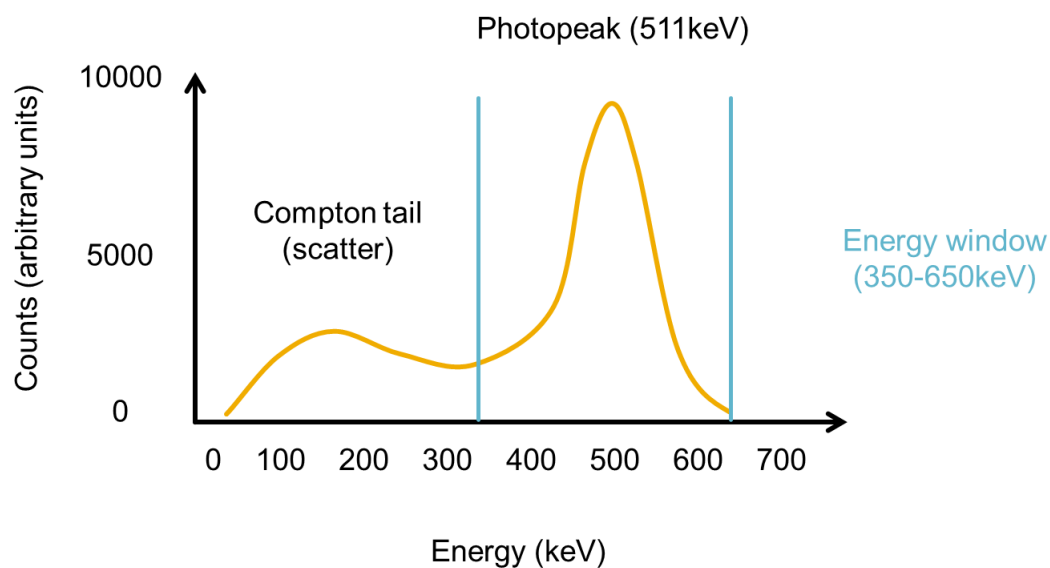


Figure 2.7: Photopeak of events indicating the range of energies detected in typical PET scan. Energy window (350-650keV) applied to discriminate against scattered counts.

2.1.4 Basic PET image reconstruction

The goal of PET image reconstruction is to recover the distribution and concentration of the radio-tracer within the subject. Ideally this should produce a 3D image composed of voxels whose values are

indicative of the source intensity at each of these points. A 3D PET image is reconstructed from projections of millions of LORs recorded over the duration of a PET scan. PET reconstruction can be described using the line integral model of acquisition, such that a projection is formed from integration along all parallel LORs at an angle ϕ [57]. Each LOR is binned according to its angle of orientation (ϕ) and the minimum distance between the LOR and the centre of the gantry (s). These projections are collected for $0 \leq \phi \leq 2\pi$ into a 2D sinogram in the (s, ϕ) co-ordinate system [58], shown in Figure 2.8. A single point in an object $f(x, y)$ traces out a sinusoid in the sinogram and the superposition of all sinusoids from each point of activity in the object will give the total sinogram for the object. The line integral transform of $f(x, y)$ to $p(s, \phi)$ can be described in 2D as a Radon transform, given in equation (2.2):

$$p(s, \phi) = \mathcal{R}(f(x, y)) = \int_{-\infty}^{\infty} f(s \cos \phi - l \sin \phi, s \sin \phi + l \cos \phi) dl \quad (2.2)$$

where l , the integration variable, is the co-ordinate along the line [58]. For a fixed angle $\phi = \phi_0$, the set of parallel line integrals $p(s, \phi_0)$ is a 1D parallel projection of $f(x, y)$.

The sinogram therefore contains 1D projection data from all possible projections from the detectors in the scanner. This process is repeated for multiple axial slices in the z direction. When the sinogram for each slice is reconstructed, the image planes are stacked together to form a 3D image of patient metabolic activity, with example sinograms shown in Figure 2.9.

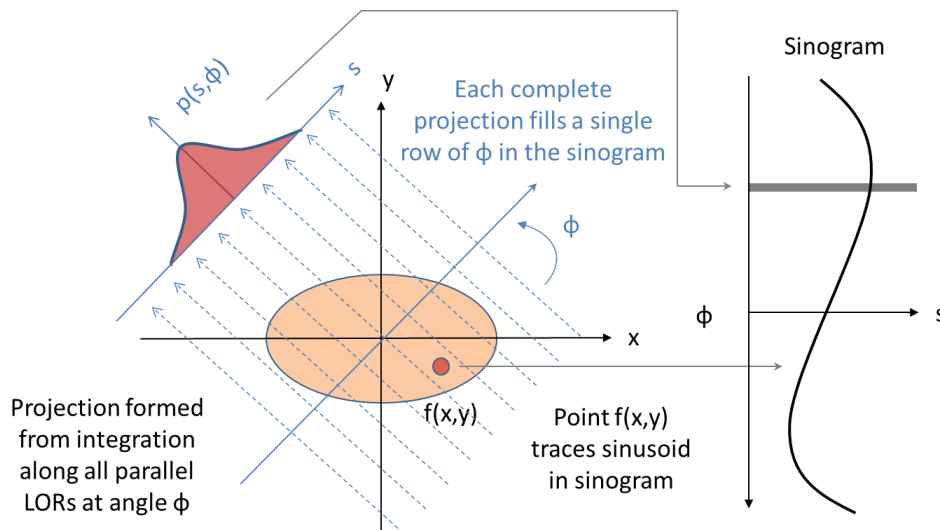


Figure 2.8: Creation of PET sinogram using projection $p(s, \phi)$, formed from integration of LORs at an angle of constant ϕ . Adapted from [57].

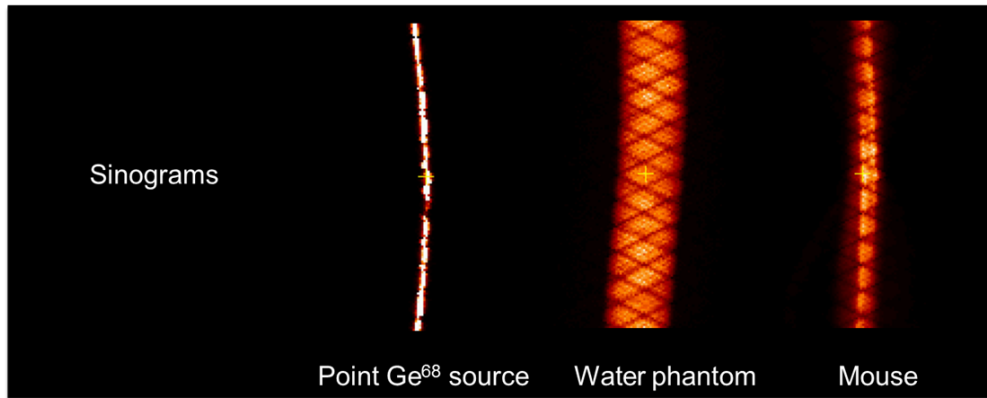


Figure 2.9: Example sinograms. The point source (left) traces out a sinusoid for a single point, whilst the cylindrical water phantom (centre) and mouse (right) sinograms show a wider distribution due to the different line integrals acquired at each projection angle. The water phantom also shows a more uniform sinogram compared to the mouse.

The PET imaging system can be modelled using equation (2.3) [57],

$$\mathbf{p} = \mathbf{H} \mathbf{f} + \mathbf{n} \quad (2.3)$$

where \mathbf{p} is the set of observations, \mathbf{H} is the known system model, \mathbf{f} is the unknown object and \mathbf{n} is the error in the observations. The purpose of image reconstruction is to find \mathbf{f} from the data \mathbf{p} , which are projections through the object. If the data is assumed to be deterministic, \mathbf{n} is a deterministic number and if known, an analytical solution for the image of \mathbf{f} can be found. An exact image solution is therefore possible if we disregard (or know) the noise term and an analytical reconstruction technique is used. An inverse of the Radon transform can be applied, giving an exact, mathematical solution for \mathbf{f} from the projections \mathbf{p} . This is attractive as analytical reconstruction methods give a simple, fast and direct solution with fairly predictable behaviour, although if the noise structure of the observations is disregarded, this can lead to images with reduced resolution and streak artefacts [57].

Central Slice Theorem

Analytical PET image reconstruction utilises the central slice theorem. This is shown schematically in Figure 2.10. It states that the Fourier transform of a 1D projection through the object f is equivalent to a profile at the same angle through the centre of the 2D Fourier transform of the object [59]. Therefore if we take $P(v_s, \phi)$ as the 1D Fourier transform of the projection $p(s, \phi)$ in the s dimension and know $P(v_s, \phi)$ in the range $0 \leq \phi \leq \pi$ then we also know $F(v_x, v_y)$, which is the 2D Fourier transform of the image in x and y . This can also be extended to three dimensions, using 2D parallel projections which correspond to a central section through the 3D Fourier transform of the object [60], [58].

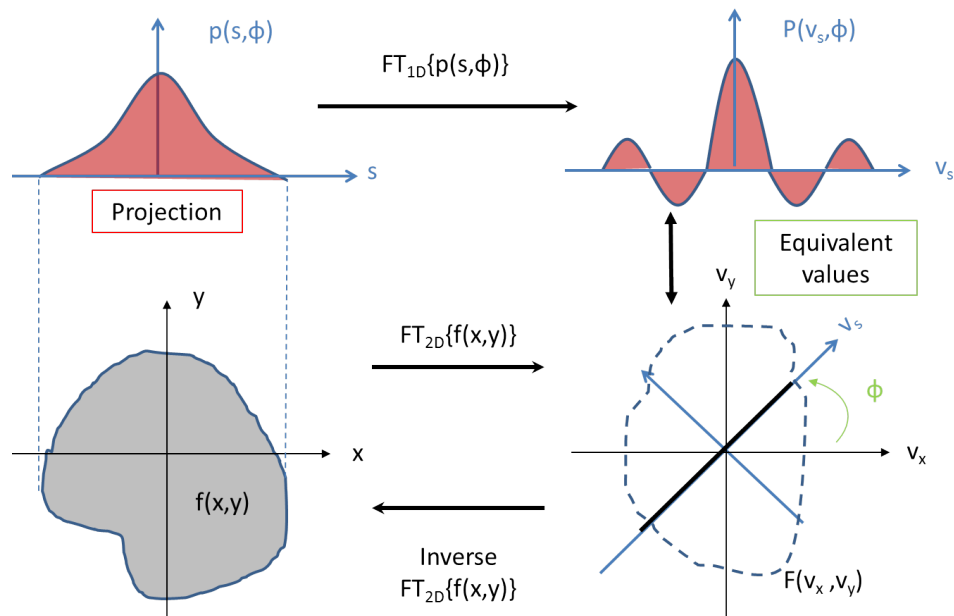


Figure 2.10: The central slice theorem states that the Fourier transform of a 1D projection is equivalent to a profile at the same angle through the centre of the 2D Fourier transform of the object. Adapted from [57].

In practice, projections of $f(x,y)$ are taken at various angles and the Fourier space is filled with radial lines according to the central slice theorem, as demonstrated in Figure 2.11 [60]. In order to perform an inverse Fourier transform on $F(v_x, v_y)$ to regain the object $f(x,y)$, therefore, the set of radial points would need to be interpolated onto a square grid. This is potentially problematic as the interpolation error will become larger as the density of radial points becomes sparser further from the centre, which will lead to a greater error in the calculation of high frequency components (the edge of Fourier space) compared to low frequency components (the centre of Fourier space) [60]. To overcome this interpolation problem, reconstruction techniques based on backprojection are used routinely in PET imaging.

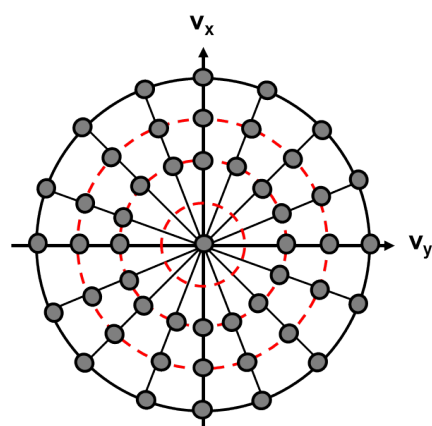


Figure 2.11: Projections of the object are collected at various angles ϕ and radially fill Fourier space (smallest concentric ring points omitted for clarity).

Backprojection

Backprojection can be described as placing a constant value of $p(s, \phi)$ back into the image array along the appropriate LOR. This process is performed on multiple LORs, creating the backprojection $b(x, y; \phi)$, as shown in Figure 2.12. Images are reconstructed by obtaining projections from a range of angles (forming the sinogram) and backprojecting them into object space at the original sampling angles [58]. The density and location of a point in image space is computed by adding all the acquired profiles from that point, but this process blurs the final image, as demonstrated in Figures 2.13(a) and 2.13(b).

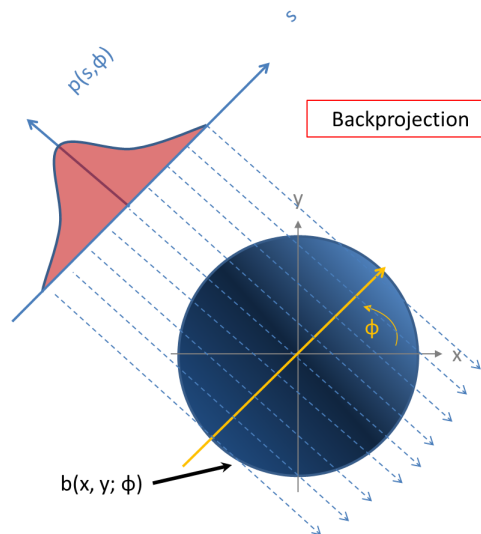


Figure 2.12: Projected data is backprojected onto $f(x,y)$ at a fixed value of ϕ to estimate the activity distribution. Adapted from [57].

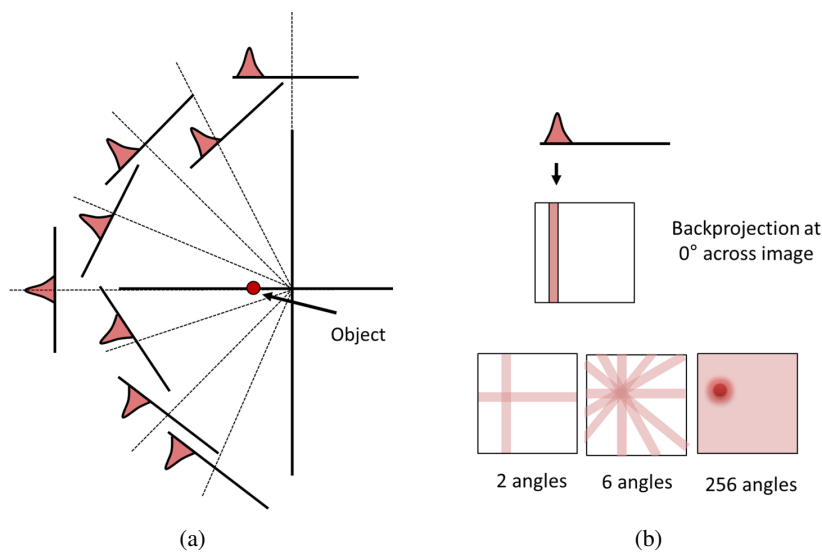


Figure 2.13: Creating a point source image. (a) Profile of object over various angles - source can lie anywhere along direction normal to scan profile, (b) Result of backprojection process, resulting in blurred point source image.

Blurred images result as backprojection enhances the low spatial frequencies in the image and therefore much of the image detail (the high spatial frequency components) is lost, as shown at the bottom of Figure 2.13(b). To reduce the impact of this artefact, the image reconstruction process is modified to accommodate the use of a filter on the sinogram before backprojection is conducted.

Filtered Backprojection (FBP)

The standard analytical PET reconstruction technique is filtered back-projection (FBP), as this accommodates for the oversampling at the origin and undersampling at the edges of Fourier space² that would result if backprojection were used on its own. This is addressed using a filter (e.g. a Ramp or Butterworth filter) [58], which is expressed mathematically in equation (2.4),

$$f(x,y) = (X p_{filtered})(x,y) = \int_0^\pi p(s,\phi)_{filtered} d\phi \quad (2.4)$$

where X is the backprojection operator, mapping $p_{filtered}$ onto the object $f(x,y)$ i.e. that $(X p_{filtered})(x,y)$ is the sum of the filtered data $p_{filtered}$ for all lines containing the point (x,y) [58]. s is in polar co-ordinates ($s = x \cos \phi + y \sin \phi$) and the filtered projections are given by

$$p(s,\phi)_{filtered} = \int_{-\infty}^{+\infty} p(s',\phi)h(s-s') ds \quad (2.5)$$

The ramp filter kernel, $h(s)$ is defined as the inverse 1D Fourier transform of the ramp filter function $|v_s|$,

$$h(s) = \int_{-\infty}^{+\infty} |v_s| \exp(i2\pi sv) dv \quad (2.6)$$

and $|v_s|$ is the one dimensional ramp filter (a section through a 2D rotationally symmetric cone filter)³.

FBP can be summarised by 4 steps, repeated for each ϕ for $0 \leq \phi < \pi$ [60]:

1. Fourier transform the projections: $P(v_s, \phi) = \text{FT}_{1D}\{p(s,\phi)\}$ for given ϕ
2. Filter the projections in frequency space: $P_{filtered}(v_s, \phi) = |v_s| P(v_s, \phi)$
3. Inverse Fourier transform the filtered projections: $p_{filtered}(s, \phi) = \text{FT}_{1D}^{-1}\{P_{filtered}(v_s, \phi)\}$
4. Backproject filtered projections to create image: Image = $f(x,y) + \Delta\phi \cdot p_{filtered}(s, \phi)$ for all s

²Due to the central slice theorem, we know that each projection corresponds to a line intersecting the centre of Fourier space and therefore the central part of Fourier space, responsible for the low spatial frequency components and the contrast of the image, is sampled to a greater degree than the edges by the projections.

³Equation (2.5) can also be expressed using the convolution theorem as $P_{filtered} = |v_s| P(v_s, \phi)$.

FBP is a popular analytical reconstruction algorithm as it is linear, implying that corrections to sinograms are equivalently applied to images, making it easier to control spatial resolution and noise. It can also be computed quickly and efficiently, but image quality suffers when confronted with noisy data.

A small perturbation in noise can lead to large changes in the image, and therefore a smoothing algorithm is used to constrain image solutions to physical values. Assuming the measured projection data is the linear sum of the true data and some uncorrelated random noise, n , i.e. $p(s, \phi)_{measured} = p(s, \phi) + n(s, \phi)$, then its power spectrum will be given by $P(v_s, \phi)_{measured} = P(v_s, \phi) + N(v_s, \phi)$. Due to the finite frequency response of the system, the signal power, $P(v_s, \phi)_{measured}$, will gradually roll off but the noise will remain approximately constant for all frequencies. As the effect of a ramp filter would be to amplify the high frequency components of the power spectrum, the signal would be dominated by noise at high frequencies [58]. Instead, a cosine apodizing window [60], such as a Hamming⁴ or Hann window, can be used to optimise the noise/resolution trade-off, although some form of radial noise streak artefacts will still be present in all images reconstructed with FBP [57]. An example cylindrical water phantom image is shown in Figure 2.14 to indicate how streak artefacts manifest in FBP images.

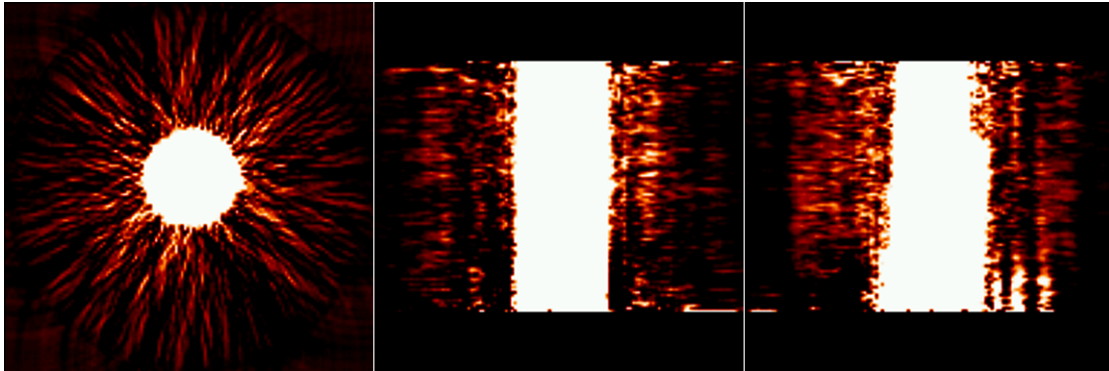


Figure 2.14: 2D FBP reconstruction of water phantom (scaled to 10% of maximum value in image), indicating streak artefacts present in transverse, coronal and axial views.

2.1.5 Further PET image reconstruction

Fully 3D PET

PET LORs can be processed in different ways due to the multiple rings of scintillator blocks in PET cameras, with the two schemes referred to as 2D or 3D mode. The differences between 2D and 3D mode are shown in Figure 2.15, where the ring difference defines from how many crystal rings away the algorithm should process LORs. In 2D mode, only LORs from direct planes (directly opposite

⁴The low pass apodizing window $\omega_{ham}(v)$ is defined as follows: $\omega_{ham}(v) = (1 + \cos(\frac{\pi v}{v_c}))/2$ when $|v| < v_c$ and $\omega_{ham}(v) = 0$ when $|v| \geq v_c$, where v_c is the cut-off frequency. This is selected using the Shannon's sampling theorem to avoid aliasing, such that $v_c \leq 1/2\Delta s$, where Δs is the radial sampling distance of the sinogram [58]. Lower v_c are also selected if the number of detected coincidences (and hence SNR) is low in order to achieve stabilization by suppressing high frequencies.

detectors) and cross planes (adjacent detectors on the opposite side, giving a ring difference of ± 1) are used. In 3D reconstruction, LORs with >1 ring difference (i.e. LORs more than one crystal ring away, known as oblique planes) are rebinned into sinograms in addition to the direct and cross planes used in 2D reconstruction [60]. The ring difference used in this work was 47 (maximum for F120 scanner) for all 3D acquisitions, with a span⁵ of 3. 3D reconstruction provides data redundancy and greater solid angle coverage, theoretically improving the sensitivity and SNR of the reconstructed image by lowering statistical noise. In practice, however, 3D mode also increases the number of scattered counts and therefore may result in decreased SNR if adequate scatter correction is not applied [57].

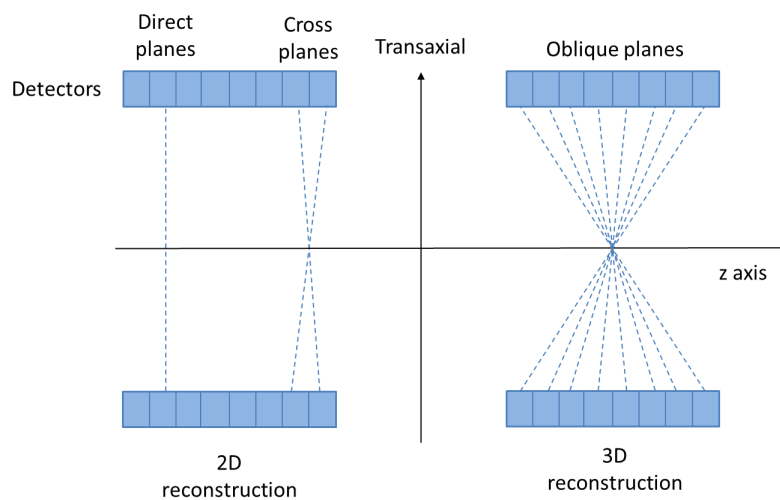


Figure 2.15: 2D and true 3D PET reconstruction. 2D uses only direct planes or those with ± 1 ring difference (cross planes), whereas true 3D uses both direct planes and oblique planes with ring difference > 1 .

3D Reprojection (3DRP)

In 2D mode, the observed intensity of a point source remains approximately constant across the FOV, but in 3D mode the scanner is more sensitive at the centre of the FOV than the edges. This causes a spatial variance, leading to truncated projections due to the finite length of scanner rings [60], [61], as shown in Figure 2.16. As a result, in 3D mode the observed intensity of a point source will change across the FOV, particularly in the axial direction unless these truncated projections are addressed.

⁵Span defines how many adjacent LORs are grouped together into the same angle, θ , between the axial and transaxial planes. A minimum span of 3 was used with the F120 to increase the size of the final sinogram and use all data available.

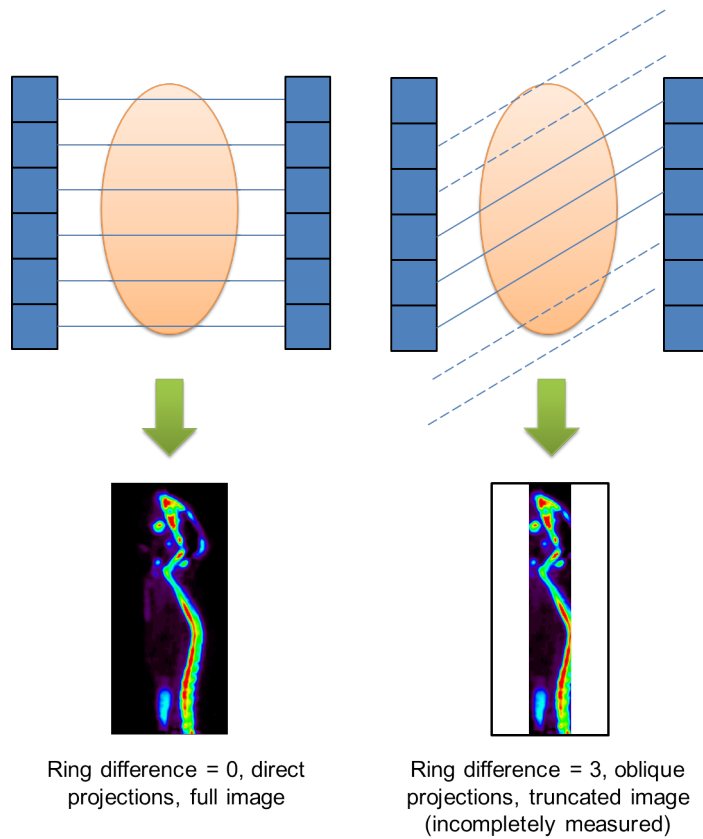


Figure 2.16: Projection truncation problem with ring difference > 1 , adapted from [62].

Originally developed by Kinahan and Rogers [61], the 3D Reprojection (3DRP) algorithm is an implementation of FBP in 3D mode which can be used when the tracer distribution extends axially over the scanner FOV and the majority of parallel projections are truncated. The only non-truncated projections are taken at $\theta = 0$, or in sampled data where $\theta < \theta_0$, where θ_0 is a small maximum obliquity angle corresponding to the maximum ring difference of a 2D acquisition. 3DRP is composed of 4 steps [58]:

1. 3DRP first reconstructs the image using 2D FBP, giving a first image estimate $f_{2D}(r)$ using the non-truncated projection subset where $\theta < \theta_0$.
2. $f_{2D}(r)$ is forward projected to extract the unmeasured parts of the 2D parallel projection set.
3. These are then merged with the measured projections to give a full set of non-truncated projections.
4. The full set of 2D projections are then filtered using a 2D Colsher's filter [63] and backprojected in 3D to give the final image (using 3D FBP). Figure 2.17 summarises the 3DRP process.

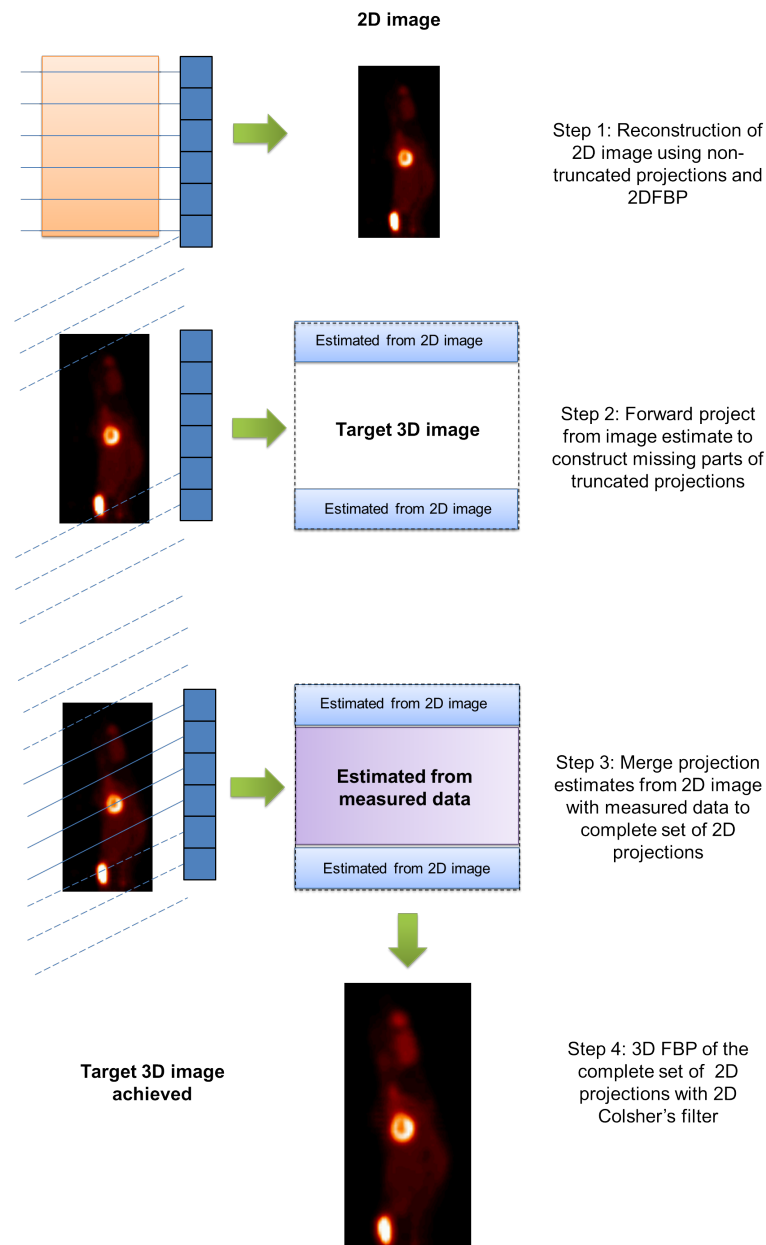


Figure 2.17: Schematic of 3DRP algorithm, adapted from [62]. Step 1 creates a first estimate of the image, which is then used in step 2 to create the truncated projections and combined with the measured data in step 3. Once a full set of 2D projections are established, they can be reconstructed into the final 3D image in step 4.

Iterative reconstruction

In reality, PET data is stochastic due to the phenomenon of positron decay, attenuation effects, scattered events, random events and the photon detection process. The noise term \mathbf{n} in equation (2.3), is hence representative of random noise, meaning that it is not possible to calculate an exact image solution and this limits the resolution of analytical image reconstruction methods. Iterative estimation can be applied to reach approximate solutions, however, by constraining solutions through regularization.

Iterative reconstruction works on the basis that the spatial resolution of a PET image can be improved by accurately modelling the system response to the detection of annihilation photons and using Poisson statistics to describe the process of nuclear decay. The trade-off is on the processing side, as the image estimates are calculated using a number of steps to successively improve an initial estimate, and this process is computationally demanding.

All iterative methods have a basic structure [58]:

1. **Image model** - Image is defined as N distinct pixels (2D) or voxels (3D).
2. **System model** - Relates unknown image to the expectation of each detector measurement. This forms an $I \times J$ matrix (H_{ij}) which relates J total voxels are related to I LORs, characterizing the probability that an emission from voxel j is detected in LOR i . The H_{ij} matrix is expressed in (2.7), where \bar{p}_i is the mean of the i -th measurement and f_j is the activity density in voxel j .

$$\bar{p}_i = \sum_{j=1}^J H_{ij} f_j \quad (2.7)$$

3. **Data/Statistical model** - Calculates expected values. The statistical model indicates the variation of the detector measurements around their expected mean values, thus establishing a measure of similarity between the measurements and the expected values. The preferred model is a Poisson distribution as it describes the physics of radioactive decay, with the raw LOR data p_i distributed as independent Poisson variables. In practice, however, the presentation of the data to the algorithm often deviates from the form of a Poisson distribution - if the number of counts per bin is high enough, a Gaussian model is used instead [58], whilst a shifted Poisson model is used if the data has been pre-corrected for random coincidences⁶.
4. **Cost/objective function** - Objective function is maximised to obtain the image estimate. Maximum Likelihood (ML) approach is commonly used, which chooses an estimate, \hat{f} , of the object, f , such that it maximises the value of \mathbf{L} , the Poisson likelihood function, given in equation (2.8).

$$\mathbf{L}(p|f) = \prod_{i=1}^{N_{LOR}} \frac{\bar{p}_i^{p_i} \exp(-\bar{p}_i)}{p_i!} \quad (2.8)$$

ML is used as the image estimate approaches the true value with low variance as the number of projections becomes large. Spatial smoothing is achieved by either stopping the algorithm before

⁶Random correction is achieved using a delayed coincidence window to measure the random counts and these counts are then subtracted from the prompt counts. This process means that the data are no longer Poisson variables, and hence a shifted Poisson is used [58]

it reaches convergence or through another operation, such as a Bayesian approach.

5. **Algorithm to optimize objective function** - Used to optimize the objective function to give the “best” image estimate. This includes the specification of the initial estimate and the stopping criteria. The Expectation Maximisation (EM) algorithm is the most commonly used.

In most applications of ML and EM, an initial image (all 1s) is forward projected into sinogram space, compared to measured sinogram data and backprojected into image space, updated by the algorithm and then forward projected into sinogram space again. This is contained in equation (2.9) [57]:

$$\hat{f}_j^{(n+1)} = \frac{\hat{f}_j^{(n)}}{\sum_{i'=1}^{N_{LOR}} H_{i'j}} \sum_{i=1}^{N_{LOR}} H_{ij} \frac{p_i}{\sum_{j'=1}^J H_{ij'} \hat{f}_{j'}^{(n)}} \quad (2.9)$$

where $\hat{f}_j^{(n+1)}$ is the next estimate of voxel j based on the current estimate (n th step) $\hat{f}_j^{(n)}$, which starts with the initial guess \hat{f}_j^0 . p_i is the set of measured LOR data, which is compared to the $\sum_{j'=1}^P H_{ik} \hat{f}_k^{(n)}$ term, which gives the expected LOR dataset gained by forward projecting the image $\hat{f}_k^{(n)}$ [58]. A multiplicative factor is formed for each projection, which is then backprojected into the image domain by the $\sum_{i=1}^{N_{LOR}} H_{ij}$ term to obtain a correction factor for the initial image estimate [57]. The current image estimate is then multiplied by the correction factor, and divided by the system model $\sum_{i'=1}^{N_{LOR}} H_{i'j}$ term which weights the desired strength of the correction factor. The process is repeated for a specified number of iterations, which are customised to produce the best image quality. Reconstruction using Ordered Subset Expectation Maximization (OSEM), for example, uses the EM algorithm but is accelerated through the use of ordered subsets, which perform the backprojection step in each subset S_b of B subsets, meaning that the image is updated during each subiteration and the complete iteration has B updates [57].

Maximum *a posteriori* (MAP) reconstruction

Despite the widespread use of OSEM in clinical PET applications, one drawback of the technique is the amplification of image noise when using an increasing number of iteration updates. This prohibits iteration of the algorithm to full convergence. Noise compensation is achieved in practice by terminating the algorithm prematurely (typically after 2–3 iterations) and by performing post-reconstruction image smoothing operations. This may, however, introduce significant levels of bias into the image, as the convergence properties of EM-based reconstruction algorithms are dependent on the underlying activity distribution (i.e. different parts of the image converge at different rates) [64], [65], [66]. As bias may have a direct impact on quantification, further “penalized” iterative techniques have been developed to try to address this issue.

Maximum *a posteriori* (MAP) is a penalized iterative reconstruction algorithm based on Bayesian principles [64], [65], [66]. Conventional MAP algorithms control the noise behaviour of the reconstruction algorithm by introducing *priors* into the reconstruction process which enforce the desired properties on the image estimate at each iteration, such as restricting differences between neighbouring voxel values or edge preservation [64], [65], [66]. The incorporation of priors as terms in the cost function of the algorithm provides a “smoothness” constraint into the reconstruction which penalises noise in successive iterations, thus allowing the algorithm to run to convergence. As with other iterative reconstruction methods, the system model can address a number of factors: the positron range between emission and annihilation, the non-collinearity of annihilation photons, as well as the intrinsic resolution, size, and location of scintillator crystals. The mathematics of MAP reconstruction with a penalized likelihood function can be found in Appendix C.

In the implementation used in this thesis, MAP is applied using a detection probability matrix, \mathbf{P} , whose elements, p_{ij} denote the probability of detecting an emission from pixel site j and detector pair i . This represents the geometric sensitivity of each image voxel in combination with an accurate detector response model, and is therefore able to model the effects of the scanner point spread function (PSF) in the reconstruction [64], [65]. The PSF corresponds to an image of a point source and characterizes the spatial resolution of the scanner. By incorporating PSF information into the backprojection process, this can alter the weighting given to LORs and provide resolution recovery, resulting in partial volume correction [67]. The \mathbf{P} matrix can be factored out as shown in equation (2.10) [64], [65],

$$\mathbf{P} = \mathbf{P}_{det.sens} \mathbf{P}_{det.blur} \mathbf{P}_{attn} \mathbf{P}_{geom} \mathbf{P}_{positron} \quad (2.10)$$

where $\mathbf{P}_{det.sens}$ is measured for a uniform cylindrical source which contains normalization factors that compensate for variations in detector pair sensitivity, $\mathbf{P}_{det.blur}$ is the sinogram blur matrix which models photon pair collinearity, inter crystal scatter and penetration, \mathbf{P}_{attn} is the measured attenuation, \mathbf{P}_{geom} is the geometric projection matrix, whose elements (i,j) correspond to the probability that a photon pair produced in voxel j reaches the front face of detector i assuming no attenuation and perfect collinearity, and $\mathbf{P}_{positron}$ is set to the identity matrix for ^{18}F , for which the positron range is sub-millimetre.

MAP images have been shown to exhibit higher resolution, reduced noise, minimal streak artefacts and greater quantitative accuracy than those produced using 3DRP reconstruction in both phantom and *in vivo* datasets [53], [64], [66], [68]. An image comparison between 3DRP and MAP for a mouse injected with ^{18}F -FDG is shown in Figure 2.18. These images can also be produced using relatively low count statistics with MAP, making it ideal for the early frames of dynamic PET applications. The drawback is the processing time required - compared to 3DRP, which uses only a single backprojection step and

no forward projection steps, reconstructing the same dataset with MAP takes typically 9-10 times longer [66], [69].

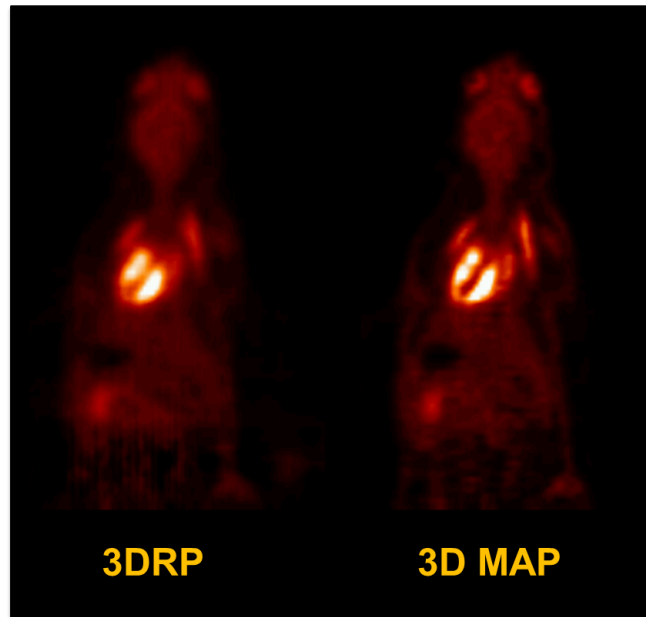


Figure 2.18: Comparison between 3DRP and 3D MAP images, reconstructed by the author, with MAP showing less streak artefacts, higher resolution and less noise, resulting in a sharper image.

2.1.6 Maintaining image quantification accuracy

A number of corrections must be applied to PET data to ensure the voxel values in reconstructed images provide accurate measurements of activity concentration *in vivo*.

- Decay correction
- Deadtime correction
- Randoms correction
- Normalization
- Scatter correction
- Attenuation correction (discussion in following section, addressed fully in Chapter 8)
- Calibration

Decay correction is applied by calculating the exponential decay of the tracer activity over the course of a scan, such that data acquired at a time, t , into a scan is corrected back to the activity at the beginning of the scan (time t_0). Half-lives for the most common PET radioisotopes are given in Table 2.1.

Radioisotope	Half-life
^{11}C	20.5 minutes
^{13}N	9.97 minutes
^{15}O	122.2 seconds
^{18}F	109.8 minutes

Table 2.1: Half-lives of commonly used PET radiotracer isotopes [70].

Deadtime correction is applied to account for counts lost due to the detector scintillators and electronics being saturated at high count rates. In preclinical imaging, a scale factor based upon repeated measurements of a decaying source [69] is applied to all detectors to accommodate for this effect.

Randoms correction is applied to remove random events, which were defined in Section 2.1.3. The rate of random coincidences on an LOR is shown in (2.11),

$$R_{ij} = 2t r_i r_j \quad (2.11)$$

where R_{ij} is the random coincidence rate on the LOR defined by detector channels i and j , r_i is the singles rate at detector channel i , r_j is the singles rate at detector channel j and t is the coincidence resolving time. As t is known, if r_i and r_j can be measured, R_{ij} can be calculated for each line of response [71]. The singles rates should be much higher than the coincidence rates, meaning that R_{ij} has good statistical quality but can be biased if measurements of r_i or r_j are inaccurate.

The correction applied in this thesis used a delayed coincidence window. In this scheme, the coincidence window from one detector of the pair is opened at a time significantly greater than the coincidence window duration time (τ in Figure 2.4). This means that no true events are registered using this scheme, and therefore any coincidences registered in the time shifted coincidence window will attributed to random events. Once measured, this estimate of the random counts is subtracted from the total detected events [65]. The advantage of this method is that the delayed channel has identical dead-time properties to the prompt channel, but the delayed window method has reduced statistical quality of the randoms estimate compared to the previously mentioned singles-based method as it relies on coincidence event rates. Method have thus been developed to smooth the data and improving the noise characteristics of random coincidence estimates in both 2D [72] and 3D PET [73].

Normalization is applied to correct for geometric differences in crystal positioning and different crystal efficiencies, to try to ensure that all LORs produce the same result for radioactivity placed anywhere inside the FOV. Geometric differences refer to the fact that each detector may register a different amount

of activity as a consequence of the different angles of the incoming gamma rays. In addition, each crystal is unique according to the manufacturing process and has a different detection efficiency. To correct for these effects, long (6-8 hours) scans are performed. In this work, the standard microPET normalization cylinder filled with ^{18}F was used to create the normalization sinogram. The LOR data were inverted and normalized such that the mean value of the sinogram was 1.0 and the normalization sinogram was added into every image reconstruction process.

Scatter correction is applied to correct for scattered events which were also defined in Section 2.1.3. Incorrectly assigned LORs can add a non-uniform, smooth background uptake to the data, reducing contrast in reconstructed images. Scattered events can be identified by their lower energies compared to true events, although the detector energy resolution is insufficient to correct for all scatter. Single scatter formulae are also applied to the data according to source and object geometry to correct for observed scatter [74].

Calibration is applied to produce PET images with standardized activity concentration units. For this thesis, a mouse-sized cylindrical phantom filled with ^{18}F fluoride dissolved in water was imaged using the same protocol as those used in murine PET studies with all other corrections applied. An aliquot of activity was withdrawn for cross-calibration in a well counter and the measured value was assigned to the uniform signal region of the image produced and then transferred into the header of the normalization file, such that every future reconstruction produced images in terms of Bq/ml.

2.1.7 Attenuation correction

Attenuation occurs as annihilation photons traverse tissues with different electron densities and depths, leading to differing levels of lost counts between detector pairs in the PET scanner ring, with an example attenuated LOR shown in Figure 2.19. This results in decreased levels of activity concentration in the final PET images compared to the true activity distribution and therefore attenuation correction (AC) is required for accurate quantification [75], [76]. AC requires knowledge of the linear attenuation coefficient (μ values in cm^{-1}) for 511-keV photons along each line of response of the PET scanner. AC can be performed using CT-based, PET-based or MR-based methods, with transmission scanning and CT-based methods used routinely and considered gold standards in both clinical and preclinical imaging [28], [69], [75], [76], [77], [78].

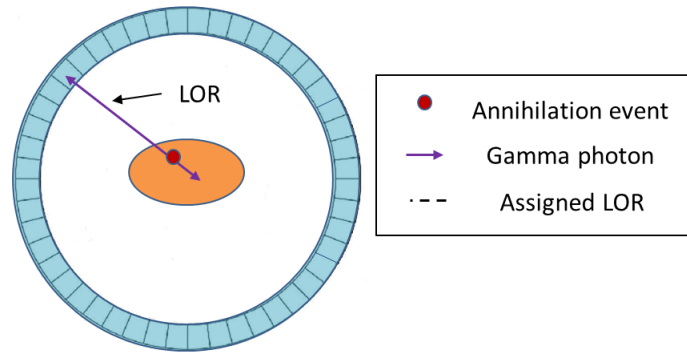


Figure 2.19: Reduction of registered LORs due to attenuation. In this example, one gamma photon from pair is detected but the other is attenuated by the body, so no LOR is recorded and the coincidence event is lost.

CT based attenuation correction in PET/CT

CT images are created in direct relation to the electron density and atomic number (Z) of tissues and can therefore be used to calculate AC for PET (CTAC). A CT scan is conducted before the PET tracer is administered, with the resulting intensity levels providing a photon attenuation map of the subject at typical diagnostic CT energies (30–130keV). Regions of greater attenuation having a higher signal intensity on the CT images, indicated in Figure 2.20. As linear attenuation co-efficient values depend on the energy of the radiation administered, the μ values attained from CT must be scaled to the energy of PET photons (511keV) using a proportional relationship that is formed using bilinear interpolation [76], [77]. A bilinear relationship is used to account for differences in the ratio of CT to PET attenuation co-efficients in tissue and cortical bone [80] and is applied after the CT image is resliced into the PET resolution and voxel size. The bilinear conversion method uses a linear relationship with one slope for regions that are a mixture of air and soft tissue ($-1000 < H < 0$, in Hounsfield Units, H.U.) and a second slope for regions that are a mixture of soft tissue and bone ($H > 0$) [80]. The conversion relationship (for tissue) used in small animal PET/CT [77] is shown in equation (2.12),

$$\mu_{PET, x} = \mu_{CT, x} \times \frac{\mu_{PET, H_2O}}{\mu_{CT, H_2O}} \leq \mu_{PET, Bone} \quad (2.12)$$

where μ is the linear attenuation co-efficient and x is the unknown tissue type. A maximum value is set as $\mu_{PET, Bone}$, as the absorption of bone relative to water at CT energies is higher than at 511keV [77]. This produces μ maps with continuous values, which are forward projected into an attenuation sinogram to be added into the PET image reconstruction process. Errors in CTAC approaches can occur due to misalignment between PET and CT data, inaccuracy in converting tissue attenuation co-efficients from the CT energy range to 511keV and beam hardening artefacts [76], [77], [78].

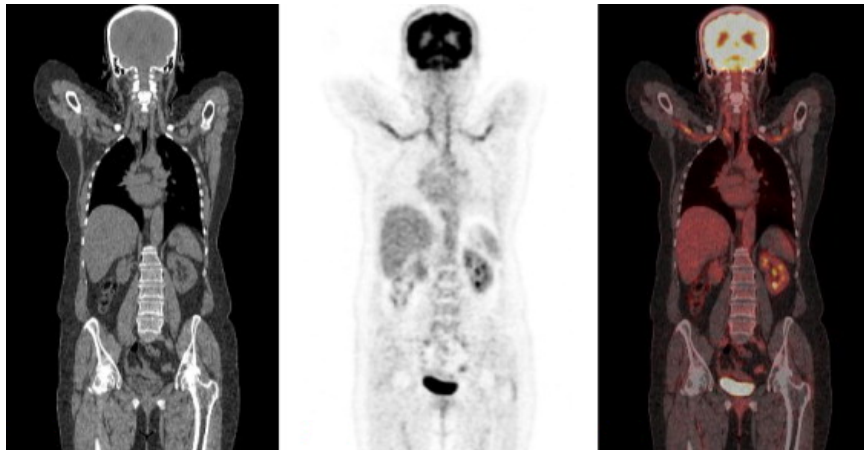


Figure 2.20: From left: CT, PET and PET/CT images reproduced with permission from [79]. Bone is resolved with high contrast and signal intensity on CT due to its large attenuation factor.

Transmission source based methods in stand-alone PET

Attenuation correction in a stand alone PET scanner can be performed with a transaxially rotating, positron emitting (e.g. ^{68}Ge) point source which moves around the subject in a transmission scan and is compared to a “blank” scan, which is taken while the PET scanner is empty. The 511keV photons emitted from the source are detected by the PET detectors in singles mode⁷ for approximately 10 minutes for both transmission and blank scans as the rotating source is moved in and out of the FOV in a helical manner, with the difference between transmission and blank scans shown in Figure 2.21. Transmission scanning-based AC (TXAC) hence provides a direct measurement of attenuation at 511keV by measuring the fraction of gammas absorbed along each LOR in the transmission scan compared to the blank scan and provides attenuation information which is aligned with the PET emission data. The resulting transmission sinogram can hence either be used directly in the reconstruction process or the reconstructed attenuation image can be forward projected to create attenuation factors for each LOR [80].

A different energy source, such as ^{137}Cs [5], [80] or ^{57}Co [78], may also be used, although the detected photon energies have to be scaled to 511keV.

⁷This is usually performed in coincidence mode but due to low SNR seen in phantom experiments with the ^{68}Ge transmission source in the Cambridge split magnet scanner, transmission scans were conducted in singles mode for the experiments covered in this thesis.

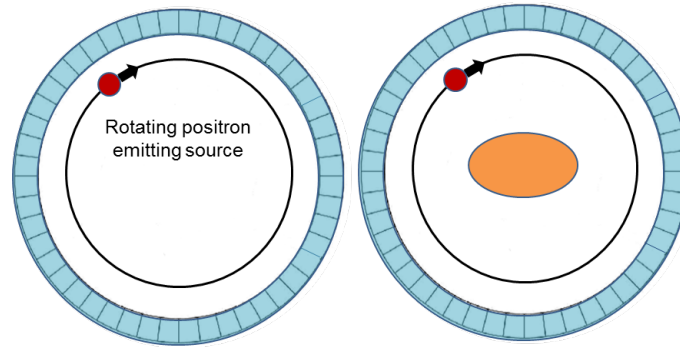


Figure 2.21: A blank scan is performed using the rotating source, which spirals into and out of the scanner to cover all possible LOR trajectories from the emitting object. This process is then repeated in the transmission scan before injection of PET tracer with the subject inside the scanner.

The ratio of the PET sinograms created by the transmission and the blank scans gives the attenuation sinogram, which provide an estimate of the linear attenuation co-efficients of the patient by applying the Beer-Lambert Law [78], [81], shown in equations (2.13) and (2.14) and Figure 2.22.

$$N = N_0 \exp^{-\mu x} \quad (2.13)$$

where N is the number of detected photons, N_0 is the original number of photons, μ is the linear attenuation co-efficient (in cm^{-1}) for the material and x is the distance the photons travel inside the material (in cm). The denser the material, the higher the μ value, as tissue and water at 511keV have values between $0.094\text{-}0.100\text{cm}^{-1}$, lung is between $0.018\text{-}0.030\text{cm}^{-1}$ but cortical bone gives μ values of $0.130\text{-}0.172\text{cm}^{-1}$ [75], [81], [82].

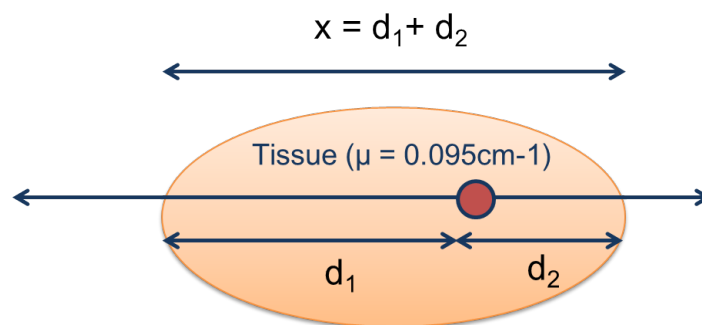


Figure 2.22: The attenuation of an LOR from a body of size x depends on the size and μ value of the body and not the point at which the gamma rays are produced.

$$\frac{N}{N_0} = \exp^{-\mu d_1} \exp^{-\mu d_2} = \exp^{-\mu x} \quad (2.14)$$

N_0 is measured using the blank scan and N is measured using the transmission scan, with distances

d_1 and d_2 defined in Figure 2.22. The attenuation sinogram is created by rearranging equation (2.13) into equation (2.15) and is used to create a corrected emission sinogram multiplying it with the normalized emission sinogram (which is produced by multiplying the emission sinogram with the normalization sinogram). The count rate of each resulting image voxel (reconstructed from the corrected emission sinogram) is therefore corrected according to its measured local attenuation.

$$\ln \frac{N_0}{N} = \ln \frac{(\text{Blank})}{(\text{Transmission})} = \mu x \quad (2.15)$$

Additionally transmission images can be reconstructed from the natural logarithm of the attenuation correction sinograms, forming μ value maps. To compensate for photon scatter and the variation of attenuation with energy, these images can be segmented into regions and their measured linear attenuation coefficients scaled to their theoretical values for 511keV photons [77]. New attenuation correction sinograms can then be created by forward projection through the scaled transmission image. It must be noted, however, that by segmenting and scaling these images, this no longer takes account of any local variation or inhomogeneities in the subject's attenuation distribution and this can be a setback in regions with variable density such as the lungs [75]. The main drawbacks of TXAC, using either the sinogram or image-based method, are due to the fact that the PET detectors are used for the data collection. As a result, high levels of noise propagate into the final reconstructed images, lower resolution μ maps (compared to CT) are produced and TXAC requires much longer acquisition times compared to CT (> 10mins compared to ≈ 20 s) [77], [78], [81].

Existing MR-based attenuation correction approaches for PET/MR

A major challenge in PET/MR is providing adequate attenuation correction without access to CTAC or TXAC due to the limited space available in PET/MR scanner bores. Using MRI as a basis to provide attenuation correction for PET is problematic as the MR signal is produced according to the proton density of tissues, without the need for ionising radiation, and therefore a direct measurement of attenuation cannot be performed [76], [82], [83], [84]. Additional corrections must also be made to accommodate for confounding hardware (e.g. RF coils in Figure 2.23), to accommodate for MR signal artefacts (e.g. from metallic implants) and to accommodate for the limited MR FOV which truncates the resulting μ maps in whole body imaging [75], [76], [82].

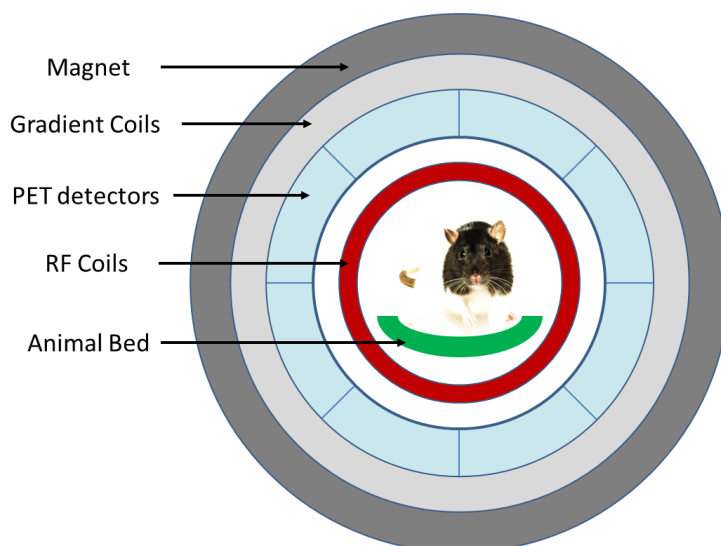


Figure 2.23: Schematic representation of PET/MR insert scanner, showing subject, RF coils and animal bed as sources of attenuation.

Two main approaches to perform MR-based attenuation correction (MRAC) have been developed: segmentation-based methods and atlas-based methods. The segmentation methods work on the assumption that the attenuation co-efficients of soft tissue at 511keV are fairly uniform [10], [82], [84] and therefore most visualised tissue types can be assigned a population average linear attenuation co-efficient to approximate their attenuation.

MRI images are therefore segmented into tissue types and organ classes, which are each assigned a pre-determined linear attenuation co-efficient value [75], [76], [81], [82], [84] as illustrated by Figure 2.24 for a simulated mouse phantom. The more accurate the segmentation process, the closer the MRAC will approximate the AC provided by transmission scans and CT. The simplest segmentation-based method used in clinical whole body PET/MR studies employs the 2-point DIXON technique [85]. 2 point DIXON acquires an in phase and out of phase gradient echo MR image of fat and water, acquired by adjusting the echo time (TE) of the sequence. If an MR signal echo is acquired when fat and water are exactly out of phase (spins at 180° to each other) their signals will cancel and likewise if they are acquired in phase, their signals will add together⁸. These images can therefore be treated as simultaneous equations, (the mathematics are included in Appendix D) and added together to give a water (soft tissue) image and subtracted to give a fat image. These images can hence be used to divide the body into tissue classes (air, lung, soft tissue and fat) and then assign average attenuation factors for each class [84]. More recent techniques for brain imaging have incorporated information from ultrashort echo time

⁸Fat and water signals dephase at different rates due to their different Larmor precessional frequencies, which result due to their differing chemical composition. They are in phase immediately after the RF excitation pulse and will be in phase at a time equivalent to the inverse of their chemical shift i.e. if the chemical shift between water and fat is 220Hz at 1.5T, they will be in phase at 1/220s later, so the TE is set to 1/220s (4.5ms) [86] to achieve an in phase image when acquiring the echo. These terms are explained in future sections on MR theory.

(UTE) sequences (further details can be found in Appendix D) which have been used to add an additional bone class into the segmentation approach [75], [76], [87].

These approaches are computationally simple and do not require information other than the MR scan but segmentation may be affected by the fact that different tissue types can produce similar signal intensities. In particular it is difficult to separate air and bone, which appear similar on MR but markedly different on CT due to the high attenuation factor of bone. A further problem lies in the fact that many MR essential imaging components (e.g. RF coils) will attenuate photons to a greater degree than the patient tissues [87] but these components do not appear on regular MR images.

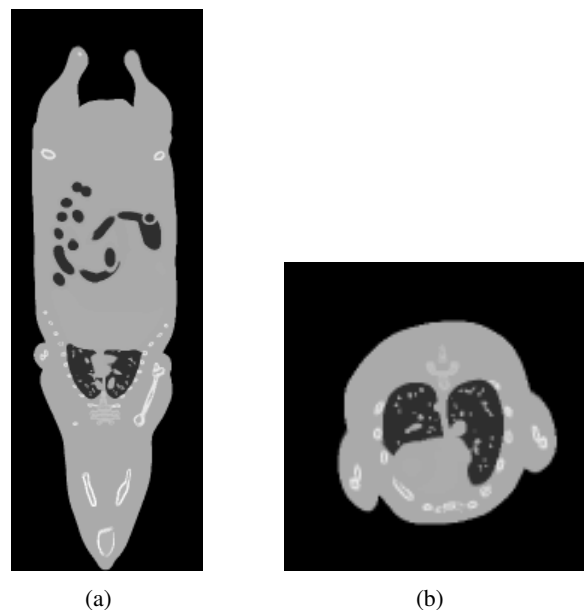


Figure 2.24: Example attenuation maps with tissue classification, simulated from the mouse whole body (MOBY) phantom (a) axial and (b) transaxial views [88]. Black areas (air) are assigned the lowest attenuation factor value, whilst white areas (bone) are assigned the highest attenuation factor value, with a range of grey values assigned to other tissues.

The other approach to MRAC uses an atlas created from an archive of MRI and CT/transmission scan images, which allows for both continuous attenuation co-efficient values to be assigned and can utilise the superior level of anatomical segmentation of tissue classes available from CT images [75], [82], [83], [89], [90], [91]. After the examination, individual MR data from a PET/MR scan is transformed into MR atlas space and a pattern recognition method is used to create a pseudo-CT image from a CT atlas (shown in Figure 2.25). The disadvantage of the atlas procedure is that a large image database is required to account for inter-individual anatomical variability (particularly in large abnormalities such as tumours) and truncated organs that lie outside the FOV may not be taken into account.

There has been limited discussion of the various MRAC methods in preclinical work, except in rabbits [89], [92], but even in PET/MR clinical studies reported so far, a consensus on the best method for

MRAC has yet to be reached [75], [81], [82], [83], [87], [93]. Currently, segmentation-based MRAC methods (using DIXON in combination with UTE [75]) are applied to brain imaging in humans but their translation to whole body imaging is complicated by misregistration problems, tissue segmentation/classification failures (e.g. mis-segmenting the lung region as an air or tissue class), UTE sequences (for bone segmentation) needing too long an acquisition time to be feasible for whole body imaging and variations in inter-subject and intra-subject lung-density [75], [76].

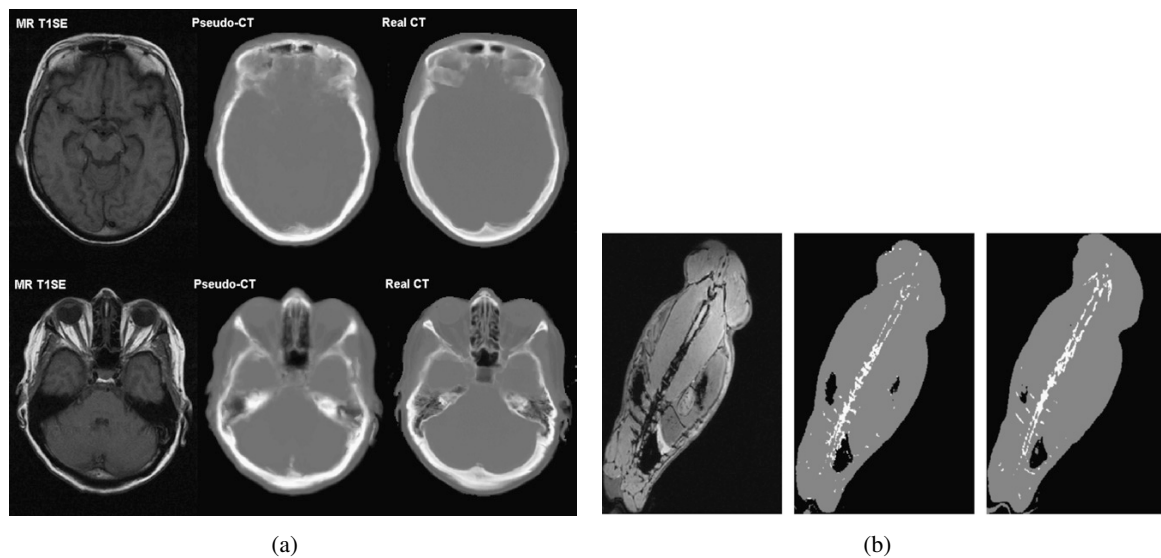


Figure 2.25: (a) Pseudo-CT (centre, with raw MR on left and reference CT on right) created from human brain MR using atlas approach to provide μ map for attenuation correction. (b) Three tissue classification scheme (raw MR on left, segmented MR centre, segmented CT right) used to create whole body rabbit μ map. Images reproduced with permission from [89].

Alternative approaches for PET/MR attenuation correction

PET emission data can also be used to generate estimates of attenuation, and has been used in preclinical studies to give an outline of the animal body which is then used as single, segmented tissue region in a similar approach to the segmentation-based MRAC approaches [77], [78].

In humans, this is adapted further using the Maximum Likelihood Reconstruction of Attenuation and Activity (MLAA) iterative algorithm to construct attenuation maps from the emission data. Proposed by Nuyts et al. [94] MLAA uses likelihood optimization in iterative reconstruction to gain an estimate of linear attenuation co-efficients, based on the observation that the absolute likelihood of a maximum likelihood expectation maximization (MLEM) emission image is always higher when attenuation is taken into account, compared to no attenuation correction. Nuyts et al. extended MLAA for use with MAP by incorporating a priori information about the attenuation co-efficients into the algorithm [94]. This method has since been expanded to be used to fill in gaps in truncated CTAC and MRAC maps [95] and also been extended to include time of flight (ToF) information [96] (see Appendix B for ToF explanation)

to further improve its μ map estimates. In ToF-MLAA, an original segmentation-based MRAC μ map is created and ToF information is applied to locate inconsistencies between the emission and transmission data, which can be used to fill in truncation artefacts on segmentation-based MRAC maps.

Other possibilities to estimate AC from PET alone include using TOF data in conjunction with low dose annulus-shaped positron emitting sources to separate out attenuation data from emission data in a simultaneous PET/MR scan [97], [98]. Unfortunately, TOF technology is not supported in rodent PET scanners, which limits the adaptation of advanced PET-based AC techniques [99].

2.1.8 Dynamic PET acquisition

If images have been fully corrected and calibrated, dynamic reconstruction can be used to examine tracer time courses. Data can be histogrammed and reconstructed to create a single “static” frame, giving the average tracer distribution over the duration of the scan or can be further segmented into dynamic “bins” to create image time frames, shown in Figure 2.26. Shorter bins (e.g. 5-10s) are used at the start of the scan to capture the passage of the tracer in its early stages and are gradually lengthened over the course of the scan to increase the count statistics in each frame (and hence the SNR) as the tracer equilibrates in tissue, such that after 45-60 minutes the bins are typically 300-600s long.

Subject motion between frames is common and can cause misalignment errors both between emission frames or between attenuation correction sinograms and emission frames, resulting in ROI delineation errors and quantification errors. To avoid this, inter-frame and intra-frame motion must be assessed in dynamic PET studies and frames co-registered to each other to reduced these errors.

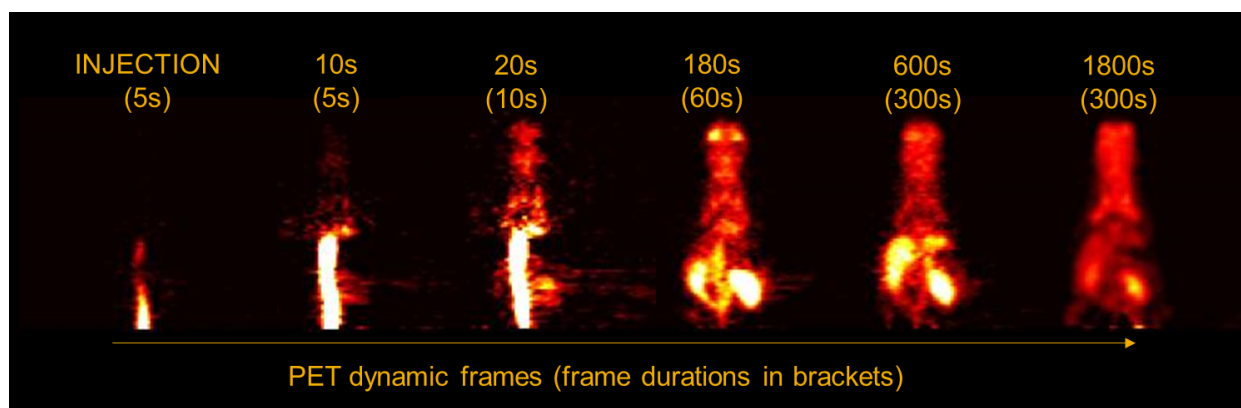


Figure 2.26: Dynamic whole body ^{18}F -FDG PET image frames of a mouse, reconstructed using 3DRP (coronal view). The tracer is administered via a tail vein cannula and proceeds to the heart, which then distributes the tracer throughout the mouse. Earlier images are much noisier due to the lower frame durations required to visualise the rapid initial kinetics.

2.1.9 Motion correction of dynamic PET data

Motion artefacts can also be reduced by binning each dynamic frame into cardiac or respiratory gating frames, according to ECG or respiratory pillow recordings. This often results in increased noise, however, as the count statistics are reduced by the number of cardiac cycles specified, as shown in Figure 2.27 for 3DRP and Figure 2.28 for MAP.

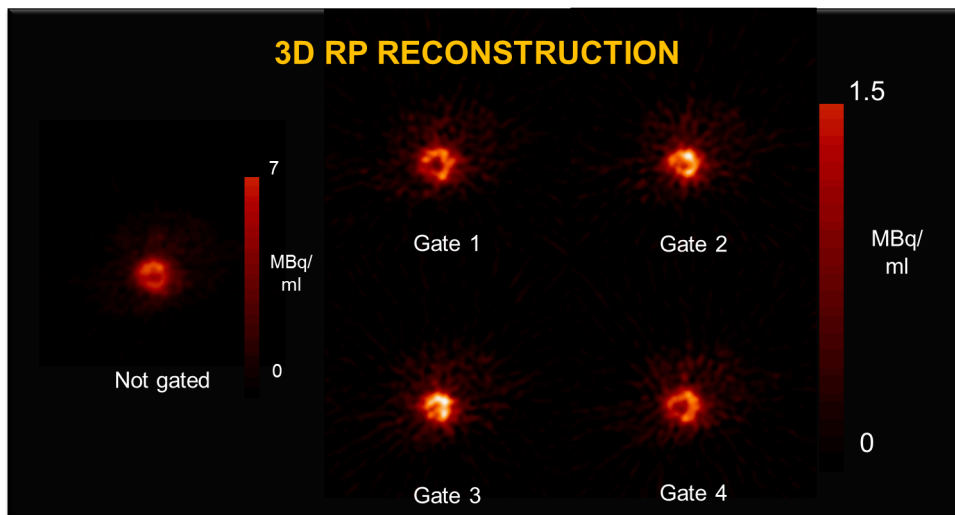


Figure 2.27: Left: Late frame (taken 40 minutes into scan, 300s duration) ^{18}F -FDG cardiac image of mouse heart reconstructed using 3DRP without cardiac gating. Right: Frames 1-4 created using ECG triggers to show systole to diastole phases of heart cycle. Global noise is increased in gated images compared to ungated image.

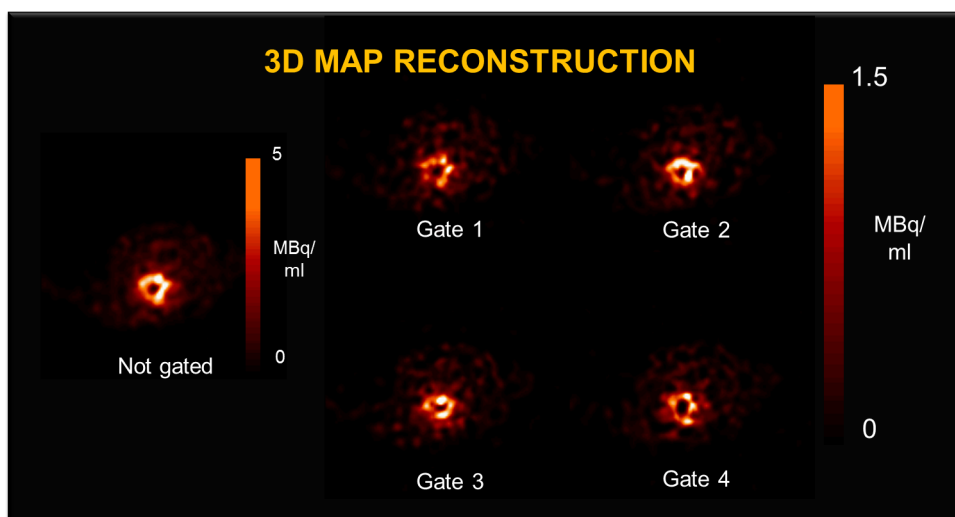


Figure 2.28: Left: Late frame (taken 40 minutes into scan, 300s duration) ^{18}F -FDG cardiac image of mouse heart reconstructed using 3D MAP without cardiac gating. Right: Frames 1-4 created using ECG triggers to show systole to diastole phases of heart cycle. Global noise is increased in gated images compared to ungated image.

As each frame must be reconstructed separately, the reconstruction time is multiplied by the number of

frames present in the acquisition. Cluster computing techniques were employed in this thesis to process the data in a realistic time frame, comprising three different cluster data processing centres (DPCs). Each DPC had 32 cores with 32GB of RAM each, two of which were run on the Windows Server 2008 operating system and the last DPC run using CentOS 6 Linux. Image reconstruction jobs were created using microPET manager software (Siemens Molecular Imaging, version 2.4.1.1, 2005) and sent to each of the DPCs via the IDL scheduler and task manager. This enabled up to 32 jobs to be processed in parallel on each of the DPCs, with an approximate maximum reconstruction time of 20 minutes per frame for MAP reconstructions. This enabled dynamic PET data of approx. 50 frames in length to be reconstructed, with the addition of cardiac gating, within 3 hours.

2.2 MRI scanning

MRI harnesses the phenomenon of nuclear magnetic resonance (NMR), which describes how nuclei with intrinsic angular momentum behave in a magnetic field after application of a characteristic radiofrequency (RF) frequency pulse. Water is a major constituent of biological material and therefore the interrogation of proton nuclei signals can be used in a medical context to create morphological images *in vivo*. The signals observed in MRI depend heavily on the exact chemical environment that protons experience, which allows for excellent contrast between tissue types by discrimination of different signal intensities. Diseased tissue is identified non-invasively by observing signal changes on MR images as a result of physiological change within the body. MRI uses non-ionising radiation (the RF pulses used for excitation of nuclei are of a frequency - and therefore energy - lower than that of visible light) and there are no known side-effects associated with exposure to the strong magnetic fields required to produce MR images, although prolonged RF excitation is limited to reduce the RF specific absorption rate (SAR) and avoid excessive heating of the body.

2.2.1 Background MRI physics

In a static magnetic field, populations of spin $\frac{1}{2}$ protons are separated into two energy levels as their spins align parallel (spin up, lower energy) or anti-parallel (spin down, higher energy) to the field. From quantum mechanics, the energy of separation is given by $\Delta E = \hbar\omega_0$, where ω_0 is the Larmor frequency and \hbar is the reduced Planck's constant [100]. The Larmor equation, given in equation (2.16), relates the proton resonance frequency to the static B_0 field,

$$\omega_0 = \gamma B_0 \tag{2.16}$$

where γ is the gyromagnetic ratio, -42.577 MHz/T. The protons obey a Boltzmann distribution such that, at room temperature, the limit of $\Delta E \ll k_B T$ is reached (where k_B is the Boltzmann constant and T is the temperature) and the ratio of populations in each spin state can be approximated in equation (2.17):

$$\frac{N_{\uparrow}}{N_{\downarrow}} = \exp\left(\frac{\Delta E}{k_B T}\right) \rightarrow 1 + \frac{\hbar\gamma B_0}{k_B T} \quad (2.17)$$

where N_{\uparrow} is the population of spins in the upper level and N_{\downarrow} is the population of spins in the lower level. This leads to an excess of spins in the lower energy level (roughly two parts per 10^5 for a magnetic field strength of 3T at room temperature) and allows for the creation of the MRI signal when an RF pulse excites spins between energy levels [100], schematically illustrated in Figure 2.29. The relaxation of the transverse component of the net magnetisation back to equilibrium gives rise to an observable signal. The MR signal is an induced current created due to the passage of the net magnetisation of the spins through a receiver coil.

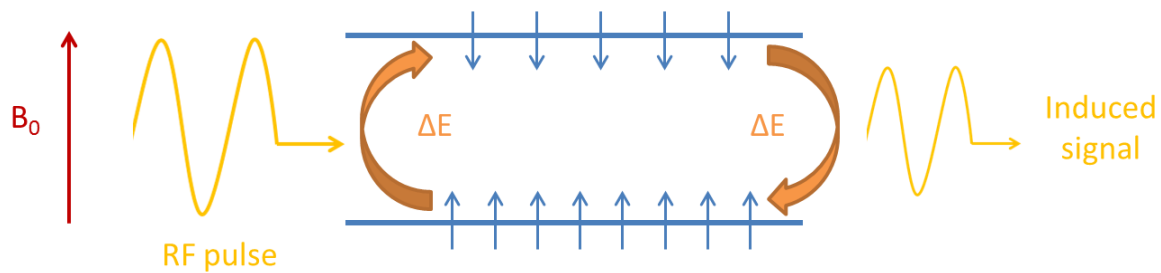


Figure 2.29: Boltzmann distribution determines proton spin populations within a magnetic field B_0 and an observable signal is created after RF excitation.

2.2.2 Scanner hardware

MRI requires a homogeneous static magnetic field (B_0) of typical magnitude 1.5–3T for clinical applications in humans ($\simeq 50\,000$ times stronger than the Earth’s magnetic field). The magnet is composed of a large superconducting coil which is cooled below its critical temperatures by cryogenics (e.g. liquid Helium), thus lowering its resistance to zero and allowing an unhindered flow of current to create the magnetic field. Gradient coils are placed within the bore of the magnet to apply orthogonal magnetic fields (G_x , G_y and G_z) to encode MR signals in 3D and create images. The preclinical MRI scanner used in this thesis is displayed in Figure 2.30. The NMR spectrometer generates RF pulses and a configuration of transmitter and receiver RF coils relay the pulses and detect the signal induced respectively. Surface coils are designed to rest next to the tissue of interest whereas volume coils envelope the tissue - both work most effectively when the coil is filled with the volume of interest.



Figure 2.30: Bruker Biospin 4.7T MRI scanner for small animals installed at the WBIC.

2.2.3 Creation of images

Signal echo generation

The MR signal originates from the net magnetic moment of sample, M_0 , which describes the sum over spin states within the volume and precesses around B_0 at ω_0 (the B_0 direction is conventionally taken as the z direction). A frame of reference rotating at ω_0 is chosen to make M_0 appear stationary and parallel to B_0 . A circularly polarised, oscillating magnetic field (B_1) is then applied by an RF pulse at ω_0 from the transmitter coil in a direction perpendicular to B_0 (i.e. at resonance along the x axis in the rotating frame). B_1 therefore acts as a vector on M_0 , causing the magnetisation to precess around the x axis at frequency $\omega_1 = \gamma B_1$ for the duration of the pulse. The pulse is timed to tip the magnetisation from the z axis down into the x - y plane (90° pulse), where a receiver coil can detect the induced signal generated by the free rotation of the magnetic moment. If the pulse is applied for twice this time, it will flip the magnetisation onto the $-z$ axis (a 180° pulse). Similarly if the pulse were left on for a third of the 90° pulse time, it would produce a 30° pulse and a vector component of the magnetisation would be visible in the x - y plane. This property is referred to as the flip angle of the pulse [86].

After the RF pulse is applied, the signal in the x - y plane decays exponentially in a free induction

decay (FID). The signal dephases as different spins experience different magnetic field inhomogeneities and spin-spin interactions, meaning that the spins develop differing precessional frequencies. Signal echoes are obtained using two methods, spin echo (SE) and gradient echo (GE), which dephase and rephase the spins into coherency, producing an echo at the echo time (TE). Figure 2.31 illustrates the GE concept, which utilizes positive and negative magnetic gradient lobes of equal area to generate signal echoes. Spins precess faster if they experience a higher magnetic field and this change in precessional frequency results in spins in a higher field dephasing from those in a lower field. If the gradient lobe is reversed, the spins will rephase and form an echo. As the rephasing process in GE only uses an opposite sign gradient lobe, the dephasing process is governed by both magnetic field inhomogeneities and spin-spin interactions, and the FID is dependent on the relaxation constant $T2^*$ [86].

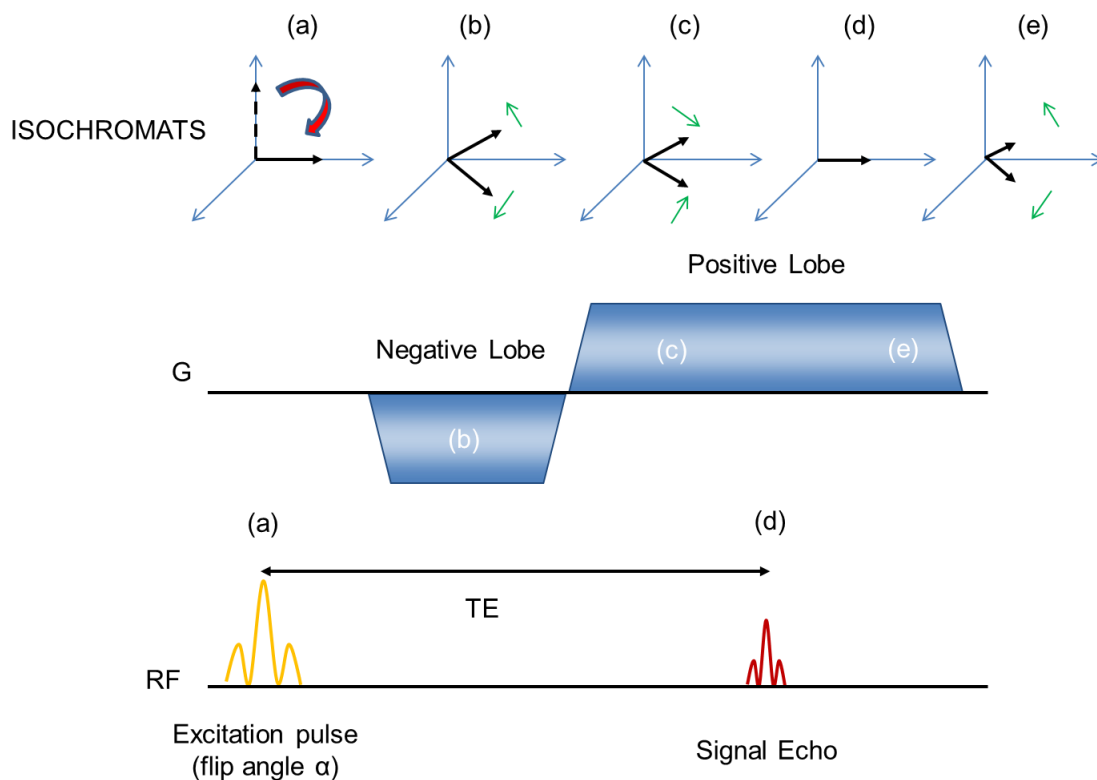


Figure 2.31: Gradient echo formation: (a) 90° pulse to tip M_0 into x-y plane, followed by (b) a rapid decay due to dephasing of the signal using the negative gradient lobe until application of (c), the positive gradient lobe. Spins that were precessing at a low frequency now precess at a higher frequency as the gradient is adding rather than subtracting from the overall magnetic field experienced, and vice versa. Rephasing now occurs, resulting in (d) echo formation (lower magnitude due to exponential decay of M_0). Spins continue to precess after echo, shown in (e). Adapted from [86].

Figure 2.32 illustrates the SE concept, which uses the application of 180° RF pulses to rephase the echo signal. Spins which are dephasing after a 90° pulse have their phase reversed by a 180° pulse but continue to dephase in the same direction as before, as they experience the same magnetic field

inhomogeneities that affected their precessional frequencies. This results in the spins rephasing at a time equal to the delay between the 90° and 180° pulses, forming a signal echo. Echo formation in this manner is most commonly referred to using the “runners on a track” analogy. Spins are represented by athletes of varying speeds running until a whistle is blown to tell them to run directly back to their starting position. The faster runners have further to go than the slower runners, so assuming their speeds are constant, all runners will arrive at the starting line together. As this method relies on reversing the phase of the signal, the decay is governed by spin spin interactions rather than magnetic field inhomogeneities and the decay of the signal echo heights is governed by the relaxation constant T2 [86].

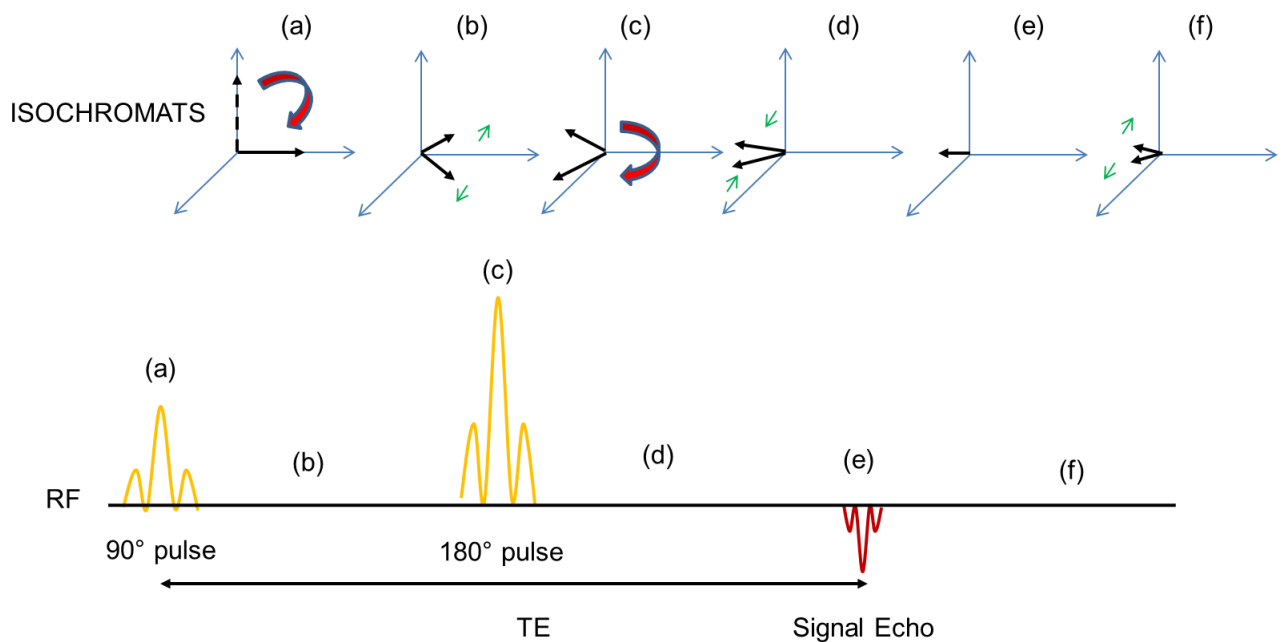


Figure 2.32: Spin echo formation: (a) 90° pulse is applied to rotate spins into transverse plane, (b) spins then dephase naturally until (c) 180° is applied. This flips all spins 180° on transverse plane (i.e. $+y$ axis to $-y$ axis). (d) This does not change the spins precessional frequencies but does reverse their phase, therefore spins which were dephasing faster than others are now rephasing faster. (e) As a result, an echo is formed which is used to record the MR signal. (f) The spins then continue to dephase as before, unless another 180° is applied. Adapted from [86].

Spatial encoding

The echo signal can be encoded in space by applying gradient fields in addition to the main field B_0 . A 3D volume is encoded by three orthogonal gradient fields: the slice selection gradient (G_{SS}), the phase encode gradient (G_{PE}) and the frequency encode gradient (G_{FE}).

The slice select gradient determines the 2D plane (or slab) of the patient which is excited by the RF pulse. By convention, the slice select direction is taken to be the z axis⁹ to align with the axis of the

⁹An axial slice acquisition is assumed by convention.

magnet bore and the direction of B_0 . The gradient coils apply a linear gradient along the z direction, with spin precessional frequencies determined by equation (2.18) [101].

$$\omega = \omega_0 + \Delta\omega = \gamma(B_0 + G_z \cdot z) \tag{2.18}$$

The spins within a patient therefore precess at different rates according to the local magnetic field, allowing for any slice to be excited. The width of the slice is determined by the bandwidth ($\Delta\omega$) of the RF pulse and gradient strength (G) of the slice select gradient, demonstrated in Figure 2.33.

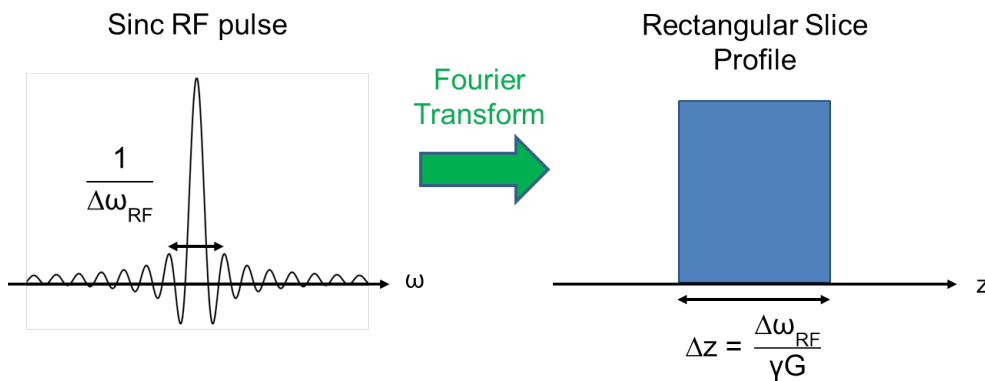


Figure 2.33: Slice excitation using RF pulse, indicating how bandwidth of RF pulse dictates size of slice excited.

The central frequency of the RF pulse determines the slice position, illustrated in Figure 2.34. Figure 2.35 depicts how three slice excitations can be achieved using three different RF frequency pulses.

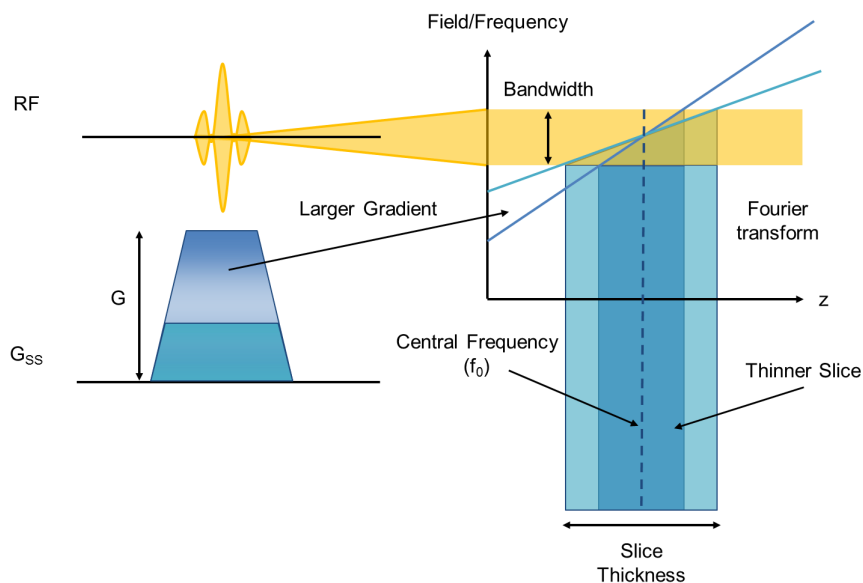


Figure 2.34: Slice select gradient, used to excite protons using an RF pulse within a desired region. Adapted from [86].

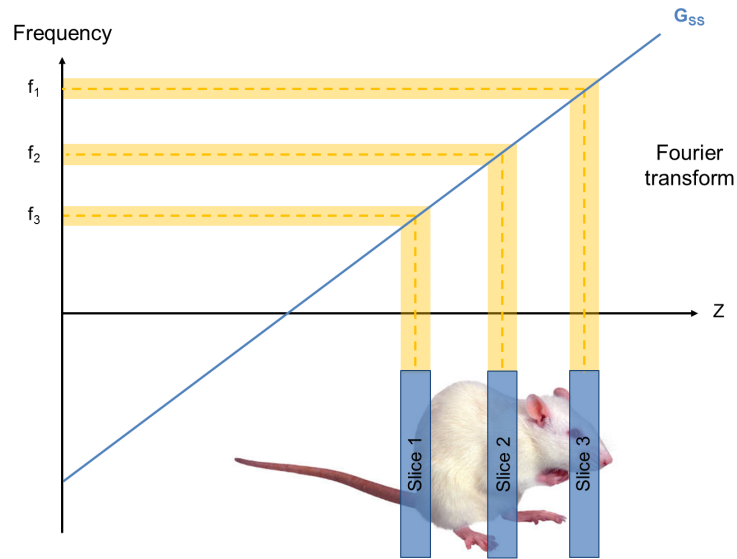


Figure 2.35: Different frequency RF pulses can be used to select different slices. Adapted from [86].

To acquire an orthogonal slice, $G_x \cdot x$ or $G_y \cdot y$ can be used in place of $G_z \cdot z$ in equation (2.18). An oblique slice acquired at any angle through the patient, can be acquired by using a combination of G_x , G_y and G_z , whose application can be characterised generally by a 3D spatial rotation matrix [101]¹⁰.

The G_{FE} and G_{PE} gradient fields (orthogonal to G_{SS}) encode the patient's spatial frequencies into k space (see Figure 2.38) with axes k_x and k_y in 2D acquisitions, using equations (2.19) and (2.20) [101]:

$$\Delta k_{FE} = \frac{\gamma}{2\pi} G_{FE}(t) \cdot m \cdot \Delta t \quad (2.19)$$

where k_{FE} = the unit interval of k space in the frequency encoding direction, G_{FE} is the magnetic gradient applied in frequency encoding direction in mT/m, m is the sampling number in the frequency encoding direction and Δt is the sampling interval (reciprocal of sampling frequency) in ms.

$$\Delta k_{PE} = \frac{\gamma}{2\pi} \Delta G_{PE}(t) \cdot n \cdot t \quad (2.20)$$

where k_{PE} = the unit interval of k space in the phase encoding direction, ΔG_{PE} is the magnetic gradient applied in the phase encoding direction in mT/m, n is the sampling number in the phase encoding direction and t is the duration of the phase encoding gradient in ms. Equation (2.21) defines an arbitrary k space trajectory [101],

$$k = \frac{\gamma}{2\pi} \int_0^t G_{PE}(t) dt \quad (2.21)$$

¹⁰To obtain a transverse slice rotated through angle ϕ from the x axis, $G_x = G_{SS} \cos \phi$ and $G_y = G_{SS} \sin \phi$ [86].

The frequency encoding (or readout) gradient is applied at the same time as the MR signal is measured, such that it assigns a unique precession frequency (governed by equation (2.16)) to a distinct spatial location along the gradient direction [101]. The measured signal frequency will thus be a mixture of the different frequency components, each corresponding to a different spatial location, and a Fourier transform can be used to determine these frequency components, as shown in Figure 2.36.

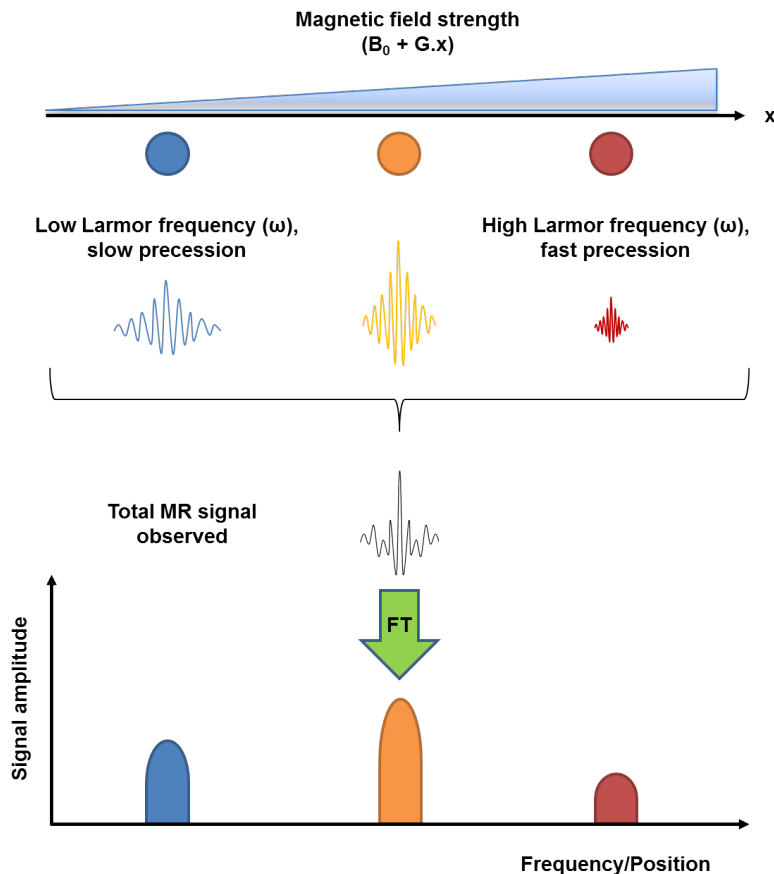


Figure 2.36: Frequency encoding (FE) schematic. With the FE gradient applied, frequencies are encoded according to their spatial positions and the total signal consists of a range of resonance frequencies. A Fourier transform hence produces a projection of the objects [86], [101].

The phase encoding gradient is applied whilst the magnetization is in the transverse plane but before the readout gradient. Whilst the gradient is applied, the precession of nuclei in the gradient direction will speed up or slow down according to their position, leading to phase differences between spins [101]. When the gradient is switched off, the spins will revert to their original frequencies but keep their resulting phase differences [86]. The phase encode gradient lobe area is therefore varied to introduce different amounts of linear phase variation to the signal and thus measure the signal produced in the object at different spatial frequencies, as demonstrated in Figure 2.37. Greater phase differences will be encoded between the spins with increasing gradient strength. To create an image of the object, all possible spatial frequencies must be interrogated in this manner, and the results recorded in k space.

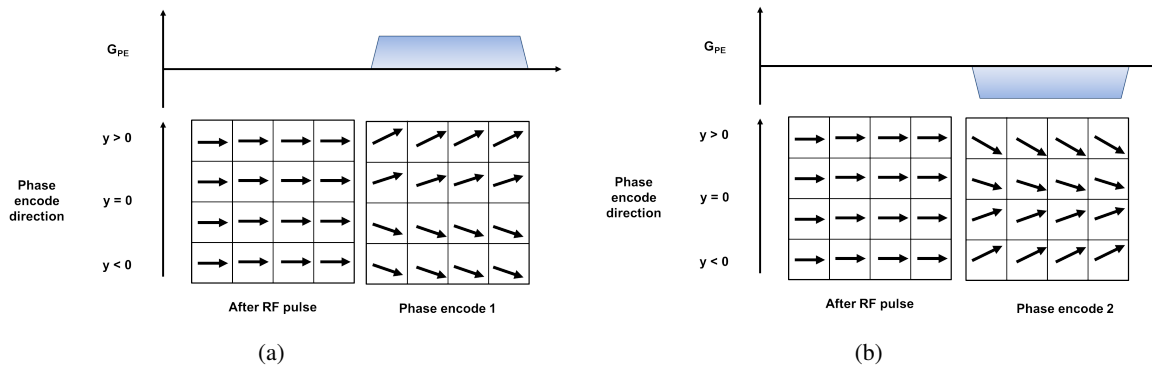


Figure 2.37: Phase encoding schematic for 16 pixel image [101]. Whilst no gradient is applied, the transverse magnetisations (arrows) are in phase. When a positive gradient is applied (left), the magnetisations dephase according to their position along the gradient direction and a position-dependent phase difference is formed. A similar process, but with the dephasing occurring in the opposite direction, is seen with a negative gradient (right).

k space sampling

A simple MR pulse sequence captures one line of k space at a time and must therefore be repeated within a repetition time (TR) and with different phase encode gradient values to sample the whole space, as shown in Figure 2.38. In this example Cartesian k space sampling scheme, we begin at $(0,0)$ ¹¹ and move to $(-k_{FE}, -k_{PE})$ with the application of negative phase encode and negative frequency encode lobes. The application of the larger positive frequency encode moves the readout along the k space line to $(k_{FE}, -k_{PE})$. Once all k space values are filled, k space is 2D inverse Fourier transformed back into real space to create the image [86].

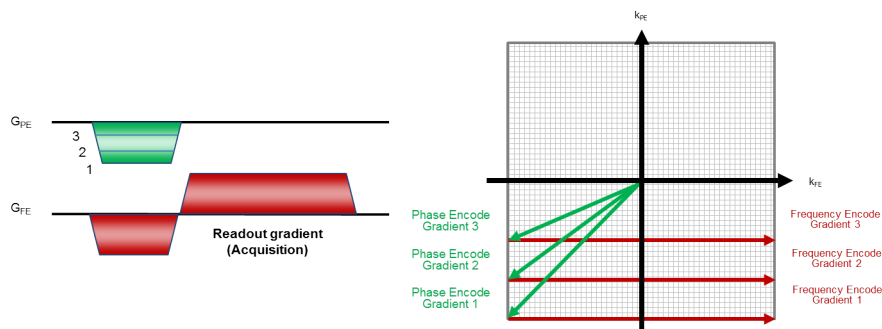


Figure 2.38: k space diagram of a simple Cartesian k space sampling scheme, with each phase encoding step associated with a separate k space line.

MR pulse sequences

All these components can be represented in a pulse sequence diagram which describes how the gradients and RF pulses are applied. All pulse sequences have the same fundamental components, beginning

¹¹When no gradients are applied, we get the signal from the whole object, referred to as zero spatial frequency.

with RF excitation and acquiring echo signal data using three orthogonal gradient fields (slice select, frequency encode and phase encode) to spatially encode the signal [102]. An example of a 2D gradient echo imaging pulse sequence is shown in Figure 2.39.

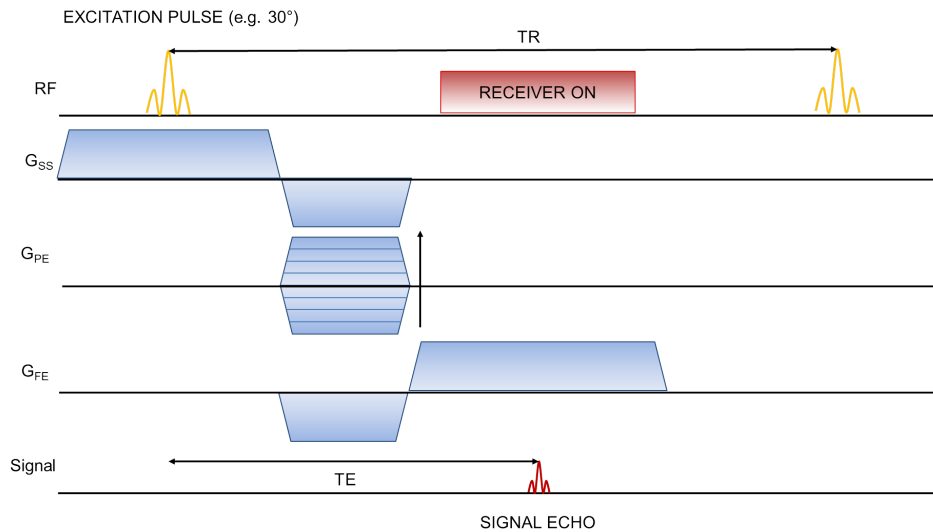


Figure 2.39: 2D MRI pulse sequence diagram for gradient echo acquisition. RF pulse excites a slice determined by the slice select gradient, whose signal echo is then rephased and encoded in k space using a combination of the phase and frequency encoding gradients. The phase encode gradient is changed each TR to record a different line of k space in the readout direction from the signal echo.

MRI images can also be acquired in 3D mode, where a slab of the patient is excited by the RF pulse instead of a slice and a second set of phase encoding gradients are added in the slice select direction to encode spatial frequencies in 3D k space (an additional k_z direction is added to the k_x and k_y directions used for frequency and phase encoding). An example of a 3D pulse sequence is shown in Figure 2.40.

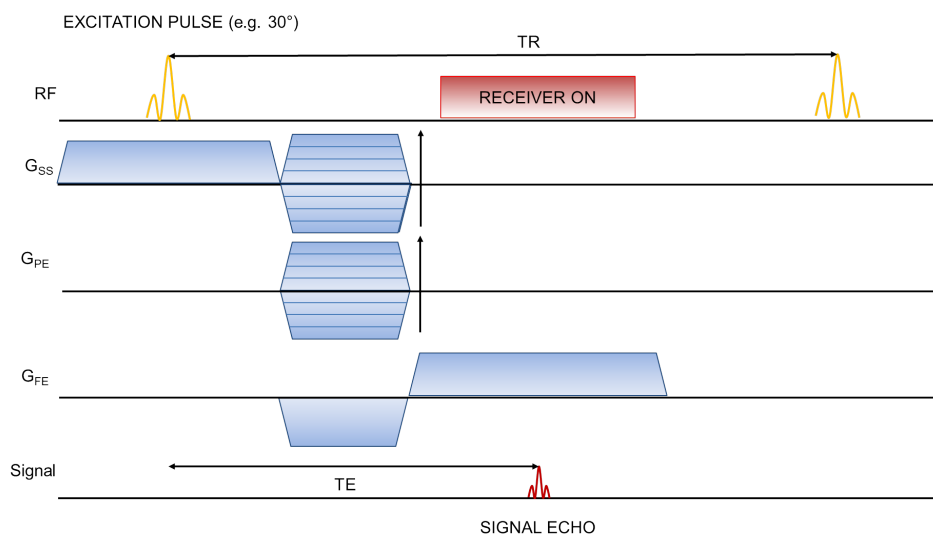


Figure 2.40: 3D MRI pulse sequence diagram, showing second phase encoding gradient on slice select axis to provide additional encoding of slab excited using RF pulse.

Once 3D k space is filled, the data undergo a 3D Fourier transform to create an image. By acquiring a slab, slices are obtained with more uniform slice profiles, as shown in Figure 2.41.

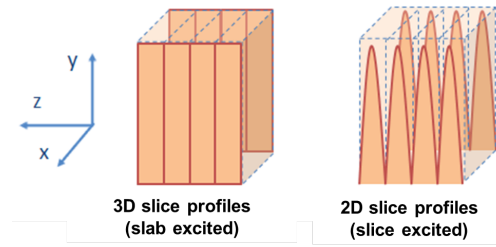


Figure 2.41: Slice profiles schematic, adapted from [103]. 2D acquisition (right) gives gaussian slice profiles, with more signal coming from the centre of each slice than the edges. Dotted blue lines indicate the gaps between successive slices which are used to reduce cross-talk. In 3D, (left) slices are rectangular and contiguous, meaning that signal is derived uniformly from each slice.

The main disadvantage of 3D acquisition is that the total scan time required for the 3D sequence is equal to the 2D scan time (no. of averages \times no. of phase encode lines \times TR) multiplied by the number of additional phase encode lines obtained in 3D [102].

2.2.4 Relaxation rates and image contrast

The relaxation of the magnetisation signal is modelled in the Bloch equations [104] using first order kinetics, which assume that nuclear spins undergo relaxation at different rates along the z axis and the x-y plane.

- **T1 is a time constant that describes the spin lattice relaxation time**, the exponential recovery of the longitudinal magnetisation along the -z axis back to equilibrium as a result of thermal energy exchanges between the spin system and the surrounding environment [102].
- **T2 is a time constant that describes the spin-spin relaxation time**, the exponential decay of the transverse magnetisation within the x-y plane as a result of individual proton magnetic moment interactions. Protons experience slightly different magnetic fields dependent upon their local environment and hence precess at different frequencies, as governed by the Larmor equation. The protons thus relax at different rates, leading to the net magnetisation to fall as the individual moments move out of phase with each other [102].
- **T2*, the relaxation constant of the FID** which incorporates the effect of T2 relaxation, inhomogeneity in the magnetic field and differences in susceptibility, as described in equation (2.22),

$$\frac{1}{T2^*} = \frac{1}{T2} + \frac{1}{T2'} \quad (2.22)$$

where T_2' is inversely proportional to the magnetic field inhomogeneity ΔB in each imaging voxel [102].

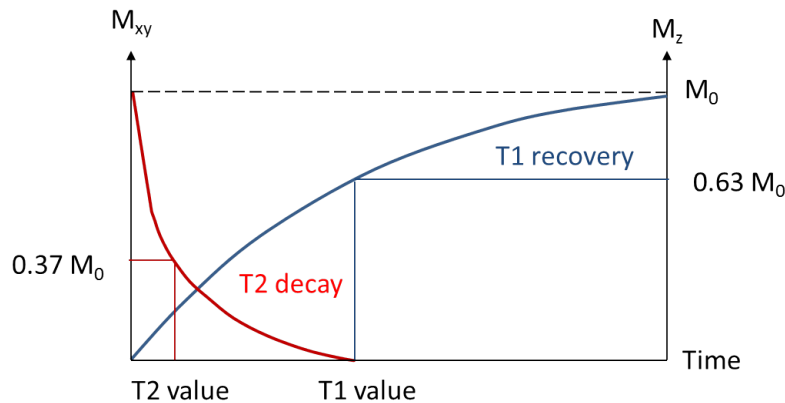


Figure 2.42: T1 recovery and T2 decay profiles after a 90° pulse.

Tissue MR signal depends upon the different T1 and T2 values of that tissue, shown in Figure 2.43. Contrast is defined as the ability to distinguish between intensity values in an image, with high contrast and high SNR indicating a high quality image [86]. Pulse sequences are designed to optimise tissue contrast and create images “weighted” toward a relaxation effect, with examples shown in Figure 2.44.

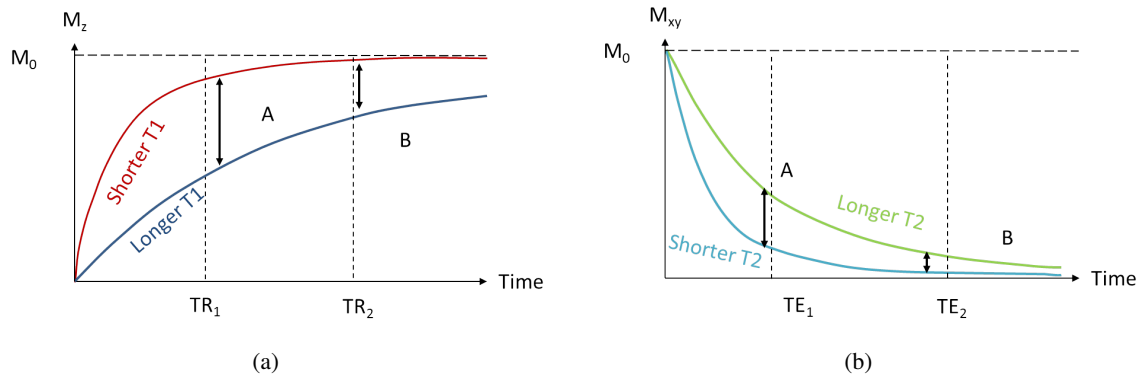


Figure 2.43: The effect of different T1 and T2 values on tissue signal (A=high contrast, B=low contrast).

The greater the weighting, the more sensitive the signal intensity becomes to differences in the relaxation parameter. T1-weighted images are typically used to differentiate between white and grey matter in the brain, as white matter appears brighter due to its lower T1 value. T2-weighted images are frequently used to image edema, as water appears brighter due its longer T2 value [105].

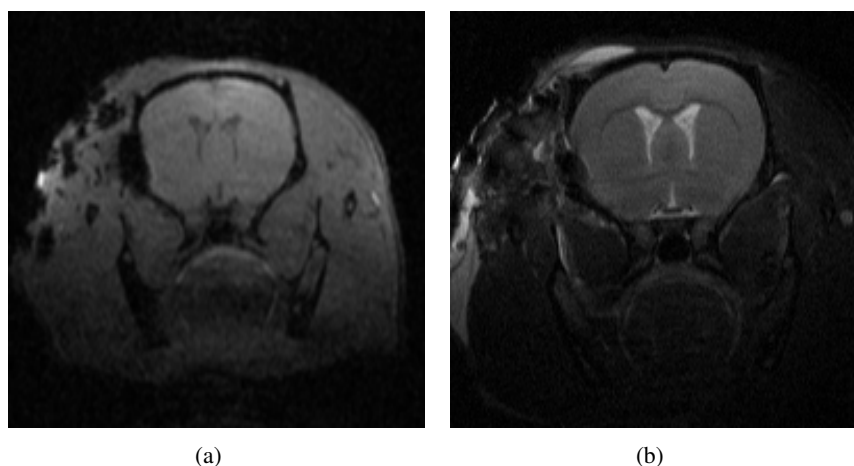


Figure 2.44: (a) T1-weighted and (b) T2-weighted image of a rat brain.

In addition to the natural MR contrast created by tissues, contrast agents can be injected into the subject via venous cannulas to improve the specificity of MR images and to increase SNR. The tail vein or femoral vein is used in rodents.

Gadolinium-based contrast agents (such as those shown in Figure 2.45) are paramagnetic due to the Gd chelation in the ligand, which possesses seven unpaired electrons. These contrast agents are designed to be non-toxic (Gd is toxic in its elemental form), stable *in vivo* and are completely eliminated from subjects within 24 hours. As a result of their paramagnetic nature, Gd-based contrast agents shorten the T1 (and T2) of tissues where they accumulate, giving an enhanced signal on T1 weighted images [106]. This effect is used most often in brain oncology, particularly in glioblastoma where highly vascular tumours will be greatly enhanced thanks to a large presence of contrast agent resulting from the breakdown of the blood brain barrier (BBB) [107].

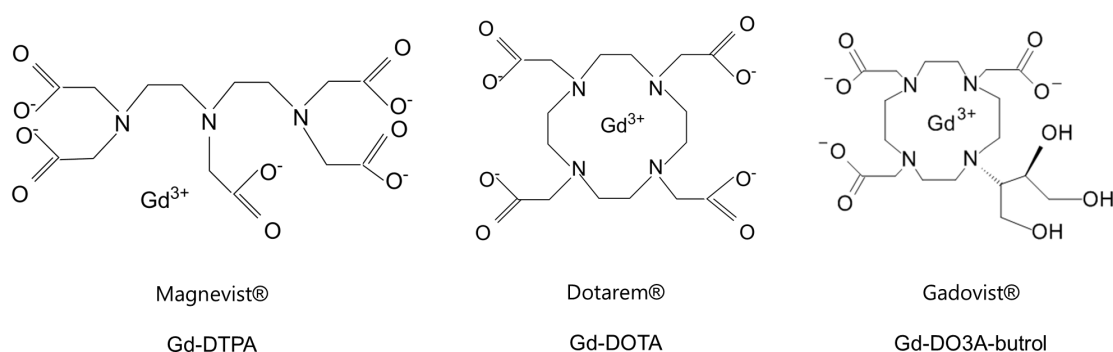


Figure 2.45: Chemical structure of MR contrast agents Magnevist, Dotarem and Gadovist [108], which display high levels of stability, indicating that it is difficult to remove the Gd ion from the chelate. Different structures give rise to different relaxivities, which indicate how much of an effect each contrast agent has on T1 and T2 in tissue.

The following sections detail the MRI pulse sequences used throughout this thesis.

2.2.5 Structural MRI pulse sequences - FISP MRI

The majority of MRI imaging pulse sequences required for PET/MR studies are anatomical sequences which have much higher resolution than PET data. A simple sequence used to perform mouse whole body imaging with good SNR is the Fast Imaging with Steady Precession (FISP) sequence, shown in Figure 2.46. The transverse magnetisation is rewound, meaning that the signal contains FID enhanced with echo and coherent transverse components. This gives more signal than spoiled gradient echo (see next section) but a more complex signal weighting. FISP images are proton density (PD) weighted at low flip angle ($\alpha < 20^\circ$) and at $\alpha > 45^\circ$ it depends on the ratio of T1/T2 [86].

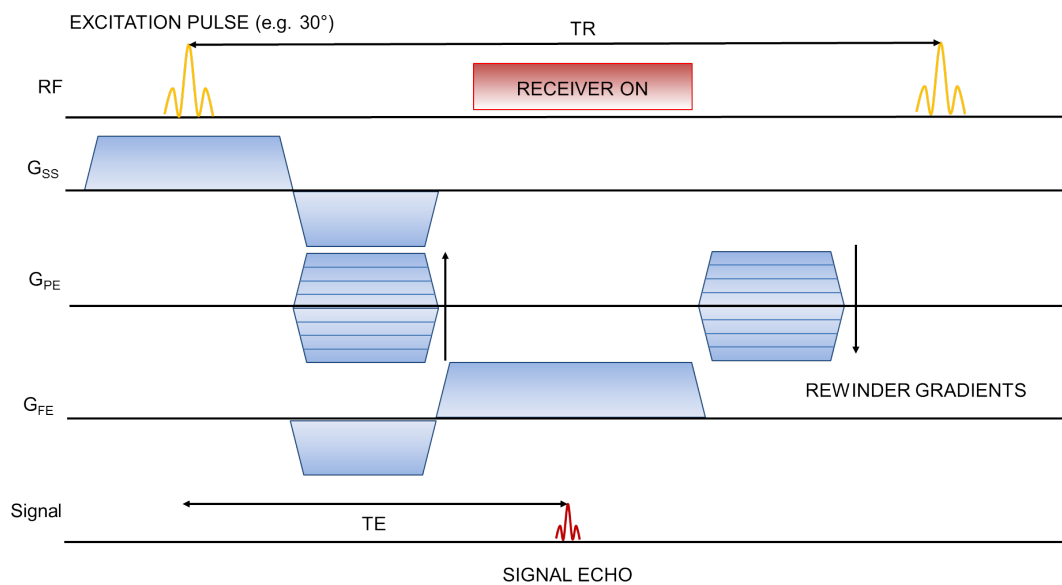


Figure 2.46: FISP pulse sequence. To increase the available signal, rewinder gradients in the phase encode direction are added to the standard gradient echo sequence. The signal therefore contains the FID enhanced with echo and fresh transverse components.

Gradient echo sequences such as FISP are favoured for cardiac imaging due to their short TRs which enable rapid imaging and their high image contrast between the moving blood and myocardium [86]. FISP can be used in cine acquisitions to acquire cardiac motion gated images of the different temporal phases of the cardiac cycle via triggering from ECG traces, as shown in Figure 2.47 for both prospective and retrospective gating schemes.

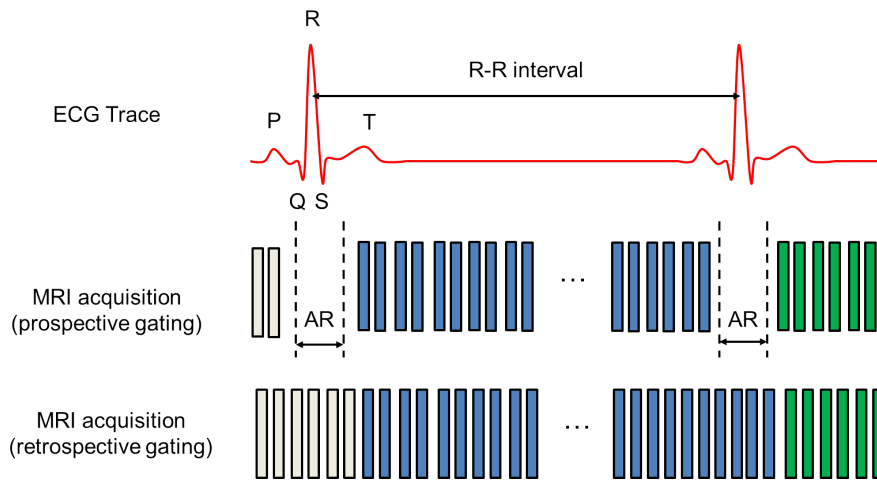


Figure 2.47: ECG triggered imaging schematic, adapted from [86], with PQRST phase labelled ECG trace (top row). Each box represents a FISP sequence acquisition, which acquires one line of k space data. This is repeated throughout the cardiac cycle using either prospective (middle row) or retrospective gating (bottom row). In prospective gating, an arrhythmia rejection window (AR) is used, during which the MRI sequence is not acquired to allow for variations in subject heart rate. In retrospective gating, the sequence is allowed to run independent of heart rate, with the ECG trace only used to trigger and update the phase encoding gradient to acquire the next line of k space. The position of the data within the cardiac cycle is determined after data collection.

To speed up image acquisition and to reduce image blurring from respiratory motion, segmented k space schemes are used to acquire multiple k space lines per heart beat for the different temporal phases of the heart cycle. Each image is therefore composed from data gathered over several heart beats, as shown in Figure 2.48.

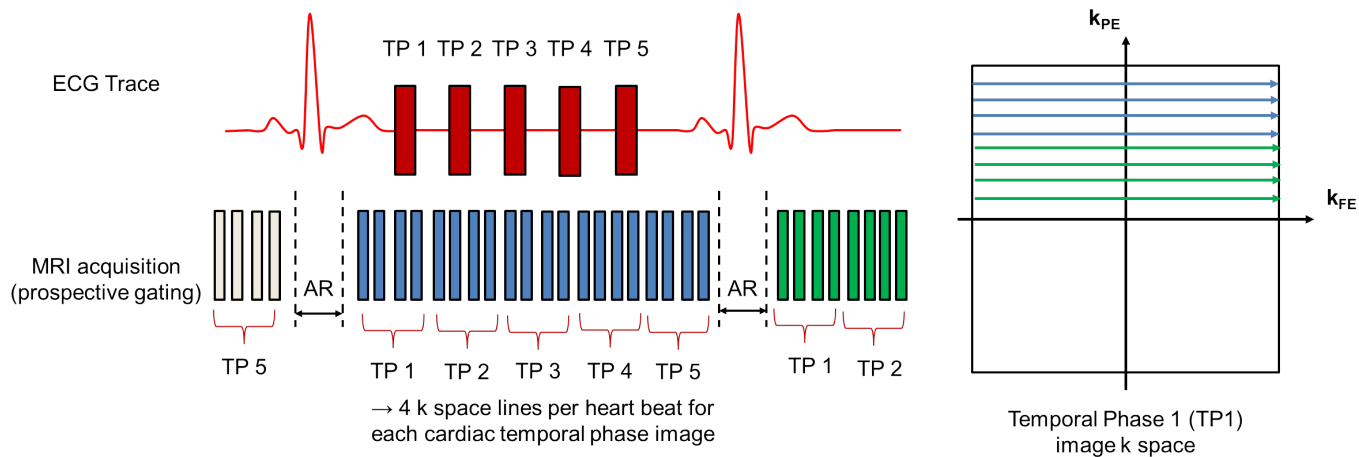


Figure 2.48: Segmented k space data acquisition schematic, used to acquire multiple lines of k space for each temporal phase (TP) of the cardiac cycle per heartbeat. In this example, k space is segmented such that 4 lines are acquired at once (i.e. 4 phase encode gradients are used), leading to an acceleration in acquisition time by a factor of 4.

2.2.6 Structural MRI pulse sequences - FLASH MRI

An alternative to FISP for structural imaging is the Fast Low Angle SHot (FLASH) technique. Image contrast generated by FISP is dependent on the flip angle of the sequence and the ratio of T1/T2 [86], giving high contrast between fluid and solid structures. In contrast, FLASH produces PD or T1 weighted images (depending on the flip angle used¹²), which generates images with high white/grey matter contrast in the brain [86]. Signal saturation occurs if pulses are applied before the longitudinal magnetisation has fully relaxed (thus exciting only a component of the magnetisation) and the effect is continuous with each subsequent pulse until the excitation and relaxation processes form a steady state. Sequences such as FLASH employ spoiling techniques to destroy magnetisation in the x-y plane before each new excitation [109], thus allowing for rapid acquisition of T1 weighted images [110], [111].

FLASH employs both a spoiling gradient in the slice select direction and phase offsets in the RF excitation pulses to spoil any remaining magnetisation in the transverse plane, with each spoiling method shown in Figures 2.49 and 2.50 respectively. Without any spoiling applied, there can be interference between different phase encoded signals from different excitations which can lead to FLASH band artefacts appearing parallel to the frequency encode direction in the images [109].

In gradient spoiling (see Figure 2.49), the residual transverse magnetisation is destroyed by applying a different gradient for each sequence repetition to dephase the non-echo forming parts of the signal.

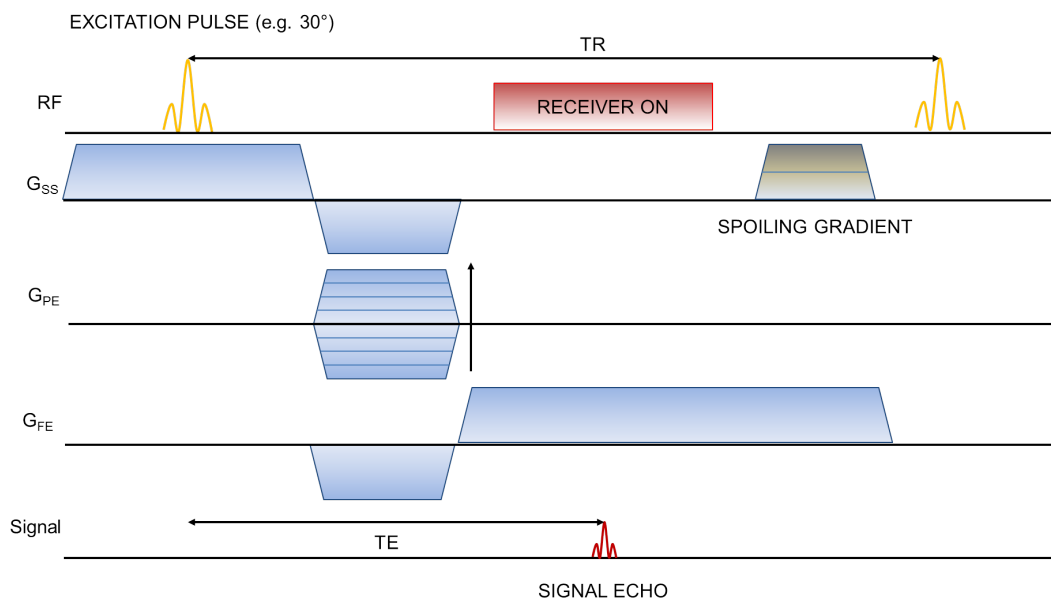


Figure 2.49: FLASH pulse sequence diagram, showing slice select spoiling gradient and extended readout gradient for spoiling. The spoiling gradients are of varying size to stop spoiled signals forming echoes [86].

¹²As seen later in equation, (2.25), the FLASH signal depends on the T1 of the tissue under study. The Ernst angle gives the maximum signal from a sequence where repeated RF excitations are made, $\alpha_{Ernst} = \cos^{-1}(\exp(-\frac{TR}{T1}))$. Images produced with $\alpha > \alpha_{Ernst}$ are T1 weighted and are PD weighted when $\alpha < \alpha_{Ernst}$ [86].

For phase spoiling (see Figure 2.50), a phase offset is applied to each successive RF excitation pulse, such that residual magnetisation in the x-y plane always points in a different direction, preventing any magnetisation building up [112], [113]. Usually phase encodes are rewound (as in FISP) to avoid spatial inhomogeneities.

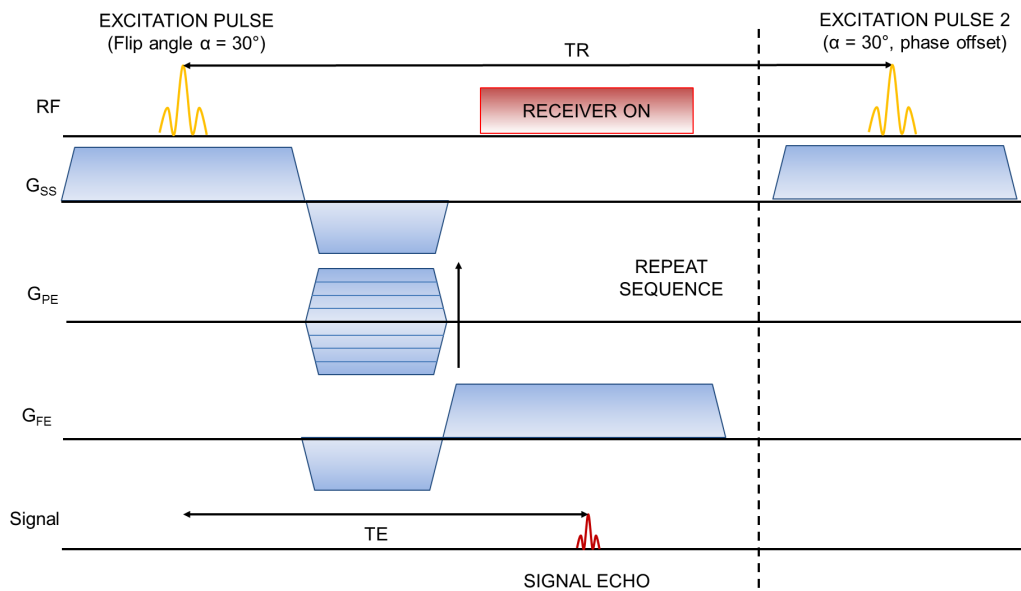


Figure 2.50: FLASH pulse sequence diagram, showing phase offsets in RF pulses to produce spoiling.

FLASH can also be combined with ECG signals to give gated cardiac images by acquiring segmented k space data, as shown in Figure 2.48. This process is repeated over several heartbeats to fill k space completely [86].

If no ECG signal is available, a self-gating sequence such as IntraGate FLASH (IG-FLASH) can be used on Bruker small animal MRI systems, which uses a navigator slice signal (positioned as a saturation slice above the lungs and heart) to estimate the stages of the cardiac cycle from the blood signal within the saturation slice. This navigator provides retrospective gating for cardiac and respiratory motion, although blood appears black on IG-FLASH images (in contrast to its usual white appearance on FLASH images) due to signal suppression by the regional flow saturation band [114]. The modified pulse sequence is shown in Figure 2.51, with data taken over a series of heart beats, gated according to the navigator signal.

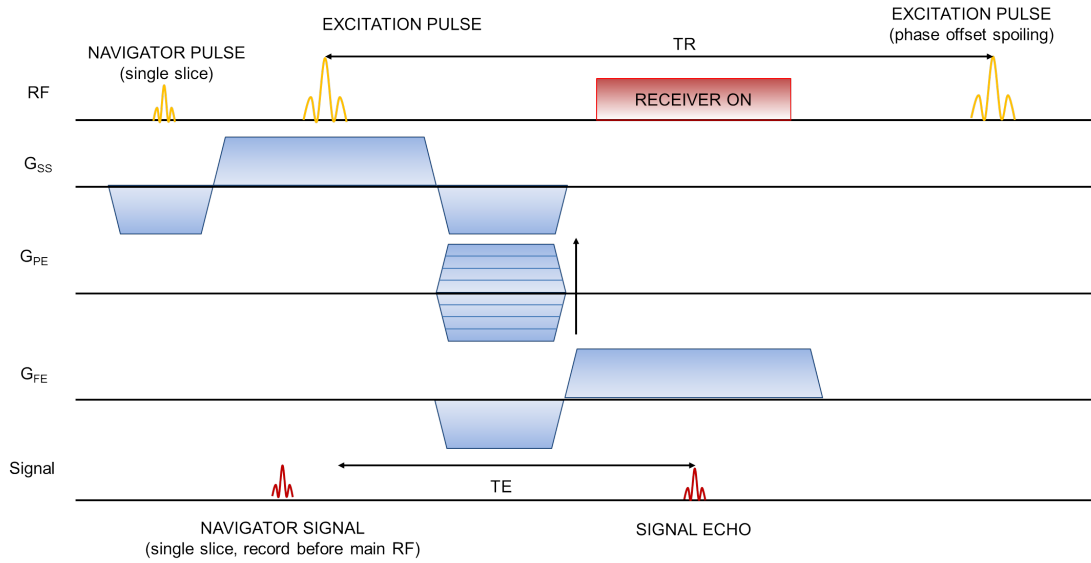


Figure 2.51: FLASH pulse sequence diagram, with additional saturation slice added above heart. Navigator signal derived from refocusing of saturation slice. Navigator is used to estimate the cardiac cycle stage and retrospectively gate the segmented FLASH acquisition.

2.2.7 Structural MRI pulse sequences - RARE MRI

Rapid Acquisition with Relaxation Enhancement (RARE) describes a fast spin echo MRI sequence used to produce high resolution, T2 weighted structural images. This sequence is based on the spin echo principle illustrated in Figure 2.32 but instead of simply encoding a single echo signal using the slice select, frequency and phase encoding gradients, fast spin echo sequences also employ phase rewinder gradients to undo the dephasing of the spins. A phase encoding step of equal strength but opposite sign is applied after the acquisition of each echo in the train, with the result that different phase encoding can be applied for each echo, as shown in the pulse sequence diagram in Figure 2.52.

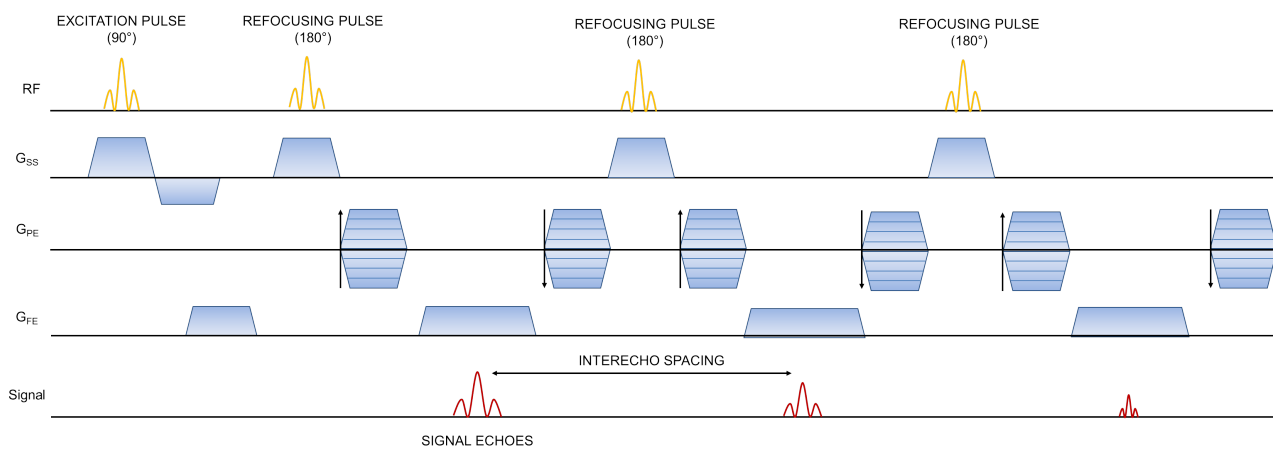


Figure 2.52: RARE pulse sequence diagram, with echo train length (RARE factor) of 3. Interecho spacing denotes the fixed time between successive echoes and arrows on phase encoding direction indicate direction of changing phase encoding (rewinder gradients).

In RARE, one line of k space is sampled in each of the intervals between successive refocusing pulses and each echo is used to fill a different segment of k space¹³, a different third in the case of Figure 2.52, illustrated in Figure 2.53. The echo train length in each TR (i.e. number of echoes generated in time to next 90° pulse) defines the acceleration of the sequence compared to standard spin echo and is also known as the RARE factor of the sequence [86]. The RARE factor is 3 in Figure 2.52 and the whole sequence repeats after TR with different phase encoding steps.

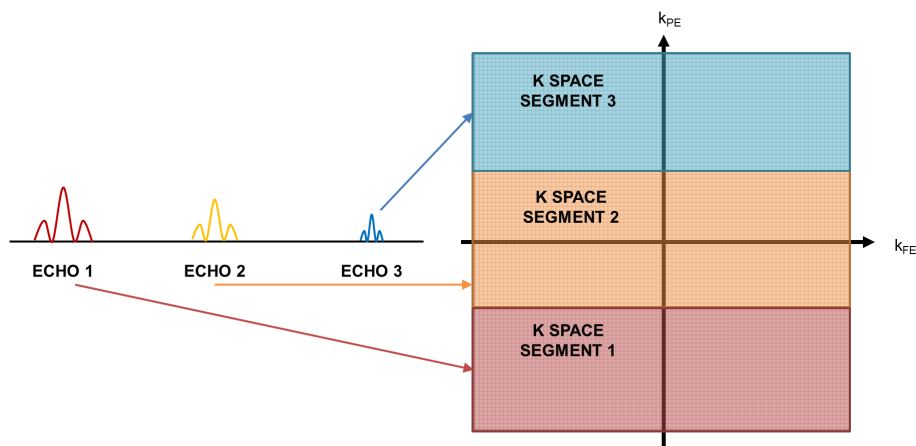


Figure 2.53: RARE data acquisition in k space with RARE factor of 3, adapted from [86]. Effective TE is given by time from initial excitation to echo which covers the central k space segment, which gives the majority of contrast in the image (echo 2 in this case).

As different segments of k space are acquired with different echoes, different lines of k space have different levels of T2 weighting and therefore very high RARE factors are not recommended, as signal from late echoes will be attenuated as a consequence of T2 relaxation.

2.2.8 Vascular MRI pulse sequences - Time of flight MR angiography

Magnetic Resonance Angiography (MRA) produces images of blood flow through a patient, making blood vessels appear distinct from tissue and produces rodent angiograms non-invasively. Time of flight MRA (TOF-MRA) uses a spoiled gradient echo sequence with short TR and TE to utilise the signal produced from moving spins inside flowing blood as indigenous contrast [86], [115].

When a gradient acts on stationary spins, the spins acquire a phase shift proportional to the magnitude and duration of the applied gradient. By balancing the gradients, no net phase shift exists after slice selection or at signal acquisition for static spins, although moving spins at a constant velocity acquire an induced phase shift, explained in Figure 2.54.

¹³To avoid N/2 Nyquist ghosting artefacts in the image, which result from slight mispositioning of alternate echoes due to small gradient imperfections, phase correction is applied [86]. This stops the mis-registration of alternating k space lines by using a 1D FT of a reference scan taken without phase encoding to calculate the required phase correction.

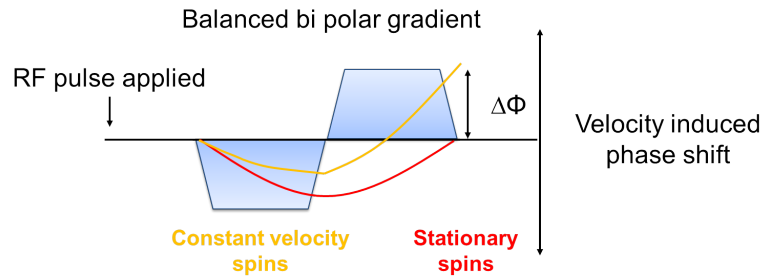


Figure 2.54: Phase shift created using equal area (balanced) bipolar gradients, adapted from [86].

Bipolar gradient lobes are added to MRA pulse sequences to provide flow compensation in the slice select and frequency encoding directions [115], as explained in Figure 2.55.

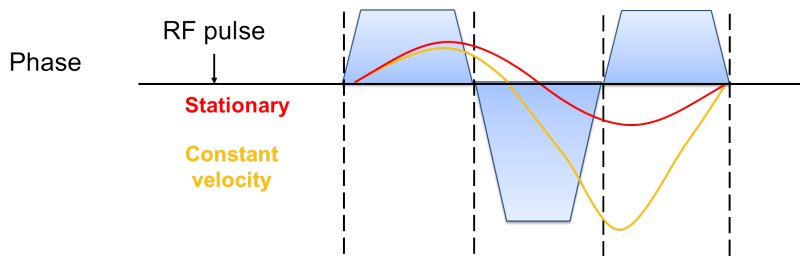


Figure 2.55: Gradient moment nulling. Zero net phase shift using equal area (balanced) tri-lobed gradients (1:2:1 configuration) for flow compensation, which act to unwind phase shift from moving spins.

The pulse sequence diagram for 2D TOF MRA (essentially a FLASH sequence with flow compensation) is shown in Figure 2.56. Short TR and short TE mean that tissue slice signal is saturated from stationary spins, whilst unsaturated spins flowing into the imaging slice yield MR signal.

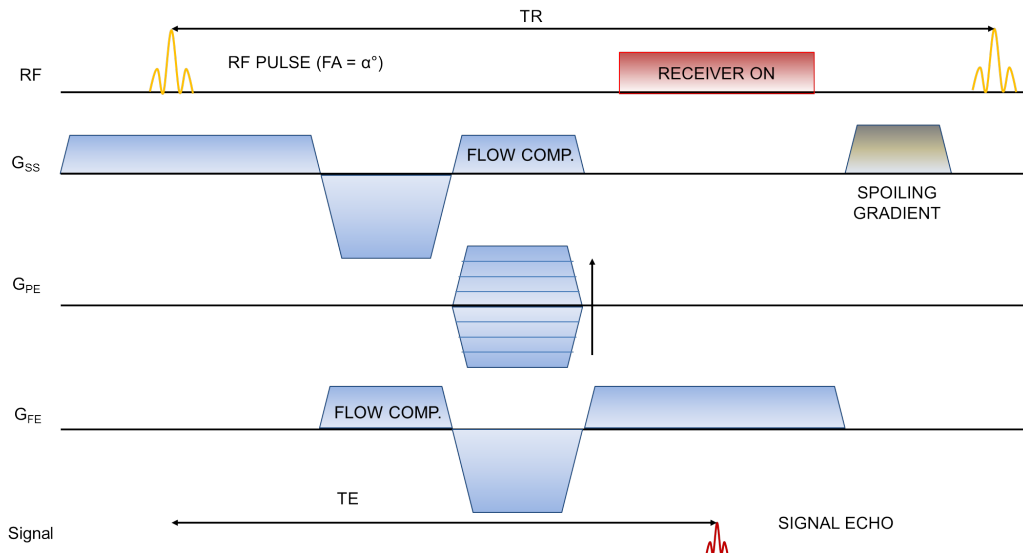


Figure 2.56: 2D TOF MRA pulse sequence, with tri-lobed velocity compensation gradients on slice select and frequency encoding axes. The phase encode gradient remains unbalanced - there are flow compensation schemes for the phase encode gradient [115], but in most 2D TOF MRA applications, the short duration of the phase encode gradients minimizes the effect of motion during their application [116].

Figure 2.57 illustrates how TOF-MRA uses a saturation RF pulse to suppress the tissue signal from a slice and records the increased signal from unsaturated protons which flow into that slice in the artery. The signal magnitude produced on the angiography image depends on the speed at which the spins are moving through the imaging slice, as illustrated in Figure 2.58. When blood is stationary ($v = 0$), it becomes saturated the same way as tissue of slice thickness z , but due to the long T_1 of blood it will appear with reduced signal on a T_1 weighted FLASH image. When the blood velocity reaches $v = \frac{z}{2TR}$, there will be increased MR signal from blood due to the partial inflow of unsaturated spins over a TR . The maximum signal is reached when the blood can completely transport itself across the slice thickness over a TR , i.e. $v \geq \frac{z}{TR}$, as there is the maximum inflow of unsaturated spins to the slice [86].

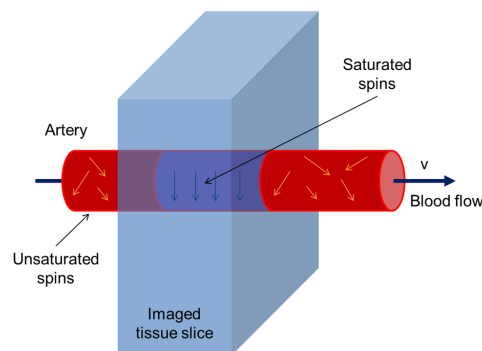


Figure 2.57: Schematic of TOF MRA signal generation through imaging slice.

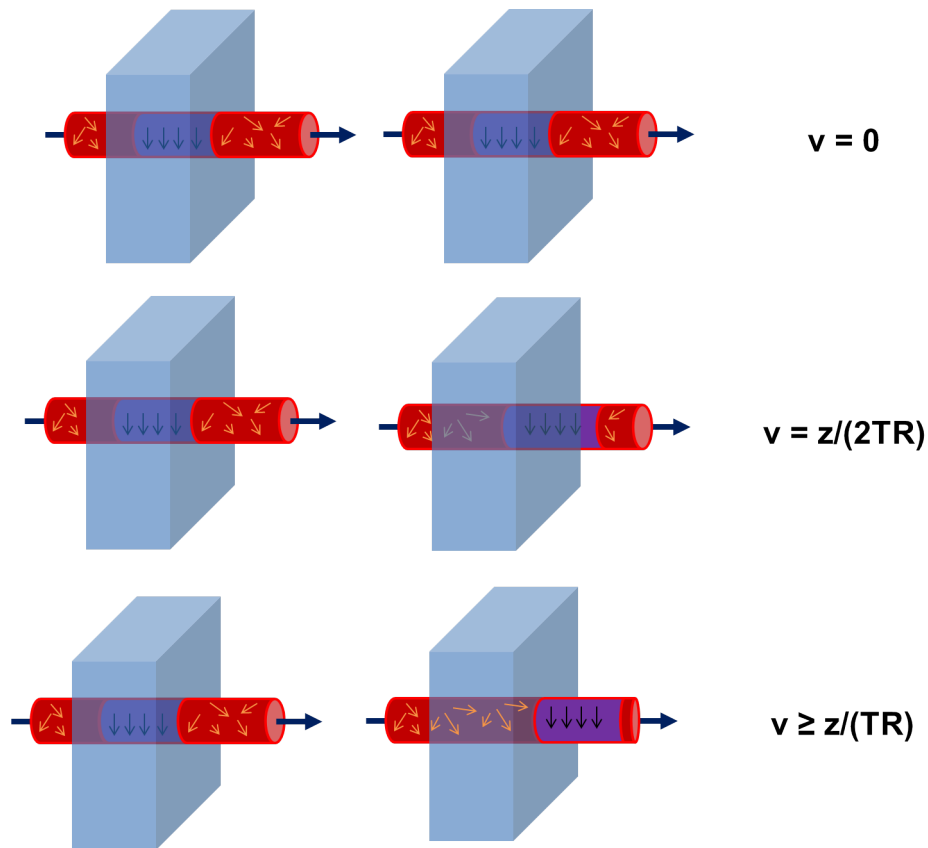


Figure 2.58: TOF effect response to blood flow speed, where v is the blood flow speed, TR is the repetition time of the MRA sequence and z is the slice thickness. No enhancement seen at $v = 0$, partial signal seen when $v = z/(2TR)$ and maximum signal seen when $v \geq z/TR$.

The TOF-MRA sequence is repeated for multiple slices taken perpendicular to the flow direction to maximise the inflow effect [86]. Maximum intensity projections (MIPs) are used to view the results, which project rays through each 2D slice to find the maximum pixel value along the line and then repeat this process after rotating the data at 5° intervals up to 180° . Finished MIPs of stacked slices are interpolated to display the results in 3D, as shown in Figure 2.59.

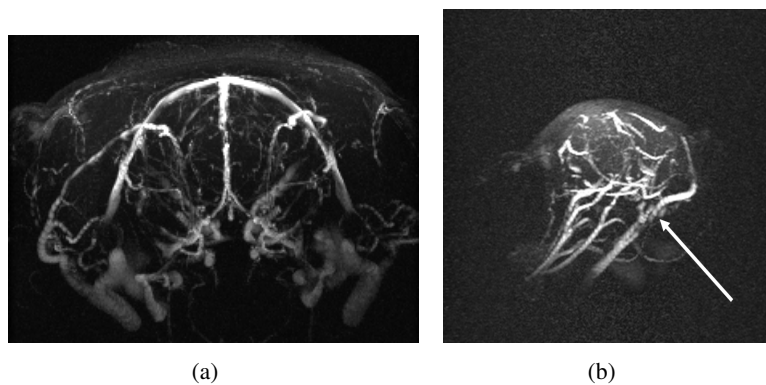


Figure 2.59: (a) 2D TOF MRA rat brain MIP, axial view (b) TOF MRA mouse brain MIP in 3D, showing contrast between bright blood vessels (arrow) and dark tissue in sagittal view.

2.2.9 Dynamic MRI pulse sequences - DSC MRI

The dynamic MRI sequences used in this thesis are all used in conjunction with injections of Gadolinium based contrast agents. Dynamic susceptibility contrast (DSC) MRI is used to assess perfusion *in vivo* [117], [118], [119], [120] by tracking a bolus of exogenous, paramagnetic contrast agent through the brain. Since the transit time of the bolus is only a few seconds, high temporal resolution imaging is required to observe the wash in and wash out of the contrast agent through the brain [121], [122].

Echo Planar Imaging

The high speed required to perform bolus tracking requires a T2*-weighted (gradient echo-based) Echo Planar Imaging (GE-EPI) sequence. The high speed of acquisition (<1s per frame) is achieved by scanning rapidly through multiple lines of k space in the frequency encode direction during each FID and using the phase encode gradient to “jump” from one k space line to the next, shown in Figures 2.60 and 2.61.

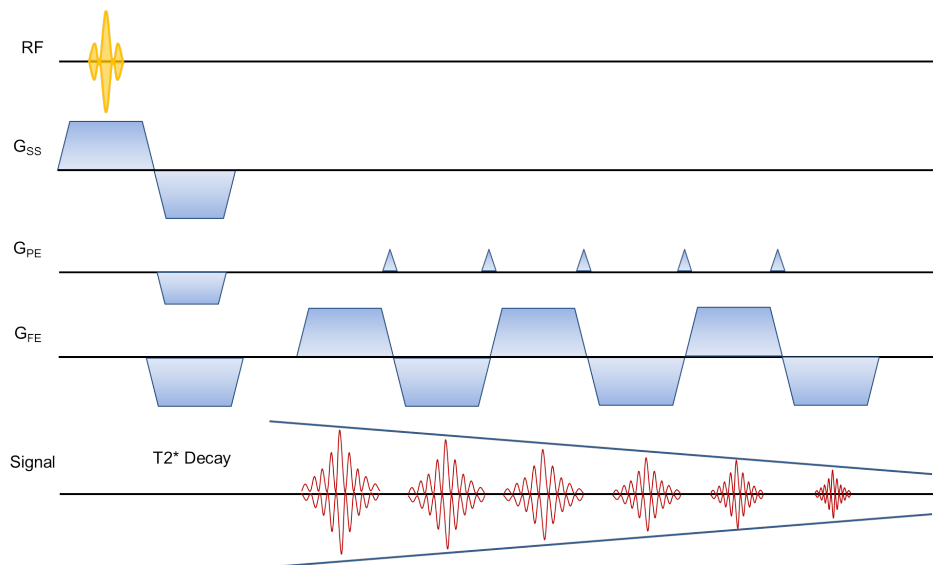


Figure 2.60: Blipped GE-EPI pulse sequence, with multiple k space line readout using a single shot gradient echo technique.

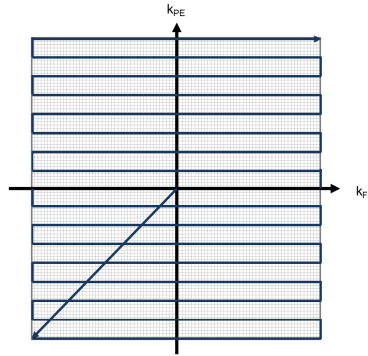


Figure 2.61: GE-EPI k space diagram. Each blip changes the phase encoding of the signal and is followed by a frequency encode gradient to read out each line of k space, which allows for rapid imaging that is limited by rate of gradient switching.

Interpretation of DSC MRI signal

Gadolinium-based contrast agents are paramagnetic and therefore the first passage of a contrast agent bolus through the cerebral vasculature produces a transient signal drop on $T2^*$ weighted EPI images. This effect results from local magnetic susceptibility changes within the vasculature, resulting in spins dephasing due to microscopic changes in the magnetic field, and this effect dominates over $T1$ relaxation enhancement [121]. The $T2^*$ mechanism is therefore preferred to $T1$ for cerebral perfusion studies, as it produces stronger signals in the first passage of the bolus, allowing the bolus to be tracked at high speed through the brain. The signal drop can be expressed as a change in $R2^*$ ($1/T2^*$) shown in equation (2.23) [123].

$$\Delta R2^* = -\frac{1}{TE} \ln \left(\frac{S(t)}{S_0} \right) \quad (2.23)$$

$\Delta R2^*$ is assumed to be proportional to the concentration of contrast agent [124] and is also assumed to be unaffected by vessel size (i.e. both large blood vessels and smaller ones from the microvascular contribute to the signal in gradient echo $T2^*$ EPI) [125]. The exact proportionality constant depends on the tissue under study, the contrast agent used, the field strength of the magnet and the pulse sequence parameters [121]. It is used as a measure of contrast agent concentration-time curves in various regions of interest (ROIs). To attain perfusion information such as cerebral blood flow (CBF), the ROI signal-time course can be analysed in conjunction with an arterial input function (AIF), defined as the concentration-time curve from arterial voxels directly feeding the ROI. The mathematics of this process are described in detail in Chapter 3. An example of the conversion of the signal loss into a concentration time curve is illustrated in Figure 2.62.

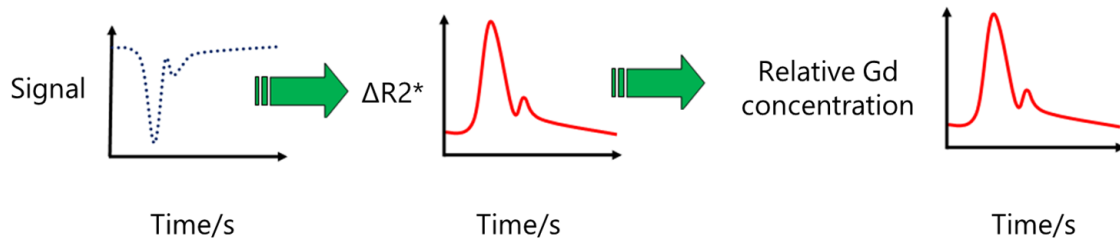


Figure 2.62: Schematic signal conversion using equation (2.23). Note that the Gadolinium concentration is only *proportional* to the change in $R2^*$.

2.2.10 Dynamic MRI pulse sequences - DCE MRI

Dynamic contrast enhanced MRI (DCE MRI) is used to assess BBB permeability by measuring quantitative changes in injected MRI contrast agent concentrations over time. DCE MRI is performed by observing signal enhancement on T1-weighted images due to the apparent change in T1 from the presence of the paramagnetic contrast agent within the vasculature, expressed in equation (2.24) [126], [127], which assumes a linear relation between $R1$ ($\frac{1}{T1}$) and contrast agent concentration in the fast exchange limit [106].

$$\frac{1}{T1^*} = \frac{1}{T1_0} + r1 \times [CA] \quad (2.24)$$

where $T1_0$ is the initial T1, $T1^*$ is the apparent T1 observed, $[CA]$ is the contrast agent concentration and $r1$ is the relaxivity of the contrast agent in mMs^{-1} . The relaxivity ($r1$) value defines the exact relationship between the observed change in T1 and concentration of contrast agent for each MR contrast agent, which is also dependent on field strength and temperature [106], [128]. Shortening of T1 occurs via thermal vibration of metal ions, creating oscillating magnetic fields which correspond to the change in energy (ΔE) between spin states and result in stimulated emission from high to low energy states.

FLASH using Variable Flip Angles (VFA) for DCE MRI

T1 is attained by analysing the FLASH signal (assumed to be perfectly spoiled, i.e. there is no build up of steady state transverse magnetization) from variable flip angle (VFA) acquisitions, using equation (2.25). FLASH is used to acquire T1 maps as it is considerably faster than standard inversion recovery techniques. The FLASH sequence used to perform DCE MRI in this thesis uses both phase and gradient spoiling, as described in Figures 2.49 and 2.50. It was also acquired in 3D, following the acquisition scheme of Figure 2.40. A 3D sequence was used as they have better flip angle accuracy than 2D se-

quences, due to multi-slice 2D sequences having poor slice profiles, leading to a distribution of flip angle values across each slice and a resulting error in the T1 values attained [129], [130].

To create a T1 map, typically between 3 and 8 different flip angles (FA) over a range of values from 2-50° are acquired in a single 4D acquisition, as different tissue types have different T1 values and a range of contrasts are required to measure these accurately.

$$S(t) = S_0 \exp\left(\frac{-TE}{T2^*}\right) \left(\frac{\sin \alpha (1 - \exp(\frac{-TR}{T1}))}{1 - \cos \alpha \exp(\frac{-TR}{T1})} \right) \quad (2.25)$$

where α is the flip angle of the pulse, TE is the echo time, TR is the repetition time, S(t) is the observed signal for each flip angle and S_0 is the equilibrium signal for each flip angle.

The majority of previous work [131], [132] rearranges the FLASH signal equation and extracts the apparent T1 using a linear plot (see equation (2.26)) of $\frac{S}{\sin \alpha}$ against $\frac{S}{\tan \alpha}$ for each flip angle, as shown in (2.27),

$$y = m x + c \quad (2.26)$$

$$\frac{S}{\sin \alpha} = \frac{S \exp(\frac{-TR}{T1})}{\tan \alpha} + S_0 \exp(\frac{-TE}{T2^*}) \left(1 - \exp(\frac{-TR}{T1}) \right) \quad (2.27)$$

The gradient, m, is therefore taken as $\exp(\frac{-TR}{T1})$ and can be re-arranged to calculate T1, as shown in equation (2.28). It is vital that the baseline T1 values are accurate in order to give accurate contrast agent concentration-time curves and should be measured on an individual basis if possible to account for variation in T1 between subjects [129], [130], [133], [134].

$$T1 = \frac{-TR}{\ln(m)} \quad (2.28)$$

Once the baseline T1 value is known, the apparent T1* value due to the presence of contrast agent must be measured, as shown in Figure 2.63. This is done by selecting a single FA (typically in the range 8-20°) which provides optimum contrast throughout the subject and repeating this single FA scan multiple times during the administration of contrast agent injection. Whilst the T1 map can take up to several minutes to acquire, ideally the repeated single FA scans will have acquisition times of $\approx 3-5$ s to record the contrast agent dynamics accurately [133], [134], [135].

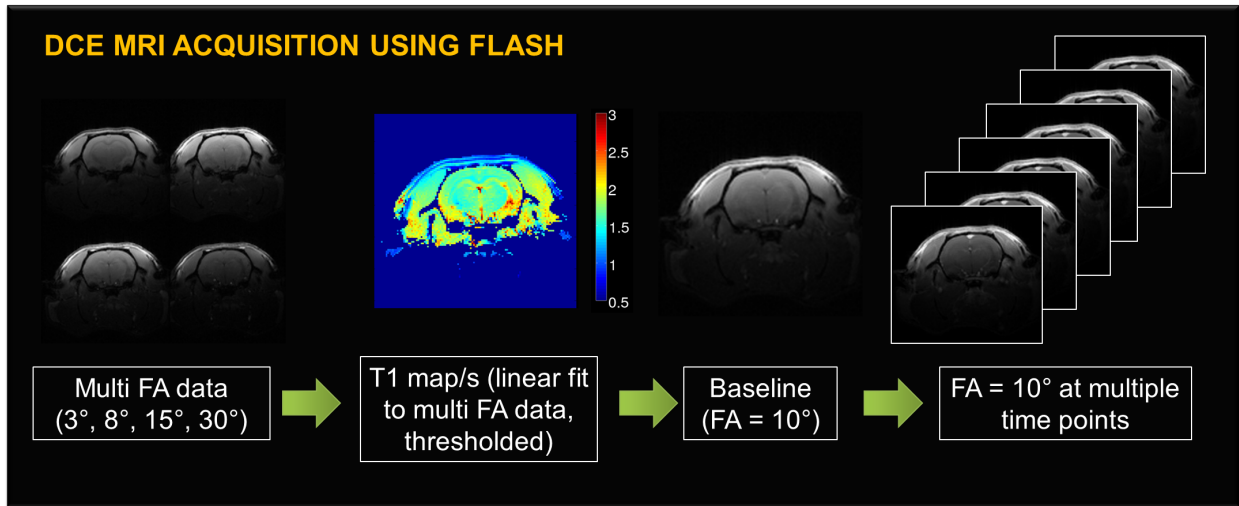


Figure 2.63: Stages of DCE MRI acquisition, beginning with VFA FLASH and using this to form a baseline T1 map. The FLASH signal baseline is then taken and the signal ratio between the baseline and scans taken after contrast agent has been administered is used to calculate the apparent T1 due to the presence of contrast agent during the dynamic scan.

The relationship between the FLASH signal and the concentration of a contrast agent in each of these single FA acquisitions is determined by combining equations (2.24) and (2.25) into equation (2.29), where S_{rel} is the relative signal i.e. the ratio between the baseline signal and the signal seen in the dynamic image and T_{10} is the baseline T1 value. This assumes that the FLASH sequence was perfectly spoiled, signal attenuation due to Gd-mediated T2 shortening is negligible and the contrast agent is uniformly distributed within each voxel [136], as shown in Figure 2.64.

$$[CA] = \frac{\ln \left(\frac{\exp \left(-\frac{2TR}{T_{10}} \right) \cos \alpha (1 - S_{rel}) + \exp \left(-\frac{TR}{T_{10}} \right) (S_{rel} \cos \alpha - 1)}{\exp \left(-\frac{TR}{T_{10}} \right) (\cos \alpha - S_{rel}) + S_{rel} - 1} \right)}{TR \cdot r_1} \quad (2.29)$$

Once the concentration at each scan point is known, these can be combined together with the times each scans were taken to give a dynamic profile of the contrast agent concentration in a region over a series of DCE MRI time frames.

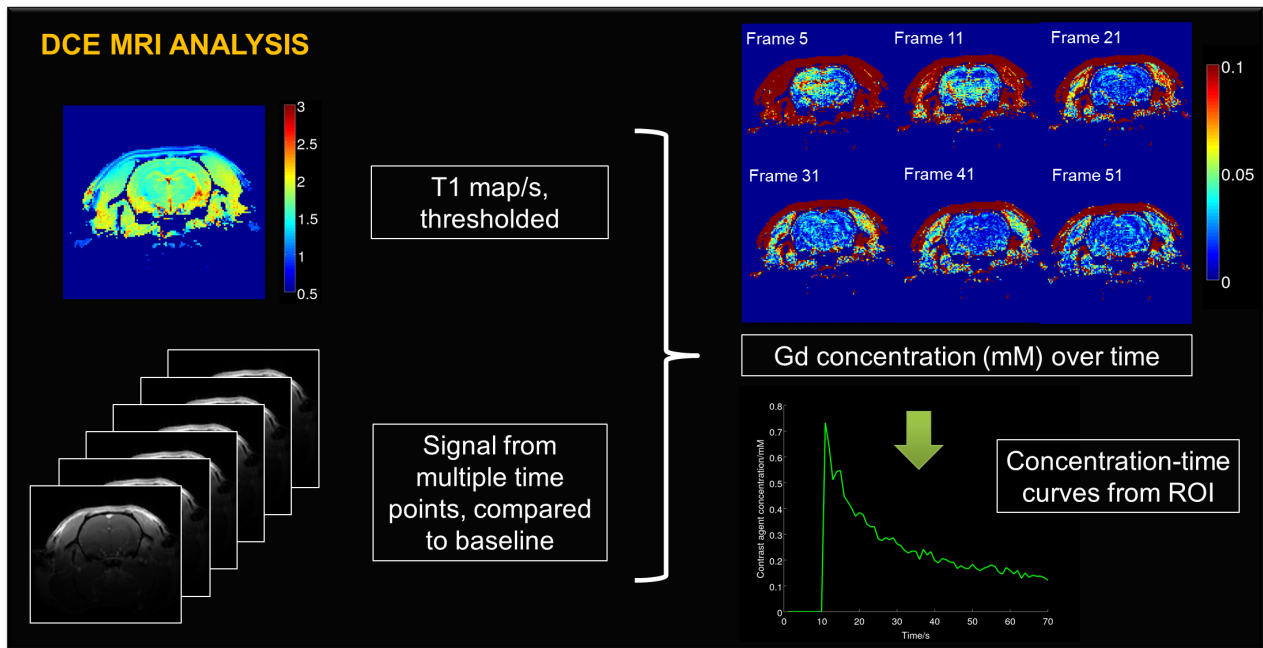


Figure 2.64: Baseline T1 map is used in conjunction with signal ratio between the FLASH baseline and FLASH scans taken after contrast agent has been administered. This produces the absolute concentration of contrast agent *in vivo* at the time points of each dynamic scan. ROIs can then be drawn in tissues of interest to give concentration-time curves.

2.2.11 Perfusion MRI pulse sequences - Arterial spin labelling

Arterial Spin Labelling (ASL) is an alternative method of measuring perfusion using MRI, but unlike DSC MRI it is entirely non-invasive as it uses magnetically labelling protons in the endogenous, freely diffusible blood supply to act as a tracer. Blood is labelled using an inversion (180°) pulse proximal (i.e. upstream) from the tissue of interest [121], [125]. Perfusion is measured as a small signal change (1–2%), which is observed when labelled blood perfuses into tissue. Inverted spins present in the blood travel to the capillary bed and exchange with the water molecules in the tissue, which reduces the total tissue magnetisation [121], [125]. An image is taken in both this state (the “tag” image) and without any labelling applied (the “control” image). The “tag” image is then subtracted from the “control” image to give a perfusion image, which is used to extract cerebral blood flow (CBF) [121], [125].

There are two types of ASL: Pulsed ASL (PASL) and Continuous ASL (CASL). In PASL, arterial spins are labelled by a spatially selective inversion pulse and the bolus of arterial blood passes transiently through the tissue of interest, whilst in CASL the labelled blood establishes a steady state with the tissue, requiring a longer tagging time [121], [125]. In this thesis, the PASL Flow-sensitive Alternating Inversion Recovery (FAIR) technique was used to perform 2D single slice ASL and is shown in Figure 2.65. PASL was used due to its higher labelling efficiency than CASL and single slice ASL was used due to the relatively long (12 minutes) acquisition time of FAIR.

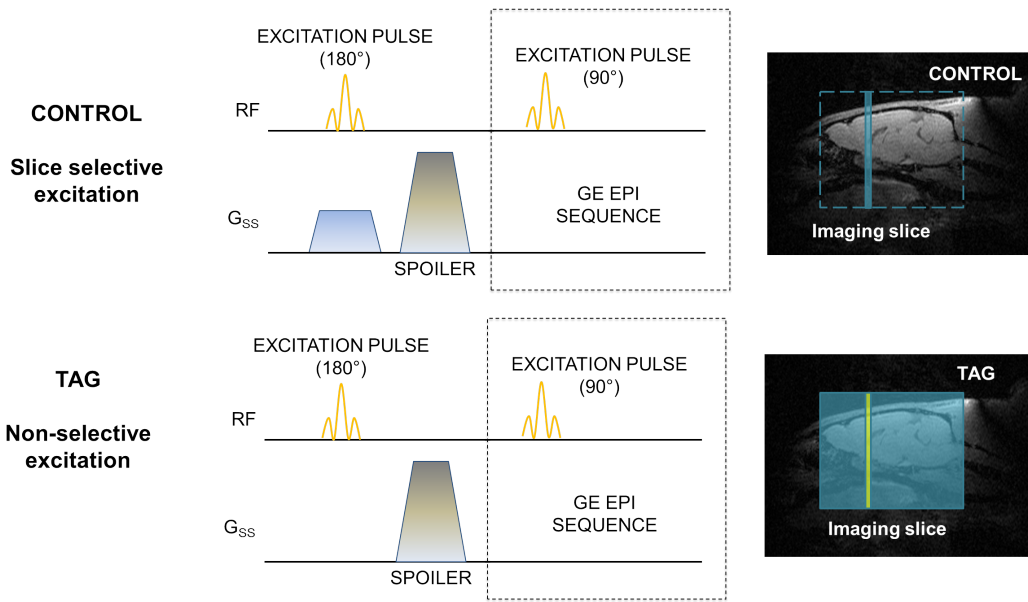


Figure 2.65: FAIR “tag” and “control” image pulse sequences (left) used to perform ASL, with image slice planning shown on the right [86], [137]. The non-selective inversion pulse is applied to the whole head to give the “tag” image while the control image is produced using a slice selective inversion pulse slightly wider than the image slice. For simplicity only the slice select gradient is shown and the box indicates an EPI sequence, shown in Figure 2.60.

In FAIR, a frequency selective inversion pulse is applied with and without a slice select gradient to produce the “control” and “tag” images respectively. This ensures that in the “control” image spins are only inverted at the imaging location, whilst in the “tag” sequence the pulse inverts spins over the global region. The magnetization for the “tag” image is inverted and therefore takes a negative sign, so the change in magnetisation is defined as follows in equation (2.30),

$$\Delta M = M_{\text{control}} - M_{\text{tag}} \quad (2.30)$$

where ΔM is the change in magnetisation, M_{control} is the positive magnetisation from the “control” image and M_{tag} is the negative magnetisation from the “tag” image.

The simplest way to calculate CBF from these images assumes that magnetisation transfer between bound and free water is compensated for and the T1 of blood is approximately the same as that of tissue [137]. The Bloch equation [104] for longitudinal magnetisation in the presence of perfusion can therefore be set out in equation (2.31),

$$\frac{dM}{dt} = \frac{M_0 - M}{T1} + f M_b - \frac{f}{\lambda} M \quad (2.31)$$

where M is the longitudinal magnetisation of the tissue, with equilibrium value M_0 , M_b is the magneti-

sation of the inflowing blood, f is the perfusion rate or CBF and λ is the partition coefficient of water molecules between tissue and blood, which is 90ml/100g for the rat brain [138]. According to this equation, the tissue T1 relaxation rate is effectively increased by $\frac{f}{\lambda}$ giving an apparent T1*, shown in equation (2.32),

$$\frac{1}{T1^*} = \frac{1}{T1} + \frac{f}{\lambda} \quad (2.32)$$

λ is generally assumed constant, so therefore if a T1 map is determined from the “control” images and a T1* map is computed from the “tag” images, the CBF can be calculated in [ml 100g⁻¹ min⁻¹]. The T1 maps are calculated using several different inversion times (TI) acquired using the sequence, where the inversion time defines the time between the labelling pulse and the delay to acquisition readout. The signal at each of the multiple TIs is then plotted against TI and fitted to the inversion recovery equation (2.33) to calculate T1 in each case. The inversion recovery equation is derived from the Bloch equation for T1 relaxation after a 180° pulse [104].

$$M_z(TI) = M_0 \left(1 - 2 \exp\left(-\frac{TI}{T1}\right) \right) \quad (2.33)$$

2.2.12 Summary of MR pulse sequences

Pulse sequence	Typical time to acquire	Contrast used	Application in thesis
FISP	6 minutes	T1 weighted	Whole body mouse structure
FLASH-IG	10 minutes	T1 weighted	Cardiac self-gating MR and whole body mouse structure
RARE	6 minutes	T2 weighted	Rat brain structure
TOF MRA	8 minutes	T1 weighted, flow comp.	2D Time of flight MR angiography
EPI	<1s per frame, 100+ frames	T2* weighted, Gd [CA]	Rat brain perfusion, first pass DSC MRI AIF
FLASH VFA	T1 map (7 FA) = 5mins, Single FA = 41s	T1 weighted, Gd [CA]	Rat brain permeability, DCE MRI AIF
FAIR	12 minutes (20 TI)	T1 weighted	Rat brain perfusion, ASL

2.3 Chapter summary

The physical basis of PET and MRI scanning techniques have been respectively outlined. The hardware of both modalities has also been discussed, with the process of signal detection explained for both techniques. A brief overview of image formation in both PET and MRI has also been provided to give an understanding of the image reconstruction techniques and pulse sequences used throughout this thesis. Finally, dynamic PET and MRI scanning procedures were examined in this Chapter. The analysis procedures required to convert dynamic PET and MR image signals into quantitative parameters are discussed in the next Chapter.

Chapter 3

Current quantitative methods in small animal PET and MR

This Chapter contains an overview of current analysis techniques used in dynamic PET and MRI to produce quantitative images and parametric maps. Both modalities rely on compartmental modelling to express the tracer and contrast agent kinetics respectively, and both PET and MRI models each require an arterial input function (AIF) to facilitate the use of such models. As such, the accurate and non-invasive determination of the AIF is important to produce quantitative analysis of imaging data and a variety of techniques used to extract AIFs in PET and MRI are discussed in this Chapter.

3.1 Quantification in PET

A summary of PET analysis techniques is shown in Figure 3.1, indicating the varying levels of analysis which can be performed on PET data, with the most powerful and complex being voxel by voxel parametric mapping, achieved through tracer kinetic modelling.

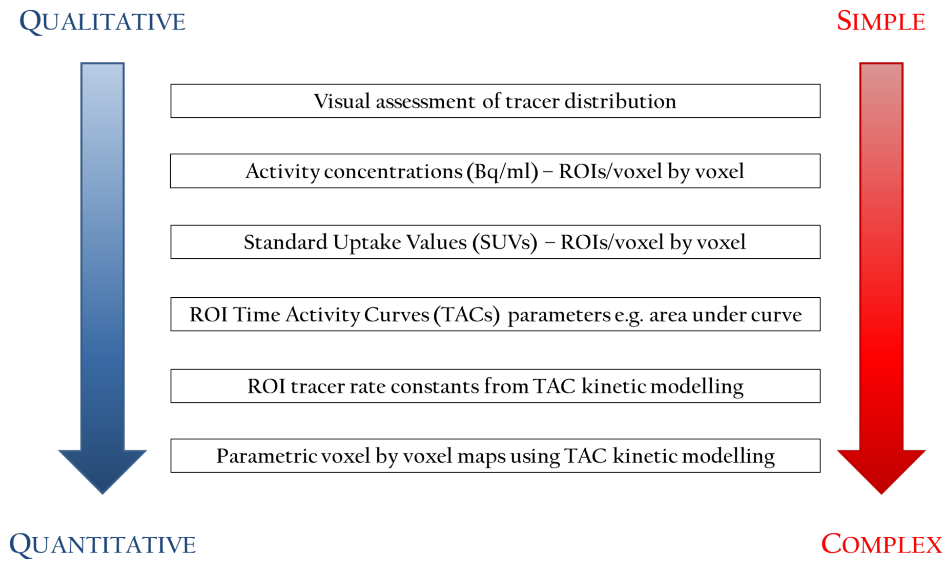


Figure 3.1: Progression in analysis of PET data to complex, quantitative techniques.

3.1.1 Standard uptake values (SUVs)

Standard uptake values (SUVs) provide a simple, semi-quantitative measurement of tracer uptake which can be compared across subjects on an ROI or voxel by voxel basis [139]. SUVs are defined in equation (3.1), in units of g/ml for small animals and can be defined as both the mean or maximum SUV across the ROI. The main advantage of SUVs lies in their simplicity - they can create a parameter map without dynamic PET measurements or invasive blood sampling.

$$\text{SUV}(t), [\text{kg/l}] = \frac{\text{Activity concentration}(t), [\text{MBq/l}]}{\left(\frac{\text{Injected Activity, [MBq]}}{\text{Body weight, [kg]}} \right)} \quad (3.1)$$

SUVs are used as a biomarker of disease in clinical oncology [140], [141], [142] for both diagnosis and cancer staging, due to ^{18}F -FDG accumulating in tumour tissue as a consequence of a higher rate glycolysis known as the Warburg effect [143]. SUV gives an indication of an individual's response to therapy, as a decreased SUV will indicate decreased ^{18}F -FDG uptake and therefore a lower rate of glycolysis and a less aggressive tumour [142].

The biggest drawback with using SUV measurements is their time dependence and lack of direct physiological meaning. Over time, tracer uptake in ROIs will change and therefore many oncological studies are performed using a “late” scan performed an hour (or more) after tracer has been administered to the patient, as a longer uptake phase often results in a better lesion-to-background contrast ratio. The SUVs calculated are therefore compared at this “late” time point across patients [142], [144], [145]. The

optimal time to compare SUVs across patients (or subjects in preclinical imaging) varies according to the kinetics of the tracer involved, in addition to factors such as the metabolic state of the subject for ^{18}F -FDG [146]. An example showing how the distribution of ^{18}F -NaF changes over a 2 hour period is shown in Figure 3.2 to illustrate how SUVs can change with time.

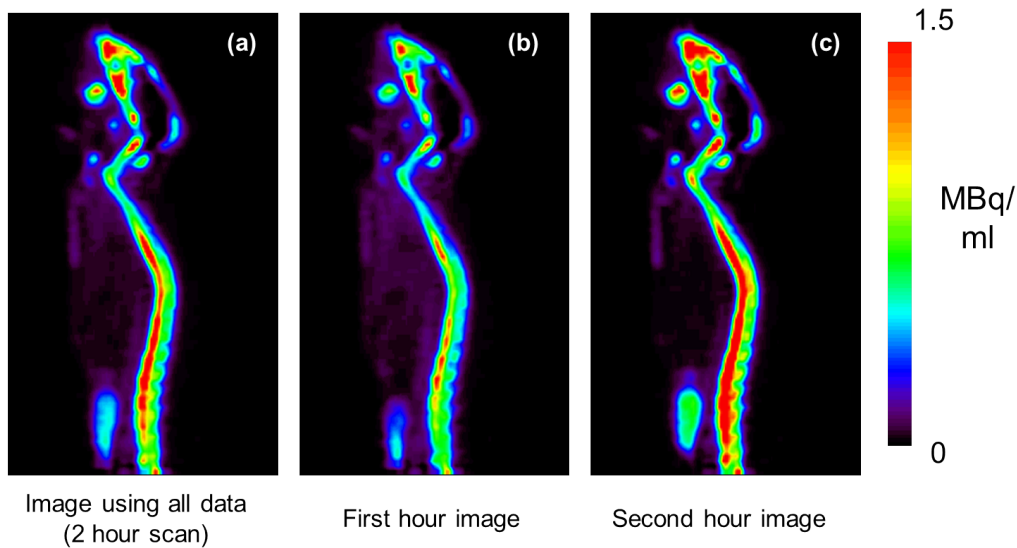


Figure 3.2: Comparison of ^{18}F -NaF whole body mouse PET images (sagittal view) reconstructed with MAP 3D for (a) entire PET 2 hour acquisition, (b) first hour and (c) second hour. Image (c) would be used to calculate SUV values as the tracer kinetics have stabilised, giving a higher SNR image with stable activity concentration.

3.1.2 Compartmental modelling of tracer kinetics

PET imaging produces quantitative images of radioactivity measurements, meaning that if suitable imaging conditions are used the tracer measurements should be influenced by the underlying physiology of the target region. Kinetic modelling of dynamic PET data allows for non-invasive quantification of physiological processes (e.g. utilization of glucose) and their alterations in various pathologies without the time dependency of SUVs [147], [148]. Each kinetic model compares the input of the system to the output using a series of stages, known as compartments, to model how the system (i.e. the imaging subject) processes the input.

PET tracer input and output

For PET tracers, the input to the system is typically defined as the tracer concentration in arterial plasma over time, known as the arterial input function (AIF), $C_p(t)$. This is defined as the input because each tracer is distributed around the body after injection via the arterial system, using the heart as a pump. The AIF is therefore ideally measured from an artery feeding the ROI and it is imperative that it is measured

accurately to ensure the analysis produces kinetic model parameters which will define the rates governing the physiological process under study correctly.

If blood samples are unavailable or if accounting for a tracer's metabolites in plasma is problematic, a reference region approach can be used to generate parametric maps of tracer kinetic parameters. This involves using the tracer concentration time courses from a region with negligible (or at least very low) tracer specific uptake to compare to the tracer concentration time courses found in the ROI [149]. This is most often used to generate estimates of the binding potential¹ for reversibly bound ligands [150].

To directly measure the AIF in humans, arterial blood samples must be taken throughout the duration of the scan and the extracted plasma activity measured. The sample data is then plotted to show how the tracer concentration within the vasculature decreases over time, as the tracer moves from plasma into various organs and tissues. Figure 3.3(a) shows the theoretical form of the AIF, whilst Figure 3.3(b) shows an AIF measured in a rat from plasma samples taken from the femoral artery.

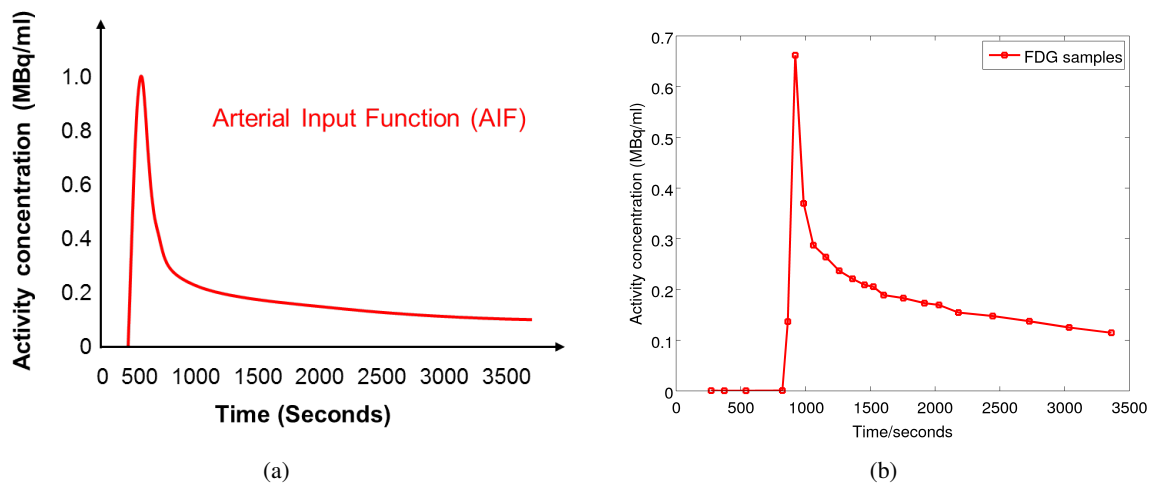


Figure 3.3: (a) Schematic showing archetypal AIF curve and (b) AIF measured from blood plasma samples taken from rat femoral artery.

The output for PET tracer kinetic models are the tracer concentrations in the ROI over time, known as time activity curves (TACs), $C_t(t)$. TACs are taken directly from PET images and show a characteristic increase of tracer concentration with time, which complements the decreasing tracer concentration seen in the AIF. Figure 3.4 illustrates the typical shapes of an AIF and a myocardial TAC for ^{18}F -FDG.

¹The non-displaceable binding potential is acquired using reference region methods, which is defined as the sum of non-specific, i.e. binding to other than the target molecule, and free radioligand concentrations in tissue. Additionally all reference region models assume the ratio of K_1/k_2 (explained in the next section) are roughly equal in the reference region and the ROI.

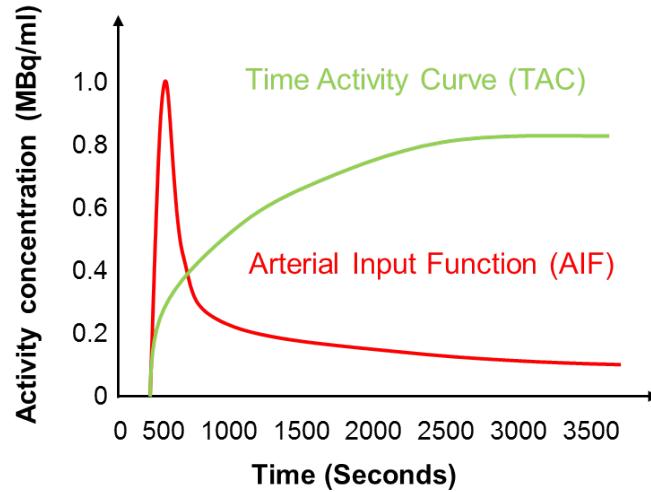


Figure 3.4: Typical curve profiles of AIF and myocardial ROI TAC for ^{18}F -FDG.

The system can therefore be modelled as applying a convolution to the AIF with the system impulse response function, $R(t)$, to create the output TAC [151]. This is expressed mathematically in equation (3.2):

$$C_t(t) = C_p(t) \otimes R(t) = \int_0^t C_a(\tau)R(t - \tau) d\tau \quad (3.2)$$

where $C_p(t)$ is the AIF, $C_t(t)$ is the TAC and $R(t)$ is the impulse response function. A compartmental model is selected which will best estimate the shape of $R(t)$ (expressed as a series of exponentials, which are the sum of each compartment's response to the bolus input [152]) and thus explain how the measured AIF is converted into the observed TAC. Each compartment of the selected model defines one possible state of the tracer, specifically its physical location (e.g. intravascular space) and/or its chemical state (e.g. its binding state to different tissue elements and receptors) [152]. The compartment model therefore describes the various transformations the tracer can undergo as it passes between compartments, such as the movement of a molecule from the vascular to the extracellular space or the phosphorylation of a molecule of ^{18}F -FDG [151].

The concentration in the first compartment is designated as C_p for the AIF (the tracer concentration in arterial plasma), with the tissue compartments numbered from 1 to N . The concentration in the first tissue compartment designated as C_1 and so on. The net flux into each compartment is defined as the sum of all outflows subtracted from the sum of all inflows, represented by arrows going in and out of compartments [151], [152]. The magnitude of the flux into each compartment is the product of the rate constant and the concentration from the source compartment. For example, a reversible one tissue compartment model (see Figure 3.5) can be expressed as shown in equation (3.3) [151]:

$$\frac{dC_1(t)}{dt} = K_1 C_p(t) - k_2 C_1(t) \quad (3.3)$$

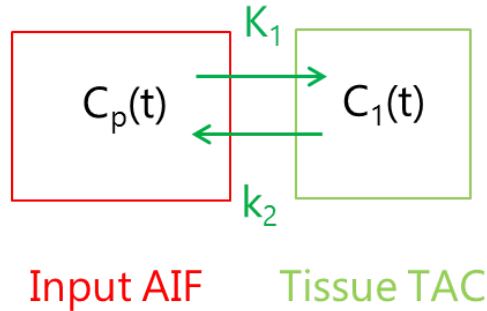


Figure 3.5: Reversible one tissue compartment model, used to describe water flow in body and applicable for diffusible blood flow tracers such as $^{15}\text{O-H}_2\text{O}$ [151].

For the reversible one tissue compartment system, the solution of the differential equation (3.4) gives the impulse response of the system (sum of N exponential decays from N tissue compartments) as shown in equation (3.4),

$$R(t) = K_1 \exp^{-k_2 t} \quad (3.4)$$

As we know that the tissue curve is a convolution of the AIF and impulse response from equation (3.2), we can express the tissue curve using equation (3.5). Equation (3.5) can then be used to find rate constants for this model. This process can be extrapolated for models with more compartments to find all required rate constants [151].

$$C_t(t) = K_1 \exp^{-k_2 t} \left(\int_0^t C_p(s) \exp^{k_2 s} ds \right) \quad (3.5)$$

Compartmental model selection

The two tracers used in this thesis, $^{18}\text{F-FDG}$ and $^{18}\text{F-NaF}$, both use an irreversible two tissue compartment binding model, shown in Figure 3.6 for $^{18}\text{F-FDG}$ [29], [31], [153] with its equations shown in (3.6) and (3.7). The first compartment shows how the tracer is transferred from the blood plasma into the tissues within the subject. The second compartment is described as irreversible, with $k_4 \approx 0$, as the phosphorylation step in tissue is irreversible for $^{18}\text{F-FDG}$ [29], [31], [153].

$$\frac{dC(t)_1}{dt} = K_1 C_p(t) - k_2 C_1(t) - k_3 C_1(t) + k_4 C_2(t) \quad (3.6)$$

$$\frac{dC(t)_2}{dt} = k_3 C_1(t) - k_4 C_2(t) \quad (3.7)$$

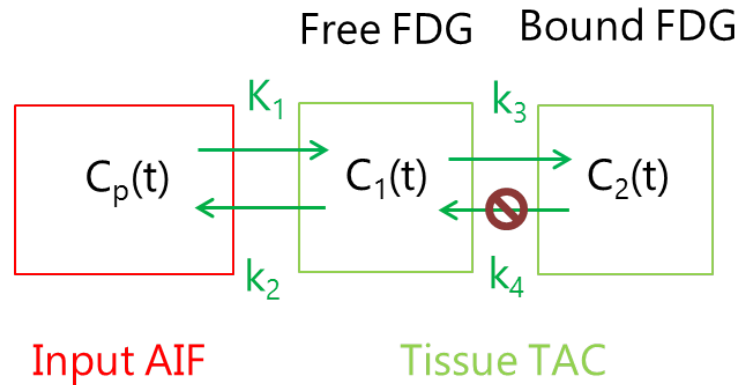


Figure 3.6: Two compartment model, with irreversible phosphorylation step trapping ^{18}F -FDG in tissue. No metabolite measurements are required to perform full kinetic modelling with this tracer [151].

This model can be solved with the impulse response being a summation of individual impulse responses for each compartment (with $k_4 \approx 0$) [29], [31], [153],

$$R(t) = R_1(t) + R_2(t) = K_1 \exp^{-(k_2+k_3)t} + R_1(t) \otimes k_3 \quad (3.8)$$

$$R(t) = K_1 \exp^{-(k_2+k_3)t} + \frac{K_1}{k_2+k_3} \left(k_3 - k_3 \exp^{-(k_2+k_3)t} \right) \quad (3.9)$$

$$R(t) = \frac{K_1 k_3}{k_2+k_3} \left(1 + \frac{k_2}{k_3} \exp^{-(k_2+k_3)t} \right) \quad (3.10)$$

The TAC and AIF can now be used as part of a curve fitting procedure to extract the rate constants. Alternatively, this model can be linearized and solved graphically using a Patlak plot [154] for irreversibly bound tracers, as expressed in equation (3.11), where the gradient is the rate constant K_i . K_i is a combination of K_1 , k_2 and k_3 (see equation (3.12)) and corresponds to the influx constant of the tracer. An example Patlak plot is shown in Figure 3.7.

$$\frac{C_t(t)}{C_p(t)} = K_i \frac{\int_0^t C_p(t) dt}{C_p(t)} + V \quad (3.11)$$

$$K_i = \frac{K_1 k_3}{k_2 + k_3} \quad (3.12)$$

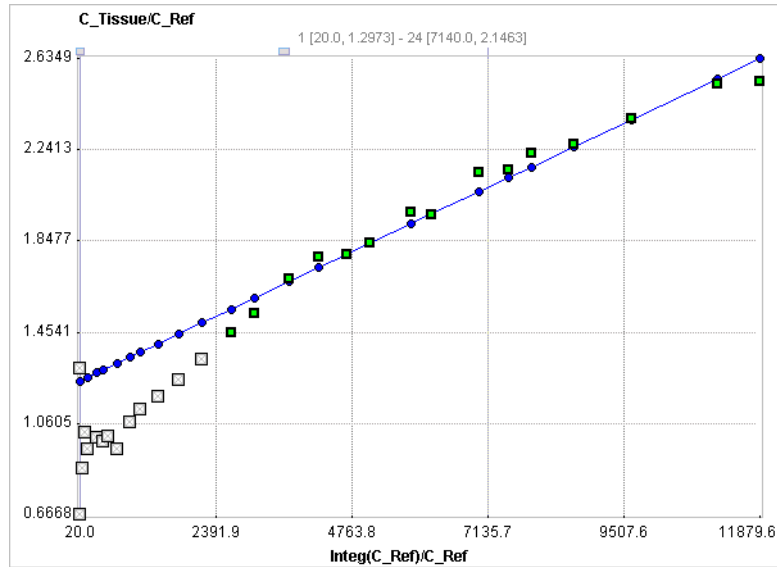


Figure 3.7: Example Patlak plot. Straight line is fitted to data to attain influx constant for tracer. Initial 10-20 minutes are not used in fit as they depend upon the administered tracer bolus.

3.1.3 Arterial input function derivation methods

An AIF is required to apply any form of kinetic model to PET tracer data and the gold standard in the clinic is between 20–30 \approx 1-2ml arterial blood samples taken serially throughout the scan [155]. The sampling scheme depends on the tracer and its kinetics, but typically samples are taken rapidly ($<5s$) in the first 2 minutes to characterise the AIF peak and these intervals are gradually lengthened to 5–10 minute intervals towards the end of the scan [156]. The sample volumes are usually reduced to 30-100 μ l in rat studies to avoid ex-sanguination [39], [157], [158].

In rats, arterial blood samples are taken via a catheter inserted into the femoral artery [39], [157], [158]. Sampling intervals are initially very short (between 5-15s) in the first 1-2 minutes to ensure the peak of the AIF is properly sampled, as the high heart rates of rats and mice mean that tracers distribute very quickly [39], [157], [158]. The time between samples is gradually lengthened after this period (e.g. to 20s for the next minute then at 5, 7, 10, 20, 30, 60, 90 minutes post-injection [39]), as the timing resolution does not have to be as high to accurately sample the AIF. Once taken, blood samples are

spun down in a centrifuge to extract the blood plasma and their radioactivity measured in a well counter. Tracer metabolite concentrations are also measured if they are required for the kinetic model [37], [41]. The serial sampling process may, however, disturb the physiology of the animal and the blood samples collected will be at limited temporal resolution at a remote site from the ROI, and so will experience dispersion both within the animal and along the cannula line [52].

In mice this process is complicated by low total blood volumes ($\sim 2\text{ml}$ [106], [159]), which makes serial blood sampling difficult, as limited volumes of blood can be collected. Although some groups have been able to perform serial blood sampling in mice by cannulating the femoral artery [160], femoral vein [36] or aorta [68] and extracting very small samples ($10\text{-}15\mu\text{l}$ [160]), many non-invasive methods have been considered, particularly for longitudinal studies in mice.

Alternative techniques to serial blood sampling which attempt to extract direct estimates of the blood activity concentrations have also been tested in rats [37], [158], [161], [162], [163], [164], [165], [166] and mice [35], [51]. These primarily use femoral arterio-venous shunts, which comprise a catheter surgically inserted between a major artery and a vein (such as the carotid artery and the jugular vein [37]) to allow for a small fraction of blood to flow outside the body through the catheters, whose activity can be measured by a probe and blood flow measured with a flowmeter or ultrasound [37], [161]. Coincidence microprobes which measure gamma emissions [51], [52], [158], [161], [163], [164] or β probes which measure positron emissions [37], [162], [165], [166] have all been used on rodents in previous work to perform rapid blood activity measurements with temporal resolution $<10\text{s}$ [158], [162] and sample volumes as low as 220nl for mice [35]. Two examples of such probes are shown in Figure 3.8. The downside of these techniques is the specialist equipment and technical personnel required to perform them, as well as the fact that repeat measurements (as part of a longitudinal study) cannot be performed due to the surgical techniques involved. In PET/MR there is the added complication of the length of the magnet bore, the restricted access to the subject and the high magnetic field, such that all equipment must be deemed MR safe to be used in the environment.

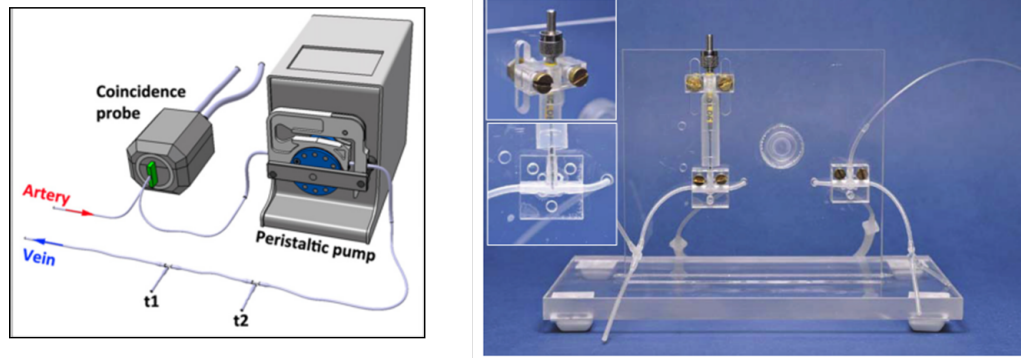


Figure 3.8: Left: Swisstrace coincidence probe wired into arteriovenous shunt circuit to continuously measure AIF in mice, reproduced with permission from [51]. Right: Coincidence probe gantry setup required to measure AIF directly in rats, reproduced with permission from [162].

The use of standard AIFs derived for a mouse population [167] have also been suggested, as well as hybrid AIFs which are scaled by a single, late blood sample taken at the end of the PET scan to calibrate them to an individual mouse [168]. The drawback of the population AIF method is that it is customized for a particular animal disease model, and so requires an empirical calculation of the mean (population) AIF and cannot adapt to individual variations in the dietary state and anaesthesia of the animal, which may lead to poor estimation of metabolic status [169]. Additionally it does not account for variations in injection speed, volume or catheterization site, meaning that a highly repeatable injection protocol using a power injector is required [52].

3.1.4 Challenges of using image derived AIFs

In humans, the AIF can be derived non-invasively by extracting an activity time course from arterial voxels on dynamic PET images, in areas such as the carotids [156], [170]. Rodent arteries are, however, frequently too small to be resolved on PET images and therefore their small size demands that image-derived input functions be extracted from the left ventricle of the heart [29], [33], [36], [53], [171], [172]. The restricted spatial resolution of small animal PET scanners (1-2mm FWHM [99]) makes it challenging to accurately place an ROI in the blood pool of the heart due to partial volume effects. The vascular radioactivity is also blurred between tissues due to the spillover effect between hot and cold regions at low spatial resolution. This results in signal contamination, which typically reduces the AIF peak height, increases the width of the AIF peak and raises the tail of the curve at later time points [173], [174].

Many alternate methods have been developed to address these problems with image-derived AIFs (ID-IFs) in preclinical studies, such as ensemble-learning independent component analysis (EL-ICA) [51], non-negative matrix factorization [175] and factor analysis (FA) [37], [176]. FA describes the covariance

relationships among multiple variables in terms of a few underlying, but unobservable, random quantities called factors. FA is based on the fact that the image intensity in a given voxel from a region such as the mouse heart is the linear superposition of counts from the myocardial TAC, the left ventricle (the AIF) and the right ventricle, and FA transforms this old basis into a set of new basis curves i.e. to isolate the TAC and AIF signals [37], [176]. Variables within a compartment are assumed to be highly correlated but variables in different compartments have relatively small correlations. Dynamic images are hence decomposed into component images via principal component analysis, which finds the eigenvectors and eigenvalues of the covariance matrix of the time-dependent pixel signals. A similar process is followed for EL-ICA, with the component images shown in Figure 3.9. Non-negative matrix factorization sets an additional condition that negative activity concentration values are not allowed [175]. These approaches can also be scaled to the activity concentration of an arterial plasma sample taken at a late time point [37], [176], or a venous plasma sample if the tracer arterial and venous plasma concentrations have equilibrated at this late time point [170].

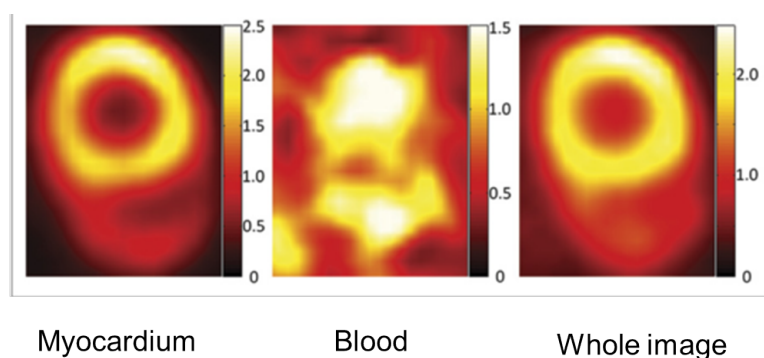


Figure 3.9: Non-invasive estimation of AIF from PET images, typically using EL-ICA [51] to separate out myocardium from heart signal and minimise spillover. Figure reproduced with permission from [51].

Partial volume correction (PVC) methods for IDIFs have also been suggested, either using reconstruction or post-reconstruction based methods. In reconstruction, algorithms such as MAP which model the PET system response, photon-pair collinearity and intercrystal penetration [64], [65] can be used to provide resolution recovery and decrease partial volume effects. Post-reconstruction methods vary widely, from empirically derived recovery co-efficient scaling factors applied to the data to recover the mean signal height [177], [178], [179] to spillover correction methods [171], to profile modelling approaches, which utilise electrocardiogram gated PET data and a 3D geometrical model of activity distribution convolved with the scanner PSF [180]. Hybrid methods also exist which use a PVC image-derived approach (such as recovery co-efficients) in the peak region of the AIF, and multiple late blood samples are used to derive the tail region before combining the data to give the full AIF [172].

Simultaneous estimation methods which take PVE and spillover into account whilst simultaneously

fitting IDIFs and model parameters have also been developed [181] although the large number of parameters have led to poor reproducibility of results by other groups [53]. Other methods include fitting a 4 parameter compartmental model to the data to describe ^{18}F -FDG tissue uptake and metabolism [182]. As yet, no consensus has been achieved in preclinical studies for the extraction of image-derived AIFs accurately and reliably.

In summary, there are 4 main ways of attaining an AIF for PET kinetic analysis:

- **Serial, arterial blood sampling** - gold standard, but requires invasive surgery, has limited temporal resolution and is highly challenging in mice.
- **β probe and/or arterio-venous shunt** - produces high temporal resolution blood sampled measurements, but requires specialized equipment, is expensive and difficult to make MR compatible.
- **Population AIFs** - a mean AIF is assumed for the subject group, from a model or from previously acquired data. This method does not accommodate for individual variations in AIF shape but can also be scaled to each animal by the use of a measured plasma sample taken at a late time point. This sample is ideally arterial plasma, but can be venous if the tracer concentration in arterial and venous plasma has reached equilibrium at the sampling time point.
- **Image-derived AIFs or IDIFs** - the AIF is extracted from an arterial ROI the PET images either directly or through a mathematical operation, such as FA. Several corrections can be applied to IDIFs, such that the measured activity concentration gives a more accurate estimate of the true input function. IDIFs can also be scaled to each animal by the use of a late plasma sample and a population IDIF can be formed from the average of multiple IDIFs.

3.2 Quantification in dynamic MR using contrast agents

Whilst PET is intrinsically quantitative if appropriate corrections and calibrations are applied, MR cannot directly measure contrast agent concentrations. Instead, extensive processing is applied to the image signal intensity to attain readings of contrast agent concentrations, as described in Chapter 2 for DSC and DCE MRI. Once this analysis has been performed, however, kinetic analysis may be performed using compartmental models in a similar way to PET tracer kinetics. Both DCE and DSC MRI require an arterial input function to compare to the contrast agent concentration-time curves from the ROI, although the time scales and models applied vary between the two MRI techniques.

3.2.1 Compartmental modelling of contrast agent kinetics in DCE MRI

In a similar manner to PET, qualitative or semi-quantitative analysis can be conducted on the concentration time curves produced by DCE MRI, including quoting time to peak and area under the curve values in healthy tissue and tumours [106]. The most powerful DCE MRI analysis method, however, uses compartment models to produce physiological parameters, such as vessel permeability [183], [184], [185], [186]. The Tofts compartment model [129], [130] is the most commonly used model and is depicted in Figure 3.10. The mathematics describing the extraction of DCE MRI parameters from this model are included in Appendix I.4².

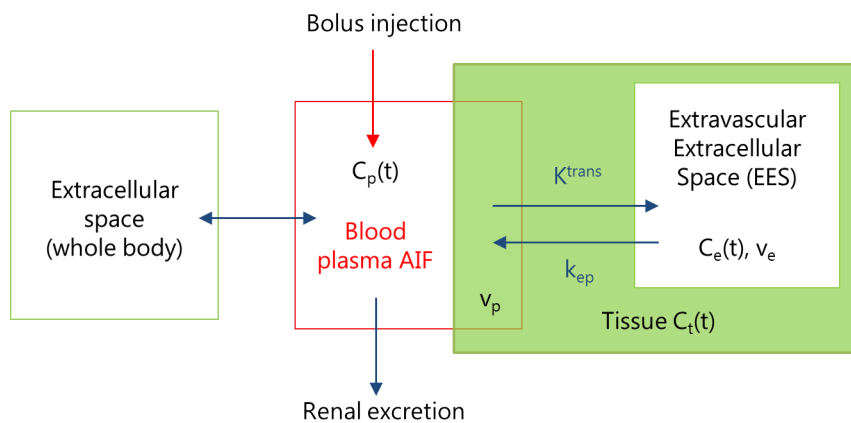


Figure 3.10: Tofts compartment model used to evaluate contrast agent kinetics in DCE MRI acquisitions [129], [130].

In similar fashion to the PET tracer compartmental model, an AIF is essential to extracting the contrast agent rate constants in DCE MRI and the AIF produced displays a similar shape to that described in Figure 3.3(a) [187]. The accuracy of the AIF is also of importance, due to the effect it has on corresponding parameter values [133], [134], [135], [188], [189] and a temporal resolution of between 3–5s is recommended to achieve acceptable accuracy in the first few minutes after injection, as the peak blood plasma concentration changes rapidly [129], [130], [133], [134]. Due to the higher resolution of dynamic MRI compared to PET (for mice and rat MR typically gives $<0.4\text{mm}$ voxels, in comparison to $>1.5\text{mm}$ for PET) image-based non-invasive AIF determination is regularly performed in both human and small animal subjects, with very few studies performing validation with blood samples due to their invasive nature.

The simplest form of MR-based AIF estimation is to draw an ROI on the feeding artery to the tissue ROI and to take the mean ROI time course as the AIF. In mice, the aorta [190] or left ventricle are often used [191], [192], [193], [194], [195]. Due to the increased size of rat brains, the linguofacial artery has

²DCE MRI is used in Chapter 7 of this thesis to provide MR AIFs only, no DCE MRI kinetic analysis was performed.

been used in rats [196], [197]. A detailed summary of alternative DCE MRI AIF extraction techniques is included in Appendix I.3.

3.2.2 Analysis of cerebral perfusion using DSC MRI

For DSC MRI, indicator dilution theory is used to express the behaviour of a contrast agent bolus as it passes through the vasculature and to attain estimates of cerebral blood flow (CBF), cerebral blood volume (CBV) and mean transit time (MTT), which defines the average time a particle of contrast agent takes to pass through the tissue [121], [125]. It is assumed that the BBB is intact, the contrast agent remains intravascular and does not have an effect on CBF itself, and that the change in T1 relaxation is negligible [121]. As mentioned in Chapter 2, EPI sequences are used to quickly acquire a T2* weighted image where the induced change in magnetic susceptibility due to the presence of contrast agent results in a proportional decrease in signal.

Contrast agent AIF in DSC MRI

An AIF is also required in this analysis process, but in DSC MRI the AIF is defined as the contrast agent concentration-time curve during the first pass phase of the injection bolus. In an ideal AIF, the recirculation of the tracer, as well as the dispersion and delay of the bolus, should be negligible, although this is difficult to achieve in practice [121]. The AIF is extracted from images using the signal-time course from voxels within the feeding artery of the tissue ROI to minimize the effects of delay and dispersion, which can result in curve spreading [120], [198], [199], [200]. A schematic DSC MRI AIF annotated with its main features is shown in Figure 3.11.

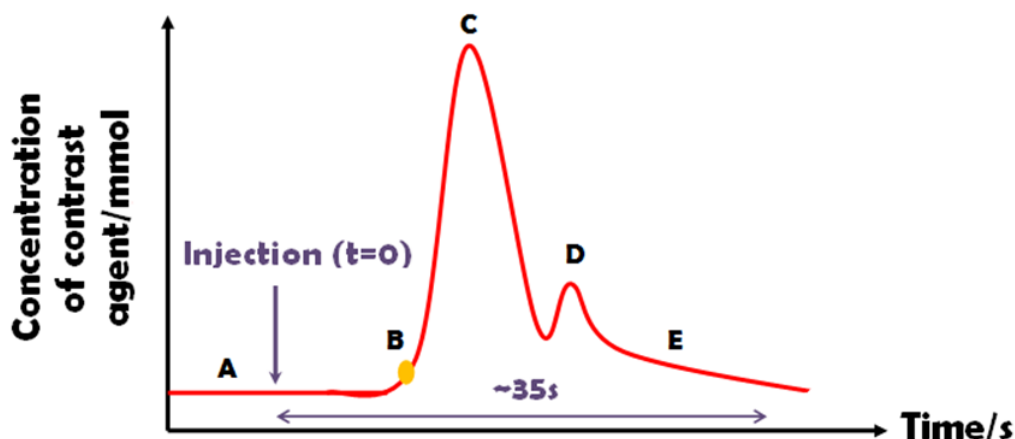


Figure 3.11: Theoretical AIF for DSC MRI, indicating the (A) steady state, (B) bolus arrival time (BAT), (C) time to peak (TTP) of first pass, (D) recirculation peak (second pass of bolus) and (E) decay to steady state.

An example extraction of an AIF from arterial voxels is shown in Figure 3.12. A clear first pass curve shape is seen but no recirculation peak due to the noise present in the data. DSC MRI cannot directly measure the contrast agent concentration, as outlined in the conversion between EPI signal and $\Delta R2^*$ given in equation (2.23). $\Delta R2^*$ is assumed proportional to the concentration of contrast agent, although the exact proportionality constant depends on the tissue of interest, the contrast agent used, the field strength of the magnet and the pulse sequence parameters used [121].

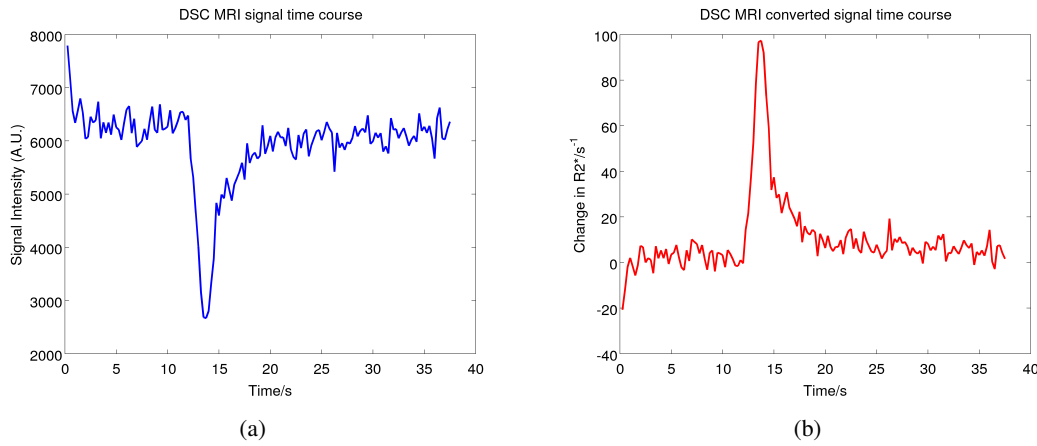


Figure 3.12: (a) DSC MRI signal from arterial voxels and (b) converted $\Delta R2^*$ time course.

Gamma variate fitting to AIF data

The image-derived AIF in DSC MRI is usually noisy due to the high temporal resolution required to visualise the first pass bolus, resulting in low spatial resolution images. AIF smoothing is performed by fitting a gamma variate function to the first pass, which is an accepted model for indicator dilution curves generated from a bolus [201]. The fitting of the gamma variate removes any recirculation peaks and residual signal from the AIF, which may disrupt the ideal bolus curve shape [202], [203].

The gamma variate function used in this work fitted curves of the form [202],

$$C_{\text{gamma}}(t) = 0 \text{ for } t \leq D \quad (3.13)$$

$$C_{\text{gamma}}(t) = A \cdot (t-D)^B \exp^{-t \cdot C} \text{ for } t > D \quad (3.14)$$

where D was set to the bolus arrival time and the other parameters were determined in a 3 parameter fit. If the fit is successful, $C_{\text{gamma}}(t)$ is treated as equivalent to a smoothed $\text{AIF}(t)$ for the analysis. Example AIFs from DSC MRI data and fitted gamma variate functions are shown in Figure 3.13.

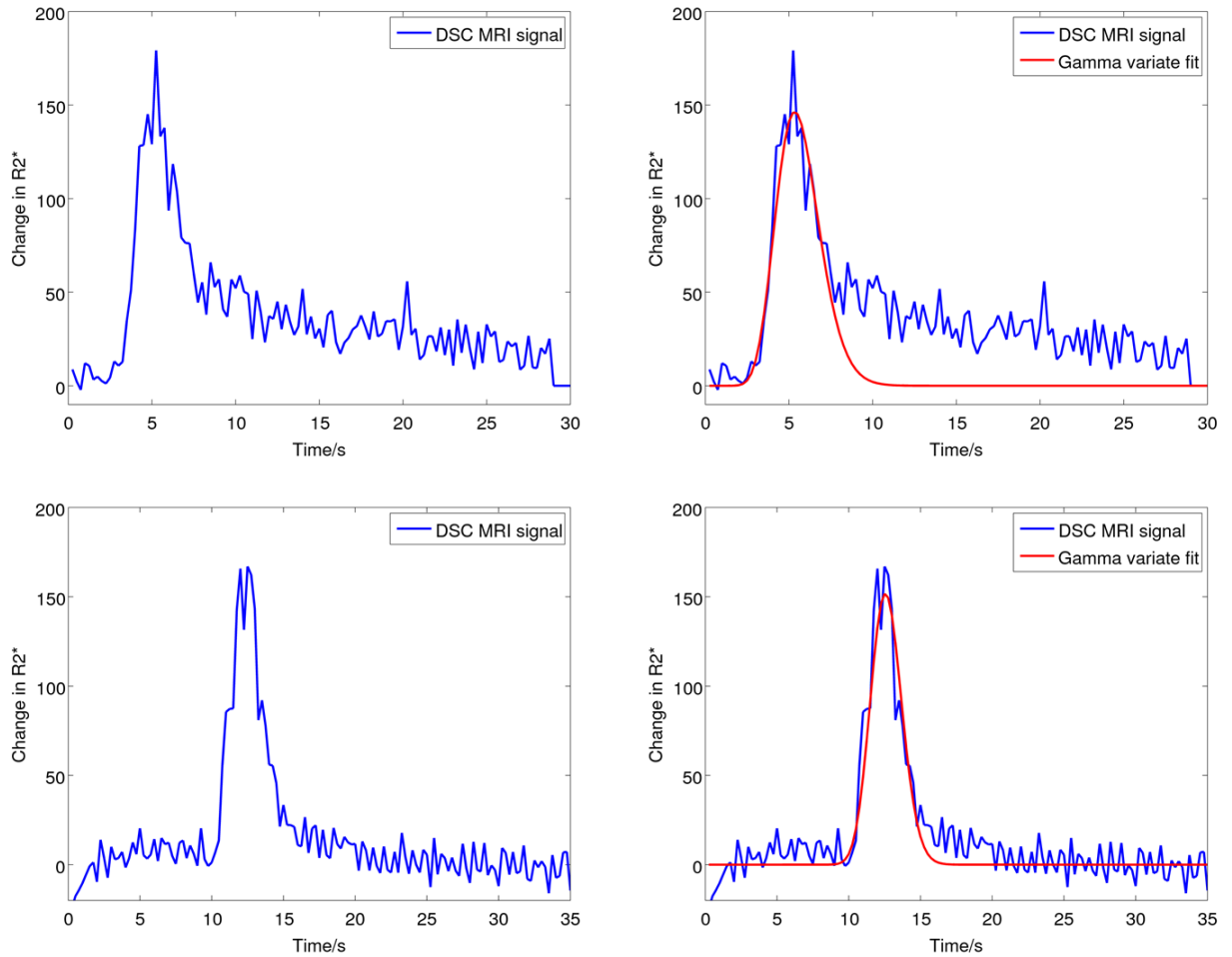


Figure 3.13: Left: AIF profiles taken from middle cerebral artery for 2 rat DSC MRI datasets. Right: Gamma variate functions (red) fitted to both datasets.

Perfusion parameter estimation

Ideally we model the contrast agent injection as an infinitely short bolus [120], but the tracer becomes dispersed as it travels through the vasculature. To attain estimates of CBF, CBV and MTT from this data, the concentration-time curve (from either an ROI or on a voxel by voxel basis) is assumed to be the convolution of the first pass AIF and the impulse response function of the system, as expressed in equation (3.15). It is also assumed that the proportionality constant between $\Delta R2^*$ and the concentration of contrast agent is constant in all tissues and in blood [121].

$$C_T(t) = C_{\text{ideal}}(t) \otimes \text{AIF}(t) = \text{CBF} \cdot \text{AIF}(t) \otimes R(t) = \text{CBF} \cdot \int_0^t \text{AIF}(\tau) R(t-\tau) d\tau \quad (3.15)$$

where $R(t)$ is the residue function [118] describing the fraction of contrast remaining in the system at time t and C_{ideal} is the true concentration in tissue. CBF can hence be calculated using the deconvolution of the tissue concentration curve ($C_T(t)$) and the measured $\text{AIF}(t)$. As equation (3.15) is ill-posed, however,

Fourier based deconvolution may give non-physical answers for the residue function and underestimate CBV [121]. Modern methods therefore use singular value decomposition (SVD) [117], [118], [120], [204] to perform deconvolution, which rewrites equation (3.15) in terms of matrices by assuming that the AIF(t) and R(t) are constant over small intervals (Δt). The exact mathematics of this process are detailed in Appendix E.

Although methods exist to perform quantitative analysis of absolute values of CBF and CBV using DSC MRI [205], [206], their accuracy has been debated [121], [204], [207], [208]. The approach most often used to calculate absolute CBF is based on Zierler's area to height relation and the central volume theorem, which assumes that the BBB is intact with little transfer of tracer from the capillary to the Extravascular Extracellular Space (EES) [119]. The absolute CBV can be calculated using equation (3.16) by scaling the $\Delta R2^*$ data to the contrast agent concentration with a proportionality constant and a correction factor that represents the brain density and the hematocrit of the subject, given in equation (3.17).

$$CBV = \frac{k_H}{\rho} \frac{\int_0^t C_T(t) dt}{\int_0^t AIF(t) dt} \quad (3.16)$$

$$k_H = \frac{1 - Hct_{large}}{1 - Hct_{small}} = 0.73 \quad (3.17)$$

where Hct_{large} (~ 0.45 [195]) and Hct_{small} (~ 0.25) are the hematocrit values in large and small blood vessels respectively and ρ is the brain density (1.04g/ml) [119], [120]. The normalization to the AIF accounts for the fact that as more tracer is injected, a greater concentration is observed in the ROI. Once calculated, CBV can be used to find absolute CBF and MTT using equations (3.18) and (3.19),

$$CBF = \frac{k_H}{\rho} \frac{\int_0^t C_T(t) dt \cdot C_{ideal, max}}{\int_0^t C_{ideal}(t) dt \int_0^t AIF(t) dt} \quad (3.18)$$

$$MTT = \frac{CBV}{CBF} \quad (3.19)$$

If only relative measurements of CBF are required (e.g. between two brain hemispheres in stroke patients or in lesion penumbra mismatch studies) the relative rCBF can be taken as the maximum of the R(t) [118], [120].

If further calibration is required for absolute values of CBF and CBV, the proportionality constant for DSC MRI can be determined by cross calibration with ^{15}O -H₂O PET [209].

Optimising AIF extraction for DSC MRI in small animals

As DSC MRI is primarily used in the brain, AIFs are usually taken directly as the mean signal from the middle cerebral artery ROI in rats [210], [211], similarly to humans [121], [199], [207], [212]. Model and population AIFs are not used as bolus administration speeds can vary greatly between different subjects. Automatic arterial voxel selection algorithms using thresholds to locate large peak heights and short bolus arrival times for AIF determination are favoured over manual methods as they are operator independent, more efficient and create standardized, reproducible results [204], [213] by selecting voxels which fulfil certain criteria [212] or by applying cluster analysis [199]. Whilst these automated algorithms are common in human DSC MRI analysis, very few have been used in small animal scanning due to the complexity of the analysis process.

To the best of the author's knowledge, only Yeh et al. [214] used a simple AIF peak height threshold in rats and Pike et al. [186] used a high peak threshold and an early bolus arrival time threshold in mice to identify suitable voxels for AIF extraction.

The local magnetic susceptibility changes caused by the passage of contrast agent create both a change in MR signal magnitude and a localized phase shift which can be detected on complex MR images [215], [216] and therefore the AIF can also be measured using the phase of the DSC MRI signal instead of the magnitude [217], [218]. The relationship between contrast agent concentration, C , and phase shift ($\Delta\phi$) is linear and is detailed in equation (3.20) [215],

$$C = \frac{\Delta\phi}{\omega_0 TE \chi_M f_g} \quad (3.20)$$

where ω_0 is the Larmor frequency, TE is the echo time, χ_M is the molar susceptibility for Gd ($\chi_M \approx 0.00034M^{-1}$) and f_g is a factor which depends on the geometry of the artery. $\Delta\phi$ is defined as $\Delta\phi(t) = \arg(\mathbf{S}(t)) - \arg(\mathbf{S}(t=0))$, where $\mathbf{S}(t)$ is the DSC MR signal time course. Phase-based measurements depend on the orientation of the blood vessel relative to the B_0 and therefore f_g is maximised at 1/3 for a parallel co-figuration i.e. when the vessel is approximated as a long cylinder and aligned with B_0 .

The linearity of equation (3.20) means that estimating the AIF is more straight-forward and can be done more accurately, which is a key advantage of phase-based DSC MRI techniques. There is also no dependence on hematocrit values involved when estimating the contrast agent concentrations for AIFs (unlike non-linear magnitude measurements) [217], [218]. $\Delta\phi$ should also be less affected by T1 inflow enhancement and variations in contrast agent relaxivities [215], [219]. Finally, phase-based measurements have a higher potential SNR than the signal magnitude ($\Delta R2^*$) method due to its larger dynamic range [217], [219], [220].

The major problem with phase based techniques is that of aliasing, whereby if the phase shift for a passage of contrast agent is greater than π (relative to the baseline phase), the signal will be phase wrapped. This is likely to happen in the early peak phase of the AIF, and techniques such as pairwise subtraction must be employed to combat this effect [218]. Physiological motion induced phase shifts may also need to be corrected for [219].

In previous studies in rats [215], $\Delta\phi$ measurements could only estimate the peak AIF Gd concentration to within 45%, although recent work in pigs [216] has demonstrated the feasibility of a fully quantitative AIF determination from phase-based measurements in the carotid arteries.

3.3 Chapter Summary

This Chapter has detailed the theory behind kinetic modelling and AIF extraction in PET, DCE MRI and DSC MRI. The importance of the AIF in all of these analysis protocols has been explored, with particular reference to the challenges faced in determining an accurate AIF non-invasively. This is of particular note in murine studies, where invasive methods are limited. The use of structural MR to provide improved ROI delineation and PVC for PET IDIFs in mice explored in detail in the following two Chapters.

Chapter 4

Comparison of image-derived input functions for use in ^{18}F -FDG murine studies

As discussed in Chapters 2 and 3, PET images are intrinsically quantitative but are limited by low spatial resolution. This results in partial volume effects, which can lead to inaccuracies in TAC extraction and subsequent errors in compartmental modelling analysis. The hypotheses addressed in this Chapter were as follows:

- 1. MR information can improve ^{18}F -FDG IDIFs and their corresponding kinetic parameters in mice by providing PVC through the geometric transfer matrix (GTM) method.*
- 2. Cardiac motion corrupts IDIF measurements and should be accounted for in murine myocardial PET/MR studies.*
- 3. The vena cava ROI can be used as an alternative IDIF extraction site to the LVBP in mice.*

This Chapter evaluates the performance of the 3DRP and MAP reconstruction algorithm in the extraction of IDIFs from an ^{18}F -FDG murine study. The IDIF results were compared both with and without cardiac gating applied to ascertain the effect of cardiac motion on the IDIFs. The left ventricular blood pool (LVBP) and vena cava (VC) ROIs were both evaluated as IDIF extraction sites, with ROI delineation provided from co-registered MRI images. Cardiac MR data was also used to provide an adaptation of the GTM partial volume correction method to assist in IDIF extraction.

4.1 Introduction

As outlined in previous Chapters, PET is a quantitative imaging technique with very high sensitivity and specificity, able to detect tracer activity concentrations down to the picomolar range, making it ideally suited to functional imaging investigations. Parametric mapping can be performed using SUVs [140], although the time dependent nature of such measurements has led to questions about the specificity of SUVs in reflecting the physiological process of interest [139] and the emphasis in small animal imaging has shifted towards the use of biomarkers obtained with compartmental modelling of tracer kinetics [41]. In murine studies, ^{18}F -FDG is commonly used to quantify glucose metabolism in the brain [51] and heart [29], [33], [53] by analysing the rate constants extracted from a two compartment model, which requires knowledge of the AIF and TACs from ROIs.

Due to the limited total blood volume of mice, image-based methods of AIF extraction are desirable, as these techniques eliminate the need for surgically complex, invasive catheterization procedures which provide limited temporal resolution sampling of the AIF and may disrupt animal physiology [53]. This also avoids the inherent time delay and dispersion effects associated with blood sampling. The limited spatial resolution of PET images, combined with the small vessel size of mice, however, makes accurate IDIF extraction particularly challenging in murine studies and there is, as yet, no consensus on the optimal IDIF extraction method.

4.1.1 ROI selection for IDIF extraction

In human brain PET studies, the carotid arteries are used to extract an IDIF [170], [221] but in mice the carotids are too small to be delineated on PET images, and an IDIF must be extracted from a much larger ROI, such as the left ventricular blood pool (LVBP) in the mouse heart [29], [36], [51], [53], [181], [182]. The LVBP ROI of a mouse is shown anatomically in Figure 4.1 on inversion recovery (IR) FLASH Late Gadolinium Enhancement (LGE)¹ images taken after a contrast agent has been administered, with the myocardium muscle surrounding it. The ROI is drawn in diastole phase as heart is relaxed and blood pool is largest in this phase.

¹IR FLASH is a form of ultrafast GE sequence with very short TR and TE. To increase image signal, the magnetisation is prepared with a single 180° inversion pulse and with a positive gradient lobe on the slice select axis. To perform LGE, data acquisition is centred around the inversion time (TI) when the healthy myocardium signal is nulled in order for the infarcted regions to be highlighted. k space readouts are acquired in a segmented manner over multiple heartbeats.

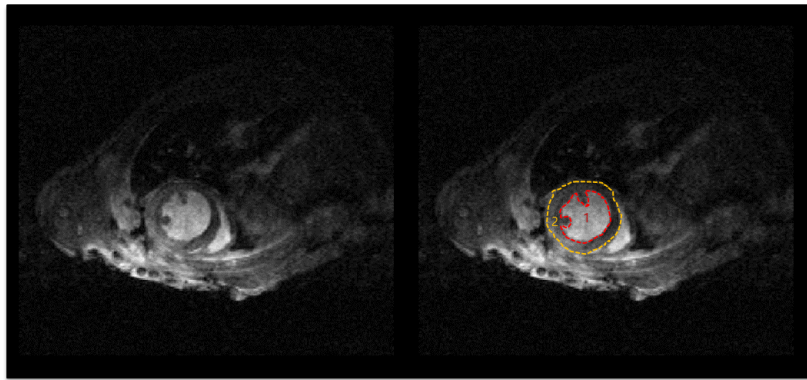


Figure 4.1: Identification of the LVBP (region 1, red) and myocardium (region 2, orange) in diastole from cardiac gated IR FLASH LGE images.

More recently, the vena cava has been suggested as an alternative site to extract an IDIF [33], [52]. It is located below the mouse heart, and when mouse tracer injections are administered, the tracer passes through the vena cava to the heart from the tail vein. Due to the high heart rate of mice, the distribution of tracer between venous and arterial blood occurs at a much faster rate than in humans and therefore it has been hypothesised that a vena cava (VC) ROI could be used in place of an arterial ROI to extract an IDIF for kinetic analysis, with promising results having been reported using OSEM images for both mice [33], [52] and rats [52]. The VC is not adjacent to other high activity areas which reduces spillover and is observed in the early, high temporal resolution frames of the dynamic PET acquisition taken directly post-injection. This also means that IDIFs from the VC ROI require limited post-processing to extract. The anatomy of the inferior vena cava in the transverse view is shown using FISP MR in Figure 4.2.

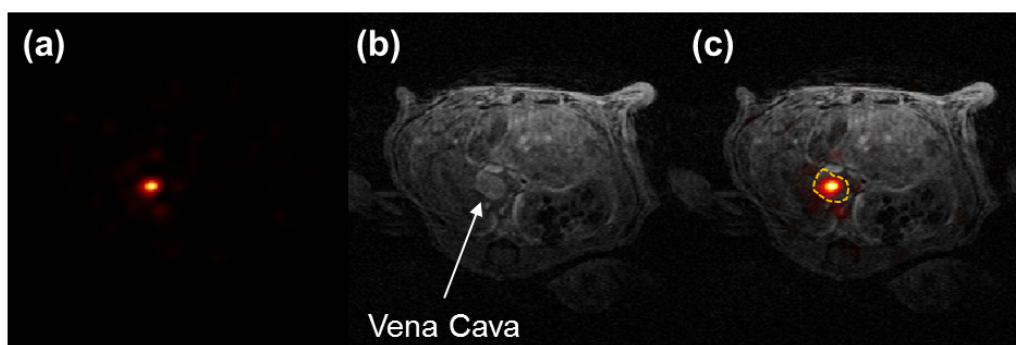


Figure 4.2: Identification of the vena cava on (a) ^{18}F -FDG MAP early frame image (15s after injection start, frame duration of 5s) and (b) Whole body FISP MR images. A fusion of the PET and MR images is shown in (c).

4.1.2 Complications arising from partial volume effects and spillover

Partial volume effects (PVE) result in underestimations of activity in small structures from a combination of two factors: firstly due to the finite spatial resolution of the scanner spreading the signal from the

object, and secondly the sampling of object activity distributions into a voxel grid [67].

The spatial resolution of the PET scanner is determined by reconstructing images of a ^{22}Na point source (the NEMA standard) located at different, standardized radial and axial locations within the FOV [99]. The Full Width Half Maximum (FWHM) of the line profiles taken through the voxel with the maximum intensity in the reconstructed images in the corresponding direction (radial, tangential or axial) is quoted as the resolution of the scanner [26].

The PVE blurring from the limited resolution of the system is seen clearly when imaging objects of diameter ≤ 2 -3 times the resolution of the scanner, with smaller diameter objects becoming affected to an even greater degree. Objects with diameters approximately equal to the resolution of the scanner (or less) are severely blurred and their mean signal values decrease substantially as a result [67], [222], as shown in Figure 4.3. This signal blurring effect on the image can be defined as the 3D convolution of the object activity distribution with the PSF of the scanner [67], [222].

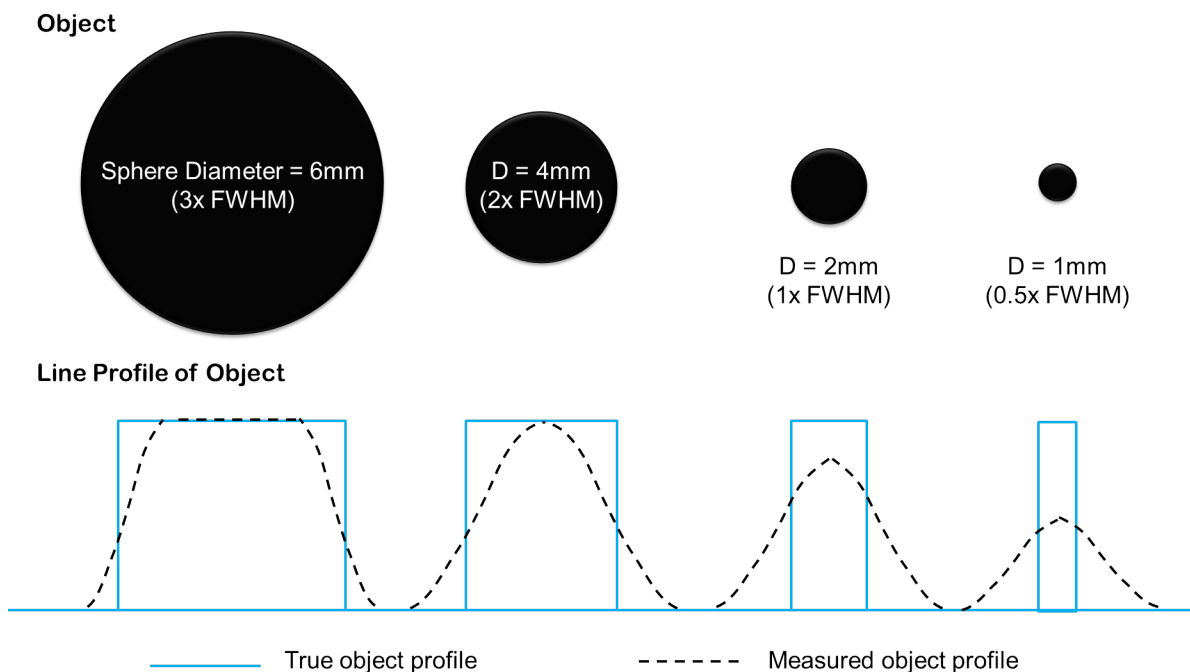


Figure 4.3: PVE effect demonstrated using uniform activity spheres. Observed signal intensity is underestimated compared to true profiles depending on object size (D), as determined by scanner spatial resolution (FWHM). Observed diameter of objects (measured from line profile) also appears to increase, meaning that small sources appear larger but dimmer on images. To measure object shape and activity accurately, object size must be $>2 \times \text{FWHM}$ ($D > 2\text{mm}$). Adapted from [223].

As a result of the 3D image blurring effect due to the finite spatial resolution of the system, there is significant spillover of tracer activity signal between adjacent high and low signal regions. A “cold” region located adjacent to a “hot” region therefore appears to have an activity concentration that is higher than its true value due to the signal spread from the “hot” region, as illustrated in Figure 4.4. In addition

to spill-out from the “hot” regions into the background, there is also spill-in from the background to the object, resulting in images of small sources appearing larger and dimmer in PET images.

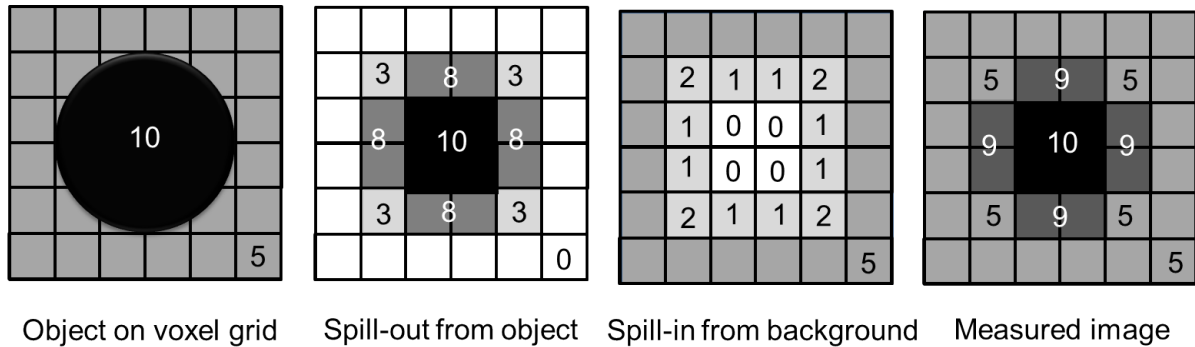


Figure 4.4: Effect of spillover on measured activity distribution. Spillover is seen due to spill-out at the edges of the high activity object into the background and spill-in from background back into the object edge voxels. The summation of the two effects is seen in the measured image [222].

The effect of image sampling also leads to PVE, as shown in Figure 4.5. Tracer activity distributions do not exactly match the voxel grid and voxels will often contain contributions from different tissue types, leading to the signal in that voxel becoming an average of the signal contributions from each of the tissue types present.

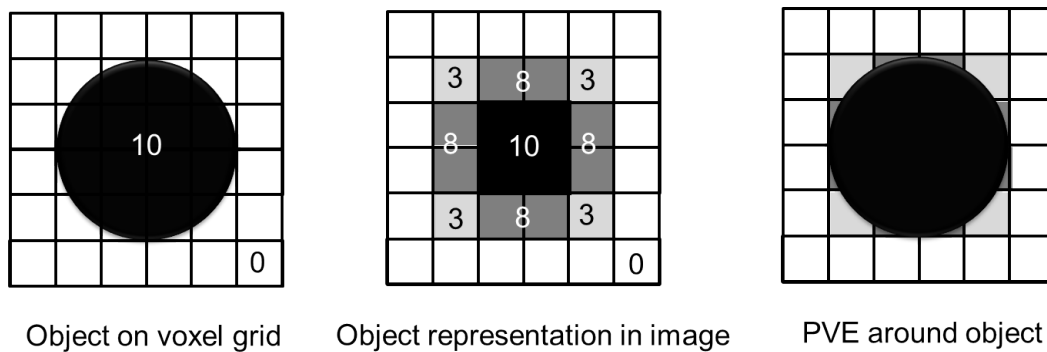


Figure 4.5: Pixels on edges of object contain both source and background activity, with resulting signal taken as the mean of the contributions from these 2 regions. This results in image blurring at the edge of the object [222].

This value is typically between 1.5-2mm at the centre of the FOV for scanners designed to perform small animal imaging [99], and structures with a diameter $<3 \times$ the FWHM of the reconstructed image resolution [222] are affected by PVE, as illustrated in Figure 4.3. This means that even large structures such as the LVBP (typical diameter between 3-4mm [53]) or VC (typical diameter of approx. 2mm [52]) can be significantly affected by PVE, both as a result of the finite resolution of the scanner and from image sampling. In addition, PVE can be time-dependent due to cardiac, respiratory or gross subject motion [67].

Figure 4.6 shows a PET ^{18}F -FDG image of the LVBP region 40 minutes after tracer injection, indicating high tracer uptake in the myocardial muscle as expected and the spreading of the signal due to PVE. The zoom inset of Figure 4.6 indicates the large spillover from the myocardium to the LVBP region, resulting in increased signal in the LVBP region. The spillover effect is also time-dependent [67], as at early time points when the LVBP has large activity and the myocardium muscle tissue has very low activity, due to the tracer travelling to the heart first before being distributed around the mouse body via the vasculature.

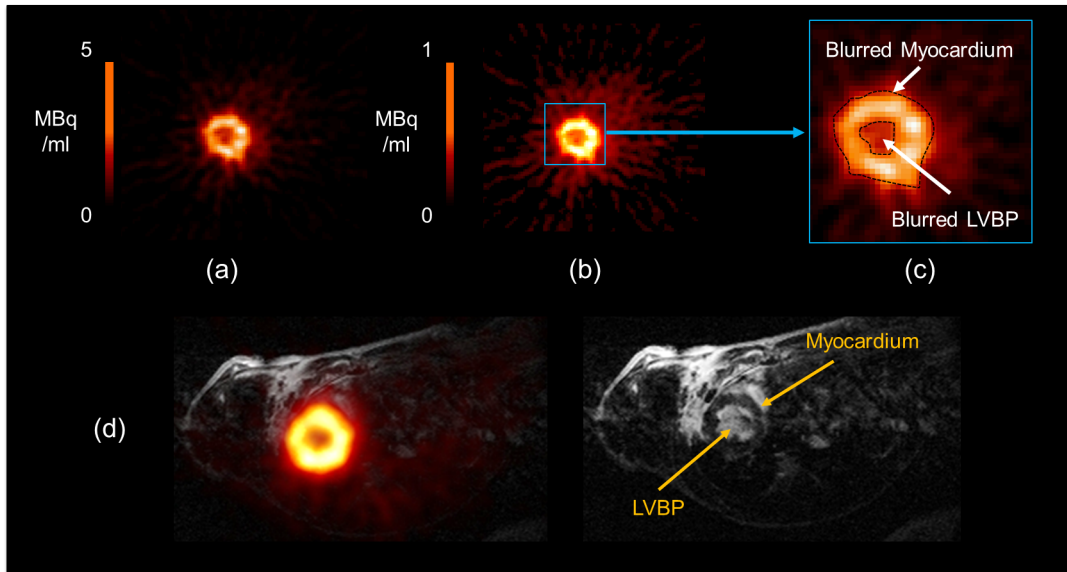


Figure 4.6: (a) 3DRP late frame reconstruction (transverse view) of mouse heart. This image is thresholded at a lower value in (b), with a zoomed in view shown in (c) to illustrate the contamination of the low activity LVBP region through spillover from the high activity myocardium region surrounding it. Co-registered MR data is shown in (d) to illustrate the spread of PET signal between anatomical regions.

4.1.3 Use of geometric transfer matrix (GTM) method to provide partial volume correction

PVC methods can be conducted either in the reconstruction process or on images formed post-reconstruction [67], [222]. The geometric transfer matrix (GTM) method [224] uses high resolution MRI data as an anatomical prior to perform PVC on PET images. The method [224] first assumes that the measured activity concentration, $g(\mathbf{r})$, is the convolution of the underlying true activity concentration, $f(\mathbf{r})$, and the scanner PSF, $h(\mathbf{r})$, described mathematically using equation (4.1), where \mathbf{r} is a three dimensional vector in image space and \mathbf{r}' is a three dimensional vector in object space,

$$g(\mathbf{r}) = \int_{FOV} f(\mathbf{r}') h(\mathbf{r}, \mathbf{r}') d\mathbf{r}' \quad (4.1)$$

The second assumption [224] is that the PET signal comes from N spatial domains, known as D_i , meaning that equation (4.1) can be expressed as follows in equation (4.2),

$$g(r) = \sum_{i=1}^N \int_{D_i} T_i h(r, r') dr' \quad (4.2)$$

These domains are each assumed to have homogeneous uptake (of tracer concentration T_i), i.e. that uptake in the LVBP and myocardium ROIs will be different, but homogeneous within each region. Equation (4.2) can hence be re-written as equation (4.3),

$$g(r) = \sum_{i=1}^N T_i \int_{D_i} h(r, r') dr' \quad (4.3)$$

The final assumption of the method is that the PSF is both spatially invariant and isotropic across the FOV². A global, gaussian PSF is assumed and calculated from a spatial resolution measurement with a ^{22}Na point source [99]. Equation (4.4) shows how the calculated PSF can then be integrated over D_i to give the regional spread function (RSF) [224] of the tissue domain D_i .

$$\text{RSF}_i(r) = \int_{D_i} h(r, r') dr' \quad (4.4)$$

The domain of calculation for the PSF convolution with the true objects is then restricted to only the ROI, rather than the entire image. The mean value observed within ROI _{j} is thus given by equation (4.5), where n_{pix} is the number of pixels in ROI _{j} .

$$t_j = \frac{1}{n_{pix}} \sum_{i=1}^N T_i \int_{ROI_j} \text{RSF}_i(r) dr \quad (4.5)$$

True activity concentrations (T_i) are then found by re-expressing the modelled, observed concentrations (t_j), taken as the mean within the ROI, with a matrix of weighting factors ω_{ij} , shown in equations (4.6) and (4.7).

$$t_j = \sum_{i=1}^N \omega_{ij} T_i \quad (4.6)$$

$$\omega_{ij} = \frac{1}{n_{pix}} \int_{ROI_j} \text{RSF}_i(r) dr \quad (4.7)$$

²In reality, the geometry of the detector ring means that the resolution at the centre of the FOV is higher than at the edges.

The weighting factors represent the contribution of each domain D_i to any ROI j and therefore can be expressed for each component of non-zero activity, forming a matrix shown in equation (4.8). This system of linear equations, known as the geometric transfer matrix, is then solved to fit the weighting factors to the measured signal [224].

$$\begin{pmatrix} t_1 \\ \vdots \\ t_n \end{pmatrix} = \begin{pmatrix} \omega_{11} & \omega_{21} & \cdots & \omega_{N1} \\ \vdots & \vdots & \vdots & \vdots \\ \omega_{1N} & \omega_{2N} & \cdots & \omega_{NN} \end{pmatrix} \times \begin{pmatrix} T_1 \\ \vdots \\ T_n \end{pmatrix} \quad (4.8)$$

The off-diagonal terms of the matrix ($i \neq j$) hence represent the fraction of each activity T_i spilled over from domain D_i and found in ROI j . The contribution of each domain to the ROI is defined and the fitted weighting factors can be used to find the corrected signals for the ROIs. These corrected signals should more accurately reflect the true activity concentrations if the region outlines and the underlying homogeneous uptake assumptions were correct [224].

In previous work, the GTM method was found to increase the accuracy of image derived input functions for kinetic modelling in the brain by segmenting the carotid arteries using co-registered patient head and neck MRI or CT data [156], [221], [225] and has been used in rat brains to correct for spillover between regions which may affect calculation of binding potentials for ^{11}C -raclopride [226]. In this Chapter, the corrected blood component extracted from the LVBP ROI using the GTM method was then used as a PVE corrected IDIF in mice.

4.1.4 Alternative PVC approach - MAP reconstruction

An alternative approach to correcting for PVE in preclinical imaging is to apply iterative reconstruction algorithms which already have PSF modelling built-in [67], [222], such as MAP, which was outlined in Chapter 2. This has been reported to provide resolution recovery, reduced noise, fewer streak artefacts and greater quantitative accuracy in MAP images compared to FBP or 3DRP in both phantom and *in vivo* datasets [53], [66], [68]. These images can also be produced using relatively low count statistics with MAP, making it ideal for the early frames of dynamic PET acquisitions. MAP has also been reported in the literature as giving good agreement with late blood samples and accurate kinetic analysis results when used with cardiac gating [29], [53], [68], [174].

MAP spatial resolution is object dependent and higher activity regions tend to converge faster [68]. As signal spreading from the PSF is already accounted for in MAP, applying GTM to MAP images requires knowledge of the residual PSF after iterative reconstruction. This is difficult to estimate accurately [227] and therefore the GTM approach was only used on images reconstructed using 3DRP.

In this Chapter, a selection of PVC methodologies for IDIF extraction in mice are tested using a cardiac ^{18}F -FDG dataset previously acquired with the Cambridge split magnet PET/MR system. Standard 3DRP and MAP reconstruction methods were compared, both with and without cardiac gating applied, to evaluate the effects of PVE and cardiac motion on murine IDIFs. IDIFs derived using both reconstruction algorithms were attained across two separate ROI regions - the LVBP and VC, with both regions identified using co-registered MRI data. The arterial and venous IDIFs were compared to ascertain if the VC ROI offered a possible alternative to the LVBP for IDIF extraction in mice, as previously reported results have suggested for mice [33] and rats [52]. Finally, the GTM method was applied to the LVBP ROI using co-registered MRI data as an anatomical prior to improve ROI delineation and hence provide MR-based PVC to 3DRP IDIFs derived from the LVBP.

4.2 Materials and Methods

4.2.1 Animal models

Previously acquired sequential cardiac MR and ^{18}F -FDG PET data³ used to study the effects of the surgically-induced myocardial infarction in mice [30], [228] were analysed to compare various approaches to murine IDIF extraction. Twelve male C57/BL6 mice were anaesthetised using pentobarbital and subjected to a 30 min occlusion of the left anterior descending branch of the left coronary artery, followed by reperfusion 2 hours later. Six of these mice received an experimental drug treatment ($1.2\mu\text{mol/l}$ Riociguat, given 5 mins before onset of reperfusion via tail vein injection) during surgery and six were control mice treated with intravenous saline [30], [228]. After surgery, each mouse underwent cardiac MRI imaging followed by a PET scan in a single imaging session.

No blood samples were available from this dataset and therefore only relative comparisons between IDIF techniques were able to be conducted. Inversion recovery (IR) FLASH was used to perform late Gadolinium enhancement (LGE) MR imaging, with the magnetisation prepared with a single 180° inversion pulse and with a positive gradient lobe on the slice select axis. The LGE MR image provided an indication of myocardial viability and overlaid ^{18}F -FDG PET showed how this related to glucose utilization in the mouse heart. To perform LGE, data acquisition was centred around the inversion time (TI) when the healthy myocardium signal is nulled in order for the infarcted regions to be highlighted. k space readouts are acquired in a segmented manner over multiple heartbeats. An example PET/MR image from the mouse dataset is shown in Figure 4.7.

³Used with the permission of Dr Guido Buonincontri, Dr Carmen Methner and Dr Thomas Krieg. All cannulations were performed by Dr Carmen Methner.

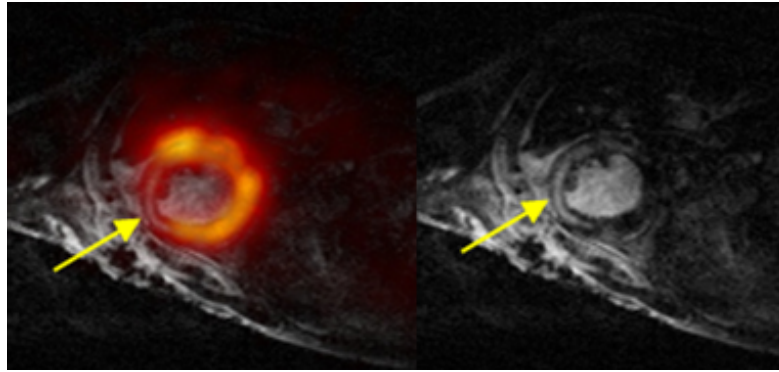


Figure 4.7: Co-registered PET/MR images showing myocardial infarction as hyperintense region on LGE MRI taken in diastole (left) and corresponding decreased uptake region in ^{18}F -FDG 3DRP PET image (right), indicated by yellow arrow.

4.2.2 Sequential PET/MR imaging

For all mice, MRI imaging was performed on a 4.7T Bruker BioSpec 47/40 scanner (Bruker Inc., Ettlingen, Germany) before the animal bed was immediately transferred to the Cambridge split-magnet PET/MR system [25], [26] for PET acquisition. The same bed configuration was used and the imaging conducted in the same session to minimize animal movement and improve the accuracy of co-registration between PET and MR datasets.

All mice were secured prone on the scanner bed on top of a Bruker mouse heart surface coil, with the centre of the mouse shoulder blades aligned with the magnet isocentre. Appropriate monitoring was employed: cardiac pads were attached to the animals front paws, a respiratory pillow was placed underneath the animal's chest and a rectal temperature probe was inserted using a lubricated cover. A heating water blanket was positioned around the animal and kept at a constant temperature of 37°C throughout the experiment. The mice were anaesthetised, using 3% isoflurane in 1l/min O_2 for induction and taken down to 1.5-2% isoflurane in 1l/min O_2 throughout for maintenance, whilst monitoring the animal to keep the respiration rate steady at 30-45 breaths per minute. Prospective gating of cardiac MRI sequences was achieved using the ECG monitoring signal from cardiac pads on the front paws⁴.

The protocol workflow for all mice is summarised in Figure 4.8.

⁴Respiratory gating did not provide improvements in resolution or co-registration so was not applied to keep SNR high in frames with low count statistics [53].

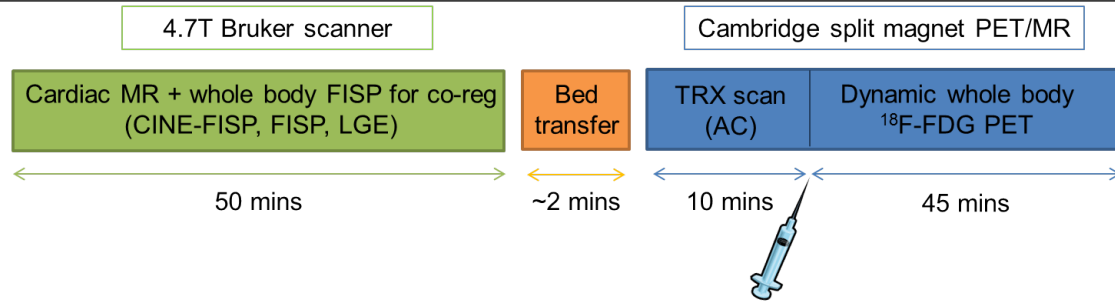


Figure 4.8: Workflow of sequential PET/MR protocol. Injections conducted from outside the magnet bore via tail vein cannula. TRX = transmission scan for PET attenuation correction (AC).

A birdcage transmitter coil of 12cm was used for MR signal excitation and a 2cm mouse cardiac surface coil was used for MR signal reception. FISP MRI (TR/TE 8/4ms, 30mm FOV, matrix $256 \times 256 \times 128$, planar resolution $120 \times 120 \mu\text{m}^2$, 0.5mm slice thickness, NEX = 2) was conducted over the whole mouse body to provide co-registration to the PET and the IR FLASH LGE MRI (FLASH TR 7ms, TR 550-750ms, TE 2.8ms, 35mm FOV, matrix 256×256 , planar resolution $140 \times 140 \mu\text{m}^2$, FA = 60° , bandwidth 64kHz, 8 slices, 0.8mm slice thickness, 0.2mm gap between adjacent slices, selective inversion 0.8mm thickness with 5ms sech shaped pulse, NEX = 1) was conducted over the mouse heart within 15 minutes after contrast agent (Gadovist, Bayer 0.3mmol/kg) was injected intravenously through the tail vein *in situ* from a cannula that ran from the mouse outside the magnet bore. The IR FLASH LGE sequence began with an inversion pulse and acquired a full multi-slice FLASH image at the nearest inversion time (TI) to the healthy myocardium tissue null signal point [30], [228].

After transfer to the PET scanner, a 10 minute transmission scan was conducted using a ^{68}Ge source in singles mode on all mice to estimate the correction required to compensate for the attenuation caused by the MR animal bed, heart coil and mouse body. The ^{18}F -FDG was manually administered as an intravenous bolus injection (mean: $26 \pm 25 \text{MBq}$, range: 7–88MBq) through the tail vein lasting approximately 15s, from the same cannula used for contrast agent injection that ran from the mouse outside the magnet bore. It was immediately followed by a saline flush injection. PET emission data was acquired in list mode for 45 minutes.

Images were reconstructed by the author using 3DRP into the following dynamic frames: $12 \times 5\text{s}$, $12 \times 10\text{s}$, $12 \times 30\text{s}$, $5 \times 60\text{s}$, $5 \times 120\text{s}$ and $4 \times 300\text{s}$. A zoom factor of 2.5 was applied to give an image of matrix $128 \times 128 \times 95$ with a transaxial pixel size of 0.35mm and a slice thickness of 0.8mm. Images reconstructed by the author with MAP used the same dynamic frame configuration, matrix size and voxel size as for 3DRP. MAP was performed using 12 subsets and 18 iterations, with a beta smoothing value of 0.005 and a uniform resolution of 1mm. Data were normalized and calibrated with corrections for decay, detector efficiency, dead time, random events and attenuation using the vendor microPET manager software (Siemens Molecular Imaging).

Each PET image dynamic frame was subsequently binned into four cardiac motion frames. The triggers used to sort the list mode data into the cardiac motion frames were derived from simultaneous ECG recordings. The diastole frame was identified and used for subsequent analysis, as the LVBP was largest at this stage and spillover from the myocardium was minimized. Data were also reconstructed in the same manner without cardiac gating applied to observe the blurring effect of motion on both the resulting images and IDIF results.

Line profiles (3 voxels wide) across both LVBP and VC ROIs were manually measured by the author in both 3DRP and MAP images, with and without cardiac gating applied. SUV values for the infarcted and healthy myocardium regions were calculated from a summation of gated, MAP dynamic frames forming the last 20 minutes of the scan.

4.2.3 IDIF extraction

PET images were co-registered to MRI using the SPMmouse toolbox [27] by the author. Dynamic frames were visually inspected for gross motion and no significant motion was observed between frames or between the MR images and different PET frames after co-registration.

ROIs used to extract IDIFs and TACs from images were drawn in Analyze 8.0 and converted into nifti format for signal extraction in Matlab by the author. ROIs were manually delineated from the co-registered MR images overlaid directly onto the last dynamic frame PET image for the left ventricle region in diastole. LVBP, healthy myocardium and infarcted myocardium ROIs were taken from 8 slices of the FLASH LGE MRI images, giving full coverage of the mouse heart, with an example slice showing these ROIs displayed in Figure 4.9. Central voxels within the LVBP region were taken as the IDIF ROI to minimize contamination from myocardial spillover. ROIs were viewed on all PET frames and manually refined to reduce contamination from neighbouring tissue types caused by gross or cardiac motion over the course of the scan.

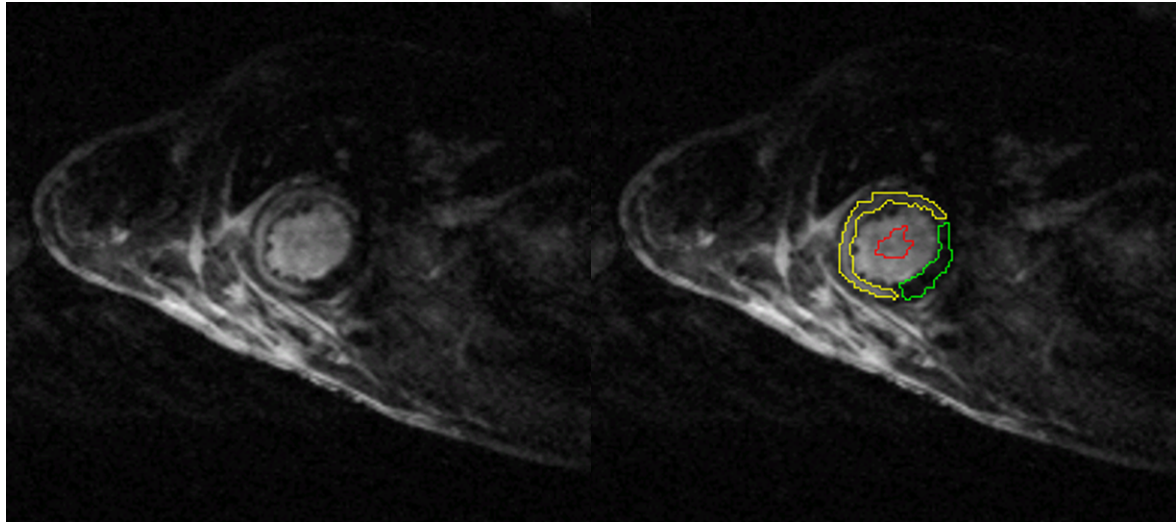


Figure 4.9: Location of PET/MR ROIs used to extract IDIF and myocardial TACs from images of diastole phase of cardiac cycle. Red region indicates LVBP ROI used for IDIF derivation, with central voxels selected to minimize contamination from inter-frame motion. Yellow region indicates infarcted myocardium ROI and green region indicates healthy myocardium ROI used for TAC derivation.

The VC ROI was segmented from 10 slices inferior to the heart region using overlaid FISP MRI and PET data, as shown in Figure 4.2 in the transaxial plane and in Figure 4.10 for the coronal and sagittal planes. Early time point PET frames were used with MR images to coincide with the passage of tracer through the vena cava, as shown in Figure 4.10. The spotted appearance of the PET images in Figure 4.10 is seen due to the limited SNR in the early time point PET frames due to their short duration. The SNR of these images is restricted further when gating is applied.

FISP MRI data was not acquired for Mouse 5 from the control group and the PET emission scan for this mouse was not started until 20s after the tracer injection had been administered due to a technical fault in the PET scanner software. As a result, the tracer bolus had already reached the LVBP region when PET data acquisition began and therefore it was not possible to extract any VC IDIFs from this mouse, so only 5 control mice datasets are used in the VC ROI analysis.

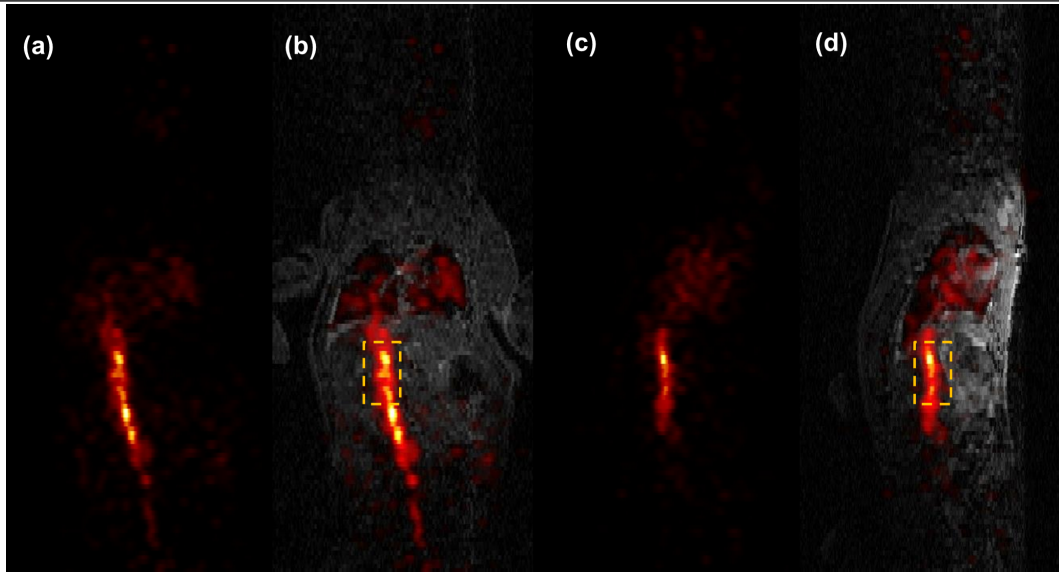


Figure 4.10: Location of vena cava ROI used to extract IDIFs on cardiac gated MAP images. Coronal view is shown in (a) PET data (early frame, 15s after injection, 5s duration) and (b) FISP MRI data with the sagittal PET view shown in (c) and the sagittal MR view in (d). Orange box indicates region of vena cava analyzed to attain IDIF estimate.

Once all ROIs were delineated, the mean values of the LVBP and VC ROIs for each dynamic frame were used to generate activity time courses, designated as IDIFs, for both 3DRP and MAP PET images, with and without cardiac gating applied. Healthy myocardium and infarcted myocardium TACs were generated in the same manner using the myocardium ROIs.

4.2.4 Application of GTM method to LVBP ROI IDIFs

Five ROI classes were required to conduct the GTM PVC method on this mouse dataset and were manually delineated from co-registered, high resolution FLASH MR LGE images overlaid on the last dynamic PET frame by the author. The ROIs were then manually inspected through all other dynamic PET frames to ensure they were not overtly affected by motion over the time course of the scan.

The five ROI classes were as follows: (a) LVBP, (b) infarct, (c) healthy myocardium, (d) body and (e) background. Figure 4.11 displays ROIs covering the LV lumen (red), infarct region (yellow), healthy myocardium (green), body (blue) and background (black). These ROIs were extracted from 8 slices of the FLASH LGE MRI images, giving full coverage of the mouse heart.

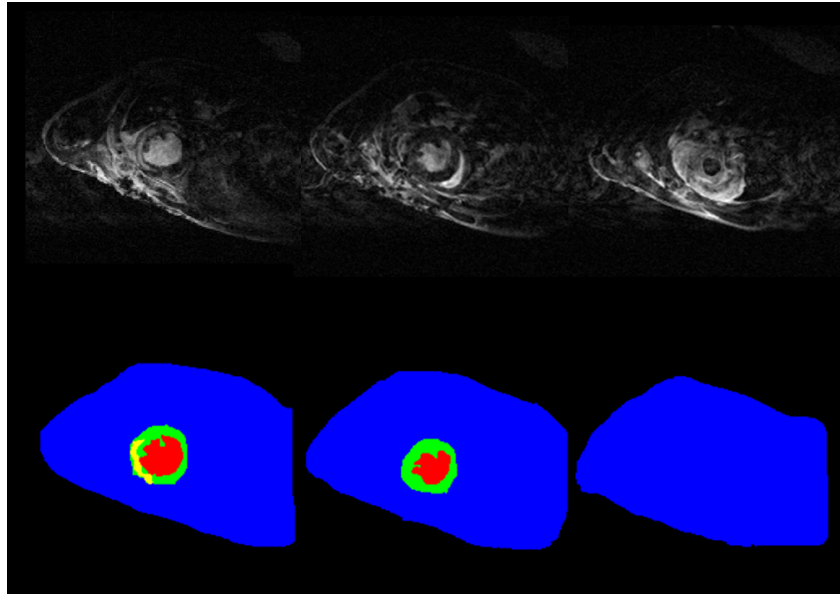


Figure 4.11: Top row: FLASH MRI images of mouse heart. Bottom row: Illustration of ROI regions extracted for single subject across 3 slices.

Segmented classes were convolved with a 1.8mm (FWHM) 3D isotropic Gaussian function representing the scanner PSF [26], as shown in Figure 4.12. The signal from each PET frame was modelled as a linear combination of the signal from the 5 convolved ROI classes to find the corrected contributions from each region. The GTM method was applied to each frame of the dynamic PET scan, and the extracted LVBP co-efficients (region (a) in Figure 4.12) for each frame were plotted as the corrected IDIF. The healthy and infarcted myocardium co-efficients (regions (b) and (c) in Figure 4.12) were used to generate their respective corrected TACs.

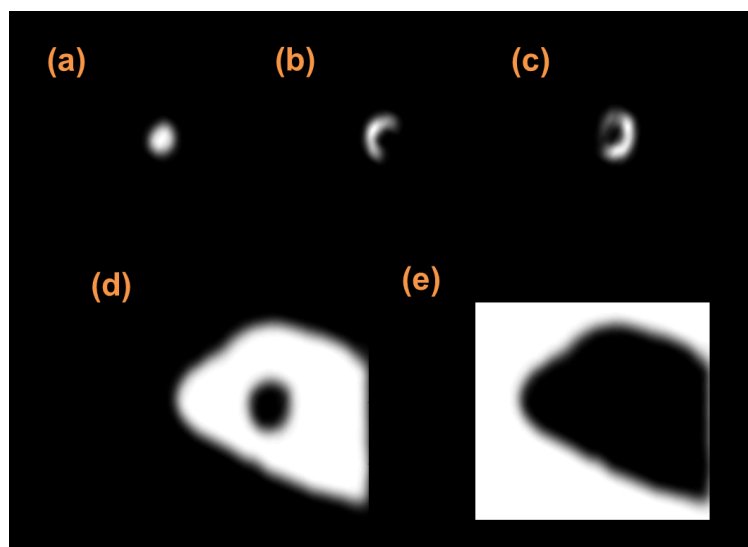


Figure 4.12: PVC GTM method of IDIF determination using 5 ROI classes delineated from MR and convolved with scanner PSF: (a) LVBP, (b) infarct, (c) healthy myocardium, (d) body and (e) background. PET signal was modelled as a linear combination of these classes and the fitted LVBP values (region (a)) were used as the corrected IDIF.

4.2.5 Conversion of IDIFs from whole blood to plasma

All extracted IDIFs represent the signal from whole blood and so were converted to the signal from plasma. This was to ensure they matched the definition of the AIF, which is taken as the activity concentration in arterial plasma, as this represents the tracer available to tissue. This conversion was performed using equation (4.9), which employs empirically derived numerical factors to convert between blood and plasma activity concentrations *in vivo* for mice [51], [182]:

$$A_{\text{Plasma}} = A_{\text{WholeBlood}} \times (0.39 \times \exp^{-0.19t} + 1.117) \quad (4.9)$$

where A_{Plasma} is the IDIF, $A_{\text{WholeBlood}}$ is the activity concentration derived directly from the LVBP on PET images and t is the time during the scan.

4.2.6 Kinetic modelling

All resulting plasma IDIFs were then used in compartmental modelling of the mouse data using PMOD software (v2.5, PMOD technologies Inc.). A two compartment irreversible model was assumed for ^{18}F -FDG detailed in Chapter 3. Model bi-exponential curves (an accepted model for mouse IDIFs [31], [54]) were fitted to the extracted IDIFs where possible before analysis to smooth the data. Patlak analysis (linear graphical analysis, shown in equation (3.11) in Chapter 3) [154] was performed on each IDIF and its corresponding healthy and infarcted myocardium TACs to calculate the influx rate constant, K_i , in units of ml/g/min in those respective regions. An example of the different Patlak plots produced using the measured data and the smoothed fitted data is shown in Figure 4.13. If bi-exponential fits were not achieved using the PMOD software, for example if the curve was contaminated with spillover from the myocardium or if the noise was very high, the measured IDIF was smoothed using a running average.

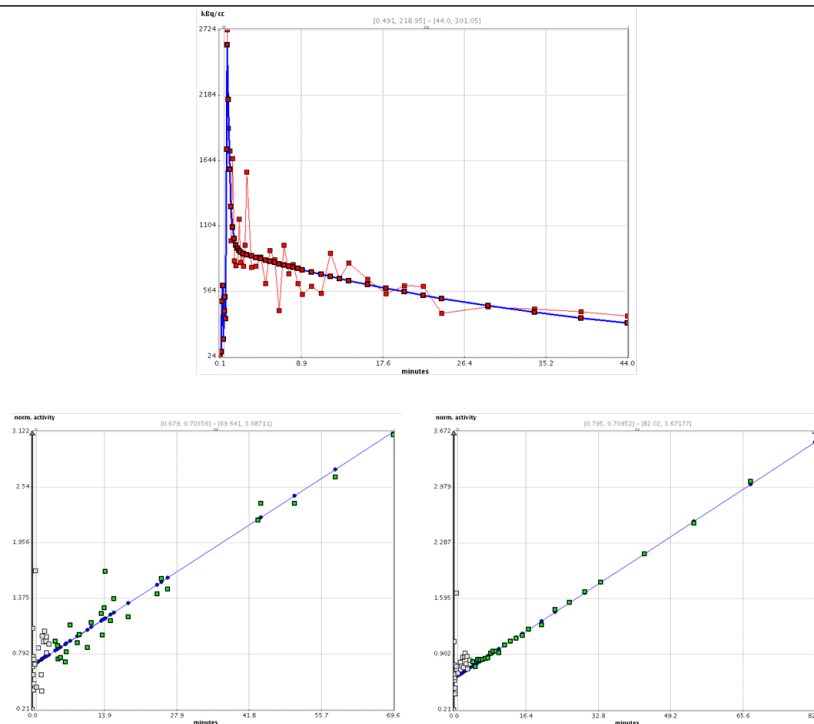


Figure 4.13: Fitting bi-exponential models to IDIFs for Patlak plot analysis. Top row: Extracted IDIF for single subject in red, with bi-exponential model fit in blue performed using PMOD software. Bottom row: Patlak plots produced using measured (not smoothed) IDIF (left) and fitted IDIF (right).

K_i values were compared to literature for validation, as no blood samples were taken with this previously acquired dataset. K_i values obtained from healthy and infarcted myocardium ROIs were also compared between treated and untreated MI mice groups.

4.3 Results

4.3.1 3DRP and MAP image comparison

Improved resolution and contrast were seen in MAP cardiac images when compared to corresponding 3DRP images, which agreed with previously published results [33], [53], [68]. Mouse heart images for a single subject are shown in Figure 4.14 with their corresponding line profiles (3 voxels wide).

As expected, line profiles indicated that MAP was found to reduce the spillover error and displayed reduced noise compared to 3DRP, causing the LVBP region to have a much lower activity in the late dynamic frames and the healthy myocardium region to have higher activity peaks. This is expected at the late stage of the PET scan when the tracer uptake is high in the myocardial muscle and has left the bloodstream. The line profiles seen in Figure 4.14 also show broader peaks in the 3DRP images as a result of PVE, which has been corrected for in the MAP images.

The application of gating to the data also has a profound effect on the resulting reconstructed images. By reducing the effect of cardiac motion, in both 3DRP and MAP images increased contrast is seen between the blood pool and the myocardium in diastole, as well as sharper definition of myocardial peak profiles when compared to line profiles taken from non-gated images. The line profile which displayed the best contrast and least spillover was taken from the gated MAP images, which was expected due to the smoothing, PVC and motion correction being applied.

The corresponding images and line profiles for an early frame for the VC ROI are displayed in Figure 4.15. The tracer is observed to be travelling from the tail vein through the VC into the mouse heart and a single peak is seen in the line profiles. It can be seen again that the MAP images and line profiles give greater contrast between the peak and the background compared to the 3DRP images. The effect of cardiac gating in this case, however, results in increased noise in the 3DRP gated images and line profiles due to low count statistics in these high temporal resolution frames. The MAP gated line profile does show an increase in peak height, but also shows an increase in noise due to reduced count statistics.

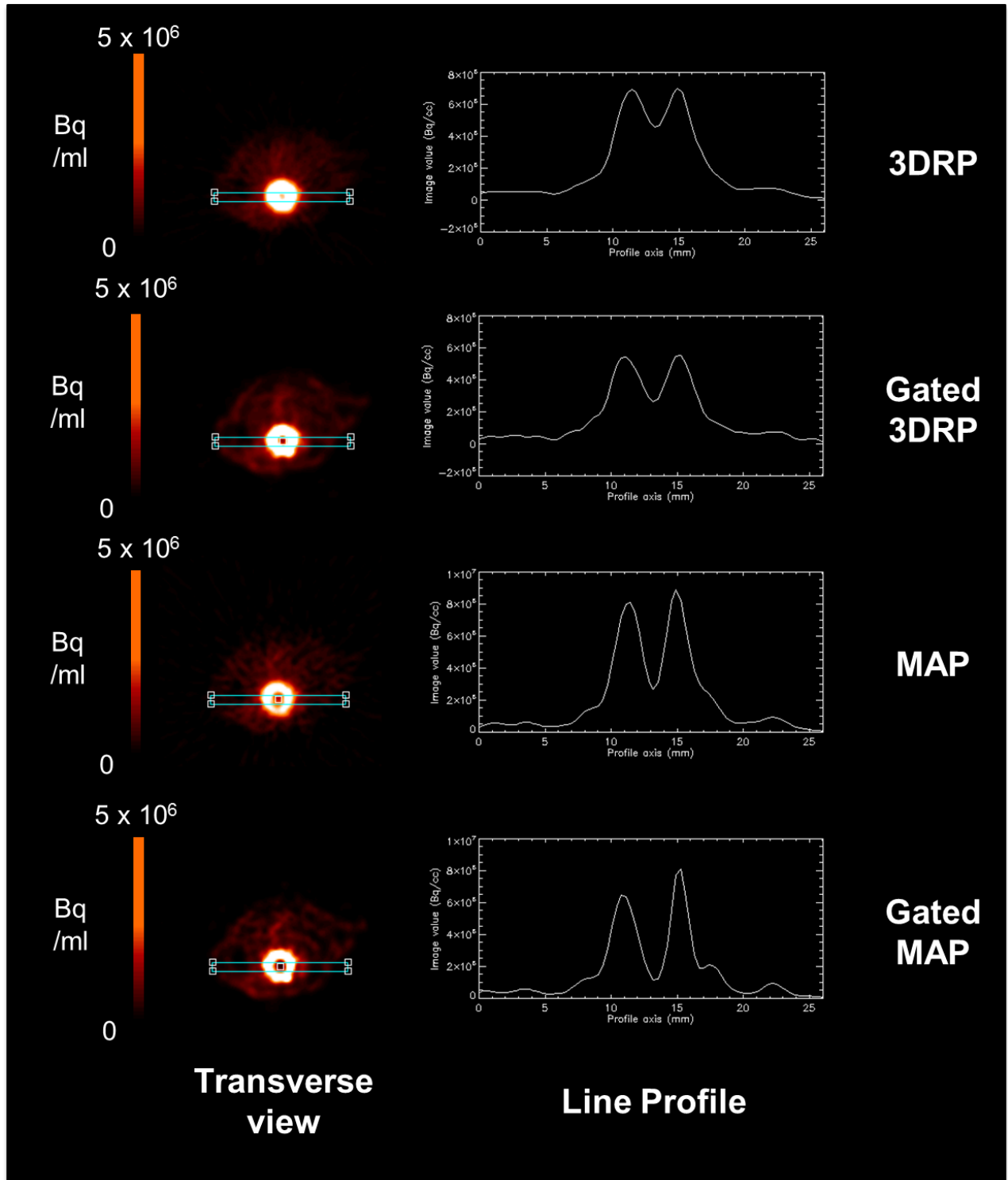


Figure 4.14: Comparison of line profiles (3 voxels wide) using 3DRP and MAP for left ventricle. Left column: Comparison of last frame (40-45mins, 5 minute duration) mouse heart images created using 3DRP and MAP in the transverse view, with and without cardiac gating applied. Right column: Line profiles produced using each technique, with greatest resolution of mouse heart achieved using MAP with cardiac gating applied.

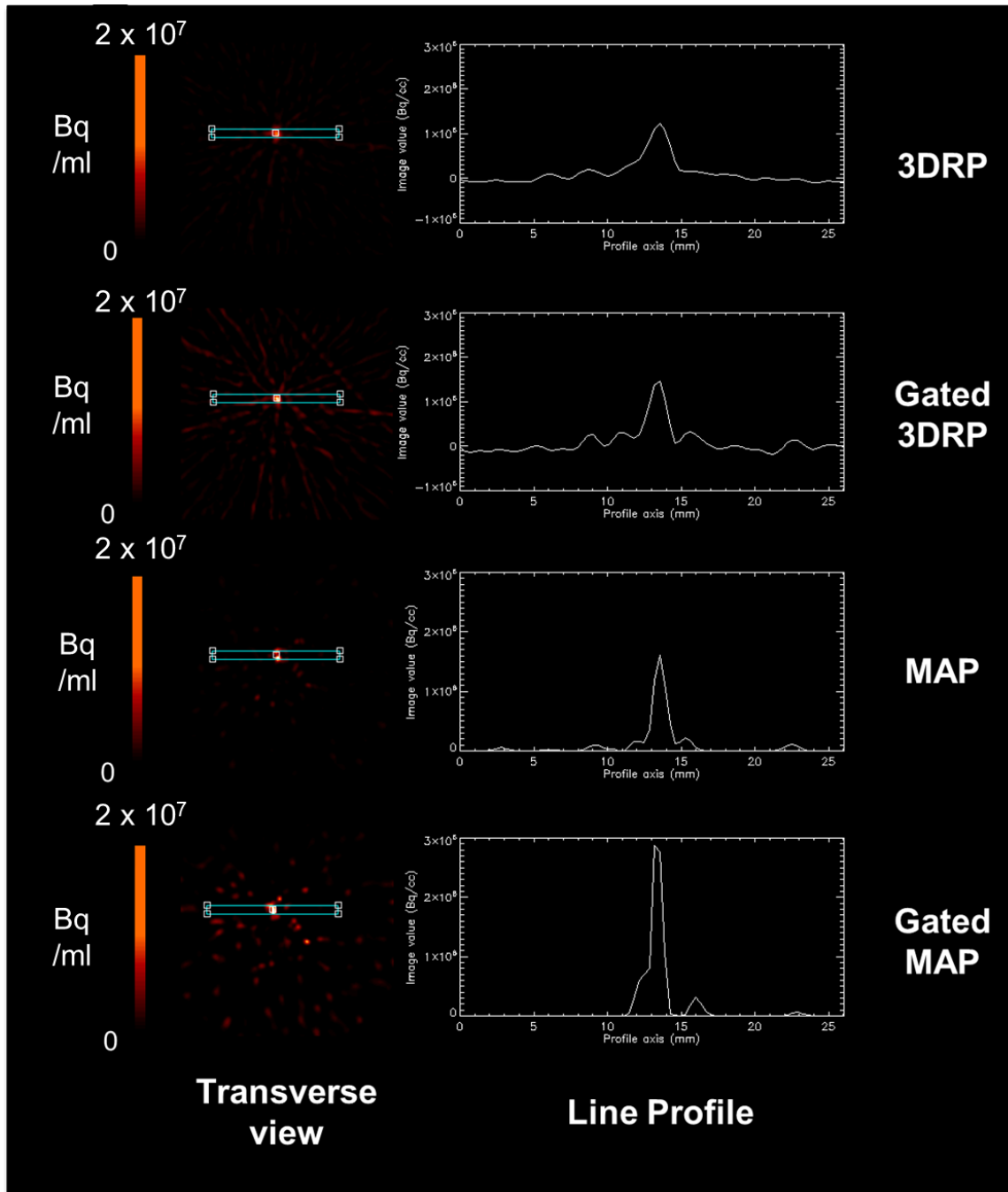


Figure 4.15: Comparison of line profiles (3 voxels wide) using 3DRP and MAP for vena cava. Left column: Comparison of early frame (approx. 15s post injection, 5s duration) mouse inferior vena cava images created using 3DRP and MAP in the transverse view, with and without cardiac gating applied. Right column: Line profiles produced using each technique, indicating increased noise in gated images due to low count statistics.

4.3.2 Differences in SUV between control and drug treated mouse groups

An example mouse from each of the treatment groups is shown in Figure 4.16⁵. The infarcted region is identified by decreased PET tracer uptake in the untreated mouse myocardium and increased signal in LGE MRI from contrast agent uptake, indicating that a larger infarct is present.

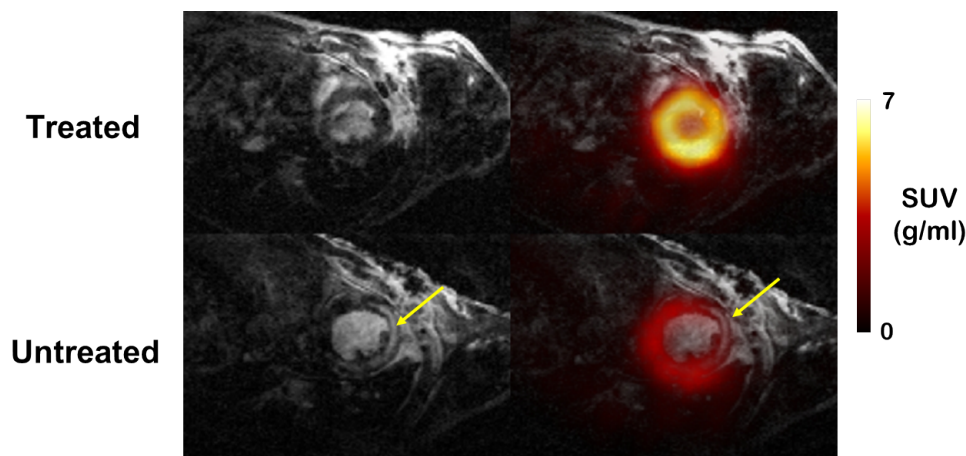


Figure 4.16: Co-registered SUV PET (3DRP) and LGE MRI short axis views of the infarcted mouse heart. Top row: mouse treated with Riociguat, bottom row: untreated (control) mouse. Infarcted region indicated by arrow.

SUV values were taken from the last 20 minutes of a dynamic 45 minute acquisition. For both groups ($n=6$ in each), SUV values for the healthy myocardium remained roughly constant, with the control group having a mean SUV of $3.9 \pm 2.2 \text{ g/ml}$ and the drug treated group a mean SUV of $3.6 \pm 1.4 \text{ g/ml}$ (two means Student's t test, p value = 0.729) when taken from cardiac gated images reconstructed with MAP. The infarcted regions showed a slightly decreased SUV in the control group of $2.5 \pm 1.0 \text{ g/ml}$ compared to $3.2 \pm 1.2 \text{ g/ml}$ in the drug treated group (two means Student's t test, p value = 0.208). There was a mean difference in SUV values between the healthy myocardium and infarcted regions of 1.4 g/ml in the control group and 0.4 g/ml in the drug treated group, with a Student's t test between the healthy and infarcted region mean values giving a p value of 0.031 for the control group and a p value of 0.176 for the drug treated group. This result indicated a significant reduction in function of the infarcted myocardium in the control group.

The SUV values confirmed results found in previous analysis of this data - a significantly larger average infarct size was found in the control group compared to the drug treated group, based on gold standard measurements from LGE MRI [30], [228]. The results from the control and drug treated groups for the different IDIF extraction techniques are therefore discussed separately in the following sections

⁵The control mouse shown here has the largest infarct of the cohort and the drug treated mouse has the smallest infarct, which may indicate why the difference in healthy myocardium values appears so high in this image as the effect of the drug is most strongly seen when comparing these two mice

of this Chapter. A full discussion of the efficacy of the drug Riociguat evaluated using both PET and MR can be found in [30] and [228].

4.3.3 IDIFs extracted from LVBP ROI

As shown in Figures 4.17 and 4.18, similar healthy myocardium TACs are achieved for both reconstruction algorithms, with and without cardiac gating applied in both mouse groups. In the drug treated group (see Figure 4.18), the TACs for healthy and infarcted myocardium were found to be very similar in shape but in the control mouse group the infarcted tissue displayed a much lower activity concentration at late time points (see Figure 4.17). This indicated a lack of viable tissue in the infarcted regions, as it cannot utilize the ^{18}F -FDG, and this result is consistent with the larger infarct sizes found in that group using LGE MRI [30], [228]. The 3DRP IDIFs shown on the left hand side Figure 4.17 are shown to have higher tails at later time points compared to the MAP IDIFs on the right hand side, with the ungated 3DRP IDIF shown to be extremely similar to the infarct TAC. This indicates that even if central voxels from the LVBP ROI are used to manually extract an IDIF from ungated 3DRP images (as demonstrated in the red ROI outline in Figure 4.9), the IDIFs produced are contaminated with TAC signal as a result of PVE and spillover.

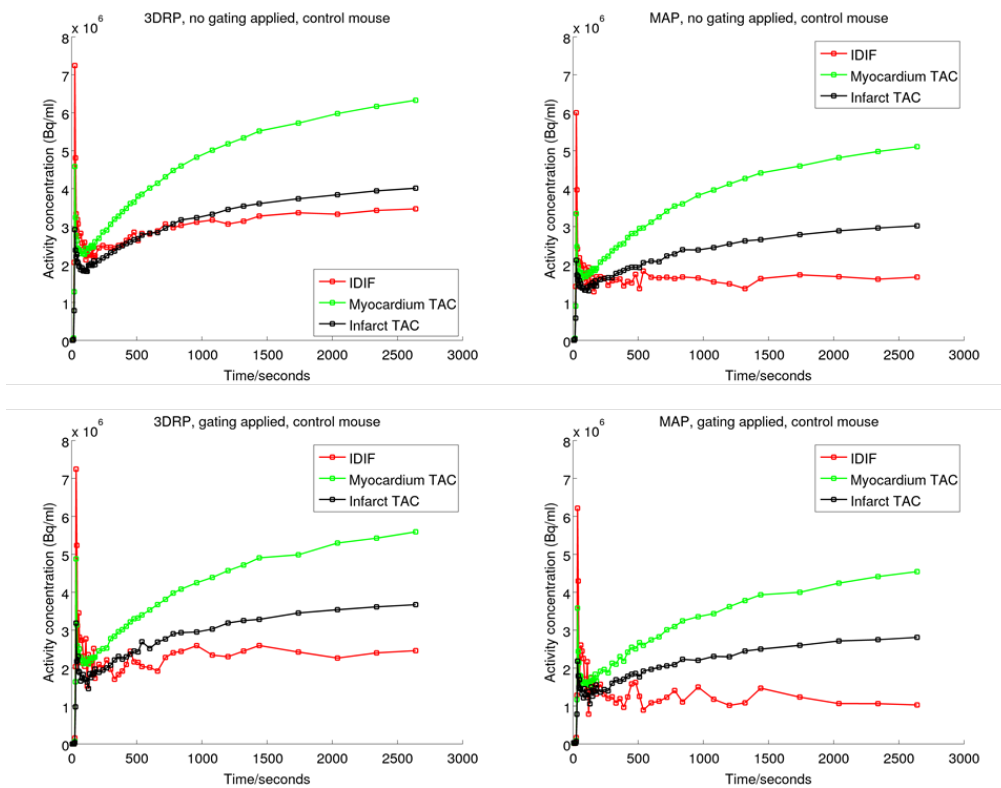


Figure 4.17: Comparison of IDIFs and myocardial TACs for control mouse, extracted from 3DRP and MAP images, with and without cardiac gating applied.

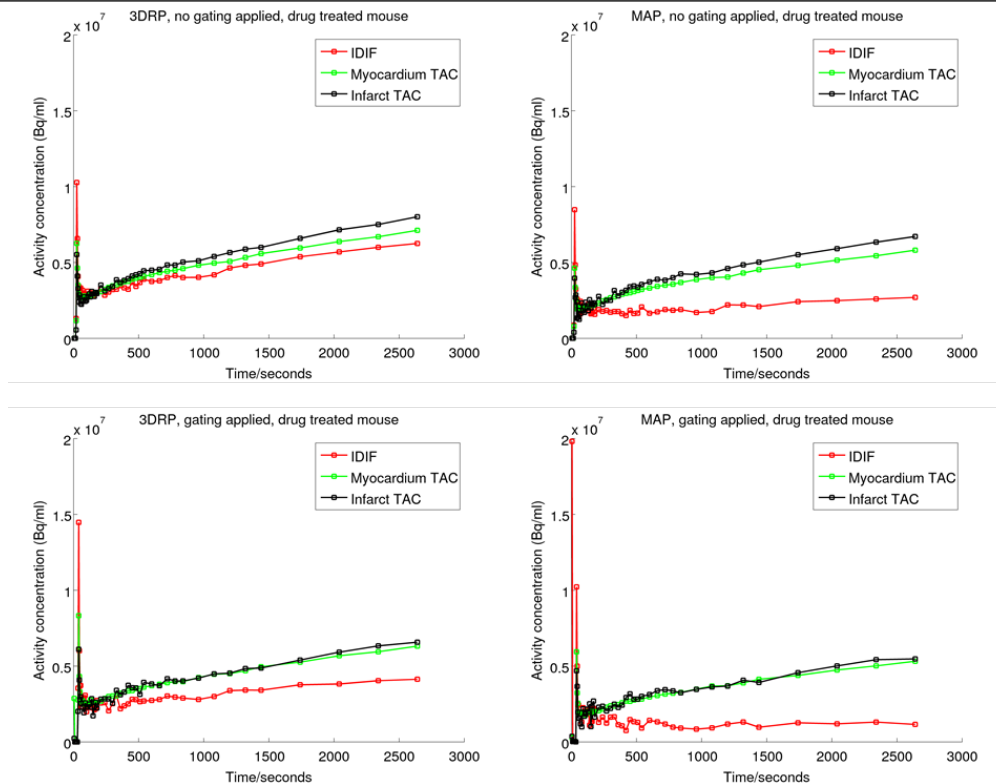


Figure 4.18: Comparison of IDIFs and myocardial TACs for drug treated mouse, extracted from 3DRP and MAP images, with and without cardiac gating applied. Note the scale on the y axis has been changed from $8 \times 10^6 \text{Bq/ml}$ in Figure 4.17 to $2 \times 10^7 \text{Bq/ml}$ to accommodate the MAP IDIF peak with gating applied.

The IDIFs and TACs displayed for all techniques with cardiac gating in Figures 4.17 and 4.18 show noisier profiles than their ungated counterparts, indicating that some gross motion is still present and affecting the gated data to a greater degree due to the decreased count statistics in the gated image frames. This is clearer in the IDIF profiles than in the TACs as the smaller LVBP ROI is more susceptible to small displacements due to motion.

The IDIF peak heights are similar for both 3DRP and MAP algorithms, with and without gating applied (see Table 4.1 for a full comparison of IDIF peak heights across all extraction methods), due to the lack of myocardial spillover in early time frames, but at late time points the extracted IDIFs show substantial differences depending on the extraction technique used. In similar fashion to the line profiles shown in Figure 4.14, IDIFs derived using MAP instead of 3DRP have lower activities at late time points due to a reduction in PVE and spillover. Applying cardiac gating to reduce spillover contamination from motion further improves the IDIF tail. The ungated 3DRP data, in particular, is seen to be affected by significant spillover, such that the IDIFs are very similar to the myocardial TACs. None of the 3DRP ungated IDIFs could be fitted with the bi-exponential IDIF model in PMOD as a result.

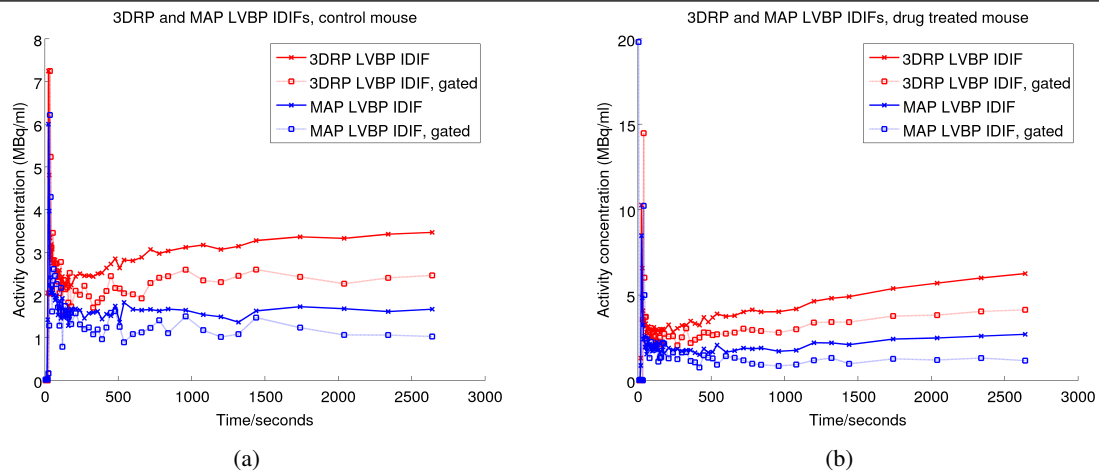


Figure 4.19: Summary of IDIFs derived from LVBP ROI for (a) control mouse and (b) drug treated mouse. Both cases show IDIFs with lower value tails due to decreased spillover when using cardiac gating (dotted lines) and MAP (blue), compared to 3DRP (red). Note the y axis scale of 8MBq/ml in 4.19(a) and 20MBq/ml in 4.19(b) to accommodate the gated MAP IDIF peak.

Figure 4.19 summarises the IDIFs shown in Figures 4.17 and 4.18. Similar changes in IDIF curve shape caused by the application of PVC through MAP and motion correction through gating is seen across both mice.

4.3.4 Comparison of LVBP IDIFs and VC IDIFs

The use of the VC ROI for IDIF extraction is displayed in Figure 4.20 for the control group mouse and in Figure 4.21 for the drug treated mouse. The VC IDIFs were found to have lower tail values and a much smoother curve shape for both 3DRP and MAP algorithms when compared to the LVBP IDIFs. Similar results were observed in both mouse groups, as shown in Figures 4.20 and 4.21. No clear differences in IDIF curve shape were observed between gated and ungated VC IDIFs, suggesting that the VC is not adversely affected by cardiac or gross motion.

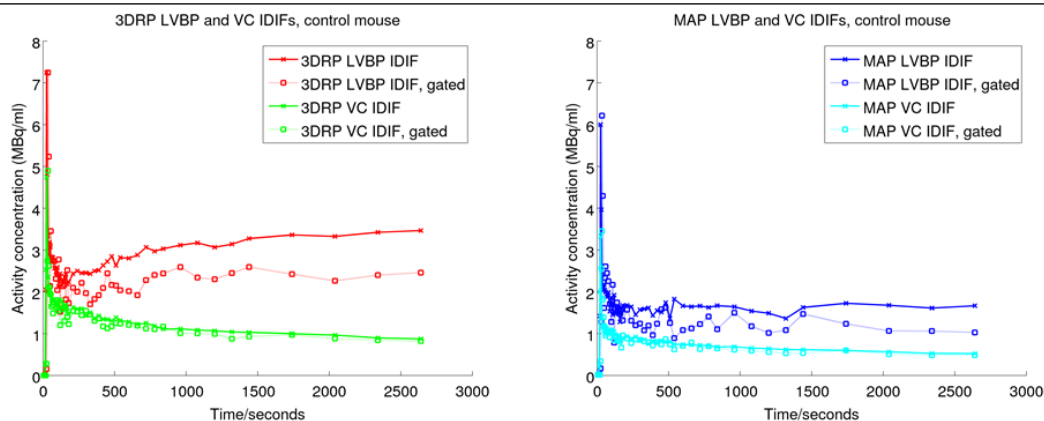


Figure 4.20: IDIFs extracted from LVBP and VC ROIs using 3DRP and MAP reconstruction techniques for control mouse. Green indicates 3DRP VC IDIFs, cyan indicates MAP VC IDIFs.

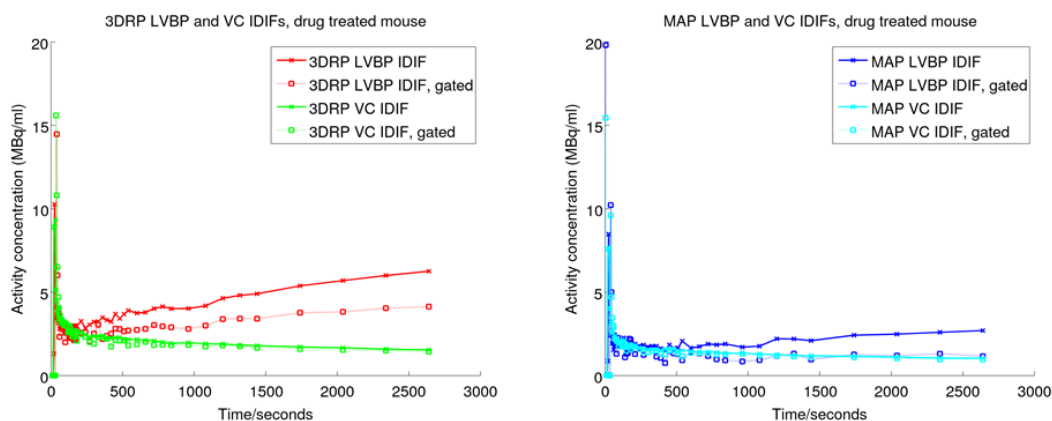


Figure 4.21: IDIFs extracted from LVBP and VC ROIs using 3DRP and MAP reconstruction techniques for drug treated mouse. Green indicates 3DRP VC IDIFs, cyan indicates MAP VC IDIFs.

4.3.5 Comparison of LVBP IDIFs with GTM correction to VC IDIFs

LVBP IDIFs extracted using the GTM method to correct for PVE and cardiac gating to correct for motion were found to have a greater resemblance to those extracted from the VC ROI than the uncorrected 3DRP IDIFs, as shown in Figure 4.22.

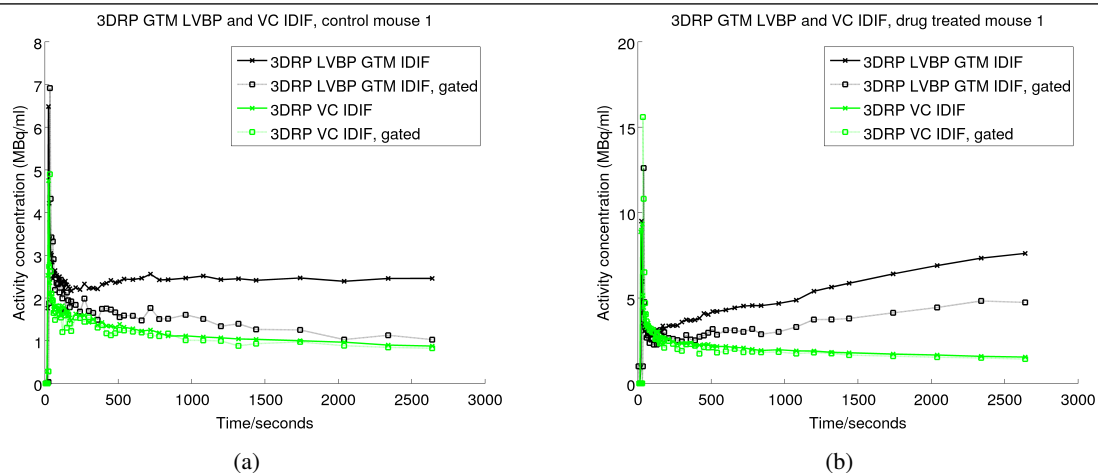


Figure 4.22: Comparison of GTM IDIFs (black) to VC IDIFs for sample control and drug treated mice.

A second set of GTM and VC IDIFs for a different control mouse and drug treated mouse are shown in Figure 4.23. This illustrates the variability of the IDIFs produced when using the GTM method, although the drug treated mouse IDIFs on the right hand side of Figure 4.23 indicate that some PVC corrected IDIFs appear to have similar curve shapes to the VC ROI IDIFs when gating is applied.

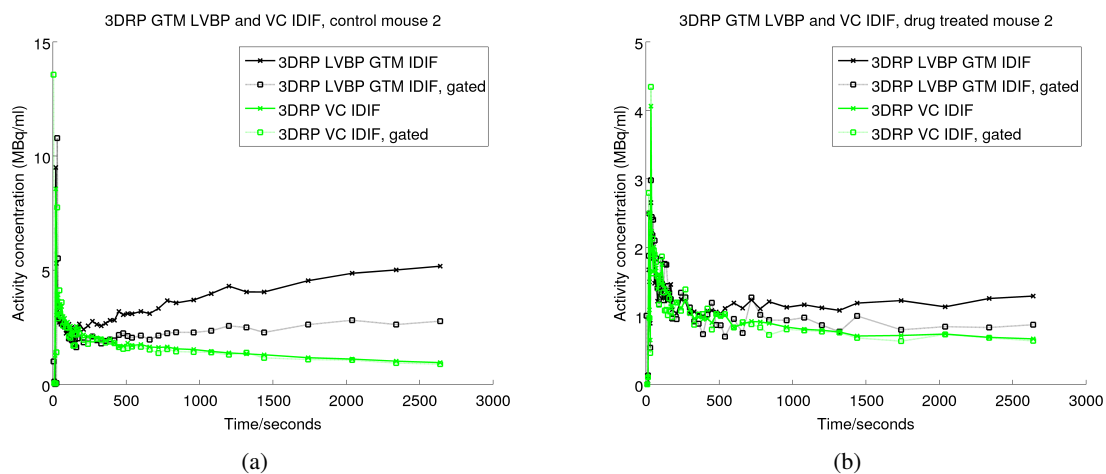


Figure 4.23: Comparison of GTM IDIFs to VC IDIFs for second set of control and drug treated mice.

In all 4 mice shown in Figures 4.22 and 4.23, cardiac gating is seen to have limited effect on the VC IDIFs, in contrast to the clear effect gating has on the GTM IDIFs. This implies that the VC ROI is less affected by motion than the LVBP ROI. Gated GTM IDIFs are compared with all other gated IDIFs (both 3DRP and MAP) in Figures 4.24 and 4.25. Both 3DRP and MAP VC IDIFs are, in fact, most similar to the MAP LVBP IDIFs rather than the GTM 3DRP LVBP IDIFs for the example mice from both groups. The lowest IDIF tail values (i.e. those assumed to have the least contamination from myocardial spillover) were generated using the VC ROI and cardiac gated MAP images.

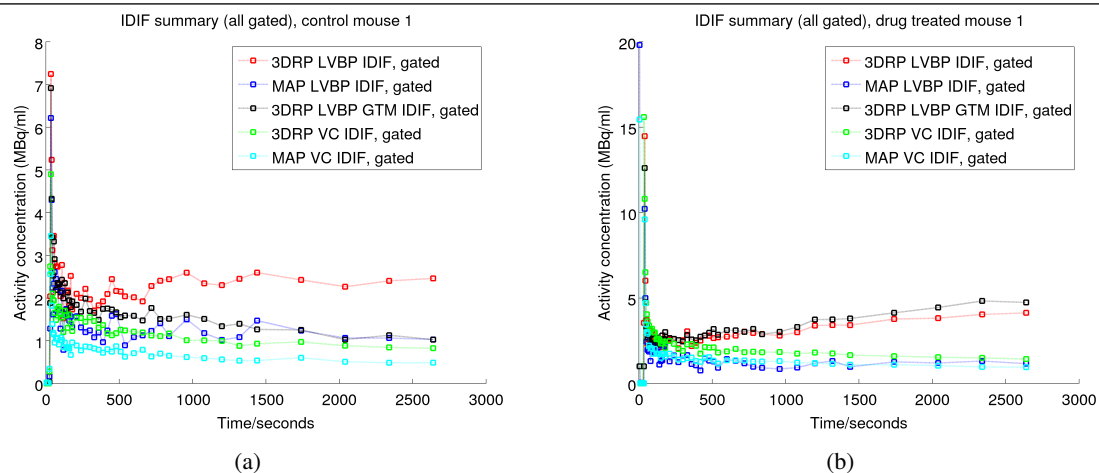


Figure 4.24: Gated GTM method compared to all previously discussed methods for (a) control mouse and (b) drug treated mouse.

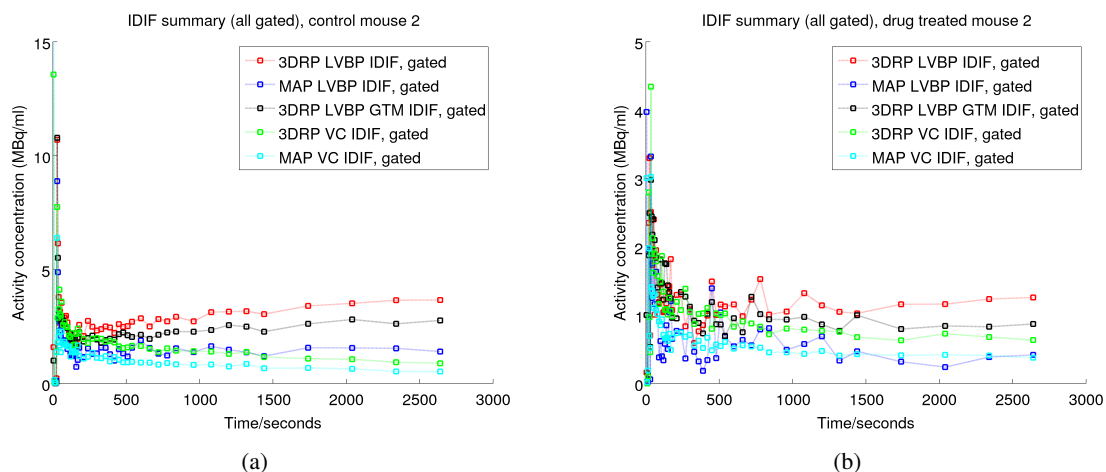


Figure 4.25: Gated GTM method compared to all previously discussed methods for (a) second control mouse and (b) second drug treated mouse.

4.3.6 IDIFs generated for all mice - LVBP ROI

A summary of all IDIFs for the control mouse group taken from the LVBP ROI is shown in Figure 4.26, with the corresponding IDIFs for the drug treated mouse group shown in Figure 4.27. The drug treated group, shown in Figure 4.27, show greater uniformity on average in their ungated IDIF shapes compared to the control mice group, although after the application of both PVC and gating all IDIFs from both groups appear more similar. In both sets of graphs, the largest contamination in the IDIFs from myocardial TAC signals due to spillover is seen in the uncorrected 3DRP data. This contamination is reduced through the application of gating to remove blurring due to cardiac motion in all mice, giving more uniform IDIFs throughout the mouse group if gating is applied. PVC from either the application of the GTM method or from the use of the MAP reconstruction algorithm also has a similar effect in

reducing the spillover effect from the myocardial TAC, resulting in an IDIF shape that decays over time. In addition, if both PVC through either GTM or MAP is applied in conjunction with cardiac gating, a greater decrease in spillover to the IDIF shape is seen, indicating that both PVC and motion should both be accounted for in IDIF extraction techniques in mice to give the best separation of IDIFs and TACs.

Table 4.1 details the respective peak heights derived for each LVBP IDIF, with the values normalized to injected dose (by dividing each value by the injected dose) shown in Table 4.2. Significant differences (paired Student's t test, $p < 0.05$) were seen across the entire mouse cohort ($n=12$) between the 3DRP peak heights and the gated 3DRP peak heights, the 3DRP peak heights and the GTM 3DRP peak heights and the 3DRP peak heights and the MAP peak heights, indicating the large effect PVC and motion correction have on the IDIFs. P values > 0.05 were seen between the gated GTM IDIF and the gated MAP IDIF peak heights due to their increased variances. Control mouse 2 was seen to have a gated MAP IDIF peak height twice the size of any other IDIF peak (17.6g/ml in Table 4.1) and drug mouse 1 was also seen to have a much higher peak (6.1g/ml) with gated MAP than any other IDIF extraction method. This effect is most likely due to the application of gating, which separates the dynamic frames into phases of the heart cycle and in so doing decreases the number of counts used to reconstruct each of the PET frames. Due to their short duration, early time point frames already have limited numbers of counts available and low SNR before gating is applied, meaning that these frames they can appear very noisy after gating is applied. The gated 3DRP data are reconstructed analytically and therefore their images (and their IDIF peaks) are not as strongly affected as the gated MAP data, which is constructed iteratively and with a smoothing prior, as discussed in Chapter 2. The noise spike in the gated MAP IDIFs of some mice indicates a bias in the images due to a non-optimal prior and iteration subset being applied for the high level of noise. This effect was monitored in the analysis, as a noisy IDIF can affect its corresponding parameters produced in kinetic analysis.

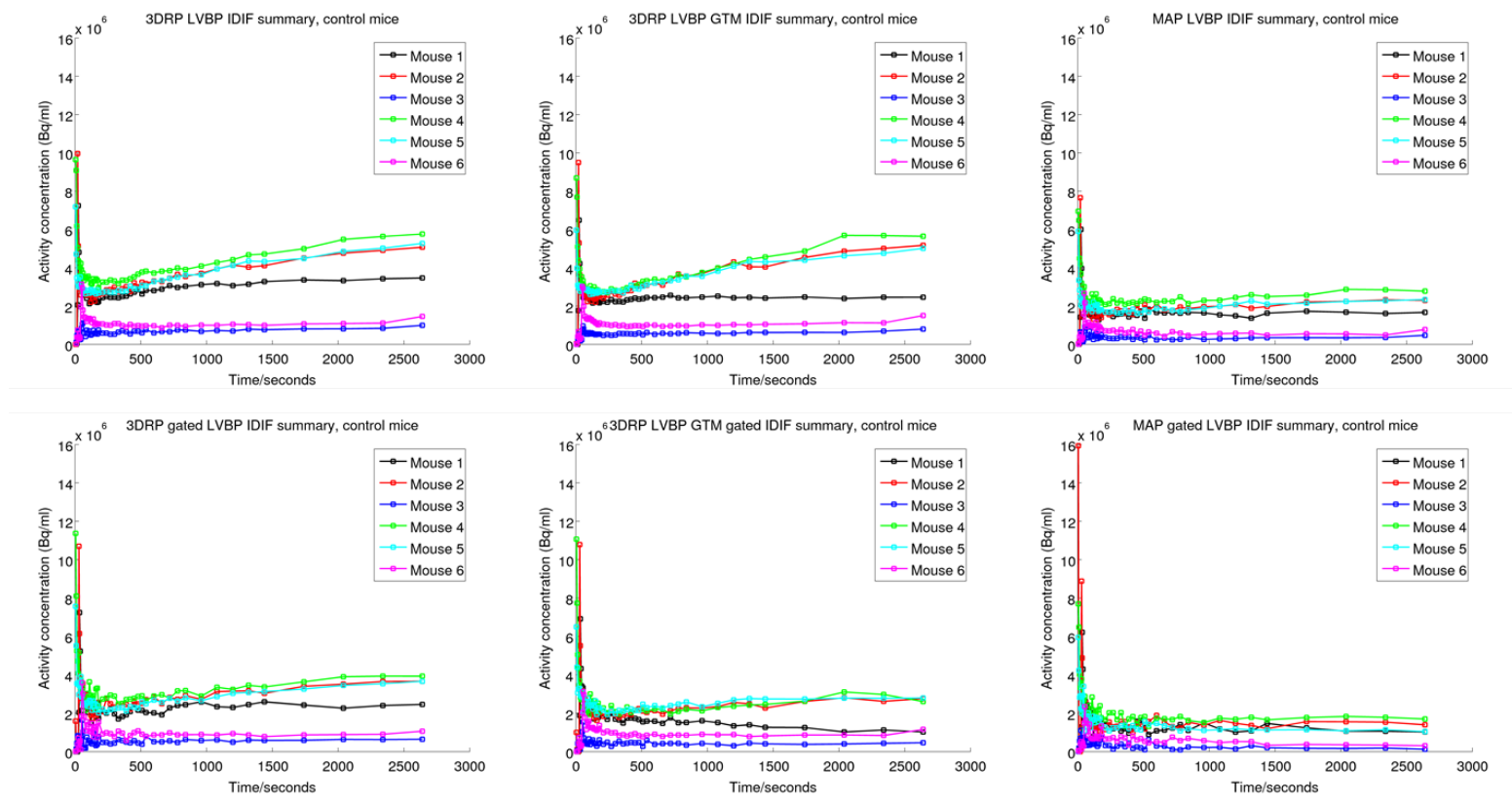


Figure 4.26: Summary of all IDIFs extracted from LVBP ROI for control mice group. Top row: (left) 3DRP IDIFs, (centre) GTM applied to 3DRP IDIFs and (right) MAP IDIFs. Bottom row: (left) 3DRP IDIFs extracted from cardiac gated images, (centre) GTM applied to gated 3DRP images and (right) MAP IDIFs extracted from cardiac gated images.

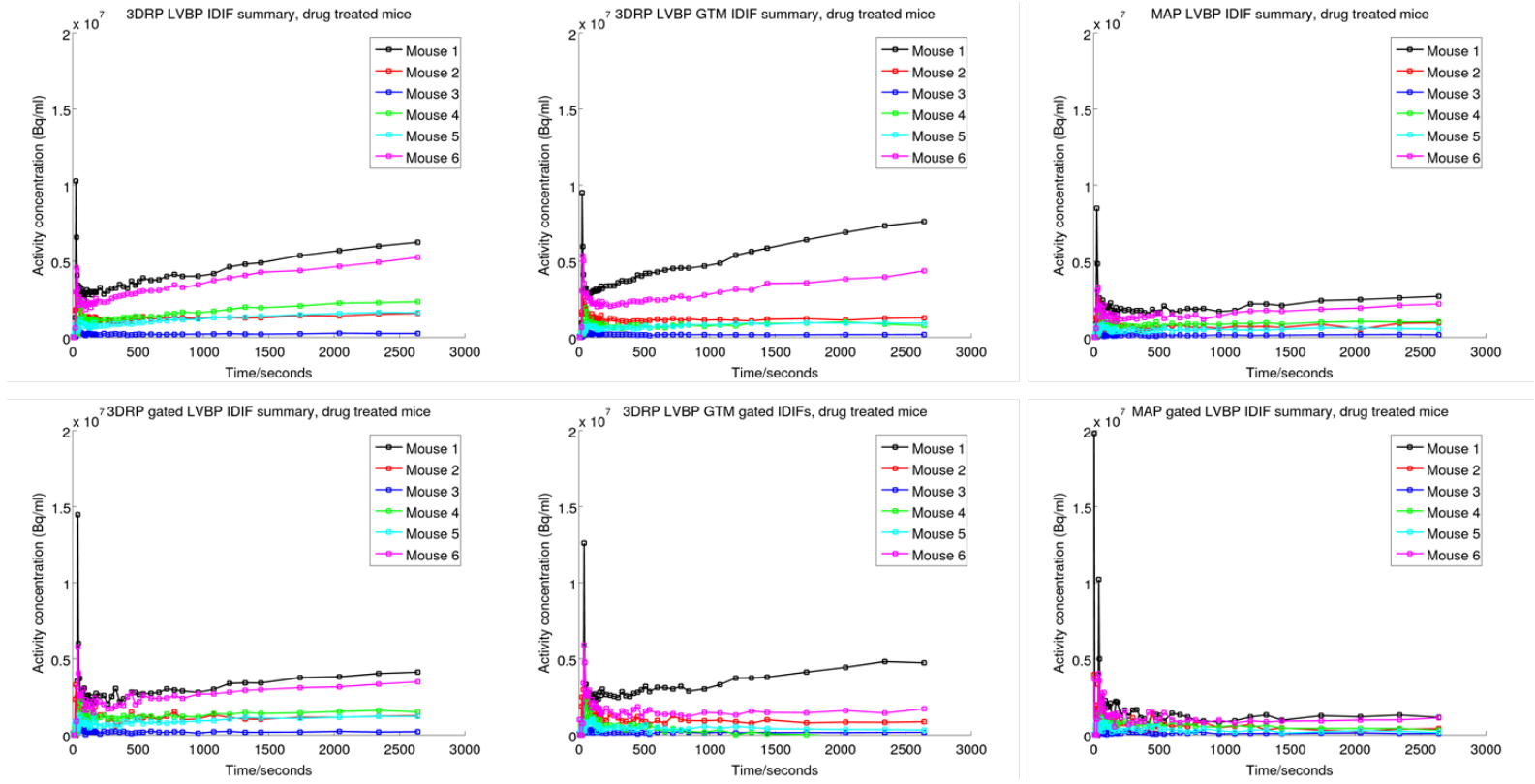


Figure 4.27: Summary of all IDIFs extracted from LVBP ROI for drug treated mice group. Top row: (left) 3DRP IDIFs, (centre) GTM applied to 3DRP IDIFs and (right) MAP IDIFs. Bottom row: (left) 3DRP IDIFs extracted from cardiac gated images, (centre) GTM applied to gated 3DRP images and (right) MAP IDIFs extracted from cardiac gated images.

Mouse	3DRP	3DRP, gated	3DRP GTM	3DRP GTM, gated	MAP	MAP, gated
Control 1	7.2	7.2	6.5	6.9	6.0	6.2
Control 2	10.0	10.7	9.5	10.8	7.7	15.9
Control 3	1.1	1.6	1.0	1.5	0.9	1.1
Control 4	9.6	11.4	8.7	11.1	7.0	7.7
Control 5	7.2	7.6	6.0	6.5	5.9	5.9
Control 6	3.1	3.6	3.0	3.1	2.7	2.3
Drug 1	10.3	14.5	9.5	12.6	8.5	19.8
Drug 2	2.8	3.3	2.7	3.0	2.5	4.0
Drug 3	0.5	0.9	0.5	0.7	0.5	0.5
Drug 4	2.5	2.7	2.0	2.4	1.6	1.8
Drug 5	1.6	1.3	1.0	1.0	0.8	1.0
Drug 6	5.3	5.8	5.4	5.9	3.3	4.0
Mean±Std (All)	5.1±3.6	5.9±4.4	4.6±3.4	5.5±4.2	3.9±2.9	5.9±6.1
Mean±Std (Controls)	6.4±3.6	7.0±3.8	5.8±3.3	6.7±3.9	5.0±2.6	6.5±5.2
Mean±Std (Drug)	3.8±3.5	4.7±5.0	3.5±3.4	4.3±4.5	2.9±2.9	5.2±7.3

Table 4.1: Comparison of peak height activity concentration values in MBq/ml for different IDIF methods using LVBP ROI, mean value for each group of mice.

Mouse	3DRP	3DRP, gated	3DRP GTM	3DRP GTM, gated	MAP	MAP, gated
Control 1	4.7	4.7	4.2	4.5	3.9	4.0
Control 2	11.0	11.8	10.5	11.9	8.5	17.6
Control 3	5.7	8.3	4.8	7.8	4.7	5.6
Control 4	3.9	4.6	3.5	4.4	2.8	3.1
Control 5	11.0	11.6	9.1	9.9	9.0	9.1
Control 6	5.8	6.6	5.6	5.8	4.9	4.3
Drug 1	3.2	4.5	2.9	3.9	2.6	6.1
Drug 2	5.5	6.6	5.3	6.0	4.9	7.9
Drug 3	1.4	2.6	1.3	2.0	1.4	1.5
Drug 4	5.3	5.7	4.2	5.1	3.5	3.9
Drug 5	5.2	4.1	3.1	3.3	2.7	3.3
Drug 6	4.0	4.3	4.0	4.4	2.5	3.0
Mean±Std (All)	5.5±2.8	6.8±2.9	4.9±2.6	5.8±2.8	4.3±2.4	5.8±4.3
Mean±Std (Controls)	7.0±3.2	7.9±3.3	6.3±2.8	7.4±3.1	5.6±2.5	7.3±5.5
Mean±Std (Drug)	4.1±1.6	4.6±1.4	3.5±1.4	4.1±1.4	2.9±1.2	4.3±2.3

Table 4.2: Comparison of peak height activity concentration values (MBq/ml), normalized to injected activity (MBq/g), for different IDIF methods taken from LVBP ROI, mean value for each group of mice.

4.3.7 IDIFs generated for all mice - VC ROI

Figures 4.28 and 4.30 summarise the IDIFs derived from the VC ROI for the control and drug mice groups respectively. Zoomed in versions with a maximum activity concentration of 10MBq/ml are shown in Figures 4.29 and 4.31. In contrast to the LVBP IDIF shapes, the VC IDIFs derived using either 3DRP images or MAP images are much smoother and much more uniform in appearance throughout both mouse groups. The application of cardiac gating has a limited effect on the VC IDIFs, indicating that motion in this region does not affect IDIF extraction to the same extent as in the LVBP. The MAP VC IDIFs also do not display any clear differences in either peak height or curve shape (on average) when compared to their 3DRP VC IDIF counterparts, with the exception of mouse 2 in the control group gated MAP VC IDIFs, which has a peak height twice the size of any other VC IDIF peak height when gating is applied (27.6 in Table 4.3 and 30.8 in Table 4.4). This again is most likely due to the decreased counts in the gated image frames resulting in a noise spike in the MAP data and is seen to a greater extent in the VC than the LVBP ROI in control mouse 2.

The peak heights for the IDIFs from the VC ROI are displayed in Table 4.3, with the normalized to injected activity values displayed in Table 4.4. No significant differences (paired Student's t test, $p < 0.05$ for significance) in peak height were detected between IDIFs formed using the VC ROI method compared to the LVBP ROI method, except for the drug mouse group using gated 3DRP IDIFs.

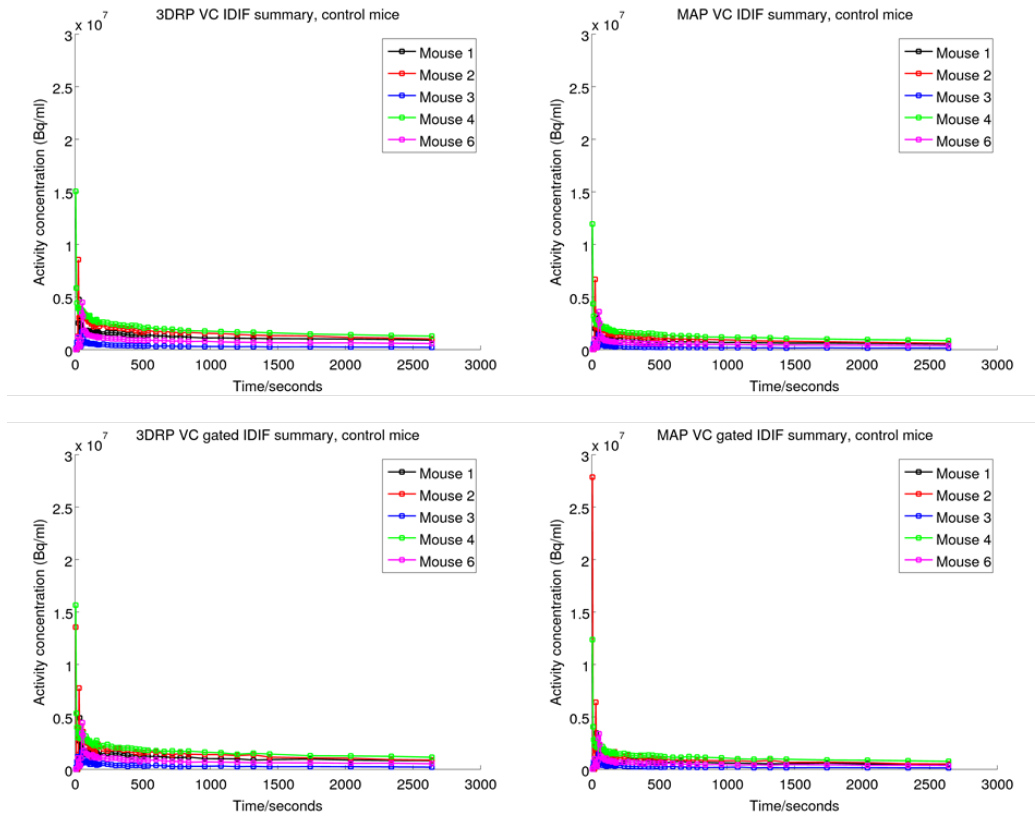


Figure 4.28: Summary of VC IDIFs for control mice group. Top row: (left) Ungated 3DRP IDIFs, (right) Ungated MAP IDIFs. Bottom row: (left) Gated 3DRP IDIFs, (right) Gated MAP IDIFs.

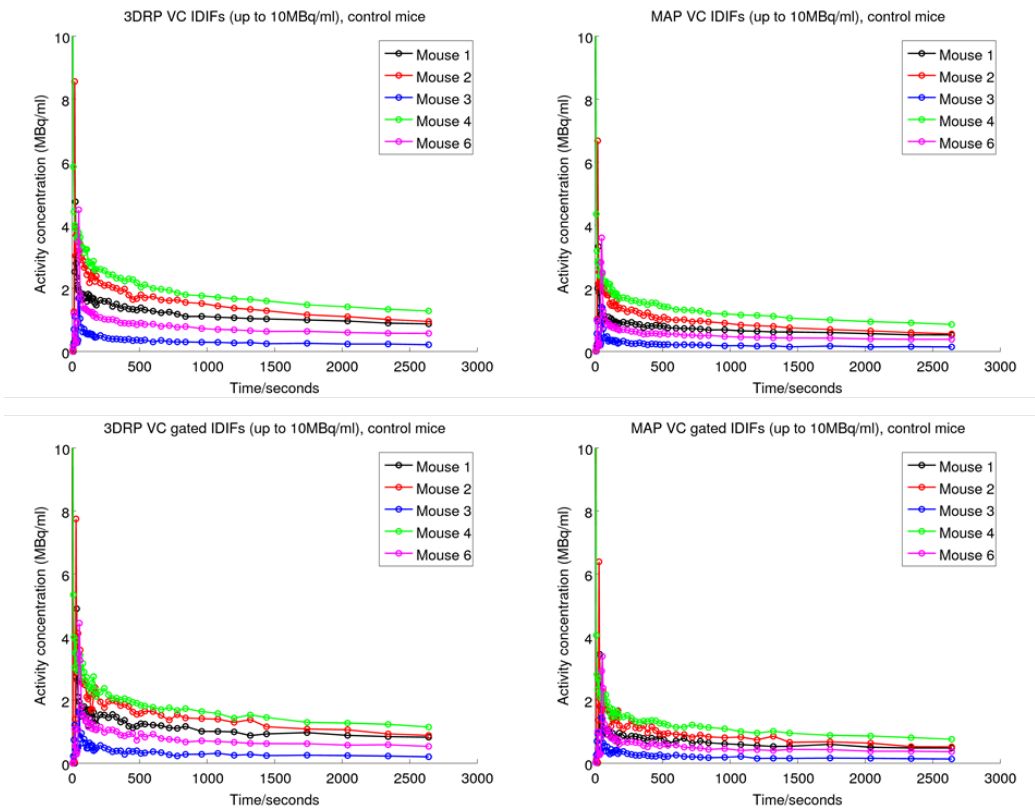


Figure 4.29: Zoomed in version of Figure 4.28, with maximum activity concentration of 10MBq/ml.

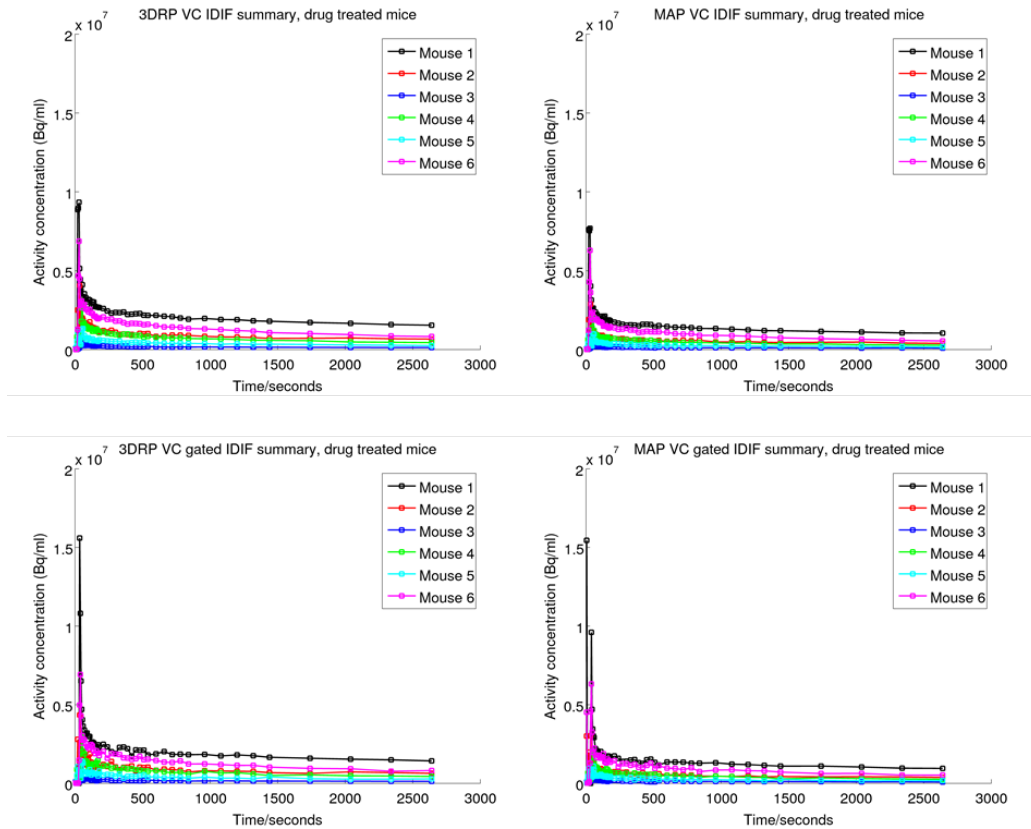


Figure 4.30: Summary of VC IDIFs for drug treated mice group. Top row: (left) Ungated 3DRP IDIFs, (right) Ungated MAP IDIFs. Bottom row: (left) Gated 3DRP IDIFs, (right) Gated MAP IDIFs.

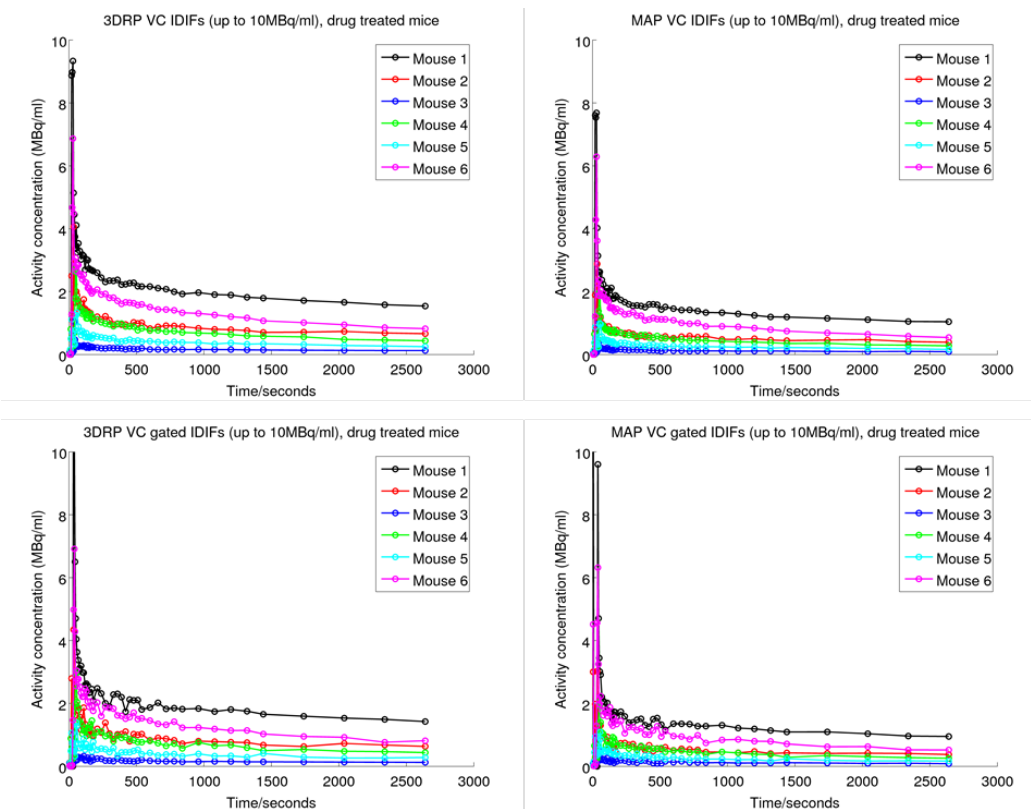


Figure 4.31: Zoomed in version of Figure 4.30, with maximum activity concentration of 10MBq/ml.

Mouse	3DRP	3DRP, gated	MAP	MAP, gated
Control 1	4.8	4.9	3.3	3.5
Control 2	8.6	13.6	6.7	27.7
Control 3	1.7	1.7	1.4	1.5
Control 4	15.1	15.6	11.9	12.4
Control 6	4.5	4.4	3.6	3.4
Drug 1	9.3	15.6	7.7	15.4
Drug 2	4.1	4.3	2.9	3.0
Drug 3	1.5	1.1	1.0	1.0
Drug 4	2.8	3.0	2.0	2.0
Drug 5	1.3	1.4	1.0	1.1
Drug 6	6.9	6.9	6.3	6.3
Mean \pm Std (All)	5.5 \pm 4.2	6.6 \pm 5.7	4.3 \pm 3.4	7.0 \pm 8.4
Mean \pm Std (Controls)	6.9 \pm 5.2	8.0 \pm 6.2	5.4 \pm 4.1	9.7 \pm 11.0
Mean \pm Std (Drug)	4.3 \pm 3.2	5.4 \pm 5.4	3.5 \pm 2.8	4.8 \pm 5.6

Table 4.3: Comparison of peak height activity concentration values in MBq/ml for different IDIF methods using VC ROI, mean value for each group of mice.

Mouse	3DRP	3DRP, gated	MAP	MAP, gated
Control 1	3.1	3.2	2.1	2.2
Control 2	9.5	15.0	7.4	30.8
Control 3	8.8	8.4	7.2	7.3
Control 4	6.3	6.3	4.8	5.0
Control 6	8.3	8.2	6.7	6.3
Drug 1	2.9	4.8	2.4	4.8
Drug 2	8.1	8.7	5.8	6.0
Drug 3	4.3	3.0	2.9	2.7
Drug 4	5.9	6.4	4.2	4.4
Drug 5	4.3	4.4	3.2	3.5
Drug 6	5.2	5.2	4.7	4.7
Mean \pm Std (All)	6.0 \pm 2.3	6.7 \pm 3.4	4.7 \pm 1.9	7.1 \pm 8.0
Mean \pm Std (Controls)	7.1 \pm 2.6	8.2 \pm 4.3	5.6 \pm 2.2	10.3 \pm 11.6
Mean \pm Std (Drug)	5.1 \pm 1.8	5.4 \pm 1.9	3.9 \pm 1.3	4.4 \pm 1.1

Table 4.4: Comparison of peak height activity concentration values (MBq/ml), normalized to injected activity (MBq/g), for different IDIF methods taken from VC ROI, mean value for each group of mice.

In summary, the cardiac gated MAP data produces IDIFs from the LVBP ROI with the least spillover contamination from myocardial TACs and is the most consistent across both mouse groups. This suggests that gated MAP IDIFs from the LVBP ROI should be used in future studies but also that the VC ROI is a promising alternative, as it is less affected by motion than the LVBP. For the VC ROI to be used in the future, however, the technique would require further validation by blood sampling to ensure it is an appropriate estimate of the AIF in mice.

4.3.8 Kinetic modelling results (K_i values)

K_i values were calculated for all IDIFs and compared across the healthy and infarcted myocardium regions for the two mouse groups. The K_i values for the LVBP IDIFs are shown in Table 4.5, whilst the K_i values for the VC IDIFs are shown in Table 4.6 and the results for the GTM PVC IDIFs are shown in Table 4.7. All TACs were taken from the same images as their respective IDIFs i.e. gated IDIFs were analyzed with gated TACs and ungated IDIFs with ungated TACs.

LVBP ROI IDIF K_i values				
TAC ROI	3DRP	3DRP, gated	MAP	MAP, gated
Control, myocardium	0.018 ± 0.009	0.026 ± 0.014	0.051 ± 0.012 [†]	0.060 ± 0.015 [†]
Treated, myocardium	0.014 ± 0.021	0.025 ± 0.019	0.047 ± 0.021	0.085 ± 0.034
Control, infarct	0.011 ± 0.005	0.013 ± 0.007	0.025 ± 0.008 [†]	0.033 ± 0.006 ^{*†}
Treated, infarct	0.005 ± 0.002	0.026 ± 0.020	0.033 ± 0.006	0.073 ± 0.024 [*]

Table 4.5: K_i values in ml/min/g for IDIF methods using LVBP ROI, mean value for each mouse group (n=6). *p < 0.05, paired Student's t test, indicating significant difference between control and drug treated groups in infarcted region. [†]p < 0.05, paired Student's t test, indicating significant difference between healthy and infarcted myocardium in this mouse group.

VC ROI IDIF K_i values				
TAC ROI	3DRP	3DRP, gated	MAP	MAP, gated
Control, myocardium	0.080 ± 0.029 [†]	0.078 ± 0.032 [†]	0.104 ± 0.042 [†]	0.098 ± 0.041 [†]
Treated, myocardium	0.079 ± 0.031	0.072 ± 0.028	0.099 ± 0.041	0.095 ± 0.038
Control, infarct	0.057 ± 0.021 [†]	0.056 ± 0.023 [†]	0.071 ± 0.027 [†]	0.062 ± 0.022 [†]
Treated, infarct	0.071 ± 0.022	0.067 ± 0.022	0.083 ± 0.022	0.086 ± 0.027

Table 4.6: K_i values in ml/min/g for IDIF methods using VC ROI, mean value for each mouse group (n=5 for controls, n=6 for drug treated group). [†]p < 0.05, paired Student's t test, indicating significant difference between healthy and infarcted myocardium in this mouse group.

LVBP IDIF K_i values after GTM applied		
TAC ROI	MR ROIs	MR ROIs, gated
Control, myocardium	0.069 ± 0.028 [†]	0.090 ± 0.041 [†]
Treated, myocardium	0.065 ± 0.024	0.096 ± 0.030
Control, infarct	0.024 ± 0.015 ^{*†}	0.036 ± 0.016 ^{*†}
Treated, infarct	0.063 ± 0.021 [*]	0.081 ± 0.028 [*]

Table 4.7: K_i values in ml/min/g for GTM IDIF methods using LVBP ROI, mean value for each mouse group (n=6). *p < 0.05, paired Student's t test, indicating significant difference between control and drug treated groups in infarcted region. [†]p < 0.05, paired Student's t test, indicating significant difference between healthy and infarcted myocardium in this mouse group.

Previously reported K_i values calculated using IDIFs for the healthy myocardium in mice range widely due to the dependence of ^{18}F -FDG uptake on mouse dietary status. For non-fasted mice, similar to those analyzed in this study, the values range between 0.08 to 0.22±0.08ml/min/g [29], [182], with common values reported around 0.1 ml/min/g (0.15±0.08ml/min/g [33], 0.13±0.04ml/min/g [36], 0.11±0.03ml/min/g [53], 0.13±0.07ml/min/g [181]). Bearing this variability in mind, from Table 4.7

it appears that the best agreement with literature for the healthy myocardium results is achieved using the MAP reconstruction algorithm with cardiac gating applied in the LVBP ROI (which yields a K_i of $0.086 \pm 0.027 \text{ ml/min/g}$ for the drug treated group) or the VC ROI ($0.098 \pm 0.041 \text{ ml/min/g}$ for the controls and $0.095 \pm 0.038 \text{ ml/min/g}$ for the drug treated group). The GTM method with cardiac gating applied to 3DRP images also gives similar results ($0.090 \pm 0.041 \text{ ml/min/g}$ for the controls and $0.096 \pm 0.030 \text{ ml/min/g}$ for the drug treated group) for the group as a whole. This indicates that the best agreement with literature myocardium values is reached when PVC and motion correction are applied to the IDIFs in this study. The large variance seen in the GTM K_i values compared to those measured with MAP LVBP gated IDIFs indicates that the MAP PVC technique is more consistent and would be the most promising for future work, as all VC ROI based techniques require further validation with blood sampling.

Significant differences in K_i values in the infarcted region of the myocardium between the two mouse groups were seen only when using the gated MAP, ungated GTM and gated GTM IDIF methods (paired Student's t test, $p < 0.05$), indicating that the application of PVC and motion correction to improve IDIF extraction can give significant K_i results. In addition, all IDIF extraction methods (except for the gated and ungated 3DRP in the LVBP ROI, which had no PVC applied) also saw a significant difference between the healthy and infarcted myocardium in the control group. In the drug treated group, however, no IDIF methods found the difference between K_i values from healthy and infarcted myocardium to be significant (two means Student's t test, $p < 0.05$).

4.4 Discussion

4.4.1 Influence of reconstruction algorithm and cardiac gating on IDIFs

It was found that the use of the LVBP ROI and 3DRP images produced IDIFs contaminated with myocardium TACs, with significant spillover effects seen, even if cardiac gating was applied to reduce motion blurring effects and co-registered high resolution MR images were used to locate and delineate ROIs. PVC is therefore essential to separate the blood and myocardium time curve components in quantitative imaging studies.

The MAP algorithm reconstructs images with greater contrast and recovered resolution compared to 3DRP due to its accurate modelling of the system response [64], [65], which was found to be particularly useful when using the LVBP ROI for IDIF extraction. PVE and spillover are further reduced when MAP is combined with cardiac gating to reduce blurring due to motion, resulting in IDIFs with the least spillover contamination from myocardial TACs in this study, which also agreed with previous

work which compared 3DRP and MAP IDIFs in the mouse heart [53], [68]. The greatest differences between 3DRP and MAP IDIFs occurred at late time points, as spillover is a time-dependent process and myocardial tracer uptake is greatest at late time points. MAP reconstruction in conjunction with cardiac gating was also found to produce the most consistent IDIFs across both mouse groups due to the reduction in noise found when using MAP in place of 3DRP and due to the smoothing applied to MAP images. The K_i values produced using the cardiac gated MAP IDIF, $0.060\pm 0.015\text{ml/min/g}$ (control) and $0.085\pm 0.034\text{ml/min/g}$ (drug treated), were also found to have the best agreement with the literature, particularly in the drug treated group, as healthy myocardium values have been previously quoted in the range between $0.08\text{-}0.22\text{ml/min/g}$ [29], [33], [36], [53], [181], [182]. This was expected as the K_i values for the “healthy” myocardium of the control mice are likely to be lower and more similar to the infarcted region due to the larger infarct sizes seen in that group. The disadvantage of using MAP is that it is a non-linear reconstruction technique and it is therefore difficult to calculate the residual PSF of the image data for further PVE correction. It is also dependent on the exact reconstruction parameters specified, such as post-reconstruction filtering to provide smoothing, MAP priors, number of iterations and sizes of subsets. MAP reconstructions also need a much longer processing time compared to 3DRP, to the extent where an extensive DPC cluster is required to process the dynamic data within a reasonable time frame.

The reduced PVE and spillover seen in both images and IDIFs when cardiac gating was applied to 3DRP and MAP data suggests that simultaneous PET/MR acquisition may be of benefit in future cardiac studies, as this would provide improved co-registration between modalities (and between dynamic PET frames as these could each be co-registered to anatomical data). Gross motion errors due to the sequential nature of the scans (e.g. shifts in mouse torso positioning) would also be reduced and temporally co-registered MRI data could be acquired to provide further motion correction for the PET images.

4.4.2 IDIFs derived from the VC ROI

The VC ROI was found to be large enough to be adequately resolved on microPET images from the Cambridge PET/MR scanner and was easily identified in the early time frames of the acquisition using co-registered MR data. The mean VC diameter for mice in this study was $2.24\pm 0.34\text{mm}$ measured from MR FISP images (previously reported as $2.54\pm 0.30\text{mm}$ [33]). This was larger than the FWHM spatial resolution of the scanner at 1.8mm [229] and the positron range for ^{18}F , which is approx. 1mm [20], [52]. It is also located in a region with few areas of high uptake in close proximity (e.g. the myocardium or kidneys) and therefore was shown to experience much less spillover than the LVBP ROI in late time frames. The VC ROI mean recovery co-efficient across the mouse group (explained in full detail in Chapter 5) was estimated from FISP MR images as 0.43 ± 0.05 for 3DRP, indicating that both the peak and mean activity concentration values estimated from the VC ROI may still be

significantly underestimated without some form of PVC applied. This would indicate that the peak activity concentration of PVE-corrected VC IDIFs may actually be much higher than the results presented here and it would require further investigation with serial blood sampling to see if the VC IDIF is an accurate representation of the AIF in mice, particularly at early time points.

The VC IDIF tail regions displayed a slow decline in activity concentration, consistent with ^{18}F -FDG uptake and retention in tissue, in contrast to the increase seen in the 3DRP LVBP IDIFs due to myocardial spillover. The lowest IDIF tail values (indicative of the greatest reduction in spillover) were generated from cardiac gated MAP images in the VC ROI. Using the VC ROI, there was much less variation between 3DRP and MAP IDIFs across the mouse groups, indicating that PVE and spillover are reduced in the VC ROI compared to the LVBP ROI. There was also a smaller change in IDIF curve shapes between gated and ungated data when compared to the LVBP ROI and all IDIFs were smoother than their LVBP ROI counterparts, indicating that the VC ROI is less vulnerable to both cardiac and gross motion.

LVBP IDIFs extracted using either the GTM method or MAP reconstruction to provide PVC were both found to appear similar to VC IDIFs if cardiac gating was also applied, as expected from the literature [33]. This demonstrated that if PVE and motion are corrected for, arterial IDIFs and venous IDIFs from mice appear very similar. This result may have interesting implications. This could provide evidence that due to the high cardiac output of mice [33], [52], their arterial and venous tracer concentrations are similar (as has been shown in blood samples taken at late time points for ^{18}F -FDG [181]) and therefore a venous ROI (which is more accessible and less susceptible to spillover/motion effects) could be used to extract IDIFs for use in kinetic analysis of mouse PET/MR data.

This is desirable as the use of gating was shown to have a limited effect in the VC ROI. As it can be difficult to record accurate ECG readings in animals with arrhythmogenesis [33], this is an advantage. Additionally as good results were achieved using either 3DRP or MAP for IDIF extraction in the VC ROI, this indicates the need for PVC in this region is also reduced and that an IDIF from the VC ROI would require limited post-processing to extract. The VC ROI does require a high specification microPET scanner, however, as it requires accurate readings to be recorded from short duration ($\leq 5\text{s}$) time frames and a large FOV to encompass both the organ under study for TAC extraction and the VC.

The variation in K_i values generated by Patlak analysis was found to be greater when using the VC IDIFs compared to the LVBP IDIFs, as the higher and sharper peaks generated by the VC IDIFs resulted in higher IDIF AUC. The mean K_i values from the VC IDIFs, however, more closely resemble those quoted in the literature, and this agrees with previous results which validated the use of the VC ROI using both a β probe and serial manual blood sampling in rats [52] and achieved good estimates of the

cerebral metabolic rate of glucose in mice [52].

To fully validate the assumption that a venous ROI can be used to derive an estimate of the AIF for mice, however, serial arterial blood sampling [35], [68] would be required in future work, but this would most likely need to be carried out using an MR-compatible blood sampler for simultaneous PET/MR studies [51], [230]. These blood samples could also be used to validate IDIFs extracted from MAP images in the LVBP ROI and to assess if a correction for ^{18}F -FDG uptake by red blood cells is required, as mice exhibit slower kinetics of ^{18}F -FDG across red blood cell membranes compared to humans and therefore an image-derived approach which relies on whole blood signals to estimate the AIF may not be appropriate [53]. Previous murine studies of the quantitative performance of 3DRP and MAP in cardiac ^{18}F -FDG PET have indicated that MAP (even with cardiac gating applied) still overestimates the AIF tail according to serial blood sampling data, but does provide a higher estimate of the AIF peak due to the limited temporal resolution of the blood samples [68].

4.4.3 Evaluation of GTM method for IDIF PVC

An adaptation of the GTM method for mice has been shown as a viable but unstable alternative to providing PVC through the use of MAP reconstruction for IDIF extraction from the LVBP ROI. The GTM method (with cardiac gating applied) produced similar IDIFs to gated MAP data, resulting in mean K_i values for the mouse groups of 0.090 ± 0.041 ml/min/g (control) and 0.096 ± 0.030 ml/min/g (drug treated). These gave reasonable agreement to the literature 0.08-0.22 ml/min/g value [29], [33], [36], [53], [181], [182]. There was considerable variation in the individual GTM LVBP IDIF curve shapes compared to the MAP-based LVBP IDIFs, reflected in the increased variance in the control group K_i value for GTM. The GTM method therefore requires both accurately co-registered MR images to aid in ROI delineation, in addition to an accurate ECG trace to provide adequate PVC for IDIF extraction from 3DRP images in the LVBP ROI.

The main drawback of the GTM method is its reliance on accurate PET and MR co-registration, as even a small mismatch in ROI positioning can lead to large errors in IDIFs, shown in the variable GTM IDIFs produced across both groups in Figures 4.26 and 4.27. A few mice in each group still show slightly increasing activity concentrations at late time points, even after GTM and gating have been applied. For more details on the effect of ROI delineation on GTM accuracy, Appendix F details a comparison of results to those produced shown when GTM was applied with non-optimal ROIs. GTM could be used as an alternative PVC technique, however, if MAP images are not available. GTM could be of greater benefit and produce more precise IDIFs in a simultaneous PET/MR acquisition, where co-registration errors and motion between the modalities are minimized. Further validation of the GTM method in a

simultaneous PET/MR scanner would also be advisable, again using gold standard serial blood sampling from an MR-compatible blood sampler such as Swisstrace [51], [230].

4.4.4 Observed differences between treated and control groups after kinetic analysis

Similar K_i values which agreed with previously reported results were noted for the healthy myocardium in both the control and drug treated mouse groups when the PVC IDIF extraction methods were used. In addition, all IDIF methods also displayed a decrease from the healthy myocardium region to the infarcted region for both control and drug treated mouse groups, indicating a decrease in glucose utilization rates, as expected from the reduction in SUV results in the infarcted region. The decrease in K_i value between the healthy myocardium and infarcted region in the control group agreed with the greater mean difference in SUV seen in the control group (1.4g/ml) compared to the drug treated group (0.4g/ml) when comparing healthy and infarcted myocardium regions. With the exception of the IDIFs extracted from the LVBP ROI with no form of PVC applied, the differences in K_i values between the healthy and infarcted myocardium in the control group were found to be significant, but not significant in the drug treated group (Student's t test, $p < 0.05$). These results further support the previous analysis of this data [30], [228] which found that the drug treated group had significantly smaller infarct volumes than those found in the control group, according to LGE MRI.

Between the control and drug treated mouse groups, only the gated MAP, ungated GTM and gated GTM IDIF methods saw a significant difference (Student's t test, $p < 0.05$) between K_i values calculated in the infarcted region of the myocardium, with the drug treated group displaying higher values of K_i which are closer in value to that of healthy myocardium. This suggests that, after PVC and motion correction are applied to the IDIF for analysis, the effect of the drug (which results in smaller infarct sizes) on glucose utilization uptake rates can now be appreciated, providing additional support in favour of the drug's efficacy to previous work [30], [228].

4.5 Conclusions

PVC has been shown to be crucial for deriving IDIFs in mouse PET studies. The inclusion of cardiac gating in IDIF extraction procedure was also shown to be highly desirable, as motion correction reduces spillover from the myocardium region into the LVBP ROI, which is used for the IDIF extraction. IDIF curve shapes with the least contamination due to spillover from myocardial TACs, reduced PVE and reduced noise were produced from the LVBP ROI when the MAP reconstruction algorithm was used to provide PVC and cardiac gating was used to apply motion correction. This method also produced K_i

values for the healthy myocardium which agreed best with those previously reported in the literature. It was found that an adaptation of the GTM PVC method could also be used to produce improved IDIF estimates from the mouse heart by utilising the high-resolution and excellent soft-tissue contrast of MR to give improved ROI delineation compared to PET, which was seen to be vital to achieve accurate results with the proposed GTM method. As a result of applying either MAP or GTM to provide PVC, significant differences in K_i were found between areas of healthy and infarcted myocardium muscle for the control group. In the drug group these differences were not found to be significant, indicating the ability of the drug to reduce both infarct sizes and retain functionality in the mouse heart, which supported the previously published of this data [30], [228]. IDIFs extracted from the VC ROI were most similar to the gated MAP IDIFs from the LVBP ROI, indicating that the VC ROI is less affected by PVE, spillover and motion compared to the LVBP, and could be used to produce a surrogate IDIF in mice studies if it is further validated with serial blood sampling.

4.6 Chapter Summary

Several methods of IDIF extraction were applied to ascertain the effect of partial volume correction and motion correction on ^{18}F -FDG mouse PET data acquired using the Cambridge split magnet PET/MR scanner. An adaptation of the MR-based GTM method of partial volume correction was developed and the IDIFs produced using this method were compared to those found when using MAP image reconstruction. IDIF curve shapes attained using both these methods exhibited less contamination from myocardial spillover, with the best results achieved using cardiac gated MAP images. The use of the VC ROI as an alternative to the LVBP ROI for extracting the IDIF was also explored and showed promising agreement with the IDIFs produced using gated MAP images. The next Chapter will explore the further use of the iterative reconstruction algorithm MAP and the VC ROI in determining IDIFs, as well as the use of the recovery co-efficient method for PVC in ^{18}F -NaF mouse studies.

Chapter 5

Evaluation of image-derived input function techniques for use in ^{18}F -NaF murine studies

This Chapter investigates the transfer of the techniques discussed in Chapter 4 to ^{18}F -NaF murine studies. The hypotheses addressed in this Chapter were as follows:

- 1. MR information can improve ^{18}F -NaF IDIFs in mice by providing PVC through the RC method.*
- 2. The vena cava ROI can also be used as an alternative IDIF extraction site for tracers with different biodistributions to ^{18}F -FDG.*

The use of the VC and LVBP ROIs to extract IDIFs from PET images of mice is again evaluated to ascertain if the same techniques used for ^{18}F -FDG are optimal for a tracer with similar kinetics but a different bio-distribution, such as ^{18}F -NaF. The recovery co-efficient method for PVC based upon anatomical measurements taken from co-registered MRI images was used in place of the GTM method. All IDIF extraction methods were tested and validated against plasma samples taken at the end of each animal's PET scan to ascertain if IDIF techniques can provide appropriately scaled estimates of AIF curves.

5.1 Introduction

One of the great strengths of PET is the wide variety of tracer compounds which can be used, allowing small animal PET imaging to be applied in the evaluation of a range of disease models. Radioactive ^{18}F labelled sodium fluoride (^{18}F -NaF) is a PET tracer used to perform bone imaging and can be used to in-

investigate metabolic, inflammatory, degenerative and traumatic bone disease [231], [232], [233]. ^{18}F -NaF PET provides assessment of bone disease with a higher accuracy than ^{99m}Tc Single Positron Emission Tomography (SPECT) and the fact that ^{18}F -NaF does not bind to plasma proteins [231], [233]. In addition to qualitative work, quantitative ^{18}F -NaF studies are being employed as a novel way of assessing treatment performance via bone metabolism [231], [234], [235] and in the detection and evaluation of atherosclerosis plaques in cardiovascular work [232], [236], although the use of quantitative ^{18}F -NaF PET in rodent studies has been limited [234], [237], [238]. To harness the full potential of dynamic PET in murine studies and perform accurate kinetic modelling, this Chapter investigates different methods of extracting image-derived input functions (IDIFs) from sequentially acquired ^{18}F -NaF PET and MR images.

5.1.1 ^{18}F -NaF tracer kinetics in mice

Following injection, the activity distribution of ^{18}F -NaF throughout the subject differs from that described in previous Chapters for ^{18}F -FDG. The tracer bolus¹ is initially injected through the cannulated tail vein of the mouse and travels through the vena cava (VC) to the heart. After reaching the heart, ^{18}F -NaF does not bind to myocardial muscle but is distributed throughout the mouse body via the vasculature and rapidly cleared from plasma. ^{18}F -NaF binds to bone and other calcifications, with a sample timecourse shown in Figure 5.2. The mechanism of uptake is the deposition of ^{18}F -NaF on the surface of newly formed hydroapatite crystals at sites of bone formation. The fluoride ion is believed to exchange with hydroxyl groups in the hydroapatite crystals on the surface of the bone matrix to form fluoroapatite [231] and therefore ^{18}F -NaF becomes concentrated with high and rapid uptake at sites of newly mineralizing bone. The rate limiting step for ^{18}F -NaF bone uptake is blood flow, and therefore the initial ^{18}F -NaF distribution represents blood flow variations between bones [231], [233].

A two compartment model was assumed for ^{18}F -NaF [233], as shown in Figure 5.1. This model is the same mathematically as the irreversible two compartment model used for ^{18}F -FDG analysis (which assumes that $k_4 \approx 0$) outlined in Chapter 3 and therefore the same analysis methods can be used to calculate rate constants K_1 , k_2 , k_3 and K_i , including Patlak plot analysis for K_i . For ^{18}F -NaF, K_i is related to the Ca^{2+} influx from plasma to the trapped bone compartments, giving an indication of the bone remodelling and apposition rates as ^{18}F -NaF is rapidly cleared from blood [233].

¹Followed by a saline flush.

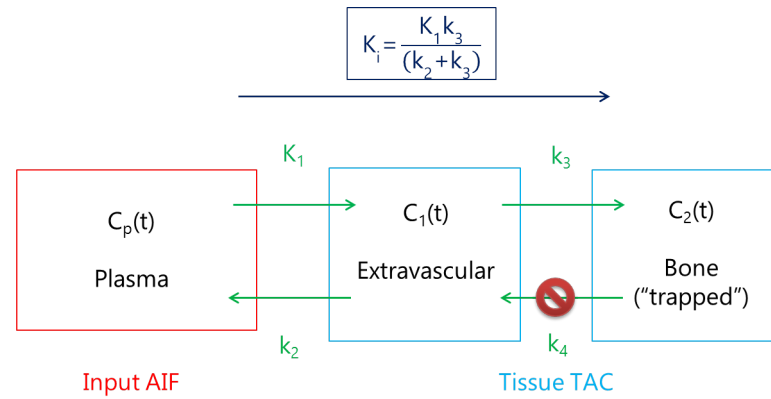


Figure 5.1: ^{18}F -NaF two compartment model. K_1 and k_2 represent forward and reverse transport from plasma, k_3 and k_4 represent “trapping” and release from bone compartment. No metabolite products are required to perform full kinetic modelling with this tracer.

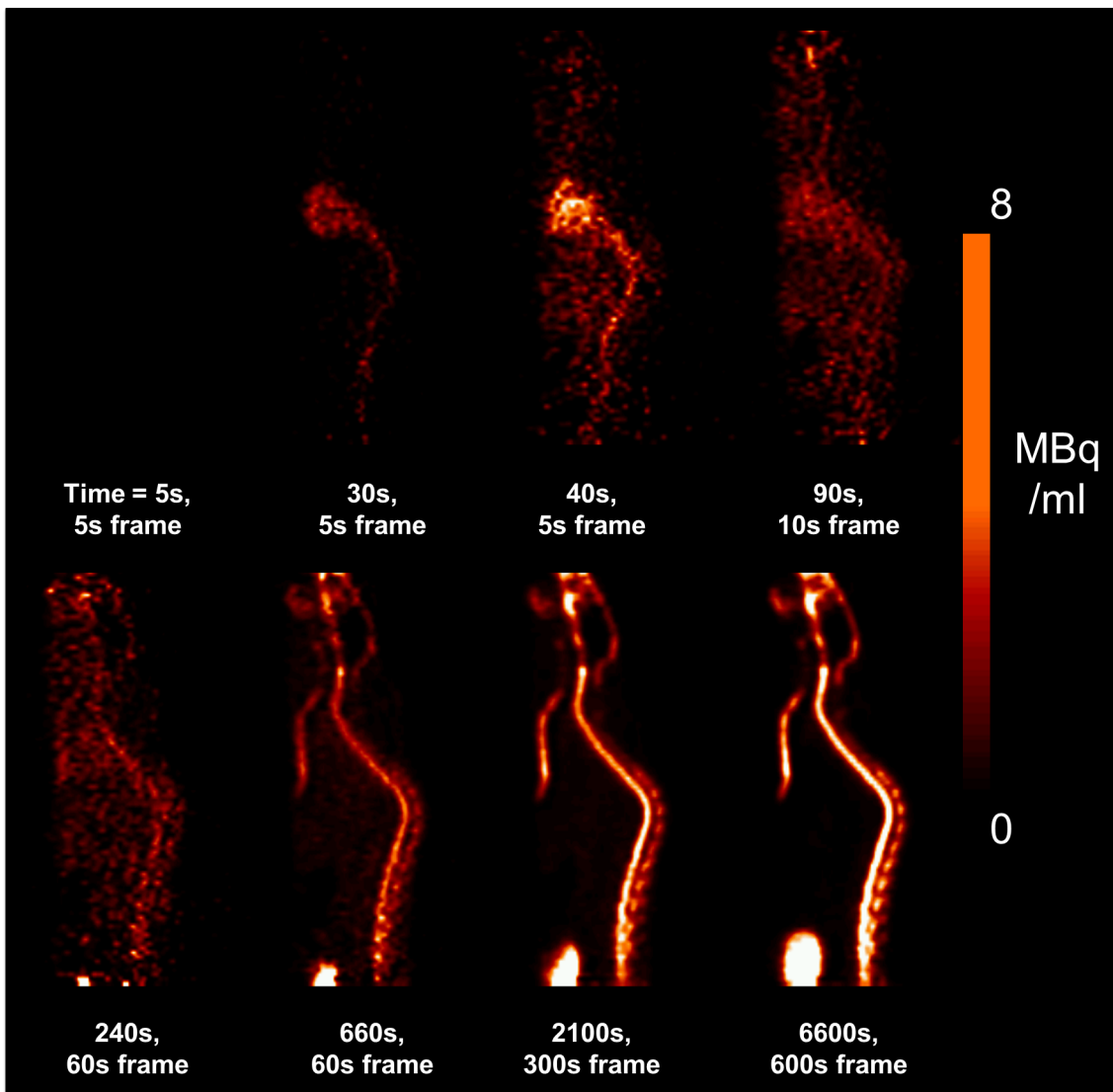


Figure 5.2: ^{18}F -NaF 2 hour (7200s) dynamic time course in mouse, MAP reconstruction, sagittal view. Selected frames from 2 hour scan illustrate how tracer distributes in mouse body over time, with frame start timings and durations indicated below each image. The tracer is distributed through the blood stream after reaching the heart and binds to the mouse skeleton.

5.1.2 ^{18}F -NaF IDIF and TAC extraction

The bolus can be visualised in the vena cava during early dynamic PET frames, with a sample frame shown in Figure 5.3. The VC ROI can therefore be used for IDIF extraction from early PET dynamic frames. The LVBP ROI has previously been used to extract IDIFs from early PET image frames in rat ^{18}F -NaF studies [237]. In this Chapter, IDIFs extracted from both the LVBP and VC ROIs were compared to assess their performance in mice.

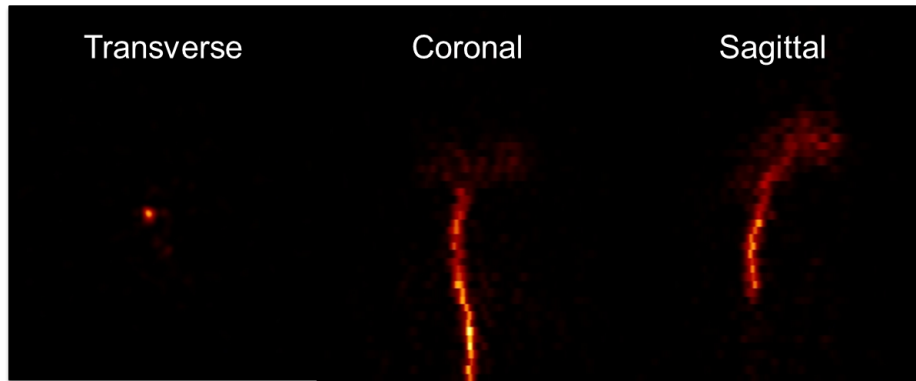


Figure 5.3: Signal from vena cava displayed in early time frame dynamic MAP PET (approx. 20s post injection, 5s duration) in transverse, coronal and sagittal views.

A comparison between an early frame used for LVBP and VC ROI delineation in IDIF extraction and a late frame used for ROI delineation in TAC extraction from the mouse skeleton is shown in Figure 5.4. ROI delineation must be carefully performed to ensure the LVBP and VC ROIs do not overlap with any part of the mouse skeleton in order to avoid significant spillover at late time points [231].

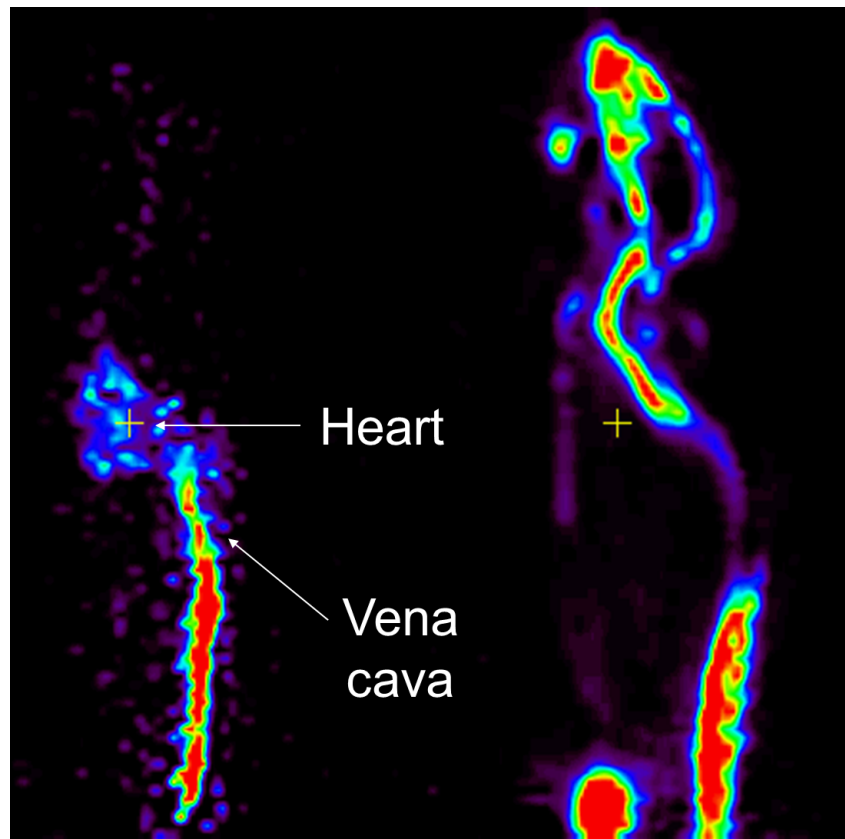


Figure 5.4: ^{18}F -NaF activity distribution *in vivo*, sagittal view, MAP reconstruction. Early frame (left) displays the tracer bolus travelling to the heart via the vena cava (5s bin, approx. 20s post injection). Late frame (right), displays uptake throughout the mouse skeleton, with the skull and spine clearly visible (600s bin, 6600s into scan). Centre of LVBP indicated by yellow cross on both images.

The proximity of the LVBP and VC ROIs to the mouse skeleton is shown with overlaid FLASH MR in Figure 5.5. This figure indicates the importance of accurate co-registration of MR data when performing ROI delineation. Each LVBP and VC ROI delineated from an early frame must be propagated to each dynamic frame and inspected for motion in order to minimise spillover effects and ensure that each ROI is correctly located within the structure of interest.

In addition to spillover, ^{18}F -NaF IDIFs also suffer from signal reduction from PVE. As ^{18}F -NaF does not accumulate in myocardial muscle like ^{18}F -FDG, it was difficult to delineate regions of homogeneous tracer concentration on all ^{18}F -NaF PET time frames. The assumption that each delineated ROI exhibits homogeneous uptake is required to successfully perform the GTM method discussed in Chapter 4, and therefore an empirical, alternative PVC method was used in this Chapter instead of the GTM approach. The RC method has previously been used in conjunction with cardiac gating and MAP reconstruction to produce ^{18}F -FDG IDIFs from the LVBP ROI which agreed with blood samples taken from mice at late time points [53], [68], [174].

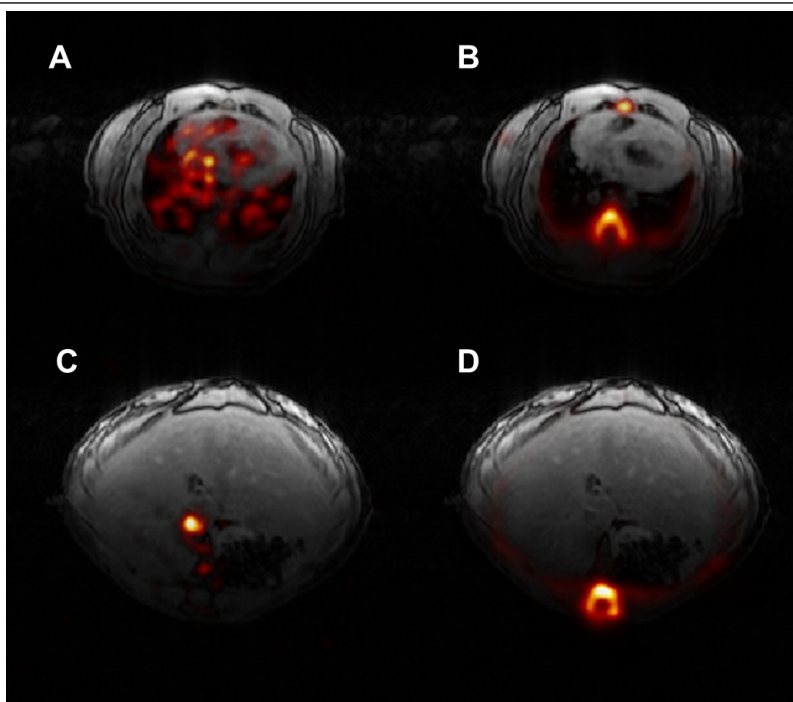


Figure 5.5: ^{18}F -NaF activity distribution *in vivo*, transverse view, MAP reconstruction, overlaid on co-registered FLASH MR. (A) Early frame, LVPB ROI, (5s bin, approx. 20s post injection). (B) Late frame, LVPB ROI, (600s bin, 6600s into scan), (C) Early frame, VC ROI, (D) Late frame, VC ROI.

5.1.3 Use of recovery co-efficient method to provide PVC

PVE results in a loss of signal within an image ROI due to the limited spatial resolution of the scanner and the finite size of the image voxel grid. This effect becomes more pronounced as the size of the object under study decreases, and is a major issue in small animal PET scanning, as shown in Chapter 4. Partial volume recovery co-efficients (RC) for regions of known size can be calculated and used to scale the observed mean signal for that ROI back to the true signal expected from an ROI of that size, but must be empirically derived from phantom scans [67], [177], [178].

A typical phantom for this application consists of several tubes or spheres of known diameter which are all filled with a tracer solution and a larger compartment filled with the same solution. The large compartment is selected to be of sufficient diameter that it is unaffected by PVE. The tracer activity is measured from the large compartment and compared to the observed activity in the smaller compartments, which should exhibit a decrease in mean activity due to PVE. The decrease in activity concentration values with decreasing tube diameter can be plotted and used to estimate the required RC for each compartment [53], [178], [179]. Larger RC corrections will be required as the diameter of the object decreases [222]. In addition, the large compartment is sampled and cross-calibrated with a well counter to ensure the accuracy of the readings.

Once a relationship between RC and object size has been established using a phantom, object diameters can be measured to calculate their respective RC, as illustrated in Figure 5.6. The RC technique in this Chapter utilised co-registered MRI images² to accurately measure the anatomical dimensions of structures *in vivo*, such as the LVBP and VC ROIs. The mean signal taken from these regions was then corrected for PVE using the calculated RC factors [67], [178].

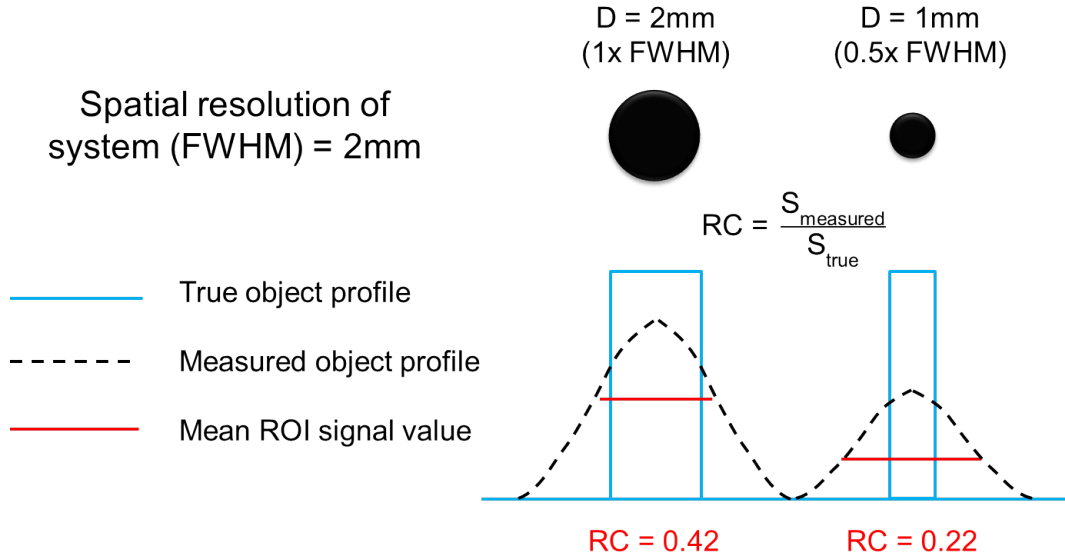


Figure 5.6: Object diameter is measured using MRI scans and required RC factor needed to scale the mean value observed back to the true value can be calculated.

RCs were calculated from signal ratios [222] defined using equation (5.1), where the true signal is not affected by PVE and the measured signal is reduced from its true value as a result of blurring from PVE. The calculated RCs were then used to correct the amplitude of signals using equation (5.2).

$$RC = \frac{\text{Signal}_{measured}}{\text{Signal}_{true}} \quad (5.1)$$

$$\text{Signal}_{true} = \frac{\text{Signal}_{measured}}{RC} \quad (5.2)$$

IDIFs were extracted from 3DRP and MAP PET images of 19 mice injected with ^{18}F -NaF. IDIFs attained from both LVBP and VC ROIs were contrasted, both with and without PVE correction provided by the RC method. The last points of all IDIFs were compared to plasma activity concentrations measured from blood samples taken at the end of the 2 hour ^{18}F -NaF PET scan. This study (to the author's

²Registration performed manually by the author in SPMmouse using anatomical landmarks, with estimated accuracy in LVBP and VC regions of <1mm.

knowledge) is the first to assess the performance of VC IDIFs for tracers other than ^{18}F -FDG in mice.

5.2 Materials and Methods

5.2.1 Phantom scans used to calculate recovery co-efficients (RC)

A microPET NEMA-NU4 2008 phantom (abbreviated to NEMA phantom for future use) was selected to provide the RC calibration measurements, and is displayed in Figure 5.7. The NEMA phantom is made from poly(methyl methacrylate) (PMMA) plastic and is primarily used for evaluating the performance of PET scanners [99]. It comprises 2 large cavity regions inside a cylinder - the first half is a single region of inner diameter 30mm and height 30mm which can be filled with PET tracer to give a “hot” region and the second half houses 5 small tubes of diameter 5mm, 4mm, 3mm, 2mm and 1mm (all of height 30mm)³. The tubes are radially aligned around the phantom’s z axis and can also be filled with PET tracer via a connection to the larger cavity to give “hot” regions of varying size. This gives the NEMA phantom a total filling volume of 20.66ml. The first half also includes 2 smaller cavities inside the large cavity, each of inner diameter 8mm and height 15mm - one is filled with water and the other filled with air to give “cold” regions.

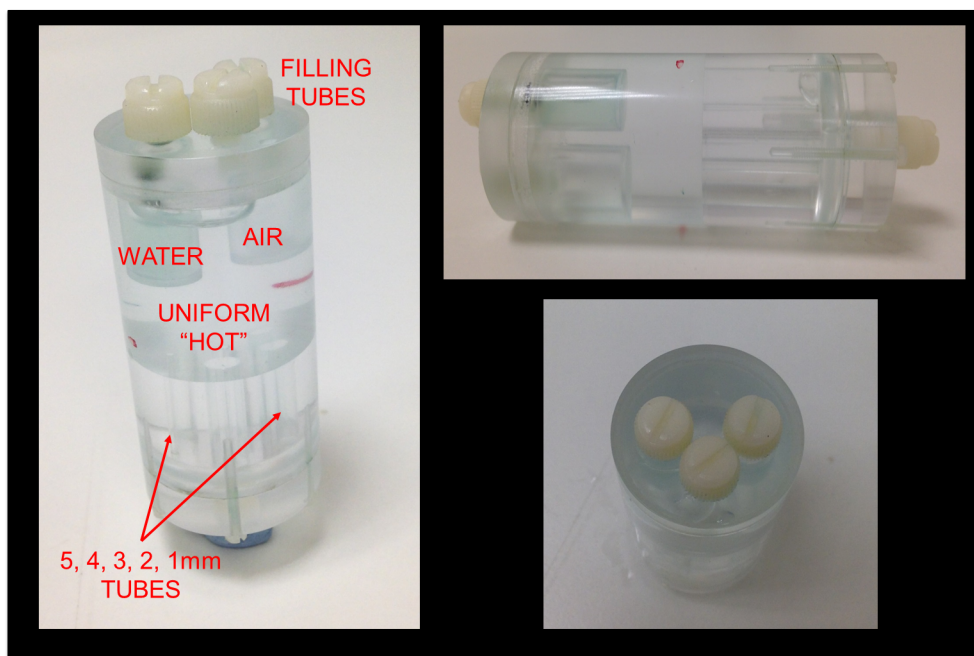


Figure 5.7: NEMA phantom photographs. The central compartment and five tubes of diameter 5, 4, 3, 2 and 1mm are filled with a water-based tracer solution. The two smaller compartments are filled with air and water respectively. Filling holes sealed with plastic screws.

³An additional 1mm filling cylinder was added to the NEMA design in the centre of the bottom cavity by Dr Rob Hawkes to improve the speed and uniformity of the filling procedure. This also enabled easier extraction of a sample to measure the phantom activity when the phantom was positioned horizontally on the scanner bed.

To perform the RC phantom calibration scan, the NEMA phantom was filled with 16.14MBq of ^{18}F -NaF (1ml) by the author and allowed to mix thoroughly for 30 minutes. The activity concentration was measured once the phantom was positioned on the scanner bed by inserting a syringe into the additional filling tube added at the base of the NEMA design and withdrawing a $\sim 160\mu\text{l}$ sample from the large compartment into an eppendorf tube. The sampling time was noted to correct for radioactive decay and the sample activity measured using a well counter (3 inch NaI crystal, Harwell Instruments, Canberra UK Ltd. using GENIE 2000 software).

An emission listmode dataset was then acquired for 2700s using the Cambridge Split Magnet PET camera (Focus 120). The data was reconstructed using 3DRP and MAP into $12\times 5\text{s}$, $12\times 10\text{s}$, $12\times 60\text{s}$, $2\times 300\text{s}$ and $2\times 600\text{s}$ dynamic bins, with a zoom factor of 2.5 applied to give an image of matrix $128\times 128\times 95$ with a transaxial pixel size of 0.35mm and a slice thickness of 0.80mm. Images reconstructed using MAP were reconstructed using 12 subsets and 18 iterations with a beta smoothing value of 0.005, giving a uniform resolution of 1mm. A 10 minute transmission scan was conducted in singles mode using a ^{68}Ge source the following day with the phantom *in situ*. Data were normalized and calibrated with corrections for decay, detector efficiency, dead time, random events and attenuation using the vendor microPET manager software (Siemens Molecular Imaging).

RCs were calculated by the author drawing circular ROIs onto images of the NEMA phantom (example images are shown in the Results section in Figure 5.10) using ASIPRO analysis software. This consisted of a 20mm ROI covering 5 slices in the main compartment of the NEMA phantom and smaller circular ROIs of diameter 5mm, 4mm, 3mm, 2mm and 1mm^4 were each manually drawn over 5 slices for each of the tubes. The ROIs were originally drawn on the 3DRP images and the same ROIs used to analyse both 3DRP and MAP datasets. The main cylinder ROI was assumed to have a large enough diameter to be unaffected by PVE in comparison to the tubes. To calculate the RCs, the observed mean activity concentration in the ROI for each of the smaller tubes in the last dynamic frame of both the 3DRP and MAP images was divided by the mean activity concentration extracted from the central ROI covering the main cylinder, as shown in equation (5.3). These values were plotted against the known tube diameter and a quadratic relation fitted to the data.

$$\text{RC} = \frac{\text{Signal}_{\text{tube}}}{\text{Signal}_{\text{uniform}}} \quad (5.3)$$

⁴Due to the small size of the tubes, the diameters were slightly overestimated - ASIPRO used ROIs spanning 15 voxels (5.25mm) for the 5mm tube, 12 voxels (4.2mm) for the 4mm tube, 9 voxels (3.15mm) for the 3mm tube, 6 voxels (2.10mm) for the 2mm tube and 3 voxels (1.05mm) for the 1mm tube.

5.2.2 Animal models

19 ApoE(-/-/CCR5) mice which were part of a larger atherosclerosis disease model evaluation experiment contributed data to this study⁵. 6 of these mice were control, wild type mice (3 males and 3 females, 26-35g) and were scanned at 26-27 weeks of age whilst 2 mice (1 male and 1 female, 30-45g) were kept on a high fat diet for 24 weeks and were scanned at 55 weeks of age. The remaining 11 mice (4 males and 7 females, 26-42g) were kept on a high fat diet for 18 weeks and were scanned at 26-30 weeks of age.

5.2.3 Sequential PET/MR imaging

All 19 mice (6 in control group, 13 in ApoE group) were scanned by the author using the sequential PET/MR workflow as described in the previous Chapter (see Figure 4.8), replacing ^{18}F -FDG with ^{18}F -NaF and conducting the PET emission scan for 2 hours instead of 45 minutes. Additionally the MR sequences were modified from those required for a cardiac mouse MR study to a whole body mouse MR study. All mice were secured prone on the scanner bed on top of a Bruker mouse heart surface coil, with the centre of the mouse shoulder blades aligned with the magnet isocentre. Appropriate monitoring was employed: a respiratory pillow was placed underneath the animal's chest and a rectal temperature probe was inserted using a lubricated cover. A heating water blanket was positioned around the animal and kept at a constant temperature of 37°C throughout the experiment. The mice were anaesthetised, using 3% isoflurane in 1l/min O₂ for induction and taken down to 1.5-2% isoflurane in 1l/min O₂ throughout for maintenance, whilst monitoring the animal to keep the respiration rate steady at 30-45 breaths per minute.

MRI was performed on a Bruker BioSpec 47/40 4.7T scanner (Bruker Inc., Ettlingen, Germany), acquiring prospectively self-gated FLASH IG (TR/TE 384/2.4ms, planar resolution $160\times 160\mu\text{m}^2$, 50 slices, thickness 1mm, matrix $256\times 256\times 50$) and TOF angiography (TR/TE 18/4ms, NEX=3, spatial resolution $160\times 160\mu\text{m}^2$, 48 slices, thickness 1.2mm, matrix $256\times 256\times 48$). The animal bed was then directly transferred to the Cambridge split magnet PET/MR scanner and a 10 minute transmission scan was conducted in singles mode using a ^{68}Ge source once the mouse was inside the magnet bore. A bolus intravenous injection of ^{18}F -NaF tracer (mean activity = $27\pm 13\text{MBq}$ over 19 mouse group, range 12-62MBq) was then administered through the tail vein cannula.

Dynamic PET emission list mode data were acquired for 7200s and reconstructed by the author using 3DRP and MAP into multiple dynamic frames: $12\times 5\text{s}$, $12\times 10\text{s}$, $12\times 60\text{s}$, $9\times 300\text{s}$, $6\times 600\text{s}$. A zoom

⁵Data were provided courtesy of Agnese Irtle, Dr Janet Maguire, Dr Joe Bird and Dr Anthony Davenport. Cannulations were performed by Vicki Pell and blood sampling by Dr David Williamson.

factor of 2.5 was applied to give an image of matrix $128 \times 128 \times 95$ with a transaxial pixel size of 0.35mm and a slice thickness of 0.80mm. Images reconstructed using MAP were reconstructed using 12 subsets and 18 iterations with a beta smoothing value of 0.005, constrained to give a uniform resolution of 1mm. Data were normalized and calibrated with corrections for decay, detector efficiency, dead time, random events and attenuation using the vendor microPET manager software (Siemens Molecular Imaging). All PET and MR images were co-registered using SPMMouse by the author [27].

To accommodate both a whole body MR protocol to image the mouse aorta for the atherosclerosis study and the 2 hour ^{18}F -NaF PET scan within a reasonable time frame for each mouse, it was not experimentally viable to attach leads to record cardiac ECG signals and perform a separate, gated cardiac MRI exam. As a result, no cardiac gating signals were available to be applied to the PET data. The FLASH IG sequence described previously was used to perform prospective cardiac gating to the whole body MRI data. Respiratory motion gating was not applied (see Appendix G for full explanation) to maintain SNR in the early frames of the dynamic scan which had low count statistics.

At the end of the PET scan, 10 of the 19 mice were immediately extracted from the PET/MR scanner and a $\approx 160\mu\text{l}$ blood sample was taken via cardiac puncture⁶. The timing of the sample was noted before the mouse was sacrificed using an IP injection of pentobarbitol. Each blood sample was transferred to a microbalance (Mettler Toledo, AT261 DeltaRange, Sanyo Electric Co. Ltd.) and its weight noted. The tube weight was then subtracted to ascertain the blood volume in each tube (blood density assumed as 1.05g/ml [239]) before inserting into a well counter (3 inch NaI crystal, Harwell Instruments, Canberra UK Ltd.) using GENIE 2000 software for 100s to measure its radioactivity in counts per second (cps). Cps were converted into kBq/ml using a conversion factor of 531.4cps/kBq and the calculated blood volume. Each blood sample was centrifuged at 10000rpm for 4 minutes to separate out clear blood plasma which was then pipetted into a pre-weighed 200 μl eppendorf. The plasma sample was then weighed using the microbalance and its radioactivity measured using the well counter in kBq/ml as described above, with the exception that mouse plasma had an assumed density of 1.025g/ml [240]. The time of each blood and plasma measurement was also noted using an external clock and each measurement was corrected for delay back to the injection time.

5.2.4 IDIF and TAC extraction

IDIFs were extracted from LVBP and VC ROIs segmented from overlaid FLASH MR, TOF MR and MAP/3DRP PET images (see Figure 5.5 for overlaid FLASH IG and PET images in LVBP and VC ROIs, and Figure 5.8 for the identification of the VC ROI using TOF MR) in a similar manner to IDIFs

⁶The remaining 9 were required for additional scans and histological analysis, so a terminal blood sample using cardiac puncture could not be taken.

extracted in the previous Chapter for mice injected with ^{18}F -FDG. LVBP and VC ROIs were drawn in Analyze 8.0 and converted into nifti format for signal extraction in Matlab by the author. ROIs were manually delineated from the co-registered MR images overlaid directly onto the last dynamic frame PET image for the LVBP ROI and an early time frame for the VC ROI.

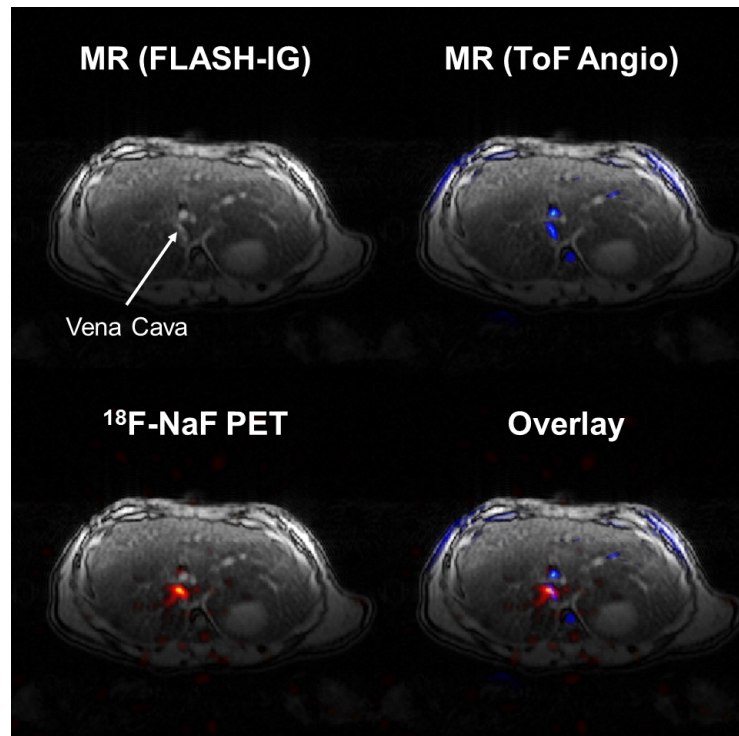


Figure 5.8: Detection of VC ROI from ^{18}F -NaF images. Clear VC signal on early time frame PET images (approx. 10s post injection, 5s duration) with overlay of FLASH MR images (top left, arrow indicates VC region). ToF angiography (blue overlay) confirms location to have high blood flow as expected for major blood vessel.

A 10 slice region covering the whole mouse heart was used to provide the LVBP ROI and a 10 slice region in the upper portion of the vena cava was used to provide the VC ROI for IDIF determination. The VC ROI selected region is shown in Figure 5.9. All ROIs were viewed on all PET frames and manually refined to reduce contamination from neighbouring tissue types caused by gross or cardiac motion over the course of the scan.



Figure 5.9: Overlay of VC PET signal (left) with FLASH MR (centre) and ToF angiography in blue (right). Yellow box indicates region used to derive VC IDIF.

The lower lumbar spine was selected as the bone TAC ROI because it was easily identifiable and displayed a reasonably consistent TAC profile across all mice. TAC profiles (not adjusted for injected activity) are shown in full in Appendix H. The lumbar spine ROI was segmented from last dynamic frame of the scan using the same 10 slices used to extract the VC ROI and again viewed on all PET frames and manually refined to reduce contamination from inter-frame motion.

5.2.5 Implementation of RC PVC method in IDIF extraction

PVC was applied to IDIFs by assuming the LVBP and VC ROIs could be approximated by cylinders. Whilst this approximation is adequate for the shape of the VC ROI, it is less appropriate for the LVBP ROI (see Figure 5.5 for a comparison of the cross sectional views of the LVBP and VC ROIs on FLASH MR images). The empirically derived RC factors applied may not have been entirely accurate in magnitude for the LVBP ROI as the geometry of the region affects how spillover and PVE will alter the observed signal profile on images. The LVBP ROI has, however, provide PVC from the RC method successfully when it has been approximated as a cylinder in previous murine studies [53].

RC factors were applied by measuring the LVBP and VC diameters on FLASH MR images and dividing each IDIF by the calculated RC factor. The RCs were taken from a quadratic plot of object diameter and RC factor made from the experimental results of the NEMA phantom measurements. Additionally a tissue background correction (previously suggested for ^{18}F -FDG [33] in mice and ^{18}F -NaF in humans [241], [242] when using similar PVC methods) was applied to compensate for tissue uptake in the LVBP and VC ROIs due to spillover. A background TAC was extracted from a surrounding tissue ROI (circle of diameter 2.5cm in nearby liver region), which gave a consistent background uptake signal throughout all frames. The corrected IDIFs were calculated as shown in equation (5.4) for all frames [33], [241],

$$\text{IDIF}_{\text{corr}} = \frac{\text{IDIF} - ((1 - \text{RC}) \times \text{TAC}_{\text{background}})}{\text{RC}} \quad (5.4)$$

where the IDIF is the mean value from the LVBP or VC ROI, RC is the estimated recovery co-efficient for the ROI measured using FLASH MR data, $\text{TAC}_{\text{background}}$ is the liver background TAC and $\text{IDIF}_{\text{corr}}$ is the corrected IDIF after the RC method has been applied.

5.2.6 Conversion of IDIFs from whole blood to plasma

All extracted IDIFs represented the activity concentration from whole blood and required conversion to plasma to estimate the AIF. To the author's knowledge, no standard conversion function between whole blood and plasma ^{18}F -NaF concentrations for mice currently exists and no serial blood sampling was available in this study, so previously published relations were evaluated for their suitability in conjunction with the single blood and plasma samples acquired for each mouse.

A porcine study [243] evaluated the relation between whole blood and plasma concentrations and reported a constant factor within each animal over the duration of a 2 hour scan. Whole blood to plasma conversion factors reported for each of the 7 pigs varied between 1.1 and 1.25 [243]. This result was further supported by a human study which reported a constant ratio of approximately 1.25-1.30 over the course of a 1 hour PET scan in a sub-group of normal, female patients for both venous and arterial blood samples [241], although other normal, female patients in this study reported a linearly decreasing value of between 1.6 and 1.4. The mean ratio was found to be a linearly decreasing ratio of between 1.5 and 1.35 over 1 hour for a group of 10 women. In this study, a mean ratio between the available plasma and whole blood samples in mice of 1.24 ± 0.04 was found, indicating agreement with the porcine study [243] and the first human group [241]. 1.24 was therefore used as a constant conversion ratio to increase the derived IDIF activity to plasma IDIF activity⁷.

After conversion from whole blood to plasma, activity concentration values from the last dynamic frames of the RC and non-RC corrected IDIFs were compared to plasma sample activity concentrations measured using the well counter to evaluate their quantitative accuracy.

5.2.7 Kinetic modelling

The accuracy of 4 groups of IDIFs were evaluated using kinetic analysis: uncorrected IDIFs, RC corrected IDIFs, IDIFs scaled such that their last time point agreed with their measured plasma sample

⁷In this application of the RC method, the RC correction was applied *before* the conversion factor of 1.24 was used to convert the IDIF into a plasma IDIF.

activity concentration and RC corrected IDIFs which were also scaled to the plasma samples. The PVC correction from the RC method was applied to IDIFs only; lumbar spin bone TACs were measured directly from the 3DRP or MAP images the IDIFs were extracted from.

All resulting plasma IDIFs were analyzed using the two compartment model shown in Figure 5.1 using PMOD software (v2.5, PMOD technologies Inc.). Model bi-exponential curves (an accepted model for mouse IDIFs [31], [54]) were fitted to the extracted IDIFs before analysis to smooth the data, as described in Chapter 4 and shown in Figure 4.13. Patlak analysis (linear graphical analysis, shown in equation (3.11) in Chapter 3) [154] was performed on each IDIF and its corresponding lumbar spine TAC to calculate the apparent uptake constant, K_i , in units of ml/g/min. As each injection and saline flush took approximately 15s to complete and a dynamic bin size of 5s was selected for the early frames⁸ only 5-6 points were available in the first 90s to characterize the peak of the IDIF. The kinetic parameter K_i was therefore analyzed and calculated using the Patlak method as this kinetic parameter depends on the AUC of each IDIF and is less sensitive to variations in IDIF peak height.

5.3 Results

5.3.1 NEMA phantom RC calibration

The activity concentration of the NEMA phantom was confirmed by an aliquot measured in the well counter as $0.538 \pm 0.005 \text{ MBq/ml}$. In the 3DRP image the large cylindrical region had an activity concentration of $0.537 \pm 0.058 \text{ MBq/ml}$, whilst in the MAP image the activity concentration was calculated as $0.567 \pm 0.080 \text{ MBq/ml}$.

Partial volume effects were clearly visible in the smaller tubes when tube diameters $< 2 \times \text{FWHM}$ of the scanner spatial resolution (1.8mm [229]) as expected. Blurring is seen clearly in both 3DRP and MAP images of the phantom shown in Figure 5.10, with the 1mm diameter tube almost disappearing from both images.

⁸5s was the minimum bin size to allow for appropriate SNR to visualise the LVBP/VC ROIs in early frames

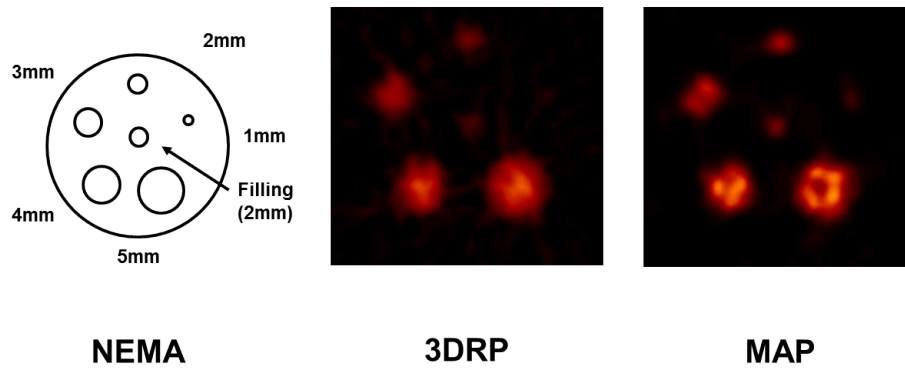


Figure 5.10: NEMA phantom emission images. (Left) Schematic of NEMA phantom tubes, showing decreasing tube diameters in clockwise direction: 5mm, 4mm, 3mm, 2mm, 1mm. (Centre) 3DRP reconstruction, 600s frame duration and (Right) MAP reconstruction, 600s frame duration on same image scale (0-0.8MBq).

The calculated RC values for the NEMA phantom are shown in Table 5.1. The 5mm tube was largely unaffected (3DRP RC= 0.80 ± 0.07 , MAP RC= 0.81 ± 0.09), but did show larger PVE than the F120 standard value of 0.93 reported from previous NEMA tests [99]. Performance dropped from the 4mm tube onwards, as shown in the table below. A drastic drop from the 2mm to the 1mm tube is seen in both 3DRP and MAP datasets as the diameter of the object becomes less than the spatial resolution of the system. The higher RC values generated by MAP indicated the gain in resolution recovery and reduction in PVE performed by the reconstruction algorithm compared to 3DRP.

Rod size	Measured 3DRP RC	Measured MAP RC	F120 reference RC
5mm	0.80 ± 0.07	0.81 ± 0.09	0.93
4mm	0.75 ± 0.07	0.79 ± 0.09	0.86
3mm	0.59 ± 0.05	0.62 ± 0.07	0.75
2mm	0.39 ± 0.04	0.52 ± 0.08	0.48
1mm	0.17 ± 0.02	0.17 ± 0.02	0.15

Table 5.1: Comparison of recovery co-efficients attained from the NEMA phantom in the Cambridge Split Magnet Scanner and a standard F120 scanner (as reported in previous NEMA tests [99]).

Graphs of the relation between the RC value and the tube diameter are shown in Figure 5.11, and broadly agree with previously published work [53], [68]. Quadratic relations were fitted between tube diameter and recovery co-efficients for both 3DRP and MAP (see Figure 5.11(b)), giving R^2 values of 0.996 and 0.981 respectively. These relations were therefore used in the *in vivo* mouse PVC work to compute RCs for the LVBP and VC ROIs.

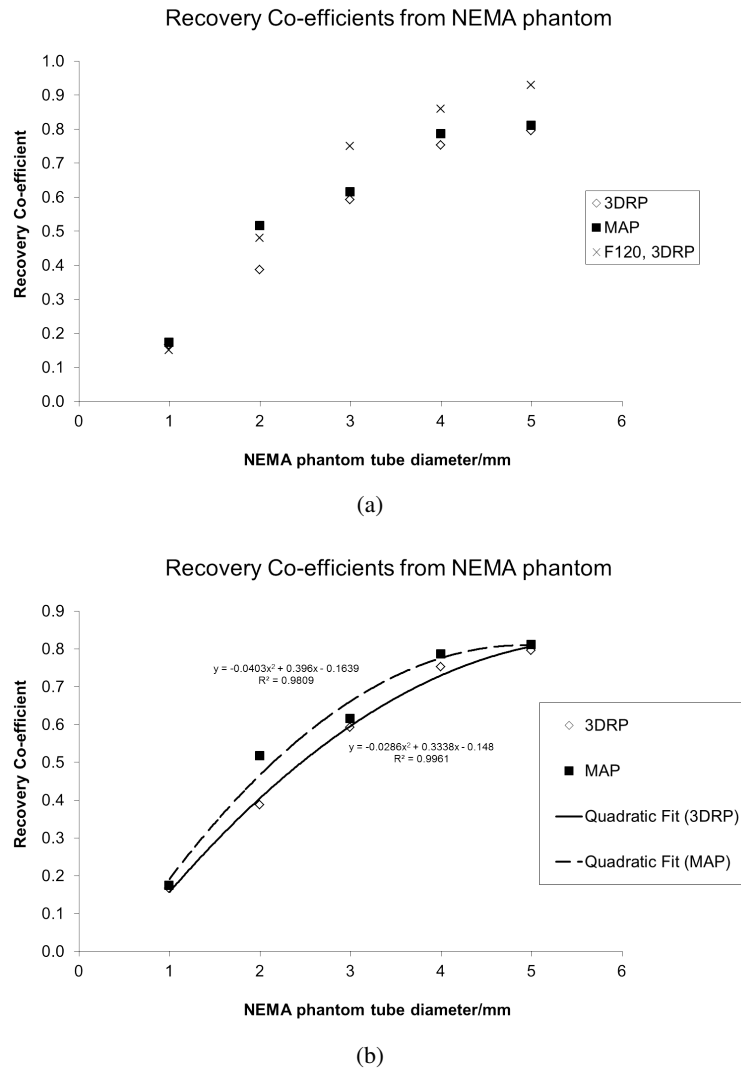


Figure 5.11: NEMA phantom RC calibration graphs. (a) Comparison to F120 NEMA results [99], (b) Quadratic trends fitted to RC relation with tube diameter.

5.3.2 Influence of reconstruction algorithm and ROI location on IDIFs

In contrast to the ^{18}F -FDG results shown in the previous chapter, no clear differences in IDIF shape or peak height were seen between reconstruction algorithms for LVBP IDIF from all 19 mice injected, with an example shown in Figure 5.12. This indicates that the LVBP ROI is less affected by PVE in the case of ^{18}F -NaF compared to ^{18}F -FDG.

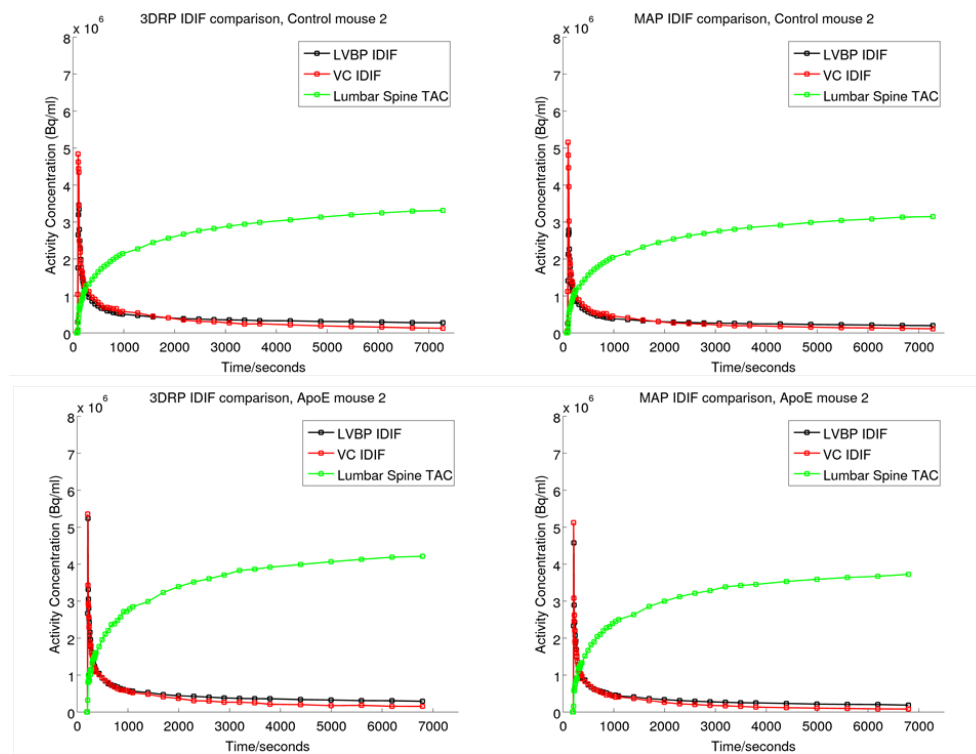


Figure 5.12: Comparison of IDIFs extracted from 3DRP (left column) and MAP (right column) images for 2 mice from cohort. Similar IDIFs are attained from both LVBP and VC ROIs, with the VC IDIFs displaying slightly lower tails.

There was little variation between LVBP and VC IDIFs using either 3DRP or MAP reconstruction over the cohort, as shown in Figures 5.13 and 5.14 for the control mice and high fat diet ApoE mice respectively. There was a slightly larger mean peak height found in the VC IDIFs using both 3DRP and MAP reconstruction, although these were mainly due to a single control mouse and a single ApoE mouse in each group. In addition, the variation in IDIF tail shapes slightly increased across the ApoE mouse group compared to the control group in both the LVBP and VC ROIs, perhaps as a result of their more varied physiology. The mean IDIF peak heights for each of the techniques across the mouse groups are detailed in Appendix H in Table H.1 and the mean IDIF AUCs are shown in Table H.2. Peak height differences were significant between the IDIFs from the LVBP and VC ROIs with the MAP algorithm for both the control group ($n=6$) and ApoE group ($n=13$). In terms of AUC, significant differences (Student's paired t test, $p<0.01$) were seen between LVBP IDIFs formed using 3DRP and MAP for both groups.

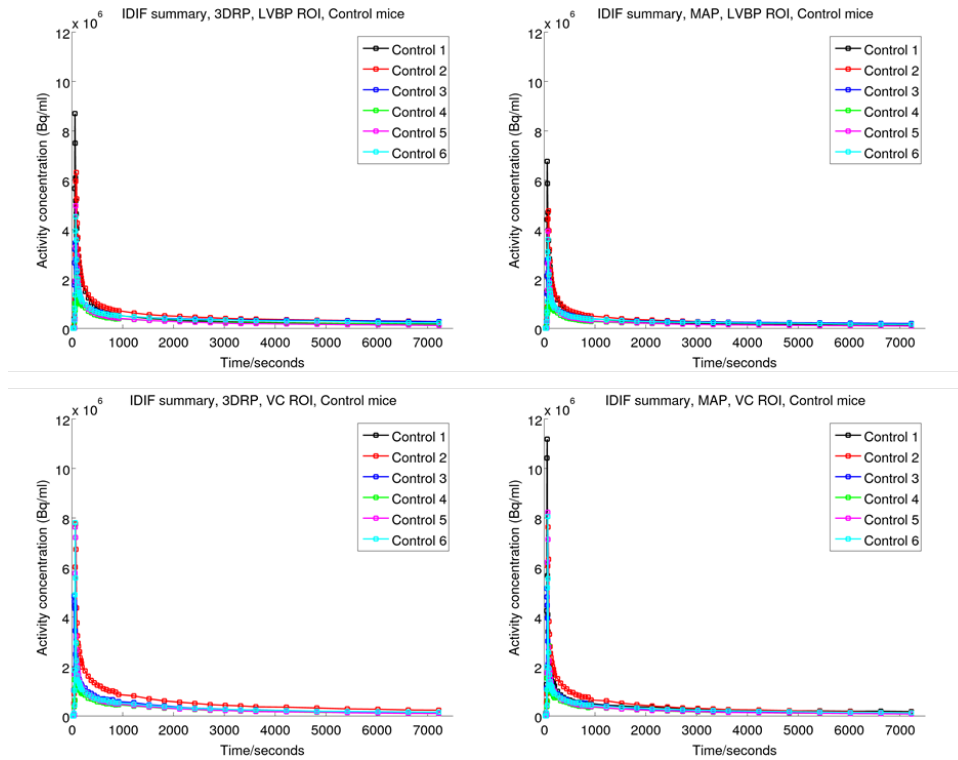


Figure 5.13: Overview of IDIFs extracted from 3DRP and MAP images for LVBP and VC ROIs across all control mice (n=6).

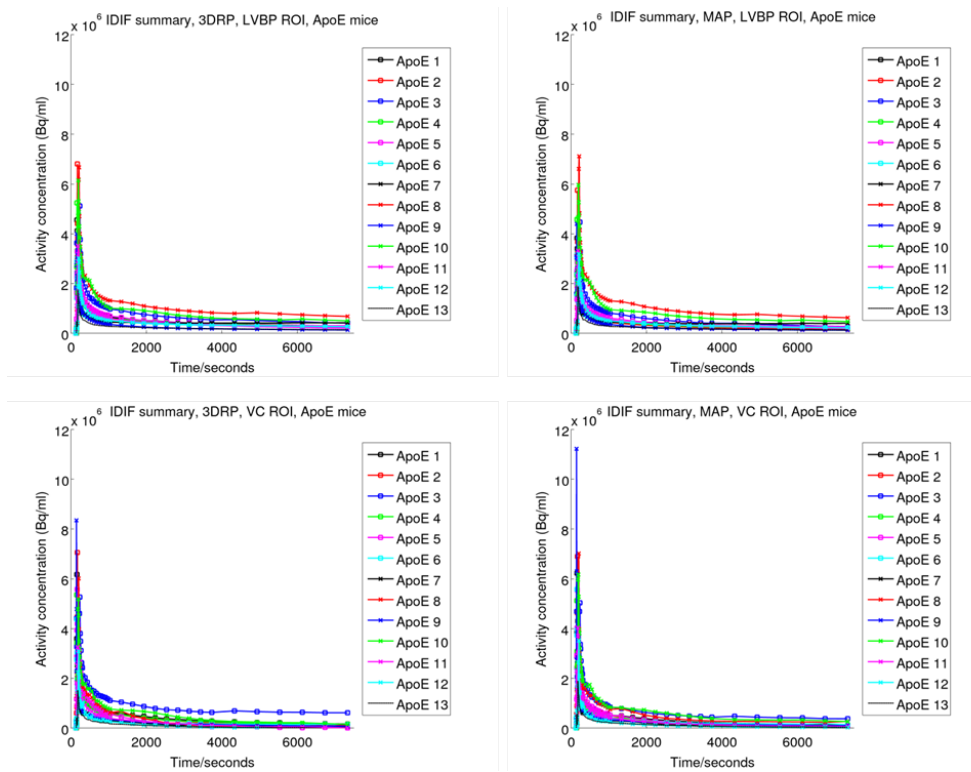


Figure 5.14: Overview of IDIFs extracted from 3DRP and MAP images for LVBP and VC ROIs across all high fat diet ApoE mice (n=13).

Mouse	3DRP LVBP	MAP LVBP	3DRP VC	MAP VC	Plasma sample
Control 1	0.217	0.138	0.239	0.175	0.137
Control 2	0.275	0.198	0.161	0.116	0.135
Control 3	0.148	0.092	0.125	0.080	0.149
Control 4	0.287	0.162	0.193	0.128	0.113
ApoE 1	0.514	0.336	0.772	0.471	0.202
ApoE 2	0.364	0.233	0.193	0.102	0.124
ApoE 3	0.379	0.332	0.006	0.122	0.129
ApoE 4	0.302	0.279	0.164	0.170	0.051
ApoE 5	0.527	0.502	0.064	0.092	0.075
ApoE 6	0.846	0.778	0.171	0.334	0.209
Mean	0.386 ± 0.201	0.305 ± 0.204	0.209 ± 0.209	0.179 ± 0.126	0.132 ± 0.049

Table 5.2: Comparison of last plasma IDIF frame values with plasma samples. All values in MBq/ml.

The comparison of the last time point of the IDIFs produced from both groups with the late plasma samples is detailed in Table 5.2 and illustrated in Figure 5.15 and Figure 5.16. Figure 5.16 visually displays the results for the entire cohort of plasma samples ($n=10$). All IDIF methods were found to produce values that were of the correct magnitude but were biased to larger values compared to the measured results and had a greater variation across the mouse group. The extra noise present in the 3DRP images compared to the smoothed MAP images contributed to a greater overestimation of the plasma sample values by 3DRP. The LVBP results for both 3DRP and MAP were also found to be significantly different to the measured samples (Student's paired t test $p \leq 0.05$; 3DRP $p=0.002$, MAP $p=0.02$).

The best agreement with the plasma samples in this study was found using the MAP VC method, which produced a mean value of 0.179 ± 0.126 MBq/ml compared to the measured 0.132 ± 0.049 MBq/ml. The VC method had lower bias to the plasma sample on average compared to the LVBP method for both 3DRP ($158 \pm 115\%$ compared to $326 \pm 190\%$) and MAP ($154 \pm 80\%$ compared to $265 \pm 202\%$). This was expected as this method provided PVC and the VC ROI was less susceptible to motion, as detailed in Chapter 4. It also agrees with previous work which reported bias in the last points of IDIFs compared to plasma samples of 575% from the LVBP ROI using OSEM with ^{18}F -FDG compared to 38% for the VC ROI [33].

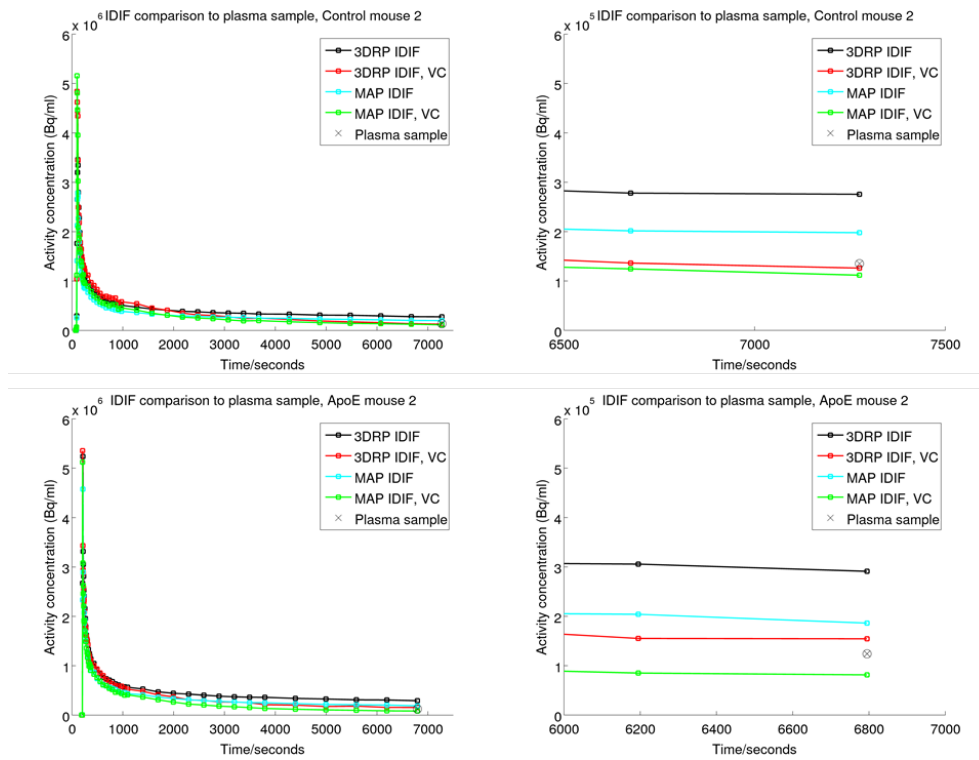


Figure 5.15: Comparison of IDIFs extracted from 3DRP and MAP images for 2 mice from cohort. Left column: IDIFs from LVBP and VC ROIs, right column: Zoom inset comparison of final IDIF values with plasma samples.

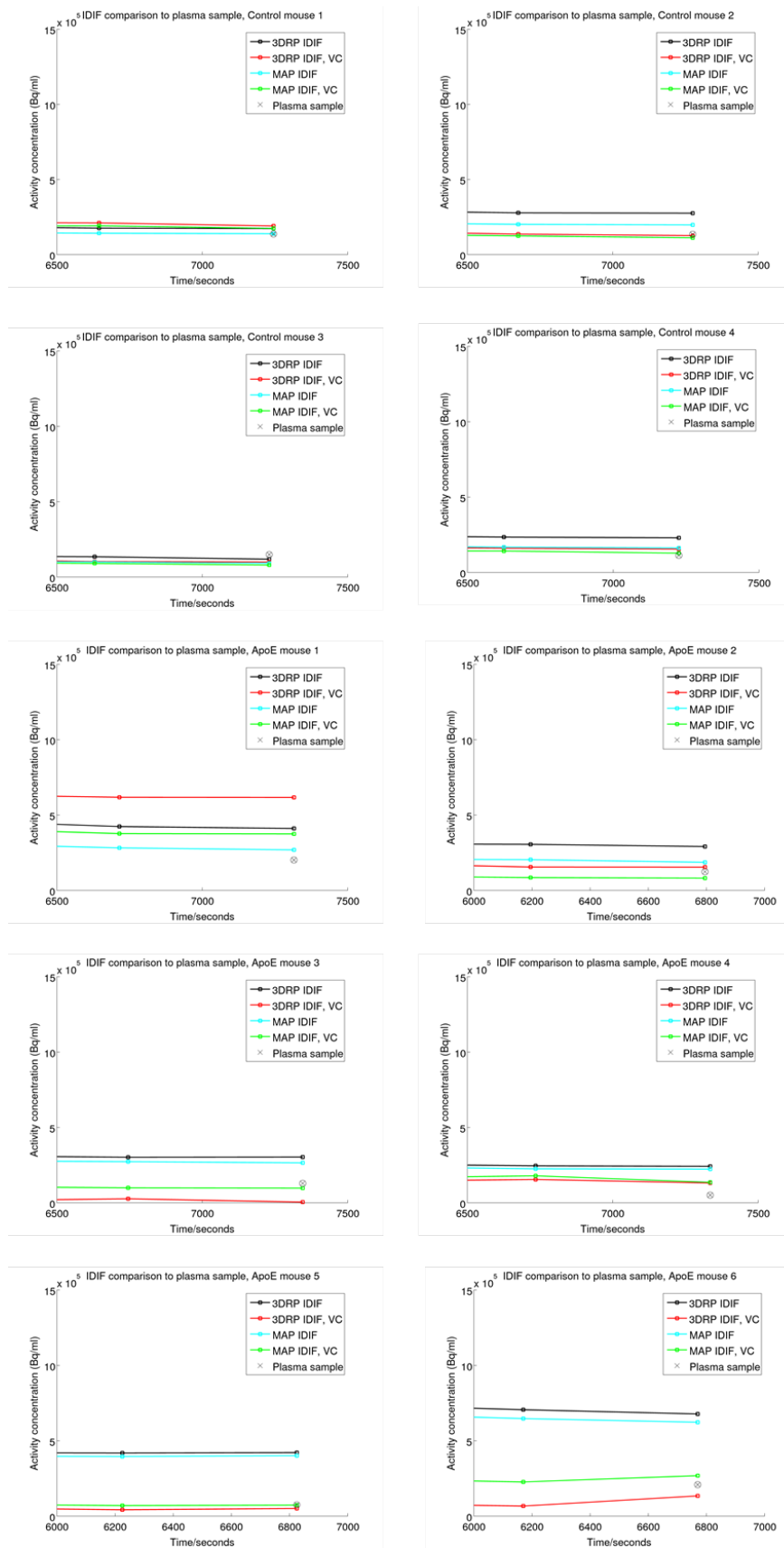


Figure 5.16: Overview of IDIFs extracted from 3DRP and MAP images across entire cohort using zoom inserts. Greater agreement with plasma samples seen with VC IDIFs across mouse group.

5.3.3 Application of RC method for IDIF PVC

The mean LVBP diameter for the entire mouse cohort was $3.68 \pm 0.34\text{mm}$, giving a mean RC of 0.71 ± 0.04 for 3DRP and 0.74 ± 0.03 for MAP. The vena cava diameter was almost half the size at $1.73 \pm 0.29\text{mm}$, giving mean RC values of 0.35 ± 0.07 for 3DRP images and 0.40 ± 0.07 for MAP images. The application of the RC correction is shown in Figures 5.17 and Figure 5.18 for a sample control and a sample ApoE mouse.

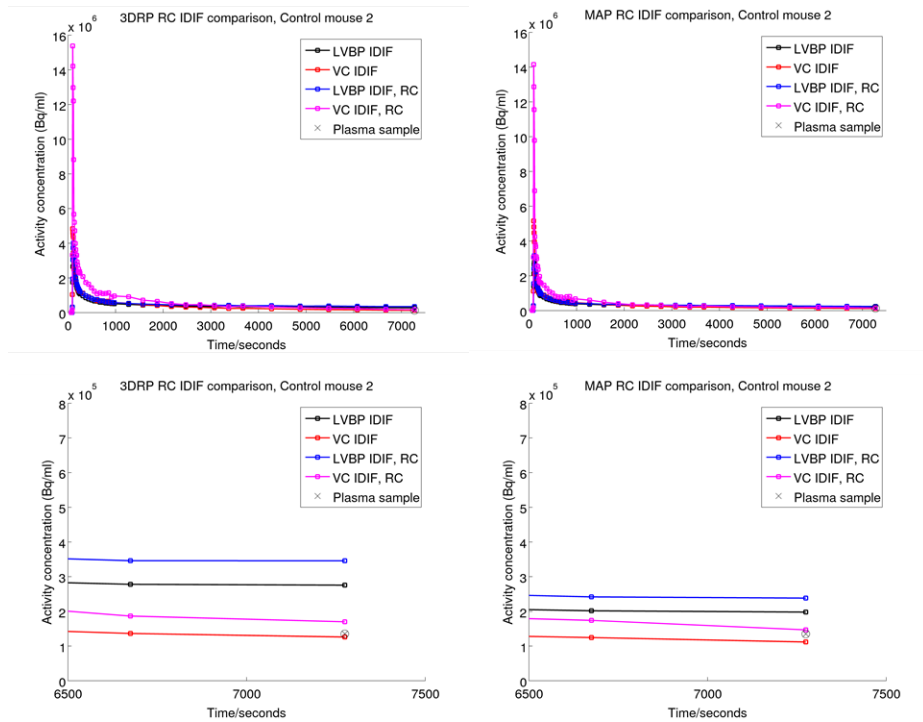


Figure 5.17: Application of RC method to LVBP and VC IDIFs for control mouse.

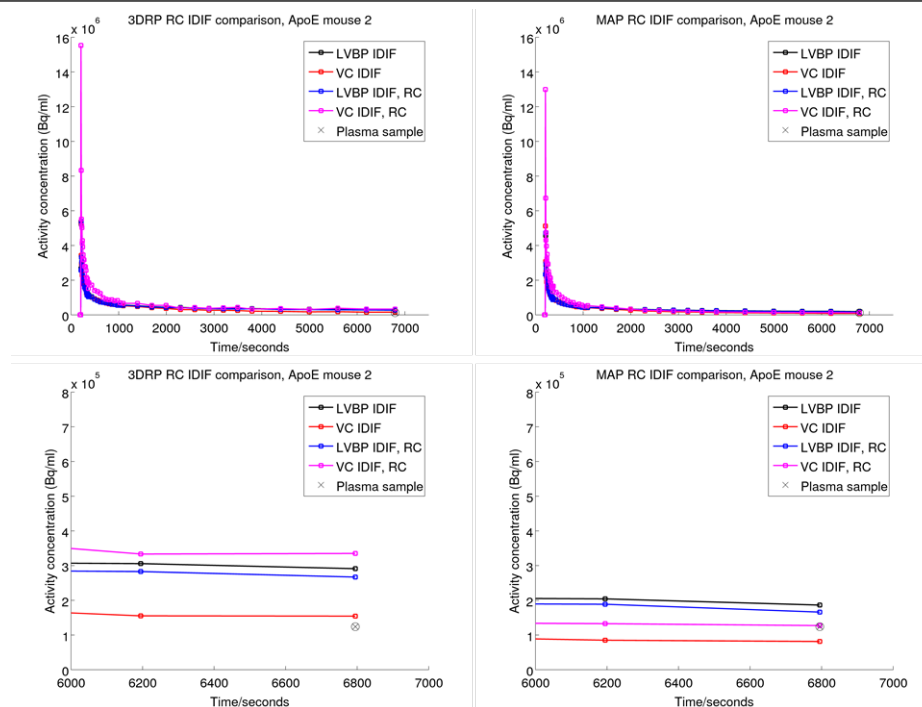


Figure 5.18: Application of RC method to LVBP and VC IDIFs for high fat diet ApoE mouse.

Although effective in some mice, the application of the RC method did not provide any of the previously extracted IDIF method with a consistent improvement across the mouse group according to the late plasma samples. All IDIFs corrected using the RC method had an increase in the bias and/or variation to the late plasma samples compared to the non-RC corrected IDIFs, as shown in Table 5.3 for all mice ($n=10$).

IDIF Method	Mean value (last time point)	Bias (%) to well counter measurement
3DRP LVBP	0.386 ± 0.201	326 ± 190
3DRP LVBP RC	0.399 ± 0.215	348 ± 233
MAP LVBP	0.305 ± 0.204	265 ± 202
MAP LVBP RC	0.306 ± 0.214	260 ± 237
3DRP VC	0.209 ± 0.209	158 ± 115
3DRP VC RC	0.327 ± 0.392	252 ± 221
MAP VC	0.179 ± 0.126	154 ± 80
MAP VC RC	0.249 ± 0.175	200 ± 139
Plasma sample	0.132 ± 0.049	-

 Table 5.3: Last IDIF time point activity concentrations (all in MBq/ml) compared to plasma sample measured in well counter for all mice ($n=10$, 4 control mice and 6 ApoE mice).

5.3.4 Kinetic modelling results (K_i values)

The calculated mean K_i values using the IDIFs for the lumbar spine ROI are detailed in Table 5.4. To the author’s knowledge, no previous ^{18}F -NaF murine studie have quoted kinetic rate constants and so full validation of the IDIFs discussed in this chapter with reported K_i values was not possible⁹.

IDIF Method	3DRP LVBP	MAP LVBP	3DRP VC	MAP VC
Control group	0.061±0.015	0.083±0.022	0.063±0.012	0.083±0.018
Control group, RC	0.054±0.018	0.082±0.025	0.052±0.017	0.073±0.016
ApoE group	0.054±0.016	0.068±0.018	0.108±0.046	0.112±0.040
ApoE group, RC	0.054±0.021	0.067±0.045	0.089±0.045	0.095±0.045

Table 5.4: Comparison of mean K_i values for IDIFs and RC IDIFs (n=19, n=6 for control group, n=13 for ApoE group) for lumbar spine ROI. All values in g/min/ml.

The mean lumbar spine K_i value for 3DRP in the LVBP ROI for the control group was 0.061 ± 0.015 g/min/ml, which matched well with 0.063 ± 0.012 g/min/ml for the VC ROI. In contrast, for the ApoE group the value for 3DRP in LVBP ROI was 0.054 ± 0.016 g/min/ml and 0.108 ± 0.046 g/min/ml in the VC ROI. This pattern was mirrored in the MAP results, giving the control group a mean K_i value of 0.083 ± 0.022 g/min/ml in the LVBP ROI and 0.083 ± 0.018 g/min/ml in the VC ROI, whereas the ApoE group displayed mean K_i values of 0.068 ± 0.018 g/min/ml in the LVBP ROI and 0.112 ± 0.040 g/min/ml in the VC ROI. The increase in K_i values seen between the 3DRP and MAP IDIFs for both groups indicates how the significant decrease in IDIF AUC from 3DRP to MAP IDIFs can affect the resulting PET kinetic parameters. Both sets of VC IDIFs also show a significant difference in K_i values (two mean Student’s t test, $p < 0.05$) between the two groups of mice, which is not seen with the LVBP IDIFs.

The RC method had a very limited effect on the LVBP K_i results, but the VC ROI mean K_i values were reduced by $\approx 15\%$ in each mouse group. The 3DRP VC K_i value for the control group reduces from 0.063 ± 0.012 g/min/ml to 0.052 ± 0.017 g/min/ml (paired Student’s t test, p value = 0.15) after the RC method was applied, whilst the MAP VC K_i value reduces from 0.083 ± 0.018 g/min/ml to 0.073 ± 0.016 g/min/ml (p value = 0.08). Similar decreases were seen in the ApoE group values - the 3DRP VC K_i value dropped from 0.108 ± 0.046 g/min/ml to 0.089 ± 0.045 g/min/ml (p value = 0.005) and the MAP VC K_i value dropped from 0.112 ± 0.040 g/min/ml to 0.095 ± 0.045 g/min/ml (p value = 0.005).

The K_i values attained when using the plasma samples to scale the tail of each AIF, are shown in

⁹Published results in humans suggest a K_i value calculated using Patlak analysis for the lumbar spine of 0.024-0.036 g/min/ml [241], [242], [244] for healthy subjects, with an increase to K_i values of 0.103 ± 0.6 g/min/ml in Paget’s disease affected bones [242].

Table 5.5. Examples of the scaled IDIFs are illustrated in Figure 5.19 for the two mice (one from each group).

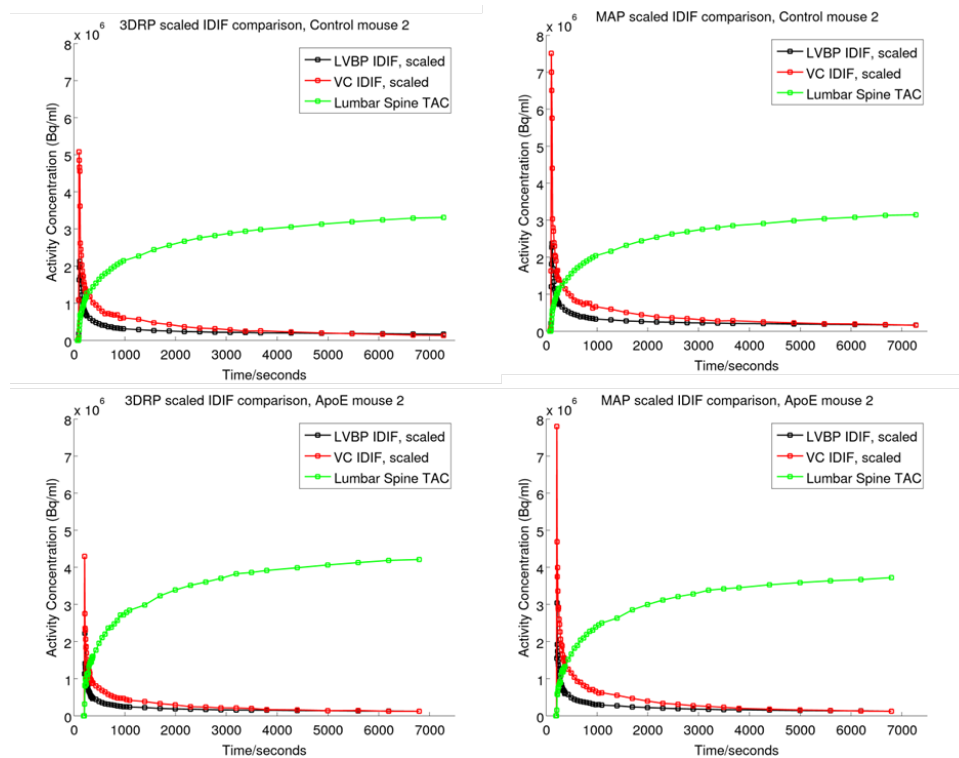


Figure 5.19: Scaled IDIFs extracted from 3DRP (left column) and MAP (right column) images for 2 sample mice. Same scale is used as in Figure 5.12, indicating the difference in the peak height after applying a global factor scaling from the plasma sample.

IDIF method	3DRP LVBP	MAP LVBP	3DRP VC	MAP VC
Control group	0.060±0.019	0.081±0.028	0.063±0.015	0.083±0.023
Control group, RC	0.053±0.023	0.077±0.031	0.055±0.018	0.070±0.020
Control group, scaled	0.097±0.018	0.079±0.010	0.085±0.020	0.069±0.010
Control group, scaled, RC	0.096±0.018	0.078±0.011	0.076±0.033	0.065±0.017
ApoE group	0.055±0.021	0.067±0.020	0.110±0.040	0.112±0.026
ApoE group, RC	0.057±0.028	0.067±0.024	0.083±0.047	0.089±0.041
ApoE group, scaled	0.198±0.062	0.212±0.095	0.151±0.094	0.207±0.082
ApoE group, scaled, RC	0.193±0.060	0.210±0.093	0.179±0.079	0.205±0.077

Table 5.5: Mean K_i values for all scaled IDIFs ($n=10$ for blood sampled data; $n=4$ for controls, $n=6$ for ApoE) using lumbar spine ROI. All values in g/min/ml.

For the control group, reasonable agreement is seen between the MAP LVBP and MAP VC K_i values produced by sample scaled IDIFs and unscaled IDIFs, but there is a increase of between 25-40% between K_i values produced using scaled and unscaled 3DRP LVBP and 3DRP VC IDIFs. The sample scaled

values (with the exception of 3DRP LVBP) all broadly agree on a K_i of between 0.070-0.085g/min/ml, suggesting that the K_i values attained for the control group by MAP LVBP or MAP VC IDIFs alone are reasonably accurate, according to the single plasma sample taken in this study.

The scaled IDIFs for the ApoE group produced increased K_i values with greater variances compared to their respective unscaled IDIFs, with all of these being significantly different (paired Student's t test, $p < 0.04$) except for the 3DRP VC IDIFs. The ApoE group increased K_i values were also significantly different to the control group K_i values when using the scaled IDIFs (two means Student's t test, $p < 0.02$). Like the control group, all sample scaled values broadly agree for the ApoE group on a K_i of between 0.150-0.215g/min/ml. The unscaled 3DRP and MAP VC IDIFs were closest to these values, although there was a much larger gap in this case than between the scaled and unscaled VC IDIF K_i values for the control group.

5.4 Discussion

5.4.1 IDIF accuracy compared to plasma samples

LVBP and VC ROIs were successfully located and delineated from PET images using overlaid MR high resolution FLASH and ToF angiography images. All IDIFs extracted using either 3DRP or MAP with the LVBP or VC ROI all showed an overestimation of the IDIF tail compared to measured plasma samples. This disagreement between measured AIFs and IDIFs has been previously reported in ^{18}F -NaF human studies [241] where serial, arterial blood sample values are underestimated by IDIFs in the early part of the curve and overestimated in the last dynamic time frames. Although only one blood sample was available, the results from this study indicated that a low but significant spillover from surrounding structures was present (see Figure 5.20). Typical spillover into VC or LVBP regions from spinal or rib cage bones was of the order of 0.1-0.2MBq/ml across the mouse group in late time frames, compared to background noise in air which varied over the mouse group between 0.002-0.003MBq/ml (2000-3000Bq/ml), which suggests the large bias in the image-based measurements to the well counter measurements in Table 5.3 (typically between 100-300%) could be accounted for by the spillover effect from nearby bones. This suggests that further PVC and motion correction must be applied to IDIFs to give better agreement with gold standard blood sampling results. In addition, the 3DRP images were noisy (particularly in early, short duration frames which had lower counts) and were not smoothed, which may have contributed to their greater disagreement to the samples than the MAP IDIFs, as observed in previous studies [68].

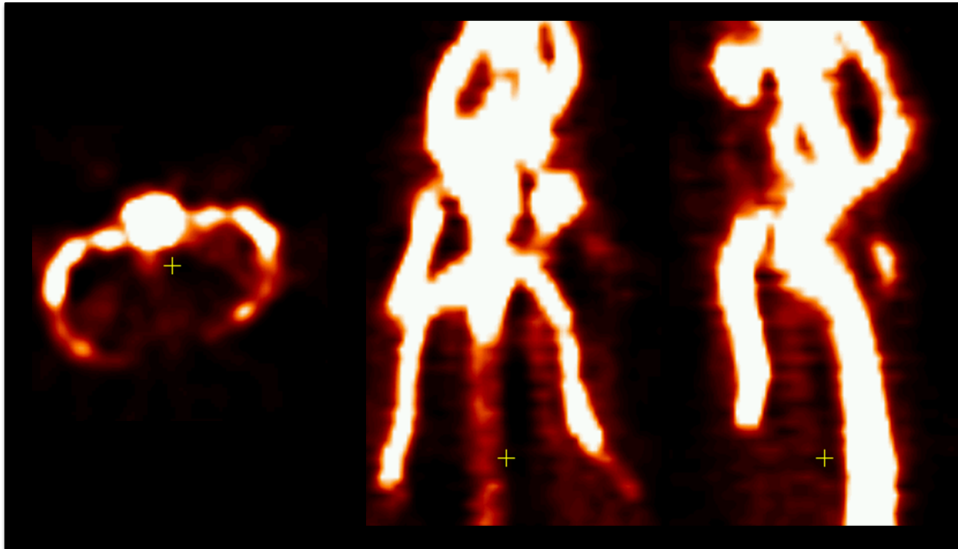


Figure 5.20: MAP image with 10% signal threshold applied, indicating non-zero (typically between 0.1-0.2MBq/ml) spillover from mouse bones into LVBP and VC ROIs at late time points, making accurate IDIF extraction challenging. Centre of VC ROI indicated by yellow cross.

Each sample was assumed to be arterial plasma as it was taken from the heart 2 hours post-injection. In human studies which performed ^{18}F -NaF PET scans with serial blood sampling, arterial and venous samples were compared and it was concluded that venous samples taken at late time points of a 1 hour scan were sufficient to scale population ^{18}F -NaF IDIFs accurately [241]. As the time of the scan was much longer in this case and mice have a higher cardiac rate than humans, it was assumed that the concentration of ^{18}F -NaF in arterial and venous plasma had equilibrated at this point. The samples may actually have had a greater amount of venous plasma than arterial plasma in them, and the concentration of ^{18}F -NaF in venous plasma may have been lower than expected for arterial plasma, contributing to the disagreement with the IDIFs. As only one blood sample was available per mouse, it is difficult to isolate the exact cause of the disagreement in this case and also to be certain of the validity of the agreement with the IDIFs.

There was greater variation in the IDIFs produced by the ApoE group compared to the control group, both in their overall curve shapes (more variable peak heights and less consistent “shoulder” regions of the curves) and in their increased disagreement with the plasma samples taken. This suggests that the physiology caused in the ApoE model by the high fat diet may have had an effect on the IDIFs, as the control group were found to produce much more consistent IDIFs, particularly in the tail region of the curve.

5.4.2 IDIFs derived from the VC ROI

Limited difference was seen between ^{18}F -NaF IDIFs derived using either 3DRP or MAP techniques, indicating that PVE had a limited effect on the IDIFs in this case, although a small difference between LVBP and VC IDIFs was observed, with the VC IDIFs exhibiting better agreement to the late plasma samples. The VC ROI was less affected by motion compared to the LVBP ROI, as previously discussed in Chapter 4, and the tracer bolus appears more concentrated within the vena cava at low count rates, as shown in Figure 5.2. No PET cardiac gating information (ECG) was available in this study so it is difficult to know the extent to which gating the PET data to provide motion correction would improve the LVBP results. In addition, the ribcage appears to cause greater spillover to the LVBP ROI than the spine bone does to the VC ROI.

This is an interesting result, as the VC ROI should provide a venous output function, rather than an arterial input function (AIF), yet in mice the VC ROI appears to produce IDIFs which more closely resemble the measured plasma samples (which were believed to be arterial plasma). This suggests that the distribution of ^{18}F -NaF tracer from venous to arterial blood may well occur at a very high rate in mice and therefore it may be possible to use a venous ROI in place of an arterial ROI to derive an IDIF, although full, serial blood sampling over the time course of the scan would again be required to confirm this hypothesis.

5.4.3 Effect of IDIF on K_i parameter

In both groups, for both LVBP and VC ROIs, using MAP IDIFs instead of 3DRP IDIFs resulted in increased K_i values. This was due to the decreased IDIF AUC found with the MAP IDIFs compared to the 3DRP IDIFs (see Table H.2 in Appendix H for full breakdown of values), which occurred because MAP IDIFs were taken from images with less PVE and were less noisy due to smoothing being applied in the reconstruction process.

Although the LVBP IDIF K_i values broadly agree between the mouse groups (3DRP LVBP: controls = $0.061 \pm 0.015 \text{g/min/ml}$, ApoE = $0.053 \pm 0.022 \text{g/min/ml}$; MAP LVBP: controls = $0.083 \pm 0.022 \text{g/min/ml}$, ApoE = $0.068 \pm 0.018 \text{g/min/ml}$), the increased variation in the ApoE VC IDIFs lead to significantly larger K_i values with greater variance being reported compared to the control mice VC IDIFs, for both 3DRP and MAP. This indicated that the cardiac motion in the LVBP region (which is larger absent in the VC ROI) may actually obscure physiological differences in kinetic analysis and motion correction, if available, should be applied in future ^{18}F -NaF murine studies.

The plasma sample scaling method was found to produce IDIFs with much larger K_i values compared

to unscaled IDIFs, particularly in the ApoE group where unscaled IDIF K_i values were significantly lower than scaled IDIF values. The scaled IDIFs also produced consistent ranges of K_i values for all IDIF extraction techniques (controls: 0.070-0.085g/min/ml, ApoE: 0.150-0.215g/min/ml) and showed significant differences in K_i values between the control and ApoE groups. This suggests that the physiological differences between the mouse groups highlighted by the unscaled VC IDIFs may well exist but would require additional data with full serial blood sampling to validate this hypothesis.

5.4.4 Evaluation of RC PVC method

According to the plasma sample results, the RC PVC method does not appear to offer an improvement over standard IDIFs derived from either 3DRP or MAP images for ^{18}F -NaF murine studies. The last IDIF frame activity concentrations are often moved further away from the plasma sample values after the application of the RC method, especially for the 3DRP results, as shown in Figures 5.17 and 5.18, resulting in greater biases to the single sample plasma concentrations, shown in Table 5.3. K_i values do not differ significantly after application of the RC method to IDIFs from the LVBP, but a significant drop in K_i values was seen between RC and non-RC corrected IDIFs from the VC ROI in the ApoE group for both 3DRP and MAP. This would suggest that the larger RC corrections used on VC IDIFs due to the smaller size of the VC ROI result in significantly lower K_i values in the ApoE group.

The limited effectiveness of RC in this study can be attributed to the fact that it is an empirical method which assumes uniform ROI dimensions and only applies a simple scaling factor to increase the mean signal extracted from the ROI, as shown in Figure 5.6. It does not provide resolution recovery or correct for the profile signal spilling out from the region into other structures. PVE was also not seen to a great extent in this dataset, as observed in both the IDIF curve shapes and the relatively similar RC values produced by 3DRP and MAP in the phantom data. This was in contrast to the extensive PVE affecting the LVBP IDIFs in Chapter 4, which may also explain why no large gains in IDIF accuracy were seen with the MR-based RC PVC method in this Chapter.

5.4.5 Improvements to experimental protocol

Ideally a fully homogeneous mouse population would have been available for analysis of the IDIF methods. 13 ApoE mice which were subjected to a high fat diet were included in this study in addition to 6 control mice to ascertain the effect of the different IDIF extraction methodologies in a larger group of mice. This also produced n=10 total mice with blood samples taken instead of just n=4 if only control mice had been used. As the IDIFs produced by the ApoE mice were found to be much more variable than the control mice IDIFs, future work examining IDIF methodology would ideally focus only on a

large group of control mice to remove the confounding factor of physiological variation in the analysis of the techniques.

The cardiac puncture method used in this study, although reasonably effective, produced only one late blood sample for IDIF validation, and this sample was taken after the mouse's PET scan had finished and the mouse removed from the magnet bore. Decapitation to attain arterial blood was not performed as the mice aorta were required intact for further evaluation via CT imaging as part of a broader atherosclerosis study. Other methods which use distal tail vein incisions to extract multiple blood samples [53] could be considered for future work, although the combined PET/MR scanner bore and magnetic field environment makes blood sampling in this manner extremely challenging.

Future work pursuing accurate IDIF extraction in mice would benefit from a fully established relation between whole blood and plasma ^{18}F -NaF activity concentrations in control mice, which would require serial arterial blood sampling. Serial blood samples would also provide a better validation of each IDIF technique, as they would provide consistent activity concentration readings from arterial plasma. This is extremely difficult to perform in mice, but could potentially be done through the use of an (expensive) MR compatible blood sampling device such as Swisstrace [51] or cannulation of the mouse femoral arteries [160], aorta [68] or tail vein [36], but these methods require highly trained and specialized personnel to perform them and could be vulnerable to dispersion in a long cannula line which feeds outside the MR bore.

5.5 Conclusions

A range of IDIF extraction techniques were tested on a 19 mouse ^{18}F -NaF dataset. The last dynamic frame activity concentrations of these IDIFs were compared to late plasma samples for 10 of these mice. Both the LVBP and VC ROI were located using MR TOF angiography images and delineated from high resolution MR images, and were then used to extract IDIFs from 3DRP and MAP images. The MAP VC IDIFs provided the best agreement with the measured plasma samples and increased K_i values for the lumbar spine in both the 6 control mice and the 13 ApoE mice. Significant differences in K_i values between the 2 mouse groups were evident when the VC IDIFs were used, and these were not seen with the LVBP IDIFs. The MAP VC IDIFs also provided K_i values with the best agreement to K_i values produced when using the plasma samples to scale their corresponding IDIFs for both mouse groups. These results both indicate that the VC ROI was less affected by motion than the LVBP ROI. The VC ROI therefore could be suitable for future IDIF use in murine ^{18}F -NaF studies, with the use of co-registered FLASH and ToF angiography used to assist in optimized VC ROI segmentation, although further work including serial blood sampling would be required to validate this technique. The RC IDIF

correction method was not found to increase the accuracy or precision of any of the extracted IDIFs or their respective K_i values, indicating that the required PVE correction was relatively small in murine ^{18}F -NaF studies and more complex MR-based PVC methods may be required in future work.

5.6 Chapter Summary

The empirical RC method of partial volume correction was tested for use in dynamic ^{18}F -NaF studies in mice, but was not found to produce IDIF tails with better agreement to late plasma samples than uncorrected IDIFs, suggesting more complex methods of PVC would be required to provide subtle improvements to ^{18}F -NaF IDIFs in mice by accommodating for spillover from nearby bones to a greater extent. IDIFs derived from the LVBP and VC ROIs were, however, found to be similar using both 3DRP and MAP images, with the VC IDIFs exhibiting better agreement to the late plasma samples as the VC ROI is less affected by motion. This supports results seen in Chapter 4 which suggested that the high cardiac output of mice leads to a similar distribution of tracer within arterial and venous blood, which would recommend further investigation into the use of the VC ROI in the place of the LVBP ROI in future IDIF murine studies. Whilst the use of MR in this case is relatively limited to improved ROI delineation using the soft tissue contrast of MRI and blood flow information derived from ToF angiography, MRI sequences are also hypothesised to be able to assist in PET AIF determination by using dynamic MR data to estimate an IDIF which can be converted into a PET AIF. The testing of a DSC MRI technique used in Chapter 7 to explore this possibility is detailed in the next Chapter.

Chapter 6

Automatic AIF detection using DSC MRI in rats

In addition to aiding PET partial volume correction approaches, it may be possible to use simultaneously acquired dynamic MR data to provide an AIF for PET. DSC MRI, described in detail in Chapters 2 and 3, is one approach that could be used for this application in the brain, although there has been limited exploration of optimizing the AIF extraction process in small animal DSC MRI. The development of an automated AIF extraction approach for use in rat DSC MRI studies of the brain is described in this Chapter. The hypotheses were as follows:

- 1. Automatic voxel selection processes produce more consistent estimates of AIFs in rat DSC MRI than manual voxel selection.*
- 2. Automatically selected AIFs produce quantitative estimates of perfusion parameters with greater accuracy than manual AIFs.*
- 3. The addition of MR angiography information can aid the AIF voxel selection process.*

6.1 Introduction

6.1.1 Quantitative analysis of cerebral perfusion from MRI

One of the key physiological processes measured by dynamic MRI using contrast agent injections is cerebral perfusion, which describes the delivery of blood to the tissue capillary bed in the brain through three key parameters: cerebral blood flow (CBF), cerebral blood volume (CBV) and mean transit time (MTT). CBF measures the average blood flow rate in [$\text{ml } 100\text{g}^{-1} \text{min}^{-1}$], CBV measures the total volume

of blood in [$\text{ml } 100\text{g}^{-1}$] and MTT measures the average time for any given particle of contrast agent to traverse through the tissue in seconds [121].

Dynamic Susceptibility Contrast MRI (DSC-MRI) uses $T2^*$ -weighted EPI imaging to track an intravenous bolus of paramagnetic contrast agent through the cerebral vasculature, via a change in the $R2^*$ relaxation parameter, which is proportional to the change in gadolinium-based contrast agent concentration as outlined in Chapter 2. This data can then be used to estimate CBF, CBV and MTT *in vivo*, as discussed in Chapter 3. DSC-MRI perfusion data has been employed in a variety of conditions, including the evaluation of ischemia [245], [246], [247], traumatic brain injury [248], Alzheimer's disease [249] and the hemodynamics and cerebral tissue physiology of lesions [204], [250], [251].

As described in Chapter 3, the concentration time curve of the feeding artery to the ROI is required as an input to the perfusion compartmental model in DSC MRI and is known as the arterial input function (AIF). A schematic AIF annotated with its main features is shown in Figure 3.11, with an example AIF derived from an ROI manually drawn on the middle cerebral artery of a rat shown in Figure 3.12. AIF shape and height must be measured correctly to give accurate perfusion quantification from either modality, as CBF and CBV scale linearly with area under the AIF [117], [118], [124], [213], [252].

As it has been hypothesized that dynamic MR data could be used to provide an estimate of a PET AIF if PET tracer and contrast agent are injected together [54], it is vital that any MR image based techniques of AIF extraction are thoroughly validated before being used to provide information for another modality. DSC MRI is one approach that could be used for this application, although there has been limited exploration of optimizing the AIF extraction process in small animal DSC MRI.

6.1.2 Development of an automatic AIF selection method

Manual voxel selection to produce AIFs non-invasively from images is a standard technique in small animal DSC MRI analysis and relies on the observer correctly selecting arterial voxels with the largest signal change from the DSC MRI images. Automatic arterial voxel selection algorithms for AIF determination are favoured over manual methods in clinical studies as they are operator independent and create standardized, reproducible results on a reduced timescale by selecting voxels which fulfil certain criteria [199], [204], [212], [213]. To reduce variability and manual error in operator-selected AIFs, the simplest form of automation applies various thresholds on voxel signals [207], [212] to identify voxels which produce curves which are most similar to an ideal arterial signal curve, i.e. high peak height, sharp rise time and narrow bolus profile. The preclinical development of one such method is discussed in this Chapter. The method is an advancement on previous work which used manual selection [211] or a single peak height threshold in rats [210], [214] and mice [186].

Arterial Spin Labelling (ASL) can also be used to measure absolute values of CBF [121], [125], as outlined in Chapter 2, although ASL in rats is usually restricted to single slice acquisitions due to the time taken to acquire the sequence. DSC MRI perfusion results produced using both manual and automatic voxel selection methods are compared to ASL results in this Chapter to ascertain if the automated DSC MRI analysis protocol produced improved perfusion parameter results.

6.1.3 Use of cerebral vasculature atlases for improved arterial voxel determination

To aid the automatic voxel selection process in the identification of arterial voxels for AIF determination, magnetic resonance angiography information was incorporated into the voxel selection algorithm. TOF-MRA measures the signal from flowing blood by a rapid series of slice selective RF pulses that saturate the background signal and then record the entrance of fresh magnetisation into the imaging plane [86], as described in Chapter 2. It does not require the aid of a contrast agent to visualise the vasculature and can be performed before contrast agent administration.

In this Chapter, TOF-MRA scans were used to construct a study-specific rodent probabilistic vasculature atlas, in a similar manner to other rodent [253], [254], and human [255], [256], vasculature atlases constructed from libraries of MRA images. This was done so that if individual data for a single subject was missing or corrupted, the atlas could still be used to predict the most likely position of the arteries and veins within the rat brain. Each atlas was created by co-registering an archive of MRA images into a common space to create a probabilistic map of major arteries and veins, which was used to identify areas commonly used to derive AIFs for DSC MRI, such as the middle cerebral artery (MCA)¹. A Bayesian approach for AIF determination was then added to the threshold-based automatic selection algorithm, streamlining its voxel selection for AIF extraction using prior knowledge of vascular anatomy derived from angiography atlases.

6.2 Materials and Methods

6.2.1 Animal preparation

Previously acquired data² was analysed to determine if voxels covering major vessels could be automatically detected and produce reliable estimates of first pass bolus AIFs from DSC MRI images of rat brains.

¹A branch of the internal carotid artery originating from the arterial circle roughly 2mm caudal to bregma [257].

²This data was used with the permission of Prof Jean-Claude Baron, Dr Ulf Jensen-Kondering and Dr Sohail Ejaz. All DSC MRI datasets were acquired by Alex Ward.

17 spontaneously hypertensive (SHR) male rat DSC MRI datasets were examined. 10 datasets were taken from control SHR rats (550-650g, Charles River, Margate, Kent, UK) who were part of a permanent MCA occlusion study and received sham surgery using a drill method [258]. MRI scans were conducted 3-4 hours post surgery, after a 2-3 hour PET scan³ was conducted, using the protocol previously described in [258]. These 10 rats did not display any ischemic lesions on T2 weighted anatomical scans or diffusion images (data not shown) and so were used as a “control” group to ascertain if DSC MRI could produce quantitative estimates of perfusion parameters using AIFs taken from relatively healthy rat brains.

The other 7 DSC MRI datasets were taken of SHR rats (10-12 weeks, Charles River, Margate, Kent, UK), which had undergone a temporary MCA occlusion procedure using a distal clip method [259]. The clip was removed after 45 minutes, and the wound closed after visual verification of blood flow restoration through the distal MCA. Animals were then allowed to survive for 28 days before MRI was conducted, allowing for a large ischemic region to appear, which was visible on T2 weighted anatomical scans and diffusion images (data not shown). Perfusion parameters derived from DSC MRI were compared across the healthy and affected hemispheres of these rat brains to attempt to identify the ischemic regions. These rat datasets are designated as the “stroke” rat group in this Chapter.

A further 3 SHR male rats which underwent the distal clip MCA occlusion method were scanned but did not receive an injection of contrast agent, using ASL to measure their brain perfusion in place of DSC MRI⁴.

In addition to these 20 rats (17 DSC MRI, 3 ASL), angiography data was taken from a further 7 SHR control rat datasets produced using the drill method (who did not have DSC MRI data available). This gave a total of 27 angiography datasets, which were used to build a rat cerebral vasculature atlas for use in the automatic voxel selection procedure.

6.2.2 MRI imaging protocol

All rats were scanned using a Bruker Biospec 47/40 4.7T MR scanner (Bruker Inc. Ettlingen, Germany) and secured prone on the scanner bed. A Bruker rat head surface coil was used for imaging, with the centre of the rat brain aligned with the magnet isocentre. Appropriate monitoring was employed: a respiratory pillow was placed underneath the animal’s chest and a rectal temperature probe was inserted using a lubricated cover. A heating water blanket was positioned around the animal and kept at a constant temperature of 37°C throughout the experiment. Animals were prepared under isoflurane anaesthesia (induced at 4% in 1.5 l/min O₂; maintained at 2% in 1.5 l/min O₂), whilst monitoring the animal to keep

³Four different tracers were used, as detailed in [258].

⁴To clarify, no rat dataset had both DSC MRI and ASL data available to directly compare CBF between the two techniques.

the respiration rate steady at 30-50 breaths per minute. Continuous blood oxygen saturation and heart beat were monitored using a pulse oximeter.

Each of the 17 SHR rats that underwent DSC MRI was injected with 0.5mmol/kg Gadovist (Gd-BT-D03A) through a femoral vein cannula and scanned using a single shot T2* weighted EPI sequence (TR/TE 250/9ms, in plane planar resolution $320 \times 390 \mu\text{m}^2$, flip angle = 50° , 5 slices, 1.5mm thickness, NEX = 1, 150 time frames at 250ms intervals) to perform DSC-MRI over the whole rat mid-brain. DSC MRI began 5s before tracer injection was administered and lasted 37.5s. A gradient echo EPI sequence was chosen over a spin echo EPI sequence due to its higher SNR, increased linearity of $\Delta R2^*$ and increased sensitivity to larger vascular structures [121], [122], [125]. The sequence is shown in Figure 2.60 in Chapter 2 and frames captured from the first pass bolus peak are shown in Figure 6.1. A multi gradient echo (MGE) sequence (TR/TE 1500/4.5ms, 12 echoes were spaced 7ms apart beginning with the first echo at 4.5ms and the last being at 81.5ms, 8 slices, 1mm slice thickness, 1.5mm gap between each slice, flip angle = 30° , NEX = 1, FOV = $40 \times 40\text{mm}$, $256 \times 256 \times 96$ image matrix, planar resolution $156 \times 156 \mu\text{m}^2$) was used to perform T2* mapping in the distal clip MCA occlusion group to detect ischemic lesion structure (in absence of other MR scans available for these rats to diagnose stroke). T2* maps were computed by fitting an exponential model to the MGE signal decay ($S = S_0 \exp(-\frac{TE}{T2^*})$) using the online macro in Bruker Paravision 5.0 software.

11 DSC MRI datasets were determined to be useable from the 17 datasets taken: 7 from the “control” group (sham drill method, no ischemic region detected) and 4 from the “stroke” group (distal clip method, clear ischemic region detected). Of the DSC MRI data that had to be discarded, 3 rat datasets exhibited poor DSC MRI signal, indicating that very little of the MR contrast agent reached the brain. This resulted in noise that was of similar size to the DSC MRI signal and meaning that an AIF peak could not be identified. The other 3 failed datasets recorded a “double bolus” appearing on the extracted AIFs, meaning that the manual injection was not executed in one smooth motion and followed by a smooth, saline flush. Over the course of the experiment, the injection protocol was refined to avoid these circumstances: rat cannulas were double checked with saline flushes before putting the rat into the magnet bore, the earbars and bite bars securing the rat head were double checked to minimise motion and the contrast agent was prefilled into the cannula line to enable a single flush injection to administer the entire bolus in a single motion.

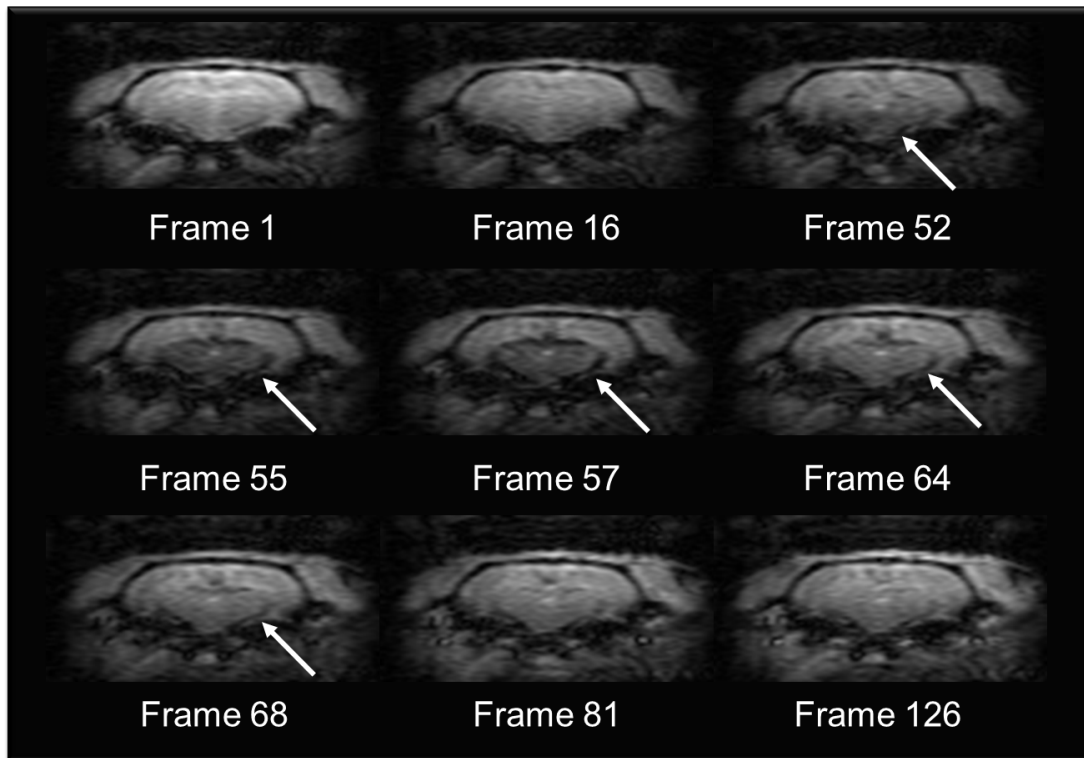


Figure 6.1: T2* weighted EPI images of first pass bolus peak in rat model, going from top left to bottom right in time order (frame duration = 250ms). Arrow highlights signal loss in vasculature due to passage of contrast agent bolus.

The 3 rats that underwent ASL were scanned using a 2D flow sensitive alternating inversion recovery (FAIR) EPI sequence with a selective excitation followed by a global excitation (TR/TE 16000/27ms, planar resolution $310 \times 620 \mu\text{m}^2$, single slice, 2 mm slice thickness, 128×64 matrix, 20 TIs in 400ms intervals from 26ms to 7626ms). A single slice in the rat striatum was used to assess perfusion by calculating CBF. CBF maps were calculated using the comparative T1 mapping method outlined in Chapter 2 and equation (2.33) using the built-in macro in Bruker Paravision 5.0 software.

All 27 rats which contributed to the angiography atlas (17 DSC MRI, 3 ASL, 7 angiography only) were scanned with a 2D T2-weighted RARE fast spin echo sequence to provide anatomical information (TR/TE 15078/36ms, NEX = 1, isotropic spatial resolution of $250 \times 250 \mu\text{m}^2$, 128 slices, 0.2mm slice thickness, 256×256 matrix, RARE factor = 8) and a 2D TOF angiography sequence (TR/TE 12/3ms, NEX = 2, spatial resolution $160 \times 160 \mu\text{m}^2$, flip angle = 80° , 64 slices, 0.7mm slice thickness, 256×256 matrix) to assess the vascular structure.

6.2.3 Construction of angiography atlas

27 SHR rat MRA datasets were used by the author to construct a study-specific vasculature probability atlas by co-registering them in a common space and averaging them together after normalisation.

First the high resolution, anatomical RARE images were manually co-registered to known atlases of rat grey matter (GM), white matter (WM) and cerebral spinal fluid (CSF) in a common space using the SPMmouse Matlab toolbox⁵ [27]. The common space was designated Paxinos space as the structural GM, WM and CSF atlases are based on the Paxinos co-ordinate system [257]. The co-registrations were performed using the bulk co-registration tool present in the toolbox, which allows the user to move and rotate the images overlaid upon atlas data. The SPM prior knowledge algorithm for affine registration was used to fine-tune the image registrations.

The segment function of SPMmouse was then used to generate normalized and modulated GM, WM and CSF maps for each rat using a probabilistic generative model. The segment function is based upon a gaussian mixture model with deformable tissue probability maps as its spatial priors, which each give the prior probability for a particular tissue at each point in the common (atlas) space which is determined by the fraction of occurrences in previous segmentations [27]. This means that the classification of each tissue type is determined by fitting a mixture of gaussian functions (1 per tissue type) to probability density histograms of the MRI image intensities. This process also estimated an RF coil coverage bias field which could be inverted using SPMmouse to compensate for non-uniform signal across the images due to their proximity to the RF receive coil [27]. This bias correction was applied to the raw data as part of the segmentation process.

In addition to segmenting the rat RARE data into GM, WM and CSF maps, the segment function also created a known transformation matrix between the native space of each rat and the common, atlas space, shown in the bottom row of Figure 6.2.

Each rat's angiography image was then re-sliced into its respective RARE image space and the RARE transformation matrix applied to the MRA images to transform them into the common space, as shown in Figure 6.2. The structural scans were used to generate the transformation matrix as they were more easily segmented and transformed to Paxinos space in SPMmouse than the MRA scans. The bias correction field determined from the anatomical RARE scans was also applied to smooth out intensity variations in the MRA images which occurred due to the proximity of the RF coil.

⁵SPMmouse is based on the human statistical parametric mapping program (SPM5) but allows the user to open files of any given voxel dimension. This approach assumes parametric statistical models at each voxel.

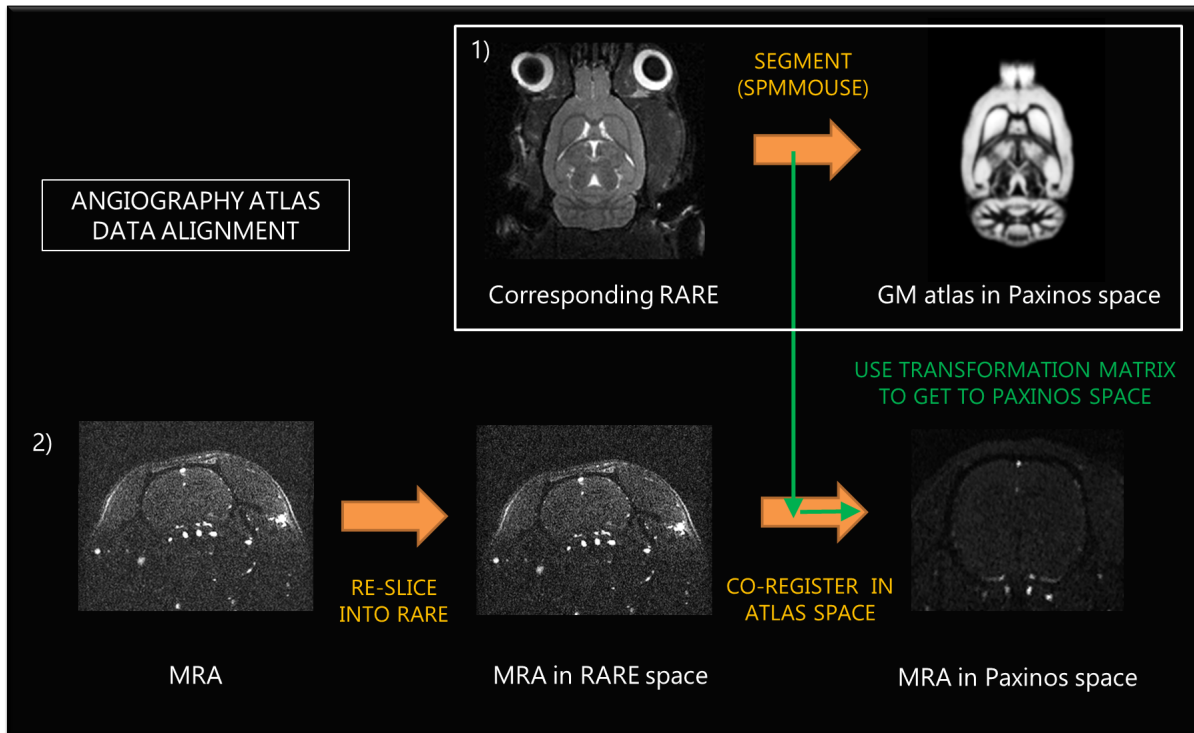


Figure 6.2: Top row: Each RARE anatomical image is co-registered to the GM, WM and CSF atlases before being segmented using SPMmouse to generate a transformation matrix. Bottom row: MRA images are re-sliced from their native space into that of the RARE images and then the transformation matrix is used to transform each rat's MRA image to the common, atlas space (green arrow).

After bias correction, a threshold was applied to the transformed MRA images to remove noise and signal artefacts. The threshold eliminated the bottom 5th percentile and top 1st percentile of MRA data. The top 1st percentile was removed in order to minimise susceptibility artefacts contributing to the AIFs. Each dataset was then normalized to its maximum signal intensity, before being averaged together to give the atlas. TOF angiography images are bright in areas of high blood flow, which are anatomically synonymous with known blood vessels, as shown in Figure 6.2. The largest signal in the atlas, corresponding to the largest artery with the biggest flow, was defined as voxels with a maximum probability of 1 whilst the background air signal was defined the minimum probability of 0. The other arteries identified using the TOF-MRA scans were then scaled between 0–1 according to their flow observed via the signal intensity of the images.

Once formed, the atlas was transformed back into the native space of each subject by the author using the inverse of the RARE transformation matrix, as shown in Figure 6.3. Once the MRA atlas was in the native RARE space of each rat, it was re-sliced into the EPI space to give a probabilistic estimates of vascular locations in EPI voxels. The atlas thus provided a spatial prior for arterial voxels for DSC MRI.

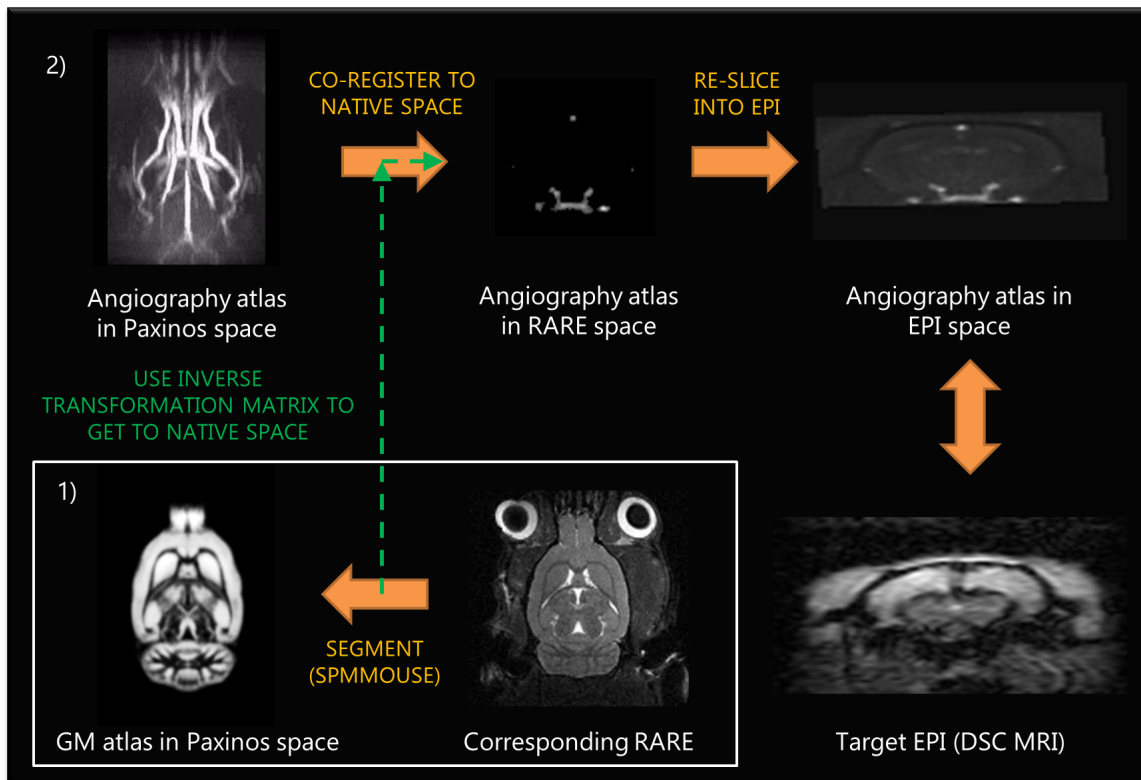


Figure 6.3: The inverse transformation saved as part of the segmentation process is used to transform the newly created vasculature atlas back into the native (RARE) space of each rat. The atlas is then re-sliced into the EPI space of the DSC MRI, which was used to give a probability of which voxels in the EPI dataset belonged to major arteries.

6.2.4 AIF extraction using an automatic voxel selection algorithm

For each rat with successful DSC MRI (11 in total, 7 “controls” and 4 “stroke” rats), an AIF was manually extracted by a single operator (the author) and compared to automatically determined AIFs. To produce a “manual AIF”, 5 voxels which displayed the largest observed signal change during the bolus passage and were located in the MCA branch area (the branch which was not occluded in any surgical procedures) were manually selected from the EPI signal data. The MCA was selected as a good estimate of the cerebral AIF after consultation with the literature [124], [204], [212], as it was close to the desired ROI and therefore should produce an AIF curve that was not adversely affected by curve spreading from delay and dispersion [121]. The signal from these voxels was converted into a $\Delta R2^*$ time course using equation (2.23), as shown schematically in Figure 2.62. The $\Delta R2^*$ time course from these voxels was then averaged to give the manually determined AIF, as shown in the example given in Figure 2.62 and Figure 3.12.

The automatic AIF determination algorithm was adapted from [212] and [260] by the author, and used a progressive voxel inclusion scheme with empirically determined thresholds to detect voxels with typical AIF characteristics. AIF criteria were selected and ranked according to their importance in iden-

tifying vasculature, as determined from analysis of previous results [119], [120], [212], [213], [260] which observed that AIFs have lower dispersion from an ideal bolus shape (a Dirac delta function) than concentration curves in other parts of the anatomy. The algorithm was applied on a voxel by voxel basis to $\Delta R2^*$ curves after they had been converted from voxel signal time courses using equation (2.23). Peak height, bolus arrival times (BAT) and time to peak (TTP) values were calculated for each voxel. Previous work recommended a total of 3–8 voxels for AIF determination [210], [212], [214], [245], and so this method was set to accept 5 voxels to compute the AIF.

The algorithm was performed over the entire image, and voxels were progressively excluded until 5 remained. Voxels were excluded if they did not meet the following criteria (applied in this order):

- (i) **Voxels with time course peaks occurring <12s from the start of the scan and with rise times <3s.** Peaks which occurred within the time that the bolus was manually observed to arrive and which exhibited short rise times between the steady state and maximum signal value were deemed likely to be blood vessels, due to high blood flow resulting in rapid signal changes.
- (ii) **Voxels with peak heights greater than the 90th percentile.** Only the highest peaks were accepted as AIF candidates due to increased bolus volume passing through major arteries. Thresholds were tested at the 50th, 60th, 70th, 75th, 80th, 85th, 90th and 95th percentiles, with the 90th percentile providing the best estimate of major blood vessels.
- (iii) **Voxels with areas under the curve (AUC) greater than the 10th percentile.** Curves with low AUC were eliminated to remove tissue voxels with dispersed peaks. Thresholds were tested at the 5th, 10th and 15th percentiles, with the 10th percentile giving optimal results.
- (iv) **Voxels with first moment of curve less than the 50th percentile.** Arterial voxels have higher height to width ratios than venous voxels due to decreased dispersion. Thresholds were tested at the 30th, 40th, 50th, 60th, 70th, 80th and 90th percentiles, finding the best discrimination between arterial and non-arterial voxels at the 50th percentile.
- (v) **Voxels with FWHM of curve less than the 50th percentile.** Arterial voxels should have a lower FWHM than venous voxels due to decreased dispersion. Thresholds were tested at the 30th, 40th, 50th, 60th, 70th, 80th and 90th percentiles, with the best discrimination found at the 50th percentile.

The application of the algorithm is illustrated in Figure 6.4 to emphasise the impact that each threshold has on the data, with a rejected voxel time course shown for each stage. Step (i) broadly identifies areas of interest using BAT, with the largest difference seen in step (ii) by the application of the peak threshold which narrows down the selected voxels to the vascular areas. Steps (iii), (iv) and (v) gradually remove voxels whose curve shapes are too broad to produce an ideal AIF.

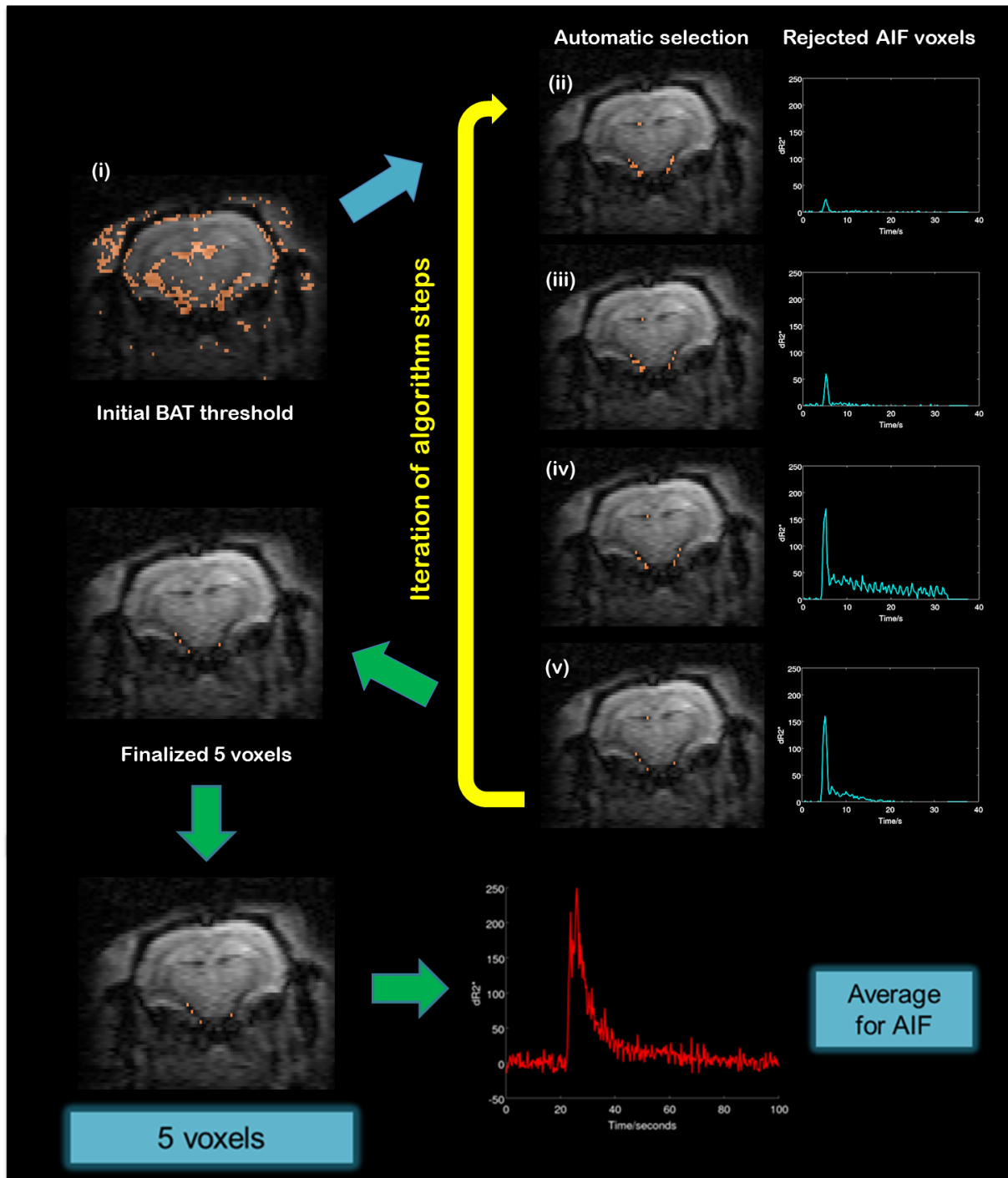


Figure 6.4: Automatically selected voxels in orange at application of each thresholding step for mouse brain. Rejected voxels at each stage are shown on the right hand side. Final voxel selection is shown on the bottom left.

If more than 5 voxels were selected, steps (ii)-(v) were then iterated (i.e. threshold values adjusted from 90th to 95th percentile for peak height threshold, AUC threshold adjusted from 50th to 60th percentile etc.) until 5 voxels remained, from which their mean time course produced an “automatic AIF”, as shown in Figure 6.4.

6.2.5 Addition of angiographic information to voxel selection algorithm

In addition to the automatically selected AIFs, a further “angiographic AIF” was computed for each of the 11 rats with successful DSC MRI. A prior knowledge constraint on the anatomical position of voxels to be in arterial regions before the first application of steps (ii) to (v) of the algorithm was applied, with only those with a probability >0.2 of being a major artery according to the vascular atlas being considered for selection using the custom algorithm. This therefore refined the search for voxels into arterial and venous regions, as shown in the overlaid atlas data in Figure 6.5. Sample voxel selections using all 3 methods are shown in Figure 6.6 for a single subject.

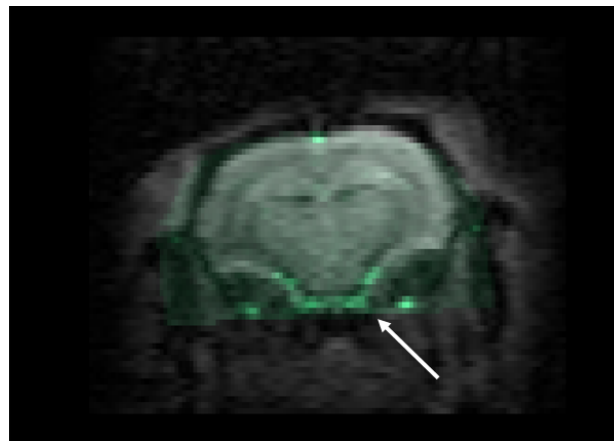


Figure 6.5: Angiography atlas information (in green) overlaid on EPI image, with arrow indicating high probability region around MCA, which was used as the primary source of AIF voxels.

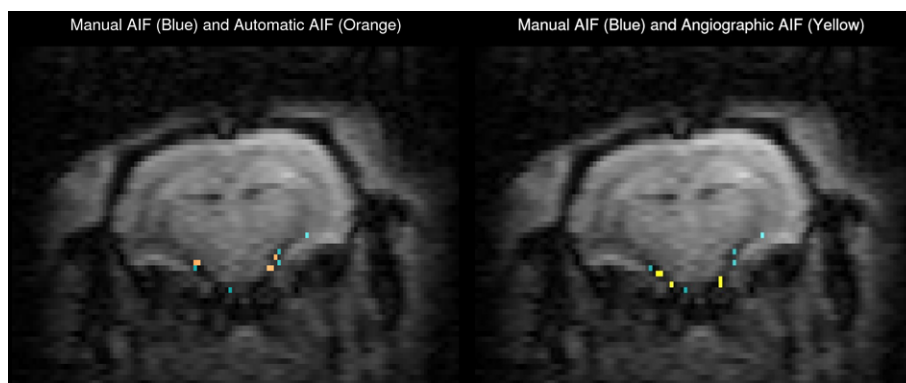


Figure 6.6: Example AIF voxel selections. Manual in blue, with automatic in orange and angiographic in yellow.

The peaks of each animal’s AIFs for each analysis method (“manual”, “automatic” and “angiographic” AIFs) were aligned such that comparisons were easier across subjects, with each animal’s AIF peak repositioned to 5.25s. Population AIFs were taken as the mean of the aligned AIFs for all 11 rats.

6.2.6 Gamma variate fitting to AIFs

Gamma variate functions, outlined in section 3.2.2 using equations (3.13) and (3.14), were fitted to the first pass AIFs of each animal to eliminate recirculation peaks (if visible in the data) and to smooth out motion effects in analysis [119], [120], [123], [203], [212], [213]. The fits were performed by the author via the `lsqcurvefit` function in Matlab with non-linear Levenberg-Marquardt fitting selected. Default parameters of [1, 0.01, 0.002] were used for gamma variate fitting parameters shown in equation (3.14) and used in the initial fit of the first 500s of each data curve. Goodness of fit was evaluated using χ^2 test values normalized to the degrees of freedom of the fit, the probability of fit ($1-\chi^2$ cumulative distribution function) and the derivatives of the fit. In addition, a qualitative assessment of fit was performed by eye. If a fit was not achieved or deemed unacceptable using the default parameters, the data selection on the x axis was shortened around the bolus peak until acceptable χ^2 values were attained ($p < 0.02$).

6.2.7 Calculation of perfusion parameters

Perfusion parameters were calculated as outlined in Chapter 3, Section 3.2.2. The response concentration-time curve ($R(t)$) was obtained using singular value decomposition (SVD) [117], [118], [119], [261], as described in Appendix E⁶. The implementation outlined in Appendix E used the standard formulas for SVD first proposed for DSC MRI analysis by Ostergaard et al. [117], [118] and did not include additional regularization. The $R(t)$ was calculated for each AIF's gamma variate and was then used to calculate voxel by voxel CBF maps, as described in equation (3.18). CBV maps were calculated on a voxel by voxel basis as described in equation (3.16) using each rat's manual, automatic and angiographic AIFs. The ratio of CBV to CBF was used to calculate voxel by voxel MTT maps, as described in equation (3.19).

Perfusion parameters in the “control” rats ($n=7$) were analysed by computing the mean CBF, CBV and MTT values from an ROI in the striatum region of each rat, as shown in Figure 6.7. The left hemisphere is displayed in the right side of the image according to radiological conventions. Sham surgery was conducted on the right side of the rat brain, so the left side was presumed to be the healthy side for comparison to literature values.

⁶All of the perfusion analysis software, including the SVD, was written by the author in Matlab

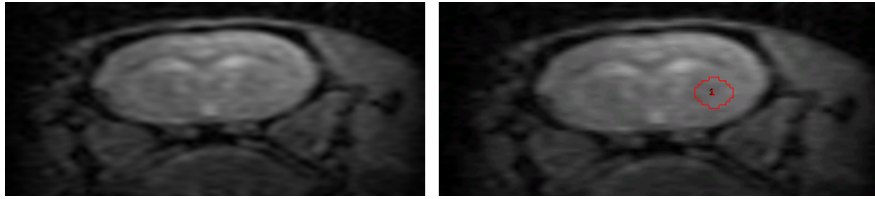


Figure 6.7: ROI selection to observe perfusion parameter values across the control rat group. The red ROI (1) was placed in healthy tissue in the left hemisphere.

In the stroke rat group ($n=4$), parameter values from both the ischemic core of the lesion and the penumbra of the lesion were compared to contralateral healthy region ROIs to assess the accuracy of both the perfusion parameters produced and their corresponding ratios between healthy and ischemic regions using each AIF determination technique. The ROIs are shown in Figure 6.8. The green ROI (2) was placed in the ischemic core region, where the largest perfusion deficit was observed, and the red ROI (1) was placed in healthy tissue contralateral to the core region. The yellow ROI (3) was placed in the penumbra region, which displayed a moderate perfusion deficit on CBF maps (as shown in Figure 6.9) and was located between the core and healthy regions.

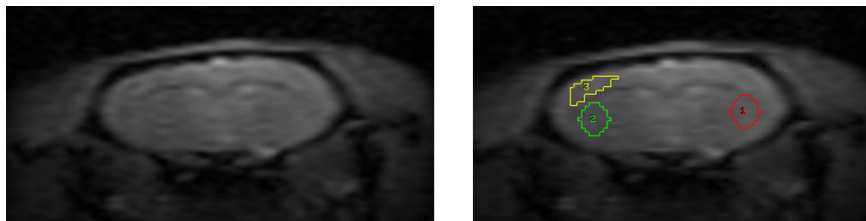


Figure 6.8: ROI selection to observe perfusion parameter ratios between ischemic and healthy regions in stroke rat group. Red ROI (1) = healthy hemisphere, green ROI (2) = ischemic core and yellow ROI (3) = ischemic penumbra.

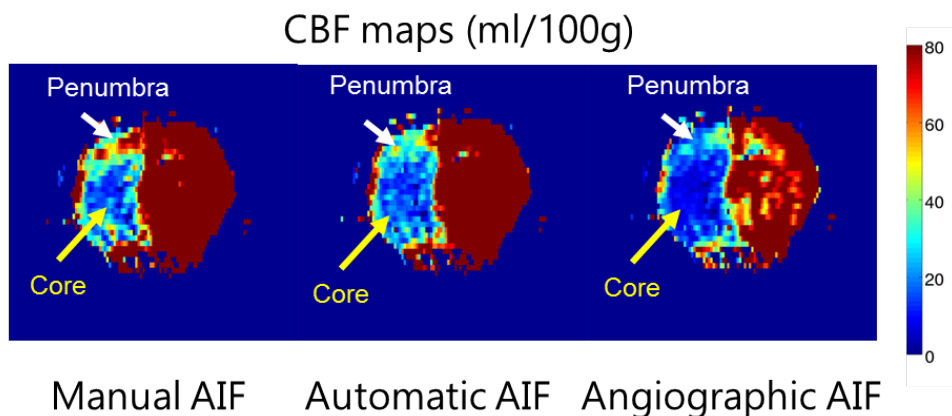


Figure 6.9: CBF maps thresholded to 80 ml/100g/min to indicate inhomogeneity within ischemic region, with core and penumbra regions indicated by arrows for all 3 AIF methods.

6.3 Results

6.3.1 Vasculature probability atlas

A comparison of the rat angiography images and their maximum intensity projections used to create the vasculature probability atlas is shown in Figure 6.10. The vascular atlas generated using 27 rat datasets is shown in Figure 6.11. The bottom row of Figure 6.11 shows the atlas after the rat brain has been segmented from the rat neck muscles and head by summing together the GM, WM and CSF atlases and eliminating any data outside of this region. The circle of Willis, the MCA and superior sagittal sinus are all clearly visible in the atlas across the whole of the rat brain and provided the highest probability estimates for use in the automatic AIF selection algorithm.

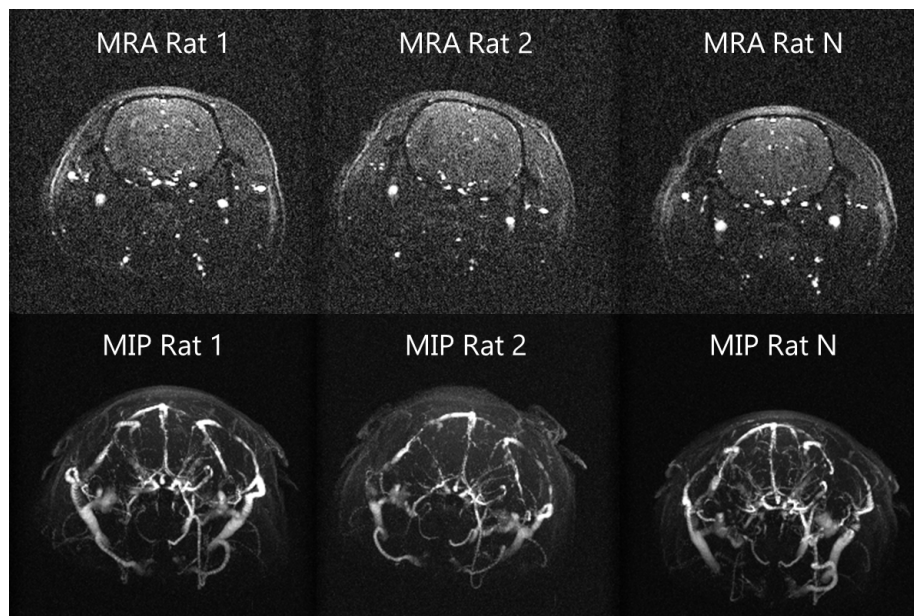


Figure 6.10: Top row: MRA images of rat brains for 3 subjects. Bottom row: MIP MRA images of the same rat brains. Largest intensity values in regions of high blood flow, corresponding to major arteries and veins.

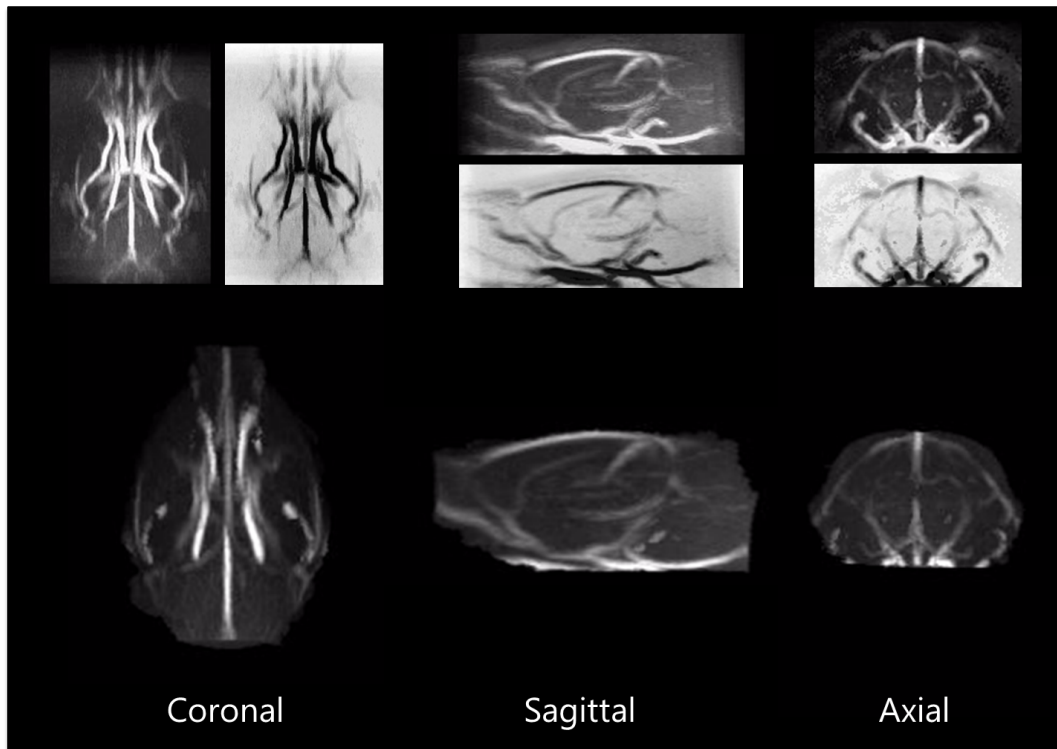


Figure 6.11: Top row: 3D MIP projections computed using ImageJ software of rat vasculature probability atlas, scaled from 1–0, shown in coronal, sagittal and axial orientations. Inverted colour scheme highlights the extent of the arteries within the brain. Bottom row: Brain segmented out from atlas data using combination of GM, WM and CSF atlases.

6.3.2 Comparison of AIFs computed using automatic and manual voxel selection

A comparison of the manual, automatic and angiographic AIFs for a single subject (“stroke” rat group) is presented in Figure 6.12. Both automatic and angiographic AIFs have a larger peak height and a more distinct bolus shape than the manual AIF. The angiographic AIF has a higher peak height than the automatic AIF but also displays greater dispersion as it has a larger FWHM, AUC and a higher tail.

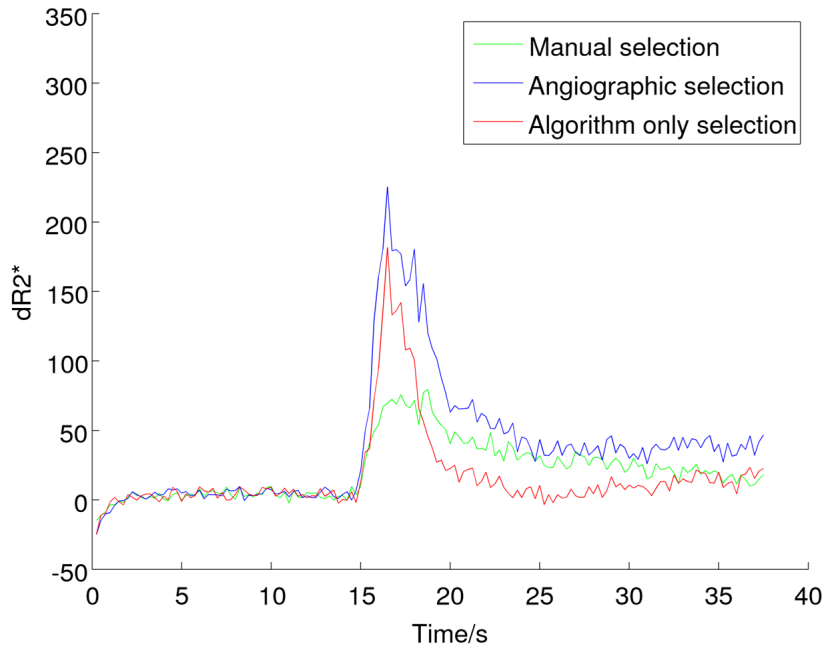


Figure 6.12: Example of manual, automatic and angiographic AIFs for single rat (“stroke” group).

Gamma variate functions were successfully fitted to all rat AIFs, with sample results shown in Figure 6.13 for the sample subject. It must be noted that due to the high noise in some sets of DSC MRI data, most likely due to inter-frame movement of the rat head⁷ the quality of the gamma variate fits is reduced in these cases compared to rats with less noisy DSC MRI. The gamma variate functions do, however, show a clear difference between the 3 AIFs produced. The manual AIF gamma function is much smaller in peak height than the automatic or angiographic AIF gamma functions, with a longer time to peak (TTP) and greater dispersion due to its increased width.

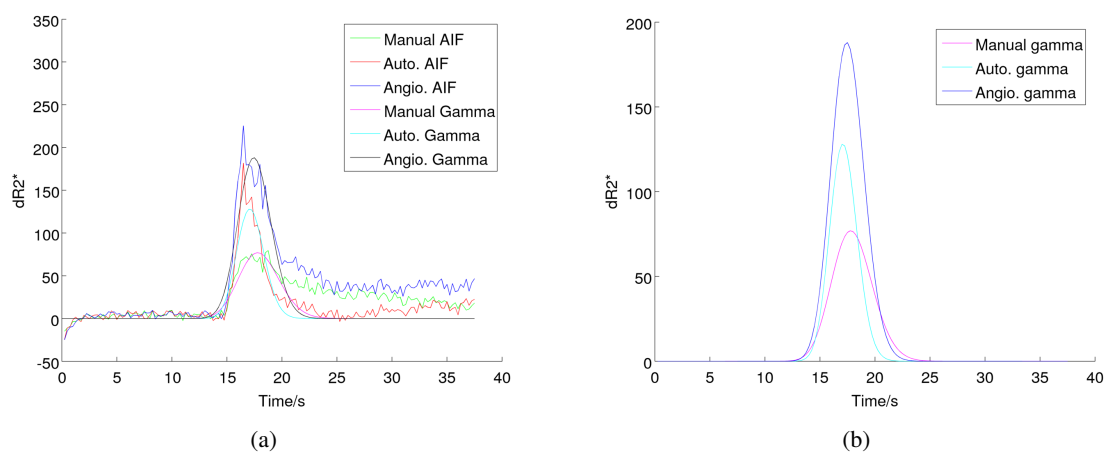


Figure 6.13: Gamma variate functions (a) fitted to sample AIF curves, (b) displayed alone for clarity. Note that the quality of the gamma variate fits is reduced in high noise DSC MRI datasets.

⁷This was attempted to be rectified through co-registration of frames using SPMmouse by the author and by Dr Steve Sawiak in FSL, but no consistent reductions in AIF noise were found after the frames were co-registered.

Manual, automatic and angiographic AIFs for all 11 rats with successful DSC MRI are displayed in Figure 6.14. Across the rat cohort, the automatic voxel selection method consistently provided both the automatic and angiographic AIFs with larger peak heights and more distinct bolus profiles compared to the manual AIFs, with a full breakdown of the curve parameters in Table 6.1 and the corresponding parameters for the fitted gamma variate functions in Table 6.2.

The TTP and FWHM values remain roughly constant across all AIF methods, with a decrease in variability of the FWHM from 3.7 ± 3.9 s for the manual AIF to 2.2 ± 0.8 s for the automatic AIF and 3.0 ± 1.5 s for the angiographic AIF. The mean peak heights for the automatic and angiographic AIFs across the entire rat cohort are nearly three times that of the manual AIFs ($\Delta R2^*$ of 157.6 ± 55.7 s⁻¹ for automatic and 173.5 ± 56.0 s⁻¹ for angiographic compared to 61.4 ± 33.3 s⁻¹ for manual). The same applied for the AUCs: $\Delta R2^*$ -s of 521.1 ± 320.4 was found for the automatic AIFs (dimensionless units) and 945.8 ± 736.8 for angiographic AIFs compared to 267.9 ± 257.1 for manual AIFs, although all AIF methods showed an error of at least 32% (angiographic AIF) in the mean value of the peak height and 62% (automatic AIF) in the mean value of the AUC. These large variations in the mean values indicate that the pathology may be affecting the AIF and that none of the AIF extraction methods are completely consistent, but the automatic and angiographic AIFs are more consistent than the manual AIFs.

The gamma variate functions display similar trends to the raw data, such as the factor of 3 in peak height between the angiographic and manual AIF gamma variates ($\Delta R2^*$ of 143.6 ± 49.2 s⁻¹ compared to 46.0 ± 26.3 s⁻¹) but do show a small reduction in the variance of the AUC values for all 3 AIF methods, although the lowest error in mean AUC only drops from 62% to 44% for the automatic AIF method, indicating that the data is smoothed but the large variation between subjects remains.

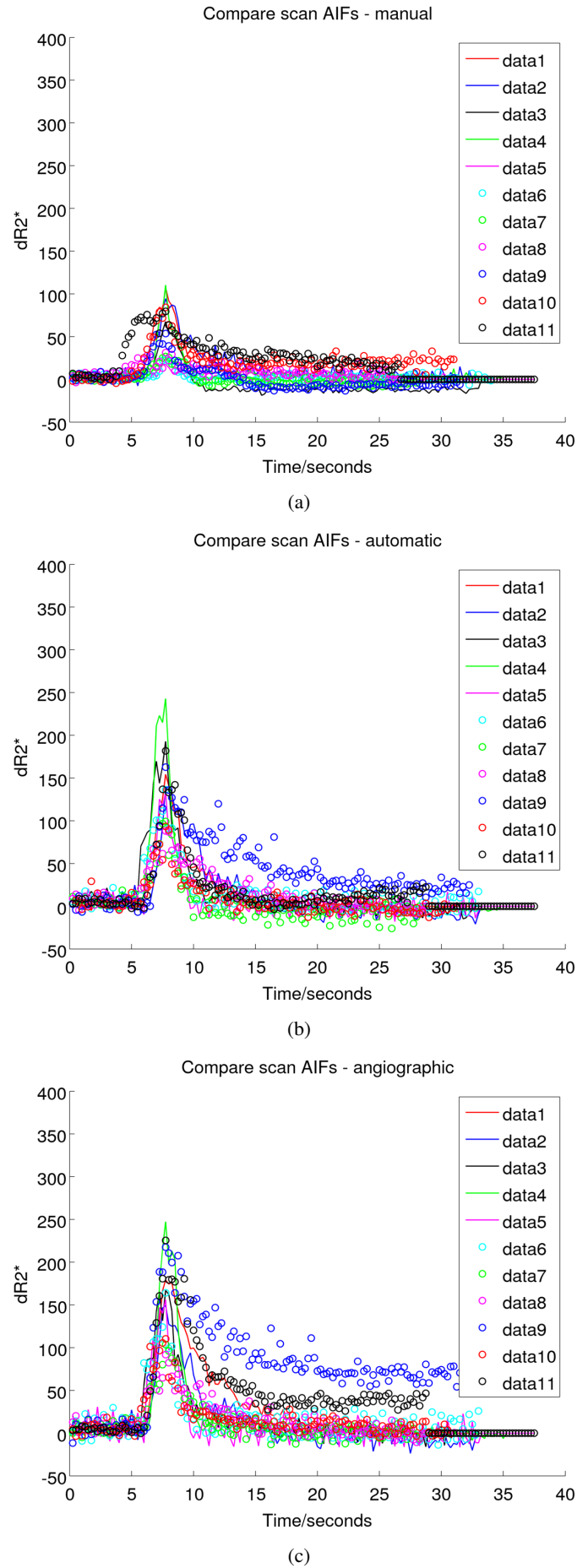


Figure 6.14: Comparison of (a) manual, (b) automatically selected and (c) angiographic AIFs for rat cohort (n=11).

AIF used	Manual AIF	Automatic AIF	Angiographic AIF
Peak Height/ $\Delta R2^*$ (s^{-1})	61.4 \pm 33.3	157.6 \pm 55.7	173.5 \pm 56.0
TTP/s	14.3 \pm 3.6	14.0 \pm 2.8	13.9 \pm 2.9
AUC/ $\Delta R2^* \cdot s$	267.9 \pm 257.1	521.1 \pm 320.4	945.8 \pm 736.8
FWHM/s	3.7 \pm 3.9	2.2 \pm 0.8	3.0 \pm 1.5

Table 6.1: DSC MRI AIF parameters for entire rat cohort (n=11).

Gamma Variate	Manual AIF	Automatic AIF	Angiographic AIF
Peak Height/ $\Delta R2^*$ (s^{-1})	46.0 \pm 26.3	116.2 \pm 49.9	143.6 \pm 49.2
TTP/s	14.3 \pm 3.3	14.3 \pm 3.1	14.4 \pm 3.2
AUC/ $\Delta R2^* \cdot s$	153.8 \pm 103.3	353.2 \pm 154.2	512.0 \pm 290.9
FWHM/s	3.2 \pm 1.5	4.0 \pm 3.0	3.3 \pm 1.3

Table 6.2: DSC MRI AIF fitted gamma variate parameters for entire rat cohort (n=11).

Significant differences were seen between the larger peak heights and AUCs generated by the automatic selection algorithm compared to manual selection (Student's paired t test, n=11, peak heights: comparing manual to automatic and angiographic AIFs $p < 0.0001$; between automatic and angiographic AIFs $p = 0.04$, AUC: comparing manual to automatic and angiographic AIFs $p < 0.05$; between automatic and angiographic AIFs $p = 0.01$). The increased peak height and AUC were also seen to give significant differences between the fitted gamma variate functions (Student's paired t test, n=11, peak heights: comparing manual to automatic and angiographic AIFs $p < 0.0005$; between automatic and angiographic AIFs $p = 0.006$, AUC: comparing manual to automatic and angiographic AIFs $p < 0.001$; between automatic and angiographic AIFs $p = 0.02$). No significant differences were seen in the TTP or FWHM parameters, either in the AIFs or their fitted gamma variates.

The population (mean) AIFs for the entire rat cohort are shown in Figure 6.15, clearly showing the increase in peak height and AUC between the automatic and manual methods. The angiographic AIF also displays a slower tail decay, indicating a slightly larger dispersion compared to the automatic AIF.

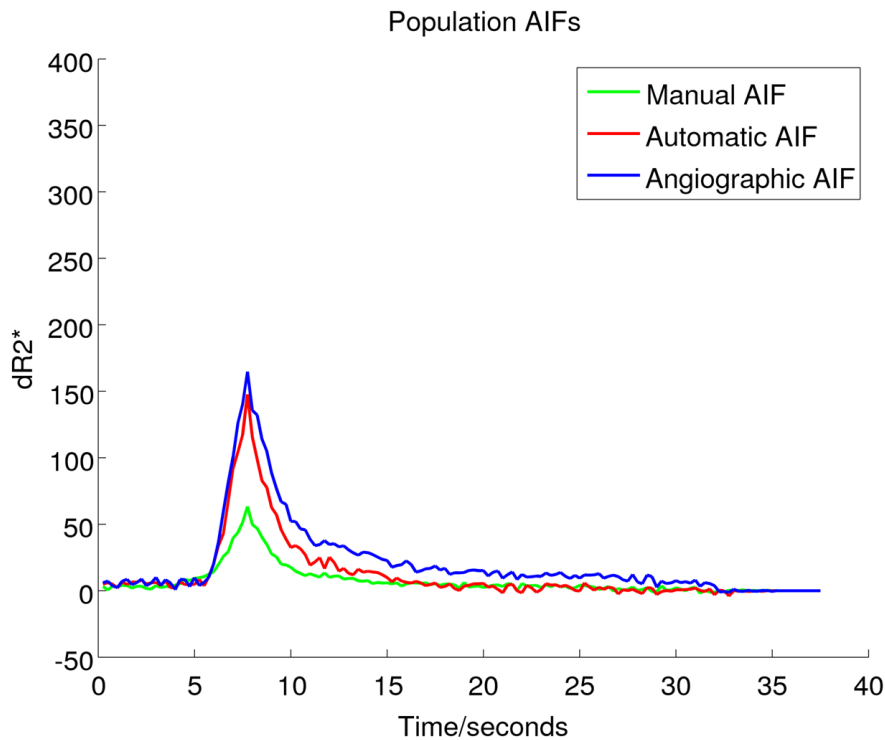
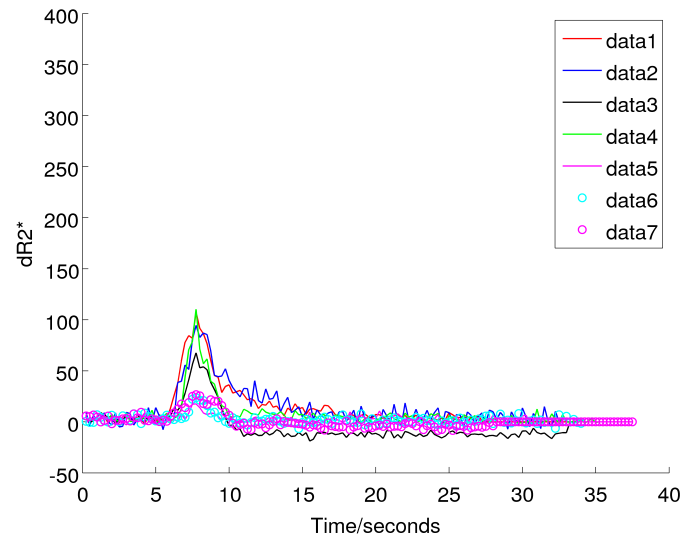
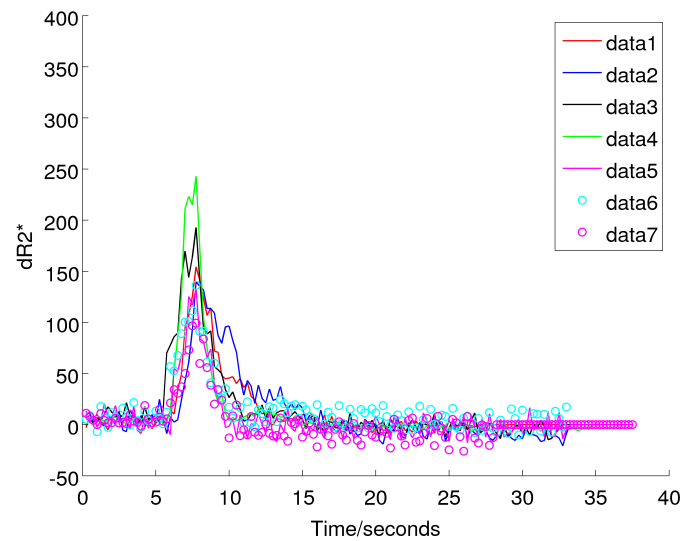


Figure 6.15: Population AIFs for entire rat cohort (n=11), showing clear difference between manual and automatic selection methods.

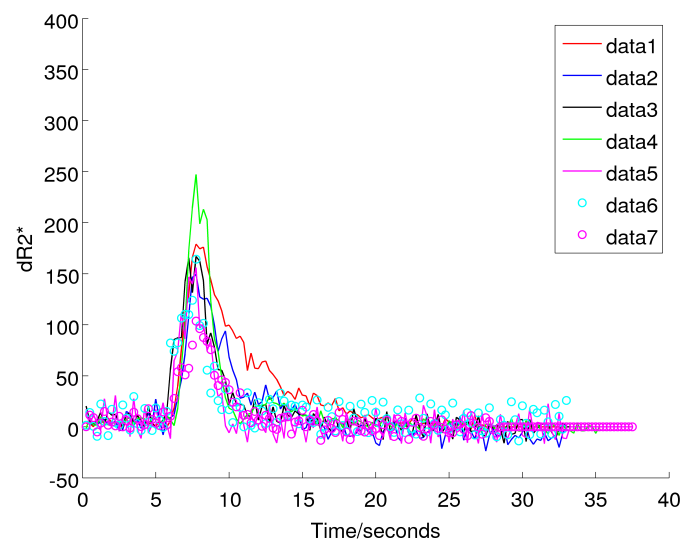
When comparing AIFs within the rat “control” group and the rat “stroke” group, similar results were found, as shown in Figures 6.16 and 6.17 respectively. Figure 6.17 indicates that AIFs taken from rats with clear ischemic regions were seen to have noisier and less consistent AIFs than the “control” group using all 3 selection techniques, indicating the variation in AIF shape with more severe pathology. The parameters for the AIF curves are listed in Table 6.3 for the “control” group and Table 6.4 for the “stroke” group.



(a)

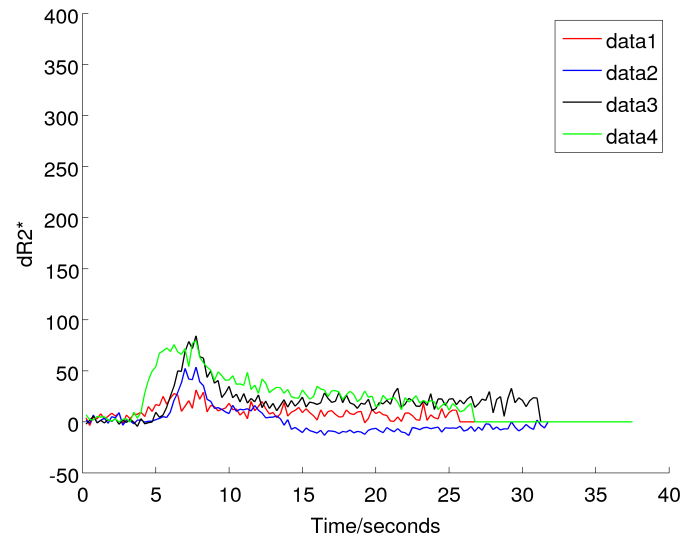


(b)

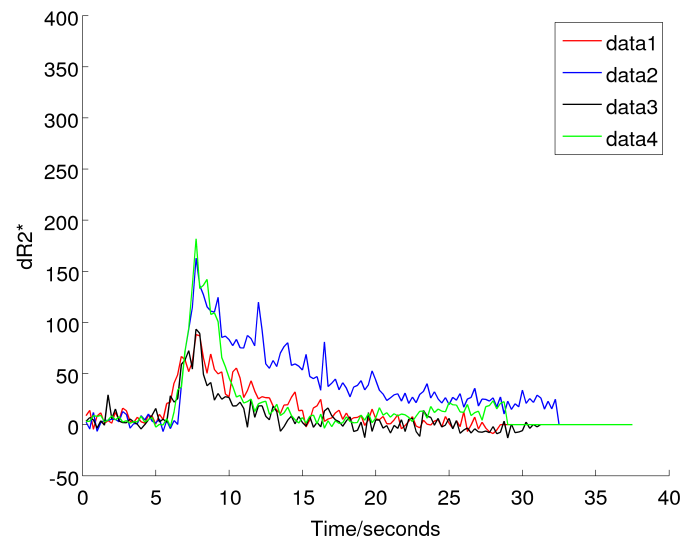


(c)

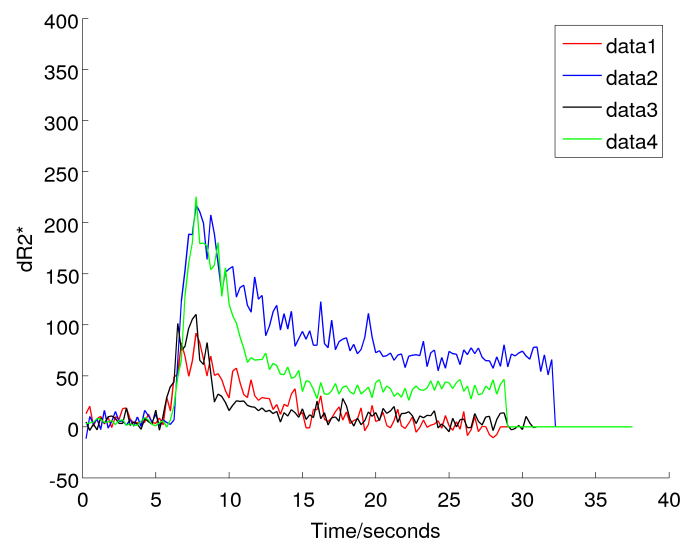
Figure 6.16: Comparison of (a) manual, (b) automatically selected and (c) angiographic AIFs for control rat cohort, scanned 3-4 hours post sham surgery with no visible ischemic regions ($n=7$).



(a)



(b)



(c)

Figure 6.17: Comparison of (a) manual, (b) automatically selected and (c) angiographic AIFs for rats with confirmed stroke, scanned 28 days post surgery using DSC MRI (n=4).

AIF used	Manual AIF	Automatic AIF	Angiographic AIF
Peak Height/ $\Delta R2^*$ (s^{-1})	61.0 \pm 39.3	172.6 \pm 57.6	180.5 \pm 51.2
TTP/s	12.9 \pm 3.4	13.4 \pm 3.2	13.1 \pm 3.2
AUC/ $\Delta R2^* \cdot s$	170.7 \pm 138.6	438.5 \pm 236.4	774.6 \pm 610.4
FWHM/s	3.9 \pm 4.5	1.9 \pm 0.4	2.4 \pm 0.8

Table 6.3: DSC MRI AIF parameters for “control” rat group (n=7).

AIF used	Manual AIF	Automatic AIF	Angiographic AIF
Peak Height/ $\Delta R2^*$ (s^{-1})	62.1 \pm 24.6	131.5 \pm 47.8	161.3 \pm 70.0
TTP/s	16.6 \pm 3.1	15.2 \pm 1.9	15.3 \pm 1.7
AUC/ $\Delta R2^* \cdot s$	437.9 \pm 348.3	665.6 \pm 432.0	1245.5 \pm 936.1
FWHM/s	3.5 \pm 3.0	2.7 \pm 1.0	4.0 \pm 2.1

Table 6.4: DSC MRI AIF parameters for “stroke” rat group (n=4).

Within each group, similar trends in peak height and AUC emerged, with a greater increase in peak height between manual and angiographic AIFs in the “control” group compared to the “stroke” group. In the “control” group, the manual AIFs displayed a mean peak height of 61.0 \pm 39.3 compared to 180.5 \pm 51.2 for the angiographic AIFs, whereas in the “stroke” group the manual AIFs displayed a mean peak height of 62.1 \pm 24.6 compared to 161.3 \pm 70.0 for the angiographic AIFs. A greater variance in AUC was noted for each of the AIF methods in the “stroke” group compared to the “control” group.

When analyzed separately, AIFs produced for the “control” rat group again displayed significant increases in peak height and AUC using the automatic and angiographic methods, although less difference between the automatic and angiographic AIFs (Student’s paired t test, n=7, peak heights: comparing manual to automatic and angiographic AIFs $p < 0.005$; between automatic and angiographic AIFs $p = 0.3$, AUC: comparing manual to automatic and angiographic AIFs $p < 0.05$; between automatic and angiographic AIFs $p = 0.07$). This was again found in their respective gamma variate functions (Student’s paired t test, n=7, peak heights: comparing manual to automatic and angiographic AIFs $p < 0.002$; between automatic and angiographic AIFs $p = 0.06$, AUC: comparing manual to automatic and angiographic AIFs $p < 0.005$; between automatic and angiographic AIFs $p = 0.1$).

No significant differences were found between any of the AIF parameters for any of the AIF determination methods in the stroke group. Although this could be due to the reduced number of subjects (n=4), it could also be attributed to the patient population and the inhomogenous nature of the ischemic region between subjects affecting the blood flow within the vasculature.

The population AIFs shown in Figure 6.18 for both rat groups also indicate a clear difference in peak height between the manual and automatic methods, with only very small differences between the angiographic and automatic method curves in the control group. The stroke rat group display much greater variation in their manually derived AIFs, indicated by the larger width of their AIFs and their dispersed bolus shapes.

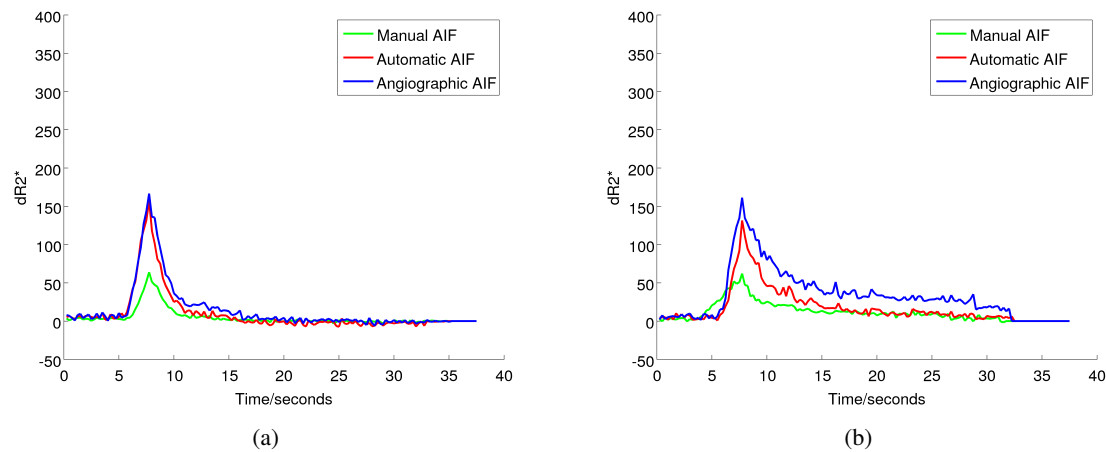


Figure 6.18: Population (mean) AIFs for (a) rat control group and (b) rat stroke group taken from DSC MRI. Both groups show clear difference between manual and automatic AIFs, with the stroke group exhibiting greater variation.

6.3.3 Perfusion parameter results - “Control” group

CBF, CBV and MTT maps for a sample control rat (designated as “data2” in the previous section) are shown in Figure 6.19. Lower values of CBV and larger values of MTT seen in the ventricles compared to the surrounding tissue, as expected from previously published parameter maps [121], [161], [248], [262], [263].

Table 6.5 summarises the perfusion parameters produced for the control rats across the cohort for the 3 AIF selection methods using a left hemisphere ROI from the rat striatum, as indicated in Figure 6.7. No significant differences (Student’s paired t test, $p < 0.05$) were found between CBF, CBV or MTT values produced using a contralateral ROI located in the opposite hemisphere of the rat brain compared to those detailed in Table 6.5 (data not shown for clarity).

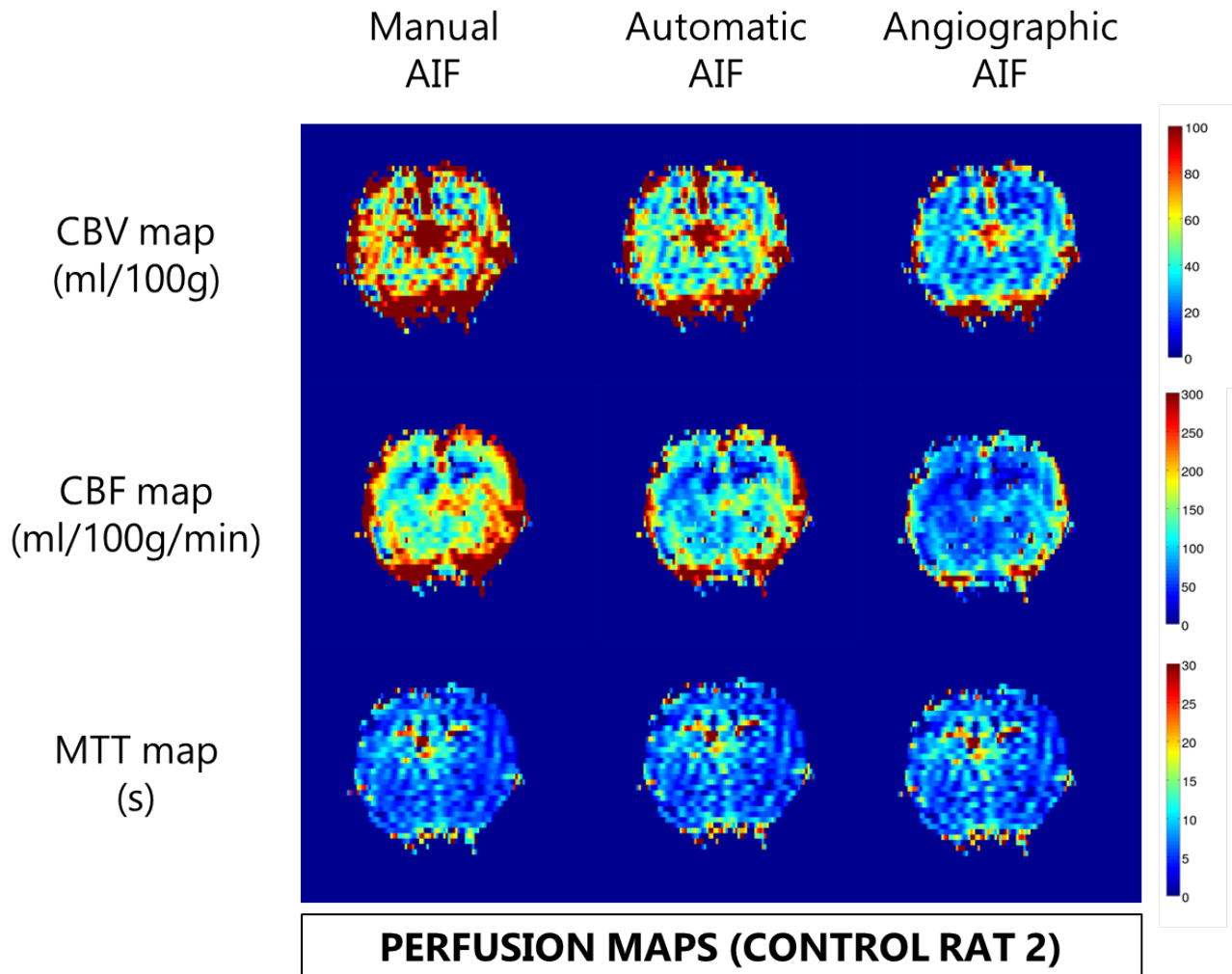


Figure 6.19: CBF, CBV and MTT parameter maps created using each of the 3 AIF determination methods for a sample rat from the control group.

AIF used	CBF (ml/100g/min)	CBV (ml/100g)	MTT (s)
Manual AIF	228±137	65±40	13.4±4.3
Automatic AIF	215±184	18±14	13.9±4.7
Angiographic AIF	154±105	13±7	13.1±4.9

Table 6.5: Control rat group perfusion parameters (n=7, mean±std).

None of the CBF, CBV or MTT parameter spatial distributions changed for any rats when different AIFs were used in the analysis, indicating that qualitative imaging is not affected by using an automated AIF in place of a manual AIF. The noise in the perfusion parameter maps and variation in mean ROI values may be due to the lack of smoothing applied in post processing or could be due to the sham surgery giving variable results across the 7 “control” rats.

There is a general consensus between previously reported absolute CBF, CBV and MTT values and those given in Table 6.5, although the range of values reported by different research groups indicates the poor reducibility of quantitative perfusion results using DSC MRI. CBF values reported from DSC MRI studies vary from $93 \pm 10 \text{ ml}/100 \text{ g}/\text{min}$ [198] to $135 \pm 29 \text{ ml}/100 \text{ g}/\text{min}$ [264], although these can also be verified against CBF values determined from ASL, which range from $84 \pm 3 \text{ ml}/100 \text{ g}/\text{min}$ [198], to $107 \pm 8 \text{ ml}/100 \text{ g}/\text{min}$ [265], to between $160 \pm 34 \text{ ml}/100 \text{ g}/\text{min}$ and $200 \pm 66 \text{ ml}/100 \text{ g}/\text{min}$ [266]. Reviews of CBF values (using a range of techniques including gold standard $^{15}\text{O}\text{-H}_2\text{O}$ PET and autoradiography) in rat brains typically quote values for absolute CBF in the range of 91-262ml/100g/min [121]. Taking this variability into account, the angiographic CBF results appear to offer the best agreement with the literature at $154 \pm 105 \text{ ml}/100 \text{ g}/\text{min}$.

CBV values also differ widely over the whole brain, reported between 4-10ml/100g [263] and at $33.39 \pm 6.51 \text{ ml}/100 \text{ g}$ for GM and $17.03 \pm 6.18 \text{ ml}/100 \text{ g}$ for WM [264]. This would suggest that only the CBV values produced by the automatic and angiographic AIFs ($18 \pm 14 \text{ ml}/100 \text{ g}$ and $13 \pm 7 \text{ ml}/100 \text{ g}$ in the striatum respectively) agree with the literature in this case, with the angiographic AIFs again giving the best agreement.

The mean MTT values indicated viable and healthy tissue on both sides of the brain as the contrast agent was able to pass freely through the vasculature [186], [210], [211], [262]. All mean MTT values (manual AIF: $13.4 \pm 4.3 \text{ s}$, automatic AIF: $13.9 \pm 4.7 \text{ s}$ and angiographic AIF: $13.1 \pm 4.9 \text{ s}$) were fairly stable across each of the techniques, as these values depend only on the ratio between CBV and CBF. Previously reported values of absolute MTT vary from 2-11s for the whole brain (3-7s, mean 6.1s [262]; 3-8s, mean 4.91s [263]; 9-11s, GM $10.7 \pm 0.9 \text{ s}$, WM $9.3 \pm 0.5 \text{ s}$, [264]), with the MTT results reported here finding broad agreement with a rat study which also used standard SVD to calculate CBF [264]. All reported MTT values appear to be slightly overestimated, perhaps due to overestimations in CBV from underestimated AIF peak heights resulting in higher MTT values.

The 3 AIF methods reported markedly different absolute values of CBF and CBV, particularly in CBV where the manual AIF data gives a CBV value that is a factor of 4 larger than those attained using the automatic and angiographic AIFs. This is due to equation (3.16), where the AUC of the angiographic AIF being 4 times as large as that of the manual AIF results in a four fold decrease in CBV value, and this effect is also seen in the CBF values, as CBF is proportional to CBV (see equations (3.18) and (3.16)). The lower values given by the angiographic AIFs for CBF ($154 \pm 105 \text{ ml}/100 \text{ g}/\text{min}$) and CBV ($13 \pm 7 \text{ ml}/100 \text{ g}$) appear to have the closest resemblance to literature and were due to the angiographic AIFs possessing the highest peak heights, indicating that these AIFs were the most accurate representations of the first bolus passage.

6.3.4 Perfusion parameter results - “Stroke” group

The MCA occlusion resulting in the ischemic stroke region within the right hemisphere of the rat brain was seen clearly as a deficit in the CBV and CBF perfusion data and a large increase in MTT for all 4 rats in the “stroke” group, with an example set of maps generated using each AIF determination method in Figure 6.20. The lesion was confirmed using T2* mapping data, where it displayed a reduction in the T2* parameter, also displayed in Figure 6.20.

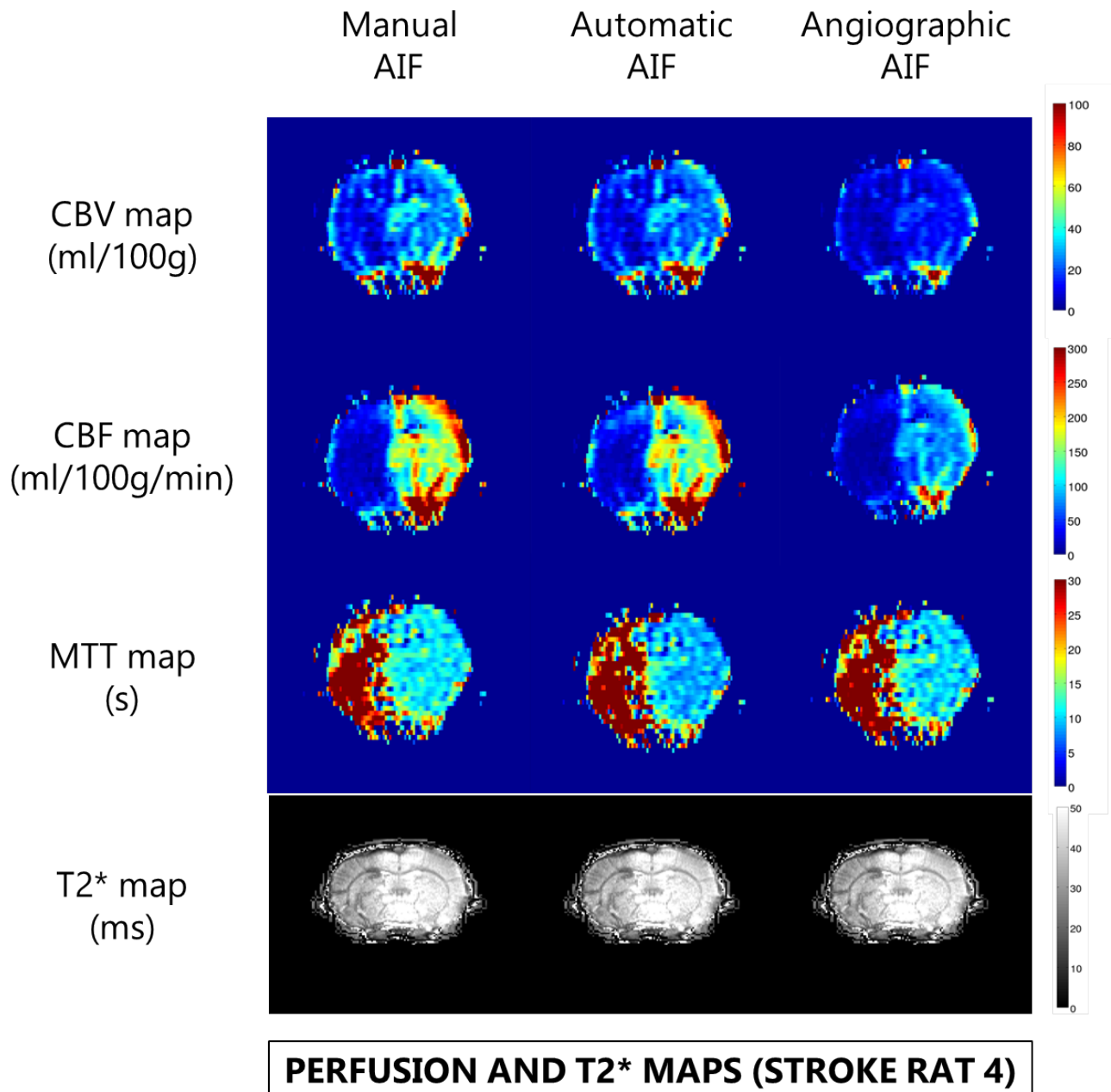


Figure 6.20: CBF, CBV and MTT images created using each AIF determined from sample “stroke” rat DSC MRI data, compared to T2* map from MRI data indicating ischemic region.

The CBF maps shown in Figure 6.20 show the same pattern of CBF reduction in the lesion area also

displayed in ASL images taken from the 3 rats who also underwent the MCA occlusion procedure using the distal clip method. An example ASL CBF map and a T2 weighted RARE image used to indicate the location of the lesion⁸ is shown in Figure 6.21.

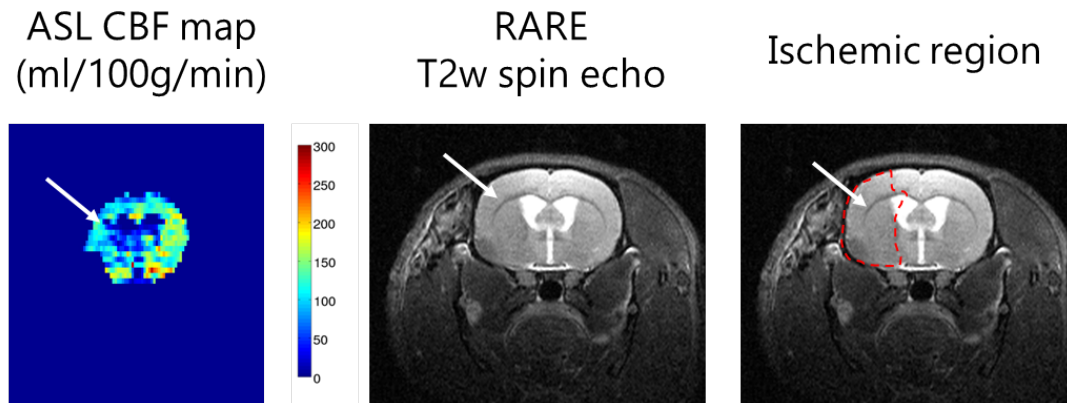


Figure 6.21: ASL and corresponding RARE anatomical images from additional rat group, who did not undergo DSC MRI but did receive MCA occlusion via distal clip method. Arrow and red outline indicates the stroke affected region.

Healthy CBF values were compared between DSC MRI and ASL in the left (healthy) hemisphere (see Figure 6.8), with the CBF, CBV and MTT values for that ROI displayed in Table 6.6. Absolute values of CBF, CBV and MTT produced for the stroke group again broadly agreed with previously reported values in the literature (MTT 2-11s [262], [263], [264], CBV 4-33ml/100g [263], [264], CBF 84-262ml/100g/min [121], [198], [262], [263], [264], [265], [266]) and with those reported in the “control” group, but also displayed large variances (≈ 50 -100% of the mean value) in all 3 AIF methods due to the noisy nature of the parameter maps produced.

AIF used	CBF (ml 100g ⁻¹ min ⁻¹)	CBV (ml 100g ⁻¹)	MTT (s)
Manual AIF (n=4)	211±99	42±31	12.1±5.6
Automatic AIF (n=4)	193±131	24±9	9.2±3.0
Angiographic AIF (n=4)	109±97	14±4	10.8±4.2
ASL (n=3)	143±4	-	-

Table 6.6: Absolute CBF values (mean \pm std) in ml 100g⁻¹ min⁻¹ healthy hemisphere of “stroke” group.

The difference between CBF and CBV values produced using the manual AIFs compared to the angiographic AIFs was seen to be as large as a factor of 2, again indicating how the increase in AIF peak height and AUC gives a proportional reduction in the values of CBF and CBV (as expected from equations (3.18) and (3.16)). CBF values produced using the angiographic AIFs (109±97ml/100g/min)

⁸These 3 rats did not have viable T2* or T2 mapping data available to identify the lesion structure.

again gave the closest match to ASL CBF values from the literature and the measured mean ASL CBF value of $143 \pm 4 \text{ ml}/100 \text{ g}/\text{min}$, indicating that the increased peak height again resulted in greater accuracy of mean quantitative CBF values calculated from DSC MRI.

The MTT values were seen to remain roughly constant (manual AIFs: $12.1 \pm 5.6 \text{ s}$, automatic AIFs $9.2 \pm 3.0 \text{ s}$, angiographic AIFs $10.8 \pm 4.2 \text{ s}$) at values which broadly agreed with the “control” group and the literature across the 3 AIF methods, which is again expected as MTT is defined as the ratio of CBV to CBF and CBF is proportional to CBV.

As the relative *ratios* of the perfusion parameters between affected and unaffected ROIs (e.g. healthy and suspected ischemia) are used in the diagnosis of stroke in the clinic [267] (e.g. CBF ratio < 0.59 and MTT ratio > 1.63 indicates ischemia [268]), ratios between the ischemic and healthy regions of the rat brains were analyzed to check if the parameter ratios were affected by using an automatic AIF voxel selection algorithm. Table 6.7 displays the CBF, CBV and MTT ratios attained for both DSC MRI and ASL in the ischemic core and penumbra regions (green and yellow ROIs in Figure 6.8) when compared to a contralateral healthy region (red ROI in Figure 6.8).

AIF used	CBF		CBV		MTT	
	Core	penumbra	Core	penumbra	Core	penumbra
Manual	0.12 ± 0.02	0.34 ± 0.21	0.32 ± 0.09	0.58 ± 0.23	3.31 ± 0.64	2.20 ± 1.16
Automatic	0.10 ± 0.01	0.35 ± 0.32	0.37 ± 0.11	0.58 ± 0.22	4.15 ± 1.24	3.45 ± 0.83
Angiographic	0.12 ± 0.05	0.36 ± 0.22	0.37 ± 0.11	0.58 ± 0.23	4.00 ± 1.45	2.97 ± 1.13
ASL	0.48 ± 0.21	0.72 ± 0.17	-	-	-	-

Table 6.7: Perfusion parameter ratios (mean \pm std) between lesion and healthy tissue in contralateral ROI for rats in stroke group scanned using DSC MRI (n=4) and ASL (n=3).

The CBF and CBV ratios between the core ischemic regions and healthy regions are consistent through all 4 rats scanned with DSC MRI and all 3 AIF measurement techniques, although slightly lower than those obtained using ASL (two mean Student’s t test, $p=0.1$ between the groups). This pattern is also seen in the penumbra regions, but with higher variance than with the core region ratios. This is mostly likely due to the inhomogeneous presentation of the penumbra region [267].

Previous DSC MRI work comparing ischemic to healthy tissue 28 days after MCA occlusion reported a CBF ratio of 0.42 (whole hemisphere) [214], which shows good agreement with the penumbra values (manual AIF 0.34 ± 0.21 , automatic AIF 0.35 ± 0.32 and angiographic AIF 0.36 ± 0.22). The ASL penumbra CBF ratio reported here (0.72 ± 0.17) did not agree as well with the literature [214], although the ASL core value (0.48 ± 0.21) does agree, indicating that PVE may be influencing the ASL results.

The increased absolute MTT values, their distribution within the brain and the MTT ratios between ischemic and healthy tissue agreed with previously reported stroke models [263], [267]. The MTT ratios displayed in Table 6.7 for the penumbra are slightly higher than those reported in literature at 48hrs - the manual AIF gives a ratio of 2.20 ± 1.16 , the automatic AIF a ratio of 3.45 ± 0.83 and the angiographic AIF a ratio of 2.97 ± 1.13 , compared to the literature value of 2.0 ± 0.4 ($n=19$) [267]⁹. Core values were not reported for comparison [267]. The rat group analyzed in this thesis is much smaller ($n=4$ compared to $n=19$) and a greater period of time has elapsed between occlusion and measurement, (48hrs in [267] compared to 28 days in this Chapter), which may also account for this disparity in MTT.

In summary, all perfusion parameter ratios were very similar between each of the 3 AIF voxel selection methods, indicating that an automatically selected AIF may produce reduced CBF and CBV absolute values which agree better with reported literature values (as shown in Table 6.6) but this is not required to produce accurate MTT values or ratios of CBF, CBV or MTT, which are the parameters most often used to define ischemic physiology.

6.4 Discussion

6.4.1 Use of cerebral vasculature probability atlases in arterial voxel selection

The rat atlas showed clear identification of the major arteries and veins within the cerebral vasculature, including the circle of willis, the MCA and the superior sagittal sinus. This was successfully applied as an additional threshold to the automatic AIF selection process and was found to increase the clustering of the selected AIF voxels as expected, resulting in the highest AIF peak heights and AUC values for the resulting AIFs. These AIFs in turn produced the lowest CBF and CBV values, in both “control” and “stroke” groups, and gave the best agreement with the range of CBF and CBV values previously published in the literature [263], [264].

A bias may have been introduced into this study-specific rat atlas by using only rat datasets who had undergone sham MCA surgery or temporary MCA occlusion to construct the atlas, and therefore this atlas would not be suitable for general use. To adapt this method to a wild type rat cohort, a database of wild type rat MRA scans would be required.

⁹[214] does not report MTT values or MTT ratios between hemispheres.

6.4.2 Comparison of automatically and manually determined first pass AIFs

The results in Figure 6.14 and Table 6.1 show that preclinical AIFs can be improved in a similar manner to clinical AIFs if voxel selection is automated [212], [213], [260]. Across both the “control” and “stroke” rat groups, the automatic AIFs had peak heights nearly three times that of the manual AIFs on average ($\Delta R2^*$: 157.6 ± 55.7 compared to 61.4 ± 33.3), with the angiographic AIFs on average slightly larger than the automatic AIFs (173.5 ± 56.0). Similar magnitude increases in peak height and AUC were also seen if the two rat groups were analysed separately. Little difference was seen between the automatic and angiographic population AIFs, meaning that either method could be recommended for future work, although the increased accuracy of CBF and CBV values found when using the angiographic AIFs in parameter analysis would recommend the angiographic method.

The use of the peak height threshold was the most effective of all thresholds applied in the automatic voxel selection algorithm and could be used on its own to simplify the procedure for higher throughput of data, as suggested in the literature [214], although the incorporation of angiographic data ensures that the algorithm converges towards a small number of voxels more quickly and that the selected voxels come from a consistent location across all rats.

The variability observed between individual subject AIFs indicates the difficulty in detecting blood vessels in DSC-MRI, resulting in poor manual AIFs produced for some control mice, such as rats 6 and 7 in the control group (see Figure 6.14). The corresponding AIFs for rats 6 and 7 when using the automatic algorithm display much larger peak heights and shapes similar to the other rats in the group, indicating that the automatic selection would be preferred to manual selection when the DSC MRI signal is low, when manual vessel identification is prone to error or when the exact shape of the injected bolus is required, for comparison with another modality, as shown in Chapter 7.

6.4.3 Perfusion parameter analysis

The “stroke” rats were easily identified in comparison to the “controls”, with a clear CBF deficit in the right hemisphere (manual AIF core to healthy ratio: 0.12 ± 0.02 , penumbra to healthy ratio: 0.34 ± 0.21) corresponding to a decrease in CBV (manual AIF core to healthy ratio: 0.32 ± 0.09 , penumbra to healthy ratio: 0.58 ± 0.23) and a large increase in MTT (manual AIF core to healthy ratio: 3.31 ± 0.64 , penumbra to healthy ratio: 2.20 ± 1.16). These traits are expected in an ischemic region according to the literature [214], [266], [267] as the tissue in that area is damaged, resulting in decreased blood flow and prolonged transit times for a bolus of contrast agent due to the damaged vasculature.

Absolute CBF, CBV and MTT values produced for both the “control” and “stroke” rat cohorts using

each of the DSC MRI AIF selection methods exhibited large variances across both rat groups, and each perfusion parameter appeared to be slightly overestimated compared to reported values. The increased AIF AUCs and peak heights provided by the automatic and angiographic AIFs, however, did lower the calculated absolute CBV and CBF values compared to the manual AIFs as expected, increasing their agreement with the broad range of literature values derived from DSC MRI and ASL. The CBF values produced in the stroke group using DSC MRI also agreed with the ASL CBF values measured for an additional 3 rats with MCA occlusion, with the greatest agreement found when the angiographic AIF was used ($109\pm 97\text{ml}/100\text{g}/\text{min}$ compared to $143\pm 4\text{ml}/100\text{g}/\text{min}$). The DSC MRI data and standard SVD deconvolution analysis conducted in this study produced quantitative estimates of perfusion with limited precision and accuracy, although the range of values quoted in the literature for these parameters indicates that this is a general issue with the technique when it is used to produce quantitative results [121], [122], [125], [207], [208]. This justifies why qualitative estimates of CBV, CBF and MTT are more commonly used and quoted in the literature for DSC MRI [261], [267].

Qualitative imaging of perfusion was not seen to be affected by the choice of AIF, as all AIFs produced parameter maps with similar ratios and spatial distributions of perfusion parameters between healthy and ischemic areas in the “stroke” group. Additionally, no significant differences between perfusion parameters measured in contralateral ROIs were reported for the “control” group. MTT values also remained approximately constant in healthy hemispheres of both “control” and “stroke” groups for each of the 3 AIFs tested for each rat, as it relied only on the ratio between CBV and CBF values. This again indicated that the automatic voxel selection method is not required in order to perform qualitative imaging accurately.

The disagreement between the ASL and DSC MRI CBF values ratios in rat brains reported here suggests that a partial volume effect may be present in the ASL data presented in this chapter. The ASL data taken in this study has a resolution of $620\mu\text{m}$ in phase encode direction, whilst the DSC MRI images have an increased spatial resolution of $390\mu\text{m}$ in phase encode direction. This also made it easier to identify the core and penumbra of the lesion directly from the CBF, CBV and MTT maps. Assuming a partial volume effect, the penumbra region of the DSC MRI region could be considered equivalent to the core region of the ASL analysis, and these values do not show a significant difference across the stroke rats examined in this chapter (manual AIF = 0.34 ± 0.21 , auto AIF = 0.35 ± 0.32 , angio AIF = 0.36 ± 0.22 , ASL = 0.48 ± 0.21 ; p value from Student’s t test between mean values >0.5).

Large noise can be seen in all of the parameter maps shown in Figures 6.19 and 6.20, indicating the extent that noise present in the DSC MRI signal data propagates into the parameter maps. This could potentially be due to the inhomogeneous nature of the tissue damage caused by the sham surgery in the control group or the ischemic lesions in the stroke group, although it could also be a result of using

simple SVD deconvolution on the raw data without applying any smoothing or further regularization to the data, other than that detailed in [117], [118], [120]. Applying Tikhonov regularization [200] or block-circulant matrices [261] to the deconvolution process could be performed in future work to refine this process. Quantifying CBF accurately using DSC MRI is known to be problematic particularly when compared to gold standard PET or SPECT perfusion measurements [121], [207], [208], [245] and different deconvolution methods have been shown to produce large variations in CBF results [120]. Further work in this area would seek to explore the effect of different smoothing techniques on the DSC MRI signal data and the effect of post-processing smoothing on the parameter maps. Additionally, professional DSC MRI perfusion software packages could be used instead of MATLAB, although (to the author's knowledge) no perfusion DSC MRI analysis programs are currently available which support rat data voxel sizes.

6.4.4 Improvements to voxel selection algorithm

To reduce the number of iterations required in the automatic method, a box ROI encompassing the lower half of the rodent brain (see Figure 6.22) was suggested as a starting point instead of the entire image in order to immediately eliminate contributions from major veins (which displayed similar arrival times, peak heights, AUC and FWHM to arterial voxels), which are mostly situated in the upper half of the rodent brain. This improvement was incorporated into the algorithm for use in DSC MRI AIF selection in Chapter 7.

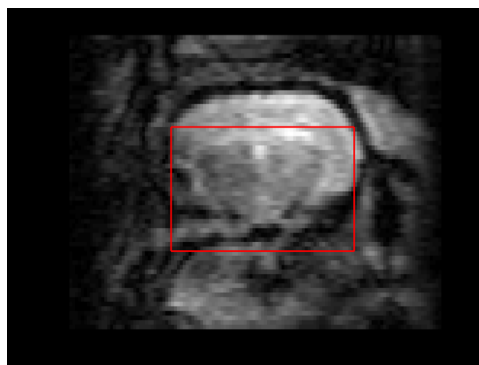


Figure 6.22: Example box ROI in red used to eliminate major veins, such as superior sagittal sinus, from automatic voxel selection.

Although more effective than manual selection, the drawback of the automated AIF method was that voxel selection thresholds had to be calculated empirically for the patient group. Future work which involved the acquisition of data from a more homogeneous patient group could investigate if the automation could be improved by using more complex selection processes which do not require empirical information, such as K means clustering, which has been used in human DSC MRI [199], [204], [206]

or Kendall's coefficient of concordance clustering analysis [269], which has been used in mouse DCE MRI. The use of the angiography information did streamline the algorithm, making the exact level of the thresholds less important, although this required a large archive of angiography data to assemble the atlas and it should be compared to other clustering-based methods to ascertain how the Bayesian probabilistic atlas approach performs against them.

Partial volume effects were found to be a cause of error in all datasets, with the typical size of a major blood vessel (0.24-1.3mm [257]) around the same size as a voxel ($0.32 \times 0.39 \times 1.5 \text{mm}^3$). Voxels are hampered by incomplete signal, leading to shape changes and subsequent bias in kinetic parameters [213], [270]. To improve on this, partial volume correction could be applied to the AIFs in future work, by comparing the AIFs to venous output functions [204] or by using tail scaling [206], [271].

6.5 Conclusions

First pass bolus AIFs were determined by selecting arterial voxels from 11 rat brain T2* weighted EPI datasets using three methods: manual voxel selection, automatic voxel selection using empirical thresholds and automatic voxel selection aided by prior knowledge of the rodent vasculature. Qualitative imaging of CBF, CBV and MTT distributions and their respective ratios between ischemic and healthy areas were shown to be unaffected by the choice of AIF, indicating that an automatically selected AIF is not essential to detect fundamental changes in physiology in preclinical models. The automatic AIF selection method did, however, produce both individual and population AIFs with larger peak heights than manual voxel selection and more consistent curve shapes, resulting in improved accuracy in estimates of absolute values of CBF and CBV in both a rat stroke model and a control rat group. The study-specific angiography atlases which were added to the algorithm streamlined voxel selection in large arteries and angiographic AIFs were found to have the highest peak heights of all 3 AIF determination methods (manual, automatic and angiographic AIFs). The angiographic AIFs produced quantitative estimates of CBF which were closest to those estimated using ASL and to the wide range of values found in the literature. The estimates of CBF, CBV and MTT across both rat datasets did, however, exhibit high variance, indicating that the analysis method in its current form requires improvement to provide consistent and accurate quantitative estimates of perfusion *in vivo*. Automatic voxel selection methods are therefore preferable to manual methods in studies which require exact and reproducible measurement of the first pass bolus AIF curve shape, such as in Chapter 7 of this thesis, where contrast agent AIFs extracted non-invasively from DSC MRI data are compared to PET tracer AIFs.

6.6 Chapter summary

A DSC-MRI methodology of using T2*-weighted EPI imaging during the first passage of a bolus of contrast agent was used to determine the arterial input function non-invasively and produce perfusion parameter maps of rat brains. The application of an automatic voxel selection algorithm was outlined, and its performance compared to manual voxel selection. AIFs with higher peak heights and AUCs were attained using the automatic method in conjunction with a vascular probability atlas compared to the manual method, and these properties were seen to give slightly improved estimates of absolute values of CBF and CBV in both control rats and rats with a large ischemic lesion. The automatic method in conjunction with angiographic information was therefore selected to be used in DSC MRI AIF determination in Chapter 7 to create consistent estimates of DSC MRI AIFs. These are compared with both PET tracer and MR contrast agent AIFs derived from blood samples within the first pass of a dual tracer and contrast agent injection bolus in Chapter 7.

Chapter 7

Comparison of AIFs derived from dual injections of Gd-based MRI contrast agent and ^{18}F -FDG in rats

This Chapter outlines an experimental comparison of PET tracer and MRI contrast agent AIFs taken from wild type rats, measured using both invasive blood sampling techniques and non-invasive dynamic MRI acquisitions. The hypotheses addressed were as follows:

- 1. There exists a technique to convert MR contrast agent AIFs into PET tracer AIFs.*
- 2. Dynamic MR data can therefore provide a non-invasive estimate of a PET AIF if a combined bolus of MR contrast agent and PET tracer are administered.*
- 3. DSC MRI images can be scaled and combined with DCE MRI data to estimate the MR contrast agent AIF.*
- 4. MR and PET AIFs have the greatest similarity in curve shapes in their initial stages, and therefore a technique which converts MR AIFs to PET AIFs in the first pass regime should be optimal.*

Gold standard AIFs derived from serial blood sampling were compared to assess if MR contrast agent AIFs could be converted successfully into PET tracer AIFs. Image-derived AIFs from MRI were determined in the first pass phase using the DSC MRI technique previously discussed in Chapter 6 and at later time points using DCE MRI. It was found that the combined DSC and DCE MRI AIFs could be converted into ^{18}F -FDG and MR contrast agent AIFs using an empirically derived set of conversion factors, which confirmed results previously reported by Poulin et al. [54]. Additionally, AIFs determined non-invasively from DSC MRI were used as to estimate PET AIFs in the first pass stage.

7.1 Introduction

Kinetic modelling requiring an arterial input function, as outlined in the literature summary of Chapter 3, and discussed in detail in Chapter 4 and 5, is a key strength of dynamic PET and is utilized in a large number of preclinical applications from cardiac metabolism studies [29], [33], [51] to oncology [32] to determining the specific binding of PET tracers in neurology [40]. As detailed in previous Chapters, the AIF is usually determined by rapid blood sampling [51], [52], [161], [162], [164] which can be both logistically challenging and has a limited temporal resolution. Non-invasive methods of AIF determination are therefore preferred, particularly in mice due to their small blood volumes, although the restricted spatial resolution of PET makes image derived input function determination challenging due to partial volume effects, as previously discussed in Chapters 4 and 5.

With the advent of simultaneous PET/MR imaging, however, one can hypothesise that a combined bolus of Gadolinium based contrast agent and PET tracer could produce a similar AIF curve profile on both dynamic MRI and PET images, thus allowing the non-invasive determination of a PET input function for subsequent kinetic analysis from MRI images alone. This could potentially negate the need for serial blood samples if no metabolite measurements were required, or at least reduce the number of blood samples required. If an MR AIF *could* be reliably converted into a PET AIF, this would also provide a platform for dual pharmacokinetic modelling from both modalities, enhancing the amount of complementary information available from a single, simultaneous PET/MR acquisition.

To be a viable alternative to blood sampling, the converted MR AIF must provide consistent estimates of PET kinetic parameters. This is potentially problematic as MR contrast agents are primarily Gd-based ligands which have different perfusion characteristics and washout rates to many PET tracers, as they are metabolised in different ways *in vivo*. In this experiment, the MR contrast agent Gadovist is used to provide a potential ^{18}F -FDG AIF, as the molecular weights are of the same order of magnitude, 181.1495g/mol for ^{18}F -FDG and 604.72g/mol for Gadobutrol (Gadovist), and as such may be expected to have similar extravasation rates from blood vessels, similar diffusion rates into the interstitium and similar excretion rates [54], [272]. Additionally, it has been shown in phantom, volunteer and patient studies that Gd-based contrast agents do not provide any substantial additional attenuation of PET tracer or have any effect on MR-based attenuation maps [273]. The molecular structures for both Gadovist and ^{18}F -FDG are shown in Figure 7.1.

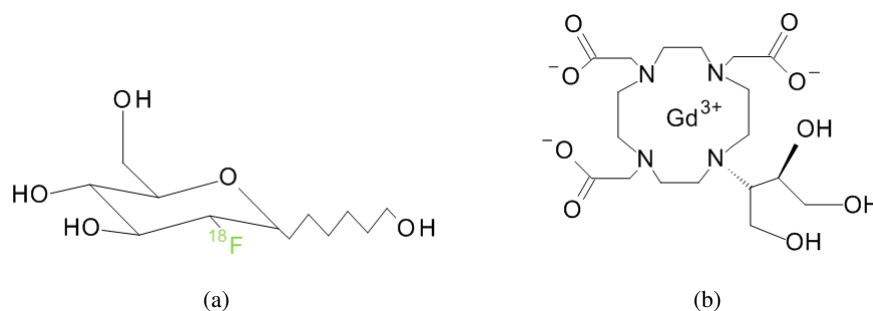


Figure 7.1: Compound structure: (a) PET tracer (Fluoro-deoxyglucose, ^{18}F -FDG) and (b) MR contrast agent (Gadovist, Gd-DO3A-butrol 6).

There remains a major difference between the 2 compounds, however, as ^{18}F -FDG is internalized and trapped via phosphorylation within cells [54], [70], [139], [272] whilst Gd-based contrast agents flow from plasma into the extravascular extracellular space (EES) [129], [130] and are not internalized in cells [106]. This difference in kinetics will most likely lead to a difference in retention times, with the PET tracer having longer retention times than the MRI contrast agent [54], [272], consequently meaning that the two compounds provide complementary but fundamentally different information. To address this, conversion methods between MR AIFs and PET AIFs must be tested to ascertain if a reliable translation between modalities is possible, as errors in PET AIF curve shapes will propagate into the kinetic parameters obtained [53], [155], [272].

7.1.1 Previous attempts to use dynamic MRI to estimate PET AIFs

Recent research [54], [272] in this area performed serial blood sampling throughout a PET scan on tumour-bearing rats after a combined bolus of Gd-DTPA and ^{18}F -FDG was administered through the cannulated femoral vein in a PET scanner. Gold standard PET tracer AIFs were measured from the activity concentrations of ^{18}F -FDG present in the plasma samples, whilst gold standard contrast agent AIFs were determined from the concentration of Gd-DTPA in each of the plasma samples. DCE MRI image-derived AIFs were obtained using a reference region methodology [274], [275] which utilized a separate Gd-DTPA bolus injection, administered at the same rate and contrast agent dose as the combined tracer/contrast agent bolus using a syringe pump. This was performed in an MRI scanner immediately before the rat was transferred from to the PET scanner for its dual bolus injection.

Bi-exponential models of the form, $(w_f \exp^{-r_f t} + w_s \exp^{-r_s t})$, convolved with a rectangular function [187], were fitted to each AIF after normalization to its maximum peak height [54]. The excretion (slow) rate constant and weighting were defined as r_s and w_s , whilst the extravasation (fast) rate constant and weighting were defined as r_f and w_f . The rectangular function represented the delay before the arrival of the contrast agent/radiotracer in blood [54], where its amplitude was defined by the concentration of

the injection and its width was defined by the duration of the injection. To convert the bi-exponential Gd AIFs and the DCE MRI image-derived AIFs to the PET AIFs, average ratios between the resulting bi-exponential rate constants and weightings which described each AIF were calculated for the rat group. These population conversion factors were then applied to the Gd AIFs and DCE MRI AIFs to convert them into normalized PET AIFs and these were scaled to MBq/ml using either a plasma sample taken from the peak of the AIF or through a normalization factor determined from the linear relation between AIF peak height and the injected activity (MBq/kg) [54]. After normalization, fitting, conversion and scaling, the Gd AIFs or DCE MRI AIFs could both be used in PET kinetic analysis. A schematic detailing the method employed in [54] is summarised in Figure 7.2 and a sample of the reported normalized and converted AIFs is shown in Figure 7.3.

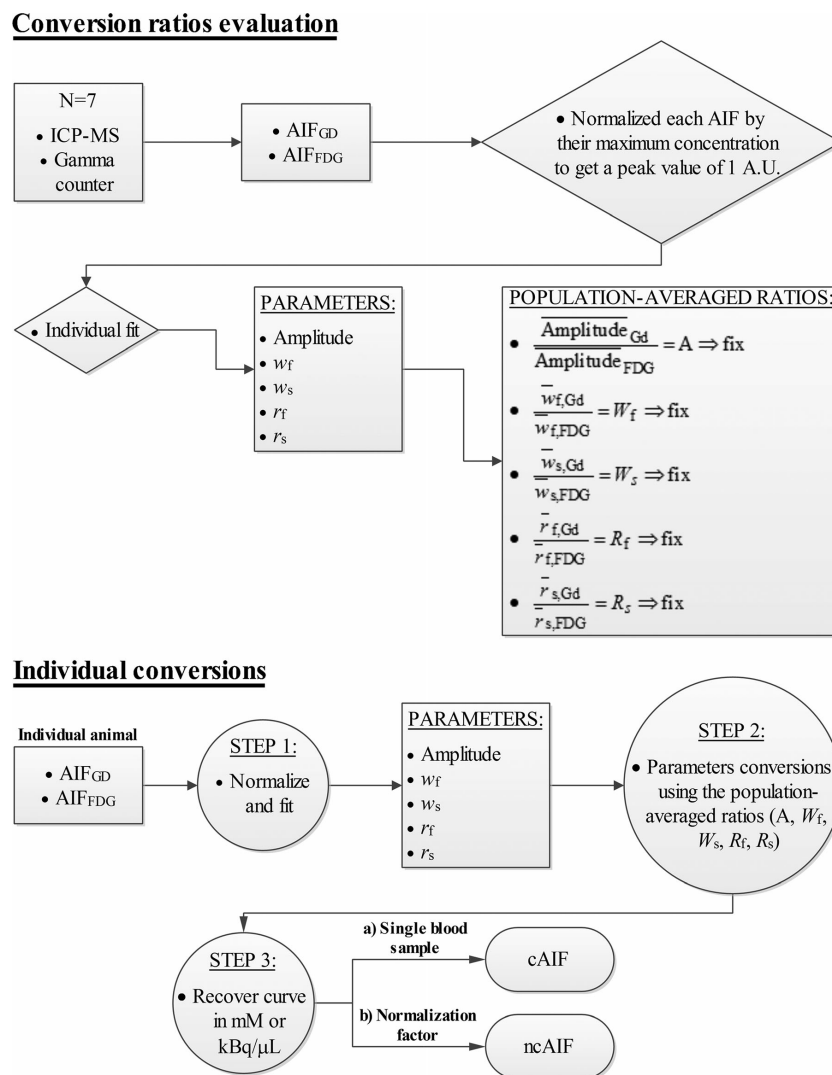


Figure 7.2: Schematic showing protocol used in [54], reproduced with permission. Plasma sample AIFs for PET tracer and MR contrast agent are normalized to their respective peak heights and fitted with a bi-exponential convolved with a top hat function. The ratios between the bi-exponential parameters of the AIFs are then averaged across the group and used to convert each Gd AIF into an ^{18}F -FDG AIF, which is then scaled to kBq/ μL using a single blood sample taken from the peak, or a factor calculated from the injected activity.

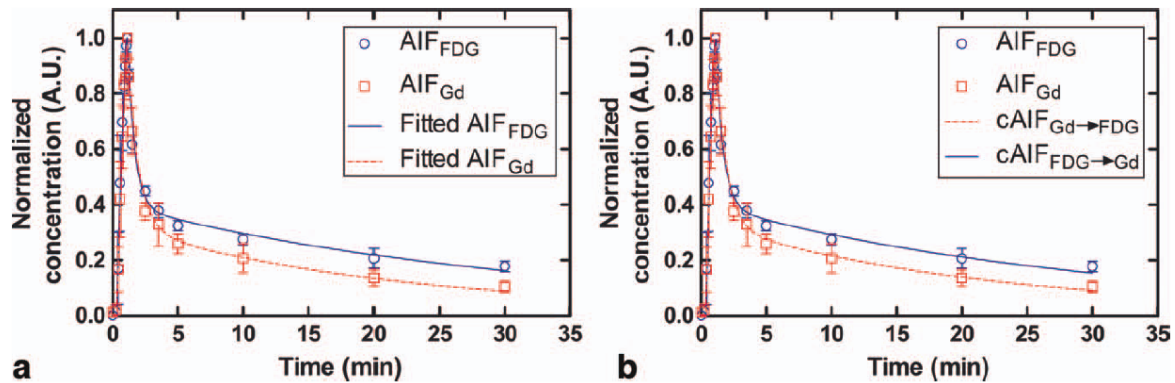


Figure 7.3: Derived PET and MRI AIFs, with corresponding converted AIFs, reproduced with permission from [54].

This method produced interchangeable AIFs between modalities (i.e. Gd contrast agent AIFs could be converted into ^{18}F -FDG AIFs and vice versa), which were found to provide consistent estimates of myocardial metabolic rate of glucose (MMRGlc) and tumour metabolic rate of glucose (TMRGlc), as well as K^{trans} , v_e and v_p parameters from DCE MRI analysis. Poulin et al. reported the divergence of the ^{18}F -FDG and contrast agent normalized curves at late times (≥ 30 minutes, shown in Figure 7.3), indicating the different retention times between the compounds which becomes more noticeable at late time points. Due to the difference in AIF curve shapes at late time points, even after normalization to peak height, an empirical calculation of the bi-exponential model conversion ratios between the AIFs was required for the chosen rat cohort.

It was hypothesized that a standardized and reproducible injection protocol resulted in the similar steep rise in the curves seen in the first few minutes of the curves and that the different *in vivo* distributions and elimination rates of the compounds were the cause of the curve divergence at later times [54]. This was also seen in the fact that the fast decay constants of their bi-exponential AIF models (r_f), which represented the rate of extravasation, were different across the 2 modalities, but the slow decay rate constants (r_s), which represented the rate of excretion, were similar for both ^{18}F -FDG and MR contrast agent AIFs [54]. This finding has limited the method's usefulness and it has yet to be translated into a clinical study. The published results do suggest, however, that the AIF shapes for both modalities are most similar within the first pass bolus phase, where the AIF shapes depend more upon the injection protocol and blood flow than on the retention rates of the compounds.

7.1.2 Overview of experimental AIF conversion protocol

As shown previously [54], [272], rapid, dynamic MRI imaging is required to provide adequate temporal sampling to measure the MR AIF accurately for conversion to the PET AIF from the combined bolus of PET tracer and MR contrast agent. DSC MRI sequences are therefore promising as these can be used to

track the passage of the combined MRI contrast agent and PET tracer bolus through the vasculature, as demonstrated in Chapter 6. This produces an estimate of the AIF within the first pass phase, where the contrast agent and tracer AIFs are believed to be most similar and therefore where conversion between them should be the most reliable. DSC MRI can also be conducted with a higher temporal sampling rate than DCE MRI when using off-the-shelf techniques. In theory, if conversion between the modalities was reliable, a converted DSC MR AIF could provide a PET AIF with greater accuracy than an IDIF taken directly from PET images, due to the superior spatial resolution of MRI resulting in reduced partial volume effects. This is of particular importance in the first pass phase of the AIF where rapid temporal sampling is desirable as standard blood sampling techniques may undersample the AIF, resulting in an aliasing effect which underestimates the true AIF peak [52], [68], [175], [276].

The drawback of this technique, as discussed in Chapter 6, is that DSC MRI relies on $\Delta R2^*$ measurements which are assumed to be proportional to changes in contrast agent concentration, rather than a direct, absolute measurement. It is also restricted to the brain and cannot provide the quantitative parametric analysis of DCE MRI (see Appendix I.4 for details), such as information on the transfer constant K^{trans} of tumours, which characterizes diffusive transport of Gd contrast agents across the capillary endothelium [189]. In addition, DSC MRI can only provide estimates of the AIF within the first pass, as it relies on the transient change in $T2^*$ which occurs as the Gd-based contrast agent bolus moves through the vasculature. This technique must therefore be combined with techniques such as DCE MRI (DCE MRI was outlined in Chapters 2 and 3) at later time points if an estimate of the PET AIF tail is also desired from an MRI AIF, but this would only be possible if the AIF conversion between modalities and the scaling between DSC and DCE data is reliable and robust.

In this work, an experimental comparison of PET tracer and MR contrast agent AIFs was conducted by imaging wild type rats injected with a combined bolus of Gadovist contrast agent and ^{18}F -FDG in an MRI scanner. Gold standard ^{18}F -FDG and Gadovist AIFs were derived from serial blood samples taken from the rats during DSC and DCE MRI acquisition using cannulas surgically inserted into each rat's femoral artery and leading outside the magnet bore. An overview of the entire experimental protocol is shown in Figure 7.4. The blood sampling protocol was performed in an MRI scanner to compare MRI image-derived AIFs to simultaneously acquired PET tracer and contrast agent AIFs from the same rats, in contrast to the protocol conducted by Poulin et al. [54], [272]. Poulin et al. compared DCE MRI image-derived AIFs (derived using the reference region method [54], [274]) taken from a separate injection of contrast agent performed later in the imaging session to their gold standard AIFs, which may not have been an identical injection despite being performed with a syringe pump. The physiological conditions of each rat may have changed between the first and second contrast agent injection, and the MR contrast agent AIF depends not only on bolus shape but also on cardiac output, vascular geometry

and the cerebral vascular resistance [121]. The approach taken in this study, however, was more likely to suffer from dispersion and delay effects as a result of the long cannulas required to take blood samples from subjects lying within the MRI bore.

The DSC MRI experiment outlined in Chapter 6 was acquired during the first pass bolus phase to ascertain how similar the initial bolus shapes were between the modalities and to see if DSC MRI AIFs could be successfully converted into PET first pass AIFs. As discussed in Chapter 6, unambiguous detection of blood vessel voxels to extract AIFs in EPI acquisitions is difficult due to low SNR and high PVE, meaning that manual selection of arterial voxels is vulnerable to human error and low reproducibility. The automatic AIF determination algorithm which was developed in Chapter 6 was hence employed along with a study-specific angiography atlas, constructed for the wild type rats scanned in this Chapter using the same process as that outlined in Chapter 6, to ensure AIF curve shapes extracted from DSC MRI datasets were as consistent and accurate as possible.

DCE MRI was acquired for a further 45 minutes (see Figure 7.4), to test if a composite DSC/DCE MRI AIF (i.e. one which used later time point DCE MRI measurements to scale DSC MRI first pass data to absolute concentrations of contrast agent *in vivo*), could be successfully converted into a PET AIF in a similar manner to the reference region DCE MRI AIF proposed by Poulin et al. [54], [272]. The DCE MRI sequence used in this study required the direct calculation of a T1 map before contrast agent was administered to relate the change in apparent T1 observed to the concentration of Gadovist contrast agent, summarised in Figures 2.63 and 2.64. The accuracy testing of Gd concentration readings attained with this DCE MRI sequence can be found in Appendix I.1 and I.2, which tested the DCE MRI sequence accuracy in both phantoms and *in vivo*, assessing its accuracy in both tissue and blood. The combined DSC and DCE MRI signals formed the total MRI image-derived AIF, which was then compared to the contrast agent AIF attained from blood sampling to assess the DSC MRI data scaling accuracy.

Once formed, the Gd contrast agent AIF and total MRI image-derived AIFs were normalized and converted into surrogate PET AIFs using the AIF conversion method outlined in Figure 7.2 and their similarity to the gold standard blood sampled PET AIFs was assessed. The DSC MRI data was also analyzed on its own and used to produce surrogate first pass PET AIFs using a gamma variate function conversion method, which were also compared to the blood sampled PET AIFs for accuracy.



	Rat brain MRI	Blood sampling	Sample analysis
12min 4s	Localizer, T2w TurboRARE, TOF MR angiography	 3 baseline samples	 5 baseline readings
4min 47s	FLASH VFA for T1 map (DCE MRI) 7 FA = [8°, 3°, 5°, 10°, 15°, 20°, 30°]		
41s	FLASH VFA baseline (DCE MRI) 1 FA = [10°]		
INJECTION	Bolus of ~100ml 2x dilution Gd and ~100ml ~20MBq FDG; 1ml saline flush		
140s	T2*w GE EPI (DSC MRI)	3-4 samples, taken as fast as possible	Each sample weighed and activity measured using well counter.
41min	Dynamic DCE MRI series 60 × 41s acq time, FLASH VFA, 1 FA = [10°]	19-22 samples, at structured time breaks (see Table 8.1 for details)	Centrifuged, plasma extracted with pipette, weighed and plasma activity measured using well counter.

Figure 7.4: Experimental timetable. 2 rats were scanned in this manner each day.

A schematic summary of all AIF data acquired and compared for each rat in this study is presented in Figure 7.5.

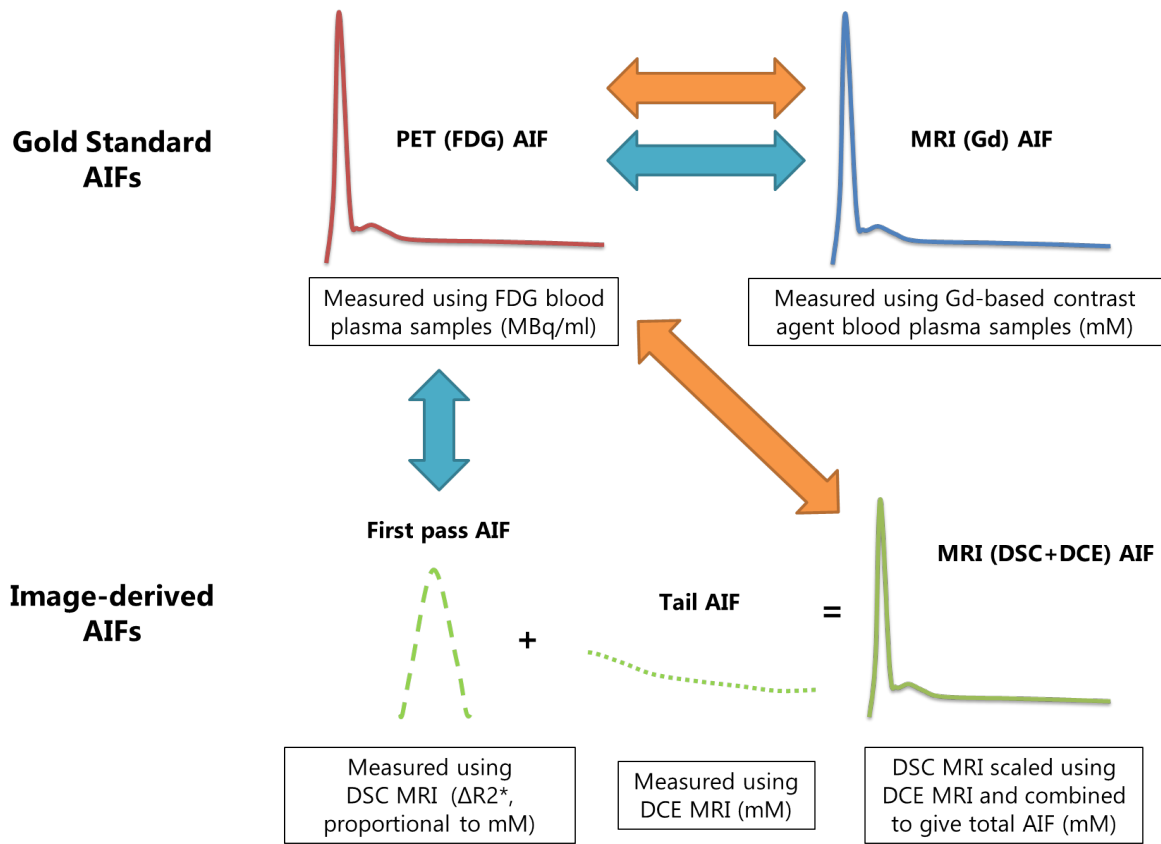


Figure 7.5: Outline of measured data and comparisons made between gold standard AIFs derived from blood plasma samples (for both PET and MRI) and image-derived AIFs from DSC and DCE MRI. DSC MRI provides first pass bolus shape at high temporal resolution, DCE MRI provides AIF tails with absolute contrast agent concentration to provide scaling. The combined DSC/DCE AIFs are compared to the blood sampled AIFs (orange arrows) using the conversion method of Poulin et al [54] and the first pass phases of each AIF are compared using the gamma variate fitting conversion method (blue arrows).

7.2 Materials and Methods

7.2.1 Animal preparation

Surgery was performed on 12 healthy, wild-type Wistar rats¹ (525 ± 92 g; Charles River Laboratories, Kent, UK) to install 1m long femoral 27G venous and arterial cannulas using PE tubing (0.4mm inner diameter) filled with heparinised saline (10 units heparin: 1ml saline). Animals were prepared under isoflurane anaesthesia (induced at 4% in 1.5 l/min O₂; maintained at 2% in 1.5 l/min O₂) before being transferred into a 4.7T Bruker Biospin MRI scanner (Bruker Inc., Ettlingen, Germany). The apparatus

¹Surgery was performed by Dr David Williamson and Dr Steve Sawiak. Assistance in blood sampling was provided by Asad Shabir and Dr Guido Buonincontri.

used in the experiment is shown schematically in Figure 7.6. Anaesthesia was maintained at 2% in 1.5 l/min O_2 for the duration of the imaging experiment, with a respiratory pillow placed underneath the animal's chest and a rectal temperature probe inserted using a lubricated cover to monitor vital signs. The level of anaesthesia was maintained to give a respiration rate of 45-50bpm across all rats, to standardise blood flow rates and reduce the impact of different blood pressures on contrast agent delivery. A flowing water heating blanket was used to maintain animal temperature at 37°C throughout the experiment.

7.2.2 MRI imaging and blood sampling, pre-injection

The imaging protocol outlined in Figure 7.4 was performed by the author using a Bruker rat head receiver volume coil and a Bruker rat body quadrature transmit coil. All scans were positioned with their central region covering the rat midbrain. T2 weighted RARE scans were acquired (TR/TE 15277/36ms, FOV $6.4 \times 6.4 \times 3.2\text{cm}$, matrix 256×256 , 0.2mm slice thickness, 128 slices, planar resolution $250 \times 250 \mu\text{m}^2$, NEX = 1, RARE factor = 8, acquisition time 6 mins 6s) to provide the structural MRI needed to implement the angiography atlas approach for automated AIF detection from DSC MRI used in Chapter 6. TOF-MRA (TR/TE 12/3.3ms, FOV $4 \times 4\text{cm}$, matrix 256×256 , 0.7mm slice thickness with 0.55mm gap, 64 slices, planar resolution $156 \times 156 \mu\text{m}^2$, NEX = 3, acquisition time 4 mins 54s) was also acquired to implement this approach, as the atlas used in the previous Chapter was for rats who had undergone MCA surgery, whereas the rats used in this study were wild type.

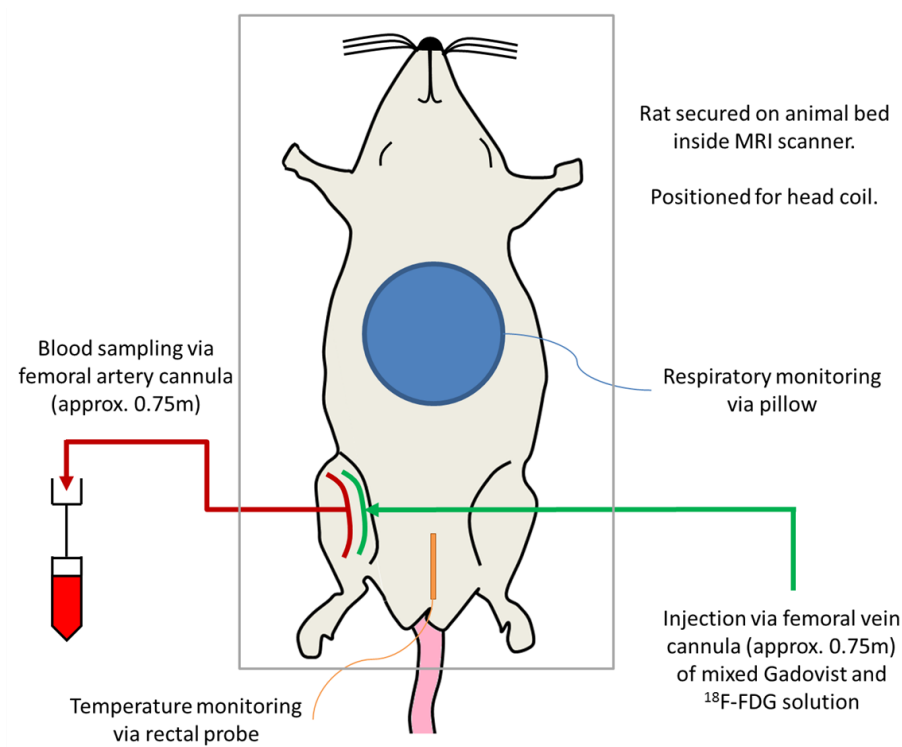


Figure 7.6: Schematic showing apparatus used in this experiment. Animal is placed in scanner to perform TOF MRA and RARE before injection of tracer and contrast agent.

The DCE MRI protocol used a variable flip angle (VFA) 3D FLASH sequence for T1 mapping comprising a $128 \times 128 \times 64$ matrix which was acquired using 7 different flip angles² (TR/TE 10/4.513ms, Flip angles = $[8^\circ, 3^\circ, 5^\circ, 10^\circ, 15^\circ, 20^\circ, 30^\circ]$, FOV = $3.84 \times 3.84 \times 3.84$ cm, slice thickness 0.5mm, planar resolution of $234 \times 234 \mu\text{m}^2$, NEX = 1, acquisition time 4 mins 47s). This scan was repeated with a single 10° flip angle (same scanning parameters, acquisition time 41s) to give a baseline for the dynamic acquisition. A flip angle of 10° was chosen to optimize the sequence sensitivity, dynamic range and SNR. The settings for this scan were then stored and copied on the scanner console to ensure that all subsequent dynamic scans would be operated with the same receiver gain as the baseline scan.

The arterial line, which extended outside of the magnet bore, was then manually opened using plastic tongs and arterial blood allowed to flow from the rat into pre-weighed $200 \mu\text{l}$ eppendorf tubes. 3 baseline samples of $50\text{--}75 \mu\text{l}$ were collected, using a plastic clamp to regulate the blood flow into the sample tubes. An external clock was started when the first baseline sample collection was begun and all sample/scan times from this point onwards were recorded with reference to the external clock to ensure accurate time-keeping. All timings are detailed in Table 7.1. This experiment therefore required 3 manual operators which were kept constant throughout: 1 operator (the author) to perform the injection and measure the blood sample activity as they were collected; 1 operator to perform the imaging and note the start and stop times of each blood sample/MRI scan, and 1 operator next to the MR scanner bore to physically collect the blood samples from the animal and communicate their start/stop times.

A combined bolus of ≈ 100 ml 0.1 mmol/kg Gadovist (prepared using $2 \times$ dilution of 1M Gadovist solution) and ≈ 100 ml, mean activity 18 ± 5 MBq ^{18}F -FDG was prepared by the author and administered into the femoral venous cannula by the same manual operator (the author) for each rat, at an approximate injection rate of 2 ml/s. This solution was immediately followed by a 1 ml saline flush, with the start and stop times of all injections noted using the external clock.

7.2.3 MRI imaging and blood sampling, post-injection

A single shot T2* weighted gradient echo EPI sequence for DSC MRI. as detailed in Chapter 6, (TR/TE $350/13.631$ ms, FOV 2.56×2.56 cm, matrix 78×64 , 1.5 mm slice thickness, 8 slices, planar resolution $330 \times 400 \mu\text{m}^2$, NEX = 1, 400 time frames, temporal resolution 0.35 s, acquisition time 140 s) was started 10 s before PET tracer and MRI contrast agent injection, as detailed in Table 7.1. Blood samples were taken as fast as possible during the first pass, immediately after injection.

After the DSC MRI had finished, 60 DCE MRI scans (using the same parameters as the baseline scan)

²This sequence was customised to repeat the 7 flip angles as part of a temporal series and store the data as a 4D image. Without this modification, incorrect T1 values were reported due to reassignments of greyscale values between flip angle acquisitions in the Bruker Paravision software.

were then conducted in parallel with the blood sampling using the timetable detailed in Table 7.1. As these scans were all conducted several minutes after the injection was administered, the high temporal resolution condition (< 5s for accurate DCE MRI parameters in compartmental modelling [134], [135], [272]) required to measure the peak region of the AIF could be relaxed and the relatively long acquisition time of 41s was deemed acceptable.

Blood samples were spaced using structured breaks (e.g. 60s breaks between samples after 20 minutes of scanning) to ensure the UK Home Office recommended limit for blood sampling was not exceeded (10% of total blood volume for each rat, assuming rats have 64ml of blood per kg body weight, giving a limit of approx. 2ml).

Summary of AIF blood sampling protocol

Time/s	MRI scans	Blood samples taken (50-75µl)
Before injection	Baseline for DCE MRI (41s)	3 baseline samples
Injection (t=0)	Start queue	Start first sample
0-140	DSC MRI (400×0.35s)	3-4 samples, as fast as possible
140-420	6 DCE MRI scans (6×41s)	4-5 samples, 15s breaks
420-600	5 DCE MRI scans (5×41s)	2-3 samples, 30s breaks
600-1200	14 DCE MRI scans (14×41s)	4-5 samples, 60s breaks
1200-2700	35 DCE MRI scans (35×41s)	6 samples, 300s breaks
Total	460 time points + baseline	22-26 (max 1.95ml blood)

Table 7.1

Each finished blood sample was rapidly transferred to a microbalance (Mettler Toledo, AT261 DeltaRange, Sanyo Electric Co. Ltd.) and its weight noted by the author. The tube weight before blood was added was then subtracted to ascertain the exact blood volume in each tube (blood density assumed as 1.05g/ml [239]) before inserting into a well counter (3 inch NaI crystal, Harwell Instruments, Canberra UK Ltd. using GENIE 2000 software) for 100s to measure its radioactivity in counts per second (cps). Cps were converted into kBq/ml using a conversion factor of 531.4cps/kBq and the calculated blood volume. The time of each measurement was noted using the external clock and corrected for radioactive decay back to the injection time. The well counter and microbalance are displayed in Figure 7.7.

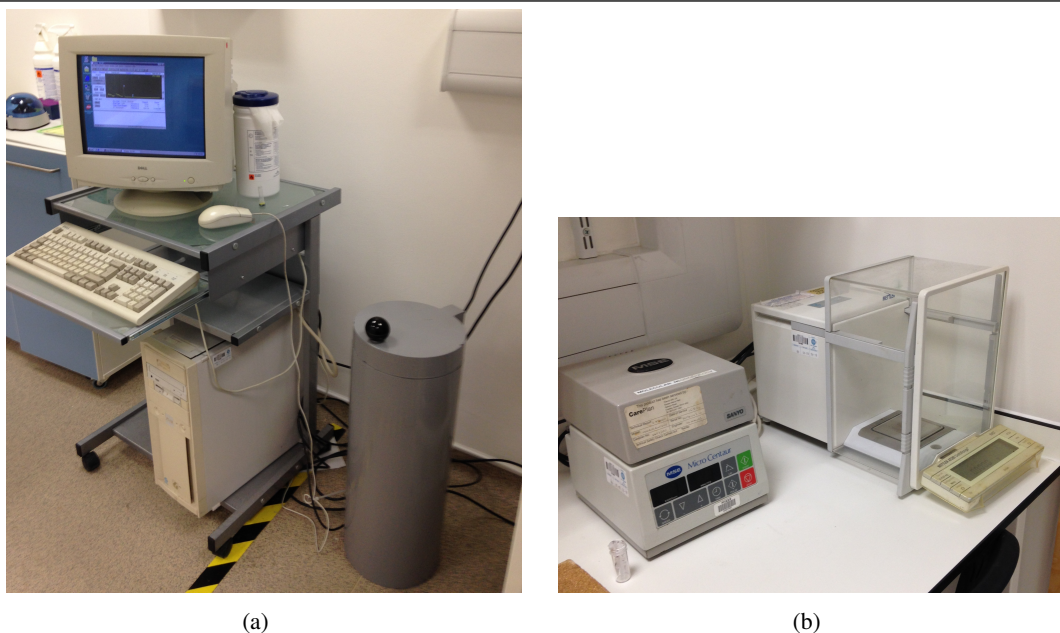


Figure 7.7: (a) Well counter used to measure tracer radioactivity in blood samples. (b) Microbalance and microcentrifuge used to weigh samples and separate blood from plasma respectively.

Each blood sample was centrifuged at 10000rpm for 4 minutes to separate out clear blood plasma which was then pipetted into a pre-weighed 200 μl eppendorf. The plasma sample was then weighed using the microbalance and its radioactivity measured using the well counter in kBq/ml as described for whole blood, with the exception that rat plasma had an assumed density of 1.025g/ml [240]. To ensure maximum plasma could be extracted from each sample, all blood samples were processed before the first plasma sample was measured and each empty eppendorf tube was pre-rinsed with heparinised saline before weighing to minimise clotting. ^{18}F -FDG AIFs were created from the activity concentrations of all measured plasma samples aligned to the times which they were extracted from the rat, adjusted for decay correction back to the injection time.

The plasma samples were then stored in a -20 $^{\circ}\text{C}$ freezer for 1 week before undergoing induced coupled plasma mass spectrometry (ICP-MS) analysis, to provide measurements of Gadolinium (and therefore contrast agent) concentrations.

7.2.4 ICP-MS analysis of plasma to determine contrast agent concentrations

The ICP-MS analysis protocol used in this study was devised by the author. All rat plasma samples were analysed by the author on a Perkin Elmer SCIEX Elan DRC II quadrupole ICP-MS (Inductively Coupled Plasma Mass Spectrometer), in the Department of Earth Sciences at the University of Cambridge, UK³. No rat blood samples were analyzed as the blood matrix was too large to be adequately processed using

³ICP-MS was conducted under the supervision of Dr Jason Day.

ICP-MS. The calibration standards were prepared as an external calibration using serial dilutions of a Gd^{157} standard (blank, 0.1, 1, 10, 100, 1000 ppb) prepared from single element high purity standards (CPI, California, USA) in high purity 1% HNO_3 (g/g, quartz distilled in house). The ICP-MS internal standards were 10 ppb Rh, In and Re and each sample was prepared in 1% HNO_3 , added online with a t-piece and mixing tube prior to the nebuliser. An independently prepared quality control standard (SPS-SW2, LGC Standards, UK) was used as a calibration standard for additional elements and was repeatedly analysed throughout the run to check for calibration accuracy (approx 5%) with a similar precision. The machinery and the samples are shown in Figure 7.8.

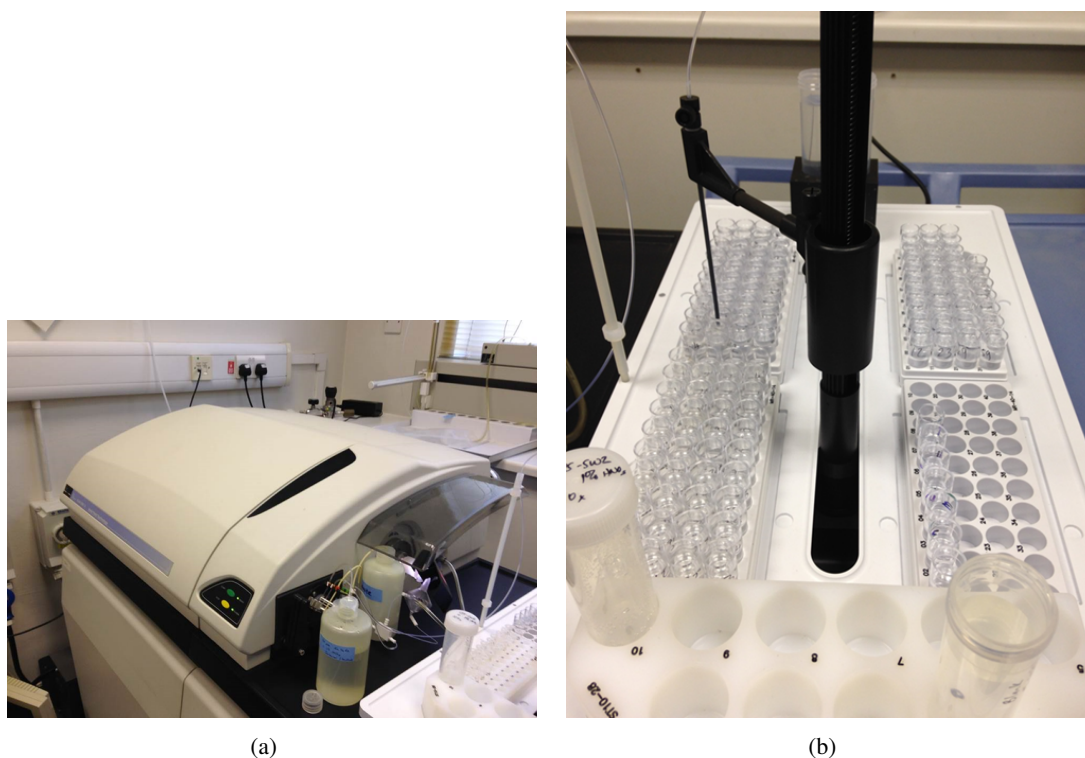


Figure 7.8: (a) ICP-MS console used to analyse samples for ^{157}Gd content. (b) Second stage diluted plasma samples inserted into measuring racks for ICP-MS analysis.

Instrumental drift was maintained at less than 2% measured for the raw intensity of the internal standards during the entire analytical run (approx. 25 solutions per rat batch, 3-5 rats per run, 3 runs in total). Additional MRI contrast agent (Gadovist) samples ($1:1 \times 10^6$ dilution factor; $1\mu\text{M}$ concentration) were run by the author to confirm the ICP-MS calibration for Gd^{157} was suitable to determine MRI contrast agent concentrations. Solutions were analysed using a Micromist FM05 microconcentric nebuliser using a pumped flow rate of $80\mu\text{l}/\text{min}$ (Glass Expansion, Australia) and a quartz cyclonic baffled spray chamber with platinum sampler and skimmer cones. ICP-MS sensitivity in this configuration was 3710 ± 70 cps/ppb for Gd^{157} . Concentration results were calculated the Elan v4.0 software with a simple linear calibration line and intercept set to zero. The raw intensities were blank subtracted and internal standard normalised before calibration calculations were performed. Samples were originally taken in $200\mu\text{l}$

ependorfs, attaining approx. $20\mu\text{l}$ plasma per blood sample. These were diluted by a factor of 1:10 using $18.2\text{M}\Omega$ deionised water before a $30\mu\text{l}$ aliquot was extracted and diluted with 1% HNO_3 into 4ml autosampler cups at a factor of 1:100 for ICP-MS analysis, giving a total dilution factor of 1:1000. The autosampler setup is shown in Figure 7.8(b). The 1% HNO_3 was doped with 10ppb Holmium to assess the precision of the sample dilutions. All results (unknowns and standards) were accurately corrected for dilutions by mass. Gd AIFs were created from the results of all measured plasma samples aligned to the times which they were extracted from the rat.

Plasma samples from 4 of the rat cohort were re-tested by the author 1 week after the original ICP-MS analysis to ascertain the reproducibility of the Gd AIF measurement.

7.2.5 AIF extraction from dynamic MRI images

DSC MRI

Arterial voxels in the middle cerebral artery (MCA) were selected using the automated angiography atlas based selection process described in Chapter 6. This was converted into $\Delta R2^*$ AIF curves using equation (2.23), which were assumed proportional to contrast agent concentration in the first pass [121] and an example of which is shown in Figure 7.9. These curves were averaged using 30s windows to smooth the signal from 0.35s temporal resolution into 30s temporal resolution frames, shown as the red line in Figure 7.9(b). This was done to compare with the blood sampled data at a similar level of temporal sampling, as the blood samples had a limited temporal resolution of between 20-40s in the first pass, depending on the rat due to dispersion within the cannula. DSC MRI data was taken at a very high temporal resolution to ensure that the any required smoothing/interpolation was possible at this stage of the analysis. Additionally the averaging process reduced the large level of noise seen in the signal, shown in Figure 7.9(a).

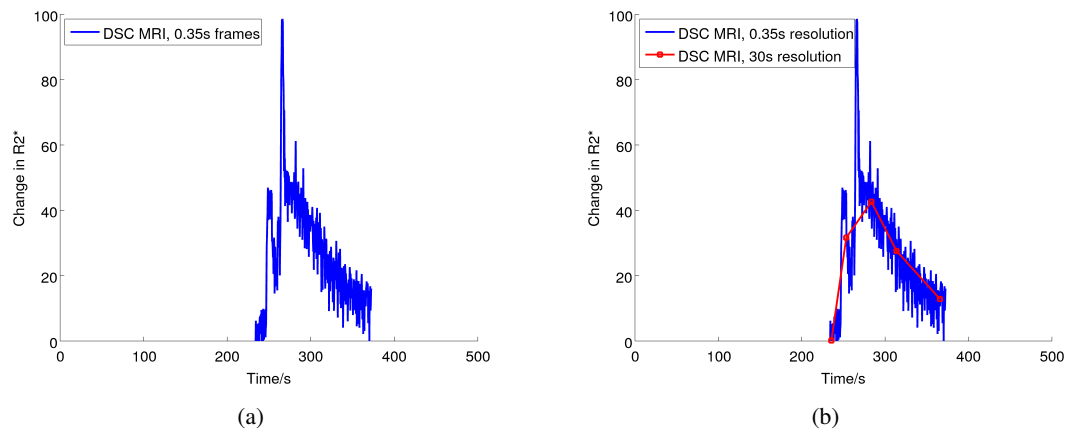


Figure 7.9: (a) DSC MRI AIF data taken from rat MCA. First 500s of overall scan time shown, indicating overall bolus shape. (b) DSC MRI AIF, with smoothed data interpolated to 30s temporal resolution shown in red.

DCE MRI

A dynamic Gadovist concentration map of the rat brain was created, applying equations (2.27) and (2.28) to create a T1 map and then applying equations (2.24) and (2.29) to convert the dynamic signal data into contrast agent concentrations. An experimentally determined relaxivity (r_1) value of 4.2mMs^{-1} was used, the details of which are contained in Appendix I.2. To account for the different relaxivities in blood and in plasma, a $\frac{1}{(1-\text{Hct})}$ factor was applied to the whole blood concentration map to convert the values to plasma concentrations [134], [136], [183], [195] where Hct is the hematocrit, which defines the volume percentage of red blood cells in blood. This conversion process assumed a fixed ratio between the concentration of Gd in whole blood and plasma and employed a hematocrit of 0.44 for rats [158], [187], [277].

The MCA voxels used to extract the first pass AIF from the DSC MRI data were re-sliced into co-registered DCE MRI data by the author and were used to extract the contrast agent AIF curve after the first pass. An example DCE later stage AIF curve is shown in Figure 7.10(b), with its corresponding first pass data (at 30s resolution) shown in Figure 7.10(a).

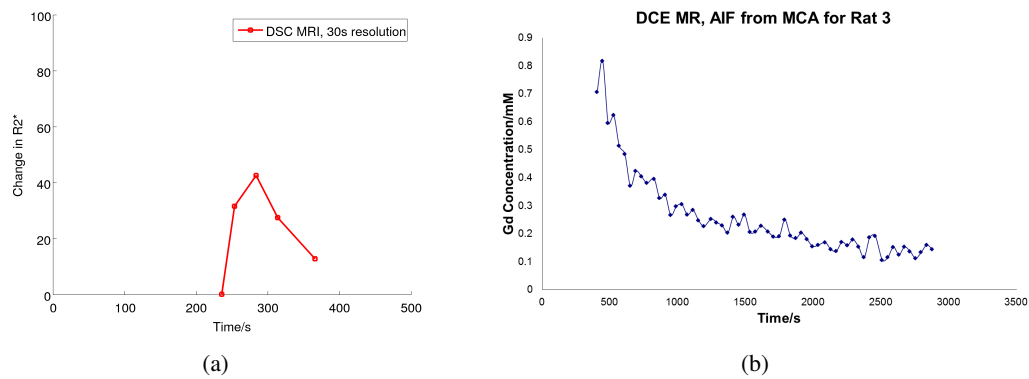


Figure 7.10: (a) DSC MRI data at 30s resolution, showing first pass of AIF in MCA. (b) DCE MRI data showing later stages of AIF taken from MCA for single rat. The first point on this concentration-time curve is used to scale the DSC MRI data to Gd concentrations in mM.

Scaling DSC MRI data using DCE MRI data

A scaling protocol (devised by the author) was attempted by taking the average $\Delta R2^*$ from the last 15 frames of each DSC MRI acquisition at 0.35s resolution and dividing that by the first value (in mM) of the corresponding DCE MRI acquisition. An empirically derived mean scaling factor of 12.6 ± 2.0 (mean \pm SEM) between $\Delta R2^*$ and mM from DCE MRI was calculated as the average for the rat cohort.

Each $\Delta R2^*$ DSC MRI AIF was then divided by this mean scaling factor to scale the DSC MRI data of each rat to values of contrast agent concentration in mM. After scaling, a small baseline was subtracted from the DSC data (now smoothed to 30s temporal resolution), such that the concentration value of the last point of the DSC data matched the concentration value of the first point of the DCE MRI data (i.e. the first DCE MRI scan in Table 7.1). It was manually checked that this also produced DSC MRI AIFs (at 30s resolution) with peaks and curve shapes which roughly matched the concentration values from plasma samples measured by ICP-MS. The DCE and scaled DSC MRI data (at 30s resolution) were then joined together to give a single MRI image-derived AIF, with an example shown in Figure 7.11. The MR AIF is taken directly from MCA in the brain, whilst femoral blood samples are delayed as they must be taken outside of the magnet bore, leading to dispersion and delay of the AIF. A delay correction which matched the peak of each blood sampled AIF to the peak of the combined MRI AIF was applied to the MR data to align it with the blood sampled AIF for comparison, as shown in Figure 7.11(b). This indicates that even with a delay correction applied, the combined DSC and DCE MRI data do not always match the Gd blood sample readings from ICP-MS (see Figure 7.22 for a comparison of all rats), most likely as a result of their different levels of temporal sampling and dispersion between the image-based AIFs and the sampled AIFs. This indicates that these effects must be accounted for when converting between MRI AIFs and a blood sample based PET AIF, in addition to converting them to MBq/ml. It

also indicates that scaling the DSC and DCE data together using mean factors derived for the rat cohort is not ideal.

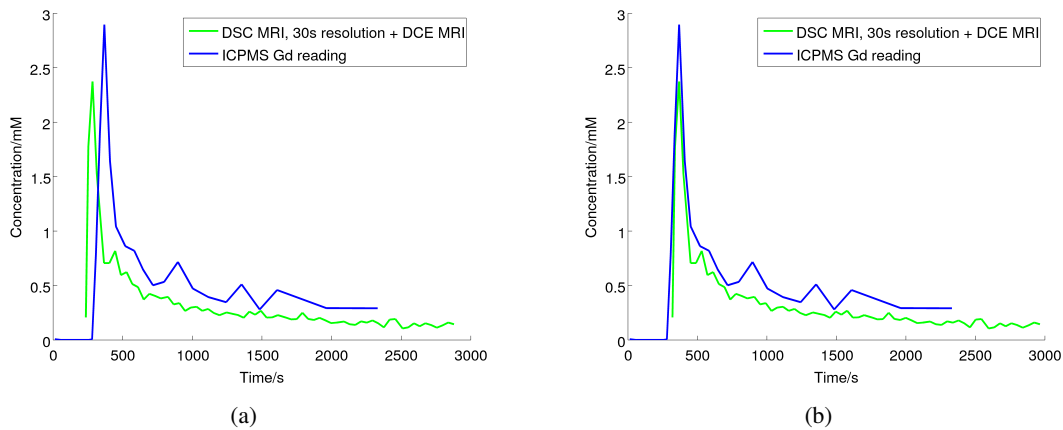


Figure 7.11: (a) Image derived MR AIF taken from a combination of DSC and DCE data compared to blood sampled ICP-MS data. (b) Delay adjusted image-derived MR AIF with peaks aligned for comparison.

7.2.6 AIF conversion method testing

All measured AIFs (FDG AIFs, Gd AIFs, DSC first pass AIFs and DSC/DCE MRI AIFs) were first normalized to their respective peak heights before two conversion methods were tested for evaluation:

1. **Poulin conversion method** This method was tested on the Gd AIFs and DSC/DCE combined MRI AIFs, using a similar conversion methodology to that described in Figure 7.2. All curves were initially fitted with a bi-exponential model (see (7.1)) using the curve fitting function of PMOD. The bi-exponential was convolved with a step function which detailed the delay between the bolus arrival and the beginning of the scan. The step function's fitted width, t_0 , described the injection duration [187]. The bi-exponential models were of the form [187]:

$$y = A_1 \exp(-k_1 t) + A_2 \exp(-k_2 t) \quad (7.1)$$

where A_1 and k_1 are the amplitude and rate constant of the (slow) excretion process, A_2 and k_2 are the amplitude and rate constant of the (fast) extravasation process and t is the time from the injection start. A calculation of the mean rat cohort ratios of the bi-exponential parameters (A_1 , k_1 , A_2 , k_2) between the ^{18}F -FDG and Gd AIFs was then performed. These mean ratios were applied to the bi-exponential parameters of the individual Gd AIFs and MR AIFs to convert them into normalized PET AIFs.

Scaling the converted, fitted and normalized Gadovist and combined MR AIFs to units of MBq/ml

for comparison to the ^{18}F -FDG AIFs was then performed using a plasma sample taken from either the peak of the ^{18}F -FDG AIF, the last point of ^{18}F -FDG AIF (the “endpoint”) or the “midpoint”. The “midpoint” was described as the crossover point between the first pass and the washout of the AIF, mathematically determined by the inequality $0.01\text{MBq/ml} \geq A_1 \exp(-k_1 t)$, where A_1 and k_1 were previously fitted to the bi-exponential model. Figure 7.12 indicates where the peak, “midpoint” and “endpoint” samples lie on a typical AIF. The “midpoint” and “endpoint” were trialled to see if the scaling could be performed with a single blood sample, ideally taken after the first pass phase where temporal sampling of the peak is not critical. All sample values were used to multiply the normalized curves from unitless values to MBq/ml.

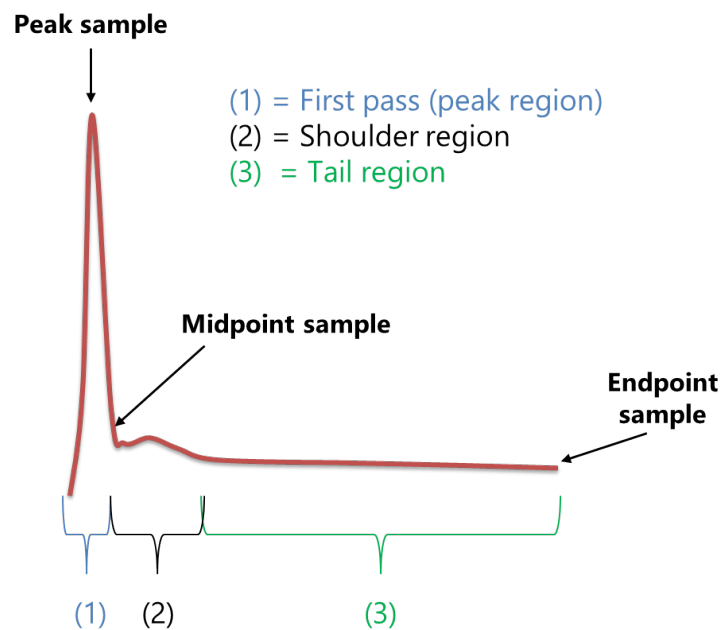


Figure 7.12: AIF schematic indicating the position of the peak, “midpoint” and “endpoint” blood samples used to scale the image-derived AIFs after conversion. The “midpoint” attempts to define a point between the first pass and tail regimes of the AIF, where a single blood sample could be taken if the high temporal sampling needed to define the peak adequately is unavailable. The “endpoint” could be taken after the scan has finished, as a “late” blood sample (as done in Chapter 5).

Alternatively, a non-invasive method was used (referred to as “dose theory”). This method assumed that higher AIF peaks would be produced when greater amounts of tracer activity (per kg) were injected and was observed using empirical measurements taken in this study. To implement “dose theory”, a linear relation was derived between the measured peak height of the ^{18}F -FDG AIF and the ^{18}F -FDG injected activity in MBq/kg and this linear relation was used to estimate the required scaling factor to take curves from unitless values to MBq/ml.

2. **Gamma variate functions** Gamma variate functions were described in Section 3.2.2 and detailed in equations (3.13) and (3.14), as well as in Chapter 6 for DSC MRI. They provide idealized bolus

profiles for first pass MR AIFs, which reduces noise, smoothes out motion effects and eliminates recirculation peaks in the curve data [119], [120], [123], [203], [212], [213] although these can result in reduced peak heights and AUC, as shown in Chapter 6. The gamma variate is also an accepted model for the first pass of PET tracer AIFs [278], and therefore we hypothesise that gamma variate can be measured using MRI and converted into a PET AIF.

The fits were performed as described in Chapter 6, via non-linear Levenberg-Marquardt fitting to the first 500s of the ^{18}F -FDG AIFs and Gadovist AIFs (i.e. 500s on from $t=0$ at injection start, which defined the first pass region of the AIF and this AIF region corresponded to the one measured using DSC MRI). Gamma variates were also fitted to all of the DSC MRI datasets (140s from $t=0$). Default parameters of [1, 0.01, 0.002] (see equation (3.14)) were used in the initial fit and goodness of fit was evaluated using χ^2 test values normalized to the degrees of freedom of the fit, the probability of fit ($1-\chi^2$ cumulative distribution function) and the derivatives of the fit. In addition, a qualitative assessment of fit was performed by eye. If a fit was not achieved or deemed unacceptable using the default parameters, the data selection on the x axis was shortened around the bolus peak until acceptable χ^2 values were attained ($p < 0.02$).

Scaling to MBq/ml for comparison of the Gd gamma variates and DSC MRI gamma variates to ^{18}F -FDG gamma variates was performed by the author using either the peak plasma sample or the non-invasive “dose theory” method to multiply the normalized curves, as described for the Poulin method.

Finally, all scaled and converted AIFs were then compared to the gold standard ^{18}F -FDG AIFs and gamma variates in terms of residuals, AUC, peak height and root mean square difference (RMSD).

7.3 Results

7.3.1 ^{18}F -FDG readings in blood and plasma samples

8 of the 12 rats scanned produced distinct PET tracer AIF curve shapes from their blood and plasma sample well counter readings, with an example shown in Figure 7.13. One rat died 25 minutes into the scanning procedure from a blood clot in the brain, whilst the other 3 gave poor results due to blood clotting and blocking the arterial cannula line, highlighting the difficulty in performing successful serial blood sampling in an MR environment.

A linear correlation between blood and plasma sample peak heights was observed ($R^2 = 0.9543$, see Figure 7.14) and the blood and plasma curve shapes matched well, as expected from the literature [51].

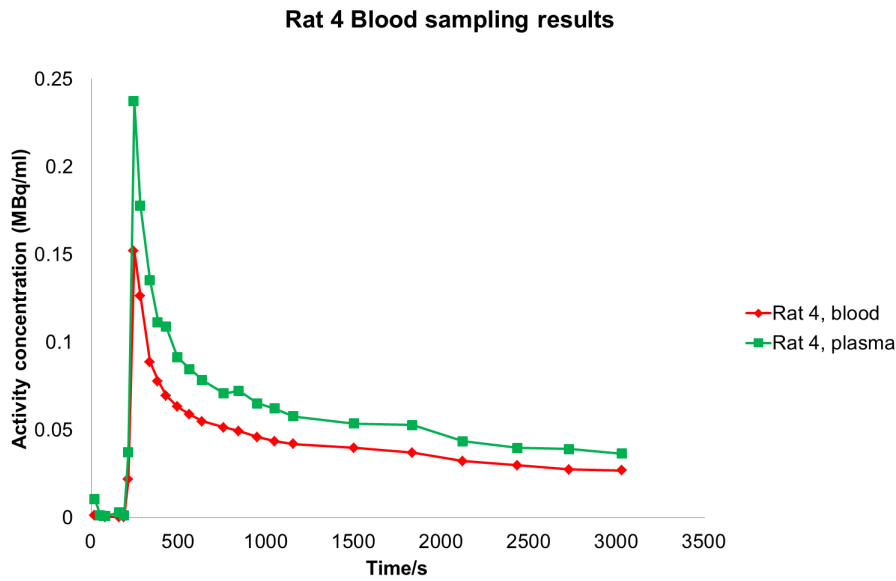


Figure 7.13: Comparison of whole blood and plasma samples of ¹⁸F-FDG from a single rat.

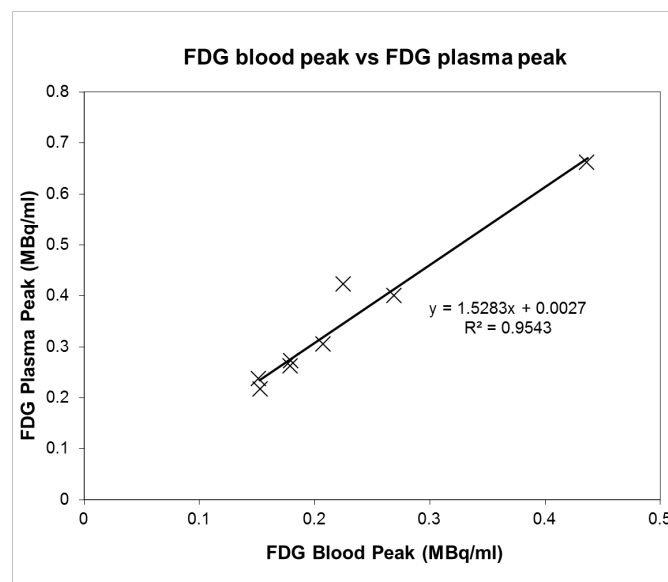


Figure 7.14: Correlation plot of ¹⁸F-FDG blood and plasma sample peak readings.

7.3.2 Repeatability of ICP-MS results for plasma samples

All ICP-MS parameters remained within 5-10% of the of the original results, although in all rats increased noise in the curves obtained was seen on the second run. This must be noted when using the ICP-MS results as a metric, particularly in the case of Rat 11, shown in Figure 7.15. It appears most likely that the freezing, thawing and re-freezing process between the first and second run may have disrupted the cells in some manner, resulting in less uniform aliquots being taken from the water-diluted samples for the second (acid) dilution stage, although further work would be required to isolate the cause of this unexpected increase in noise. The second run data were all much noisier than the first run and did not

fit the known bi-exponential AIF models from the literature [187] as well as the first run data. For the purposes of this experiment, the first run of ICPMS results were used for all rats, as it was unclear why the data from the second run was found to be different from the first run in some rats (but not all, as indicated in Figure 7.15) when the samples had all undergone the same preparation on both runs.

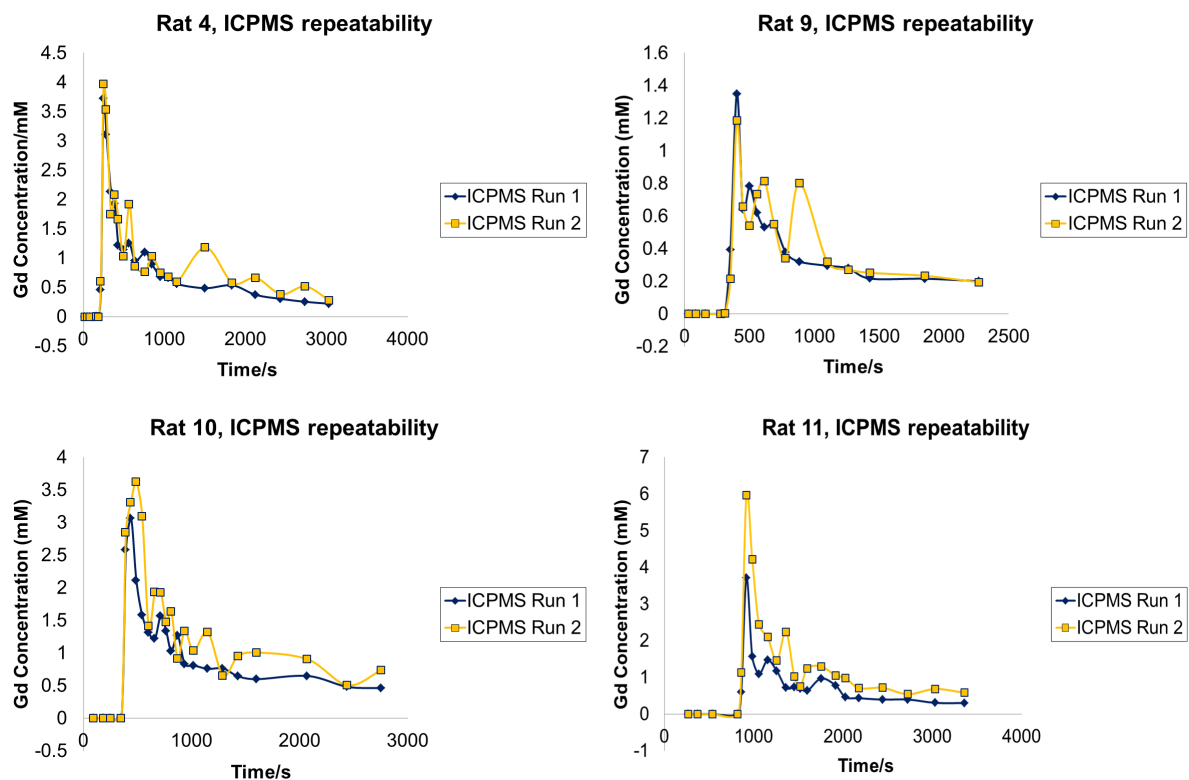


Figure 7.15: Repeatability of ICP-MS results for 4 rats, with samples prepared in an identical manner 1 week after initial ICP-MS measurement.

7.3.3 Comparison between gold standard ^{18}F -FDG and Gd-based contrast agent AIFs

Figures 7.16 and 7.17 show the raw data and the variation between individual AIFs in the rat cohort ($n=8$) for ^{18}F -FDG and Gadovist AIFs respectively.

No clear relation (linear plots, $R^2 < 0.25$) between the Gd contrast agent AIF values and ^{18}F -FDG AIF values was found at either the peak, “midpoint” or endpoint, as shown in the correlation plots in Figure 7.18. This was expected, as the volumes of tracer and contrast agent were kept approximately constant between rats ($\approx 100\text{ml}$ ^{18}F -FDG and $\approx 100\text{ml}$ Gadovist) and the Gd contrast agent dose was the same for all rats (0.1mmol/kg), the injected ^{18}F -FDG activity varied between rats (range: $13\text{--}33\text{MBq}$). The AIFs were therefore normalized before conversion between Gd/MR AIFs and PET AIFs was attempted, as there was no defined relation between mM and MBq/ml values.

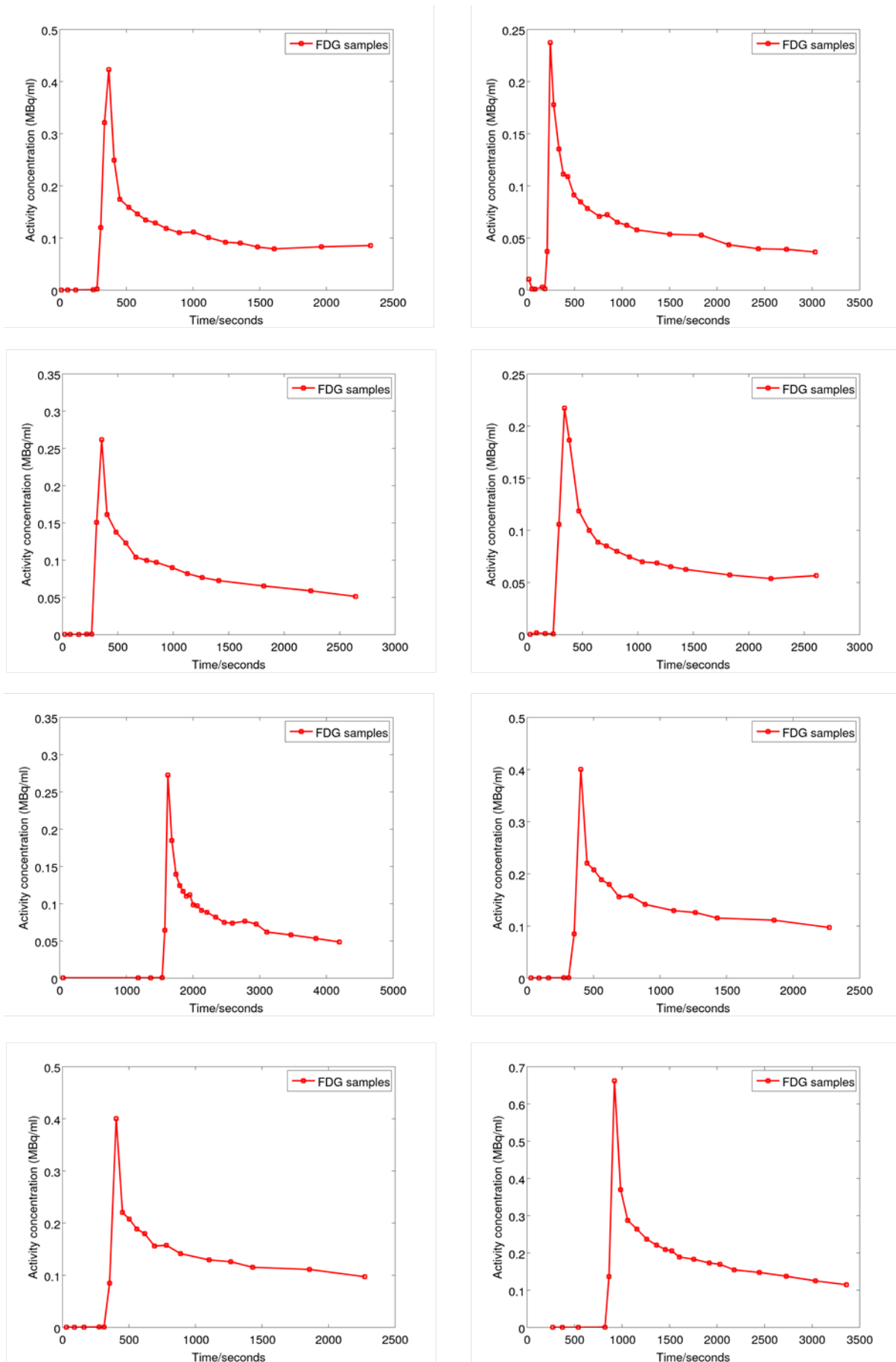


Figure 7.16: Gold standard ^{18}F -FDG AIFs measured using a radioactive well counter for 8 rats. Note different scales selected to highlight similarity of AIF shapes between rats. Peak heights vary due to different rat weights and injected activities.

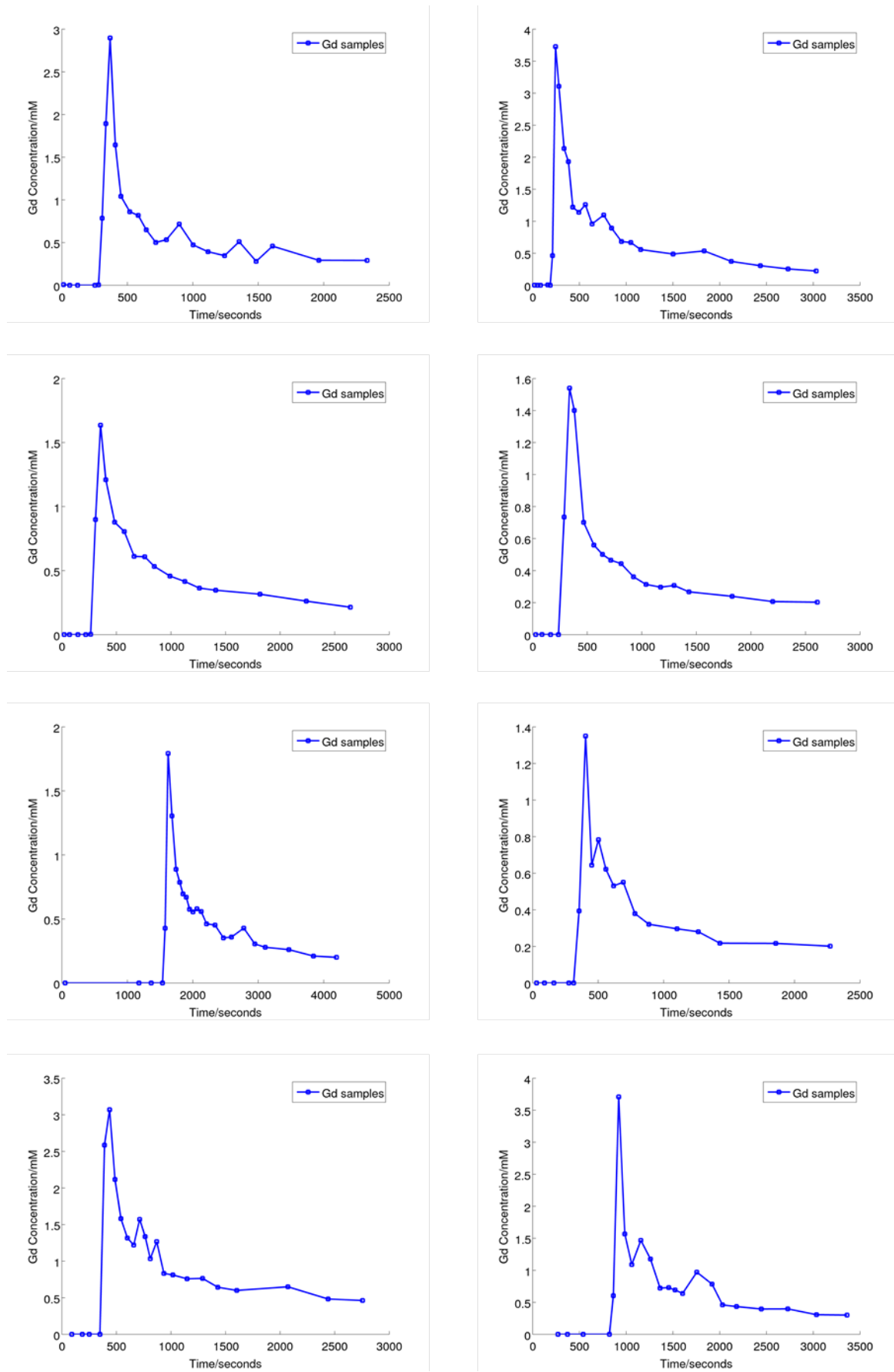


Figure 7.17: Gadovist AIFs measured using ICP-MS for 8 rats. Note different scales selected to highlight similarity of AIF shapes between rats.

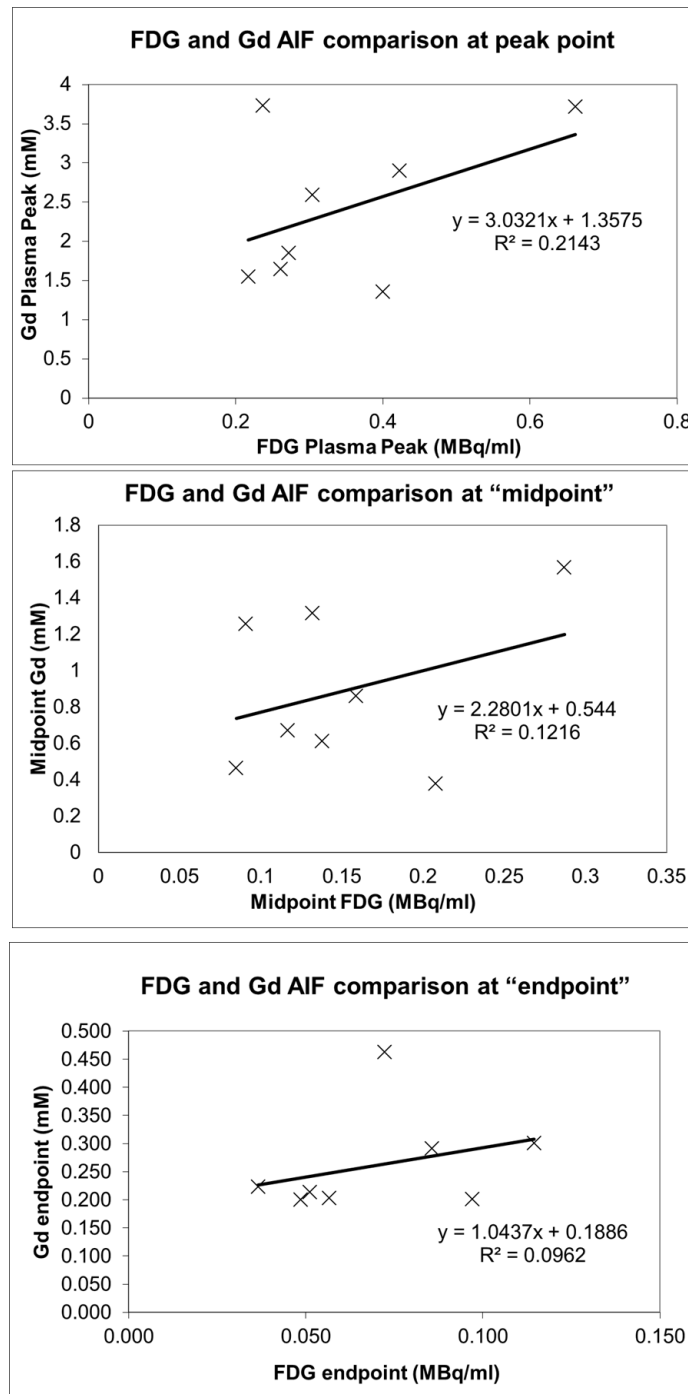


Figure 7.18: Correlation plots between ¹⁸F-FDG and Gd AIFs, taken at the peak of each AIF, the “midpoint” (the point between the first pass and the tail) and the “endpoint” (last recorded value).

Figure 7.19 shows a comparison of AIFs for each rat, after the raw data has been normalized to the maximum peak height and the bi-exponential model fitted to smooth out the noise present in the data. All rats show similar profiles for Gd contrast agent AIFs and ¹⁸F-FDG AIFs, with the expected pattern of agreement within the first pass phase that was previously published [54], with increasing disagreement into the washout region (see Figure 7.3).

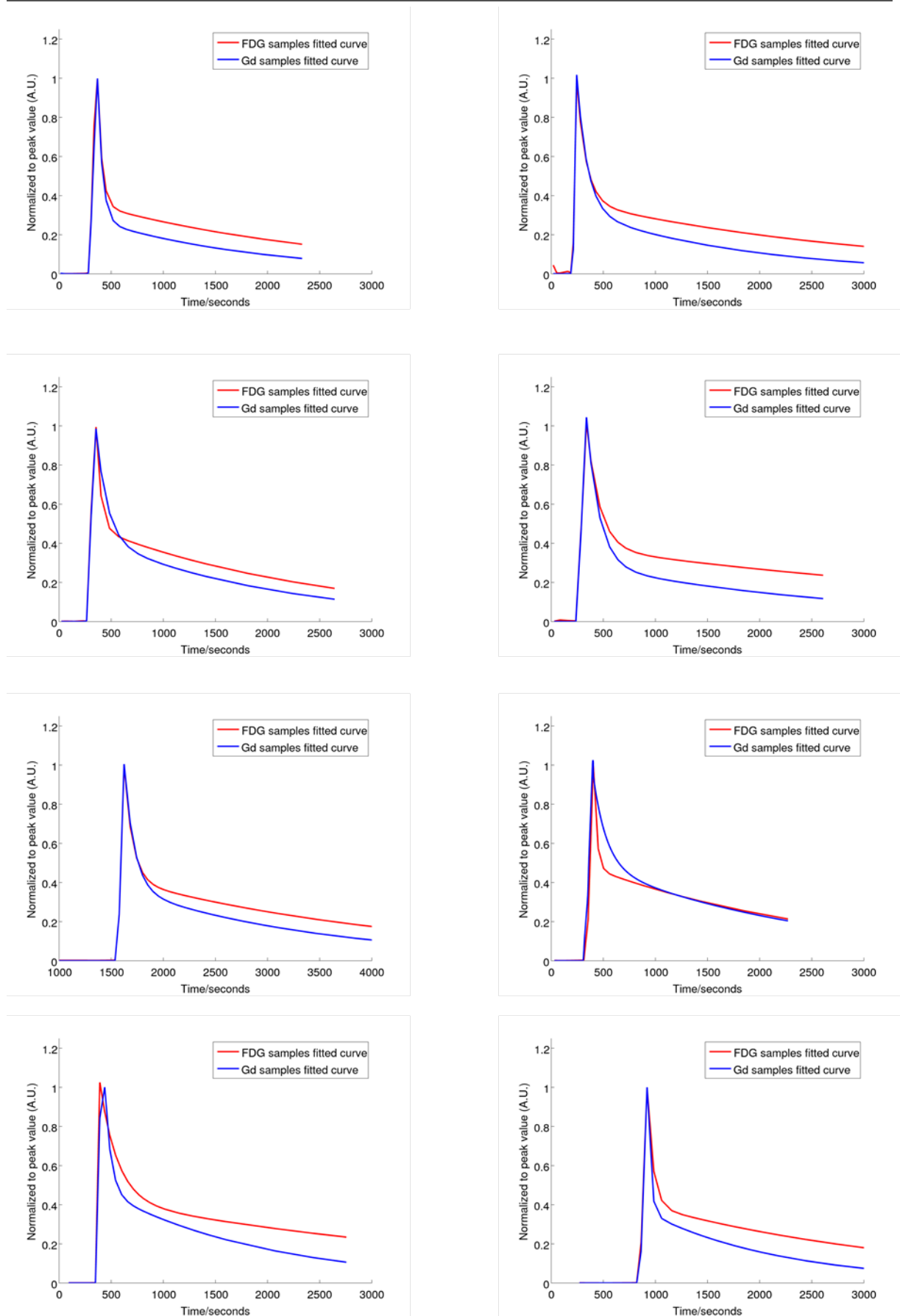


Figure 7.19: Comparison of ^{18}F -FDG and Gd contrast agent AIFs after peak height normalization and bi-exponential fitting for 8 rats. Whilst the first pass phase is similar in both modalities, at later time points the divergence between the ^{18}F -FDG and Gd curves is clear in all but 1 of the 8 rats.

7.3.4 Scaling of DSC MRI data to create combined DSC and DCE MRI AIFs

To create the combined MRI AIFs, DCE data was used to scale the DSC MRI AIFs extracted from the first pass region to values of contrast agent concentration (mM). A linear relation (see Figure 7.20) was found between the maximum DCE point (first DCE scan) and the “midpoint” of the Gd contrast agent AIFs, which occurred at similar points in the AIF profile (middle of the “shoulder” region, mathematically determined by the inequality $0.01\text{MBq/ml} \geq A_1 \exp(-k_1 t)$ from the fitted bi-exponentials).

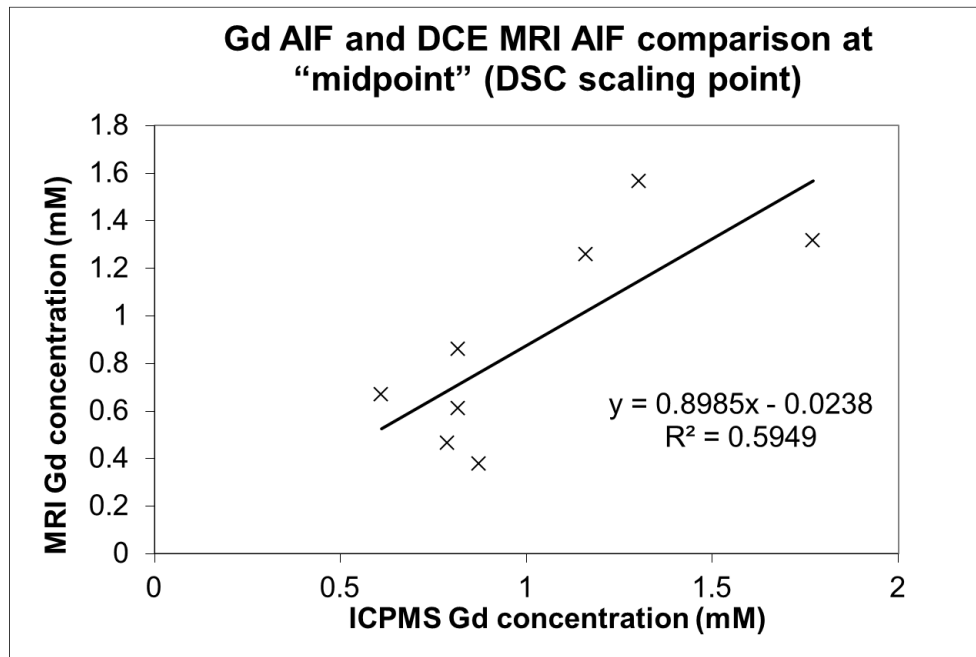


Figure 7.20: Correlation plot of “midpoint” values between Gd AIFs and first point of DCE AIFs. “Midpoint” is defined as the transition between the first pass phase and the tail phase of the AIF.

No clear relationship between $\Delta R2^*$ seen at the peak of the DSC MRI AIFs and the peak value of the blood sampled Gd AIFs was evident, as shown in Figure 7.21. This relation was improved by scaling the data using the DCE MRI curves as a baseline to add to the DSC MRI data and create the combined DSC/DCE MRI AIFs. The values shown here reflect the agreement between the peak values of the combined MRI AIFs and the Gd AIFs once a mean scaling factor for the cohort was applied to each rat’s DSC MRI data. Agreement in the linear plots increases from $R^2 < 0.30$ to $R^2 > 0.55$ for both the full temporal resolution (0.35s) DSC MRI data and the smoothed, 30s resolution data, which was used to complement the temporal resolution of the blood sampling data. Comparisons between Gd AIFs and MRI AIFs are shown in Figure 7.22 for each rat.

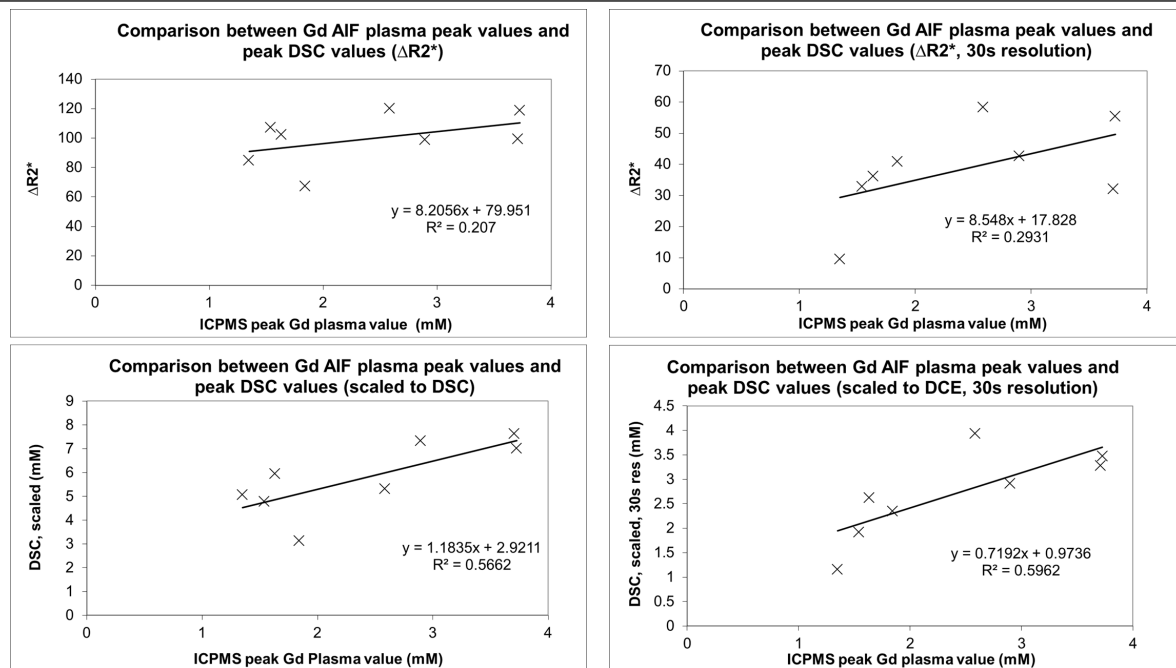


Figure 7.21: Correlation plots between DSC MRI AIF and Gd AIF peak values. Top row: (Left) Change in $R2^*$ plotted against peak Gd concentration, (Right) Smoothed $R2^*$ data at 30s resolution. Bottom row: (Left) Scaled Gd concentration from combined DSC and DCE MRI data, plotted against peak Gd concentration, (Right) Smoothed data at 30s resolution.

7.3.5 Comparison between image-derived MR AIFs and Gd-based contrast agent AIFs

A delay correction was required to align the peaks of the DSC and DCE MRI data with the blood sample data, after which better agreement was found between the scaled MRI data and the Gd contrast agent samples. This difference is a result of both dispersion present in the blood sampling line and a consequence of the delay between the sampling of the blood in the artery and the collection of the blood in each eppendorf. Neither of these effects were present in the MRI data, as measurements were taken directly from the rat brain non-invasively. A comparison of the delay corrected MRI AIFs and the blood sampled Gd contrast agent AIFs for all rats is shown in Figure 7.22.

The low temporal sampling of the blood sampled data did lead to undersampling of the AIF peak whilst the smoothed DSC MRI data at 30s resolution did not undersample it, leading to inaccuracies between the resulting AIFs, as shown in Figure 7.22, with the residuals between them (defined as Gd AIF - DSC/DCE MRI AIF) shown in Figure 7.23. Larger residuals ($> \pm 1$) are seen where the peak has been underestimated by the plasma samples compared to the combined DSC/DCE MRI AIF and are also seen when the mean scaling factor for the group was not optimum for each rat. This also resulted in mismatches between the shapes of the normalized and bi-exponential fitted MRI AIFs and both sets of blood sampled AIFs after normalization to peak height, as indicated in Figure 7.24. This indicates that combining DSC and DCE MRI data together using a mean scaling factor for the group does not produce

a good estimation of the Gd contrast agent AIF, particularly when a bi-exponential model is fitted to this data. A separate set of conversion factors were therefore calculated for the DSC/DCE MRI AIFs to change them to ^{18}F -FDG AIFs and to see if consistent conversion from MR to PET AIFs was possible using the Poulin conversion method.

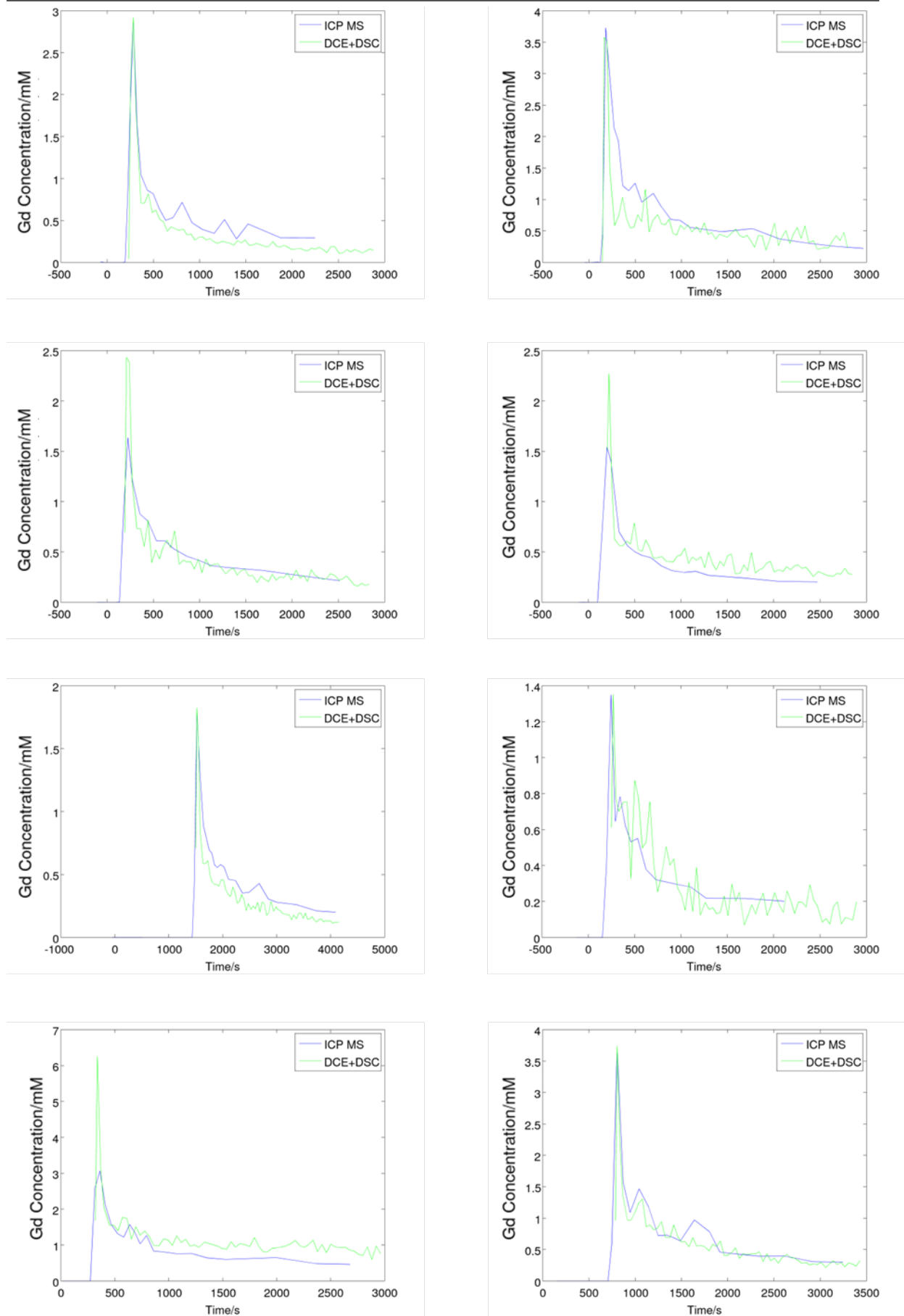


Figure 7.22: Comparison of scaled DSC and DCE MRI AIFs and Gd contrast agent AIFs for all 8 rats. There is good agreement between the MRI and blood sampled AIFs in some rats, but in others the varying temporal resolution of the blood samples led to mismatches when the mean scaling factor for the group was applied.

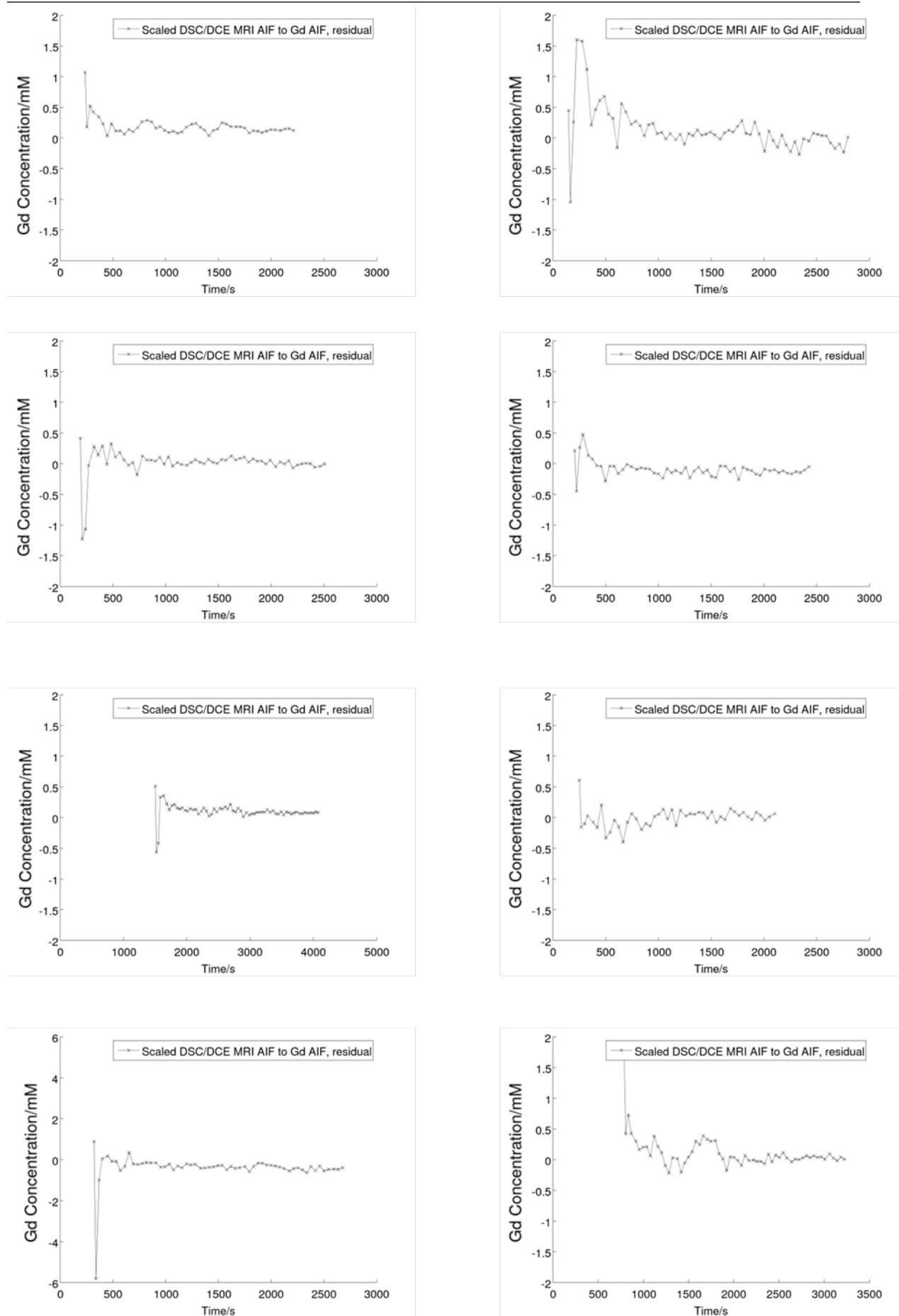


Figure 7.23: Residuals between scaled DSC/DCE MRI AIFs and Gd contrast agent AIFs for all 8 rats. Note the changed scale on rat 7 (bottom row, left) where the mismatch in temporal sampling leads to a very large residual around the peak region.

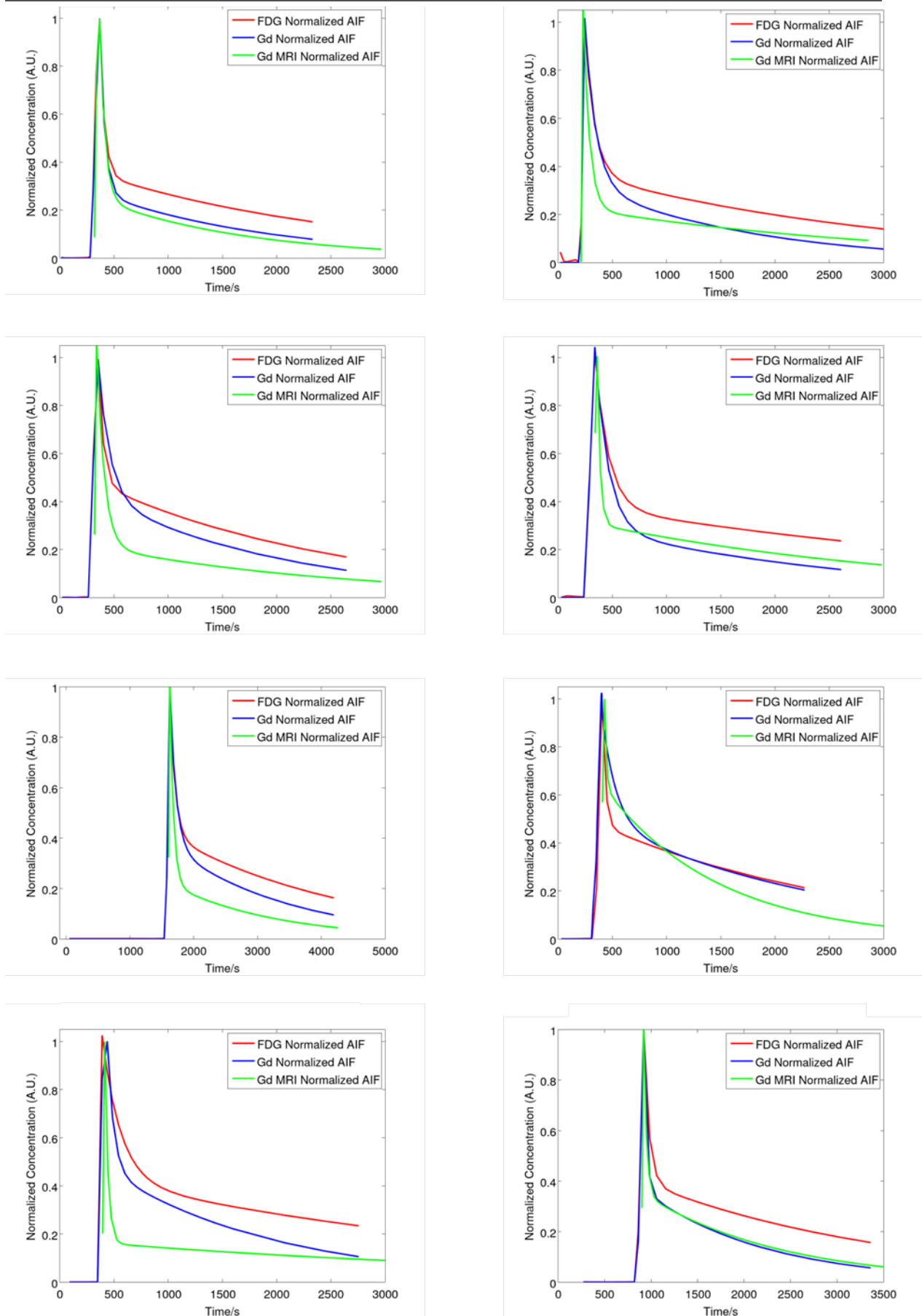


Figure 7.24: Comparison of normalized MRI AIFs, Gd contrast agent AIFs and ^{18}F -FDG AIFs fitted with bi-exponential model. Different shapes were seen in MRI AIFs compared to both blood sampled AIFs due to temporal sampling mismatch between the techniques, which then results in different bi-exponential curve shape fits.

7.3.6 Conversion between MR image-derived AIFs, Gd-based contrast agent AIFs and ^{18}F -FDG AIFs

Poulin method

The average fitted bi-exponential parameters to the ^{18}F -FDG, Gd and MRI AIFs are shown in Table 7.2. The Gd contrast agent AIFs and ^{18}F -FDG AIFs show similar A_1 and k_1 values (0.59 ± 0.05 compared to 0.63 ± 0.10 and 0.91 ± 0.54 compared to 0.99 ± 0.41), indicating agreement in the excretion (slow) rates, similarly to those previously described [54], although greater variation is reported in this study. This is most likely due to the dispersion and delays caused by the long cannulas required to perform blood sampling in the MRI scanner rather than a PET scanner. Although the amplitudes of the extravasation (fast) rates (A_2 , 0.41 ± 0.05 compared to 0.37 ± 0.08) do agree between the ^{18}F -FDG and Gd AIFs, the rate constant k_2 does not agree (34.94 ± 11.01 compared to 20.82 ± 4.47). This is expected from the known kinetic behaviour of the two compounds and was also seen in the previously published results [54], as is the decrease in k_2 reported for Gd AIFs compared to ^{18}F -FDG AIFs.

Modality	A_1	k_1	A_2	k_2
FDG AIF	0.59 ± 0.05	0.91 ± 0.54	0.41 ± 0.05	34.94 ± 11.01
Gadovist AIF	0.63 ± 0.10	0.99 ± 0.41	0.37 ± 0.08	20.82 ± 4.47
DSC/DCE MRI AIF	0.74 ± 0.13	0.48 ± 0.22	0.29 ± 0.11	26.79 ± 13.48

Table 7.2: Bi-exponential parameters of all normalized rat AIFs (n=8, mean \pm std for cohort)

The linear correlation plots between the bi-exponential parameters over the rat cohort between the ^{18}F -FDG AIFs and the Gd AIFs are shown in Figure 7.25 and the corresponding plots for the ^{18}F -FDG AIFs and the MRI AIFs are shown in Figure 7.26. Correlation is seen between both sets of amplitude parameters in Figure 7.25 for the ^{18}F -FDG and Gd AIFs, although only limited correlation is seen in the k_2 parameter. No correlation is seen in the k_1 parameter values. This pattern is also seen in Figure 7.26, although much less correlation is seen between both sets of amplitude parameters in this case, but greater correlation is seen in the k_2 parameter. These plots indicate that whilst the k_1 parameter average values for the cohort may agree between ^{18}F -FDG AIFs and Gd AIFs, they do not agree on an individual basis and this makes it difficult to convert the AIFs reliably between modalities using the method proposed by Poulin et al. [54]. The decreased correlation between the amplitude A_1 and A_2 values (and increased correlation in the k_2 value) seen in Figure 7.26 are most likely a result of the temporal mismatch, delay and dispersion between the Gd AIFs and the MRI AIFs, resulting in a different shoulder region of the bi-exponential AIFs.

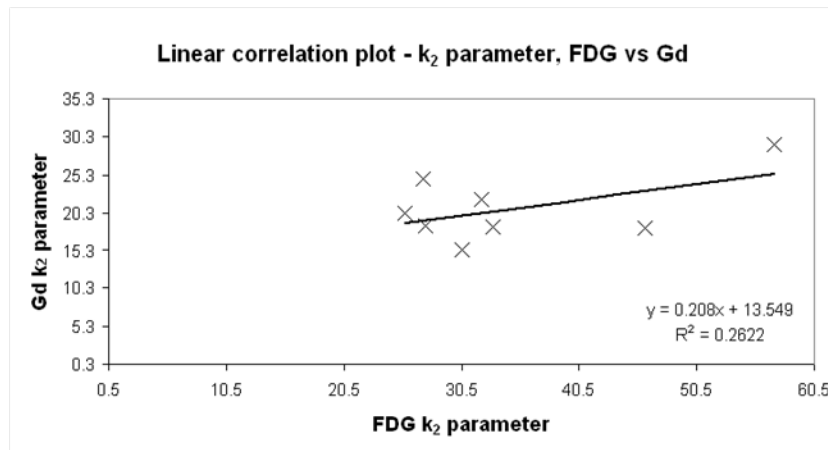
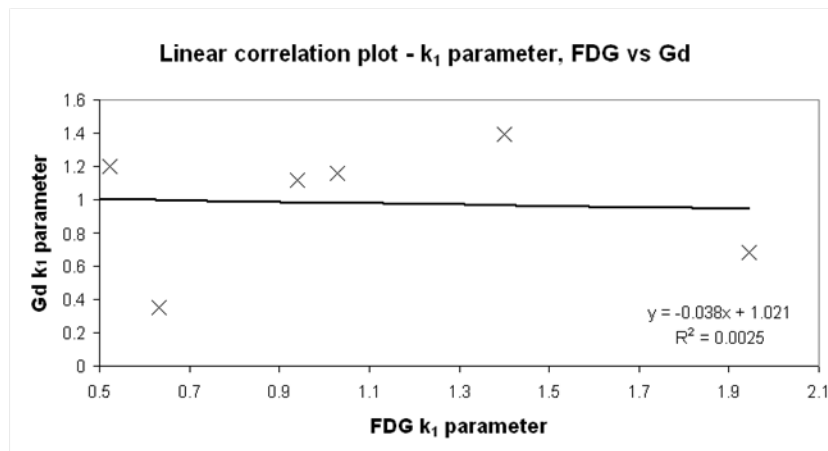
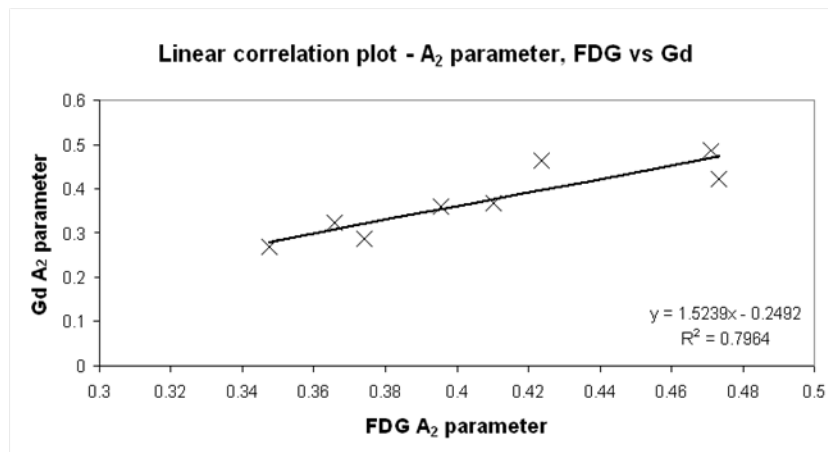
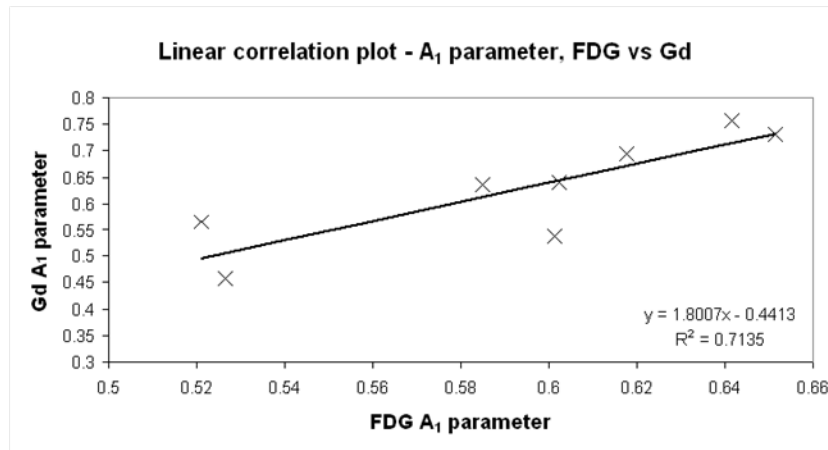


Figure 7.25: Linear correlation plot comparison of bi-exponential AIF parameters calculated for ¹⁸F-FDG and Gd AIFs. From top: Amplitude parameters A₁ and A₂, followed by rate constants k₁ and k₂. Correlation is seen between the amplitude parameters but only little correlation is seen between the k₂ parameters. No correlation is seen in the k₁ parameter.

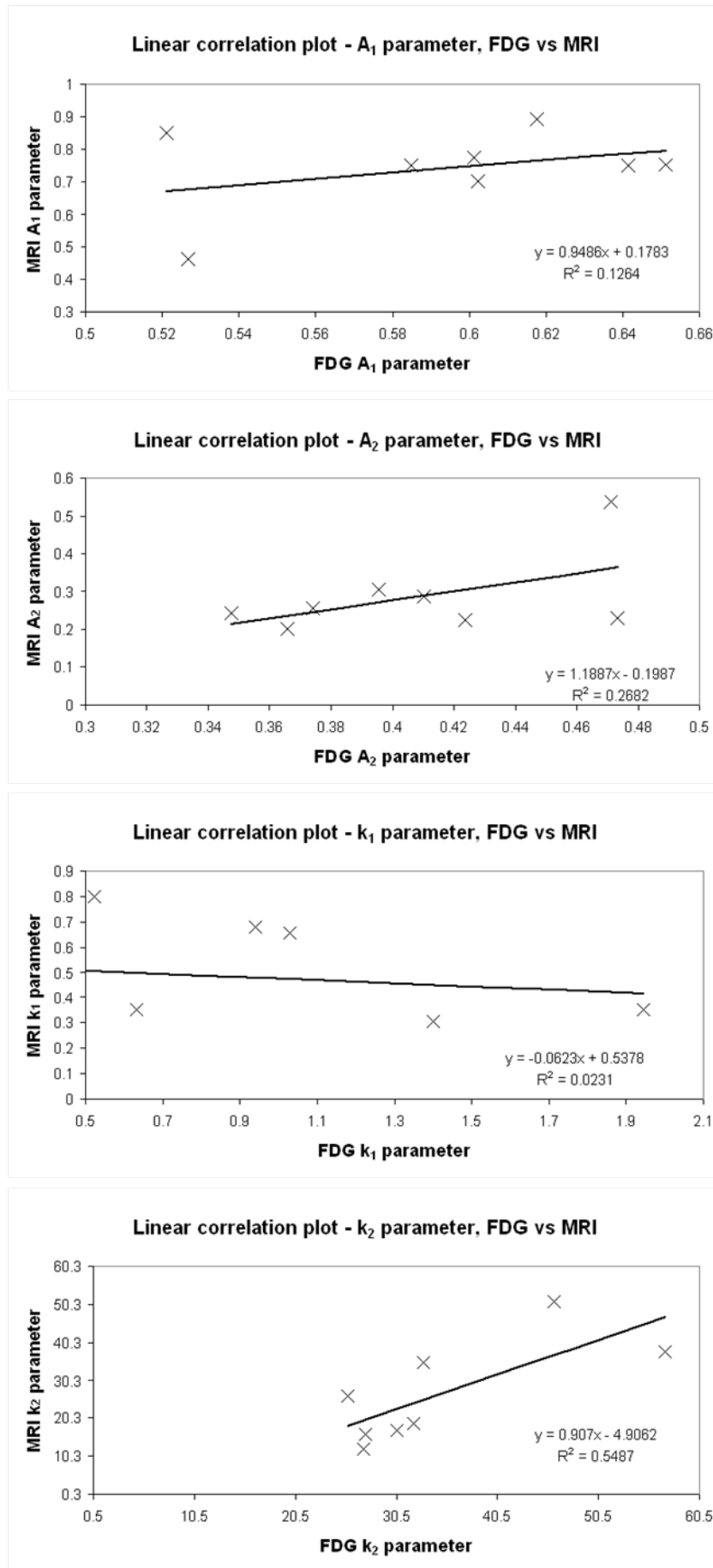


Figure 7.26: Linear correlation plot comparison of bi-exponential AIF parameters calculated for ¹⁸F-FDG and MRI AIFs. From top: Amplitude parameters A₁ and A₂, followed by rate constants k₁ and k₂. Less correlation with the ¹⁸F-FDG AIFs is seen in A₁ and A₂ compared to the Gd AIFs, but k₂ shows increased correlation.

The conversion between Gadovist AIFs and ¹⁸F-FDG AIFs was performed by taking the average ratios of their amplitudes and rate constants across the group, which are shown in Table 7.3.

Conversion	A ₁	k ₁	A ₂	k ₂
Gd to FDG	0.96±0.11	1.12±0.85	1.12±0.14	1.70±0.47
MRI to FDG	0.86±0.26	2.33±1.83	1.61±0.62	1.47±0.48

Table 7.3: Average ratios for cohort used to convert between modalities (n=8) using Poulin Method

Due to the temporal mismatch, dispersion, delay and estimated scaling between the DSC MRI and Gd contrast agent AIFs, the resulting DSC/DCE MR AIFs show little agreement between each set of rate constants for either ¹⁸F-FDG or Gd AIFs and present different curve shapes, as shown in Figure 7.24. This indicates that this combined MRI method (on average) does not produce AIFs which are similar to PET AIFs. A separate set of empirical parameter ratios were still calculated and used to convert the DSC/DCE AIFs into ¹⁸F-FDG AIFs to observe the results. These ratios are also shown in Table 7.3.

Figure 7.27 shows the normalized curves after conversion using the ratios in Table 7.3, with good agreement seen between converted Gd AIFs and ¹⁸F-FDG AIFs for 7 out of 8 rats and combined MRI AIFs also displaying good agreement in 4 of 8 rats. Figure 7.28 shows the residuals, defined as (FDG AIF - converted Gd/MRI AIF). The greatest differences are still observed between the MRI AIFs and ¹⁸F-FDG AIFs, mainly in the “shoulder” region of the AIF, even after conversion using the mean ratios derived for the rat group. Large differences were seen over a small region where the peak alignment of the MRI AIFs and ¹⁸F-FDG AIFs was not optimal. The differences in the peak and “shoulder” regions were also seen with the converted Gd AIFs compared to the ¹⁸F-FDG AIFs, but to a much lesser extent, as confirmed by the residuals, which indicated good agreement with previously published results [54]. This suggests that there is also greater variation across the DSC/DCE MRI AIFs for the rat group, possibly due to the varying degrees of temporal mismatch, dispersion and delay between the DSC/DCE MRI AIFs and the blood samples for each rat. This could also be due to inaccurate Gd concentration values estimated by DCE MRI resulting in DSC MRI scaling errors, as several rats show underestimation or overestimation of the Gd AIF in the tail phase in Figure 7.22. In addition, the scaling between DSC and DCE MRI was generalised but this appears to not be entirely accurate and would require individual optimization of the DSC to mM scaling factors to work, which is not practical when attempting to create a general method for MRI AIF to PET AIF conversion.

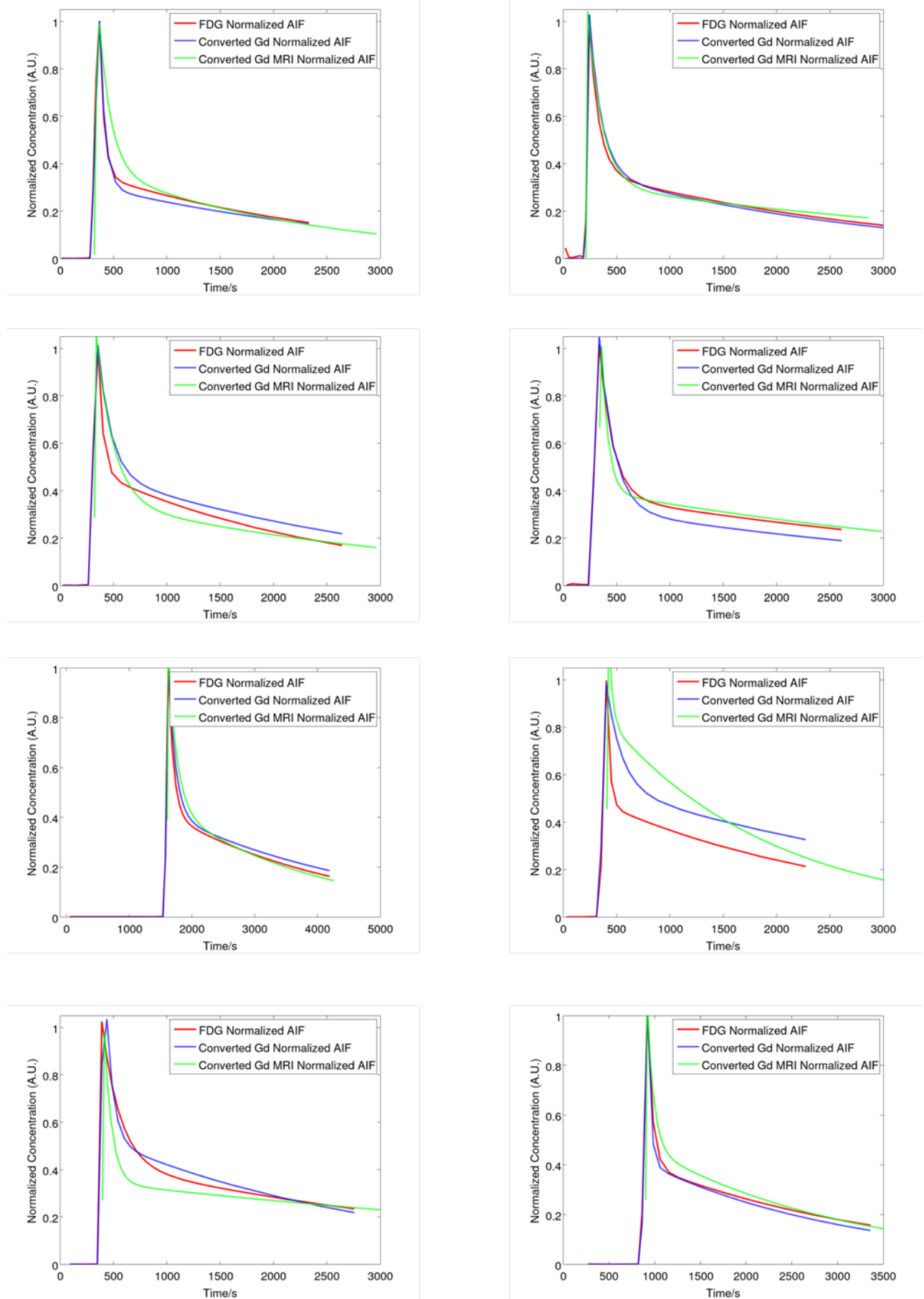


Figure 7.27: Comparison of normalized and converted DSC/DCE MRI AIFs, Gd AIFs and normalized ^{18}F -FDG AIFs (same order of plots as Figure 7.24). There is good agreement between converted Gd AIFs and ^{18}F -FDG AIFs in some rats and more limited agreements in others. Mismatch in temporal sampling results in disagreement in some rats between converted MRI AIFs and ^{18}F -FDG AIF curve shapes, even after application of the mean conversion ratios listed in Table 7.3.

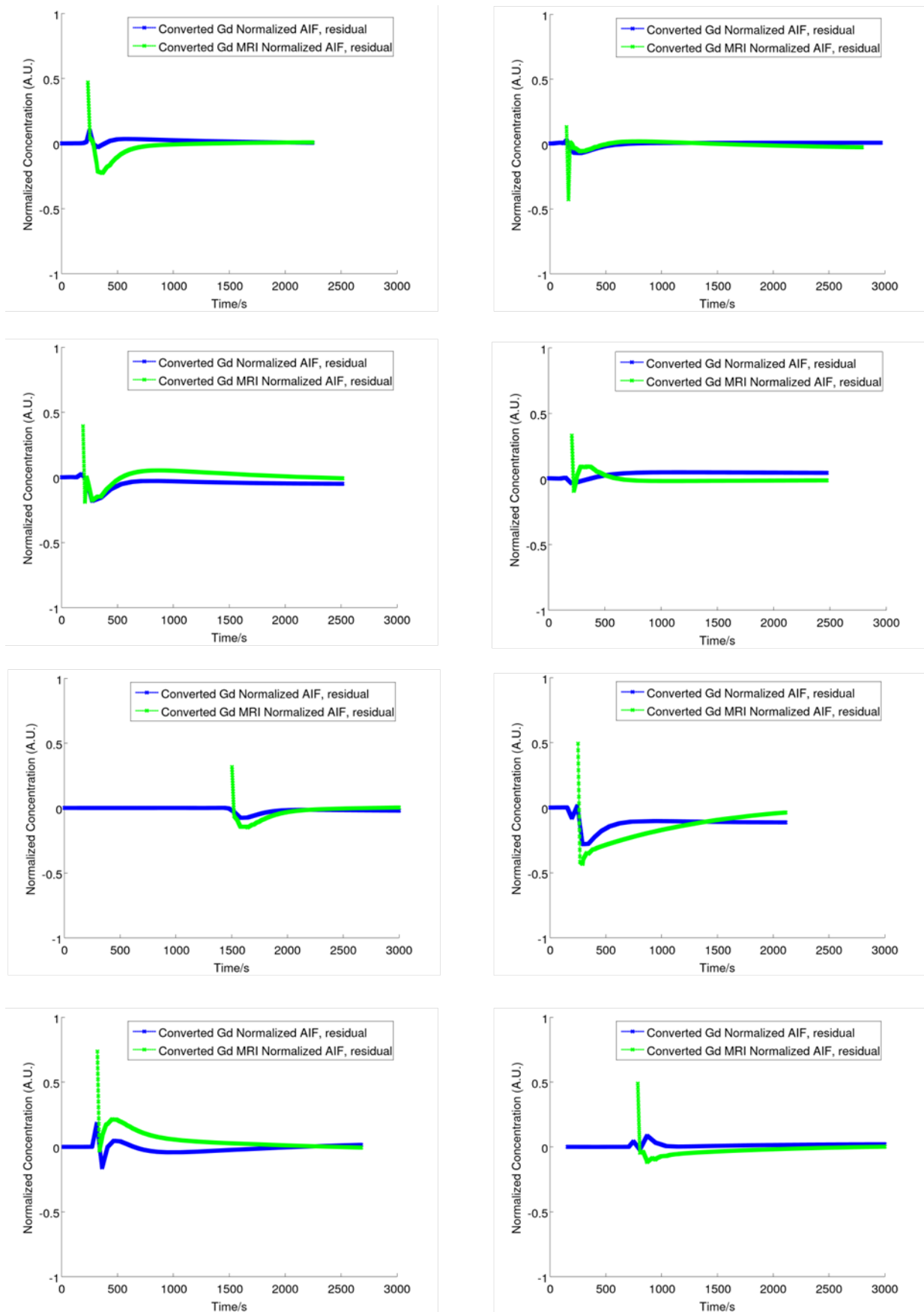


Figure 7.28: Residuals between normalized and converted MRI AIFs, Gd contrast agent AIFs and ^{18}F -FDG AIFs, indicating greatest differences seen with MRI AIFs, mainly in the “shoulder” region of the AIF. These differences also seen with the Gd AIFs, but to a lesser extent.

The linear relation between peak height, “midpoint”, “endpoint” and injected activity in MBq/kg are shown in Figure 7.29. The best correlation was found with the peak heights, which was used as the non-invasive scaling relation for the “dose theory” scaling.

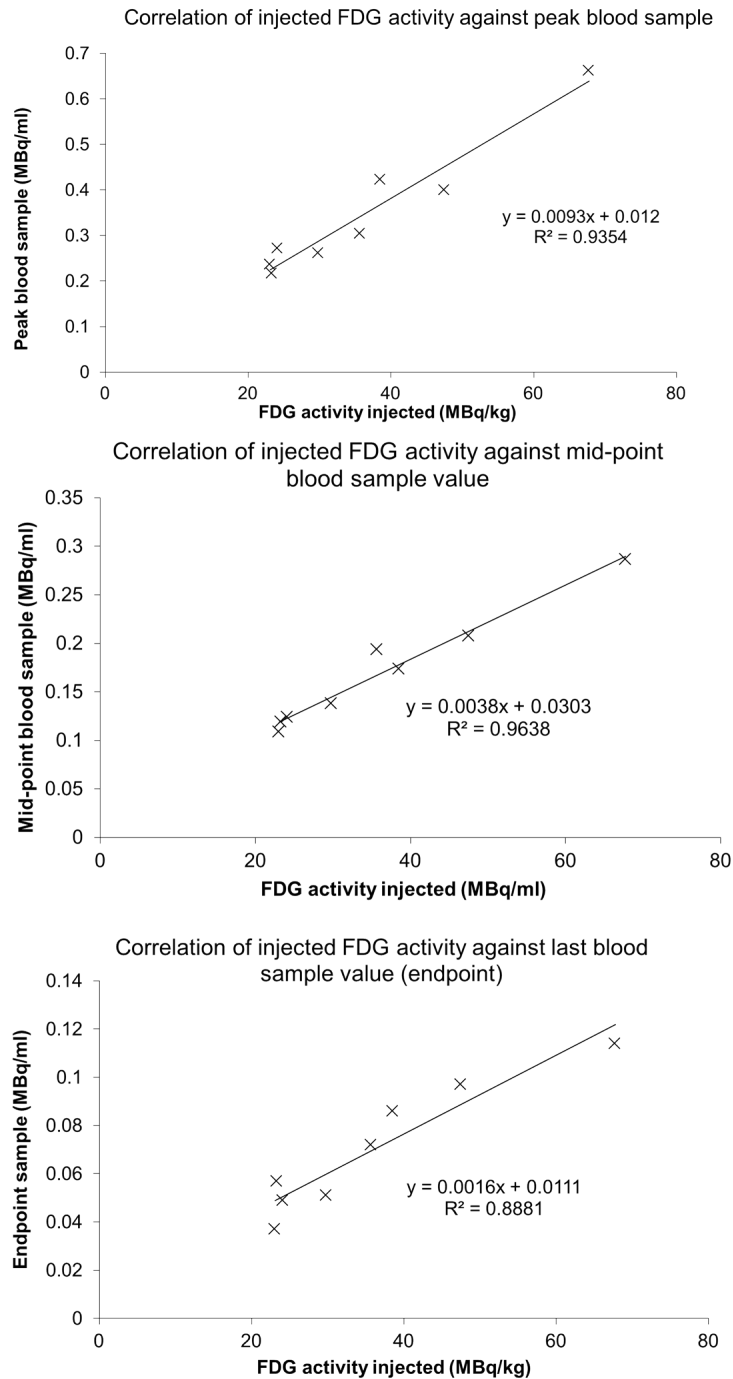


Figure 7.29: Linear relationships between injected activity and measured ¹⁸F-FDG peak heights, “mid-points” and “endpoints”. Best correlation found with peak heights.

An example of the comparison between the ¹⁸F-FDG AIF in MBq/ml and the AIFs produced using each sample scaling method (peak, “midpoint” and “endpoint”) is shown in Figure 7.30 for the Gd contrast agent AIFs, with the non-invasive scaling technique results (labelled as “dose theory”) are compared

to the peak scaled AIFs in Figure 7.31. The residuals between the ^{18}F -FDG AIFs and the scaled AIFs (defined as ^{18}F -FDG AIF - scaled AIF) are shown for the Gd AIFs in Figure 7.32.

Figure 7.33 shows the peak, “midpoint” and “endpoint” scaled MRI AIFs for all rats and Figure 7.34 shows the “dose theory” MR AIFs compared to the peak scaled AIFs. The MRI AIF residuals (compared to the ^{18}F -FDG AIFs) are shown in Figure 7.35.

The greatest differences to the PET AIFs for both Gd and MRI AIFs were found at the end of the first pass region and the beginning of the “shoulder” region, with these differences exaggerated in the MRI AIFs due to the junction between DSC and DCE MRI occurring in this region. It must be noted that the scaling in the MRI AIF residuals in Figure 7.35 is five times (± 1 compared to ± 0.2) that of the Gd AIF residuals in Figure 7.32, indicating the scale of the differences between the ^{18}F -FDG AIFs and the DSC/DCE MRI AIFs compared to the ^{18}F -FDG AIFs and the Gd AIFs.

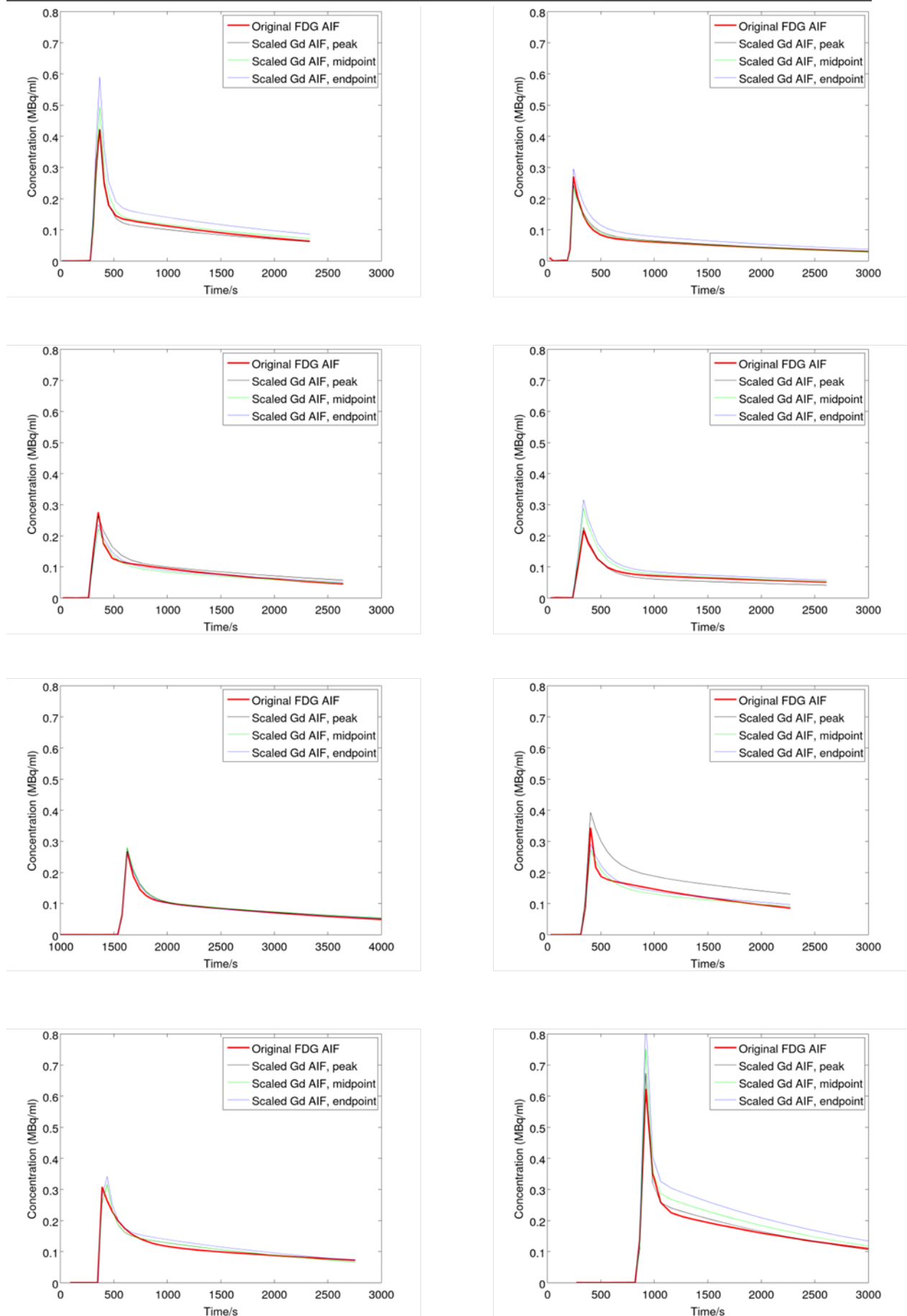


Figure 7.30: Comparison of scaling methods applied to Gd contrast agent AIFs converted into ^{18}F -FDG AIFs via the Poulin method, using blood samples taken at the peak of the AIF, the crossover point of the first pass (the “midpoint”) and the last blood sample taken (the “endpoint”).

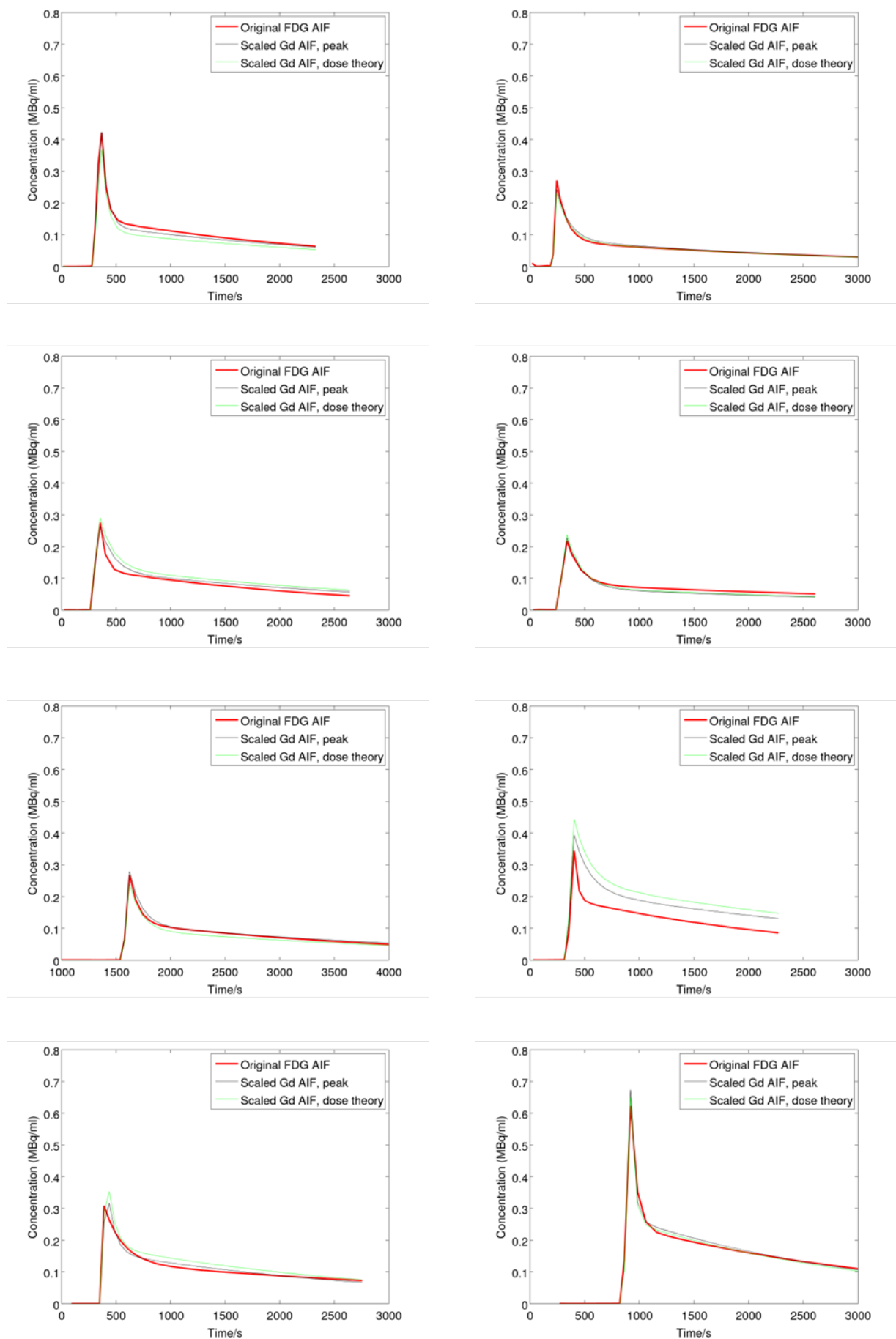


Figure 7.31: Comparison of scaling methods applied to Gd contrast agent AIFs converted into ^{18}F -FDG AIFs via the Poulin method, using a fully non-invasive dose relation scaling method. The non-invasive method appears as effective as direct scaling by the peak height for the majority of rats scanned.

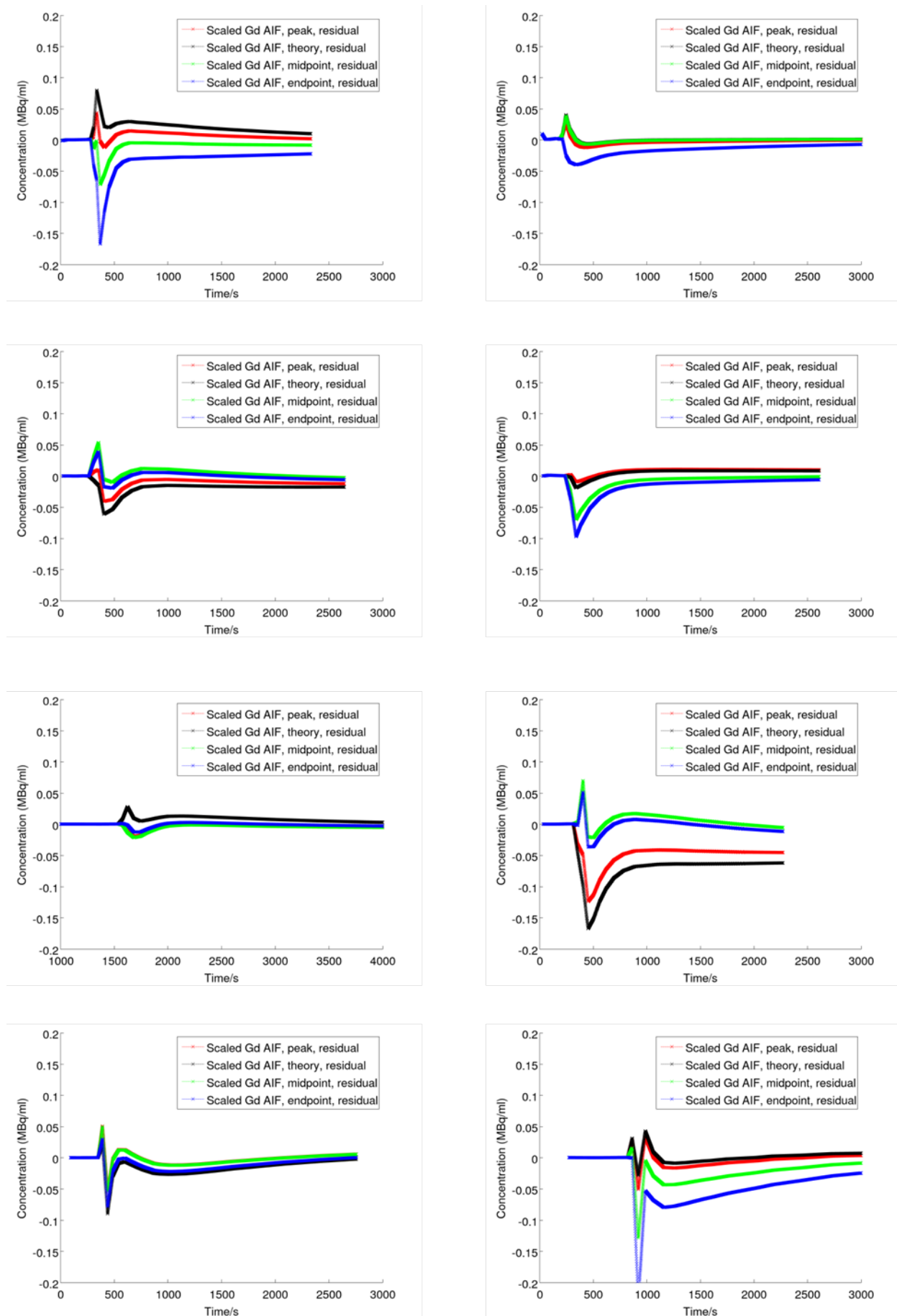


Figure 7.32: Residuals between normalized, converted and scaled Gd contrast agent AIFs and ^{18}F -FDG AIFs, indicating greatest differences in the end of the first pass and in the “shoulder” region of the AIF, with decreasing differences towards end of AIF tail.

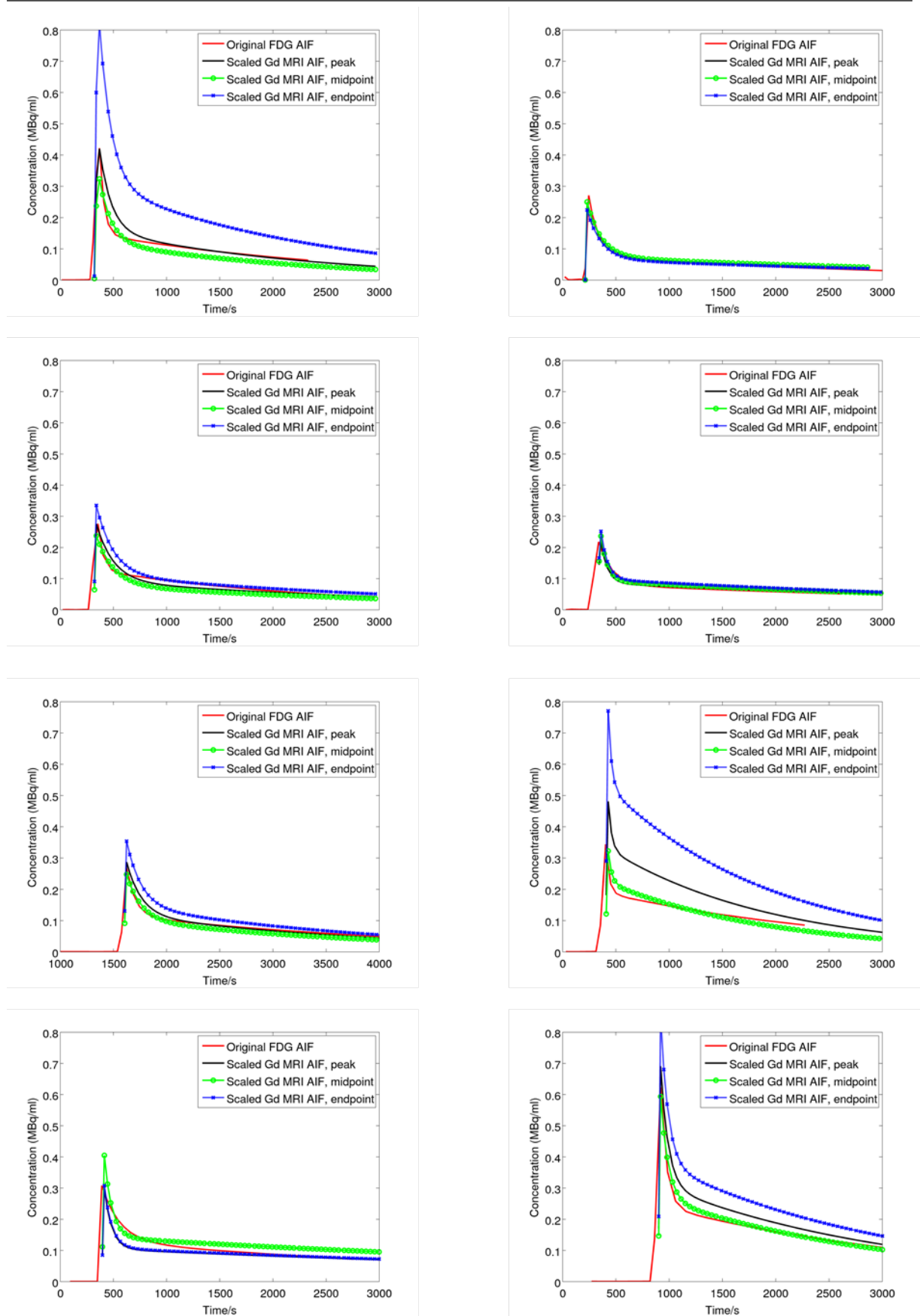


Figure 7.33: Comparison of scaling methods applied to MR AIFs converted into ^{18}F -FDG AIFs via the Poulin method, using blood samples taken at the peak of the AIF, the crossover point of the first pass (the “midpoint”) and the last blood sample taken (the “endpoint”).

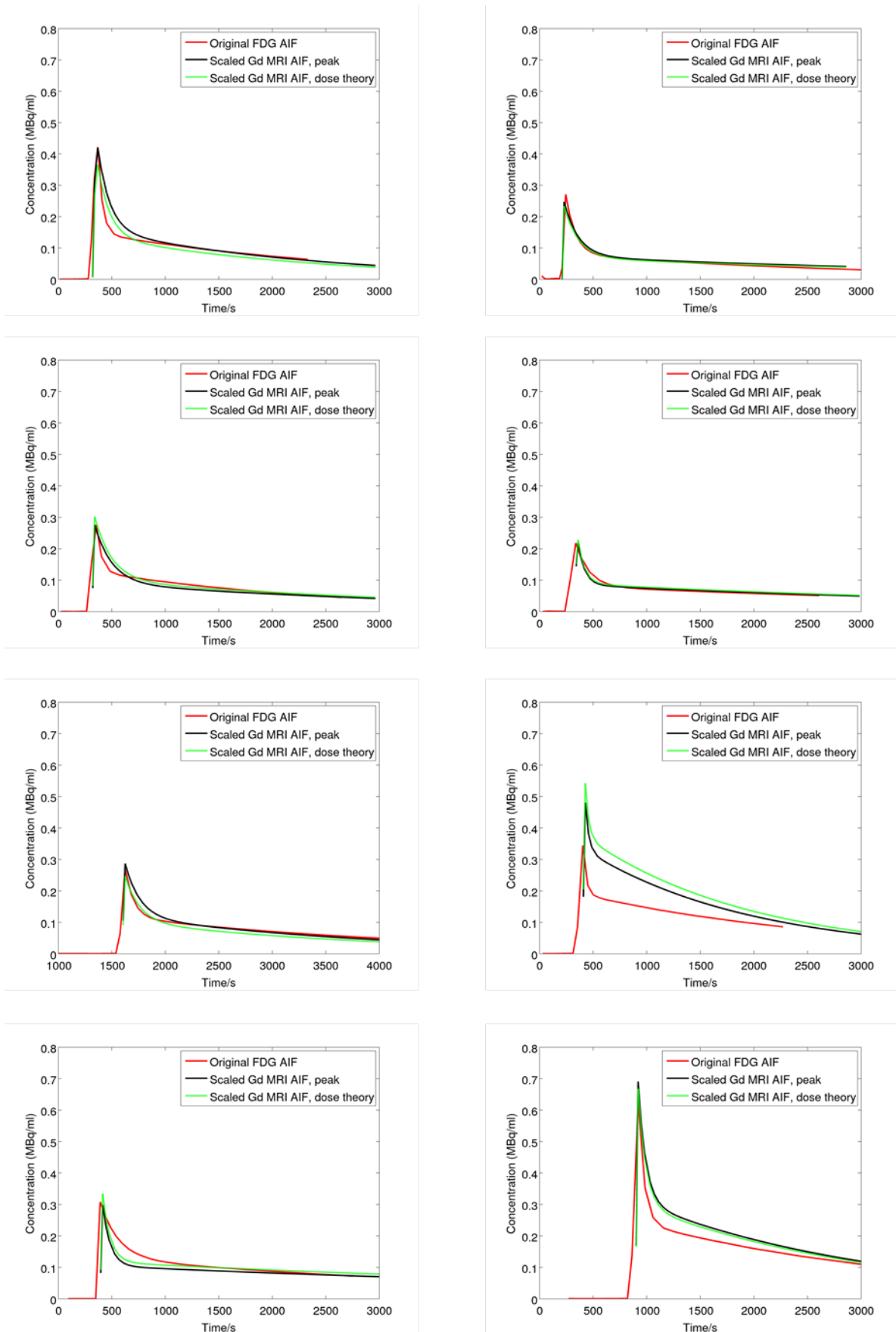


Figure 7.34: Comparison of scaling methods applied to MR AIFs converted into ^{18}F -FDG AIFs via the Poulin method, using a fully non-invasive dose relation scaling method. The non-invasive method appears as effective as direct scaling by the peak height for the majority of rats scanned.

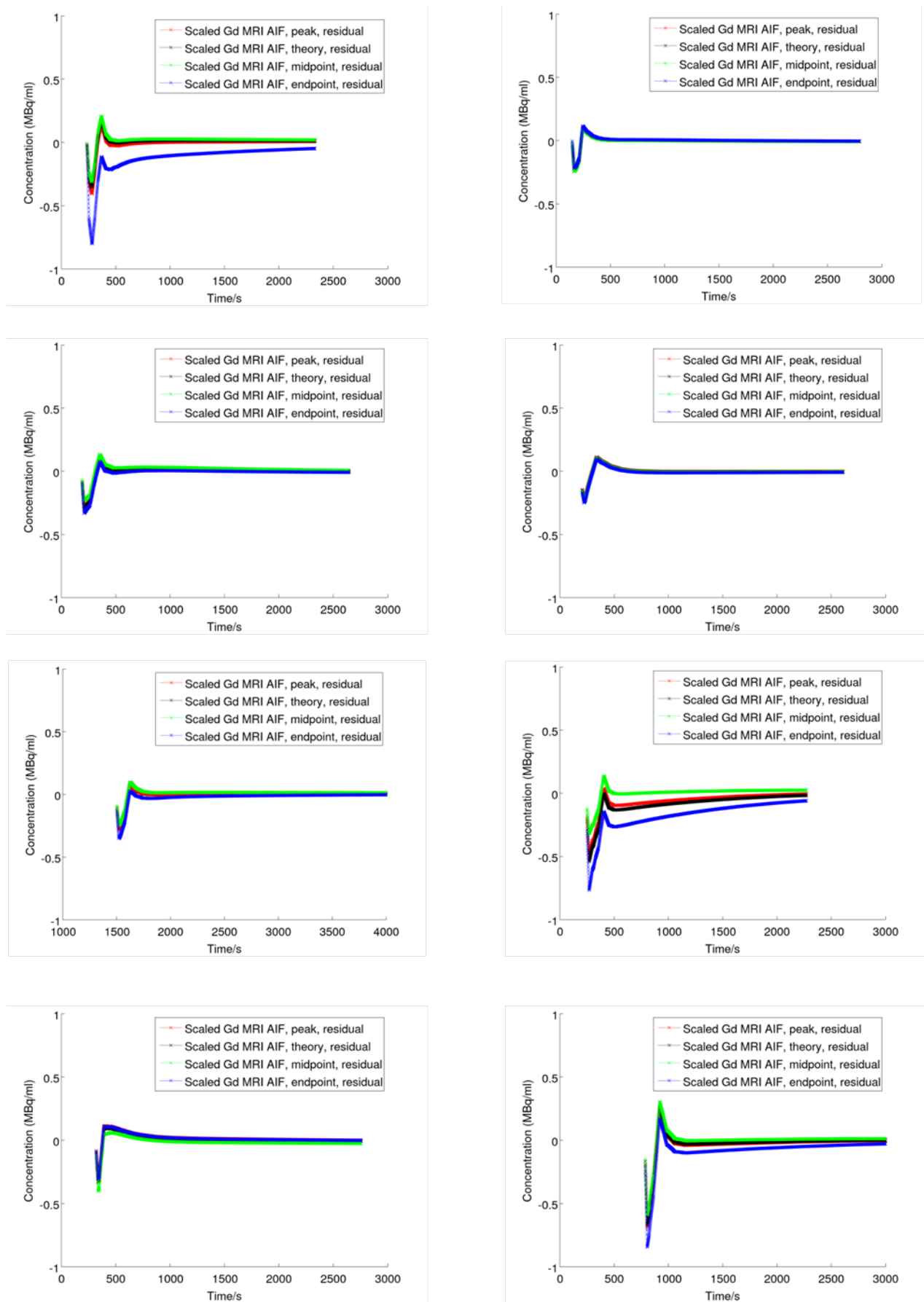


Figure 7.35: Residuals between normalized and converted MRI AIFs and ^{18}F -FDG AIFs, indicating greatest differences seen in the end of the first pass region and in the “shoulder” region of the AIF. Note difference in scale (± 0.2 to ± 1) compared to scaled Gd contrast agent AIFs, indicating level of increased differences present in the DSC+DCE MRI AIFs.

Figure 7.36 shows the AUC and peak height parameter comparisons across each of the scaling methods for both the Gd AIFs and MRI AIFs. No significant differences were found in the AUC or peak heights over the rat cohort for either Gd AIFs or MRI AIFs after scaling into ¹⁸F-FDG AIFs, except when using the “endpoint” scaling method ($p < 0.05$, paired Student’s t test), as shown in Figure 7.36. This, in addition to the large residuals seen between the “endpoint” scaled Gd AIFs and ¹⁸F-FDG AIFs indicates that a single, late blood sample would not be suitable to perform the conversion between Gd AIFs and ¹⁸F-FDG AIFs reliably. The peak or “midpoint” samples performed well, however, when using the Gd AIFs, showing good agreement between the scaled curves and ¹⁸F-FDG AIFs for 7 out of 8 rats, indicating that only limited blood samples would be required in order to scale Gd AIFs to PET AIFs.

In future work, PET AIFs should not be produced by scaling together DSC and DCE data, however, as although they give good AUC and peak height results over the cohort, their individual residuals and RMSD show considerable differences remain between them and the ¹⁸F-FDG AIFs. RMSD between the MRI AIFs and ¹⁸F-FDG AIFs before scaling but after conversion was $45 \pm 13\%$. RMSD is subsequently reduced to $20 \pm 13\%$ for the peak value scaling, $21 \pm 18\%$ for the dose/height relation scaling, $19 \pm 6\%$ for the “midpoint” scaling but increases to $48 \pm 47\%$ for the “endpoint” scaling. This again indicates that “endpoint” scaling is unsuitable but also shows that even peak height scaling still results in differences in curve shapes across the cohort for MR and ¹⁸F-FDG AIFs.

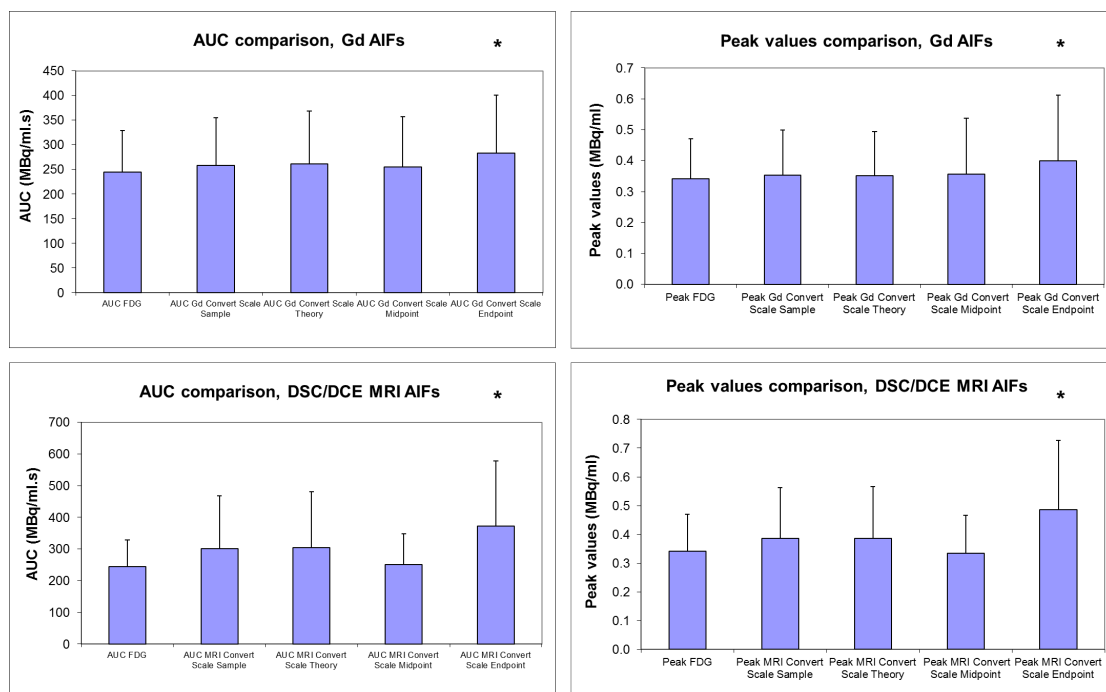


Figure 7.36: Top row: Scaled Gd AIFs comparison (Left) AUC, (Right) Peak height. Bottom row: Scaled DSC/DCE AIFs comparison (Left) AUC, (Right) Peak height. * $p < 0.05$ for paired Student’s t test.

Gamma variate method

Gamma variate functions were successfully fitted to all ^{18}F -FDG AIF, Gd AIF and MRI AIF data sets after peak height normalization. The gamma variate fits are shown in Figures 7.38, 7.39 and 7.40 respectively.

A delay correction was required to align the peaks of the DSC MRI data with the blood sample data, after which good agreement was seen between first pass bolus shapes of ^{18}F -FDG and Gd AIFs, as well as with DSC MRI data after normalization. The impact of the delay correction is shown in Figure 7.37.

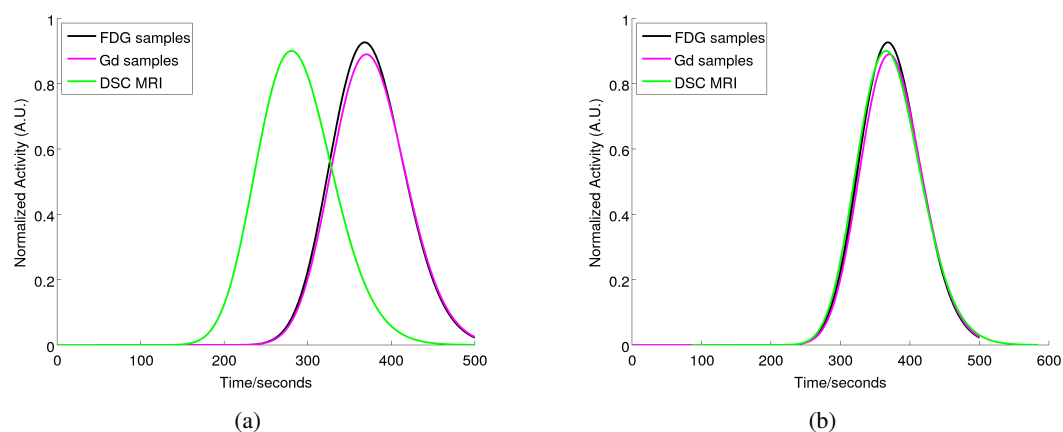


Figure 7.37: (a) Gamma variate functions fitted directly to normalized ^{18}F -FDG, Gd contrast agent and DSC MRI data for single rat (b) Gamma functions after delay adjustment to re-align peaks, showing similar shapes.

After delay adjustment the ^{18}F -FDG gamma variates (in MBq/ml) were then compared to the scaled Gd gamma variates and DSC MRI gamma variates. Good agreement with the ^{18}F -FDG gamma variates was seen with the other sets of gamma variates using either the peak plasma sample to scale the data (see Figure 7.41) or the linear relation between peak height and dose (see Figure 7.43). The residuals between the ^{18}F -FDG gamma variates for both the Gd gamma variates and the DSC MRI gamma variates for the peak scaling method are shown in Figure 7.42 and those for the dose theory scaling method are shown in Figure 7.44.

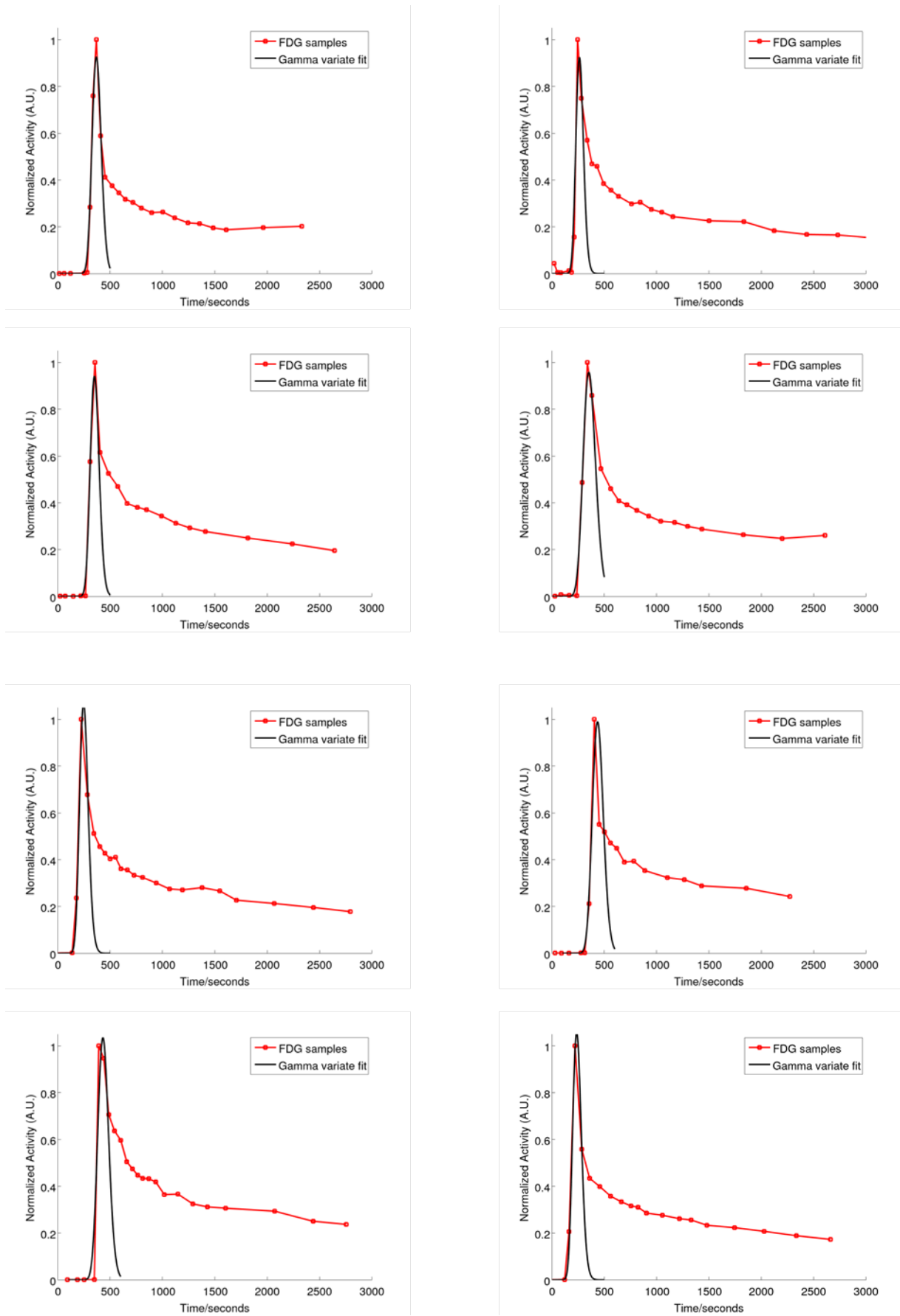


Figure 7.38: Gamma variate functions fitted to first 500s of rat ^{18}F -FDG plasma data, with good fits achieved in all but one rat (3rd row, right).

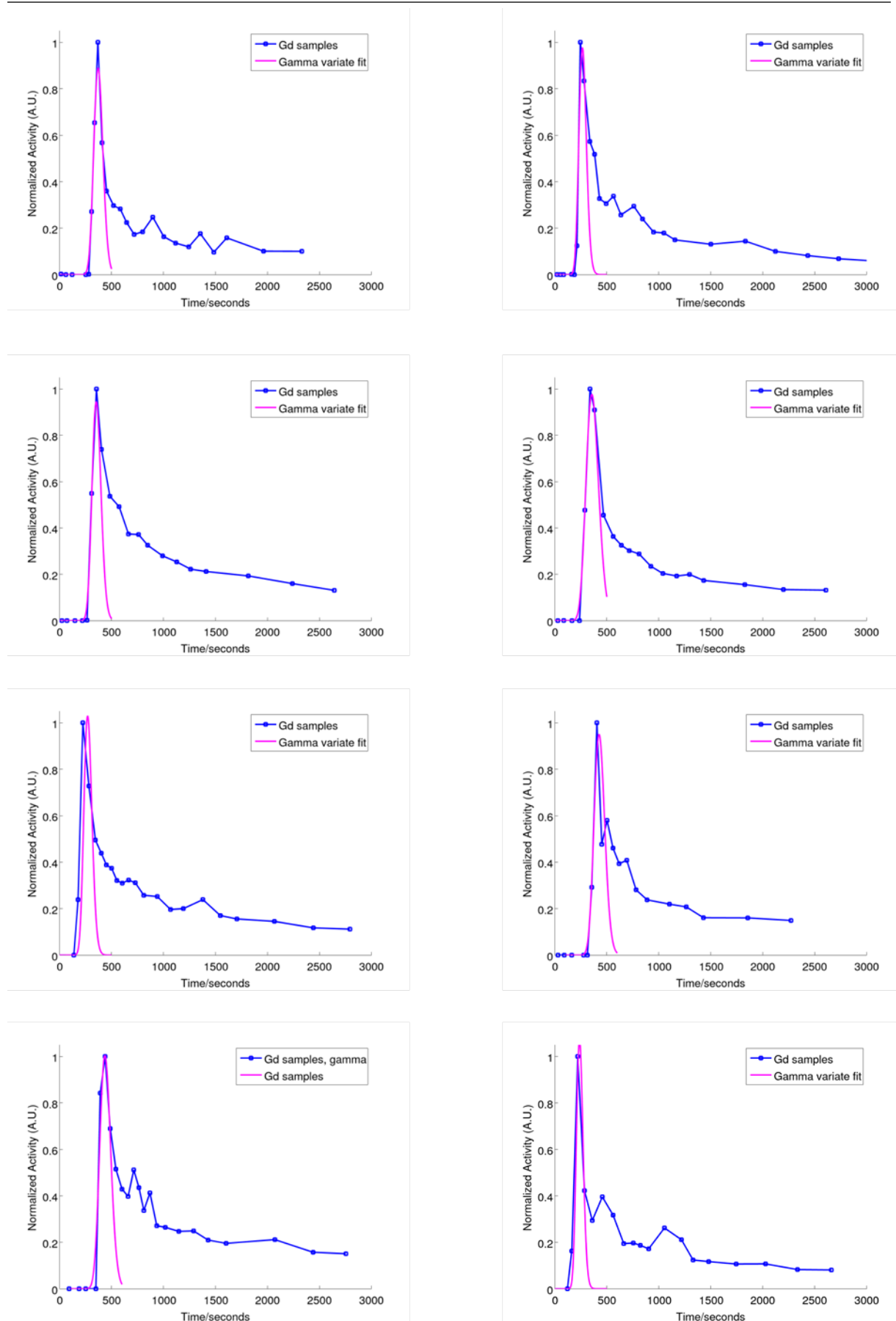


Figure 7.39: Gamma variate functions fitted to first 500s of rat Gd-based MR contrast agent plasma data, with good fits achieved in all but one rat (same rat that poor gamma fits to ^{18}F -FDG data, 3rd row, right).

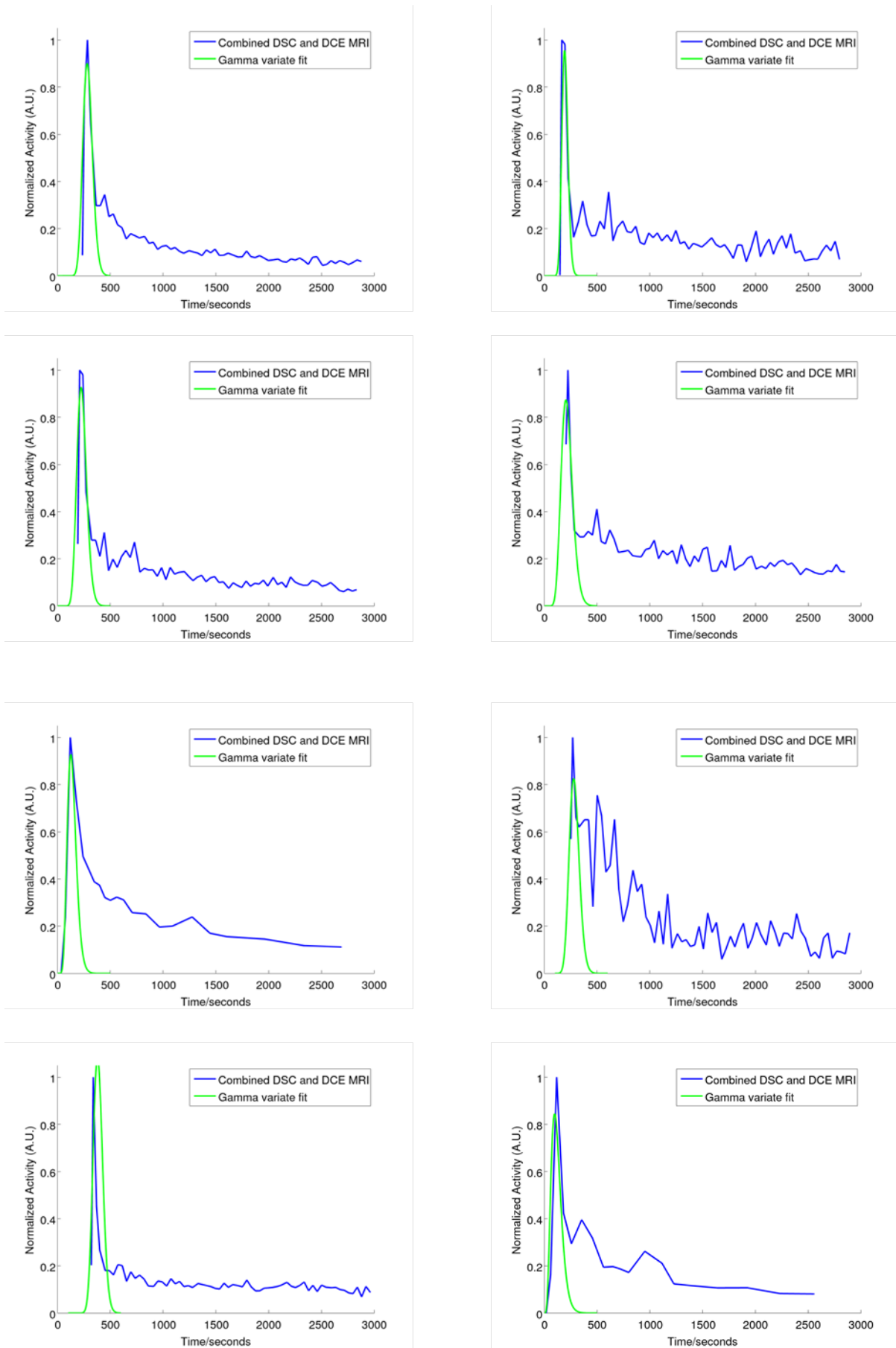


Figure 7.40: Gamma variate functions fitted to rat DSC MRI data and compared to combined DSC/DCE MRI AIF.

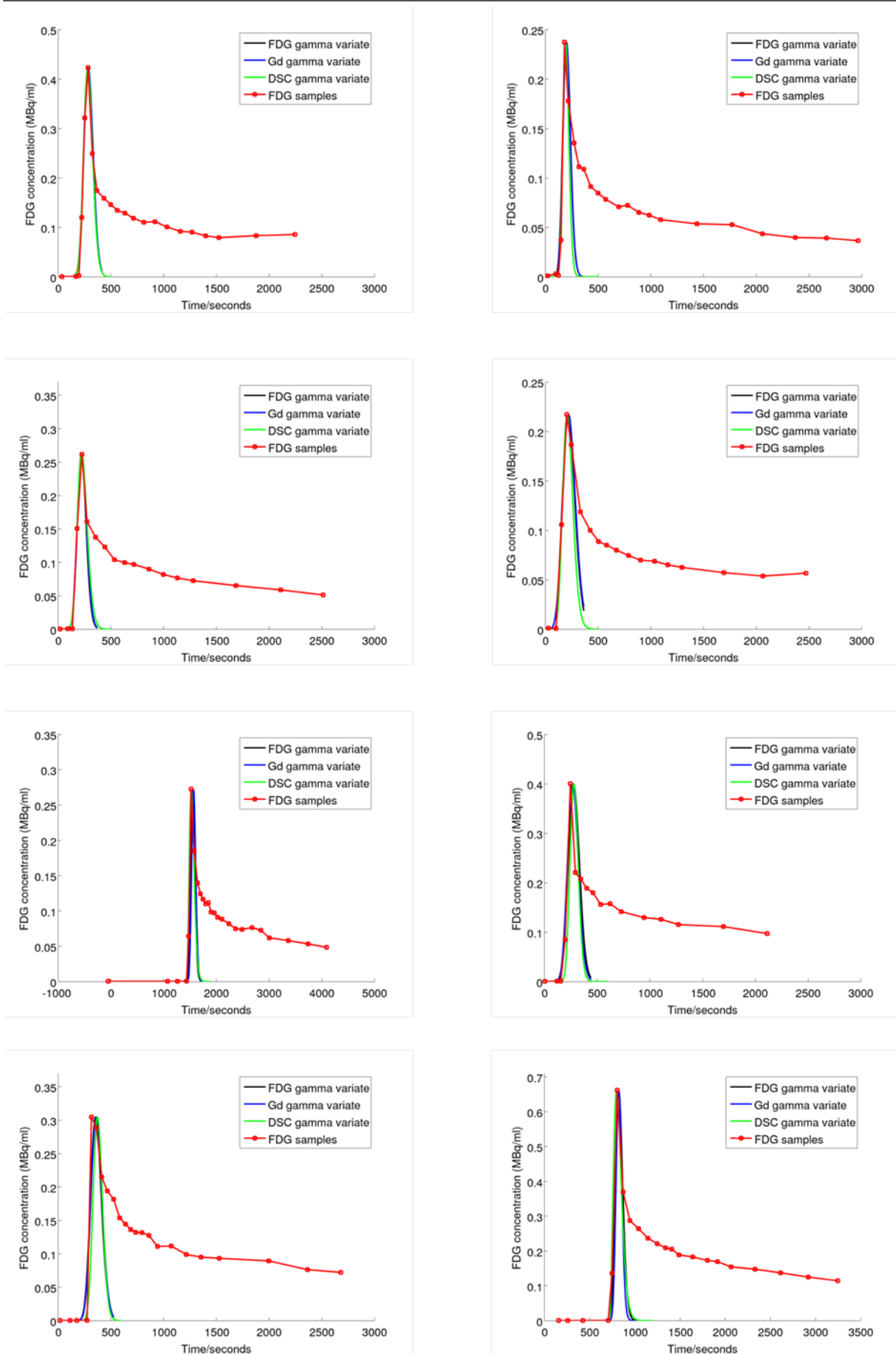


Figure 7.41: Gamma variates fitted to ^{18}F -FDG, Gd and DSC MRI data, scaled using maximum peak height plasma sample for each rat dataset. Note different activity scales on y axes for each rat due to differences in tracer dose administered.

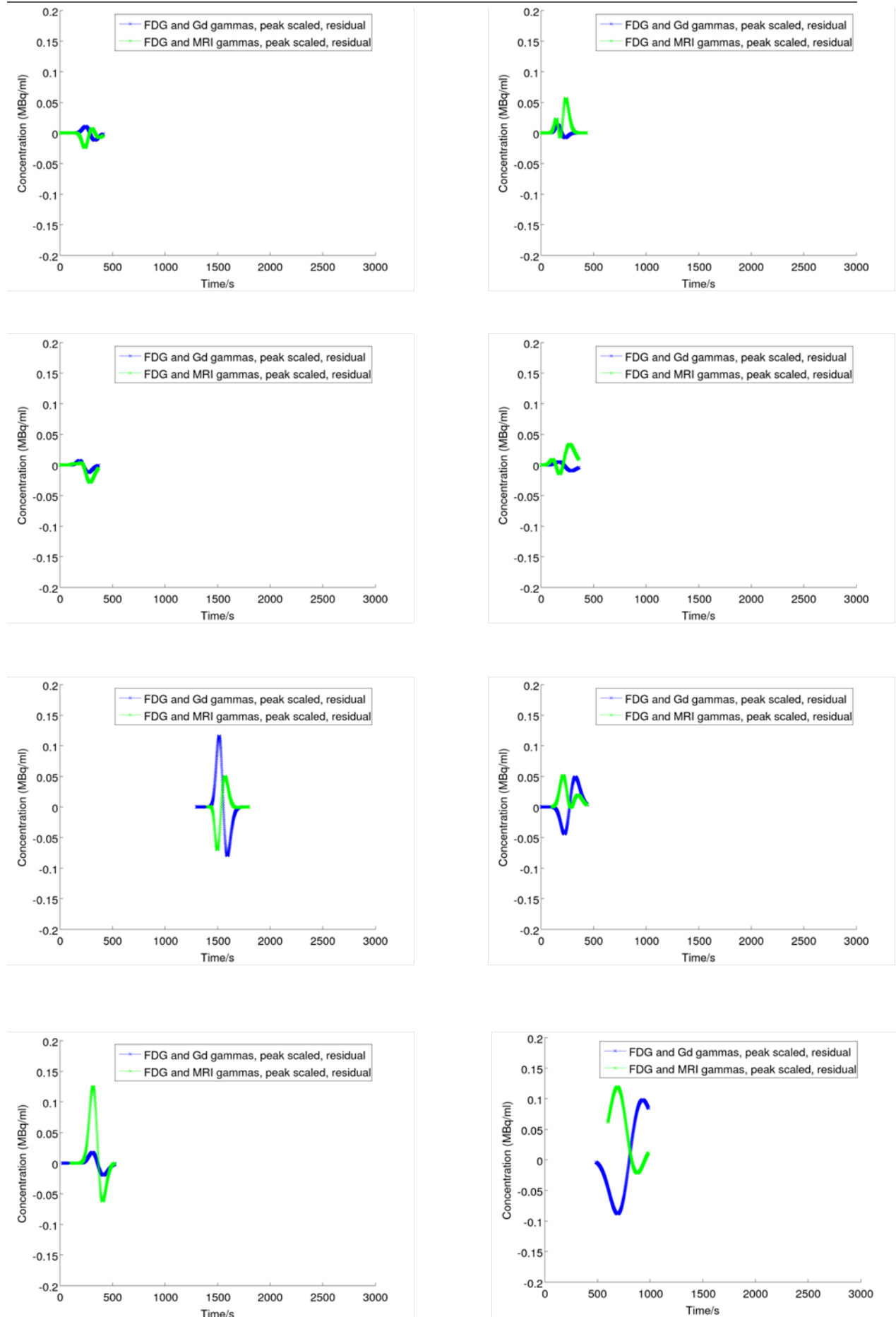


Figure 7.42: Residuals between gamma variates fitted to ^{18}F -FDG and Gd/DSC MRI data, scaled using maximum peak height plasma sample for each rat dataset. Majority of rats show a very low residual ($< \pm 0.05\text{MBq/ml}$), but those with slight misalignments of gamma variates show larger differences ($< \pm 0.15\text{MBq/ml}$).

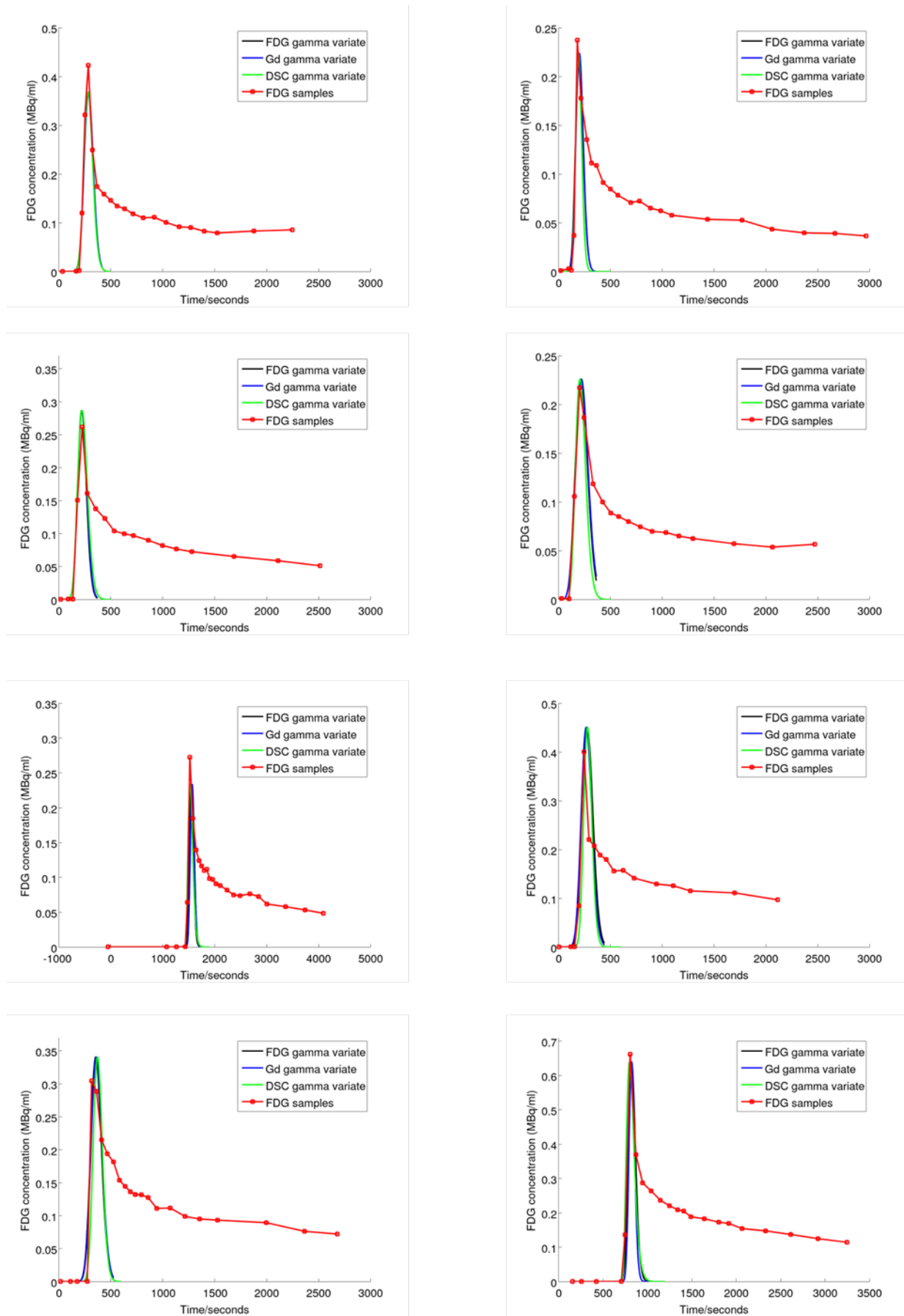


Figure 7.43: Gamma variates fitted to ^{18}F -FDG, Gd and DSC MRI data, scaled using linear relation between peak height and administered dose for each rat dataset.

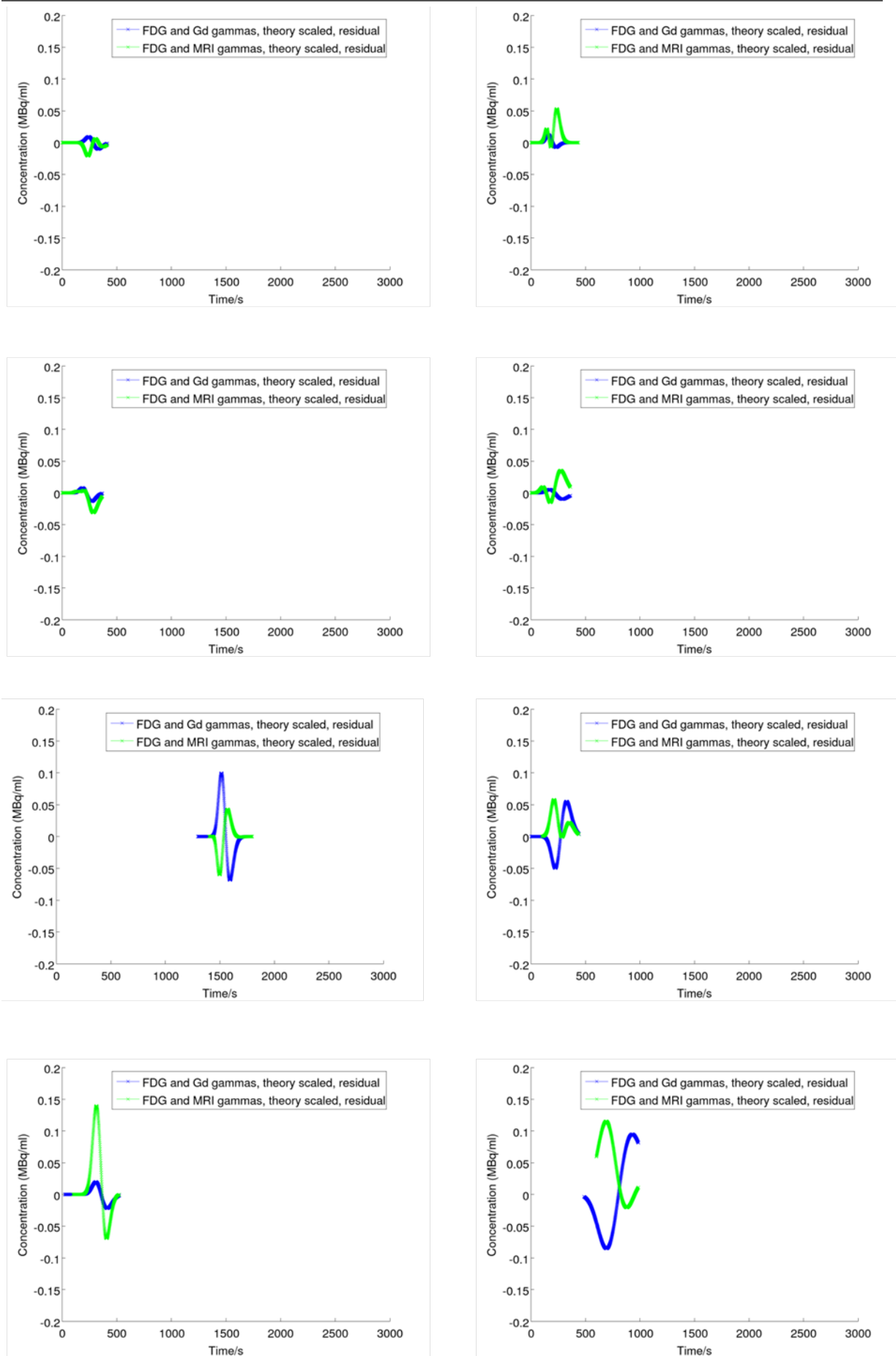


Figure 7.44: Residuals between gamma variates fitted to FDG and Gd/DSC MRI data, scaled using relation between peak height and activity of injection administered. Almost identical residuals produced between peak scaling method and linear dose relation method.

The peak scaling method and the “dose theory” scaling method both produced very similar results, indicating that non-invasive scaling performs adequately with this technique and that this process could be repeated without the need to take blood samples if the “dose theory” relation was verified for the subject group. Over all MRI gammas, the RMSD between the peak scaled gammas and the “dose theory” scaled gammas was $9\pm 4\%$. In over half the rats, however, both the Gd gamma variates and DSC MRI gamma variates show high residuals ($> \pm 0.1\text{MBq/ml}$) when compared to ^{18}F -FDG gamma variates. This could be due to problems in the fitting procedure for the gamma variates and misaligned peaks from a non-optimal delay/dispersion correction in the case of the DSC MRI gamma variates.

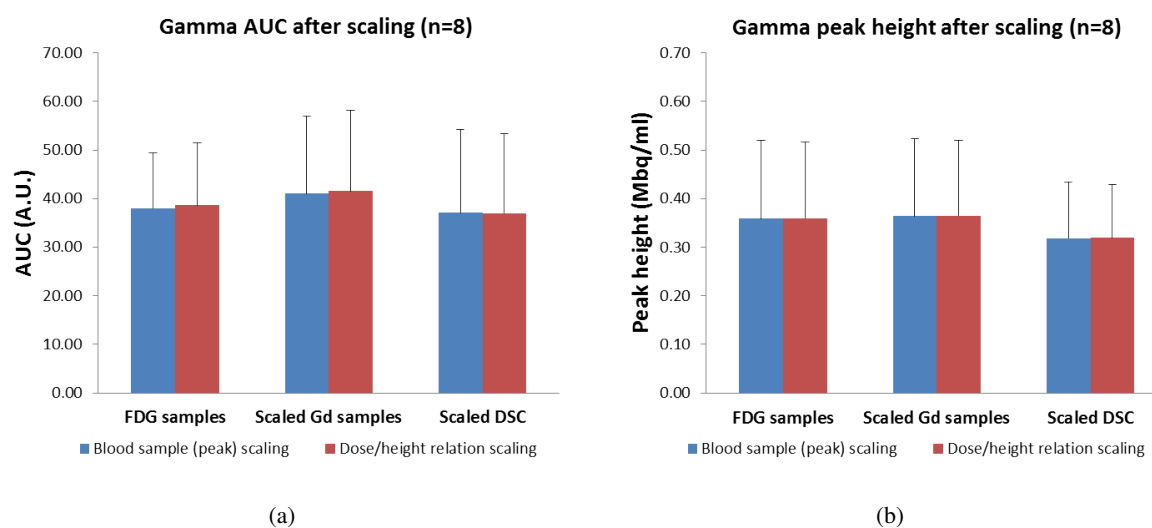


Figure 7.45: (a) Comparison of AUC values for each scaling technique after conversion using the gamma fitting method. (b) Comparison of peak concentration values for each scaling technique after conversion using the gamma fitting method.

No significant differences in AUC or peak height values were seen between normalized gammas taken from any of the modalities measured in this experiment, as shown in Figure 7.45. The changes in RMSD between gammas scaled using the “dose theory” technique were found as follows: ^{18}F -FDG/Gd gammas was $11\pm 5\%$, Gd/DSC MRI gammas was $41\pm 18\%$ and ^{18}F -FDG/DSC MRI gammas was $40\pm 17\%$. This indicated that larger changes were seen when comparing the gamma shapes from the DSC data directly to those found in the blood sampled data. Additionally no significant differences were seen when comparing peak value scaling to peak height/dose relation scaling techniques for any of these comparisons. This indicates that kinetic modelling using the AUC may provide suitable estimates using a converted DSC MRI AIF but full kinetic modelling results which rely on the exact AIF shape may not be accurate using this technique.

7.4 Discussion

7.4.1 Experimental challenges

Collecting the blood sampling data for each rat involved a number of logistical problems. The main one concerned preventing the rat blood from clotting inside the long cannula line which extended from the MRI bore. Clotting led to 4 of the 12 rat datasets collected using this protocol being unusable as the sampling line became blocked, disrupting the measurement process. Steps were taken to minimise these errors in later datasets and it was recommended that each blood sampling tube should be pre-rinsed with heparinised saline and that at least 3 manual operators are required to perform this protocol. The 3 operators have distinct roles: a timer, a blood sampler and an injector/data processor, enabling the parallel processing of the well counter data whilst the blood samples were being collected in order to maximise plasma yield before each blood sample clots.

A further complication was the lack of an MR-compatible syringe pump to regularise the injection rates for each rat, so it is unknown whether the individual variation between subjects is solely due to their physiology or whether manual injection rates of slightly different volumes of mixed ^{18}F -FDG/Gd solution could be the problem. As shown in Figure 7.46, narrower AIFs were observed using MRI than with the Gadovist blood samples although this effect was largely removed for most rats when the AIFs were converted using the cohort ratios of amplitude and rate constants for bi-exponential model.

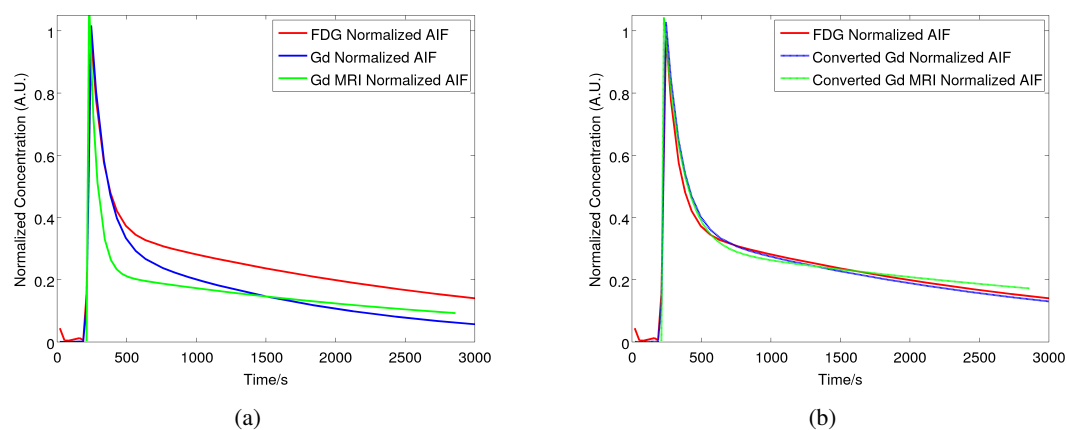


Figure 7.46: (a) Sample normalized blood sampled and MR-derived AIFs for single subject, showing a much narrower MR-derived AIF compared to the Gadovist AIF from ICP-MS. (b) Converted AIFs using cohort ratios of amplitude and rate constants for bi-exponential model shows that this dispersive effect is removed when an average ratio is used.

Another difficulty arose from the fact that a combined bolus of PET tracer and MRI contrast agent was required to perform this experiment. In most PET studies a slow injection rate is preferred such that the bolus first pass phase is elongated and reduced temporal resolution is required to adequately sample

the AIF peak [52], [68], [279], whereas a rapid injection of a small volume is preferred in DSC and DCE MRI [106], [121], [122], [135]. A rapid injection gives a narrow bolus and ensures high SNR in the first pass AIF phase (by maximising intra to extravascular magnetic susceptibility differences), which in turn enables more accurate CBF measurements to be performed [122]. The rapid bolus injection in this study thus enforces high temporal resolution to achieve adequate sampling in the peak and “shoulder” regions of the AIF. In future studies, the bolus injection rate and contrast agent dose should be optimized to achieve a high SNR MRI AIF that best reflects the PET AIF curve shape.

Another issue with the combined bolus approach was that due to the combined volume of ^{18}F -FDG and Gadovist solution, some of the original injection was seen as an initial peak before the flush was administered in each rat as shown in the high temporal resolution 0.35s data in Figure 7.47(a). The smoothing of the data to 30s frames does not detect this prebolus, as shown in Figure 7.47(b). This small difference between the initial injection and flush peaks may be reduced if injections were regulated via a syringe pump [129], [130], which would lead to improved results in analysis as the low resolution 30s frames would capture the bolus curve shape more accurately.

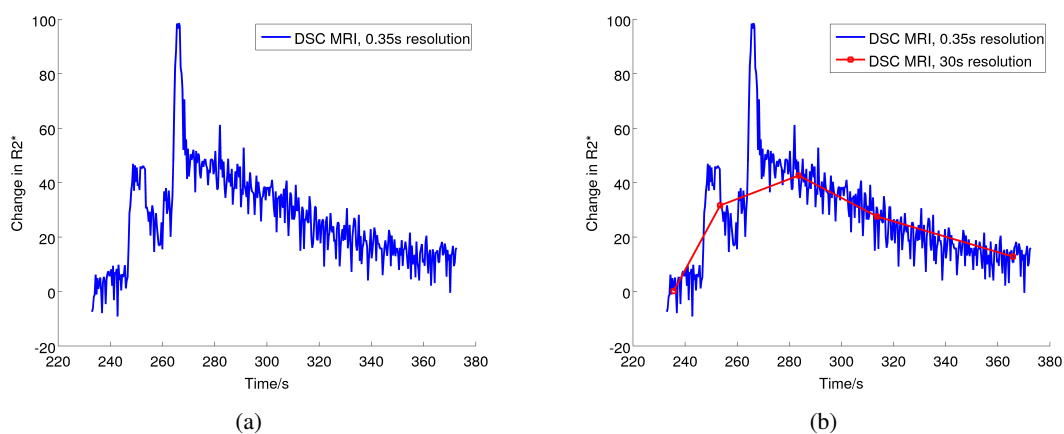


Figure 7.47: (a) DSC MRI data taken from rat MCA, with 2 distinct peak contributions from the original injection and then the saline flush. (b) DSC MRI interpolated to 30s temporal resolution, showing overall single bolus shape when data is smoothed.

Further work would employ a syringe pump and perform only a single rat scan per day to regulate the volume of PET tracer injected each time. An experimental measurement of cannula dispersion in a flow phantom would be recommended, forming a “top hat” function of tracer within the measurement cannula and measuring how dispersion spreads out the tracer bolus along the cannula [280], [281], [282]. Once the dispersion caused by the cannula is known, additional bi-exponential dispersion models could be applied to the sampled AIF data to accommodate for dispersion of the tracer bolus within the rat body itself between the femoral veins/arteries and the brain [52], but these dispersion models would also need to be independently verified with serial blood samples.

7.4.2 Contrast agent concentration results from ICP-MS

ICP-MS is a very accurate measurement technique, and it was therefore unexpected that the differences between the first and second runs of Gd measurements for 4 rats would be as large. It was also observed that the second run was noticeably noisier than the first, as shown in Figure 7.15. This effect should be explored further, as all samples were prepared using the same dilution protocol by the same operator in the same surroundings, with separate calibration experiments performed on each measurement day that were in agreement. Hydrochloric acid was used in the second dilution stage to disrupt the plasma cell integrity and should have ensured that all Gadovist within the sample was released into solution for measurement, although all second ICPMS runs displayed *higher* Gadovist concentrations indicating that the acid may not have been as effective as hoped in the first run. It appears most likely that the freezing, thawing and re-freezing process may have disrupted the cells in some manner, resulting in less uniform aliquots being taken from the water-diluted samples for the second (acid) dilution stage. A much more complex effect may be at work, however, as rats 10 and 11 appear to have much greater disparity between their first and second runs than rats 4 and 9 in Figure 7.15.

7.4.3 Comparison with previously reported AIF conversion results

Similar results for the Gadovist AIFs and ^{18}F -FDG AIFs were reported compared to the previous study conducted by Poulin et al. [54], [272] and this work agrees with their conclusion that MR AIFs require significant normalization, conversion and scaling to be used as an alternative to PET AIFs. Both AIF shapes and AUC values reported here agreed with those previously published [54] for both Gadovist and ^{18}F -FDG AIFs, in addition to the similar average (slow) excretion rate constants and different average (fast) extravasation rate constants being reported from the fitted bi-exponential model. Linear correlation plots between the rate constants, however, indicated that although on average the excretion rate constants agreed between the Gadovist and ^{18}F -FDG AIFs, there was no linear correlation in this value seen across the rat cohort. Whilst the initial AIF stages displayed similar steep rises which were attributed to the rapid bolus injection protocol, the difference in clearance rates resulting in differing AIF shapes at late time points can be contributed to a number of factors. The cell internalization rates for the compounds will be different as ^{18}F -FDG is phosphorylated and trapped in tissue whilst the MR contrast agent is not internalized [106], [122]. Furthermore the extravasation rate of ^{18}F -FDG can depend on glucose transporters, unlike Gd-based contrast agents, which rely on passive transport alone [54]. The different molecular weights of the compounds may also have contributed to the different washout rates and diffusivities from plasma and therefore the AIF curve shape differences at late time points.

The success of the specific bi-exponential ratio-based Poulin conversion method using this dataset

confirms that the conversion of Gd AIFs to ^{18}F -FDG AIFs is viable but highly complex. The accuracy of this conversion varied between rats, as indicated by the linear correlation plots in Figures 7.25 and 7.26. These plots showed correlation in the amplitude parameters (A_1 and A_2) of the fitted biexponentials but no correlation in the excretion rate constant k_1 and limited correlation in the extravasation rate constant k_2 , indicating that the average conversion ratios would have limited success over the cohort as a whole. Bearing this in mind, successful scaling of converted Gd and MRI AIFs which produced similar AUC and peak values to the gold standard ^{18}F -FDG AIFs was achieved. These results were found when scaling was performed using either the “dose theory” relation or with blood samples. For scaling to be successful, the blood sample had to be taken from either the peak of the curve or from the “midpoint” (designated as the area between the first pass phase and the washout). Each of these scaling methods provided good agreement between converted Gd AIFs with ^{18}F -FDG AIFs, with the “midpoint” shown to give slightly less variance over the group, as this aligned the “shoulder” regions of the AIFs. If a blood sample taken at the end of the scan (the “endpoint”) was used to provide scaling, however, this produced converted Gd AIFs that were significantly different from ^{18}F -FDG AIFs. This was an important result, as it demonstrated that the Poulin method cannot successfully convert MRI AIFs to ^{18}F -FDG AIFs if only a single, late blood sample (e.g. taken after the PET scan has finished) is available. This implies that unless the “dose theory” relation is used, some form of invasive blood sampling must be conducted in the early stages of scanning, which would require extensive surgical expertise. It must be noted, however, that although parameters such as AUC were not significantly different after conversion from Gd AIFs and DSC/DCE combined AIFs to ^{18}F -FDG AIFs, meaning that parameters such as K_i would be well estimated (as shown previously [54], [272]), the subtle changes in AIF curve shapes would likely result in differences in K_1 , k_2 and k_3 using this conversion methodology. This is particularly true for K_1 if the peaks are not aligned fully, as it is highly dependent on the AIF bolus peak shape.

The main problem with the conversion technique used by Poulin et al. [54] is its reliance on known conversion ratios for bi-exponentials between modalities. In addition to the variance between subject groups, the variance between individual subject AIFs shown in this study indicates that using mean group values may not always produce accurate conversion ratios for AIFs. This technique is therefore not practical for translation to the clinic due to the required pre-measurement of patient cohort bi-exponential ratios from blood sampling data.

Another problem found with this conversion technique was the difficulty in attaining exact quantitative results of Gd-based contrast agent concentrations from DSC, DCE or combined DSC/DCE MRI (as shown in Figure 7.20). Poulin et al. themselves elaborated on this issue in a follow-up paper to their main work [272]. In their second paper, their reference region DCE MRI methodology was refined to stop underestimation of the Gd AIF peak by applying a linear correction, which related the apparent

reference region DCE MRI AIF peak height to the reported peak height from the Gd plasma samples. In this work, the DCE MRI method also struggled to always attain accurate estimates of the AIF tails (see Figure 7.22) and the DSC MRI method required scaling with DCE MRI to produce a linear relation between DSC MRI peak height and Gd contrast agent peak concentration values, as shown in Figure 7.21. This non-linearity in the DSC MRI signal compared to contrast agent concentration was most likely due to the different blood vessels sizes in the image, the proton diffusion rate and the sequence parameters that were used, such as the TE, [122] as the automatic method voxel selection method should have reduced operator error in the AIF from manual voxel selection.

Furthermore, the combining of DSC and DCE data as a single MRI AIF was subject to a mean scaling factor which was only validated at 30s resolution. It was also assumed that a mean scaling factor would hold for all rats, which was not always the case, as seen in Figures 7.22 and 7.23. Even after conversion to ^{18}F -FDG AIFs using empirically derived bi-exponential ratios, in some rats considerable differences remain between DSC/DCE AIFs and ^{18}F -FDG AIFs due to temporal sampling mismatch, dispersion, delay and difficulty in accurate scaling of DSC MRI data to mM. The temporal sampling mismatch and dispersion from the cannula line, in particular, cause the shapes of combined DSC/DCE MRI AIFs after normalization to be considerably different to the ^{18}F -FDG AIFs, particularly in the “shoulder” region (see Figure 7.24), which is required for full kinetic analysis.

Scaling the data using plasma samples did reduce the errors found between the DSC/DCE MRI AIFs and ^{18}F -FDG AIFs, with no significant differences reported in peak height, AUC or RMSD for any scaling method except for the “endpoint” method, although the residuals between the scaled MRI AIFs and the ^{18}F -FDG AIFs in Figure 7.35 were much larger than those reported for the scaled Gd AIFs in Figure 7.32. If the Poulin approach were to be used in future studies, a DCE MRI technique which covered all of the AIF would be recommended to remove any DSC/DCE scaling issues. It would also be required to have at least $<5\text{s}$ temporal resolution to ensure the AIF was not undersampled - this could be achieved using previously reported phase based methods [283], [284] or segmented k space “keyhole” techniques [54]. Phase based DCE MRI also produces a signal that is linear with Gd concentration over a wide range (rather than requiring T1 mapping to be performed to calculate Gd concentrations), has high SNR compared to magnitude data and is less vulnerable to T1/T2 relaxation effects [283], [284]. Potential drawbacks include phase drift of magnets over time, aliasing due to the 2π range of phase measurements (an appropriately small TE would be required to minimise this, at the expense of sensitivity to changes in concentration) and the difficult implementation of a projection-based AIF measurement [283].

It must be noted however, that the use of DCE MRI to replace PET AIFs at late time points is of much less value as the temporal resolution of PET can be equivalent to MR at this point and little extra

information is gained by having high temporal resolution within the tail region of the AIF. PET image-derived methods may therefore be just as accurate as a converted MRI AIF for late time points. Blood samples to measure PET metabolites within the blood may also have to be taken anyway at late time points, meaning that MRI techniques that focus on the first pass of the AIF may be of greater use rather than those which attempt to retrieve the entire PET AIF.

7.4.4 Evaluation of gamma variate AIF conversion and scaling method in first pass

Fitting gamma variate functions to the first 500s of ^{18}F -FDG, Gd and DSC AIFs provided reasonable agreement between all modalities after data was normalized to peak height and the delay due to the long cannula running out of the magnet bore was taken into account. The good fits achieved in all but 1 rat for all modalities (rat 6, 3rd row, right in Figures 7.38, 7.39 and 7.40) indicate that the gamma variate model represents the first pass stage of the AIF well and can be used to smooth data for analysis and reduce noise. It does, however, idealize the bolus shape and would therefore be of limited use in studies which require more than the first pass of the AIF for their kinetic analysis, as it could only be used to adjust the measured AIF peak height and rising slope in this case.

The increased variation between the DSC MRI gamma variates taken directly from the rat brain and the blood sampled Gd gamma variates is likely to be a consequence of both natural dispersion along the cannula from the rat body to the sample collection point, the limited temporal resolution of the current blood sampling technique and the various mismatches in temporal sampling between MRI and blood sampling for each rat. This dispersive and temporal sampling effect should be investigated in future work using an MR-compatible version of a blood sampler with high temporal resolution [51], [230] which could then isolate the magnitude of each of these effects, as well as standardizing blood sample measurements between rats.

Figure 7.48 indicates the problems with the gamma variate conversion technique, particularly shown in the large residuals for rat 5 shown in Figures 7.42 and 7.44. Firstly the fitting procedure in some rats may not have been optimal and produced gamma variate curve fits which were slightly too wide or too narrow than the data (seen in the disagreement between the ^{18}F -FDG and Gd curve shapes in Figure 7.48 but not in Figure 7.37). Secondly, assuming that the fitting procedure was accurate, it appears that some rats showed different levels of dispersion between the blood samples and MRI data, resulting in the differences in curve shapes seen in Figure 7.48(a). Finally the delay adjustment calculated from the 30s resolution DSC MRI and blood sampled data (peak to peak alignment) was found to have limited success in some rats (see Figure 7.48(b)), giving a temporal displacement of the curves and giving large residuals in Figures 7.42 and 7.44.

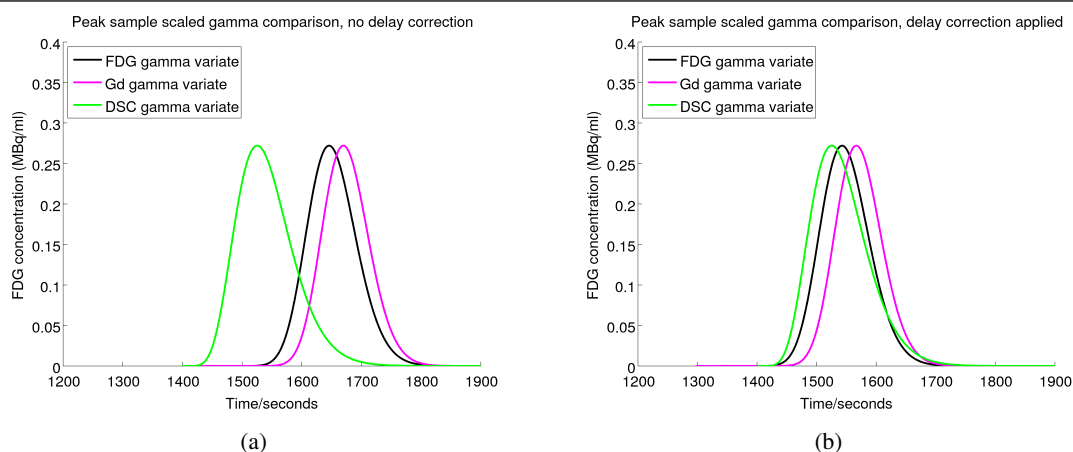


Figure 7.48: (a) Scaled gamma variate functions for ^{18}F -FDG, Gd contrast agent and DSC MRI data for single rat. (b) Same gamma variates, after delay adjustment attempts to re-align peaks. Differences in residuals seen previously occur due to curve misalignment from poor delay correction, rather than from a change in shape of the gamma variate between modalities.

The AUC, peak height (see Figure 7.45) and RMSD results all indicate that the differences seen between the ^{18}F -FDG, Gd and DSC MRI gamma variate residuals in Figures 7.42 and 7.44 should be noted but may not be vital in ensuring accurate PET kinetic parameters are created from surrogate MRI AIFs. Patlak analysis, for example, relies on the AUC of the AIF and TAC to provide estimates of K_i , meaning that as long as MR AIFs provide similar AUCs to PET AIFs, accurate estimation of K_i would be possible⁴ [231], [276], [285]. Full kinetic analysis, however, relies more heavily on the exact shape of the AIF, particularly K_1 , which is dependent upon the bolus peak of the AIF and is indicative of blood flow and perfusion [170], [209], [231], [245], [285]. To ascertain how accurate the converted MRI gamma variates need to be, full validation in a simultaneous PET/MR acquisition would be required. Kinetic parameters K_i , K_1 , k_2 , k_3 and k_4 could then be compared between blood sampled AIFs, PET image-derived AIFs (with PVC and motion correction applied) and converted MRI AIFs.

If fully validated, the use of a non-invasive, surrogate gamma variate from MRI would be of most use in perfusion studies which require a first pass AIF (e.g. ^{15}O - H_2O PET tracer [286]), although the exact technique demonstrated in this work will need to produce more consistent and accurate results for it to be considered a viable alternative to serial blood sampling or PET image-derived AIFs at this time. To extend the gamma variate technique to further preclinical studies, simultaneous PET/MR capabilities could be employed further in hybrid image input function approaches [170], [172]. It would be desirable that MRI gamma variates are used as a substitute for PET AIFs in the first pass phase using a similar technique to that detailed in this Chapter, and that later points in the AIF could be extracted either from blood samples (if metabolite analysis is required) or simultaneously acquired PET images, in order to avoid complications from the different washout rates of the PET tracers and MR contrast agents.

⁴ K_i values were not calculated for this study as no PET TACs were available.

7.5 Conclusions

Serial blood sampling data taken from rats injected with a combined bolus of Gadovist and ^{18}F -FDG inside the MRI bore of a scanner confirmed previously published results [54], indicating that MRI contrast agent AIFs can be converted into PET AIFs, but only after normalization and conversion. This was performed using ratios derived from fitted bi-exponentials to accommodate for the different physiological kinetics of the two compounds, and although image-derived combined DSC/DCE MRI AIFs exhibited greater variation than blood sampled contrast agent AIFs, they could potentially be used as ^{18}F -FDG AIFs if only PET parameters depending on the AIF AUC are required (as suggested in the similar AUC values in Figure 7.45). More consistent results were achieved when first pass AIFs taken from DSC MRI, which were fitted with gamma variate functions and then converted into ^{18}F -FDG first pass AIFs, either through scaling with a single plasma sample from the AIF peak or completely non-invasively using a linear relation between AIF peak height and injected activity. These results were achieved using off-the-shelf DSC MRI sequences which are readily available and easily implemented. Although temporal sampling mismatches, dispersion and delay are present between the DSC MRI AIFs and PET AIFs displayed in this Chapter, this technique has the potential to be used in preclinical simultaneous PET/MR imaging studies to provide non-invasive estimates of PET AIFs from MR images in the first pass phase, assuming consistent conversion protocols are applied.

7.6 Chapter summary

This Chapter has explored the viability of converting MRI contrast agent AIFs into PET tracer AIFs for kinetic modelling in rats. Blood sampling data taken from rats which had been injected with a combined bolus of ^{18}F -FDG and Gd contrast agent inside an MR scanner confirmed the results of previous work published by Poulin et al. [54] for a combined bolus administered in a PET scanner. This Chapter also proposed the use of DSC MRI (instead of DCE MRI, as proposed by Poulin et al. [54]) in the first pass as a possible substitute AIF for PET. A gamma variate fitting and conversion protocol was shown to be the most promising for converting DSC MRI AIFs into ^{18}F -FDG AIFs, although requires further validation in a simultaneous PET/MR experiment with dispersion correction to confirm if the conversion technique is consistent and accurate enough to replace serial blood samples. The final experimental Chapter of this thesis explores how structural MRI may be used to perform attenuation correction as a substitute for PET transmission scanning in mice when traditional attenuation correction methods are not available.

Chapter 8

Direct evaluation of MR-based attenuation correction for mice

All PET kinetic modelling analysis discussed in previous Chapters relies on accurate PET image quantification, which is achieved through the application of a range of corrections to measured PET data, as detailed in Chapter 2. Whilst the majority of these corrections can be adapted from PET to PET/MR in a relatively straightforward manner, new methods of attenuation correction (AC) have been developed to adapt to the limited space available in preclinical PET/MR scanner bores, which restricts access to transmission scan (TXAC) or CT-based AC methods (CTAC). The hypotheses addressed in this Chapter were as follows:

- 1. Accurate quantification of murine PET images requires attenuation correction.*
- 2. There exists an MR-based method that can provide adequate AC for murine PET/MR studies.*

This Chapter details the testing of an MR-based segmentation attenuation correction (MRAC) method for use in a preclinical PET/MR environment, which was validated using the transmission scan capabilities of the Cambridge split magnet PET/MR scanner.

8.1 Introduction

Accurate quantification of PET images requires the application of various corrections to the measured data, as outlined in Chapter 2, Section 2.1.6. These corrections are vital to ensuring that any IDIFs or TACs extracted from PET data reflect the underlying physiology of the subject and therefore produce the correct results under kinetic analysis.

Attenuation correction (AC) accounts for lost counts in LORs due to the absorption of photons within the material of the imaged object. As previously discussed in Chapter 2, alternative attenuation correction methods must be considered for use in PET/MR studies due to the limited space available in PET/MR scanners. MR images can be used to provide AC by creating segmented tissue maps with assigned attenuation co-efficient values, as outlined in Chapter 2, but these must be validated against established PET AC methods which employ ionizing radiation before they can be used routinely in PET/MR imaging.

In preclinical PET/MR, there has been limited exploration of the accuracy of MR-based attenuation correction (MRAC) techniques due to the small size of the subjects involved. Many preclinical PET groups ignore this correction altogether [28], [146], even when performing kinetic analysis [33], [52], as it is typically around 20-30% of the total signal in mouse phantom studies [77], [78], much lower in magnitude than the correction required for clinical applications in humans. For comparison, the magnitude of the required attenuation correction for PET is 1.3 for a 3cm diameter mouse, 1.6 for a 5cm rat and 45 for a 40cm diameter human [77], such that approximately 90% of photon pairs from the centre of the human body are attenuated [81]. The fractions of photons transmitted through the length of a mouse sized phantom was reported as 79% in comparison to 14% for its human equivalent [28]. Other studies have argued that attenuation correction provided by CT or transmission scanning is required in both rats and mice to provide quantitatively accurate PET data [16], [28], [77], [78], [287]. Some research groups do note, however, that a correctly scaled uniform correction (i.e. this assumes the mouse is a cylinder with uniform attenuation and applies a single global scaling factor to this region [77]) places the average activity concentration around the correct magnitude for the mouse but does not compensate for the cupping artefact caused in line profiles as a result of attenuation [77]. PET/MR studies in rabbits [92] have shown that a simple MRAC segmentation based approach using 4 tissue classes (air, tissue, fat and bone) and CT templates for RF coils and the bed produced PET images with adequate attenuation correction, but this has yet to be investigated in rodent PET/MR studies.

In this Chapter, we test the hypothesis that a simple MR whole body scan which is thresholded and segmented to form a two class (air and tissue) attenuation co-efficient μ map can provide adequate AC (when compared to a gold standard method) for mouse PET scanning after being forward projected to form a PET attenuation sinogram. Two slight variations to the default MRAC two class segmentation approach were also tested, namely changing the lung region designation from air to either lung tissue or body tissue, to ascertain how misassignment of the lung region within segmented MRAC μ map affect the resulting reconstructed PET images in mice.

To assess the accuracy of these MRAC methods *in vivo*, sequential PET/MRI data was analysed from mice scanned as part of a cardiac ^{18}F -FDG study [228]. A cardiac surface coil was used in the MR acquisition and remained in place with a standard Bruker MR animal bed throughout the PET scan (as this

configuration would be required in a simultaneous PET/MR acquisition). The attenuation effect of both the mouse body and the surrounding equipment on myocardial and whole body SUVs was investigated. Myocardial SUVs achieved using mouse whole body μ maps created from segmented MR images were compared to SUVs for the same mice produced using gold standard AC from a transmission source (TXAC) installed in the Cambridge split magnet scanner (see Figure 8.1). The SUV results generated using the 3 MRAC techniques were also compared to SUVs produced with AC calculated from the PET emission scan (EmAC), to see how the MR-based segmentation methods compared to applying a uniform correction [77], [78]. As only the TXAC method corrected for both the mouse body and the surrounding equipment (all others corrected for only the mouse body), the effect that the surface coil and mouse bed had on the resulting SUVs was also assessed.

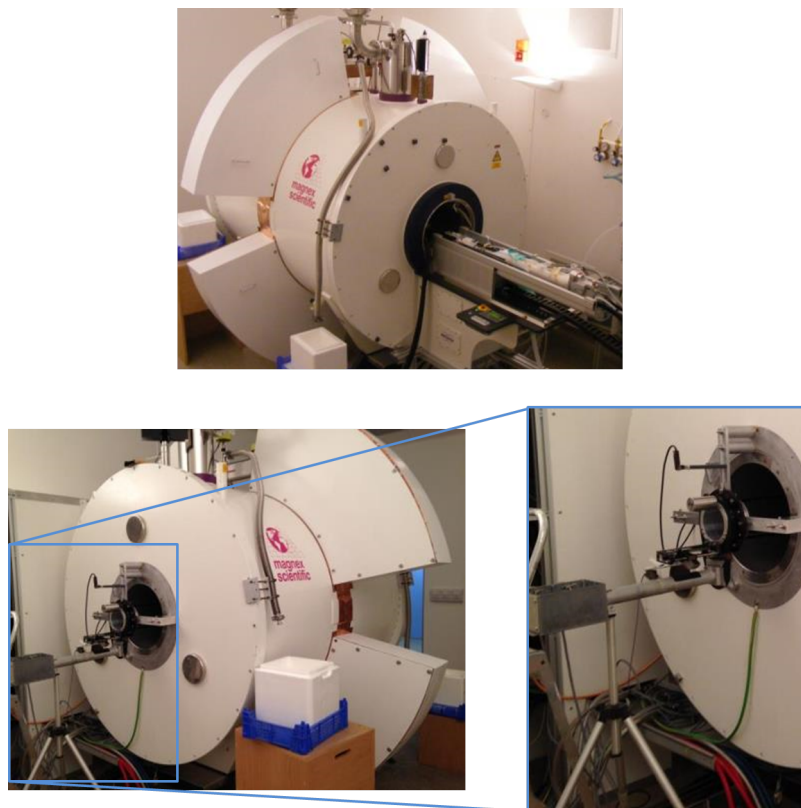


Figure 8.1: Split magnet PET/MR scanner from front (top) and back (bottom). Zoom (inset) shows transmission source mechanism.

8.2 Materials and Methods

8.2.1 Sequential PET/MR acquisition - *in vivo* imaging

Previously acquired data from sequential PET/MR scans of ten mice was used in this study, with the full PET/MR scanning protocol detailed in the Materials and Methods section of Chapter 4¹. Each mouse underwent tail vein cannulation before being placed into a 4.7T Bruker BioSpec MRI (Bruker Inc., Ettlingen, Germany) scanner. 3D FISP was acquired over the whole mouse body (TR/TE 8/4ms, slice thickness 0.5mm, NEX = 2, 0.5mm spacing between slices, FOV= 30mm, planar resolution $120 \times 120 \mu\text{m}^2$, matrix $256 \times 256 \times 128$) before the mouse was transferred on its standard Bruker animal bed (with single loop surface coil, Bruker T7027, in situ) to the Cambridge split magnet PET/MR scanner [25]. A 10 minute single pass transmission scan (^{68}Ge) was then performed with singles mode scatter correction² applied to the transmission data. Emission listmode data was acquired for 45 minutes following manual administration of a $\approx 25\text{MBq}$ ^{18}F -FDG (mean $26 \pm 25\text{MBq}$, range 7-88MBq) tracer bolus through the tail vein lasting approximately 15s seconds and followed by a saline flush.

8.2.2 Sequential PET/MR acquisition - phantom imaging

The PET/MR scanning procedure as described above was repeated using the same coil and bed configuration on a water-filled NEMA NU-4 microPET phantom by the author. The NEMA phantom was previously described in the Materials and Methods section of Chapter 5 and is shown in Figure 5.7. The NEMA phantom images reconstructed using MRAC attenuation sinograms and TXAC attenuation sinograms were compared to ascertain how a two class uniform attenuation co-efficient method performed against the transmission scan method on a phantom with well-defined hot and cold regions of known volume.

The NEMA phantom was injected with 1ml of ^{18}F -NaF solution³. The tracer was allowed to mix for 30 minutes to give a uniform activity concentration throughout the phantom before placing the uniform region in the centre of the mouse surface coil and placing the phantom inside the MR scanner to perform the FISP MRI scan. After transfer to the split magnet F120 PET scanner, the NEMA phantom had an activity of $31.2 \pm 0.2\text{MBq}$ at the start of the 45 minute emission scan. A $160\mu\text{l}$ aliquot was drawn from the phantom before it was inserted into the PET scanner via the additional feeding hole in the design to

¹ 10 mice of the 12 mentioned in Chapter 4 were analyzed. Mouse 5 from the control mouse group did not have a FISP scan taken at the time of imaging and the transmission scan data for Mouse 3 from the drug treated group was found to be corrupted. These two mice were excluded from the AC analysis.

² A single point of scatter, based upon a centre of mass calculation, is used to generate a scatter profile for each transaxial angle. The scatter profile is subtracted from the transmission profile to give a scatter-corrected profile [69].

³ ^{18}F -NaF was used in place of ^{18}F -FDG as it was freely available on site and has similar behaviour in water phantom scans.

confirm its absolute activity concentration via cross-calibration with a well counter (3 inch NaI crystal, Harwell Instruments, Canberra UK Ltd.) using GENIE 2000 software.

8.2.3 Reconstruction of images using different AC methods

The gold standard TXAC method attenuation sinograms were calculated from the ratio between the singles counts of the 10 minute blank and transmission scans for each mouse using microPET manager software for both the *in vivo* mouse data and the phantom data.

A simple two class MRAC methodology was devised by the author and explored to ascertain its effectiveness in mice. PET emission and MR images were co-registered using the SPMmouse toolbox [27], using its bulk co-registration tool. FISP MR scans of the mouse body were then thresholded in Matlab using the signal magnitude to remove noise artefacts from the edge of the FOV, leaving the body outline only. The mouse body was then segmented from the background of the MR data using the image fusion package of ASIPRO analysis software (Siemens Medical Solutions) to form a two class μ map. The mouse body was defined as a single region of tissue with uniform attenuation co-efficient of 0.095cm^{-1} , with the surrounding background and mouse lung regions assigned an attenuation co-efficient of 0cm^{-1} (air). This was the default ASIPRO MRAC μ map approach. The scheme was then modified to give two additional MR μ maps, by first segmenting the mouse lung region of the MRAC μ maps in Matlab. The first modified MRAC approach used a two class scheme, assigning the lungs a linear attenuation co-efficient of 0.095cm^{-1} , and is referred to as MRAC (tissue) in this Chapter. The second modified MRAC approach used a three class scheme, with the lung region assigned its own attenuation co-efficient of 0.032cm^{-1} , the default lung class in ASIPRO, which is referred to as MRAC (lung) in this Chapter. The ASIPRO image fusion tool was then used to forward project all 3 MRAC μ maps and to histogram them into 3D PET attenuation sinograms for use in image reconstruction in conjunction with the PET emission sinograms.

EmAC μ maps were also constructed using the ASIPRO image fusion tool by thresholding a non-AC PET emission image (see later in this section for full image reconstruction parameters) of each mouse and segmenting out the mouse body contour from the background PET signal. This region was uniformly assigned the tissue attenuation co-efficient of 0.095cm^{-1} and was then forward projected to give an attenuation sinogram.

The NEMA phantom attenuation sinograms were created using a similar process to the mouse data. Its FISP MR images were noise thresholded in Matlab and segmented into air and water⁴ regions after being loaded in ASIPRO software, with each water region within the MR FOV assigned a uniform

⁴Plastic in mouse NEMA phantom was ignored as it could not be visualised on MR images and was deemed to be of small enough dimension to provide a negligible contribution to overall attenuation.

attenuation co-efficient of 0.095cm^{-1} and each air region assigned an attenuation co-efficient of 0cm^{-1} using the default MRAC method. This was designated as the MRAC approach for the phantom, but could also have been performed by segmenting the water regions from an emission scan of the phantom and assigning uniform attenuation co-efficients to these areas.

All static PET images were reconstructed using 3DRP for the last 20 minutes of the acquisition, both with and without each AC method attenuation sinogram applied. The images were reconstructed into a matrix of size $128 \times 128 \times 95$ with a transaxial pixel size of 0.87mm and a slice thickness of 0.80mm . Data were normalized and calibrated with corrections for decay, detector efficiency, dead time, random events and attenuation using the vendor microPET Manager software (Siemens Molecular Imaging). The reconstruction software available in microPET Manager does not allow for scatter correction to be performed on non-AC corrected data, and therefore, as a direct comparison between activity concentrations found in AC and non-AC data was desired in this study, scatter correction was not applied to the PET images. The magnitude of scatter in mouse imaging is much smaller than that in human imaging, with scatter fractions of only 8% reported for mice, compared to 33% for humans [28], making the effect of scatter correction less significant [78].

A summary of how the default two class TXAC and MRAC images were created is shown in Figures 8.2 and 8.3 respectively. The μ map shown in Figure 8.2 was reconstructed using the MAPTR algorithm, a specialized version of MAP used to reconstruct transmission scan data in microPET manager [69]. A similar process to that described in Figure 8.3 for the default MRAC approach was performed to generate images using both the modified MRAC and EmAC approaches.

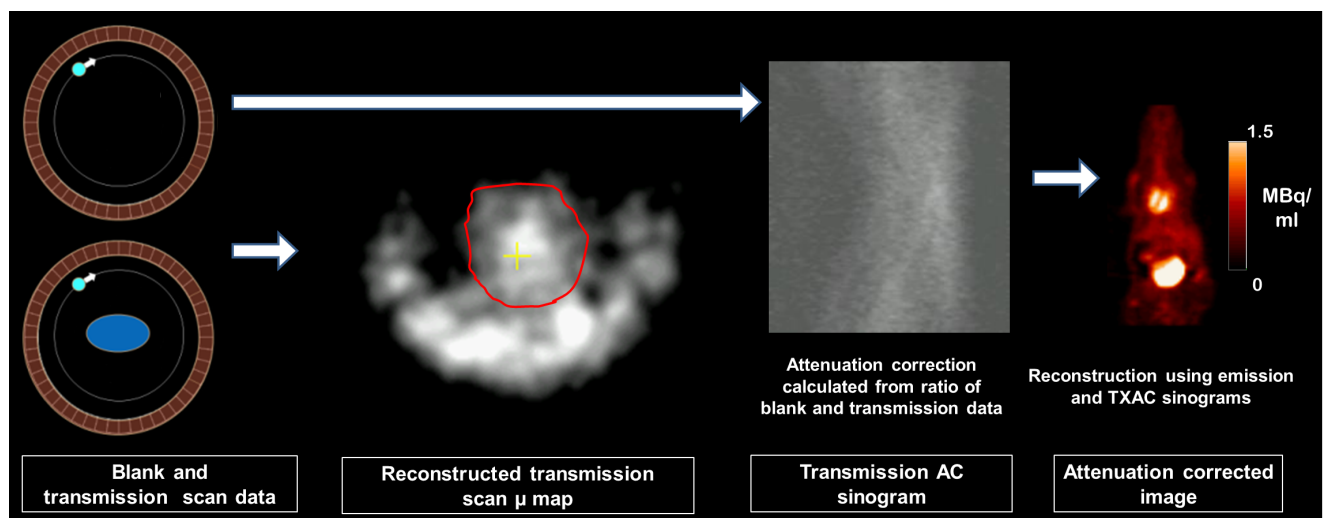


Figure 8.2: TXAC workflow. Blank and transmission scan data is used to construct the attenuation correction sinogram. The μ map shows that both the mouse body (yellow cross indicates centre of FOV aligned with mouse heart, red outline indicates approximate mouse body contour) and mouse surface coil and bed underneath it are present in the attenuation sinogram. The image on the far right comprises the last 20 minutes of scan data.

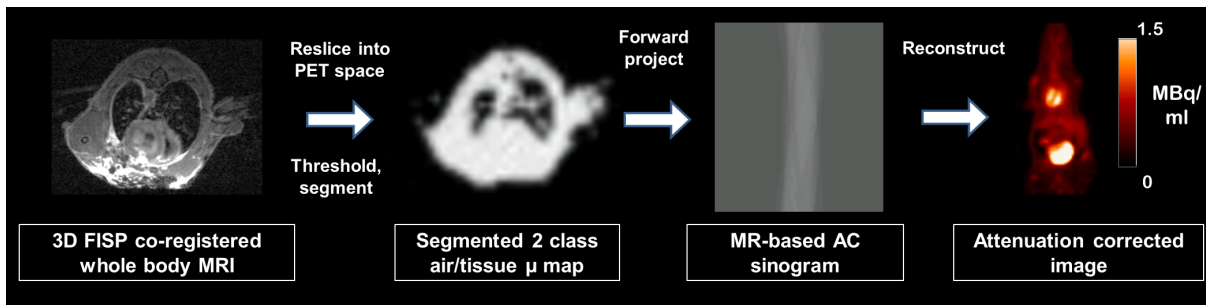


Figure 8.3: MRAC sinogram creation. Matlab was used to apply initial noise thresholds and reslice MR data. ASIPRO was then used to threshold tissue classes from the images and to forward project the segmented data into an attenuation sinogram. The image on the far right comprises the last 20 minutes of scan data.

Figure 8.4 shows the TXAC μ maps in more detail and Figure 8.5 shows the MRAC μ maps formed using the default air/tissue two class approach, with the lungs designated as air with an attenuation coefficient of 0cm^{-1} in this case. The overlaid emission scan in Figure 8.4 indicates the range of the EmAC method and also indicates that only the TXAC method corrects for the surrounding equipment such as the RF coil and animal bed.

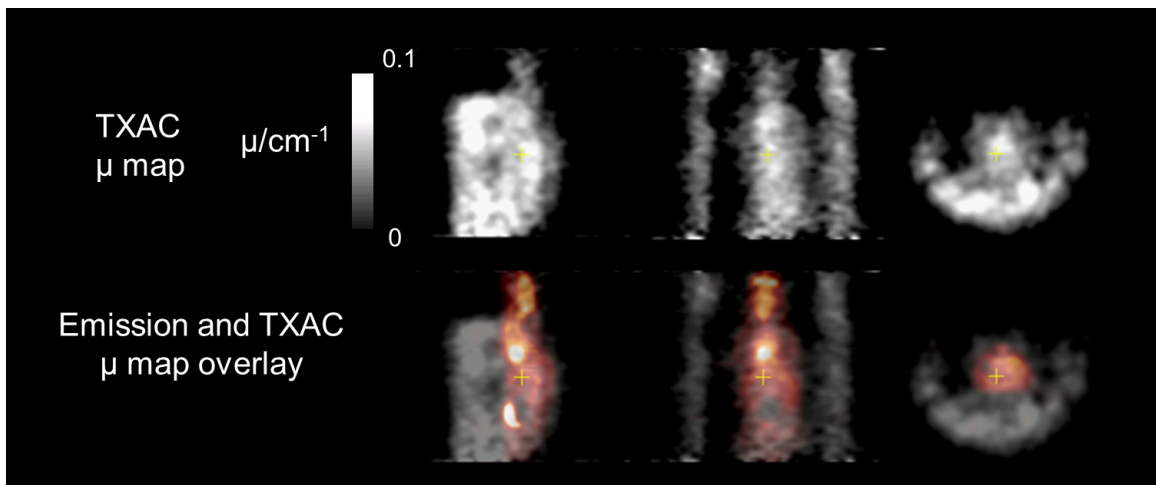


Figure 8.4: Transverse, coronal and sagittal views of TXAC μ maps with overlaid PET emission image (red). Grey areas indicate the additional equipment corrected for using TXAC.

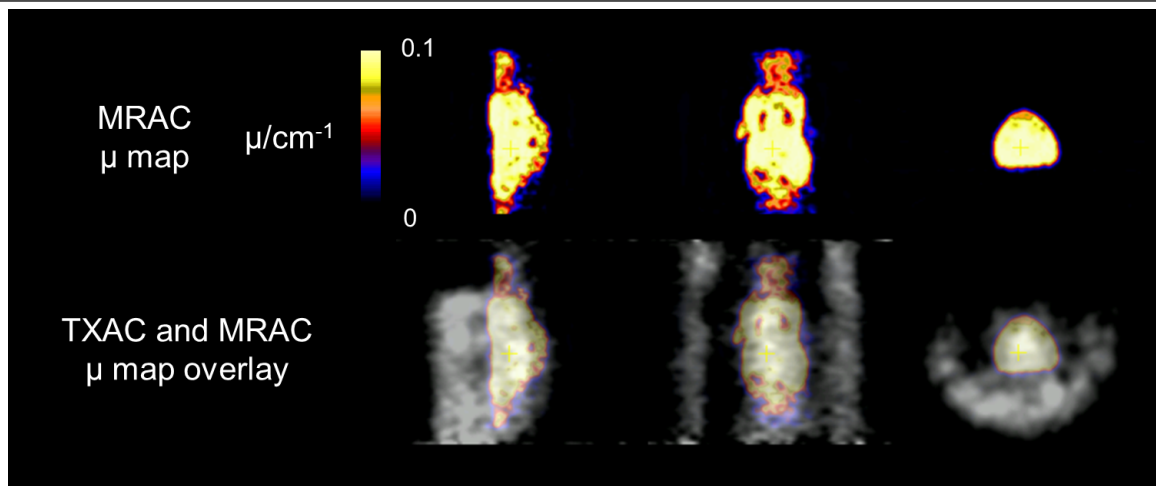


Figure 8.5: Transverse, coronal and sagittal views of MRAC μ map. Overlaid MRAC and TXAC μ maps illustrate that MRAC corrects only for mouse body whilst TXAC also corrects for surrounding equipment including the MR coil and animal bed.

8.2.4 SUV map calculation

SUV maps were calculated on a voxel by voxel basis from the summed PET images (last 20 minutes) for each AC technique using equation (3.1) from Chapter 3. Mean SUV values were then calculated for healthy myocardium and whole body ROIs. The healthy myocardium ROIs were the same as those used in Chapter 4, with an example shown in green in Figure 8.6. The whole body ROIs were segmented from the background using a signal intensity threshold on the outline of the FISP MR scans (the blue ROI in Figure 8.6).

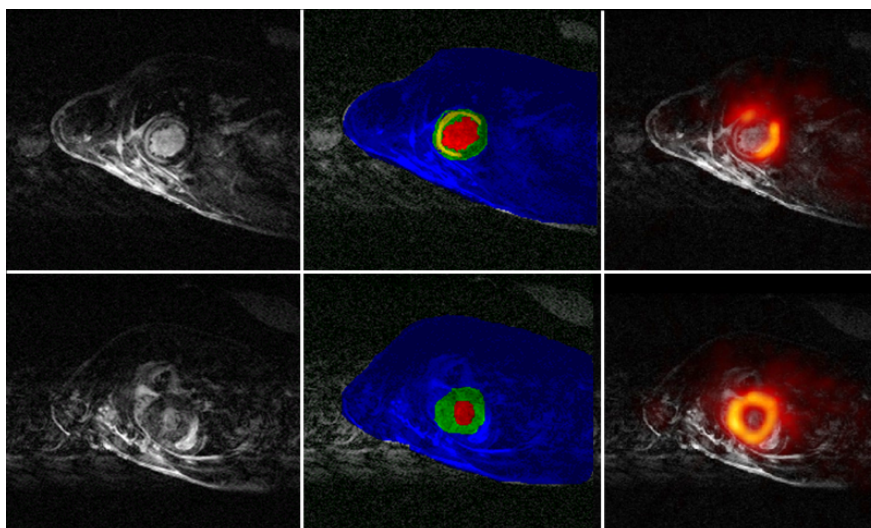


Figure 8.6: MR myocardial ROI shown over 2 different slices through mouse heart, taken from diastolic phase of cardiac cycle (previously shown in Chapter 4). Red region indicates LVBP ROI. Yellow region indicates infarcted myocardium ROI and green region indicates healthy myocardium ROI. Blue region indicates mouse body.

8.3 Results

8.3.1 Phantom results

Tracer concentration values were compared over line profiles (3 voxels wide), which are shown in Figure 8.7. Profiles for each AC method were taken across the main compartment of the NEMA phantom and across the cold air region. An aliquot taken from the NEMA phantom's large, 30mm diameter compartment was measured using a well counter with an activity concentration of 1.414 ± 0.005 MBq/ml.

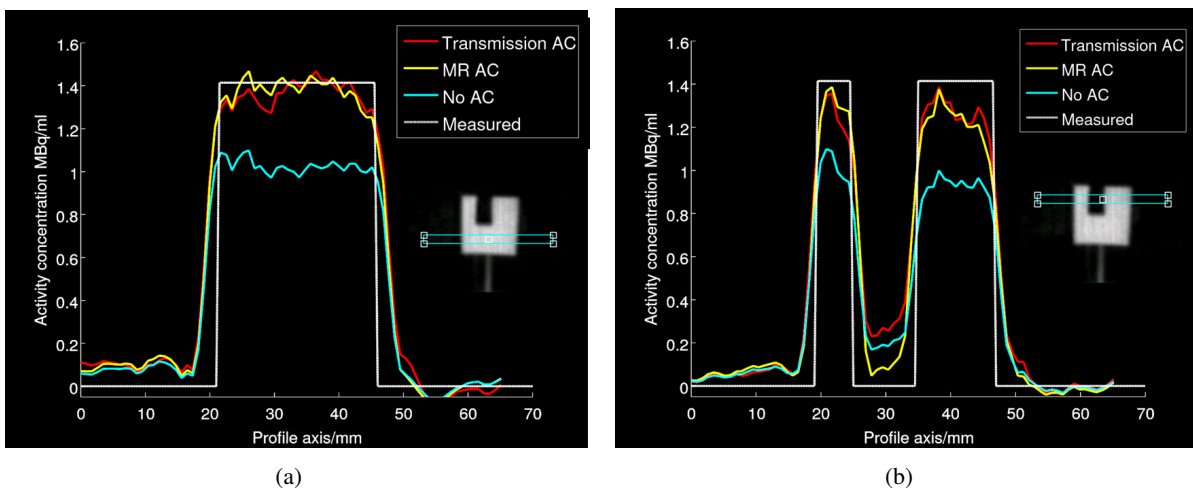


Figure 8.7: Left: Line profiles through large compartment of the NEMA phantom (hot region, tracer mixed in water) Right: Line profiles through air region of the NEMA phantom (cold region).

In the large diameter compartment of the phantom (Figure 8.7(a)), both the TXAC and segmented MRAC methods gave mean activity concentration values which agreed with those measured by the sample in the well counter, as shown in Table 8.1. These values were significantly higher (paired Student's *t* test, $p < 0.00001$) than values achieved without AC being applied, indicating the need to apply some form of AC to achieve absolute quantification in preclinical PET images. A uniform tissue value assigned to the large compartment was seen to provide adequate attenuation correction in the phantom case.

Activity concentrations in NEMA phantom, large diameter region

AC method	MBq/ml (mean \pm std)	% difference
Measured	1.41 ± 0.01	0.0
no AC	1.02 ± 0.04	-27.7
TXAC	1.35 ± 0.04	-4.3
MRAC	1.36 ± 0.04	-3.5

Table 8.1

All image line profiles exhibited non-zero noisy behaviour in the “cold” air region of the NEMA phantom (see Figure 8.7(b)), with the greatest noise present in the TXAC line profile. More noise and larger spillover of activity concentration into the “cold” region was observed in the TXAC line profile compared to the no AC applied line profile ($0.028 \pm 0.05 \text{ MBq/ml}$ compared to $0.20 \pm 0.03 \text{ MBq/ml}$), indicating that the TXAC method propagates noise into the PET emission images, which may result in overestimation of activity in “cold” regions, as indicated in Table 8.2. There is reduced noise in MRAC image profiles and a reduced bias to the actual value of 0 MBq/ml in the air region, as only uniform co-efficients are applied to each area and thus any small variations in local attenuation are not accounted for.

Activity concentrations in NEMA phantom, air region

AC method	MBq/ml (mean \pm std)
Measured	0.00 ± 0.01
no AC	0.20 ± 0.03
TXAC	0.28 ± 0.05
MRAC	0.11 ± 0.06

Table 8.2

Figure 8.8 shows how both the TXAC and MRAC methods create PET images which show a dramatic difference to images reconstructed with no AC applied. The differences seen between these images complement the 20-25% difference seen in the line profile results between no AC applied and both TXAC and MRAC. The propagation of noise by the TXAC method was also seen in the increased image artefacts seen in Figure 8.8.

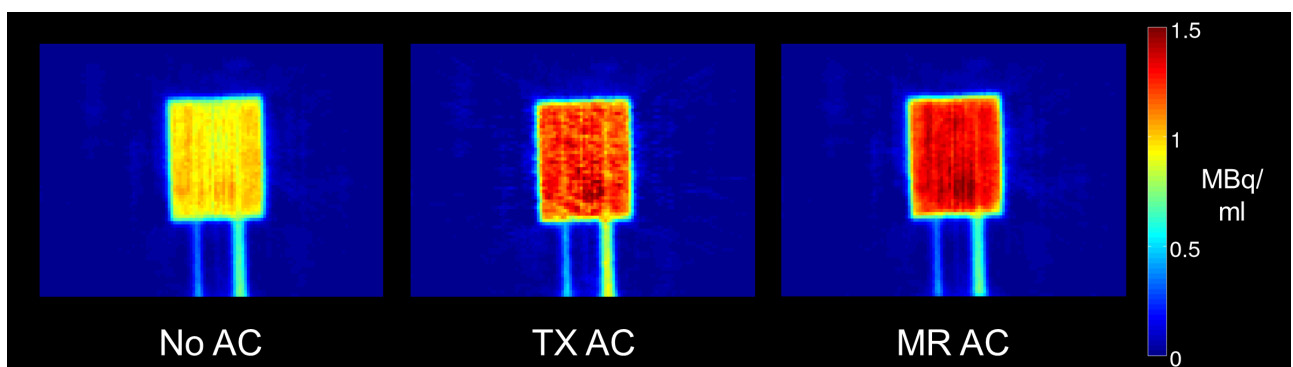


Figure 8.8: Activity concentration images of NEMA phantom with various AC methods applied. Clear difference between no AC and AC methods, with an average difference of between 20-25% across the phantom.

8.3.2 Mouse myocardial line profiles

Mouse line profiles through the myocardium region are shown in Figure 8.9. The results are similar to those found in the phantom, with a 20-25% decrease in peak activity concentrations in all orientations when any AC approach is applied compared to images with no AC. These results agree with previously published line profiles for mice in AC evaluation studies [77], [78]

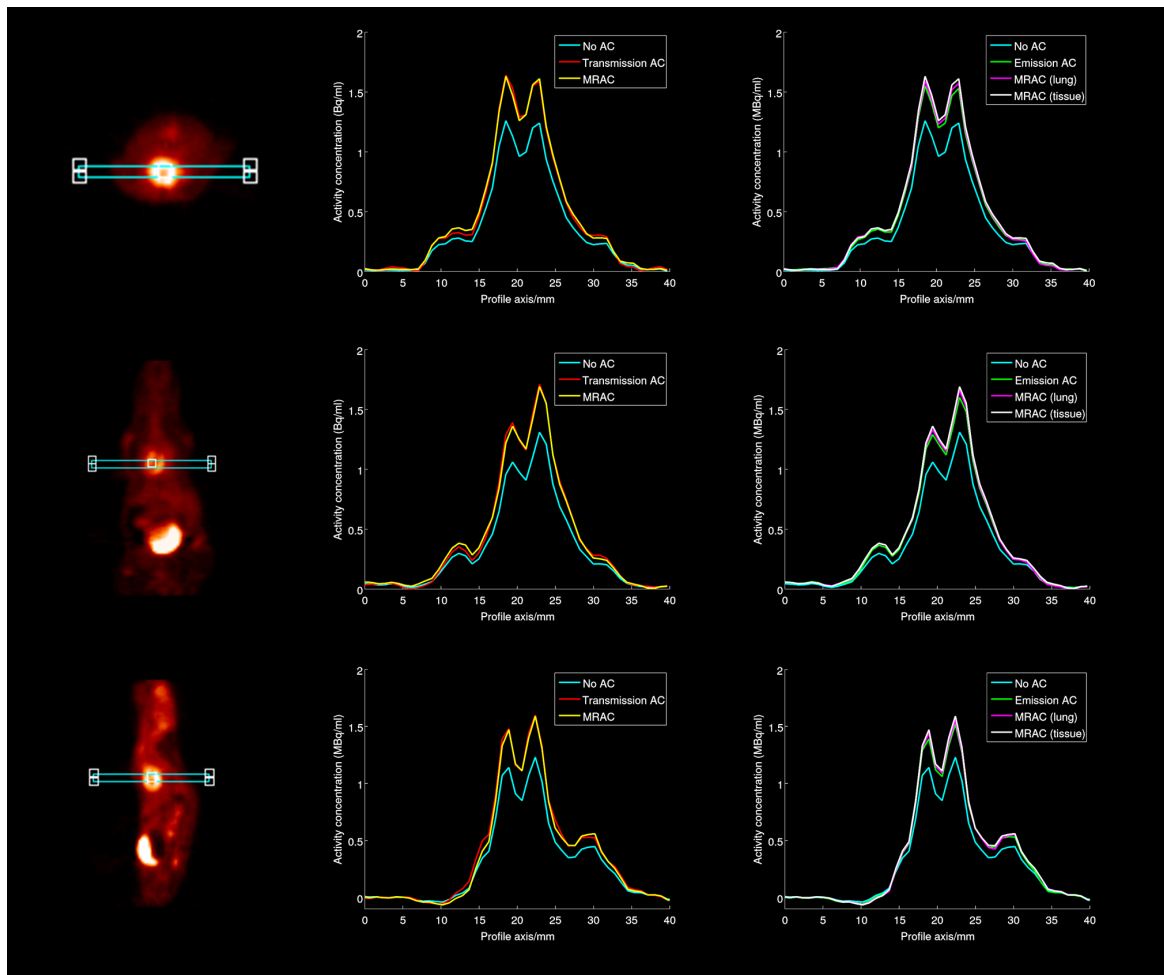


Figure 8.9: Line profiles through mouse heart for each AC method. From top: Transverse, coronal and sagittal views. Central peaks correspond to myocardium.

8.3.3 ROI SUV comparison between AC methods *in vivo*

Figure 8.10 shows the SUV maps created by each AC technique for a single subject. A clear difference in myocardial SUV can be seen between images with no AC applied and all other images, although there are only very slight differences between the TXAC image, the EmAC image and each of the MRAC images. No significant differences were found between the SUV values created using each of the AC techniques (paired Student's *t* test, all $p > 0.15$) but all mice across the group displayed significantly different values with AC applied compared to no AC (paired Student's *t* test, all $p < 0.00001$).

Tables 8.3 and 8.5 detail the relative SUV percentage differences achieved for each AC technique compared to no AC applied in the myocardium and over the whole mouse body respectively. For the myocardium, the TXAC method reported the largest mean increase across the mouse group ($22.6 \pm 0.9\%$), whilst the EmAC approach reported the lowest ($17.3 \pm 2.9\%$), with default MRAC only marginally higher at $18.5 \pm 0.9\%$. The MRAC (lung) and MRAC (tissue) techniques were closer to the TXAC values, with mean percentage differences of $20.3 \pm 0.9\%$ and $21.9 \pm 1.5\%$ respectively. The TXAC method reported the largest mean increase of $20.7 \pm 0.7\%$ compared to no AC applied for the whole body ROI, whilst the EmAC and default MRAC methods again reported the lowest increases of $16.3 \pm 3.6\%$ and $16.4 \pm 1.3\%$ respectively. The MRAC (lung) and MRAC (tissue) techniques again performed slightly better in this ROI, reporting increases of $17.0 \pm 1.3\%$ and $19.2 \pm 2.4\%$ respectively.

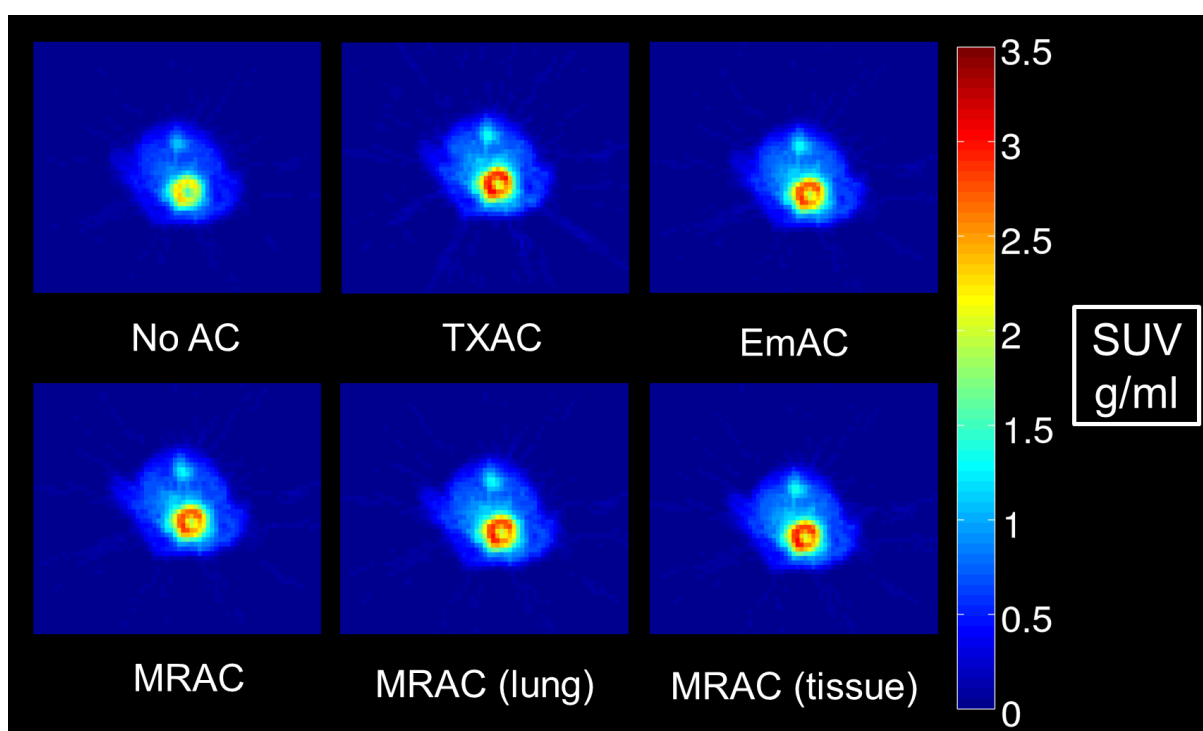


Figure 8.10: Comparison of mouse heart SUV maps (transverse view). Top row: (Left) No AC applied, (Centre) Transmission-based AC, (Right) Emission-based AC. Bottom row: (Left) MRAC, default two class (air and tissue), (Centre) MRAC (lung, tissue and air classes), (Right) MRAC (air and tissue), classifying lungs as tissue

All MRAC approaches produced myocardial and whole body SUV within 10% of TXAC values across the mouse group, as shown in Tables 8.4 and 8.6 respectively. The best agreement with the TXAC method was seen with the MRAC (tissue) method, which generated a mean difference of $0.9 \pm 2.4\%$ across the group. The largest percentage differences to TXAC were $6.3 \pm 2.8\%$ for the EmAC method and $5.0 \pm 1.6\%$ was the default MRAC method, which misclassified the lungs as air. For the whole body, the MRAC (tissue) method again reported the best agreement with TXAC, with a mean difference of $1.8 \pm 2.8\%$, whilst the EmAC and default MRAC methods reported mean differences of $5.2 \pm 3.9\%$ and

5.1±1.2%. The MRAC (lung) method in both cases showed better agreement with TXAC than the default MRAC method, but worse agreement than MRAC (tissue).

Mouse	TXAC	EmAC	MRAC	MRAC (lung)	MRAC (tissue)
1	23.9	21.8	17.9	19.3	20.3
2	23.9	22.3	18.7	21.1	22.9
3	23.2	18.6	18.1	20.2	22.1
4	21.7	17.4	19.0	20.6	22.6
5	22.3	14.7	19.1	21.4	24.9
6	21.9	18.2	18.8	20.8	22.3
7	22.2	16.0	20.3	21.5	22.8
8	21.7	13.8	17.2	19.6	20.5
9	23.4	14.6	18.2	19.3	20.0
10	21.7	15.6	17.9	19.3	20.5
Mean	22.6±0.9	17.3±2.9	18.5±0.9	20.3±0.9	21.9±1.5

Table 8.3: Percentage SUV increase (% , mean ± std) for myocardium, compared to no AC.

Mouse	TXAC - EmAC	TXAC - MRAC	TXAC - MRAC (lung)	TXAC - MRAC (tissue)
1	2.7	7.3	5.7	4.5
2	2.0	6.4	3.5	1.2
3	5.7	6.2	3.8	1.4
4	5.2	3.4	1.4	-1.1
5	8.9	4.0	1.2	-3.4
6	4.5	3.8	1.3	-0.5
7	7.4	2.5	1.0	-0.7
8	9.2	5.5	2.6	1.5
9	10.3	6.4	5.1	4.2
10	7.3	4.7	3.0	1.5
Mean	6.3±2.8	5.0±1.6	2.9±1.7	0.9±2.4

Table 8.4: Percentage SUV difference (% , mean ± std) for myocardium, compared to TXAC.

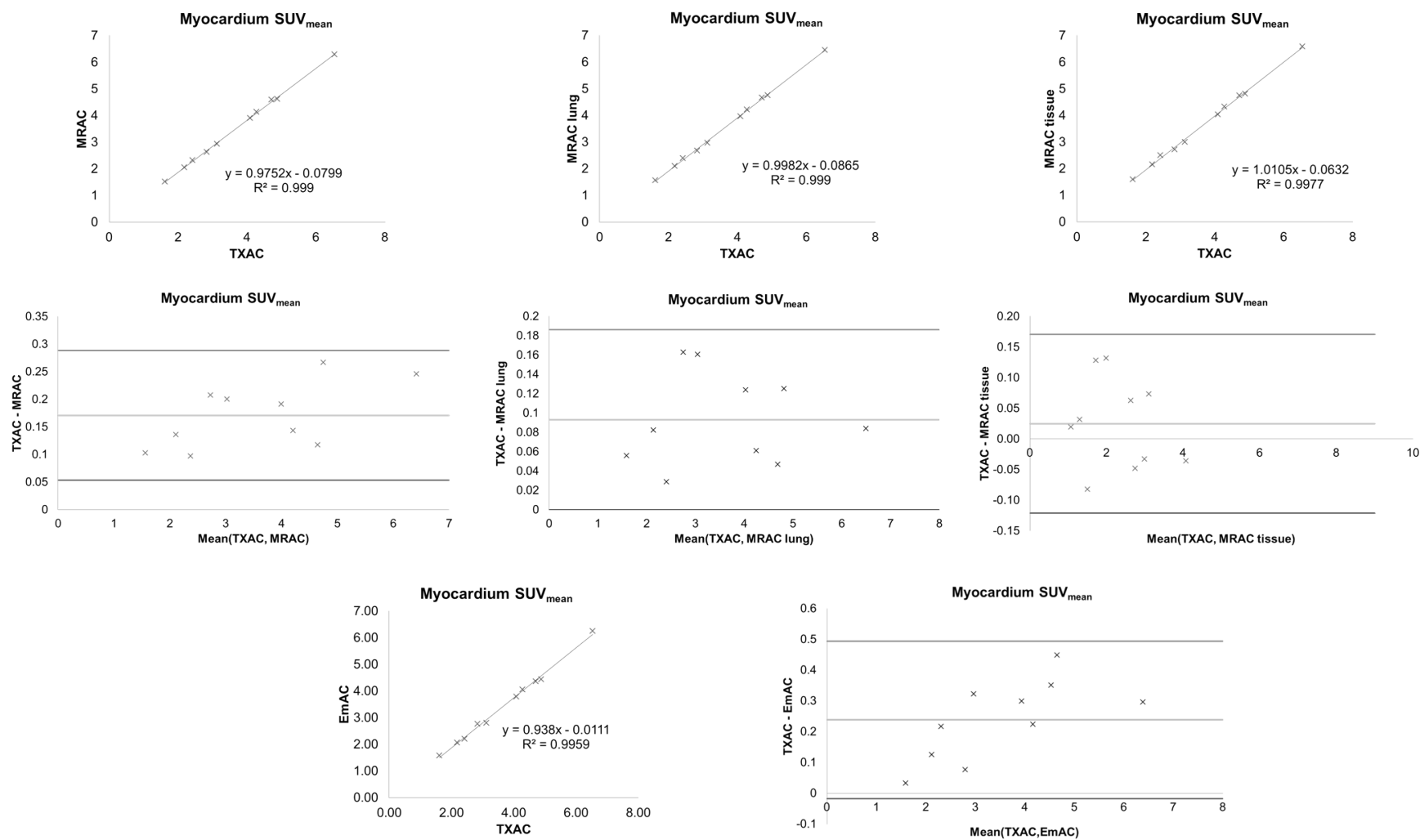


Figure 8.11: Correlation and Bland-Altman plots between mean SUV values produced using MRAC, MRAC (lung), MRAC (tissue) and EMAC against TXAC for myocardium ROI.

Mouse	TXAC	EmAC	MRAC	MRAC (lung)	MRAC (tissue)
1	21.4	23.3	15.8	16.0	15.0
2	21.3	21.6	16.8	17.9	20.8
3	20.7	16.5	14.8	16.3	19.3
4	19.9	15.7	16.2	16.9	20.3
5	20.9	13.1	17.7	18.8	22.9
6	20.3	16.8	16.9	17.9	20.1
7	22.1	15.8	19.0	19.2	21.1
8	20.3	12.1	14.5	15.4	16.5
9	20.6	13.1	16.7	16.7	18.2
10	19.9	14.9	16.0	15.5	17.8
Mean	20.7±0.7	16.3±3.6	16.4±1.3	17.0±1.3	19.2±2.4

Table 8.5: Percentage SUV increase (% , mean \pm std) for whole body, compared to No AC.

Mouse	TXAC - EmAC	TXAC - MRAC	TXAC - MRAC (lung)	TXAC - MRAC (tissue)
1	-2.5	6.7	6.5	7.5
2	-0.4	5.3	4.1	0.6
3	5.0	6.9	5.2	1.7
4	5.0	4.4	3.6	-0.5
5	9.0	3.9	2.6	-2.7
6	4.3	4.2	3.0	0.2
7	7.5	3.8	3.7	1.3
8	9.2	6.7	5.8	4.5
9	8.6	4.7	4.6	2.9
10	5.8	4.6	5.1	2.5
Mean	5.2±3.9	5.1±1.2	4.4±1.2	1.8±2.8

Table 8.6: Percentage SUV difference (% , mean \pm std) for whole body, compared to TXAC.

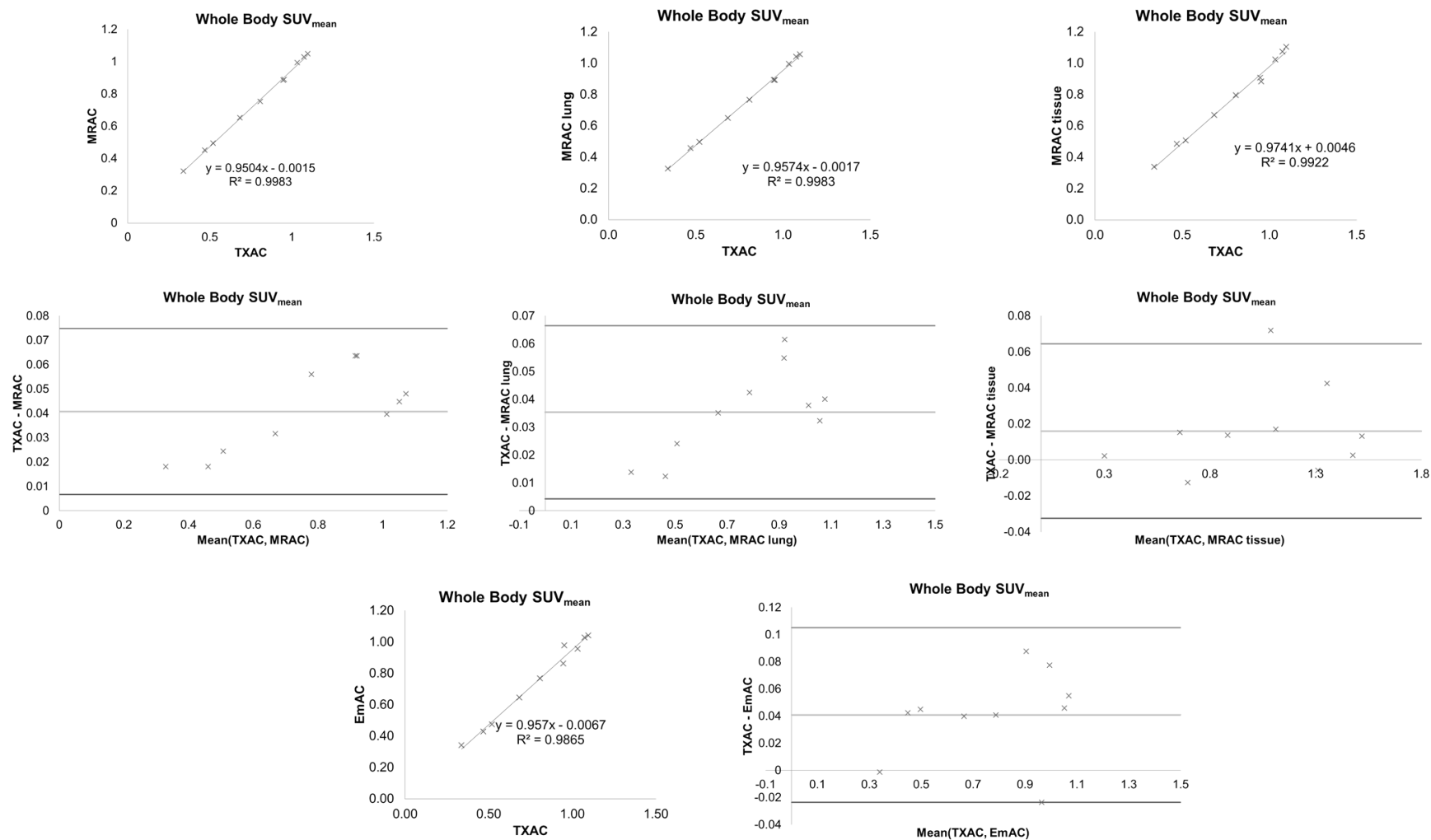


Figure 8.12: Correlation and Bland-Altman plots between mean SUV values produced using MRAC, MRAC (lung), MRAC (tissue) and EMAC against TXAC for whole body ROI.

Linear relationships were observed between all MRAC approaches and TXAC values for both myocardium and whole body values, as shown in Figures 8.11 and 8.12. Additionally Bland-Altman plots showed a small bias between the TXAC and default MRAC method over the 10 mouse group in both ROIs, which appeared to be a systematic error and was of similar size for each mouse. A small bias was also seen in the EmAC Bland-Altman plots, with a more prominent trend seen for the myocardium ROI. The bias was reduced in the MRAC (lung) comparison and further reduced in the MRAC (tissue) comparison, indicating that segmenting the lung region and re-assigning its attenuation co-efficient reduced the error between the techniques and TXAC. The mean difference for the MRAC (tissue) and TXAC methods in the myocardium region was very close to 0 and four of the 10 data points were below 0, indicating good agreement between these two techniques in this region. The higher variation of the MRAC (tissue) method in the whole body ROI did result in one data point, however, being outside the upper bound in its Bland-Altman plot, again suggesting that the MRAC (tissue) technique has the best agreement with the gold standard technique but also exhibits the greatest variation between mice of the MRAC techniques.

8.3.4 Whole-body SUV map comparison between AC methods

A comparison between the no AC and TXAC images in the transverse view over the mouse heart region is shown in Figure 8.13 for a single subject. The difference in SUV values varies with position within the mouse body. There is a 20–30% difference between the no AC and TXAC images throughout the main torso region, increasing to greater differences of up to 40% at the base of the mouse body. A similar set of images is shown for the EmAC technique in Figure 8.14. A smooth and uniform correction of 15-20% is observed in the centre of the mouse torso, and reduces towards the edges of the mouse body. The no AC and default MRAC comparison images are shown in Figure 8.15, indicating relatively uniform differences of approximately 15% is seen in the mouse torso, with greater differences seen at the edges of the mouse body of up to 40% and very low differences of approx -2–3% seen in the lung regions, as this region was designated as air in the AC sinogram. The change in SUV difference map when lung region is re-classified as lung tissue rather than air is shown in Figure 8.16, showing that the lung region now exhibits a mean difference of 10% and the main torso difference has also increased by 10%, giving greater agreement with the TXAC method. The best agreement with the TXAC SUV difference maps is seen with the lung region reclassified as tissue in Figure 8.17, although the increase towards maximum differences seen at the base of the mouse body in the TXAC results is not observed.

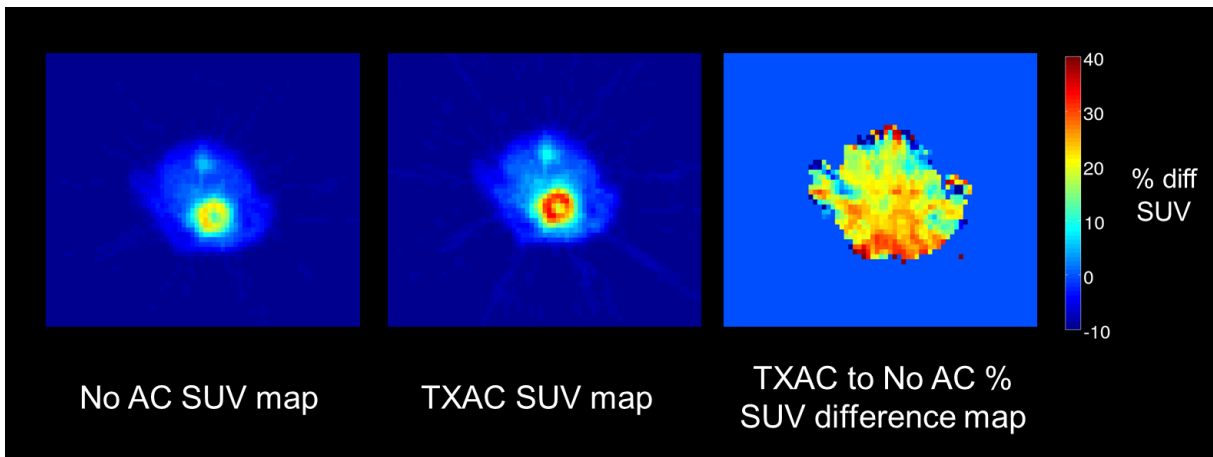


Figure 8.13: SUV map comparison between no AC and TXAC applied, showing large SUV changes in mouse myocardium region. Mouse body segmented from SUV percentage difference map and thresholded to -10 – 40% to mask noise from streak artefacts.

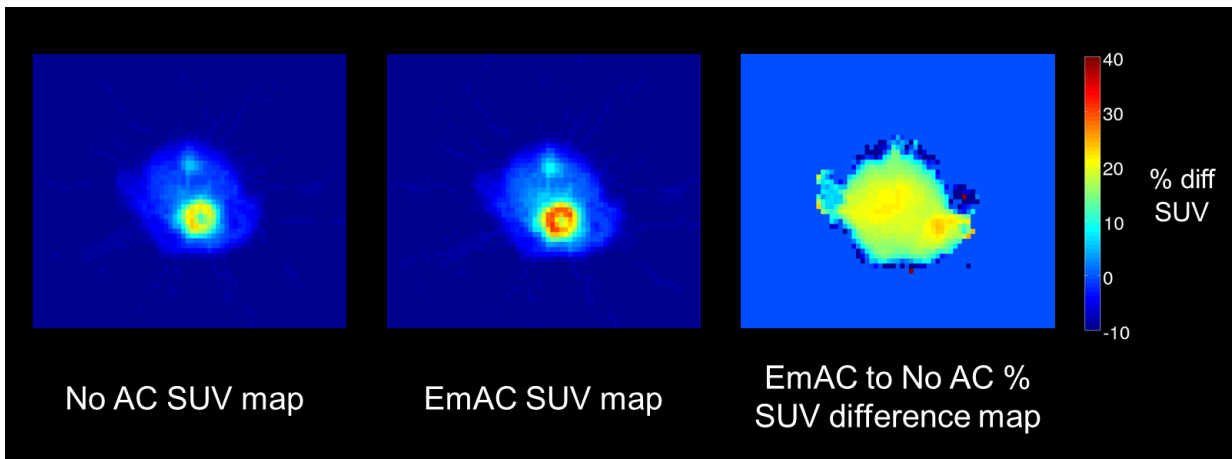


Figure 8.14: SUV map comparison between no AC and EmAC applied, showing smooth, uniform correction in mouse torso. Mouse body segmented from SUV percentage difference map and thresholded to -10 – 40% to mask noise from streak artefacts.

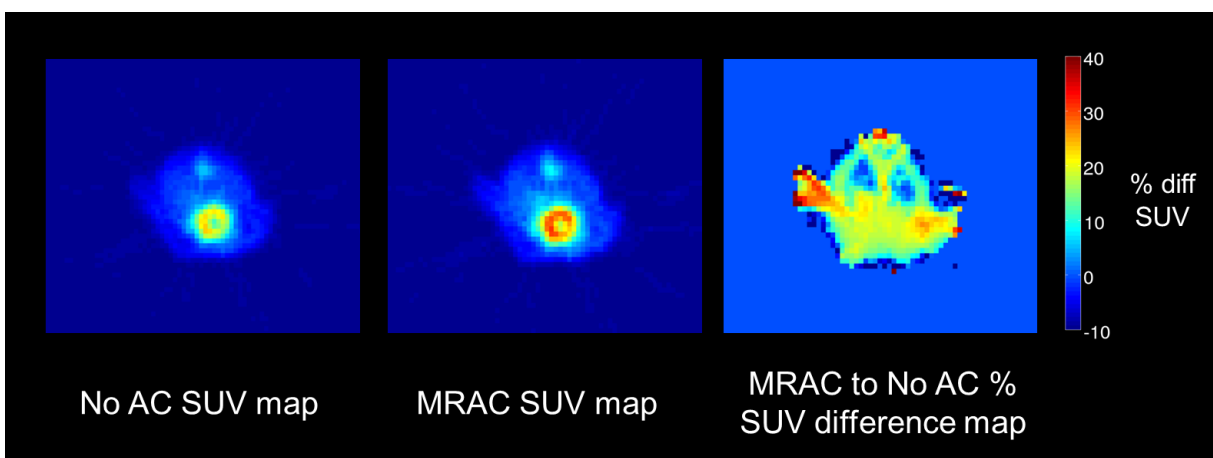


Figure 8.15: SUV map comparison between no AC and MRAC applied, showing relatively uniform changes in mouse torso, except for lungs. Mouse body segmented from SUV percentage difference map and thresholded to -10 – 40% to mask noise from streak artefacts.

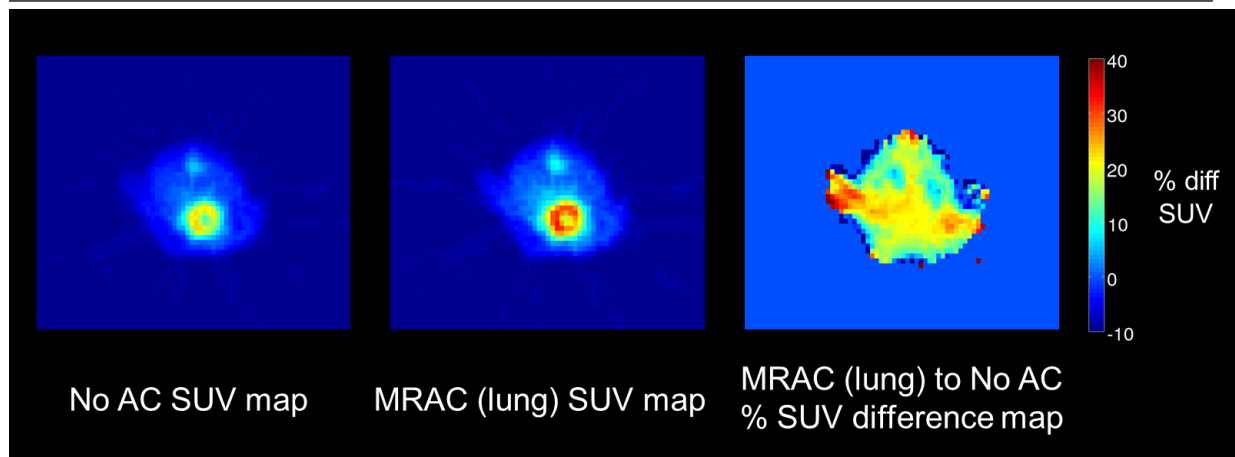


Figure 8.16: SUV map comparison between no AC and MRAC (lung) applied, showing more uniform changes throughout mouse lung region. Mouse body segmented from SUV percentage difference map and thresholded to -10 – 40% to mask noise from streak artefacts.

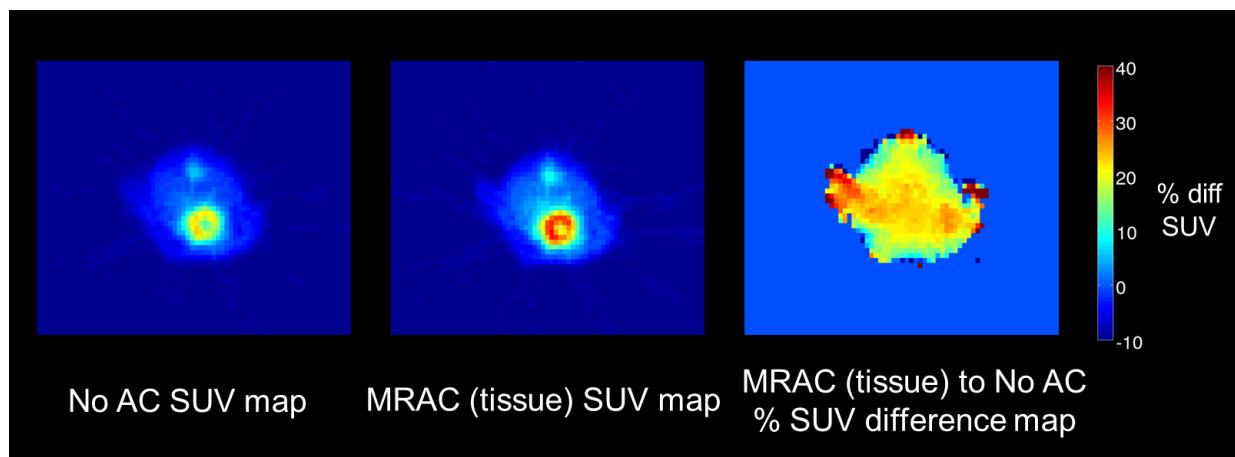


Figure 8.17: SUV map comparison between no AC and MRAC (tissue) applied, showing relatively uniform changes throughout mouse body region. Mouse body segmented from SUV percentage difference map and thresholded to -10 – 40% to mask noise from streak artefacts.

Direct comparisons between TXAC, EmAC and each MRAC method SUV images are shown in Figures 8.18, 8.19, 8.20 and 8.21. The EmAC comparison in Figure 8.18 shows large differences of >20% towards the edges of the mouse body, with the largest differences seen at the base of the mouse body. Figure 8.19 indicates reductions in SUV compared to TXAC for the default MRAC approach of up to 25% in the lung region and at the base of the mouse body. For MRAC (lung) in Figure 8.20 the difference is reduced to between 15-20% and the torso region becomes more distinct with a difference around 0%, although the large difference at the base of the mouse body remains at the same level. When the lung region is re-classified as tissue (see Figure 8.21), it now appears similar to the torso region, with a mean difference around 0% in the myocardium ROI. The large difference at the base of the mouse body again remains at a high level, with maximum differences of up to 25% seen in this mouse, indicating that this region remains undercorrected for attenuation in all approaches except TXAC.

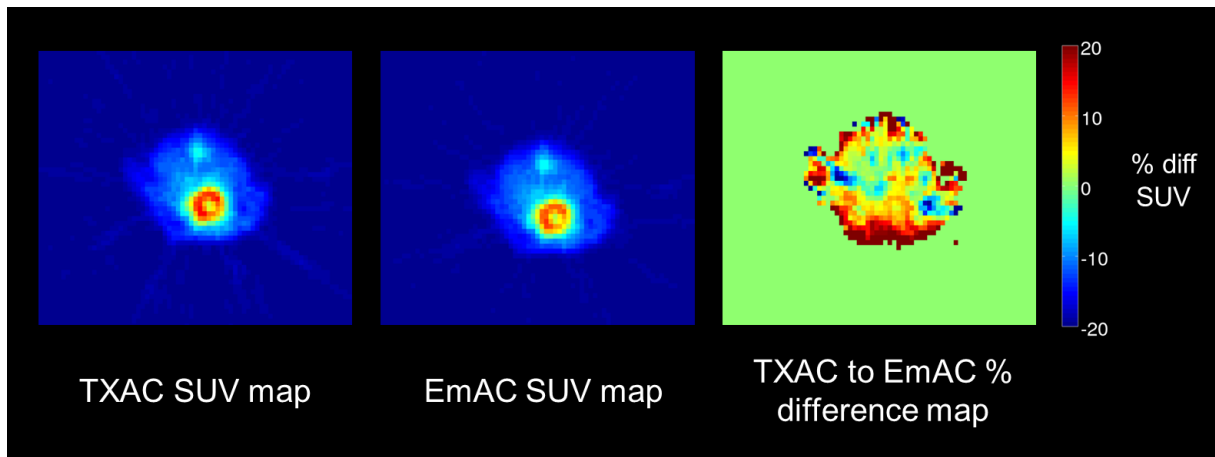


Figure 8.18: SUV map comparison between gold standard TXAC and EmAC, showing large differences throughout the mouse body. Mouse body segmented from SUV percentage difference map and thresholded to $-20 - 20\%$ to mask noise from streak artefacts.

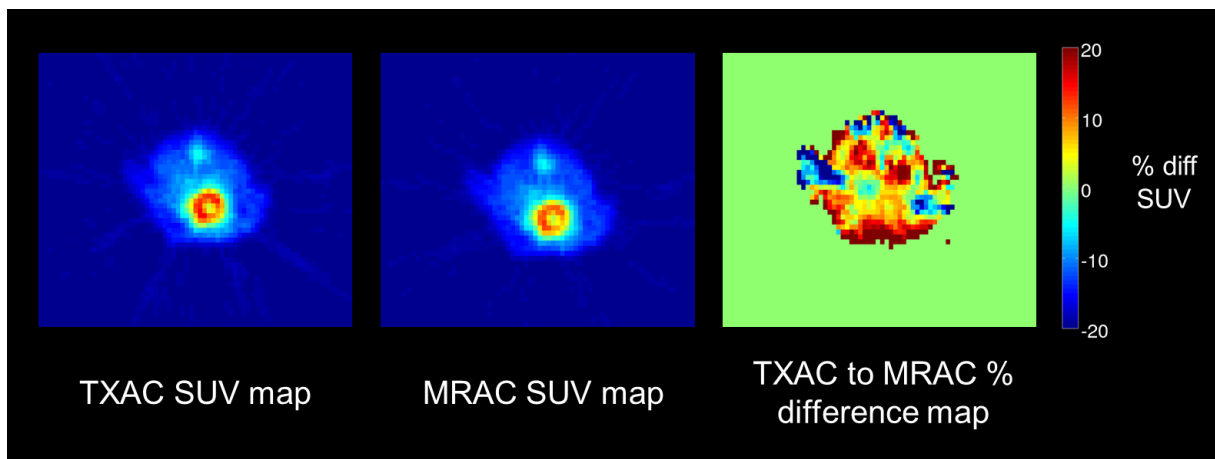


Figure 8.19: SUV map comparison between gold standard TXAC and MRAC, showing large differences in the misclassified lung region. Mouse body segmented from SUV percentage difference map and thresholded to $-20 - 20\%$ to mask noise from streak artefacts.

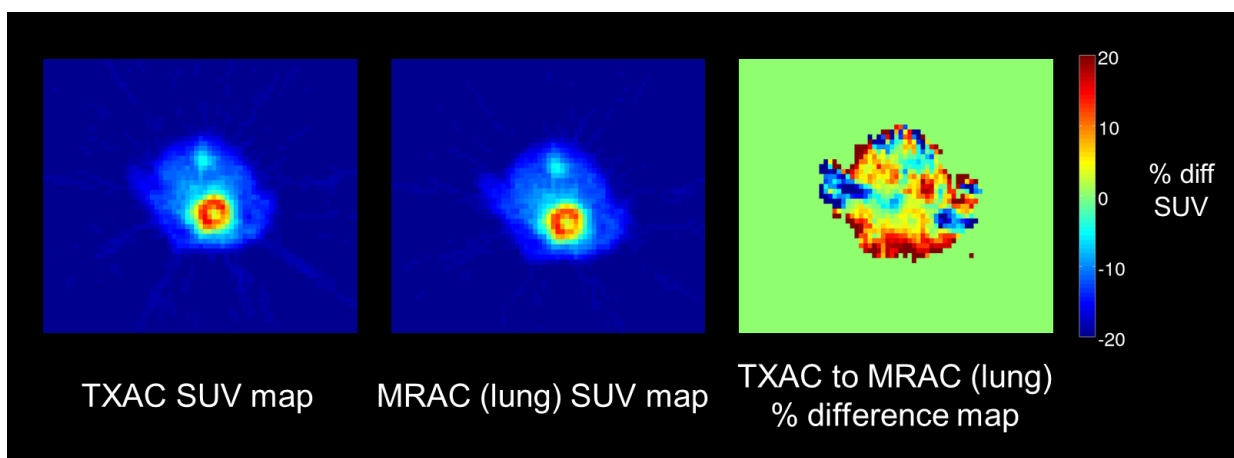


Figure 8.20: SUV map comparison between gold standard TXAC and MRAC (lung), with reduced differences in the lung region. Mouse body segmented from SUV percentage difference map and thresholded to $-20 - 20\%$ to mask noise from streak artefacts.

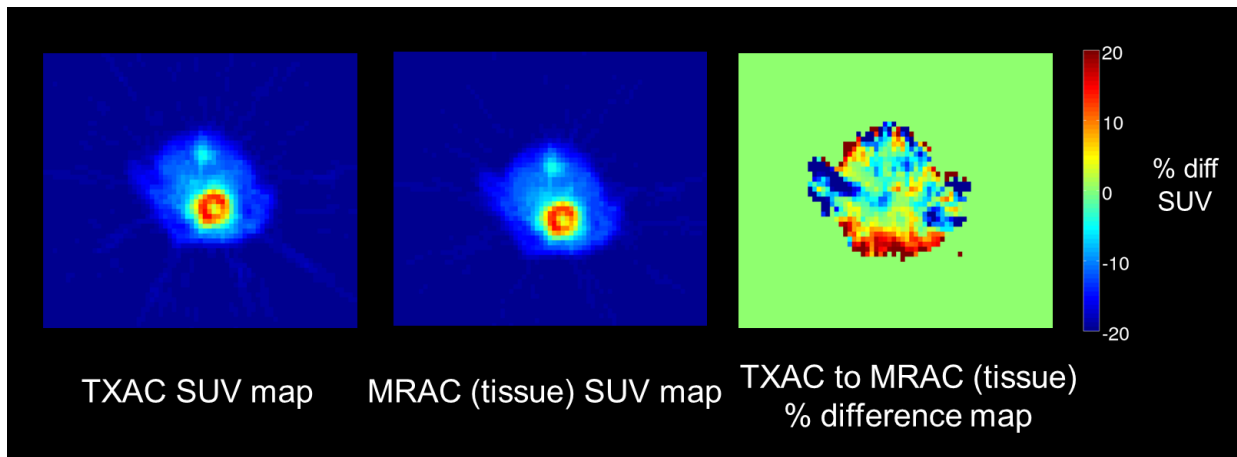


Figure 8.21: SUV map comparison between gold standard TXAC and MRAC (tissue), showing relatively small differences over mouse body. Mouse body segmented from SUV percentage difference map and thresholded to $-20 - 20\%$ to mask noise from streak artefacts.

8.3.5 Cause of disparities between TXAC and other AC methods

Differences of up to $+40\%$ across the mouse group (mean \pm std: $30.1 \pm 4.4\%$, range: $27-40\%$) between even the MRAC (tissue) and TXAC SUVs were noted in the lower mouse body directly adjacent to the coil and bed (bed and coil shown in grey in Figure 8.22 and corresponding photograph in Figure 8.23). This corresponds to the difference between the linear attenuation co-efficient maps for TXAC and MRAC, shown in Figures 8.4 and 8.5.

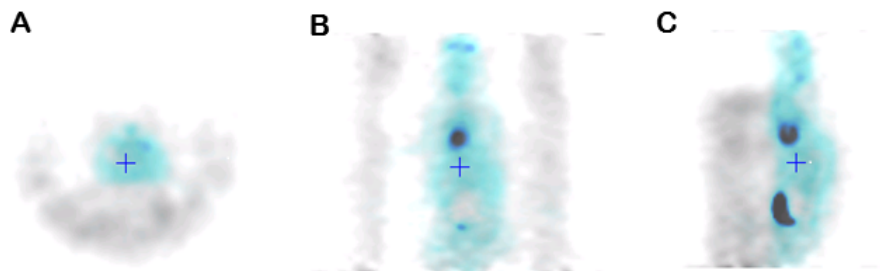


Figure 8.22: Fusion of PET emission (blue) and transmission (grey) images showing mouse, coil and bed. Greatest attenuation from grey areas appears at base of mouse body. (A) Transverse view, (B) coronal and (C) sagittal.

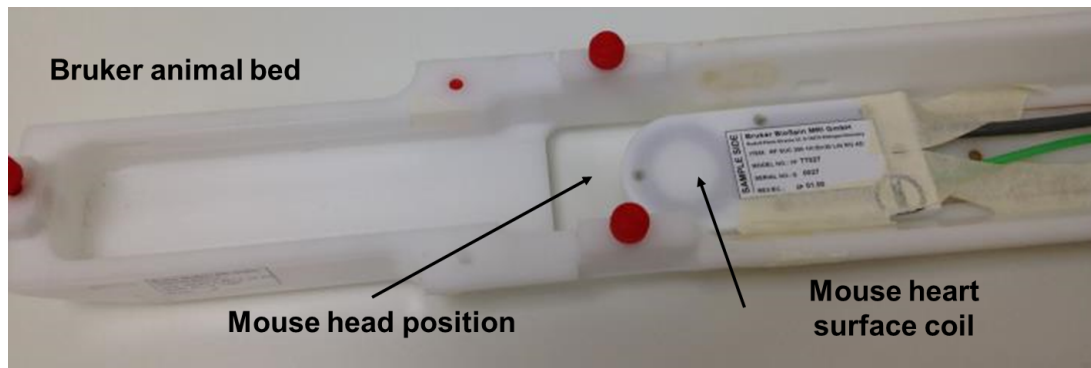


Figure 8.23: Photograph showing the mouse bed and coil used for heart imaging. Both are made from 1cm plastic, resulting in localised attenuation in the mouse PET images.

Figure 8.5 also shows all MRAC approaches also suffered in areas near the top edge of the mouse torso due to the limited range of the surface coil used for whole body acquisitions, shown in the small high percentage difference region at the top of the mouse torso in Figure 8.21. The EmAC approach also suffered in this area and on the flanks of the mouse torso.

Large negative differences (-15 – 20%), indicating that the MRAC images were over-correcting and reporting higher values than the TXAC images, were seen between TXAC and all 3 MRAC techniques on side flanks of the mice, such as in Figure 8.21. In EmAC, this region reported a positive 15–20% change, indicating it was undercorrected compared to TXAC due to the limited range of the EmAC technique. The overcorrection therefore occurred as the MRAC methods applied a uniform tissue correction over all regions of the segmented mouse body visible on the MR scan, and did not accommodate for small differences in the AC linear co-efficients within the side flank region where only very small regions, such as the mouse arms, attenuate the signal.

8.4 Discussion

8.4.1 Evaluation of tested AC methods

The TXAC, EmAC and segmented MRAC methods were found to create more accurate activity concentration and SUV map results compared to not applying AC by between 17-23% on average across the mouse group. These results were also confirmed using the NEMA phantom. The difference between SUV values and activity concentrations was found to be significant between applying AC and not applying AC (paired Student's t test $p < 0.00001$), but no significant differences were found between the SUV values produced by each of the AC techniques. This agreed with previously published comparisons of preclinical AC techniques [77], [78], which estimated the correction to be between 9-26% and also found the difference between AC and no AC applied to be significant. Line profiles (see Figure 8.9) also

showed that AC is required to attain accurate quantification in murine PET, particularly in high uptake regions, such as the myocardium for ^{18}F -FDG. These results were also supported by the similar results reported in the line profiles and SUV maps produced from the NEMA phantom data.

SUV maps of the 10 mice scanned found the TXAC, EmAC and 3 MRAC methods increased SUV values in both the myocardium ROI and over the whole body ROI when compared to not using AC, with no significant differences found between them (paired Student's t test, all $p > 0.15$). All 3 MRAC methods produced SUV values within 10% of those derived using TXAC for both the myocardium and the whole body ROIs, indicating that the MRAC techniques provide an adequate approximation of the required AC. As shown in Figures 8.11 and 8.12, a clear linear trend can be fitted between the TXAC and MRAC techniques ($R^2 > 0.99$). The SUV percentage difference measures shown in Tables 8.3 and 8.5 were found to agree with literature estimates of expected mouse attenuation [77]. These results confirm that any of the 3 segmented MRAC approaches detailed in this Chapter provide adequate myocardium SUV values in murine studies, although the best agreement with the gold standard TXAC was achieved by re-classifying the lung regions originally classified as air in ASIPRO as soft tissue, with a linear attenuation co-efficient value of 0.095cm^{-1} . This agreed with previous work in humans, which noted that lung tissue was the third most important class to segment behind soft tissue and air, as misclassification of lung regions as air could lead to errors in activity concentrations of between 25-40% [81].

The MRAC (tissue) method gave the lowest mean SUV difference of $0.9 \pm 2.4\%$ in the myocardium and $1.8 \pm 2.8\%$ in the whole body ROI and reported the smallest bias in the Bland-Altman analysis shown in Figures 8.11 and 8.12. It also reported the greatest agreement in spatial distribution of SUVs across the mouse body with TXAC, compared to EmAC and the other MRAC techniques, as demonstrated in the SUV difference maps shown in Figure 8.21. This indicates that mice lung regions are so small that the local differences in linear attenuation co-efficient resulting from lung tissue should be neglected in a segmented MRAC approach and the default MRAC map produced by ASIPRO, which classifies the lungs as air, must be modified accordingly. The MRAC (tissue) approach was found to be more accurate on average across the mouse group compared to an EmAC approach, confirming results by previous work which noted that applying a uniform AC correction across the mouse body from the PET emission scan resulted in incorrect AC estimations at the edges of the mouse body [77], [78].

The use of previously acquired data from a myocardial infarction drug study (detailed in Chapter 4, $n=10$ mice, 5 control mice and 5 drug treated mice [30], [228]) to study the effects of AC methods on PET image quantitation was non-ideal and therefore percentage differences in activity concentrations and SUV values produced using the different AC techniques were examined rather than relying on absolute values. SUVs for all mice were affected in the same manner by each AC technique, indicating that the AC effect was independent of animal model.

8.4.2 Improvements to MRAC method

All the MRAC and EmAC methods reported SUV differences of up to +40% at the base of mouse body over the mouse group, and these were attributed to local attenuation from the mouse coil casing and animal bed (see Figure 8.23), which were of comparable size to the mouse and made of polyethylene (HDPE) acrylic plastic [288] of approximately 1cm thickness each (combined thickness approximately 2cm). Acrylic plastic is used as it is inexpensive, machines well and is readily available, and fortunately it had a relatively low linear attenuation co-efficient with a theoretical value of 0.093cm^{-1} [69], [288]⁵. In this study, TXAC μ maps reported μ values similar to tissue within the bed region, with a mean linear attenuation co-efficient of $0.094 \pm 0.018\text{cm}^{-1}$ recorded across the cohort, indicating that the animal bed and coil cannot be neglected if absolute quantification is to be achieved, as it provides attenuation on a similar level to that of the mouse body itself. If available, it would be advised that CT templates of the coil and bed are added to future MRAC and EmAC maps (following a similar procedure to that applied in clinical studies [76]) to avoid local inhomogeneities in the AC accuracy towards the base of the mouse body due to presence of the animal bed and RF coil.

MRAC also suffered near the top edge of the mouse body (see maps in Figure 8.5) due to the limited range of the surface coil, although no correction for RF inhomogeneity or FOV truncation was applied in this work. Ideally MRAC should therefore be provided using a volume transmit/receive coil with an RF inhomogeneity correction applied to reduce spatial bias in the AC provided. Additional truncation artefacts could be filled in by allocating uniform attenuation co-efficients from emission scans if possible. In this study, the myocardium ROI SUV values were not affected by these truncation artefacts, so this would not be essential in future mouse cardiac studies. Likewise, the overcorrection provided by the MRAC methods at the mouse flank (caused due to the MRAC methods not accounting for local variations in μ value) could also be addressed by using the ^{18}F -FDG emission scans to crop the edges of the MRAC μ maps, although this overcorrection did not affect the myocardium ROI in this work, so again it would not be essential in future cardiac studies.

It should be noted, however, that although TXAC values were taken as the gold standard in this Chapter, this method produced low resolution μ maps and propagated noise into the final images [77], [78], [289] with the increase in noise shown most clearly in the NEMA phantom line profiles and the increased streak artefacts seen in all TXAC images. The SNR of the TXAC method was also limited as it could only be performed for a single pass of 10 minutes. Further comparison of the MRAC techniques detailed here with a CTAC approach could therefore be performed to assess the impact of TXAC image noise on the AC comparison results.

⁵The very small copper components within the RF coil may also contribute, with linear attenuation co-efficient of 0.74cm^{-1} [69], although their small size should mean that these contributions are minimized.

8.5 Conclusion

A simple, two class (tissue and air) segmentation based MRAC approach for quantitative, simultaneous PET/MR imaging has been validated against gold standard TXAC for 10 mice. Both TXAC and MRAC methods were found to give an approximately 20% increase in absolute activity concentrations and SUV values when compared to images reconstructed without AC applied in both phantom and *in vivo* datasets. MRAC was also found to provide mean SUV differences of <10% compared to TXAC in both a myocardium ROI and across the whole mouse body, which was deemed adequate for myocardial imaging in mice. To provide the best agreement with TXAC, the lung region should be re-assigned a soft tissue linear attenuation co-efficient in place of the default air linear attenuation co-efficient assigned by ASIPRO software, resulting in a reduction of the mean SUV difference to $0.9 \pm 2.4\%$ in the myocardium ROI and $1.8 \pm 2.8\%$ in the whole body ROI when compared to TXAC. Further improvements to the MRAC method could include the addition of CT templates of coils and animal beds to MRAC μ maps, as these were found to be the biggest source of disparity between the TXAC, EmAC and MRAC techniques. If even greater quantitative accuracy was required, UTE sequences could also be tested to see if they could offer a further gain in accuracy, as UTE has been shown to provide improved AC accuracy via bone identification in human studies [75], [76], [87] and in rat SPECT studies [290] of the brain and lungs.

8.6 Chapter summary

Attenuation correction in PET/MR systems must be implemented to provide comparable image quantitation results to stand-alone PET or PET/CT which utilise traditional AC approaches. In this Chapter, a two class (tissue and air) MRAC method for mice was evaluated against a gold standard TXAC method for both phantom and *in vivo* murine imaging studies. It was concluded that some form of attenuation correction was required in murine imaging and that the default two class MRAC method provided by ASIPRO should be refined with the lung region segmented from the MR images and assigned a soft tissue linear attenuation co-efficient. This simple, two class MRAC method could then be easily implemented to give myocardial SUV values within <5% accuracy of gold standard TXAC for use in quantitative, simultaneous PET/MR studies of the mouse heart.

Chapter 9

Conclusions

The PET/MR field is rapidly expanding in both clinical and preclinical arenas due to the ability of PET/MR to provide exquisite soft tissue contrast and high resolution anatomical information to complement functional information derived from PET, without the need for additional radiation exposure to the subject. This thesis has explored various uses of sequentially acquired MR images to improve the quantification of small animal PET data.

9.1 Importance of partial volume correction in murine IDIF extraction

As shown in Chapters 4 and 5, without applying some form of partial volume correction, deriving accurate PET AIFs from images is extremely difficult in murine studies. Accurate IDIFs are, however, highly desirable due to low total blood volumes in mice, which makes serial blood sampling challenging.

9.1.1 ^{18}F -FDG

In Chapter 4 it was shown that even with the application of motion correction from cardiac gating derived from mouse ECG signals, in conjunction with improved ROI delineation from co-registered, high resolution MR images, the resulting IDIFs extracted from 3DRP dynamic ^{18}F -FDG PET images showed contamination from myocardial TACs due to spillover in the LVBP ROI. Through the application of either the GTM PVC technique, or the use of the iterative PET reconstruction techniques which incorporate PSF modelling, such as MAP, this spillover effect was shown to be reduced and more realistic estimates of K_i were attained using Patlak analysis. This indicates that the application of PVC techniques in ^{18}F -FDG IDIF extraction is vital to ensuring accurate quantitative analysis of PET data, which consequently lead to detecting significant differences in K_i between infarcted and healthy myocardium tissue.

The GTM method, which used MR information as an anatomical prior to perform PVC, was found to be unstable and highly reliant upon accurate ROI delineation. The greatest reductions in spillover for LVBP IDIF determination from 3DRP images were achieved when GTM was used in conjunction with cardiac gating to provide motion correction. The MAP reconstruction algorithm used with cardiac gating was found to give the most consistent reductions in spillover affecting IDIFs, although it is a computationally expensive technique which requires a data processing cluster for images to be reconstructed within a reasonable timeframe.

Promising results were achieved when the VC ROI was used as an alternative IDIF extraction site to the LVBP ROI for IDIF determination, as both 3DRP and MAP IDIFs derived from the VC ROI displayed less contamination with tissue TACs than their LVBP counterparts. VC IDIFs also displayed more consistent IDIF shapes across the mouse cohort and were less affected by motion than the LVBP IDIFs. Although these results complement recently published work which derived IDIFs from VC ROI [33], [52], a set of serial blood samples was not available to fully validate the technique at this time.

9.1.2 $^{18}\text{F-NaF}$

In Chapter 5, a similar approach was attempted on a $^{18}\text{F-NaF}$ mouse dataset to evaluate an empirical recovery co-efficient (RC) technique, which used measurements from co-registered high resolution MR images to provide PVC for IDIFs. Less spillover was seen in all IDIFs derived from the LVBP ROI compared to those seen for $^{18}\text{F-FDG}$, as the kinetics of $^{18}\text{F-NaF}$ mean that there is no trapping of tracer within the myocardial muscle. This indicated that there was a reduced difference between the curve shapes of the 3DRP and MAP LVBP IDIFs in all 19 mice, and much greater similarity between the LVBP and VC ROI derived IDIFs. Late blood samples taken in 10 mice indicated the best IDIF agreement with plasma samples was achieved using MAP VC IDIFs, although even this method registered a mean bias of $154\pm 80\%$ across the cohort, indicating that some residual PVE or motion effects were still present in the data. The empirical RC method was not found to offer a consistent improvement to any of the IDIF extraction methods. It actually was found to increase the biases and variation for IDIF tails when compared to the measured plasma samples over the mouse cohort, for example raising the bias of the MAP VC method to $200\pm 139\%$. These results indicate that more complicated PVC methods would need to be applied to provide better agreement with late plasma samples. The VC ROI again showed it could be a viable alternative to the LVBP ROI for IDIF extraction, as it was affected less by spillover and motion, although agreement with more than one single, late plasma sample would be required to confirm this hypothesis.

Patlak analysis in Chapter 5 revealed that despite similar IDIF curve shapes being produced across the

mouse cohort, small but significant differences were seen in influx constant K_i when compared across the control and ApoE groups using the VC IDIFs and plasma sample scaled IDIFs, although these were not seen with the LVBP IDIFs. This again suggests that the VC ROI is less affected by motion than the LVBP and therefore is a promising alternative ROI for IDIF extraction in mice.

The main conclusions from the first part of this thesis can therefore be summarised as follows:

1. For tracers with large myocardial uptake, such as ^{18}F -FDG, PVC and spillover correction are essential to extract accurate IDIFs.
2. PVC and spillover correction for ^{18}F -FDG IDIFs can be provided by MR information using the GTM method, although its use is restricted due to its reliance on accurately delineated ROIs and its assumption of homogeneous uptake in each region.
3. The RC method did not provide any improvement in accuracy for ^{18}F -NaF IDIFs.
4. The use of MAP reconstruction produced the most accurate IDIF results for both ^{18}F -FDG and ^{18}F -NaF. For ^{18}F -FDG, these results were improved further by using cardiac gating to correct for motion.
5. The vena cava ROI is a promising alternative to the LVBP ROI for ^{18}F -FDG and ^{18}F -NaF IDIF extraction, as IDIFs extracted from the VC were less affected by spillover and motion. In the case of ^{18}F -NaF, VC IDIFs also agreed best with late plasma blood samples.

9.2 Relationship and conversion between PET tracer and MR contrast agent AIFs

As an alternative to PVC IDIF methods, the use of a Gadolinium contrast agent AIF derived non-invasively from MR images for conversion into a PET AIF was explored. Chapter 6 outlined the development of an automated DSC MRI analysis which used empirically-derived voxel thresholds to attain reliable estimates of an MR contrast agent first pass bolus AIF in rats. Qualitative analysis of stroke physiology was unaffected by using an automatically selected AIF in place of a manually derived AIF, but AIF peak heights and AUC increased by up to a factor of 3 when using the angiographic voxel selection method. The angiographic method used a probabilistic study-specific rodent vasculature atlas to streamline the empirical thresholds of the automatic algorithm in AIF voxel selection, and as a result produced AIFs with the largest peak heights and most distinct bolus profiles, resulting in CBF and CBV values with the best agreement to the literature. The CBF values from the angiographic method also had the best agreement with CBF values determined from ASL, although all perfusion parameters produced

using DSC MRI were found to exhibit a high variance and appeared to slightly overestimate CBF, CBV and MTT. This indicated that the current method of performing quantitative analysis of perfusion was non-ideal and could be improved upon in future work by incorporating techniques, such as Tikhonov regularization [200], into the analysis process.

The angiographic method developed in Chapter 6 was then applied in Chapter 7 to attain consistent DSC MRI AIFs for comparison to gold standard PET and MR contrast agent AIFs derived from serial blood sampling following a dual injection of ^{18}F -FDG and Gadovist in rats. The DSC MRI AIFs were also combined with AIFs from DCE MRI acquired at later time points of the scan to create a non-invasive estimate of the contrast agent AIF. The relationships observed between the blood sampled ^{18}F -FDG and Gd AIFs confirmed previously published results [54], which showed that the greatest similarity between the AIFs was observed in the first few minutes of the examination where blood flow dominates the AIF curve shape. Different AIF tail curve shapes were observed in the later stages of the examination (>10 minutes after injection), which was attributed to the difference in extravasation rates between the two compounds and the fact that ^{18}F -FDG is internalized within cells. AIF conversion between modalities was achieved using a previously described methodology, based on empirically derived bi-exponential rate constant ratios [54], giving AUC and peak height results which agreed between the converted Gd AIFs, converted DSC/DCE MRI AIFs and ^{18}F -FDG AIFs. There was more variation in the converted DSC/DCE MRI AIFs, however, than the converted Gd AIFs across the rat cohort due to dispersion and delay affecting the collection of the blood samples, as well as scaling difficulties between the DSC and DCE MRI datasets for some rats. This indicated that a combined DSC/DCE MR-based method could be used to non-invasively estimate the PET AIF but the residuals between the converted curves indicated it would be difficult to perform full kinetic modelling of tracer rate constants accurately. The conversion method also relied on empirically derived ratios from extensive blood sampling of each subject group, which is time-consuming and difficult to obtain.

An alternative AIF conversion method which focused only on the first pass of the AIF was also investigated, as this was the region where the PET tracer and contrast agent AIFs were seen to be most similar. Normalized gamma variates were first fitted to both the first pass of the ^{18}F -FDG and Gd AIFs, as well as to DSC MRI AIFs. It was found that the DSC MRI and Gd gamma variates could then be scaled to the ^{18}F -FDG gamma variates either with a blood sample taken from the peak of the ^{18}F -FDG AIF or non-invasively using a linear relation derived between the injected PET tracer dose and the PET AIF peak height. Both sets of scaled gamma variates gave more consistent AUC, peak height and residual results in the first pass of the AIF compared to the bi-exponential method. It was hypothesized that this DSC MRI method could be used to assist in PET AIF peak determination in the first pass phase, with PET image-derived methods used to extract the AIF non-invasively at later time points. The reliance

of the non-invasive conversion method on the linear scaling relation means that a similar relation would need to be established for each subject population in order for the technique to be translated into practical use on simultaneous PET/MR systems.

The main conclusions from the second part of this thesis are summarised as follows:

1. Automatically extracted DSC MRI AIFs provide are more consistent than those extracted manually and automatic AIFs produce more realistic quantitative estimates of perfusion parameters CBF and CBV. These results were improved further with the addition of angiographic information. Qualitative perfusion estimates were unaffected by AIF voxel selection technique.
2. As expected, the AIF curve shapes produced by MR contrast agents and PET tracers were different at late time points according to blood sample measurements. These results agreed with those previously reported by Poulin et al. [54].
3. Scaling AIFs extracted from DSC MRI with DCE MRI data did not produce reliable estimates of MR contrast agent AIFs, although this was most likely due to a temporal sampling mismatch and delay/dispersion inside the cannula line.
4. The conversion method proposed by Poulin et al. [54] was found to produce good estimates of AIF peak height and AUC values, but limited agreement with AIF curve shapes across the rat cohort.
5. Performing the MR to PET AIF conversion using normalized gamma variate functions gave more consistent residuals in the first pass phase of the AIF compared to the Poulin method. This suggests that future work should focus on using MR techniques which specialize in measuring the first pass of the AIF for conversion to PET AIFs, as this part of the curve had the greatest similarity between the modalities.

9.3 Attenuation correction approaches for murine PET/MR

A simple MR-based attenuation correction approach based on a two class (air and tissue) MR segmentation method was seen to provide adequate attenuation correction for quantitative PET in mice when compared to gold standard transmission scanning in Chapter 8. The small size of the mice meant that the observed attenuation effect was much lower than that in humans, resulting in a $22.6 \pm 0.9\%$ reduction in SUV within the myocardial ROI, when comparing non-AC corrected images to those created using TXAC. Although the default air and tissue MRAC method provided by ASIPRO gave myocardial SUV values that had a mean difference of $5.0 \pm 1.6\%$ in the myocardial ROI when averaged across the mouse group, the best agreement with TXAC was achieved when the lung region was assigned the linear atten-

uation co-efficient of tissue (0.095cm^{-1}), giving a mean difference of $0.9\pm 2.4\%$ in the myocardial ROI. There remained a large discrepancy of up to 40% in SUV values at the base of the mouse body between images reconstructed using the MRAC and TXAC techniques, however, even with the adjustment of the lung region, indicating that this was caused by the surrounding equipment, such as the animal bed and RF surface coil.

In conclusion,

1. AC is required in sequential PET/MR murine studies for absolute quantification
2. To perform this in a preclinical PET/MR scanner, a whole body MR scan is required and this should be used to provide a μ map template of the entire mouse body with the linear attenuation co-efficient of tissue (0.095cm^{-1}). If the lung is mis-segmented as air, this must be corrected.
3. Coil and bed μ map templates are also required to avoid a spatial bias in the AC provided.

9.4 Further Work

To build on the results of this thesis, serial blood sampling of mice in a PET/MR environment would be required using MR-compatible equipment such as the Swisstrace [51] blood sampling and measurement system to further evaluate the IDIF extraction techniques discussed in Chapters 4 and 5. A full set of arterial plasma samples is required to fully evaluate murine IDIF extraction methods for both ^{18}F -FDG and ^{18}F -NaF, particularly to see if the VC ROI can be used as an alternative to the LVBP ROI for IDIF extraction, as it is less affected by PVE and motion. Blood samples are also required to establish a standard relationship between whole blood and plasma concentrations in mice for ^{18}F -NaF. Additional analysis of PVC approaches for IDIF determination currently used in PET, such as factor analysis [37], could also be compared to those discussed in this thesis to determine the optimum IDIF extraction method for use in PET/MR kinetic modelling studies.

The use of simultaneous PET/MR imaging is desirable, as each dynamic PET frame could be co-registered to simultaneously acquired MR data. The improved co-registration between modalities would reduce errors in ROI delineation, and as a consequence would reduce IDIF spillover artefacts. This would also reduce gross motion errors resulting from organs shifting in position between sequential MR and PET scans. Simultaneous PET/MR would, however, require an alternative attenuation correction method to be used, such as the two class MRAC approach discussed in this thesis. To improve on this method, equipment such as the scanner bed and MR coils which remain within the PET FOV could be accommodated for using CT scan templates added into MRAC μ maps.

Finally, further studies into the use of MR AIFs to estimate PET AIFs in rats would also benefit from simultaneous PET/MR acquisition, as this would allow the converted MR AIFs to be tested in kinetic analysis with PET TACs and would also allow the converted MR AIFs to be compared to PET IDIFs extracted using techniques similar to those investigated in Chapters 4 and 5. Syringe pumps should also be used in future studies to standardise volumes and rates of injection, as well as using previously proposed methods [280] to account for dispersion present in long arterial and venous cannulas when performing blood sampling from inside the bore of an MRI scanner. Rapid, MR-compatible blood sampling techniques [51], [230] would also be advisable to gain higher temporal resolution estimates of a gold standard AIF in the first pass of a combined tracer and contrast agent bolus. Fast imaging sequences such as DSC MRI or phase-based DCE MRI [283], [284] could be used to provide rapid measurement of MRI contrast agent concentrations within the first pass, to ensure that this region is accurately represented when converting from an MR AIF to a PET AIF. Further work on this subject using similar DSC MRI based techniques to assist in determining the first pass of the PET AIF from MR are currently being pursued by Hasan Sari of University College London [291] and Liliana Caldeira of Forschungszentrum Jülich [292] in clinical PET/MR studies, indicating that the technique described in this thesis may have a clinical translation.

To summarise, the results presented in this thesis provide a clear platform for the use of PET/MR scanning in preclinical research for a number of applications which require quantitative results. Additionally, simultaneous PET/MR systems offer increased accuracy of co-registration and reduced motion artefacts between the modalities, which should further improve the accuracy of quantitative PET images. This research can hopefully be translated into human research and clinical studies, where quantitative imaging information can assist in diagnosis and treatment monitoring.

Eleanor Evans

June 2015

Appendix A

Spilt magnet simultaneous PET/MR

A schematic representation of the 1T split magnet design is shown in Figure A.1. The two halves of the magnet are split by approximately 80mm, with 120cm radial light guides attached to PMTs in the gap, shown in Figure 1.2. The magnet is kept at field using a cryostat using both Nitrogen and Helium cooling layers, requiring ≈ 200 l/week of N_2 and ≈ 100 l/3 weeks of He. PET scanner has been modified to increase the standard light guides from 100cm, such that the PMTs experience a field of 10 Gauss and can operate with minimal shielding. Almost identical performance to a standard Focus 120 scanner is achieved [26], with its parameters listed in Table A.1.

The drawbacks of the design lie in the low SNR achieved by the 1T MRI system (SNR scales linearly with field strength) and decreased light yield of 40% in the optical fibres compared to the standard Focus 120 light guides, resulting in an increase from $17.2 \pm 0.1\%$ to $27.1\% \pm 0.1\%$ in the FWHM of the mean photopeak energy resolution, making it more difficult to perform voxel by voxel comparisons across subjects [12]. Low SNR also precipitates longer acquisition times as more averages will be required to gain the same image quality as a higher field system.

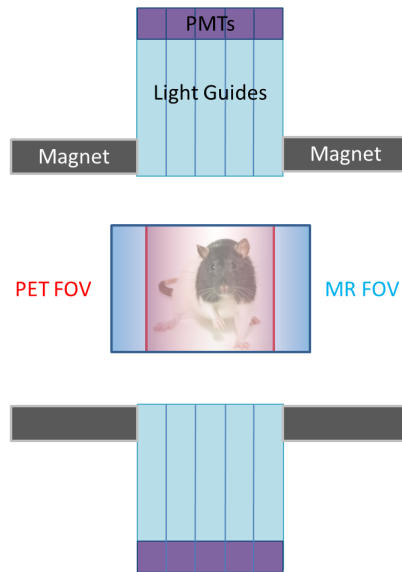


Figure A.1: Split magnet PET/MR scanner set-up.

Parameters of the MicroPET Focus 120 scanner in Cambridge split magnet design [26], [229]

Parameter	Values
Detector rings	4
Detector blocks per ring	24
Detector crystals per block	12×12
Crystal dimensions	1.52×1.52×10mm
Fibre optic dimensions	100mm bundles
PMT	Hamamatsu R5900-C12
Energy resolution	27%
Maximum spatial resolution	1.8mm FWHM
Maximum sensitivity	3.4%
Axial FOV	76mm
Transverse FOV	100mm

Table A.1

The split magnet uses custom-made split gradient coils [293] (Figure A.2) and custom-made RF coils (Figure A.3). Coil elements are not included in the gap between the two halves of the magnet to minimise attenuation and scatter. There are also four posts inserted around the centre of the magnet to brace the magnet halves against the attractive forces of the magnetic field. This results in some light guides being placed around the posts (ideally all modules would be placed at equal distances around the centre) and modified with cuts to ensure signal from all scintillator crystals is received.

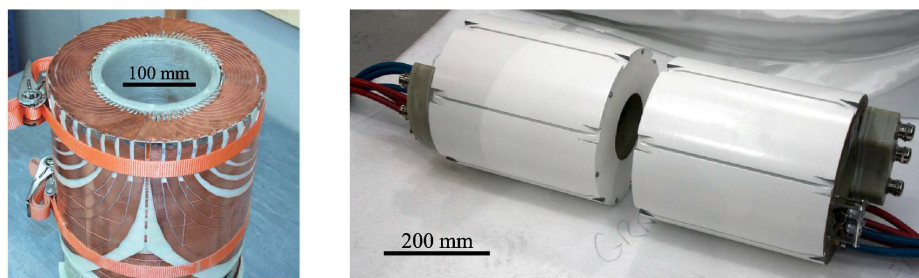


Figure A.2: Split gradient coils required for split magnet imaging. Photos used with permission of Dr Rob Hawkes.



Figure A.3: Custom-made RF coils: (a) transmission coil and (b) mouse head coil. Photos used with permission of Dr Rob Hawkes.

Appendix B

Time of flight PET

The principle of Time Of Flight (TOF) relies on the fact that the two gamma rays from each positron annihilation event will have different travel times. Taking the midpoint between the 2 detectors as d , one event must travel a distance of $d + \Delta x$ and the other must travel $d - \Delta x$ (shown as d_1 and d_2 in Figure B.1 respectively). As photons travel at the speed of light ($c, 3 \times 10^8 \text{ms}^{-1}$), the arrival time difference is $\frac{2\Delta x}{c}$ [2].

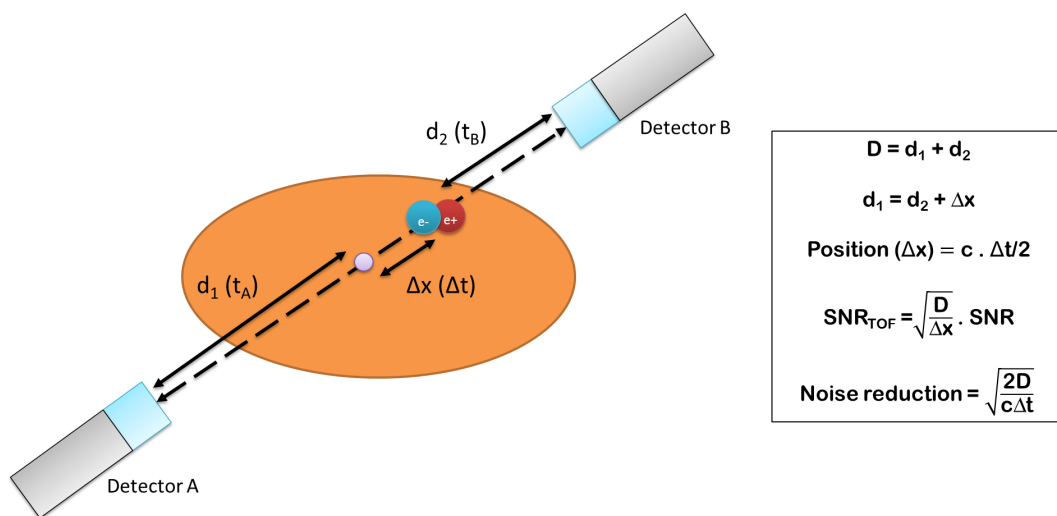


Figure B.1: Schematic illustrating PET data acquisition incorporating TOF, which can localize an annihilation event along an LOR. The spatial uncertainty on the annihilation position depends on the scanner timing resolution.

A human scanner with a timing resolution of 500ps will have a 7.5cm spatial uncertainty in the position of the annihilation event. This can then provide a probability distribution for each LOR, demonstrated in Figure B.2. This is then fed directly into the reconstruction algorithm, leading to an SNR improvement. Due to the small size of the subjects involved, no small animal scanners have yet been developed with timing resolutions capable of providing TOF capabilities [99].

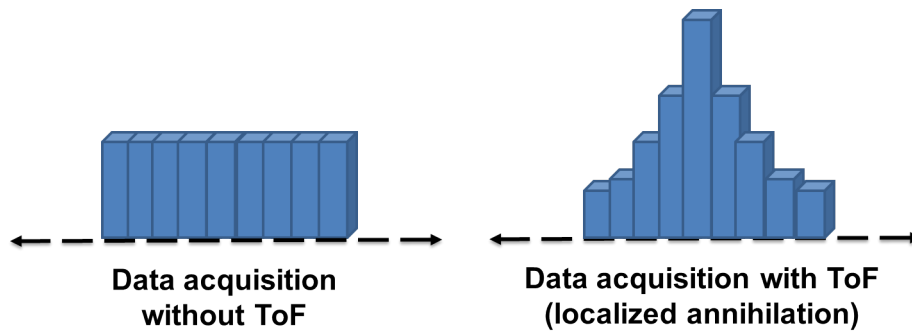


Figure B.2: LOR probability distributions, showing that TOF replaces the assignment of equal probability all along the LOR with a probability distribution.

Appendix C

Mathematics of MAP reconstruction

In iterative reconstruction, PET data are modelled as a collection of independent Poisson random variables with the log-likelihood function, L , given in equation (C.1) [65],

$$L(\mathbf{p}|\mathbf{f}) = \sum_i p_i \log \bar{p}_i - \bar{p}_i - \log p_i! \quad (\text{C.1})$$

where $\mathbf{f} \in \mathbb{R}^{N \times 1}$ is the unknown image, $\mathbf{p} \in \mathbb{R}^{M \times 1}$ is the measured sinogram (p_i is the sinogram at LOR i) and $\bar{\mathbf{p}} \in \mathbb{R}^{M \times 1}$ is the mean of the sinogram (\bar{p}_i is the sinogram at LOR i).

The mean sinogram $\bar{\mathbf{p}}$ is related to the image \mathbf{x} through an affine transform shown in equation (C.2) [65],

$$\bar{\mathbf{p}} = \mathbf{P}\mathbf{f} + \mathbf{s} + \mathbf{r} \quad (\text{C.2})$$

where $\mathbf{P} \in \mathbb{R}^{M \times N}$ is the detection probability matrix, $\mathbf{s} \in \mathbb{R}^{M \times 1}$ is the scatter in the data and $\mathbf{r} \in \mathbb{R}^{M \times 1}$ are the random counts in the data.

The randoms correction is usually performed by computing the difference between the coincidence events in the “prompt” coincidence timing window and those in a delayed window of equal duration, assuming that the mean of all the events in delayed timing window is equal to the randoms mean in the coincidence window, meaning that the precorrected data has a mean of $\mathbf{P}\mathbf{f} + \mathbf{s}$ and a variance of $\mathbf{P}\mathbf{f} + \mathbf{s} + 2\mathbf{r}$, such that the shifted-Poisson model with log-likelihood (1 in equation (C.3)) serves as a good approximation [65],

$$l(\mathbf{p}|\mathbf{f}) = \sum_{i=1}^{N_{LOR}} (p_i + 2r_i) \log ((\mathbf{P}\mathbf{f})_i + s_i + 2r_i) - ((\mathbf{P}\mathbf{f})_i + s_i + 2r_i) \quad (\text{C.3})$$

A Gibbs prior is used to regularize the reconstruction and is detailed in equation (C.4) [65],

$$G(\mathbf{f}) = \frac{1}{Z} \exp(-\beta U(\mathbf{f})) \quad (\text{C.4})$$

where $U(\mathbf{f})$ is the energy function, β is the smoothing parameter that controls the resolution of the image and Z is the normalization constant. β is incorporated to constrain the values of neighbouring voxels to similar values [65]. A β of 0.0 imposes no constraint (MAP then becomes an expectation maximization algorithm), with a large value (1.0) imposing high smoothing.

MAP image reconstruction is performed using the likelihood function (which incorporates the P matrix) with the image prior as a penalty term, as shown in equation (C.5),

$$\hat{\mathbf{f}}(\mathbf{p}) = \arg \max_{f \geq 0} l(\mathbf{p}|\mathbf{f}) - \beta U(\mathbf{f}) \quad (\text{C.5})$$

where $\mathbf{f} \in \mathbb{R}^{N \times 1}$ is the unknown image, $\mathbf{p} \in \mathbb{R}^{M \times 1}$ is the measured sinogram, where $U(\mathbf{f})$ is the energy function, β is the smoothing parameter that controls the resolution of the image and l is the shifted-Poisson log-likelihood function.

EM and OSEM approaches can exhibit high variance at high iteration numbers and are regularized through early termination of the reconstruction or post-processing image smoothing [64]. In MAP, smoothing is achieved using a prior to regularize the reconstruction, meaning that MAP does not exhibit instabilities at high iterations and once effective convergence has been reached, the iteration stopping point is not critical [64]. MAP hence provides better resolution recovery and convergence than 3D OSEM, although takes longer to process without ordered subsets to speed up the reconstruction.

Appendix D

Segmentation-based MR attenuation correction techniques for PET

D.1 2 point DIXON

In phase and out of phase gradient echo images can be combined to give images of water and fat using the two point DIXON technique [85]. In the first in-phase image, the signal is expressed in equation (D.1) [86],

$$S_{ip} = S_w + S_f \quad (D.1)$$

where S_{ip} is the in phase image signal, S_w is the water signal and S_f is the fat signal. The out of phase image signal, S_{op} , is formed at halfway between the in phase TE and the next in phase TE (i.e. if the in phase TE was 4.5ms at 1.5T, the out of phase TE will be 6.9ms) and is given in equation (D.2) [86],

$$S_{op} = S_w - S_f \quad (D.2)$$

Equations (D.1) and (D.2) are then used to find the water and fat image signals [137],

$$S_w = \frac{1}{2}(S_{ip} + S_{op}) \quad (D.3)$$

$$S_f = \frac{1}{2}(S_{ip} - S_{op}) \quad (D.4)$$

As the two images are created using different TEs, a correction for T2* differences between the images is required [86]. The two point DIXON also assumes perfect B₀ homogeneity, which can lead to phase errors accumulating between S_{ip} and S_{op}. To resolve this, a three point DIXON technique is used, which acquires a third image at a later in phase TE to calculate this phase shift and therefore accommodate for B₀ inhomogeneities [137].

D.2 Ultra short echo time (UTE) MR

Cortical bone has very short T2 values (0.42–0.50ms [294]), leading to rapid dephasing of the MR signal. This means that bone appears extremely similar to air on conventional MR images and can only be visualised if the sequence TE is of the same order of magnitude as the T2 value. Specialist ultra short echo time (UTE) sequences have hence been developed to visualise bone [294]. In order to attain a very short TE, UTE typically uses a radial k space sampling and data acquisition starts immediately after the RF pulse, during the ramp up time of the readout gradient [295]. The TE is limited by the RF deadtime, which is defined as half the RF pulse duration and the delay time needed for the system to switch from transmit to receive mode [295].

UTE is used to classify a bone class for μ maps in segmentation-based MRAC approaches, although these are limited to brain studies due to the long acquisition times required by UTE [75]. The most commonly utilised approach for this application is a dual echo UTE sequence - the first image is taken from the FID very quickly after RF excitation (TE = 50-150 μ s) and the second is a standard gradient echo image (TE typically 2-3ms) [75], [81], [290]. Tissues with short T2, such as bone, are visible in the FID image, but not the gradient echo image. As soft tissue is visible in both images, and air is visible in neither, bone can be extracted by comparing the FID and gradient echo images [81]. This approach was recently implemented in rat SPECT/MR imaging [290], where an attenuation map was created by first calculating a voxel by voxel R2 (1/T2) map from the FID and gradient echo images, as described in equation (D.5),

$$R2 = \frac{\ln(I_1) - \ln(I_2)}{TE_1 - TE_2} \quad (D.5)$$

where I₁ and I₂ are the image intensities in the FID and gradient echo image respectively, and TE₁ and TE₂ are their echo times. A binary body mask (taken from a threshold of the FID image) was used to exclude erroneous R2 values from air voxels [290]. Empirically derived R2 thresholds were then applied to the data to give a 4 class μ map (air, soft tissue, bone and lung) [290].

Appendix E

Mathematics of singular value decomposition (SVD)

Singular value decomposition (SVD) was performed to produce the residue function and calculate estimates of CBF as outlined in [117], [118] and [120].

To determine absolute CBF, Zierler's area to height relation is used as detailed in Section 3.2.2, and presented again as equation (E.1),

$$\text{CBF} = \frac{(1 - H_{large})}{\rho(1 - H_{small})} \frac{\int C_T(t) dt \cdot C_{ideal, max}}{\int C_{ideal}(t) dt \int AIF(t) dt} \quad (\text{E.1})$$

where $H_{ct_{large}}$ (~ 0.45 [195]) and $H_{ct_{small}}$ (~ 0.25) are the hematocrit values in large and small blood vessels respectively, ρ is the brain density (1.04g/ml), C_{ideal} is the true concentration in tissue (i.e. the tracer bolus is instantaneous), $C_{ideal, max}$ is its peak value, $C_T(t)$ is the measured concentration in tissue and $AIF(t)$ is the arterial input function [119], [120].

The measured concentration is a convolution of the true concentration and the AIF, shown in equation (E.2),

$$C_T(t) = C_{ideal}(t) \otimes AIF(t) = \text{CBF} \cdot AIF(t) \otimes R(t) = \text{CBF} \cdot \int_0^t AIF(\tau) R(t-\tau) d\tau \quad (\text{E.2})$$

where $R(t)$ is the residue function [117], [118] describing the fraction of contrast remaining in the system at time t . CBF can hence be calculated using the deconvolution of the tissue concentration curve ($C_T(t)$) and the measured $AIF(t)$.

Gamma variate functions as described in Section 3.2.2 (see equations (3.13) and (3.14)) were fitted

to the AIFs as described in Section 6.2.6. It was attempted to fit gamma variate functions on a voxel by voxel basis to tissue concentration-time curves for analysis with the AIF gamma variates, as described in [120], but poor fitting was achieved using this method as rat DSC MRI time courses give a reduced response compared to those found in human data, as illustrated by the lack of recirculation peaks seen in 6.14. SVD was therefore conducted with the full tissue $\Delta R2^*$ concentration-time curves and AIF $\Delta R2^*$ concentration-time curves or with the full tissue $\Delta R2^*$ concentration-time curves and gamma variate functions fitted to the AIFs. The results presented in Chapter 6 use the later of these two methods.

To perform the deconvolution, it is assumed that the functions AIF(t) and R(t) (i.e. $C_{ideal}(t)$) are constant over small intervals Δt , the time between measurements (see equation (E.3)),

$$C_T(t_j) = CBF \Delta t \sum_{i=0}^N AIF(t_i) R(t_j - t_i) \quad (E.3)$$

The convolution can then be formulated as a matrix of the form $\mathbf{A} \cdot \mathbf{b} = \mathbf{c}$ (equation (E.4)),

$$CBF \cdot \Delta t \begin{pmatrix} AIF(t_1) & 0 & \cdots & 0 \\ AIF(t_2) & AIF(t_1) & \cdots & 0 \\ \cdots & \cdots & \cdots & \cdots \\ AIF(t_N) & AIF(t_{N-1}) & \cdots & AIF(t_1) \end{pmatrix} \cdot \begin{pmatrix} R(t_1) \\ R(t_2) \\ \cdots \\ R(t_N) \end{pmatrix} = \begin{pmatrix} C_T(t_1) \\ C_T(t_2) \\ \cdots \\ C_T(t_N) \end{pmatrix} \quad (E.4)$$

Matrix \mathbf{A} be expressed as the product of an $M \times N$ column-orthogonal matrix \mathbf{U} , an $N \times N$ diagonal matrix \mathbf{W} and the transpose of an an $N \times N$ orthogonal matrix \mathbf{V} . The inverse of \mathbf{A} can therefore be written as shown in equation (E.5),

$$\mathbf{A}^{-1} = \mathbf{V} \cdot \left[\text{diag}\left(\frac{1}{w_i}\right) \right] \cdot \mathbf{U}^T \quad (E.5)$$

where w_i are the diagonal elements of \mathbf{W} and \mathbf{U}^T is the transpose of \mathbf{U} . As both the AIF and residue function vary over small timescales compared to the temporal resolution, equation (E.5) is modified such that AIF(t) and R(t) vary linearly with time during Δt and the elements of \mathbf{A} , a_{ij} can be written as follows:

$$a_{ij} = \begin{cases} \Delta t (AIF(t_{i-j-1}) + 4 \cdot AIF(t_{i-j}) + \frac{AIF(t_{i-j+1})}{6}) & \text{for } 0 \leq j \leq i \\ 0 & \text{otherwise} \end{cases} \quad (E.6)$$

The matrix \mathbf{b} is then calculated, which contains the elements of R(t), using equation (E.7),

$$\mathbf{b} = \mathbf{V} \cdot \left[\text{diag}\left(\frac{1}{w_i}\right) \right] \cdot (\mathbf{U}^T \cdot \mathbf{c}) \quad (\text{E.7})$$

In order to regularize the solution for \mathbf{b} , values smaller than 20% of the maximum value of w_i were set to 0 [120]. $R(t)$ (i.e. C_{ideal}) is then used with $C_T(t)$ and AIF(t) to calculate the CBF from equation (E.1) and (E.2).

Appendix F

Dependence of GTM PVC method on ROI delineation in ^{18}F -FDG murine studies

To ascertain the effect of “poor” ROI delineation on the effectiveness of the GTM method, PVC IDIFs were obtained in an additional way from 3DRP PET data in the LVBP ROI. This was designated as the “PET” ROI GTM method.

The five ROI classes required to conduct the GTM PVC method (as outlined in Chapter 4) were manually delineated from the last dynamic frame over 10 slices of 3DRP images covering the mouse heart. Each image was scaled between 0 and 75% of the maximum value found in the LVBP region. Rough approximations of the LVBP region in the centre of the heart, the high uptake region showing the healthy myocardium and the reduced region indicating the infarcted myocardium were manually delineated by the same operator (the author). Each image was then scaled to between 0 and 50% of the maximum value in the LVBP region and the contour of the mouse body was outlined. ROIs were manually inspected through all dynamic frames to ensure they were not overtly affected by motion. An example “PET” LVBP ROI is shown on the left hand side of Figure F.1.

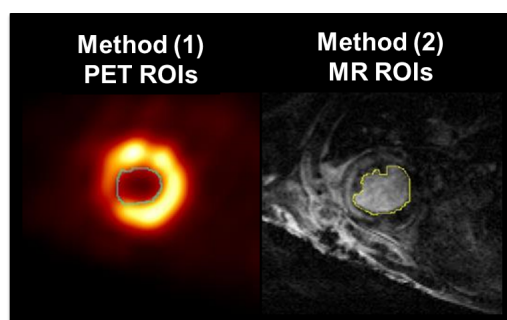


Figure F.1: GTM IDIF ROIs. (Left) Method 1: LVBP ROI drawn directly on PET data interpolated to MR space for comparison and (Right) Method 2: LVBP ROI drawn on high resolution MR.

F.1 Comparison of GTM IDIFs from “PET” or “MR” LVBP ROIs

A comparison of IDIFs extracted using the GTM methodology with “PET” and “MR” ROIs taken from the LVBP region are shown for a control and drug treated mouse in Figure F.2. The IDIFs corrected using ROIs delineated from PET alone often result in a non-physical, negative IDIF tail, particularly when gating is applied to the data. This indicates that the GTM method is over-correcting for spillover. This occurs as the LVBP and myocardium classes are not delineated accurately and therefore the LVBP signal is too high before GTM is applied, resulting in a negative value being assigned to its “corrected” co-efficient when the signal curve is fitted to the combination of all corrected signal classes. IDIFs produced using MRI to aid in the ROI delineation process, however, produce PVC corrected IDIFs with positive activity concentration values in the tail region, and the application of gating to these IDIFs lowers the tail as the signal blurring and spillover from motion is reduced. This is expected as gated PET data should align better with gated MR data, increasing ROI delineation accuracy. In summary, these results indicate the GTM method is unstable and highly dependent on accurate ROI delineation.

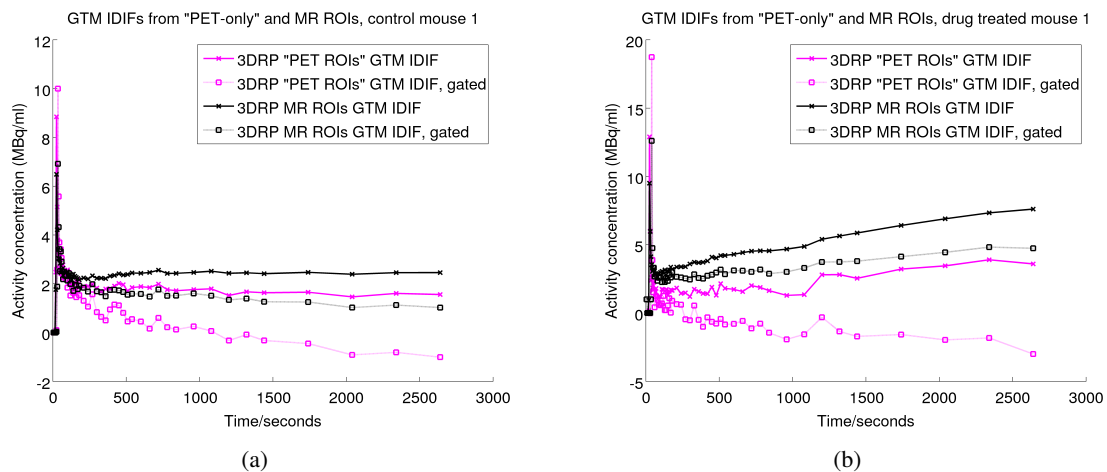


Figure F.2: Comparison of GTM IDIFs for control and drug treated mouse - “MR” LVBP ROI IDIFs are shown in black and “PET” LVBP ROI IDIFs are shown in pink, with dotted lines indicating gated IDIFs. Generally the “MR” ROIs produce more realistic IDIF estimates than those done using PET alone.

IDIFs derived for a second example set of mice using the GTM method are shown in Figure F.3, to illustrate further the variability of success when using the GTM method to provide PVC and the sensitivity of the method to ROI shape.

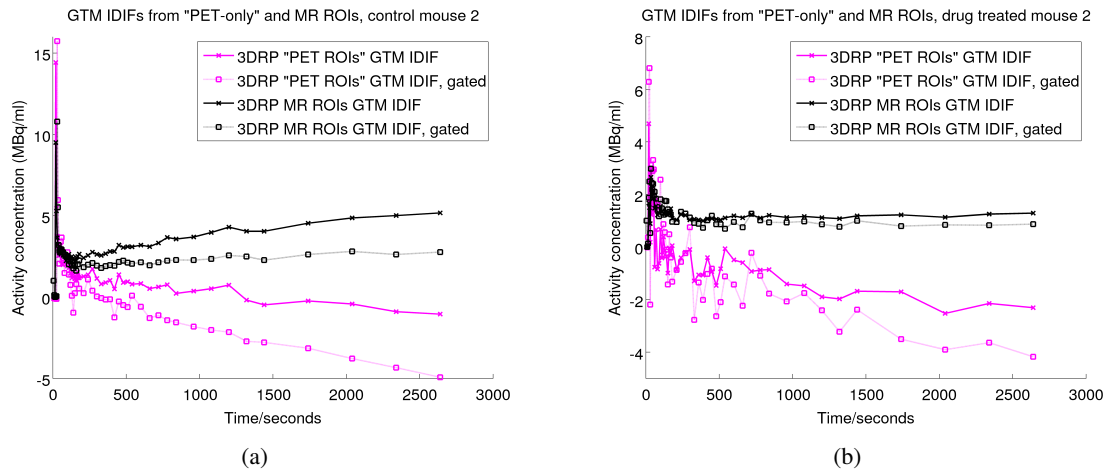


Figure F.3: Comparison of GTM IDIFs second set of control and drug treated mice - “MR” LVBP ROI IDIFs are shown in black and “PET” LVBP ROI IDIFs are shown in pink, with dotted lines indicating gated IDIFs. “PET” ROIs, with no MR to guide them, are again shown to be inaccurate as these produce an over-correction for the IDIF and give the IDIF tail negative values in both mice.

F.2 Comparison of K_i values calculated using GTM IDIFs from “PET” or “MR” ROIs

LVBP IDIF K_i values after GTM applied

TAC ROI	PET-only ROIs	PET-only ROIs, gated	MR ROIs	MR ROIs, gated
Control, myocardium	$0.196 \pm 0.137^\dagger$	$0.436 \pm 0.233^\dagger$	$0.069 \pm 0.028^\dagger$	$0.090 \pm 0.041^\dagger$
Treated, myocardium	$0.474 \pm 0.322^\dagger$	$0.620 \pm 0.351^\dagger$	0.065 ± 0.024	0.096 ± 0.030
Control, infarct	$0.068 \pm 0.101^\dagger$	$0.147 \pm 0.127^\dagger$	$0.024 \pm 0.015^{*\dagger}$	$0.036 \pm 0.016^{*\dagger}$
Treated, infarct	$0.229 \pm 0.190^\dagger$	$0.227 \pm 0.198^\dagger$	$0.063 \pm 0.021^*$	$0.081 \pm 0.028^*$

Table F.1: K_i values in ml/min/g for GTM IDIF methods using LVBP ROI, mean value for each mouse group (n=6). * $p < 0.05$, paired Student’s t test, indicating significant difference between control and drug treated groups in infarcted region. $^\dagger p < 0.05$, paired Student’s t test, indicating significant difference between healthy and infarcted myocardium in this mouse group.

As shown in Table F.1, the non-physical GTM IDIFs created by using incorrect ROIs (the “PET” ROIs) vastly overestimate the myocardial K_i values and also show a very large variance in the values reported. This again indicates the instability of the GTM method and its vulnerability to poor ROI delineation.

Appendix G

Motion correction in ^{18}F -NaF murine studies

Respiratory gating signals were taken during the PET emission scan, but were not used in the final analysis covered in Chapter 5. No great improvements in resolution or in co-registration were achieved using respiratory gating to re-bin the dynamic frames, as shown in Figure G.1 and as reported in literature for ^{18}F -FDG [53]. Respiratory gating was therefore not applied to ensure SNR was kept high in short dynamic frames with low count statistics which covered the rapid washout of ^{18}F -NaF from the mouse heart.

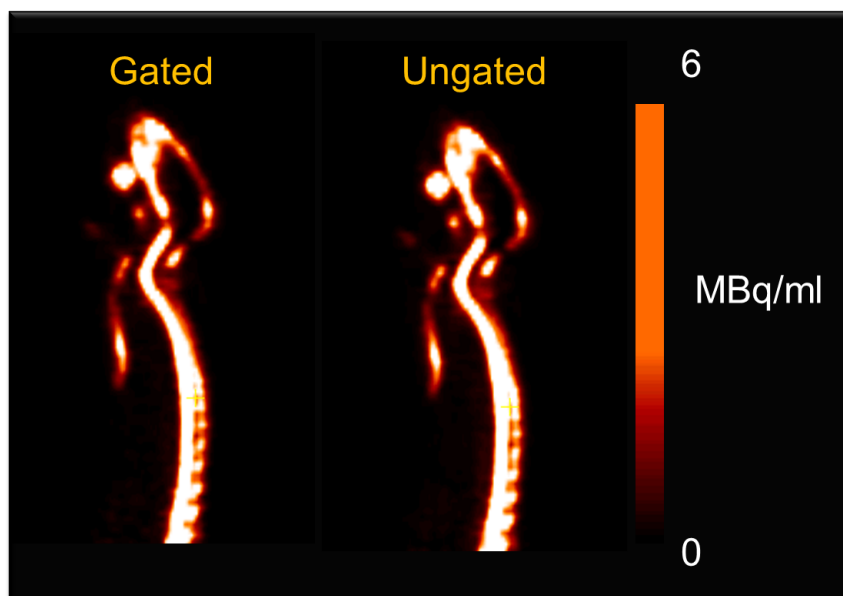


Figure G.1: Comparison of respiratory gated and ungated ^{18}F -NaF murine data. No qualitative differences in image quality seen by applying motion correction, so gating was not applied to ensure maximum count statistics were available.

Appendix H

Additional TAC and IDIF parameter data from ^{18}F -NaF murine studies

A summary of all extracted lumbar spine TACs for both control and ApoE mouse groups is shown in Figure H.1.

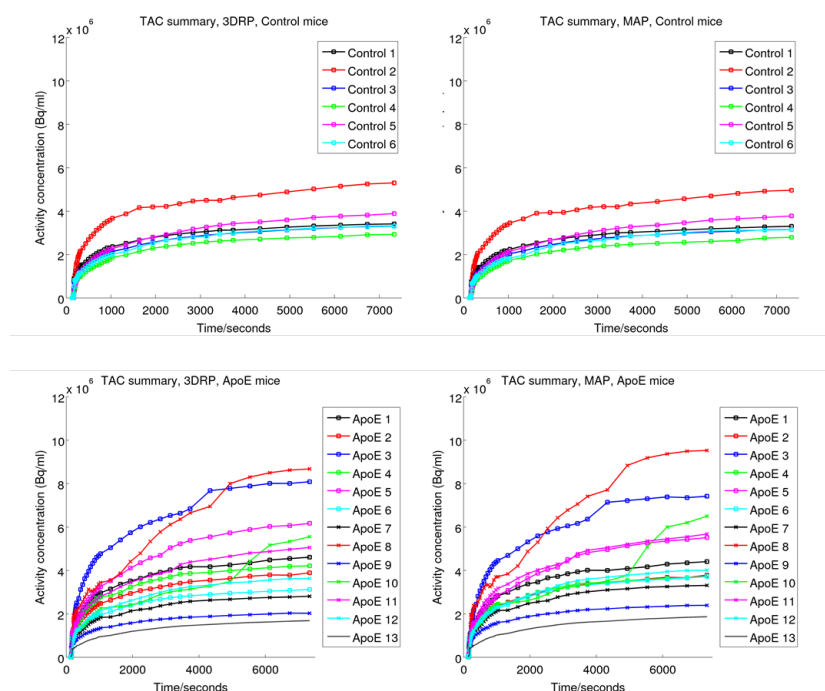


Figure H.1: Lumbar spine TACs extracted from ^{18}F -NaF murine data. Top Row: Control group TACs from (left) 3DRP images and (right) MAP images. Bottom row: ApoE group TACs from (left) 3DRP images and (right) MAP images.

Uniform, smooth shapes are seen across both groups, with higher uptakes seen in the ApoE group. ApoE 2 and ApoE 10 suffer jumps at late time points due to the scanner acquisition protocol crashing and being restarted within those time frames, fortunately this effect did not cause as a large a jump in

their respective IDIFs, and could be smoothed out in PMOD when analyzing the TACs to calculate K_i values.

The mean peak heights and mean AUC values for mouse groups are detailed in Tables H.1 and H.2. These results expand upon the summary of IDIFs shown in Figure 5.13 and 5.14, indicating how the peak heights and AUC values change with IDIF extraction technique. The AUC values, in particular, influence parameters taken from graphical kinetic analysis such as K_i .

Mouse group	3DRP LVBP	MAP LVBP	3DRP VC	MAP VC
All (n=19)	4.4±1.7	4.0±1.6	5.4±2.2	6.0±2.6
Controls (n=6)	4.8±2.0	3.9±1.8	6.8±2.4	7.2±2.9
ApoE (n=13)	4.2±1.6	4.1±1.5	4.8±1.9	5.4±2.4
Normalized to injection	3DRP LVBP	MAP LVBP	3DRP VC	MAP VC
All (n=19)	5.5±2.0	5.0±1.7	6.7±2.3	7.3±2.4
Controls (n=6)	5.6±1.6	4.5±1.4	7.9±2.1	8.4±2.7
ApoE (n=13)	5.5±2.2	5.3±1.8	6.1±2.2	6.8±2.2

Table H.1: Comparison of IDIF mean peak heights from LV and VC ROIs using 3DRP and MAP. All peak height values in MBq/ml. Bottom half of table shows results after each IDIF was normalized to injected activity (MBq/g).

Mouse group	3DRP LVBP	MAP LVBP	3DRP VC	MAP VC
All (n=19)	3119±1205	2227±1212	2654±1149	2627±2221
Controls (n=6)	2662±759	2613±755	1984±481	2165±541
ApoE (n=13)	3330±1336	2049±1362	2963±1253	2841±2668
Normalized to injection	3DRP LVBP	MAP LVBP	3DRP VC	MAP VC
All (n=19)	4087±1983	3005±2552	3461±1650	3688±4232
Controls (n=6)	3209±800	3111±532	2382±330	2579±209
ApoE (n=13)	4492±2252	2956±3105	3960±1785	4200±5094

Table H.2: Comparison of IDIF mean AUC from LV and VC ROIs using 3DRP and MAP. All AUC values in MBq·s/ml. Bottom half of table shows results after each IDIF was normalized to injected activity (MBq/g).

Differences in IDIF peak height found between 3DRP and MAP in both the LV and VC ROIs both before and after normalization to injected activity were all found to be significant (Student's paired t test, $p < 0.01$) when all IDIFs from all 19 mice were analyzed together, indicating that any difference in IDIF

extraction technique affected the resulting mean peak height for the IDIFs. For the control group (n=6), peak height differences were significant (Student's paired t test, $p < 0.01$) only when IDIFs from the LV and VC ROIs were taken from images with the same reconstruction algorithm were compared, and these differences were only significant between the LV and VC ROIs with the MAP algorithm for the ApoE group (n=13). In terms of AUC, significant differences (Student's paired t test, $p < 0.01$) were only seen between LV and VC IDIFs formed using 3DRP and between LV IDIFs formed using 3DRP and MAP. These differences were seen both when the IDIFs were analyzed together and when they were analyzed in the Control and ApoE groups.

These results suggest that, unlike the ¹⁸F-FDG results from the previous Chapter, the partial volume correction provided by MAP compared to 3DRP has slightly less of an impact on the IDIF curve shapes of ¹⁸F-NaF data, but IDIFs from the LV and VC ROIs can still be significantly different from each other.

Appendix I

DCE MRI

A DCE MRI sequence was used to scale DSC MRI data to contrast agent concentrations for comparison to blood sampled Gd AIFs and ^{18}F -FDG AIFs in Chapter 7 of this thesis. DCE MRI can also be used to extract non-invasive estimates of contrast agent AIFs and use these in compartmental modelling analysis, as detailed in Chapter 3. The validation of the DCE MRI technique, its relaxivity value calculation, an overview of DCE MRI AIF extraction techniques and the mathematics of DCE MRI kinetic theory are contained in the following sections to provide necessary background on the technique.

I.1 Validation of DCE MRI sequence *in vitro*

DCE-MRI requires a rapid FLASH VFA protocol which can perform accurate T1 mapping using multiple flip angles. A baseline, single flip angle FLASH acquisition should also be performed before any MR contrast agent is administered to act as a baseline and repeated multiple times after the injection to observe the signal change due to the presence of contrast agent. This signal change can then be used in conjunction with the baseline scan and the T1 map generated from the VFA acquisition, as detailed in Chapter 2, to estimate the shortened T1 of the tissue due to the presence of contrast agent and therefore the concentration of contrast agent according to its known relaxivity value. B_1 mapping is often conducted in clinical studies [109], [113], [296] in addition to the VFA FLASH T1 mapping protocol, to correct for variations which may bias the resulting T1 values, although small animal studies in preclinical MR scanners do not usually require this correction [193], [269] due to the smaller size of the subject meaning the preclinical volume coils provide adequate B_1 homogeneity across the subject.

The variable flip angle FLASH sequence used to perform DCE MRI in Chapter 7 was tested in an aqueous phantom study, using 7 tubes containing known concentrations of Gadovist contrast agent (see Figure I.1, tubes 1-7 = pure water, 0.16, 0.32, 0.48, 0.64, 0.8 and 0.96mM). The T1 values produced for

the phantom (see Figure I.1 and Table I.1) were of the range expected for the selected concentrations and additional T1 maps of rat brains, an example of which is shown in Figure I.2, were found to agree with literature [297], [298], [299].

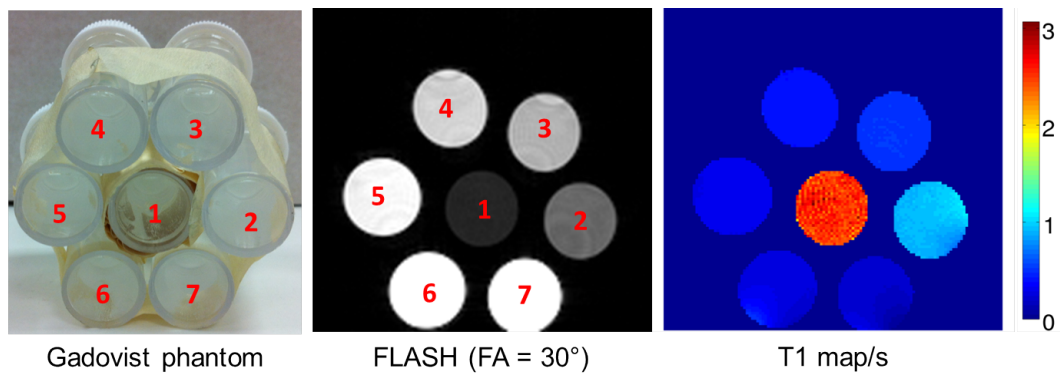


Figure I.1: Left to right: Photograph of Gadovist phantom with tube numbers; FLASH image of Gadovist phantom used for DCE MRI; T1 map produced from signal generated by multiple flip angle acquisitions.

Gadovist phantom T1 values

Tube	Concentration/mM	T1 values/s
1	0.00	2.53 ± 0.12
2	0.16	0.93 ± 0.05
3	0.32	0.52 ± 0.01
4	0.48	0.41 ± 0.01
5	0.64	0.31 ± 0.01
6	0.80	0.28 ± 0.04
7	0.96	0.20 ± 0.03

Table I.1

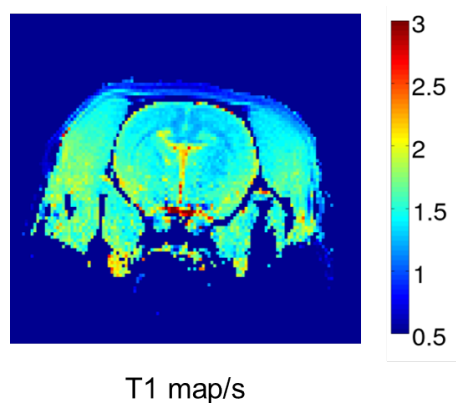


Figure I.2: T1 map of rat brain, showing longest T1 values (approx. 3s) in CSF rich region.

The phantom and *in vivo* tests additionally showed good precision of T1 measurements and uniformity of results across each tube of the water-based phantom. This indicated that B₁ homogeneity and the spoiling of the sequence was acceptable, providing good flip angle accuracy and was again confirmed with the uniformity of *in vivo* T1 results.

I.2 Relaxivity calculation

The relaxivity (r1) of a contrast agent determines how large a change in contrast agent concentration is reflected in the observed change in relaxation rate on the MRI images. The r1 value decreases with both field strength [128] and temperature [298], [300]. The relaxivity for a water based solution of Gadovist in a 4.7T scanner at 20° was determined from the values shown in Table I.1 as $4.5 \pm 0.3 \text{mMs}^{-1}$ using a linear fit of the difference in observed T1 values and the water (0mM) T1 value against concentration from equation (2.24), discussed in Chapter 2.

The phantom was then tightly wrapped in a water heating blanket with a temperature probe inserted next to the inner water tube to observe the change in the relaxivity at body temperature. The water heating blanket was set at nominal heating temperatures 35, 38 and 40°C and the phantom allowed to stabilise for 10 minutes at each temperature before measurement began. The temperature reading taken from next to the phantom inner tube was noted each time the relaxivity was re-calculated.

T1 values increased in a roughly linear fashion with temperature as expected, increasing by approx. 20% between room temperature and 37°C. This led to a change in r1 from 4.5 to 4.0mMs^{-1} (11% decrease), shown in Table I.2.

Gadovist phantom relaxivities with temperature for water at 4.7T

Water blanket setting/°C	Phantom temperature/°C	r1 value/mMs ⁻¹
Off	20.0 ± 1.0	4.5 ± 0.3
35	32.0 ± 0.5	4.3 ± 0.3
38	34.0 ± 0.5	4.2 ± 0.3
40	37.0 ± 0.5	4.0 ± 0.3

Table I.2

These results lie between the published value for Gadovist at 4.7T and 37°C in water of $3.2 \pm 0.2 \text{mMs}^{-1}$ and in bovine plasma of $4.7 \pm 0.2 \text{mMs}^{-1}$ [128], although a clinical study quoted a value of $3.3 \pm 0.2 \text{mMs}^{-1}$ for water and $4.1 \pm 0.2 \text{mMs}^{-1}$ for human plasma at 3T and 37°C [301]. Taking all of these results into account, a revised mean value of $4.2 \pm 0.3 \text{mMs}^{-1}$ was used to convert *in vivo* rat plasma T1 readings into

contrast agent concentrations. Once this relation is known, concentration time curves can be extracted from FLASH 4D datasets for kinetic analysis and AIFs can be extracted from arterial voxel regions.

I.3 Arterial input function extraction for DCE MRI in small animals

To streamline DCE MRI AIF extraction in the clinic, automated voxel-finding algorithms have been developed that usually employ thresholds on peak height and bolus arrival time to ensure that the voxels selected in the AIF ROI display the most arterial character (i.e. have a large, thin peak with a rapid decay indicative of an AIF) [260], [302], [303], [304]. More complicated algorithms exploit various clustering techniques for automatic analysis of mouse [269] or rat kidney [305] data to increase their accuracy and speed.

As accurate measurement of the AIF requires high temporal resolution at the expense of SNR and spatial resolution, leading to partial volume effects, uncertainty in individual AIF measurement can be high. A model or an experimentally-derived population AIF may then be used [134], [306], which assumes that individual AIFs do not vary greatly between subjects. This assumption has been controversial in the literature, as some would argue that individual AIFs have an effect on the parametric maps produced [194], [306] although comparisons between individual and population AIFs in rats [195], [196] and mice [189] have not found significant differences in the DCE MRI parameters produced. The accepted model for DCE MRI in small animals is a bi-exponential, [187], of the form shown in equation (I.1) [185],

$$C_p(t) = A \exp^{-k_1 t} + B \exp^{-k_2 t} \quad (\text{I.1})$$

An alternative to direct measurement of the AIF involves a reference region approach [272], [274], [275]. This approach does not directly derive the AIF but uses a reference tissue (e.g. muscle) with a well characterized signal change to compare to the ROI concentration time curve. This assumes the same theory as the AIF analysis, but uses the ratio between K^{trans} in the reference tissue and the ROI to assist in the fitting of the parameters. This method is popular in rat DCE MRI where spatial resolution is limited [272], [274].

A dual bolus approach can also be used if the required equipment is present [307] - first a small, pre-bolus of contrast agent is administered to the subject (typically 1-2/10ths of the total contrast agent dose), and a DCE acquisition is conducted with much higher temporal resolution than the typical scan. One can then measure the AIF by drawing an ROI on this high resolution dataset, before adjusting the parameters back to normal and conducting the full scan with the further 8-9/10ths of the total dose. This technique additionally requires the use of a syringe pump to standardise the contrast agent bolus administration

speed and has been successfully performed in mice [307], although complex surgery and customized equipment was required.

Finally, phase-based AIF measurement techniques have been developed in mice [283], [284] which enable very high temporal resolution sampling of the AIF in rodents, but do require extensive post-processing of the MRI signal. The AIF is taken from voxels within the mouse tail [283] or aorta/vena cava [284] where the phase change due to the passage of contrast agent is greatest and this is converted to the concentration of contrast agent present using a separate phantom calibration experiment.

I.4 Extraction of DCE MRI parameters from compartmental model

The Tofts compartmental model is assumed for the extraction of kinetic parameters from tissue concentration time curves and AIFs, as outlined in Figure 3.10. The flow of contrast agent across the endothelium is given in differential equation (I.2)

$$v_e \frac{dC_e(t)}{dt} = K^{trans} (C_p(t) - C_e(t)) \quad (I.2)$$

where v_e is the fractional volume of the Extracellular, Extravascular Space (EES, also known as the interstitial space), C_e is the concentration of contrast agent within the EES compartment, C_p is the arterial input function (AIF) of contrast agent in plasma and K^{trans} is the transfer constant between the plasma and EES compartments.

The AIF is converted from the whole blood concentration time curve using equation (I.3) [136],

$$C_p(t) = \frac{C_b(t)}{(1 - Hct)} \quad (I.3)$$

where $C_p(t)$ is the AIF, $C_b(t)$ is the whole blood curve extracted from DCE MRI images and Hct is the hematocrit of the species under study (e.g. 0.45 for mice [183], 0.44 for rats [187]).

The solution of equation (I.2) is a convolution of the AIF with the impulse response function $R(t)$, which in this case is given in equation (I.4):

$$R(t) = K^{trans} \exp^{-k_{ep} t} \quad (I.4)$$

where k_{ep} is the ratio (K^{trans}/v_e). The measured tissue concentration time curve from the ROI can therefore be expressed as shown in equation (I.5), in similar fashion to the PET tracer in equation (3.5):

$$C_t(t) = v_p C_p(t) + K^{trans} \int_0^t C_p(s) \exp^{k_{ep}(t-s)} ds \quad (I.5)$$

The shapes of the ROI enhancement curves are dependent on the values of K^{trans} , v_e and their ratio k_{ep} and are determined by a least squares fit to the ROI curve and AIF between the model values and the measured values. The initial slope of the ROI curve is given by K^{trans} , whilst the peak depends on v_e and the overall shape of the curve therefore depends on k_{ep} [129], [130].

The transfer constant K^{trans} characterizes the diffusive transport of Gadolinium-based contrast agents across the capillary endothelium [129] and is frequently used to characterize tumour biology and treatment response in both patients [134], [135], [184] and in small animal studies [185], [186], [191], [196]. These are of particular use in studies of anti-angiogenic treatments targeted at tumours [106], [130], [196].

List of Figures

1.1	Approaches to PET/MR scanner design: (a) Sequential PET and MR acquisition, (b) Simultaneous PET/MR acquisition. PMTs = Photomultiplier tubes, traditional PET detectors based on a cathode/anode ray tube. SiPMs = Silicon photomultipliers, solid state PET detectors which can operate in a high magnetic field with similar performance to PMTs. Adapted from [18].	14
1.2	Preclinical 1T split magnet simultaneous PET/MR scanner. (a) Fully shielded and (b) PMT modules and light guides visible when Faraday screen removed.	15
1.3	PET and MR images from mouse heart region in diastole, transverse view. Images were co-registered using the SPMMouse toolbox [27]. (Left) ^{18}F -FDG PET, (Centre) FISP MRI, (Right) Overlay of PET and MR images, localising tracer uptake to myocardium. .	16
1.4	2 BALB/c mice bearing CT26 tumour, images reproduced with permission from [12]. In PET/CT (top row) the tumour appears homogeneous (blue arrow), whereas T2-weighted MRI (bottom row) shows the inhomogeneous nature of the tumour, coinciding with an area of low PET tracer uptake.	17
2.1	Diagram of β^+ decay, harnessed in PET tracers.	21
2.2	Positron emission and annihilation photon coincidence detection in PET. Adapted from [56].	22
2.3	PET detector schematic showing scintillator, light guide and photomultiplier tube, with event triggering electron cascade.	23
2.4	Events 1 and 2 are detected at A and B on the detector ring, creating time stamped electrical signals. The trigger pulse from event 1 marks the start of the first coincidence time window (duration τ) and event 2 generates the second coincidence window. LOR is recorded by the coincidence circuitry if both coincidence windows overlap, as shown by the overlapping blue and red lines.	24
2.5	LOR and VOR definition. Adapted from [57].	24
2.6	Different LORs generated by true counts, scattered counts and random counts.	24

2.7	Photopeak of events indicating the range of energies detected in typical PET scan. Energy window (350-650keV) applied to discriminate against scattered counts.	25
2.8	Creation of PET sinogram using projection $p(s,\phi)$, formed from integration of LORs at an angle of constant ϕ . Adapted from [57].	26
2.9	Example sinograms. The point source (left) traces out a sinusoid for a single point, whilst the cylindrical water phantom (centre) and mouse (right) sinograms show a wider distribution due to the different line integrals acquired at each projection angle. The water phantom also shows a more uniform sinogram compared to the mouse.	27
2.10	The central slice theorem states that the Fourier transform of a 1D projection is equivalent to a profile at the same angle through the centre of the 2D Fourier transform of the object. Adapted from [57].	28
2.11	Projections of the object are collected at various angles ϕ and radially fill Fourier space (smallest concentric ring points omitted for clarity).	28
2.12	Projected data is backprojected onto $f(x,y)$ at a fixed value of ϕ to estimate the activity distribution. Adapted from [57].	29
2.13	Creating a point source image. (a) Profile of object over various angles - source can lie anywhere along direction normal to scan profile, (b) Result of backprojection process, resulting in blurred point source image.	29
2.14	2D FBP reconstruction of water phantom (scaled to 10% of maximum value in image), indicating streak artefacts present in transverse, coronal and axial views.	31
2.15	2D and true 3D PET reconstruction. 2D uses only direct planes or those with ± 1 ring difference (cross planes), whereas true 3D uses both direct planes and oblique planes with ring difference > 1	32
2.16	Projection truncation problem with ring difference > 1 , adapted from [62].	33
2.17	Schematic of 3DRP algorithm, adapted from [62]. Step 1 creates a first estimate of the image, which is then used in step 2 to create the truncated projections and combined with the measured data in step 3. Once a full set of 2D projections are established, they can be reconstructed into the final 3D image in step 4.	34
2.18	Comparison between 3DRP and 3D MAP images, reconstructed by the author, with MAP showing less streak artefacts, higher resolution and less noise, resulting in a sharper image.	38
2.19	Reduction of registered LORs due to attenuation. In this example, one gamma photon from pair is detected but the other is attenuated by the body, so no LOR is recorded and the coincidence event is lost.	41

- 2.20 From left: CT, PET and PET/CT images reproduced with permission from [79]. Bone is resolved with high contrast and signal intensity on CT due to its large attenuation factor. 42
- 2.21 A blank scan is performed using the rotating source, which spirals into and out of the scanner to cover all possible LOR trajectories from the emitting object. This process is then repeated in the transmission scan before injection of PET tracer with the subject inside the scanner. 43
- 2.22 The attenuation of an LOR from a body of size x depends on the size and μ value of the body and not the point at which the gamma rays are produced. 43
- 2.23 Schematic representation of PET/MR insert scanner, showing subject, RF coils and animal bed as sources of attenuation. 45
- 2.24 Example attenuation maps with tissue classification, simulated from the mouse whole body (MOBY) phantom (a) axial and (b) transaxial views [88]. Black areas (air) are assigned the lowest attenuation factor value, whilst white areas (bone) are assigned the highest attenuation factor value, with a range of grey values assigned to other tissues. . . 46
- 2.25 (a) Pseudo-CT (centre, with raw MR on left and reference CT on right) created from human brain MR using atlas approach to provide μ map for attenuation correction. (b) Three tissue classification scheme (raw MR on left, segmented MR centre, segmented CT right) used to create whole body rabbit μ map. Images reproduced with permission from [89]. 47
- 2.26 Dynamic whole body ^{18}F -FDG PET image frames of a mouse, reconstructed using 3DRP (coronal view). The tracer is administered via a tail vein cannula and proceeds to the heart, which then distributes the tracer throughout the mouse. Earlier images are much noisier due to the lower frame durations required to visualise the rapid initial kinetics. . . 48
- 2.27 Left: Late frame (taken 40 minutes into scan, 300s duration) ^{18}F -FDG cardiac image of mouse heart reconstructed using 3DRP without cardiac gating. Right: Frames 1-4 created using ECG triggers to show systole to diastole phases of heart cycle. Global noise is increased in gated images compared to ungated image. 49
- 2.28 Left: Late frame (taken 40 minutes into scan, 300s duration) ^{18}F -FDG cardiac image of mouse heart reconstructed using 3D MAP without cardiac gating. Right: Frames 1-4 created using ECG triggers to show systole to diastole phases of heart cycle. Global noise is increased in gated images compared to ungated image. 49
- 2.29 Boltzmann distribution determines proton spin populations within a magnetic field B_0 and an observable signal is created after RF excitation. 51
- 2.30 Bruker Biospin 4.7T MRI scanner for small animals installed at the WBIC. 52

- 2.31 Gradient echo formation: (a) 90° pulse to tip M_0 into x-y plane, followed by (b) a rapid decay due to dephasing of the signal using the negative gradient lobe until application of (c), the positive gradient lobe. Spins that were precessing at a low frequency now precess at a higher frequency as the gradient is adding rather than subtracting from the overall magnetic field experienced, and vice versa. Rephasing now occurs, resulting in (d) echo formation (lower magnitude due to exponential decay of M_0). Spins continue to precess after echo, shown in (e). Adapted from [86]. 53
- 2.32 Spin echo formation: (a) 90° pulse is applied to rotate spins into transverse plane, (b) spins then dephase naturally until (c) 180° is applied. This flips all spins 180° on transverse plane (i.e. +y axis to -y axis). (d) This does not change the spins precessional frequencies but does reverse their phase, therefore spins which were dephasing faster than others are now rephasing faster. (e) As a result, an echo is formed which is used to record the MR signal. (f) The spins then continue to dephase as before, unless another 180° is applied. Adapted from [86]. 54
- 2.33 Slice excitation using RF pulse, indicating how bandwidth of RF pulse dictates size of slice excited. 55
- 2.34 Slice select gradient, used to excite protons using an RF pulse within a desired region. Adapted from [86]. 55
- 2.35 Different frequency RF pulses can be used to select different slices. Adapted from [86]. 56
- 2.36 Frequency encoding (FE) schematic. With the FE gradient applied, frequencies are encoded according to their spatial positions and the total signal consists of a range of resonance frequencies. A Fourier transform hence produces a projection of the objects [86], [101]. 57
- 2.37 Phase encoding schematic for 16 pixel image [101]. Whilst no gradient is applied, the transverse magnetisations (arrows) are in phase. When a positive gradient is applied (left), the magnetisations dephase according to their position along the gradient direction and a position-dependent phase difference is formed. A similar process, but with the dephasing occurring in the opposite direction, is seen with a negative gradient (right). 58
- 2.38 k space diagram of a simple Cartesian k space sampling scheme, with each phase encoding step associated with a separate k space line. 58
- 2.39 2D MRI pulse sequence diagram for gradient echo acquisition. RF pulse excites a slice determined by the slice select gradient, whose signal echo is then rephased and encoded in k space using a combination of the phase and frequency encoding gradients. The phase encode gradient is changed each TR to record a different line of k space in the readout direction from the signal echo. 59

- 2.40 3D MRI pulse sequence diagram, showing second phase encoding gradient on slice select axis to provide additional encoding of slab excited using RF pulse. 59
- 2.41 Slice profiles schematic, adapted from [103]. 2D acquisition (right) gives gaussian slice profiles, with more signal coming from the centre of each slice than the edges. Dotted blue lines indicate the gaps between successive slices which are used to reduce cross-talk. In 3D, (left) slices are rectangular and contiguous, meaning that signal is derived uniformly from each slice. 60
- 2.42 T1 recovery and T2 decay profiles after a 90° pulse. 61
- 2.43 The effect of different T1 and T2 values on tissue signal (A=high contrast, B=low contrast). 61
- 2.44 (a) T1-weighted and (b) T2-weighted image of a rat brain. 62
- 2.45 Chemical structure of MR contrast agents Magnevist, Dotarem and Gadovist [108], which display high levels of stability, indicating that it is difficult to remove the Gd ion from the chelate. Different structures give rise to different relaxivities, which indicate how much of an effect each contrast agent has on T1 and T2 in tissue. 62
- 2.46 FISP pulse sequence. To increase the available signal, rewriter gradients in the phase encode direction are added to the standard gradient echo sequence. The signal therefore contains the FID enhanced with echo and fresh transverse components. 63
- 2.47 ECG triggered imaging schematic, adapted from [86], with PQRST phase labelled ECG trace (top row). Each box represents a FISP sequence acquisition, which acquires one line of k space data. This is repeated throughout the cardiac cycle using either prospective (middle row) or retrospective gating (bottom row). In prospective gating, an arrhythmia rejection window (AR) is used, during which the MRI sequence is not acquired to allow for variations in subject heart rate. In retrospective gating, the sequence is allowed to run independent of heart rate, with the ECG trace only used to trigger and update the phase encoding gradient to acquire the next line of k space. The position of the data within the cardiac cycle is determined after data collection. 64
- 2.48 Segmented k space data acquisition schematic, used to acquire multiple lines of k space for each temporal phase (TP) of the cardiac cycle per heartbeat. In this example, k space is segmented such that 4 lines are acquired at once (i.e. 4 phase encode gradients are used), leading to an acceleration in acquisition time by a factor of 4. 64
- 2.49 FLASH pulse sequence diagram, showing slice select spoiling gradient and extended readout gradient for spoiling. The spoiling gradients are of varying size to stop spoiled signals forming echoes [86]. 65
- 2.50 FLASH pulse sequence diagram, showing phase offsets in RF pulses to produce spoiling. 66

- 2.51 FLASH pulse sequence diagram, with additional saturation slice added above heart. Navigator signal derived from refocusing of saturation slice. Navigator is used to estimate the cardiac cycle stage and retrospectively gate the segmented FLASH acquisition. . . . 67
- 2.52 RARE pulse sequence diagram, with echo train length (RARE factor) of 3. Interecho spacing denotes the fixed time between successive echoes and arrows on phase encoding direction indicate direction of changing phase encoding (rewinder gradients). 67
- 2.53 RARE data acquisition in k space with RARE factor of 3, adapted from [86]. Effective TE is given by time from initial excitation to echo which covers the central k space segment, which gives the majority of contrast in the image (echo 2 in this case). 68
- 2.54 Phase shift created using equal area (balanced) bipolar gradients, adapted from [86]. . . . 69
- 2.55 Gradient moment nulling. Zero net phase shift using equal area (balanced) tri-lobed gradients (1:2:1 configuration) for flow compensation, which act to unwind phase shift from moving spins. 69
- 2.56 2D TOF MRA pulse sequence, with tri-lobed velocity compensation gradients on slice select and frequency encoding axes. The phase encode gradient remains unbalanced - there are flow compensation schemes for the phase encode gradient [115], but in most 2D TOF MRA applications, the short duration of the phase encode gradients minimizes the effect of motion during their application [116]. 70
- 2.57 Schematic of TOF MRA signal generation through imaging slice. 70
- 2.58 TOF effect response to blood flow speed, where v is the blood flow speed, TR is the repetition time of the MRA sequence and z is the slice thickness. No enhancement seen at $v = 0$, partial signal seen when $v = z/(2TR)$ and maximum signal seen when $v \geq z/TR$. 71
- 2.59 (a) 2D TOF MRA rat brain MIP, axial view (b) TOF MRA mouse brain MIP in 3D, showing contrast between bright blood vessels (arrow) and dark tissue in sagittal view. . 71
- 2.60 Blipped GE-EPI pulse sequence, with multiple k space line readout using a single shot gradient echo technique. 72
- 2.61 GE-EPI k space diagram. Each blip changes the phase encoding of the signal and is followed by a frequency encode gradient to read out each line of k space, which allows for rapid imaging that is limited by rate of gradient switching. 73
- 2.62 Schematic signal conversion using equation (2.23). Note that the Gadolinium concentration is only *proportional* to the change in $R2^*$ 74
- 2.63 Stages of DCE MRI acquisition, beginning with VFA FLASH and using this to form a baseline T1 map. The FLASH signal baseline is then taken and the signal ratio between the baseline and scans taken after contrast agent has been administered is used to calculate the apparent T1 due to the presence of contrast agent during the dynamic scan. 76

2.64	Baseline T1 map is used in conjunction with signal ratio between the FLASH baseline and FLASH scans taken after contrast agent has been administered. This produces the absolute concentration of contrast agent <i>in vivo</i> at the time points of each dynamic scan. ROIs can then be drawn in tissues of interest to give concentration-time curves.	77
2.65	FAIR “tag” and “control” image pulse sequences (left) used to perform ASL, with image slice planning shown on the right [86], [137]. The non-selective inversion pulse is applied to the whole head to give the “tag” image while the control image is produced using a slice selective inversion pulse slightly wider than the image slice. For simplicity only the slice select gradient is shown and the box indicates an EPI sequence, shown in Figure 2.60.	78
3.1	Progression in analysis of PET data to complex, quantitative techniques.	82
3.2	Comparison of ^{18}F -NaF whole body mouse PET images (sagittal view) reconstructed with MAP 3D for (a) entire PET 2 hour acquisition, (b) first hour and (c) second hour. Image (c) would be used to calculate SUV values as the tracer kinetics have stabilised, giving a higher SNR image with stable activity concentration.	83
3.3	(a) Schematic showing archetypal AIF curve and (b) AIF measured from blood plasma samples taken from rat femoral artery.	84
3.4	Typical curve profiles of AIF and myocardial ROI TAC for ^{18}F -FDG.	85
3.5	Reversible one tissue compartment model, used to describe water flow in body and applicable for diffusible blood flow tracers such as ^{15}O -H $_2$ O [151].	86
3.6	Two compartment model, with irreversible phosphorylation step trapping ^{18}F -FDG in tissue. No metabolite measurements are required to perform full kinetic modelling with this tracer [151].	87
3.7	Example Patlak plot. Straight line is fitted to data to attain influx constant for tracer. Initial 10-20 minutes are not used in fit as they depend upon the administered tracer bolus.	88
3.8	Left: Swisstrace coincidence probe wired into arteriovenous shunt circuit to continuously measure AIF in mice, reproduced with permission from [51]. Right: Coincidence probe gantry setup required to measure AIF directly in rats, reproduced with permission from [162].	90
3.9	Non-invasive estimation of AIF from PET images, typically using EL-ICA [51] to separate out myocardium from heart signal and minimise spillover. Figure reproduced with permission from [51].	91
3.10	Tofts compartment model used to evaluate contrast agent kinetics in DCE MRI acquisitions [129], [130].	93

3.11	Theoretical AIF for DSC MRI, indicating the (A) steady state, (B) bolus arrival time (BAT), (C) time to peak (TTP) of first pass, (D) recirculation peak (second pass of bolus) and (E) decay to steady state.	94
3.12	(a) DSC MRI signal from arterial voxels and (b) converted $\Delta R2^*$ time course.	95
3.13	Left: AIF profiles taken from middle cerebral artery for 2 rat DSC MRI datasets. Right: Gamma variate functions (red) fitted to both datasets.	96
4.1	Identification of the LVBP (region 1, red) and myocardium (region 2, orange) in diastole from cardiac gated IR FLASH LGE images.	102
4.2	Identification of the vena cava on (a) ^{18}F -FDG MAP early frame image (15s after injection start, frame duration of 5s) and (b) Whole body FISP MR images. A fusion of the PET and MR images is shown in (c).	102
4.3	PVE effect demonstrated using uniform activity spheres. Observed signal intensity is underestimated compared to true profiles depending on object size (D), as determined by scanner spatial resolution (FWHM). Observed diameter of objects (measured from line profile) also appears to increase, meaning that small sources appear larger but dimmer on images. To measure object shape and activity accurately, object size must be $>2 \times \text{FWHM}$ ($D > 2\text{mm}$). Adapted from [223].	103
4.4	Effect of spillover on measured activity distribution. Spillover is seen due to spill-out at the edges of the high activity object into the background and spill-in from background back into the object edge voxels. The summation of the two effects is seen in the measured image [222].	104
4.5	Pixels on edges of object contain both source and background activity, with resulting signal taken as the mean of the contributions from these 2 regions. This results in image blurring at the edge of the object [222].	104
4.6	(a) 3DRP late frame reconstruction (transverse view) of mouse heart. This image is thresholded at a lower value in (b), with a zoomed in view shown in (c) to illustrate the contamination of the low activity LVBP region through spillover from the high activity myocardium region surrounding it. Co-registered MR data is shown in (d) to illustrate the spread of PET signal between anatomical regions.	105
4.7	Co-registered PET/MR images showing myocardial infarction as hyperintense region on LGE MRI taken in diastole (left) and corresponding decreased uptake region in ^{18}F -FDG 3DRP PET image (right), indicated by yellow arrow.	109
4.8	Workflow of sequential PET/MR protocol. Injections conducted from outside the magnet bore via tail vein cannula. TRX = transmission scan for PET attenuation correction (AC).	110

- 4.9 Location of PET/MR ROIs used to extract IDIF and myocardial TACs from images of diastole phase of cardiac cycle. Red region indicates LVBP ROI used for IDIF derivation, with central voxels selected to minimize contamination from inter-frame motion. Yellow region indicates infarcted myocardium ROI and green region indicates healthy myocardium ROI used for TAC derivation. 112
- 4.10 Location of vena cava ROI used to extract IDIFs on cardiac gated MAP images. Coronal view is shown in (a) PET data (early frame, 15s after injection, 5s duration) and (b) FISP MRI data with the sagittal PET view shown in (c) and the sagittal MR view in (d). Orange box indicates region of vena cava analyzed to attain IDIF estimate. 113
- 4.11 Top row: FLASH MRI images of mouse heart. Bottom row: Illustration of ROI regions extracted for single subject across 3 slices. 114
- 4.12 PVC GTM method of IDIF determination using 5 ROI classes delineated from MR and convolved with scanner PSF: (a) LVBP, (b) infarct, (c) healthy myocardium, (d) body and (e) background. PET signal was modelled as a linear combination of these classes and the fitted LVBP values (region (a)) were used as the corrected IDIF. 114
- 4.13 Fitting bi-exponential models to IDIFs for Patlak plot analysis. Top row: Extracted IDIF for single subject in red, with bi-exponential model fit in blue performed using PMOD software. Bottom row: Patlak plots produced using measured (not smoothed) IDIF (left) and fitted IDIF (right). 116
- 4.14 Comparison of line profiles (3 voxels wide) using 3DRP and MAP for left ventricle. Left column: Comparison of last frame (40-45mins, 5 minute duration) mouse heart images created using 3DRP and MAP in the transverse view, with and without cardiac gating applied. Right column: Line profiles produced using each technique, with greatest resolution of mouse heart achieved using MAP with cardiac gating applied. 118
- 4.15 Comparison of line profiles (3 voxels wide) using 3DRP and MAP for vena cava. Left column: Comparison of early frame (approx. 15s post injection, 5s duration) mouse inferior vena cava images created using 3DRP and MAP in the transverse view, with and without cardiac gating applied. Right column: Line profiles produced using each technique, indicating increased noise in gated images due to low count statistics. 119
- 4.16 Co-registered SUV PET (3DRP) and LGE MRI short axis views of the infarcted mouse heart. Top row: mouse treated with Riociguat, bottom row: untreated (control) mouse. Infarcted region indicated by arrow. 120
- 4.17 Comparison of IDIFs and myocardial TACs for control mouse, extracted from 3DRP and MAP images, with and without cardiac gating applied. 121

- 4.18 Comparison of IDIFs and myocardial TACs for drug treated mouse, extracted from 3DRP and MAP images, with and without cardiac gating applied. Note the scale on the y axis has been changed from 8×10^6 Bq/ml in Figure 4.17 to 2×10^7 Bq/ml to accommodate the MAP IDIF peak with gating applied. 122
- 4.19 Summary of IDIFs derived from LVBP ROI for (a) control mouse and (b) drug treated mouse. Both cases show IDIFs with lower value tails due to decreased spillover when using cardiac gating (dotted lines) and MAP (blue), compared to 3DRP (red). Note the y axis scale of 8MBq/ml in 4.19(a) and 20MBq/ml in 4.19(b) to accommodate the gated MAP IDIF peak. 123
- 4.20 IDIFs extracted from LVBP and VC ROIs using 3DRP and MAP reconstruction techniques for control mouse. Green indicates 3DRP VC IDIFs, cyan indicates MAP VC IDIFs. 124
- 4.21 IDIFs extracted from LVBP and VC ROIs using 3DRP and MAP reconstruction techniques for drug treated mouse. Green indicates 3DRP VC IDIFs, cyan indicates MAP VC IDIFs. 124
- 4.22 Comparison of GTM IDIFs (black) to VC IDIFs for sample control and drug treated mice. 125
- 4.23 Comparison of GTM IDIFs to VC IDIFs for second set of control and drug treated mice. 125
- 4.24 Gated GTM method compared to all previously discussed methods for (a) control mouse and (b) drug treated mouse. 126
- 4.25 Gated GTM method compared to all previously discussed methods for (a) second control mouse and (b) second drug treated mouse. 126
- 4.26 Summary of all IDIFs extracted from LVBP ROI for control mice group. Top row: (left) 3DRP IDIFs, (centre) GTM applied to 3DRP IDIFs and (right) MAP IDIFs. Bottom row: (left) 3DRP IDIFs extracted from cardiac gated images, (centre) GTM applied to gated 3DRP images and (right) MAP IDIFs extracted from cardiac gated images. 128
- 4.27 Summary of all IDIFs extracted from LVBP ROI for drug treated mice group. Top row: (left) 3DRP IDIFs, (centre) GTM applied to 3DRP IDIFs and (right) MAP IDIFs. Bottom row: (left) 3DRP IDIFs extracted from cardiac gated images, (centre) GTM applied to gated 3DRP images and (right) MAP IDIFs extracted from cardiac gated images. 129
- 4.28 Summary of VC IDIFs for control mice group. Top row: (left) Ungated 3DRP IDIFs, (right) Ungated MAP IDIFs. Bottom row: (left) Gated 3DRP IDIFs, (right) Gated MAP IDIFs. 133
- 4.29 Zoomed in version of Figure 4.28, with maximum activity concentration of 10MBq/ml. . 133

4.30	Summary of VC IDIFs for drug treated mice group. Top row: (left) Ungated 3DRP IDIFs, (right) Ungated MAP IDIFs. Bottom row: (left) Gated 3DRP IDIFs, (right) Gated MAP IDIFs.	134
4.31	Zoomed in version of Figure 4.30, with maximum activity concentration of 10MBq/ml.	134
5.1	^{18}F -NaF two compartment model. K_1 and k_2 represent forward and reverse transport from plasma, k_3 and k_4 represent “trapping” and release from bone compartment. No metabolite products are required to perform full kinetic modelling with this tracer.	146
5.2	^{18}F -NaF 2 hour (7200s) dynamic time course in mouse, MAP reconstruction, sagittal view. Selected frames from 2 hour scan illustrate how tracer distributes in mouse body over time, with frame start timings and durations indicated below each image. The tracer is distributed through the blood stream after reaching the heart and binds to the mouse skeleton.	146
5.3	Signal from vena cava displayed in early time frame dynamic MAP PET (approx. 20s post injection, 5s duration) in transverse, coronal and sagittal views.	147
5.4	^{18}F -NaF activity distribution <i>in vivo</i> , sagittal view, MAP reconstruction. Early frame (left) displays the tracer bolus travelling to the heart via the vena cava (5s bin, approx. 20s post injection). Late frame (right), displays uptake throughout the mouse skeleton, with the skull and spine clearly visible (600s bin, 6600s into scan). Centre of LVBP indicated by yellow cross on both images.	148
5.5	^{18}F -NaF activity distribution <i>in vivo</i> , transverse view, MAP reconstruction, overlaid on co-registered FLASH MR. (A) Early frame, LVBP ROI, (5s bin, approx. 20s post injection). (B) Late frame, LVBP ROI, (600s bin, 6600s into scan), (C) Early frame, VC ROI, (D) Late frame, VC ROI.	149
5.6	Object diameter is measured using MRI scans and required RC factor needed to scale the mean value observed back to the true value can be calculated.	150
5.7	NEMA phantom photographs. The central compartment and five tubes of diameter 5, 4, 3, 2 and 1mm are filled with a water-based tracer solution. The two smaller compartments are filled with air and water respectively. Filling holes sealed with plastic screws.	151
5.8	Detection of VC ROI from ^{18}F -NaF images. Clear VC signal on early time frame PET images (approx. 10s post injection, 5s duration) with overlay of FLASH MR images (top left, arrow indicates VC region). ToF angiography (blue overlay) confirms location to have high blood flow as expected for major blood vessel.	155
5.9	Overlay of VC PET signal (left) with FLASH MR (centre) and ToF angiography in blue (right). Yellow box indicates region used to derive VC IDIF.	156

5.10	NEMA phantom emission images. (Left) Schematic of NEMA phantom tubes, showing decreasing tube diameters in clockwise direction: 5mm, 4mm, 3mm, 2mm, 1mm. (Centre) 3DRP reconstruction, 600s frame duration and (Right) MAP reconstruction, 600s frame duration on same image scale (0-0.8MBq).	159
5.11	NEMA phantom RC calibration graphs. (a) Comparison to F120 NEMA results [99], (b) Quadratic trends fitted to RC relation with tube diameter.	160
5.12	Comparison of IDIFs extracted from 3DRP (left column) and MAP (right column) images for 2 mice from cohort. Similar IDIFs are attained from both LVBP and VC ROIs, with the VC IDIFs displaying slightly lower tails.	161
5.13	Overview of IDIFs extracted from 3DRP and MAP images for LVBP and VC ROIs across all control mice (n=6).	162
5.14	Overview of IDIFs extracted from 3DRP and MAP images for LVBP and VC ROIs across all high fat diet ApoE mice (n=13).	162
5.15	Comparison of IDIFs extracted from 3DRP and MAP images for 2 mice from cohort. Left column: IDIFs from LVBP and VC ROIs, right column: Zoom inset comparison of final IDIF values with plasma samples.	164
5.16	Overview of IDIFs extracted from 3DRP and MAP images across entire cohort using zoom inserts. Greater agreement with plasma samples seen with VC IDIFs across mouse group.	165
5.17	Application of RC method to LVBP and VC IDIFs for control mouse.	166
5.18	Application of RC method to LVBP and VC IDIFs for high fat diet ApoE mouse.	167
5.19	Scaled IDIFs extracted from 3DRP (left column) and MAP (right column) images for 2 sample mice. Same scale is used as in Figure 5.12, indicating the difference in the peak height after applying a global factor scaling from the plasma sample.	169
5.20	MAP image with 10% signal threshold applied, indicating non-zero (typically between 0.1-0.2MBq/ml) spillover from mouse bones into LVBP and VC ROIs at late time points, making accurate IDIF extraction challenging. Centre of VC ROI indicated by yellow cross.	171
6.1	T2* weighted EPI images of first pass bolus peak in rat model, going from top left to bottom right in time order (frame duration = 250ms). Arrow highlights signal loss in vasculature due to passage of contrast agent bolus.	181

- 6.2 Top row: Each RARE anatomical image is co-registered to the GM, WM and CSF atlases before being segmented using SPMmouse to generate a transformation matrix. Bottom row: MRA images are re-sliced from their native space into that of the RARE images and then the transformation matrix is used to transform each rat's MRA image to the common, atlas space (green arrow). 183
- 6.3 The inverse transformation saved as part of the segmentation process is used to transform the newly created vasculature atlas back into the native (RARE) space of each rat. The atlas is then re-sliced into the EPI space of the DSC MRI, which was used to give a probability of which voxels in the EPI dataset belonged to major arteries. 184
- 6.4 Automatically selected voxels in orange at application of each thresholding step for mouse brain. Rejected voxels at each stage are shown on the right hand side. Final voxel selection is shown on the bottom left. 186
- 6.5 Angiography atlas information (in green) overlaid on EPI image, with arrow indicating high probability region around MCA, which was used as the primary source of AIF voxels. 187
- 6.6 Example AIF voxel selections. Manual in blue, with automatic in orange and angiographic in yellow. 187
- 6.7 ROI selection to observe perfusion parameter values across the control rat group. The red ROI (1) was placed in healthy tissue in the left hemisphere. 189
- 6.8 ROI selection to observe perfusion parameter ratios between ischemic and healthy regions in stroke rat group. Red ROI (1) = healthy hemisphere, green ROI (2) = ischemic core and yellow ROI (3) = ischemic penumbra. 189
- 6.9 CBF maps thresholded to 80 ml/100g/min to indicate inhomogeneity within ischemic region, with core and penumbra regions indicated by arrows for all 3 AIF methods. . . . 189
- 6.10 Top row: MRA images of rat brains for 3 subjects. Bottom row: MIP MRA images of the same rat brains. Largest intensity values in regions of high blood flow, corresponding to major arteries and veins. 190
- 6.11 Top row: 3D MIP projections computed using ImageJ software of rat vasculature probability atlas, scaled from 1–0, shown in coronal, sagittal and axial orientations. Inverted colour scheme highlights the extent of the arteries within the brain. Bottom row: Brain segmented out from atlas data using combination of GM, WM and CSF atlases. 191
- 6.12 Example of manual, automatic and angiographic AIFs for single rat ("stroke" group). . . 192
- 6.13 Gamma variate functions (a) fitted to sample AIF curves, (b) displayed alone for clarity. Note that the quality of the gamma variate fits is reduced in high noise DSC MRI datasets. 192
- 6.14 Comparison of (a) manual, (b) automatically selected and (c) angiographic AIFs for rat cohort (n=11). 194

6.15	Population AIFs for entire rat cohort (n=11), showing clear difference between manual and automatic selection methods.	196
6.16	Comparison of (a) manual, (b) automatically selected and (c) angiographic AIFs for control rat cohort, scanned 3-4 hours post sham surgery with no visible ischemic regions (n=7).	197
6.17	Comparison of (a) manual, (b) automatically selected and (c) angiographic AIFs for rats with confirmed stroke, scanned 28 days post surgery using DSC MRI (n=4).	198
6.18	Population (mean) AIFs for (a) rat control group and (b) rat stroke group taken from DSC MRI. Both groups show clear difference between manual and automatic AIFs, with the stroke group exhibiting greater variation.	200
6.19	CBF, CBV and MTT parameter maps created using each of the 3 AIF determination methods for a sample rat from the control group.	201
6.20	CBF, CBV and MTT images created using each AIF determined from sample “stroke” rat DSC MRI data, compared to T2* map from MRI data indicating ischemic region.	203
6.21	ASL and corresponding RARE anatomical images from additional rat group, who did not undergo DSC MRI but did receive MCA occlusion via distal clip method. Arrow and red outline indicates the stroke affected region.	204
6.22	Example box ROI in red used to eliminate major veins, such as superior sagittal sinus, from automatic voxel selection.	209
7.1	Compound structure: (a) PET tracer (Fluoro-deoxyglucose, ^{18}F -FDG) and (b) MR contrast agent (Gadovist, Gd-DO3A-butrol 6).	214
7.2	Schematic showing protocol used in [54], reproduced with permission. Plasma sample AIFs for PET tracer and MR contrast agent are normalized to their respective peak heights and fitted with a bi-exponential convolved with a top hat function. The ratios between the bi-exponential parameters of the AIFs are then averaged across the group and used to convert each Gd AIF into an ^{18}F -FDG AIF, which is then scaled to kBq/ μl using a single blood sample taken from the peak, or a factor calculated from the injected activity.	215
7.3	Derived PET and MRI AIFs, with corresponding converted AIFs, reproduced with permission from [54].	216
7.4	Experimental timetable. 2 rats were scanned in this manner each day.	219

- 7.5 Outline of measured data and comparisons made between gold standard AIFs derived from blood plasma samples (for both PET and MRI) and image-derived AIFs from DSC and DCE MRI. DSC MRI provides first pass bolus shape at high temporal resolution, DCE MRI provides AIF tails with absolute contrast agent concentration to provide scaling. The combined DSC/DCE AIFs are compared to the blood sampled AIFs (orange arrows) using the conversion method of Poulin et al [54] and the first pass phases of each AIF are compared using the gamma variate fitting conversion method (blue arrows). 220
- 7.6 Schematic showing apparatus used in this experiment. Animal is placed in scanner to perform TOF MRA and RARE before injection of tracer and contrast agent. 221
- 7.7 (a) Well counter used to measure tracer radioactivity in blood samples. (b) Microbalance and microcentrifuge used to weigh samples and separate blood from plasma respectively. 224
- 7.8 (a) ICP-MS console used to analyse samples for ^{157}Gd content. (b) Second stage diluted plasma samples inserted into measuring racks for ICP-MS analysis. 225
- 7.9 (a) DSC MRI AIF data taken from rat MCA. First 500s of overall scan time shown, indicating overall bolus shape. (b) DSC MRI AIF, with smoothed data interpolated to 30s temporal resolution shown in red. 227
- 7.10 (a) DSC MRI data at 30s resolution, showing first pass of AIF in MCA. (b) DCE MRI data showing later stages of AIF taken from MCA for single rat. The first point on this concentration-time curve is used to scale the DSC MRI data to Gd concentrations in mM. 228
- 7.11 (a) Image derived MR AIF taken from a combination of DSC and DCE data compared to blood sampled ICP-MS data. (b) Delay adjusted image-derived MR AIF with peaks aligned for comparison. 229
- 7.12 AIF schematic indicating the position of the peak, “midpoint” and “endpoint” blood samples used to scale the image-derived AIFs after conversion. The “midpoint” attempts to define a point between the first pass and tail regimes of the AIF, where a single blood sample could be taken if the high temporal sampling needed to define the peak adequately is unavailable. The “endpoint” could be taken after the scan has finished, as a “late” blood sample (as done in Chapter 5). 230
- 7.13 Comparison of whole blood and plasma samples of ^{18}F -FDG from a single rat. 232
- 7.14 Correlation plot of ^{18}F -FDG blood and plasma sample peak readings. 232
- 7.15 Repeatability of ICP-MS results for 4 rats, with samples prepared in an identical manner 1 week after initial ICP-MS measurement. 233
- 7.16 Gold standard ^{18}F -FDG AIFs measured using a radioactive well counter for 8 rats. Note different scales selected to highlight similarity of AIF shapes between rats. Peak heights vary due to different rat weights and injected activities. 234

- 7.17 Gadovist AIFs measured using ICP-MS for 8 rats. Note different scales selected to highlight similarity of AIF shapes between rats. 235
- 7.18 Correlation plots between ^{18}F -FDG and Gd AIFs, taken at the peak of each AIF, the “midpoint” (the point between the first pass and the tail) and the “endpoint” (last recorded value). 236
- 7.19 Comparison of ^{18}F -FDG and Gd contrast agent AIFs after peak height normalization and bi-exponential fitting for 8 rats. Whilst the first pass phase is similar in both modalities, at later time points the divergence between the ^{18}F -FDG and Gd curves is clear in all but 1 of the 8 rats. 237
- 7.20 Correlation plot of “midpoint” values between Gd AIFs and first point of DCE AIFs. “Midpoint” is defined as the transition between the first pass phase and the tail phase of the AIF. 238
- 7.21 Correlation plots between DSC MRI AIF and Gd AIF peak values. Top row: (Left) Change in $R2^*$ plotted against peak Gd concentration, (Right) Smoothed $R2^*$ data at 30s resolution. Bottom row: (Left) Scaled Gd concentration from combined DSC and DCE MRI data, plotted against peak Gd concentration, (Right) Smoothed data at 30s resolution. 239
- 7.22 Comparison of scaled DSC and DCE MRI AIFs and Gd contrast agent AIFs for all 8 rats. There is good agreement between the MRI and blood sampled AIFs in some rats, but in others the varying temporal resolution of the blood samples led to mismatches when the mean scaling factor for the group was applied. 241
- 7.23 Residuals between scaled DSC/DCE MRI AIFs and Gd contrast agent AIFs for all 8 rats. Note the changed scale on rat 7 (bottom row, left) where the mismatch in temporal sampling leads to a very large residual around the peak region. 242
- 7.24 Comparison of normalized MRI AIFs, Gd contrast agent AIFs and ^{18}F -FDG AIFs fitted with bi-exponential model. Different shapes were seen in MRI AIFs compared to both blood sampled AIFs due to temporal sampling mismatch between the techniques, which then results in different bi-exponential curve shape fits. 243
- 7.25 Linear correlation plot comparison of bi-exponential AIF parameters calculated for ^{18}F -FDG and Gd AIFs. From top: Amplitude parameters A_1 and A_2 , followed by rate constants k_1 and k_2 . Correlation is seen between the amplitude parameters but only little correlation is seen between the k_2 parameters. No correlation is seen in the k_1 parameter. 245
- 7.26 Linear correlation plot comparison of bi-exponential AIF parameters calculated for ^{18}F -FDG and MRI AIFs. From top: Amplitude parameters A_1 and A_2 , followed by rate constants k_1 and k_2 . Less correlation with the ^{18}F -FDG AIFs is seen in A_1 and A_2 compared to the Gd AIFs, but k_2 shows increased correlation. 246

- 7.27 Comparison of normalized and converted DSC/DCE MRI AIFs, Gd AIFs and normalized ^{18}F -FDG AIFs (same order of plots as Figure 7.24). There is good agreement between converted Gd AIFs and ^{18}F -FDG AIFs in some rats and more limited agreements in others. Mismatch in temporal sampling results in disagreement in some rats between converted MRI AIFs and ^{18}F -FDG AIF curve shapes, even after application of the mean conversion ratios listed in Table 7.3. 248
- 7.28 Residuals between normalized and converted MRI AIFs, Gd contrast agent AIFs and ^{18}F -FDG AIFs, indicating greatest differences seen with MRI AIFs, mainly in the “shoulder” region of the AIF. These differences also seen with the Gd AIFs, but to a lesser extent. 249
- 7.29 Linear relationships between injected activity and measured ^{18}F -FDG peak heights, “midpoints” and “endpoints”. Best correlation found with peak heights. 250
- 7.30 Comparison of scaling methods applied to Gd contrast agent AIFs converted into ^{18}F -FDG AIFs via the Poulin method, using blood samples taken at the peak of the AIF, the crossover point of the first pass (the “midpoint”) and the last blood sample taken (the “endpoint”). 252
- 7.31 Comparison of scaling methods applied to Gd contrast agent AIFs converted into ^{18}F -FDG AIFs via the Poulin method, using a fully non-invasive dose relation scaling method. The non-invasive method appears as effective as direct scaling by the peak height for the majority of rats scanned. 253
- 7.32 Residuals between normalized, converted and scaled Gd contrast agent AIFs and ^{18}F -FDG AIFs, indicating greatest differences in the end of the first pass and in the “shoulder” region of the AIF, with decreasing differences towards end of AIF tail. 254
- 7.33 Comparison of scaling methods applied to MR AIFs converted into ^{18}F -FDG AIFs via the Poulin method, using blood samples taken at the peak of the AIF, the crossover point of the first pass (the “midpoint”) and the last blood sample taken (the “endpoint”). 255
- 7.34 Comparison of scaling methods applied to MR AIFs converted into ^{18}F -FDG AIFs via the Poulin method, using a fully non-invasive dose relation scaling method. The non-invasive method appears as effective as direct scaling by the peak height for the majority of rats scanned. 256
- 7.35 Residuals between normalized and converted MRI AIFs and ^{18}F -FDG AIFs, indicating greatest differences seen in the end of the first pass region and in the “shoulder” region of the AIF. Note difference in scale (± 0.2 to ± 1) compared to scaled Gd contrast agent AIFs, indicating level of increased differences present in the DSC+DCE MRI AIFs. 257

7.36	Top row: Scaled Gd AIFs comparison (Left) AUC, (Right) Peak height. Bottom row: Scaled DSC/DCE AIFs comparison (Left) AUC, (Right) Peak height. * $p < 0.05$ for paired Student's t test.	258
7.37	(a) Gamma variate functions fitted directly to normalized ^{18}F -FDG, Gd contrast agent and DSC MRI data for single rat (b) Gamma functions after delay adjustment to re-align peaks, showing similar shapes.	259
7.38	Gamma variate functions fitted to first 500s of rat ^{18}F -FDG plasma data, with good fits achieved in all but one rat (3rd row, right).	260
7.39	Gamma variate functions fitted to first 500s of rat Gd-based MR contrast agent plasma data, with good fits achieved in all but one rat (same rat that poor gamma fits to ^{18}F -FDG data, 3rd row, right).	261
7.40	Gamma variate functions fitted to rat DSC MRI data and compared to combined DSC/DCE MRI AIF.	262
7.41	Gamma variates fitted to ^{18}F -FDG, Gd and DSC MRI data, scaled using maximum peak height plasma sample for each rat dataset. Note different activity scales on y axes for each rat due to differences in tracer dose administered.	263
7.42	Residuals between gamma variates fitted to ^{18}F -FDG and Gd/DSC MRI data, scaled using maximum peak height plasma sample for each rat dataset. Majority of rats show a very low residual ($< \pm 0.05 \text{ MBq/ml}$), but those with slight misalignments of gamma variates show larger differences ($< \pm 0.15 \text{ MBq/ml}$).	264
7.43	Gamma variates fitted to ^{18}F -FDG, Gd and DSC MRI data, scaled using linear relation between peak height and administered dose for each rat dataset.	265
7.44	Residuals between gamma variates fitted to FDG and Gd/DSC MRI data, scaled using relation between peak height and activity of injection administered. Almost identical residuals produced between peak scaling method and linear dose relation method.	266
7.45	(a) Comparison of AUC values for each scaling technique after conversion using the gamma fitting method. (b) Comparison of peak concentration values for each scaling technique after conversion using the gamma fitting method.	267
7.46	(a) Sample normalized blood sampled and MR-derived AIFs for single subject, showing a much narrower MR-derived AIF compared to the Gadovist AIF from ICP-MS. (b) Converted AIFs using cohort ratios of amplitude and rate constants for bi-exponential model shows that this dispersive effect is removed when an average ratio is used.	268
7.47	(a) DSC MRI data taken from rat MCA, with 2 distinct peak contributions from the original injection and then the saline flush. (b) DSC MRI interpolated to 30s temporal resolution, showing overall single bolus shape when data is smoothed.	269

- 7.48 (a) Scaled gamma variate functions for ^{18}F -FDG, Gd contrast agent and DSC MRI data for single rat. (b) Same gamma variates, after delay adjustment attempts to re-align peaks. Differences in residuals seen previously occur due to curve misalignment from poor delay correction, rather than from a change in shape of the gamma variate between modalities. 274
- 8.1 Split magnet PET/MR scanner from front (top) and back (bottom). Zoom (inset) shows transmission source mechanism. 278
- 8.2 TXAC workflow. Blank and transmission scan data is used to construct the attenuation correction sinogram. The μ map shows that both the mouse body (yellow cross indicates centre of FOV aligned with mouse heart, red outline indicates approximate mouse body contour) and mouse surface coil and bed underneath it are present in the attenuation sinogram. The image on the far right comprises the last 20 minutes of scan data. 281
- 8.3 MRAC sinogram creation. Matlab was used to apply initial noise thresholds and reslice MR data. ASIPRO was then used to threshold tissue classes from the images and to forward project the segmented data into an attenuation sinogram. The image on the far right comprises the last 20 minutes of scan data. 282
- 8.4 Transverse, coronal and sagittal views of TXAC μ maps with overlaid PET emission image (red). Grey areas indicate the additional equipment corrected for using TXAC. . . 282
- 8.5 Transverse, coronal and sagittal views of MRAC μ map. Overlaid MRAC and TXAC μ maps illustrate that MRAC corrects only for mouse body whilst TXAC also corrects for surrounding equipment including the MR coil and animal bed. 283
- 8.6 MR myocardial ROI shown over 2 different slices through mouse heart, taken from diastolic phase of cardiac cycle (previously shown in Chapter 4). Red region indicates LVBP ROI. Yellow region indicates infarcted myocardium ROI and green region indicates healthy myocardium ROI. Blue region indicates mouse body. 283
- 8.7 Left: Line profiles through large compartment of the NEMA phantom (hot region, tracer mixed in water) Right: Line profiles through air region of the NEMA phantom (cold region). 284
- 8.8 Activity concentration images of NEMA phantom with various AC methods applied. Clear difference between no AC and AC methods, with an average difference of between 20-25% across the phantom. 285
- 8.9 Line profiles through mouse heart for each AC method. From top: Transverse, coronal and sagittal views. Central peaks correspond to myocardium. 286

-
- 8.10 Comparison of mouse heart SUV maps (transverse view). Top row: (Left) No AC applied, (Centre) Transmission-based AC, (Right) Emission-based AC. Bottom row: (Left) MRAC, default two class (air and tissue), (Centre) MRAC (lung, tissue and air classes), (Right) MRAC (air and tissue), classifying lungs as tissue 287
- 8.11 Correlation and Bland-Altman plots between mean SUV values produced using MRAC, MRAC (lung), MRAC (tissue) and EMAC against TXAC for myocardium ROI. 289
- 8.12 Correlation and Bland-Altman plots between mean SUV values produced using MRAC, MRAC (lung), MRAC (tissue) and EMAC against TXAC for whole body ROI. 291
- 8.13 SUV map comparison between no AC and TXAC applied, showing large SUV changes in mouse myocardium region. Mouse body segmented from SUV percentage difference map and thresholded to -10 – 40% to mask noise from streak artefacts. 293
- 8.14 SUV map comparison between no AC and EmAC applied, showing smooth, uniform correction in mouse torso. Mouse body segmented from SUV percentage difference map and thresholded to -10 – 40% to mask noise from streak artefacts. 293
- 8.15 SUV map comparison between no AC and MRAC applied, showing relatively uniform changes in mouse torso, except for lungs. Mouse body segmented from SUV percentage difference map and thresholded to -10 – 40% to mask noise from streak artefacts. 293
- 8.16 SUV map comparison between no AC and MRAC (lung) applied, showing more uniform changes throughout mouse lung region. Mouse body segmented from SUV percentage difference map and thresholded to -10 – 40% to mask noise from streak artefacts. 294
- 8.17 SUV map comparison between no AC and MRAC (tissue) applied, showing relatively uniform changes throughout mouse body region. Mouse body segmented from SUV percentage difference map and thresholded to -10 – 40% to mask noise from streak artefacts. 294
- 8.18 SUV map comparison between gold standard TXAC and EmAC, showing large differences throughout the mouse body. Mouse body segmented from SUV percentage difference map and thresholded to -20 – 20% to mask noise from streak artefacts. 295
- 8.19 SUV map comparison between gold standard TXAC and MRAC, showing large differences in the misclassified lung region. Mouse body segmented from SUV percentage difference map and thresholded to -20 – 20% to mask noise from streak artefacts. 295
- 8.20 SUV map comparison between gold standard TXAC and MRAC (lung), with reduced differences in the lung region. Mouse body segmented from SUV percentage difference map and thresholded to -20 – 20% to mask noise from streak artefacts. 295
- 8.21 SUV map comparison between gold standard TXAC and MRAC (tissue), showing relatively small differences over mouse body. Mouse body segmented from SUV percentage difference map and thresholded to -20 – 20% to mask noise from streak artefacts. 296

8.22	Fusion of PET emission (blue) and transmission (grey) images showing mouse, coil and bed. Greatest attenuation from grey areas appears at base of mouse body. (A) Transverse view, (B) coronal and (C) sagittal.	296
8.23	Photograph showing the mouse bed and coil used for heart imaging. Both are made from 1cm plastic, resulting in localised attenuation in the mouse PET images.	297
A.1	Split magnet PET/MR scanner set-up.	309
A.2	Split gradient coils required for split magnet imaging. Photos used with permission of Dr Rob Hawkes.	310
A.3	Custom-made RF coils: (a) transmission coil and (b) mouse head coil. Photos used with permission of Dr Rob Hawkes.	310
B.1	Schematic illustrating PET data acquisition incorporating TOF, which can localize an annihilation event along an LOR. The spatial uncertainty on the annihilation position depends on the scanner timing resolution.	311
B.2	LOR probability distributions, showing that TOF replaces the assignment of equal probability all along the LOR with a probability distribution.	312
F.1	GTM IDIF ROIs. (Left) Method 1: LVBP ROI drawn directly on PET data interpolated to MR space for comparison and (Right) Method 2: LVBP ROI drawn on high resolution MR.	320
F.2	Comparison of GTM IDIFs for control and drug treated mouse - “MR” LVBP ROI IDIFs are shown in black and “PET” LVBP ROI IDIFs are shown in pink, with dotted lines indicating gated IDIFs. Generally the “MR” ROIs produce more realistic IDIF estimates than those done using PET alone.	321
F.3	Comparison of GTM IDIFs second set of control and drug treated mice - “MR” LVBP ROI IDIFs are shown in black and “PET” LVBP ROI IDIFs are shown in pink, with dotted lines indicating gated IDIFs. “PET” ROIs, with no MR to guide them, are again shown to be inaccurate as these produce an over-correction for the IDIF and give the IDIF tail negative values in both mice.	322
G.1	Comparison of respiratory gated and ungated ^{18}F -NaF murine data. No qualitative differences in image quality seen by applying motion correction, so gating was not applied to ensure maximum count statistics were available.	323

-
- H.1 Lumbar spine TACs extracted from ^{18}F -NaF murine data. Top Row: Control group TACs from (left) 3DRP images and (right) MAP images. Bottom row: ApoE group TACs from (left) 3DRP images and (right) MAP images. 324
- I.1 Left to right: Photograph of Gadovist phantom with tube numbers; FLASH image of Gadovist phantom used for DCE MRI; T1 map produced from signal generated by multiple flip angle acquisitions. 328
- I.2 T1 map of rat brain, showing longest T1 values (approx. 3s) in CSF rich region. 328

List of Tables

2.1	Half-lives of commonly used PET radiotracer isotopes [70].	39
4.1	Comparison of peak height activity concentration values in MBq/ml for different IDIF methods using LVBP ROI, mean value for each group of mice.	130
4.2	Comparison of peak height activity concentration values (MBq/ml), normalized to injected activity (MBq/g), for different IDIF methods taken from LVBP ROI, mean value for each group of mice.	131
4.3	Comparison of peak height activity concentration values in MBq/ml for different IDIF methods using VC ROI, mean value for each group of mice.	135
4.4	Comparison of peak height activity concentration values (MBq/ml), normalized to injected activity (MBq/g), for different IDIF methods taken from VC ROI, mean value for each group of mice.	136
4.5	K_i values in ml/min/g for IDIF methods using LVBP ROI, mean value for each mouse group (n=6). *p< 0.05, paired Student's t test, indicating significant difference between control and drug treated groups in infarcted region. †p< 0.05, paired Student's t test, indicating significant difference between healthy and infarcted myocardium in this mouse group.	137
4.6	K_i values in ml/min/g for IDIF methods using VC ROI, mean value for each mouse group (n=5 for controls, n=6 for drug treated group). †p< 0.05, paired Student's t test, indicating significant difference between healthy and infarcted myocardium in this mouse group.	137
4.7	K_i values in ml/min/g for GTM IDIF methods using LVBP ROI, mean value for each mouse group (n=6). *p< 0.05, paired Student's t test, indicating significant difference between control and drug treated groups in infarcted region. †p< 0.05, paired Student's t test, indicating significant difference between healthy and infarcted myocardium in this mouse group.	137

5.1	Comparison of recovery co-efficients attained from the NEMA phantom in the Cambridge Split Magnet Scanner and a standard F120 scanner (as reported in previous NEMA tests [99]).	159
5.2	Comparison of last plasma IDIF frame values with plasma samples. All values in MBq/ml.	163
5.3	Last IDIF time point activity concentrations (all in MBq/ml) compared to plasma sample measured in well counter for all mice (n=10, 4 control mice and 6 ApoE mice).	167
5.4	Comparison of mean K_i values for IDIFs and RC IDIFs (n=19, n=6 for control group, n=13 for ApoE group) for lumbar spine ROI. All values in g/min/ml.	168
5.5	Mean K_i values for all scaled IDIFs (n=10 for blood sampled data; n=4 for controls, n=6 for ApoE) using lumbar spine ROI. All values in g/min/ml.	169
6.1	DSC MRI AIF parameters for entire rat cohort (n=11).	195
6.2	DSC MRI AIF fitted gamma variate parameters for entire rat cohort (n=11).	195
6.3	DSC MRI AIF parameters for “control” rat group (n=7).	199
6.4	DSC MRI AIF parameters for “stroke” rat group (n=4).	199
6.5	Control rat group perfusion parameters (n=7, mean±std).	201
6.6	Absolute CBF values (mean ± std) in ml 100g ⁻¹ min ⁻¹ healthy hemisphere of “stroke” group.	204
6.7	Perfusion parameter ratios (mean ± std) between lesion and healthy tissue in contralateral ROI for rats in stroke group scanned using DSC MRI (n=4) and ASL (n=3).	205
7.1	Summary of AIF blood sampling protocol	223
7.2	Bi-exponential parameters of all normalized rat AIFs (n=8, mean±std for cohort)	244
7.3	Average ratios for cohort used to convert between modalities (n=8) using Poulin Method	247
8.1	Activity concentrations in NEMA phantom, large diameter region	284
8.2	Activity concentrations in NEMA phantom, air region	285
8.3	Percentage SUV increase (% , mean ± std) for myocardium, compared to no AC.	288
8.4	Percentage SUV difference (% , mean ± std) for myocardium, compared to TXAC.	288
8.5	Percentage SUV increase (% , mean ± std) for whole body, compared to No AC.	290
8.6	Percentage SUV difference (% , mean ± std) for whole body, compared to TXAC.	290
A.1	Parameters of the MicroPET Focus 120 scanner in Cambridge split magnet design	309

F.1	K_i values in ml/min/g for GTM IDIF methods using LVBP ROI, mean value for each mouse group (n=6). * $p < 0.05$, paired Student's t test, indicating significant difference between control and drug treated groups in infarcted region. † $p < 0.05$, paired Student's t test, indicating significant difference between healthy and infarcted myocardium in this mouse group.	322
H.1	Comparison of IDIF mean peak heights from LV and VC ROIs using 3DRP and MAP. All peak height values in MBq/ml. Bottom half of table shows results after each IDIF was normalized to injected activity (MBq/g).	325
H.2	Comparison of IDIF mean AUC from LV and VC ROIs using 3DRP and MAP. All AUC values in MBq·s/ml. Bottom half of table shows results after each IDIF was normalized to injected activity (MBq/g).	325
I.1	Gadovist phantom T1 values	328
I.2	Gadovist phantom relaxivities with temperature for water at 4.7T	329

Bibliography

- [1] P. J. Ell, “The contribution of PET/CT to improved patient management”, *Br. J. Radiol.*, vol. 79, no. 937, pp. 32–36, Jan. 2006
- [2] D. W. Townsend, “Dual-modality imaging: combining anatomy and function”, *J. Nucl. Med.*, vol. 49, no. 6, pp. 938–955, Jun. 2008
- [3] S. L. Kitson, V. Cuccurullo, A. Ciarmiello, D. Salvo, and L. Mansi, “Clinical Applications of Positron Emission Tomography (PET) Imaging in Medicine : Oncology, Brain Diseases and Cardiology”, *Curr. Radiopharm.*, vol. 2, no. 4, pp. 224–253, Oct. 2009
- [4] M. S. Judenhofer, H. F. Wehrl, D. F. Newport, C. Catana, S. B. Siegel, M. Becker, A. Thielscher, M. Kneilling, M. P. Lichy, M. Eichner, K. Klingel, G. Reischl, S. Widmaier, M. Röcken, R. E. Nutt, H. J. Machulla, K. Uludag, S. R. Cherry, C. D. Claussen, and B. J. Pichler, “Simultaneous PET-MRI: a new approach for functional and morphological imaging”, *Nat. Med.*, vol. 14, no. 4, pp. 459–465, Apr. 2008
- [5] H.-P. Schlemmer, B. J. Pichler, R. Krieg, and W.-D. Heiss, “An integrated MR/PET system: prospective applications”, *Abdom. Imaging*, vol. 34, no. 6, pp. 668–674, Nov. 2009
- [6] A. Boss, S. Bisdas, A. Kolb, M. Hofmann, U. Ernemann, C. D. Claussen, C. Pfannenbergl, B. J. Pichler, M. Reimold, and L. Stegger, “Hybrid PET/MRI of intracranial masses: initial experiences and comparison to PET/CT”, *J. Nucl. Med.*, vol. 51, no. 8, pp. 1198–1205, Aug. 2010
- [7] G. Antoch and A. Bockisch, “Combined PET/MRI: a new dimension in whole-body oncology imaging?”, *Eur. J. Nucl. Med. Mol. Imaging*, vol. 36, Suppl 1, pp. S113–S120, Mar. 2009
- [8] N. F. Schwenzer, H. Schmidt, and C. D. Claussen, “Whole-body MR/PET: applications in abdominal imaging”, *Abdom. Imaging*, vol. 37, no. 1, pp. 20–28, Feb. 2012
- [9] S. R. Cherry, “Multimodality imaging: beyond PET/CT and SPECT/CT”, *Semin. Nucl. Med.*, vol. 39, no. 5, pp. 348–353, Sep. 2009

- [10] C. Schiepers and M. Dahlbom, "Molecular imaging in oncology: the acceptance of PET/CT and the emergence of MR/PET imaging", *Eur. Radiol.*, vol. 21, no. 3, pp. 548–554, Mar. 2011
- [11] O. Ratib and T. Beyer, "Whole-body hybrid PET/MRI: ready for clinical use?". *Eur. J. Nucl. Med. Mol. Imaging*, vol. 38, no. 6, pp. 992–995, Jun. 2011
- [12] B. J. Pichler, H. F. Wehrl, and M. S. Judenhofer, "Latest advances in molecular imaging instrumentation", *J. Nucl. Med.*, vol. 49, Suppl 2, pp. 5S–23S, Jun. 2008
- [13] M. S. Judenhofer, C. Catana, B. K. Swann, S. B. Siegel, W. I. Jung, R. E. Nutt, S. R. Cherry, C. D. Claussen, and B. J. Pichler, "PET/MR images acquired with a compact MR-compatible PET detector in a 7-T Magnet", *Radiology*, vol. 244, no. 3, pp. 807–814, Sep. 2007
- [14] H. F. Wehrl, M. Hossain, K. Lankes, C.-C. Liu, I. Bezrukov, P. Martirosian, F. Schick, G. Reischl, and B. J. Pichler, "Simultaneous PET-MRI reveals brain function in activated and resting state on metabolic, hemodynamic and multiple temporal scales", *Nat. Med.*, vol. 19, no. 9, pp. 1184–1189, Sep. 2013
- [15] H. F. Wehrl, S. Wiehr, M. R. Divine, S. Gatidis, G. T. Gullberg, F. C. Maier, A.-M. Rolle, J. Schwenck, W. M. Thaiss, and B. J. Pichler, "Preclinical and Translational PET/MR Imaging", *J. Nucl. Med.*, vol. 55, Suppl 2, pp. 11S–18S, May 2014
- [16] A. Schmid, J. Schmitz, J. G. Mannheim, F. C. Maier, K. Fuchs, H. F. Wehrl, and B. J. Pichler, "Feasibility of Sequential PET/MRI Using a State-of-the-Art Small Animal PET and a 1T Benchtop MRI", *Mol. Imaging Biol.*, vol. 15, no. 2, pp. 155–165, Apr. 2013
- [17] K. Nagy, M. Tóth, P. Major, G. Patay, G. Egri, J. Häggkvist, A. Varrone, L. Farde, C. Halldin, and B. Gulyás, "Performance evaluation of the small-animal nanoScan PET/MRI system", *J. Nucl. Med.*, vol. 54, no. 10, pp. 1825–1832, Oct. 2013
- [18] S. R. Cherry, A. Y. Louie, and R. E. Jacobs, "The integration of positron emission tomography with magnetic resonance imaging", *Proc. IEEE*, vol. 96, no. 3, pp. 416–438, Mar. 2008
- [19] T. S. Ng, J. R. Bading, R. Park, H. Sohi, D. Procissi, D. Colcher, P. S. Conti, S. R. Cherry, A. A. Raubitschek, and R. E. Jacobs, "Quantitative, simultaneous PET/MRI for intratumoral imaging with an MRI-compatible PET scanner", *J. Nucl. Med.*, vol. 53, no. 7, pp. 1102–1109, Jun. 2012
- [20] A. Del Guerra, N. Belcari, M. G. Bisogni, G. Llosá, S. Marcatili, and S. Moehrs, "Advances in position-sensitive photodetectors for PET applications", *Nucl. Instrum. Meth. A*, vol. 604, no. 1–2, pp. 319–322, Jun. 2009

- [21] S. H. Maramraju, S. D. Smith, S. S. Junnarkar, D. Schulz, S. Stoll, B. Ravindranath, M. L. Purschke, S. Rescia, S. Southeikal, J.-F. Pratte, P. Vaska, C. L. Woody, and D. J. Schlyer, “Small animal simultaneous PET/MRI: initial experiences in a 9.4 T microMRI”, *Phys. Med. Biol.*, vol. 56, no. 8, pp. 2459–2480, Apr. 2011
- [22] C. Catana, D. Procissi, Y. Wu, M. S. Judenhofer, J. Qi, B. J. Pichler, R. E. Jacobs, and S. R. Cherry, “Simultaneous in vivo positron emission tomography and magnetic resonance imaging”, *PNAS*, vol. 105, no. 10, pp. 3705–3710, Mar. 2008
- [23] S. Vandenberghe and P. K. Marsden, “PET-MRI: a review of challenges and solutions in the development of integrated multimodality imaging”, *Phys. Med. Biol.*, vol. 60, no. 4, pp. R115-R154, Feb. 2015
- [24] S. España, L. M. Fraile, J. L. Herraiz, J. M. Udías, M. Desco, and J. J. Vaquero, “Performance evaluation of SiPM photodetectors for PET imaging in the presence of magnetic fields”, *Nucl. Instrum. Meth. A*, vol. 613, no. 2, pp. 308–316, Feb. 2010
- [25] A. J. Lucas, R. C. Hawkes, R. E. Ansorge, G. B. Williams, R. E. Nutt, J. C. Clark, T. D. Fryer, and T. A. Carpenter, “Development of a combined microPET-MR system”, *Technol. Cancer Res. Treat.*, vol. 5, no. 4, pp. 2345–2348, Aug. 2006
- [26] R. C. Hawkes, T. D. Fryer, A. J. Lucas, S. B. Siegel, R. E. Ansorge, J. C. Clark, and T. A. Carpenter, “Initial Performance Assessment of a Combined microPET Focus-F120 and MR Split Magnet System”, *2008 IEEE Nucl. Sci. Conf. Record*, pp. 3673–3678, Oct. 2008
- [27] S. J. Sawiak, N. I. Wood, G. B. Williams, A. J. Morton, and T. A. Carpenter, “Voxel-based morphometry with templates and validation in a mouse model of Huntingtons disease”, *J. Magn. Reson. Imaging*, vol. 31, no. 9, pp. 1522-1531, Nov. 2013.
- [28] R. Yao, R. Lecomte, and E. S. Crawford, “Small-animal PET: what is it, and why do we need it?”, *J. Nucl. Med. Technol.*, vol. 40, no. 3, pp. 157-165, Sep. 2012
- [29] M. Zhong, C. E. Alonso, H. Taegtmeier, and B. K. Kundu, “Quantitative PET imaging detects early metabolic remodeling in a mouse model of pressure-overload left ventricular hypertrophy in vivo”, *J. Nucl. Med.*, vol. 54, no. 4, pp. 609–615, Apr. 2013
- [30] C. Methner, G. Buonincontri, C.-H. Hu, A. Vujic, A. Kretschmer, S. Sawiak, A. Carpenter, J.-P. Stasch, and T. Krieg, “Riociguat reduces infarct size and post-infarct heart failure in mouse hearts: insights from MRI/PET imaging”, *PLoS One*, vol. 8, no. 12, p. e83910, Dec. 2013

- [31] K. Røe, T. B. Aleksandersen, A. Kristian, L. B. Nilsen, T. Seierstad, H. Qu, A. H. Ree, D. R. Olsen, and E. Malinen, "Preclinical dynamic 18F-FDG PET - tumor characterization and radiotherapy response assessment by kinetic compartment analysis", *Acta Oncol.*, vol. 49, no. 7, pp. 914-921, Oct. 2010
- [32] A. van Waarde, K. Shiba, J. R. de Jong, K. Ishiwata, R. A. Dierckx, and P. H. Elsinga, "Rapid reduction of sigma1-receptor binding and 18F-FDG uptake in rat gliomas after in vivo treatment with doxorubicin", *J. Nucl. Med.*, vol. 48, no. 8, pp. 1320-1326, Aug. 2007
- [33] S. L. Thorn, R. A. Dekemp, T. Dumouchel, R. Klein, J. M. Renaud, R. G. Wells, M. H. Gollob, R. S. Beanlands, and J. N. Dasilva, "Repeatable noninvasive measurement of mouse myocardial glucose uptake with 18F-FDG: evaluation of tracer kinetics in a type 1 diabetes model", *J. Nucl. Med.*, vol. 54, no. 9, pp. 1637-1644, Sep. 2013
- [34] J. W. Dalley, T. D. Fryer, F. I. Aigbirhio, L. Brichard, H. K. Richards, Y. T. Hong, J.-C. Baron, B. J. Everitt, and T. W. Robbins, "Modelling human drug abuse and addiction with dedicated small animal positron emission tomography", *Neuropharmacology*, vol. 56, Suppl 1, pp. 9-17, Jan. 2009
- [35] H.-M. Wu, G. Sui, C.-C. Lee, M. L. Prins, W. Ladno, H.-D. Lin, A. S. Yu, M. E. Phelps, and S.-C. Huang, "In vivo quantitation of glucose metabolism in mice using small-animal PET and a microfluidic device", *J. Nucl. Med.*, vol. 48, no. 5, pp. 837-845, May 2007
- [36] M. C. Kreissl, D. B. Stout, K.-P. Wong, H.-M. Wu, E. Caglayan, W. Ladno, X. Zhang, J. O. Prior, C. Reiners, S.-C. Huang, and H. R. Schelbert, "Influence of dietary state and insulin on myocardial, skeletal muscle and brain [F]-fluorodeoxyglucose kinetics in mice", *EJNMMI Res.*, vol. 1, no. 1, pp. 1-8, Jul. 2011
- [37] R. Laforest, T. L. Sharp, J. A. Engelbach, N. M. Fetti, P. Herrero, J. Kim, J. S. Lewis, D. J. Rowland, Y. Tai, and M. J. Welch, "Measurement of input functions in rodents: challenges and solutions", *Nucl. Med. Biol.* vol. 32, no. 7, pp. 679-685, Oct. 2005
- [38] S. Assadian, A. Aliaga, R. F. Del Maestro, A. C. Evans, and B. J. Bedell, "FDG-PET imaging for the evaluation of antiglioma agents in a rat model", *Neuro. Oncol.*, vol. 10, no. 3, pp. 292-299, Jun. 2008
- [39] P. J. Riss, Y. T. Hong, D. Williamson, D. Caprioli, S. Sitnikov, V. Ferrari, S. J. Sawiak, J.-C. Baron, J. W. Dalley, T. D. Fryer, and F. I. Aigbirhio, "Validation and quantification of [(18)F]altanserin binding in the rat brain using blood input and reference tissue modelling", *J. Cereb. Blood Flow Metab.*, vol. 31, no. 12, pp. 2334-2342, Dec. 2011

- [40] K. Fischer, V. Sossi, A. von Ameln-Mayerhofer, G. Reischl, and B. J. Pichler, “In vivo quantification of dopamine transporters in mice with unilateral 6-OHDA lesions using [11C]methylphenidate and PET”, *Neuroimage*, vol. 59, no. 3, pp. 2413-2422, Feb. 2012
- [41] P. Dupont and J. Warwick, “Kinetic modelling in small animal imaging with PET”, *Methods*, vol. 48, no. 2, pp. 98–103, Jun. 2009
- [42] F. C. Maier, H. F. Wehrl, A. M. Schmid, J. G. Mannheim, S. Wiehr, C. Lerdkrai, C. Calaminus, A. Stahlschmidt, L. Ye, M. Burnet, D. Stiller, O. Sabri, G. Reischl, M. Staufenbiel, O. Garaschuk, M. Jucker, and B. J. Pichler, “Longitudinal PET-MRI reveals β -amyloid deposition and rCBF dynamics and connects vascular amyloidosis to quantitative loss of perfusion”, *Nat. Med.*, vol. 20, no. 12, pp. 1485–1492, Dec. 2014
- [43] A. Schmid, H. Braumüller, H. F. Wehrl, M. Röcken, and B. J. Pichler, “Non-invasive monitoring of pancreatic tumor progression in the RIP1-Tag2 mouse by magnetic resonance imaging”, *Mol. Imaging Biol.*, vol. 15, no. 2, pp. 186-193, Apr. 2013
- [44] K. Büscher, M. S. Judenhofer, M. T. Kuhlmann, S. Hermann, H. F. Wehrl, K. P. Schäfers, M. Schäfers, B. J. Pichler, and L. Stegger, “Isochronous assessment of cardiac metabolism and function in mice using hybrid PET/MRI”, *J. Nucl. Med.*, vol. 51, no. 8, pp. 1277–1284, Aug. 2010
- [45] W. W. Lee, B. Marinelli, A. M. van der Laan, B. Sena, R. Gorbato, F. Leuschner, P. Dutta, Y. Iwamoto, T. Ueno, M. P.V. Begieneman, H. W. M. Niessen, J. J. Piek, C. Vinegoni, M. J. Pittet, F. K. Swirski, A. Tawakol, M. Di Carli, R. Weissleder, and M. Nahrendorf, “PET/MRI of inflammation in myocardial infarction”, *J. Am. Coll. Cardiol.*, vol. 59, no. 2, pp. 153–163, Jan. 2012
- [46] M. S. Judenhofer and S. R. Cherry, “Applications for preclinical PET/MRI”, *Semin. Nucl. Med.*, vol. 43, no. 1, pp. 19-29, Jan. 2013
- [47] C. Y. Sander, J. M. Hooker, C. Catana, M. D. Normandin, N. M. Alpert, G. M. Knudsen, W. Vanduffel, B. R. Rosen, and J. B. Mandeville, “Neurovascular coupling to D2/D3 dopamine receptor occupancy using simultaneous PET/functional MRI”, *PNAS*, vol. 110, no. 27, pp. 11169-11174, Jul. 2013
- [48] H. F. Wehrl, J. Schwab, K. Hasenbach, G. Reischl, G. Tabatabai, L. Quintanilla-Martinez, F. Jiru, K. Chughtai, A. Kiss, F. Cay, D. Bukala, R. M. A. Heeren, B. J. Pichler, and A. W. Sauter, “Multimodal elucidation of choline metabolism in a murine glioma model using magnetic resonance spectroscopy and 11C-choline positron emission tomography”, *Cancer Res.*, vol. 73, no. 5, pp. 1470-1480, Mar. 2013

- [49] H. F. Wehrl, P. Martirosian, F. Schick, G. Reischl, and B. J. Pichler, "Assessment of rodent brain activity using combined [(15)O]H₂O-PET and BOLD-fMRI", *Neuroimage*, vol. 89, pp. 271-279, Apr. 2014
- [50] L. Moerman, D. De Naeyer, P. Boon, and F. De Vos, "P-glycoprotein at the blood-brain barrier: kinetic modeling of 11C-desmethyloperamide in mice using a 18F-FDG μ PET scan to determine the input function", *EJNMMI Res.*, vol. 1, no. 1, pp. 1–12, Jan. 2011
- [51] M. F. Alf, M. T. Wyss, A. Buck, B. Weber, R. Schibli, and S. D. Krämer, "Quantification of brain glucose metabolism by 18F-FDG PET with real-time arterial and image-derived input function in mice", *J. Nucl. Med.*, vol. 54, no. 1, pp. 132-138, Jan. 2013
- [52] B. Lanz, C. Poitry-Yamate, and R. Gruetter, "Image-Derived Input Function from the Vena Cava for 18F-FDG PET Studies in Rats and Mice", *J. Nucl. Med.*, vol. 55, no. 8, pp. 1380–1388, Jun. 2014.
- [53] L. W. Locke, S. S. Berr, and B. K. Kundu, "Image-derived input function from cardiac gated maximum a posteriori reconstructed PET images in mice," *Mol. Imaging Biol.*, vol. 13, no. 2, pp. 342-347, Apr. 2011.
- [54] E. Poulin, R. Lebel, E. Croteau, M. Blanchette, L. Tremblay, R. Lecomte, M. Bentourkia, and M. Lepage, "Conversion of arterial input functions for dual pharmacokinetic modeling using Gd-DTPA/MRI and 18F-FDG/PET", *Magn. Reson. Med.*, vol. 69, no. 3, pp. 781-792, Mar. 2013
- [55] J. R. Stickel and S. R. Cherry, "High-resolution PET detector design: modelling components of intrinsic spatial resolution", *Phys. Med. Biol.*, vol. 50, no. 2, pp. 179–195, Dec. 2004
- [56] R. Lecomte, "Novel detector technology for clinical PET", *Eur. J. Nucl. Med. Mol. Imaging*, vol. 36, Suppl. 1, pp. S69–S89, Dec. 2008
- [57] A. Alessio and P. Kinahan, "PET Image Reconstruction", in *Nuclear Medicine*, R. E. Henkin, D. Bova, G. L. Dillehay, J. R. Halama, S. M. Karesh, R. H. Wagner and A. M. Zimmer (Eds.), 2nd Edition, vol. 1, Philadelphia, PA, USA, Mosby, Inc., pp. 271–284, 2006
- [58] M. Defrise, P. E. Kinahan and C. J. Michel, "Image Reconstruction Algorithms in PET" in *Positron Emission Tomography: Basic Sciences*, D. L. Bailey, D. W. Townsend, P. E. Valk and M. N. Maisey (Eds.), London, UK, Springer Ltd., pp.63–92, 2004
- [59] A. Kak and M. Slaney, *Principles of Computerized Tomographic Imaging*, Classics in Applied Mathematics Ed., Philadelphia, PA, USA, Society for Industrial and Applied Mathematics (SIAM), 2001

- [60] M. Defrise and P. Kinahan, "Data Acquisition and Image Reconstruction", in *The Theory and Practice of 3D PET*, B. Bendriem and D. W. Townsend (Eds.), pp. 11-53, Kluwer Academic publishers, Dordrecht, The Netherlands, 1998
- [61] P. E. Kinahan and J. G. Rogers, "Analytic 3D image reconstruction using all detected events", *IEEE Trans. Nucl. Sci.*, vol. 36, no. 1, pp. 964-968, Feb. 1989
- [62] C. Labbé, H. Zaidi, C. Morel, K. Thielemans, "Description of the STIR implementation of FBP 3DRP", *STIR Handbook*, Version 0.91, 2005, available online: <http://stir.sourceforge.net/documentation/STIR-FBP3DRP.pdf>
- [63] J. G. Colsher, "Fully three-dimensional positron emission tomography", *Phys. Med. Biol.*, vol. 25, no. 1, pp. 103-115, Jan. 1980
- [64] J. Qi, R. M. Leahy, S. R. Cherry, A. Chatziioannou, and T. H. Farquhar, "High-resolution 3D Bayesian image reconstruction using the microPET small-animal scanner", *Phys. Med. Biol.*, vol. 43, no. 4, pp. 1001-1013, Apr. 1998
- [65] J. Qi and R. M. Leahy, "Resolution and noise properties of MAP reconstruction for fully 3-D PET", *IEEE Trans. Med. Imaging*, vol. 19, no. 5, pp. 493-506, May 2000
- [66] A. Chatziioannou, J. Qi, A. Moore, A. Annala, K. Nguyen, R. Leahy and S. R. Cherry, "Comparison of 3-D maximum a posteriori and filtered backprojection algorithms for high-resolution animal imaging with microPET", *IEEE Trans. Med. Imaging*, vol. 19, no. 5, pp. 507-512, May 2000
- [67] K. Erlandsson, I. Buvat, P. H. Pretorius, B. A. Thomas, and B. F. Hutton, "A review of partial volume correction techniques for emission tomography and their applications in neurology, cardiology and oncology", *Phys. Med. Biol.*, vol. 57, no. 21, pp. R119-R159, Dec. 2012
- [68] J.-C. K. Cheng, K. Shoghi, and R. Laforest, "Quantitative accuracy of MAP reconstruction for dynamic PET imaging in small animals", *Med. Phys.*, vol. 39, no. 2, pp. 1029-1041, Feb. 2012
- [69] "MicroPET: A Whole New Perspective", *MicroPET Manager and ASIPRO Handbook*, Siemens Medical Solutions (Molecular Imaging), USA, 2005
- [70] A. M. Scott, "PET Imaging in Oncology", in *Positron Emission Tomography: Basic Sciences*, D. L. Bailey, D. W. Townsend, P. E. Valk and M.N. Maisey (Eds.), Springer, London, UK, p 311, 2005

- [71] B. E. Cooke, A. C. Evans, E. O. Fanthome, R. Alarie and A. M. Sendyk, "Performance figure and images from the Therascan 3128 positron emission tomograph", *IEEE Trans. Nucl. Sci.*, vol. 31, no. 1, pp. 640–644, Feb. 1984
- [72] M. E. Casey and E. J. Hoffman "Quantitation in Positron Emission Computed Tomography: A technique to reduce noise in accidental coincidence measurements and coincidence efficiency calibration", *J. Comput. Assist. Tomogr.* vol. 10, no. 5, pp. 845–850, Sep. 1986
- [73] R. D. Badawi, M. P. Miller, D. L. Bailey and P. K. Marsden "Randoms variance reduction in 3D PET", *Phys. Med. Biol.*, vol. 44, no. 4, pp. 941–954, Apr. 1999
- [74] C. C. Watson, D. Newport, M. E. Casey, "A Single Scatter Simulation Technique for Scatter Correction in 3D PET", in *Three-Dimensional Image Reconstruction in Radiology and Nuclear Medicine*, P. Grangeat and J-L. Arrans, Eds., Kluwer Academic Publishers, Netherlands, pp. 255–268, 1996
- [75] I. Bezrukov, F. Mantlik, H. Schmidt, B. Schölkopf, and B. J. Pichler, "MR-Based PET attenuation correction for PET/MR imaging", *Semin. Nucl. Med.*, vol. 43, no. 1, pp. 45-59, Jan. 2013
- [76] D. Izquierdo-Garcia, S. J. Sawiak, K. Knesaurek, J. Narula, V. Fuster, J. Machac, and Z. A. Fayad, "Comparison of MR-based attenuation correction and CT-based attenuation correction of whole-body PET/MR imaging", *Eur. J. Nucl. Med. Mol. Imaging*, vol. 41, no. 8, pp. 1574-1584, Aug. 2014
- [77] P. L. Chow, F. R. Rannou, and A. F. Chatziioannou, "Attenuation correction for small animal PET tomographs", *Phys. Med. Biol.*, vol. 50, no. 8, pp. 1837-1850, Apr. 2005
- [78] H. H. El Ali, R. P. Bodholdt, J. T. Jrgensen, R. Myschetzky, and A. Kjaer, "Importance of Attenuation Correction (AC) for Small Animal PET Imaging", *Diagnostics*, vol. 2, no. 4, pp. 42-51, Oct. 2012
- [79] I. Zerizer, K. Tan, S. Khan, T. Barwick, M. C. Marzola, D. Rubello, and A. Al-Nahhas, "Role of FDG-PET and PET/CT in the diagnosis and management of vasculitis", *Eur. J. Radiol.*, vol. 73, no.3, pp. 504–509, Mar. 2010
- [80] A. M. Alessio, P. E. Kinahan P. M. Cheng, H. Vesselle and J. S. Karp, "PET/CT scanner instrumentation, challenges and solutions", *Radiol. Clin. N. Am.*, vol. 42, no. 6, pp. 1017–1032, Nov. 2004
- [81] V. Keereman, P. Mollet, Y. Berker, V. Schulz and S. Vandenberghe, "Challenges and current methods for attenuation correction in PET/MR", *MAGMA*, vol. 26, no. 1, pp. 81–98, Feb. 2013

- [82] G. Wagenknecht, H.-J. Kaiser, F. M. Mottaghy, and H. Herzog, "MRI for attenuation correction in PET: methods and challenges.," *MAGMA*, vol. 26, no. 1, pp. 99-113, Feb. 2013
- [83] M. Hofmann, I. Bezrukov, F. Mantlik, P. Aschoff, F. Steinke, T. Beyer, B. J. Pichler, and B. Schölkopf, "MRI-based attenuation correction for whole-body PET/MRI: quantitative evaluation of segmentation- and atlas-based methods", *J. Nucl. Med.*, vol. 52, no. 9, pp. 1392–1399, Sep. 2011
- [84] A. Martinez-Möller, M. Souvatzoglou, G. Delso, R. A. Bundschuh, C. Chefd'hotel, S. I. Ziegler, N. Navab, M. Schwaiger, and S. G. Nekolla, "Tissue classification as a potential approach for attenuation correction in whole-body PET/MRI: evaluation with PET/CT data", *J. Nucl. Med.*, vol. 50, no. 4, pp. 520–526, Apr. 2009
- [85] B. D. Coombs, J. Szumowski, and W. Coshov, "Two-point Dixon technique for water-fat signal decomposition with B0 inhomogeneity correction", *Magn. Reson. Med.*, vol. 38, no. 6, pp. 884–889, Dec. 1997
- [86] D. W. McRobbie, E. A. Moore, M. J. Graves, and M. R. Prince, *MRI from picture to proton*, 2nd edition, Cambridge, UK, Cambridge University Press, 2007
- [87] C. Catana, A. van der Kouwe, T. Benner, C. J. Michel, M. Hamm, M. Fenchel, B. Fischl, B. Rosen, M. Schmand, and A. G. Sorensen, "Toward implementing an MRI-based PET attenuation-correction method for neurologic studies on the MR-PET brain prototype", *J. Nucl. Med.*, vol. 51, no. 9, pp. 1431–1438, Sep. 2010
- [88] W. P. Segars, B. M. W. Tsui, E. C. Frey, G. A. Johnson, S. S. Berr, "Development of a 4D Digital Mouse Phantom for Molecular Imaging Research", *Mol. Imaging Biol.*, vol. 6, no. 3, pp. 149–159, May 2004
- [89] M. Hofmann, F. Steinke, V. Scheel, G. Charpiat, J. Farquhar, P. Aschoff, M. Brady, B. Schölkopf and B. J. Pichler, "MRI-based attenuation correction for PET/MRI: a novel approach combining pattern recognition and atlas registration", *J. Nucl. Med.*, vol. 49, no. 11, pp. 1875–1883, Nov. 2008
- [90] D. Izquierdo-Garcia, K. T. Chen, A. E. Hansen, S. Förster, D. Benoit, S. Schachoff, S. Fürst, D. B. Chonde, and C. Catana, "New SPM8-based MRAC method for simultaneous PET/MR brain images: comparison with state-of-the-art non-rigid registration methods", *EJNMMI Phys.*, vol. 1, Suppl 1, p. A29, May 2014
- [91] N. Burgos, M. J. Cardoso, K. Thielemans, M. Modat, S. Pedemonte, J. Dickson, A. Barnes, J. S. Duncan, D. Atkinson, S. R. Arridge, B. F. Hutton, and S. Ourselin, "Attenuation correction

- synthesis for hybrid PET-MR scanners: application to brain studies”, *IEEE Trans. Med. Imaging*, vol. 33, no. 12, pp. 2332–2341, Dec. 2014
- [92] J. Bini, D. Izquierdo-Garcia, J. Mateo, J. Machac, J. Narula, V. Fuster, Z. A. Fayad, “Preclinical evaluation of MR attenuation correction versus CT attenuation correction on a sequential whole body MR/PET scanner”, *Invest. Radiol.*, vol. 48, no. 5, pp. 313–322, May 2013
- [93] I. B. Malone, R. E. Ansorge, G. B. Williams, P. J. Nestor, T. A. Carpenter, and T. D. Fryer, “Attenuation correction methods suitable for brain imaging with a PET/MRI scanner: a comparison of tissue atlas and template attenuation map approaches”, *J. Nucl. Med.*, vol. 52, no. 7, pp. 1142–1149, Jul. 2011
- [94] J. Nuyts, P. Dupont, S. Stroobants, R. Bennick, L. Mortelmans and P. Suetens, “Simultaneous maximum a posteriori reconstruction of attenuation and activity distributions from emission sinograms”, *IEEE Trans. Med. Imaging* vol. 18, no. 5, pp. 393–403, May 1999
- [95] J. Nuyts, G. Bal, F. Kehren, M. Fenchel, C. Michel, and C. Watson, “Completion of a Truncated Attenuation Image From the Attenuated PET Emission Data”, *IEEE Trans. Med. Imaging*, vol. 32, no. 2, pp. 237–246, Feb. 2013
- [96] R. Boellaard, M. B. Hofman, O. S. Hoekstra, and A. A. Lammertsma, “Accurate PET/MR quantification using time of flight MLAA image reconstruction”, *Mol. Imaging Biol.*, vol. 16, no. 4, pp. 469–477, Aug. 2014
- [97] V. Y. Panin, M. Aykac, and M. E. Casey, “Simultaneous reconstruction of emission activity and attenuation coefficient distribution from TOF data, acquired with external transmission source”, *Phys. Med. Biol.*, vol. 58, no. 11, pp. 3649–3669, Jun. 2013
- [98] P. Mollet, V. Keereman, J. Bini, D. Izquierdo-Garcia, Z. A. Fayad, and S. Vandenberghe, “Improvement of attenuation correction in time-of-flight PET/MR imaging with a positron-emitting source”, *J. Nucl. Med.*, vol. 55, no. 2, pp. 329–336, Jan. 2014
- [99] A. L. Goertzen, Q. Bao, M. Bergeron, E. Blankemeyer, S. Blinder, M. Cañadas, A. F. Chatziioannou, K. Dinelle, E. Elhami, H.-S. Jans, E. Lage, R. Lecomte, V. Sossi, S. Surti, Y.-C. Tai, J. J. Vaquero, E. Vicente, D. A. Williams, and R. Laforest, “NEMA NU 4-2008 comparison of preclinical PET imaging systems”, *J. Nucl. Med.*, vol. 53, no. 8, pp. 1300–1309, Aug. 2012
- [100] P. Mansfield and P. G. Morris, *NMR imaging in biomedicine*, UK edition, London, UK, Academic Press, 1982

- [101] M. A. Bernstein, K. F. King, and X. J. Zhou, "Imaging gradients", in *Handbook of MRI Pulse Sequences*, London, UK, Elsevier Academic Press, pp. 579–647, 2004
- [102] M. A. Bernstein, K. F. King, and X. J. Zhou, "Basic Pulse Sequences", in *Handbook of MRI Pulse Sequences*, London, UK, Elsevier Academic Press, pp. 579–647, 2004
- [103] R. E. Hendrick, "Gradient Echo and 3D imaging" in *Breast MRI: Fundamentals and Technical Aspects*, New York, NY, USA, Springer, p. 72, 2008
- [104] F. Bloch, "Nuclear Induction", *Physical Review*, vol. 70, no. 7–8, pp. 460–474, Oct. 1946
- [105] R. Schmidt, S. Ropele, B. Pendl, P. Ofner, C. Enzinger, H. Schmidt, A. Berghold, M. Windisch, H. Kolassa and F. Fazekas, "Longitudinal multimodal imaging in mild to moderate Alzheimer disease: a pilot study with memantine," *J. Neurol. Neurosurg. Psychiatry*, vol. 79, no. 12, pp. 1312–1307, Jun. 2008
- [106] S. L. Barnes, J. G. Whisenant, M. E. Loveless and T. E. Yankeelov, "Practical Dynamic Contrast Enhanced MRI in Small Animal Models of Cancer: Data Acquisition, Data Analysis and Interpretation", *Pharmaceutics*, vol. 4, no. 3, pp. 442–478, Sep. 2012
- [107] A. H. Jacobs, L. W. Kracht, A. Gossmann, M. A. Rüger, A. V. Thomas, A. Thiel, and K. Herholz, "Imaging in Neurooncology", *NeuroRx*, vol. 2, no. 2, pp. 333–347, Apr. 2005
- [108] S. Laurent, L. V. Elst and R. N. Muller, "Comparative study of the physicochemical properties of six clinical low molecular weight gadolinium contrast agents", *Contrast Media & Mol. Imaging*, vol. 1, no. 3, pp. 128–137, May–Jun. 2006
- [109] C. Preibisch and R. Deichmann, "Influence of RF spoiling on the stability and accuracy of T1 mapping based on spoiled FLASH with varying flip angles", *Magn. Reson. Med.*, vol. 61, no. 1, pp. 125–135, Jan. 2009
- [110] A. Haase, "Snapshot FLASH MRI. Applications to T1, T2, and chemical-shift imaging", *Magn. Reson. Med.*, vol. 13, no. 1, pp. 77–89, Jan. 1990
- [111] A. Garpebring, R. Wirestam, N. Ostlund, and M. Karlsson, "Effects of inflow and radiofrequency spoiling on the arterial input function in dynamic contrast-enhanced MRI: a combined phantom and simulation study", *Magn. Reson. Med.*, vol. 65, no. 6, pp. 1670–1679, Jun. 2011
- [112] Y. Zur, M. L. Wood, and L. J. Neuringer, "Spoiling of transverse magnetization in steady-state sequences", *Magn. Reson. Med.*, vol. 21, no. 2, pp. 251–263, Oct. 1991

- [113] V. L. Yarnykh, “Optimal radiofrequency and gradient spoiling for improved accuracy of T1 and B1 measurements using fast steady-state techniques”, *Magn. Reson. Med.*, vol. 63, no. 6, pp. 1610–1626, June 2010
- [114] A. Pohlmann, P. Boyé, B. Wagenhaus, D. Müller, M. Kolanczyk, S. Köhler, J. Schulz-Menger and T. Niendorf, “Cardiac MR imaging in Mice: Morphometry and Functional Assessment”, *Bruker Application Note (FLASH IntraGate Sequence)*, pp. 1–6, 2012, available online: www.bruker.com/fileadmin/user_upload/8-PDF-Docs/MagneticResonance/MRI/brochures/Cardiac-MRI-app-note.pdf
- [115] M. A. Bernstein, K. F. King, and X. J. Zhou, “Correction gradients”, in *Handbook of MRI Pulse Sequences*, London, UK, Elsevier Academic Press, pp. 292–362, 2004
- [116] D. A. Saloner, “Magnetic Resonance Angiography Techniques” in *MRI and CT of the cardiovascular system*, C. B. Higgins and A. de Roos (Eds.), Second edition, Philadelphia, PA, USA, Lippencott, Williams and Williams, pp. 19–36, 2006
- [117] L. Østergaard, R. M. Weisskoff, D. A. Chesler, C. Gyldensted, and B. R. Rosen “High resolution measurement of cerebral blood flow using intravascular tracer bolus passages. Part I: Mathematical approach and statistical analysis”, *Magn. Reson. Med.*, vol. 36, no. 5, pp. 715–725, Nov. 1996
- [118] L. Østergaard, D. F. Smith, P. Vestergaard-Poulsen, S. B. Hansen, A. D. Gee, A. Gjedde, and C. Gyldensted, “Absolute cerebral blood flow and blood volume measured by magnetic resonance imaging bolus tracking: comparison with positron emission tomography values”, *J. Cereb. Blood Flow Metab.*, vol. 18, no. 4, pp. 425–432, Apr. 1998
- [119] K. A. Rempp, G. Brix, F. Wenz, C. R. Becker, F. Gückel, and W. J. Lorenz, “Quantification of regional cerebral blood flow and volume with dynamic susceptibility contrast-enhanced MR imaging”, *Radiology*, vol. 193, no. 3, pp. 637–641, Dec. 1994
- [120] R. Wirestam, L. Andersson, L. Østergaard, M. Bolling, J.-P. Aunola, A. Lindgren, B. Geijer, S. Holtås, and F. Ståhlberg, “Assessment of regional cerebral blood flow by dynamic susceptibility contrast MRI using different deconvolution techniques”, *Magn. Reson. Med.*, vol. 43, no. 5, pp. 691–700, May 2000
- [121] F. Calamante, L. Thomas, and C. E. T. Al, “Measuring cerebral blood flow using magnetic resonance imaging techniques,” *J. Cereb. Blood Flow Metab.*, vol. 19, no. 7, pp. 701–735, Feb. 1999
- [122] M. S. Shiroishi, G. Castellazzi, J. L. Boxerman, F. D’Amore, M. Essig, T. B. Nguyen, J. M. Provenzale, D. S. Enterline, N. Anzalone, A. Drfler, A. Rovira, M. Wintermark, and M. Law, “Princi-

- ples of T2 *-weighted dynamic susceptibility contrast MRI technique in brain tumor imaging”, *J. Magn. Reson. Imaging*, vol. 41, no. 2, pp. 296–313, Feb. 2015
- [123] S. Heiland, T. Benner, W. Reith, M. Forsting, and K. Sartor, “Perfusion-weighted MRI using gadobutrol as a contrast agent in a rat stroke model”, *J. Magn. Reson. Imaging*, vol. 7, no. 6, pp. 1109–1115, Nov–Dec. 1997
- [124] E. J. W. Bleeker, M. A. van Buchem, and M. J. P. van Osch, “Optimal location for arterial input function measurements near the middle cerebral artery in first-pass perfusion MRI”, *J. Cereb. Blood Flow Metab.*, vol. 29, no. 4, pp. 840–852, Apr. 2009
- [125] G. Zaharchuk, “Theoretical basis of hemodynamic MR imaging techniques to measure cerebral blood volume, cerebral blood flow, and permeability”, *Am. J. Neuroradiology*, vol. 28, no. 10, pp. 1850–1858, Nov.–Dec. 2007
- [126] K. Hittmair, G. Gomiscek, K. Langenberger, M. Recht, H. Imhof, and J. Kramer, “Method for the quantitative assessment of contrast agent uptake in dynamic contrast-enhanced MRI”, *Magn. Reson. Med.*, vol. 31, no. 5, pp. 567–571, May 1994
- [127] P. Sharma, J. Socolow, S. Patel, R. I. Pettigrew, and J. N. Oshinski, “Effect of Gd-DTPA-BMA on blood and myocardial T1 at 1.5T and 3T in humans”, *J. Magn. Reson. Imaging*, vol. 23, no. 3, pp. 323–330, Mar. 2006
- [128] M. Rohrer, H. Bauer, J. Mintorovitch, M. Requardt, and H.-J. Weinmann, “Comparison of magnetic properties of MRI contrast media solutions at different magnetic field strengths”, *Invest. Radiol.*, vol. 40, no. 11, pp. 715–724, Nov. 2005
- [129] P. S. Tofts, G. Brix, D. L. Buckley, J. L. Evelhoch, E. Henderson, M. V. Knopp, H. B. W. Larsson, T.-Y. Lee, N. A. Mayr, G. J. M. Parker, R. E. Port, J. Taylor, and R. M. Weisskoff, “Estimating kinetic parameters from dynamic contrast-enhanced T(1)-weighted MRI of a diffusable tracer: standardized quantities and symbols”, *J. Magn. Reson. Imaging*, vol. 10, no. 3, pp. 223–232, Sep. 1999
- [130] P. S. Tofts, “Concepts: Measurement and MRI,” in *Quantitative MRI of the Brain: measuring changes caused by disease*, P.S. Tofts, (Ed.), Chichester, UK, John Wiley & Sons, Ltd., pp. 3–15, 2003
- [131] S. C. L. Deoni, T. M. Peters, and B. K. Rutt, “Determination of optimal angles for variable nutation proton magnetic spin-lattice, T1, and spin-spin, T2, relaxation times measurement”, *Magn. Reson. Med.*, vol. 51, no. 1, pp. 194–199, Jan. 2004

- [132] H.-L. M. Cheng and G. A. Wright, "Rapid high-resolution T(1) mapping by variable flip angles: accurate and precise measurements in the presence of radiofrequency field inhomogeneity", *Magn. Reson. Med.*, vol. 55, no. 3, pp. 566–574, Mar. 2006
- [133] A. Jackson, G. C. Jayson, K. L. Li, X. P. Zhu, D. R. Checkley, J. J. Tessier and J. C. Waterton, "Reproducibility of quantitative dynamic contrast-enhanced MRI in newly presenting glioma," *Br. J. Radiol.*, vol. 76, no. 903, pp. 153–162, Mar. 2003
- [134] G. J. M. Parker, C. Roberts, A. Macdonald, G. A. Buonaccorsi, S. Cheung, D. L. Buckley, A. Jackson, Y. Watson, K. Davies, and G. C. Jayson, "Experimentally-derived functional form for a population-averaged high-temporal-resolution arterial input function for dynamic contrast-enhanced MRI", *Magn. Reson. Med.*, vol. 56, no. 5, pp. 993–1000, Nov. 2006
- [135] A. Garpebring, P. Brynolfsson, J. Yu, R. Wirestam, A. Johansson, T. Asklund, and M. Karlsson, "Uncertainty estimation in dynamic contrast-enhanced MRI", *Magn. Reson. Med.*, vol. 69, no. 4, pp. 992-1002, Apr. 2013
- [136] B. M. Dale, J. A. Jesberger, J. S. Lewin, C. M. Hillenbrand, and J. L. Duerk, "Determining and optimizing the precision of quantitative measurements of perfusion from dynamic contrast enhanced MRI", *J. Magn. Reson. Imaging*, vol. 18, no. 5, pp. 575-584, Nov. 2003
- [137] M. A. Bernstein, K. F. King, and X. J. Zhou, "Advanced Pulse Sequence Techniques", in *Handbook of MRI Pulse Sequences*, London, UK, Elsevier Academic Press, pp. 802–830, 2004
- [138] E. Esparza-Coss, J. Wosnik and P. A. Narayana, "Perfusion in Rat Brain at 7T with Arterial Spin Labelling Using FAIR-TrueFISP and QUIPSS", *J. Magn. Reson. Imaging*, vol. 28, no. 4, pp. 607–612, May 2010
- [139] M. C. Adams, T. G. Turkington, J. M. Wilson, and T. Z. Wong, "A systematic review of the factors affecting accuracy of SUV measurements", *Am. J. Roentgenol.*, vol. 195, no. 2, pp. 310-320, Aug. 2010
- [140] P. E. Kinahan and J. W. Fletcher, "Positron emission tomography-computed tomography standardized uptake values in clinical practice and assessing response to therapy", *Semin. Ultrasound CT MR*, vol. 31, no. 6, pp. 496-505, Dec. 2010
- [141] S. Ben-Haim and P. Ell, "18F-FDG PET and PET/CT in the evaluation of cancer treatment response", *J. Nucl. Med.*, vol. 50, no. 1, pp. 88-99, Jan. 2009
- [142] R. Boellaard, "Need for Standardization of 18F-FDG PET/CT for Treatment Response Assessments", *J. Nucl. Med.*, vol. 52, Suppl. 2, pp. 93S–100S, Dec. 2011

- [143] S. J. Bensinger and H. R. Christofk, "New aspects of the Warburg effect in cancer cell biology", *Semin. Cell Dev. Biol.*, vol. 23, no. 4, pp. 352-361, Jun. 2012
- [144] R. Boellaard, M. J. O'Doherty, W. A. Weber, F. M. Mottaghy, M. N. Lonsdale, S. G. Stroobants, W. J. G. Oyen, J. Kotzerke, O. S. Hoekstra, J. Pruim, P. K. Marsden, K. Tatsch, C. J. Hoekstra, E. P. Visser, B. Arends, F. J. Verzijlbergen, J. M. Zijlstra, E. F. I. Comans, A. A. Lammertsma, A. M. Paans, A. T. Willemsen, T. Beyer, A. Bockisch, C. Schaefer-Prokop, D. Delbeke, R. P. Baum, A. Chiti, and B. J. Krause, "FDG PET and PET/CT: EANM procedure guidelines for tumour PET imaging: version 1.0", *Eur. J. Nucl. Med. Mol. Imaging*, vol. 37, no. 1, pp. 181-200, Jan. 2010
- [145] H. Zhuang, M. Pourdehnad, E. S. Lambright, A. J. Yamamoto, M. Lanuti, P. Li, P. D. Mozley, M. D. Rossman, S. M. Albelda, and A. Alavi, "Dual Time Point 18F-FDG PET Imaging for differentiating malignant from inflammatory processes", *J. Nucl. Med.*, vol. 42, no. 9, pp. 1412-1417, Sep. 2001
- [146] B. J. Fueger, J. Czernin, I. Hildebrandt, C. Tran, B. S. Halpern, D. Stout, E. Michael, M. E. Phelps and W. A. Weber, "Impact of Animal Handling on the Results of 18 F-FDG PET Studies in Mice", *J. Nucl. Med.*, vol. 47, no. 6, pp. 999-1006, Mar. 2006
- [147] G. A. Sayre, B. L. Franc, and Y. Seo, "Patient-Specific Method of Generating Parametric Maps of Patlak K(i) without Blood Sampling or Metabolite Correction: A Feasibility Study", *Int. J. Mol. Imaging*, vol. 1, pp. 185-197, Jan. 2011
- [148] E. P. Visser, M. E. P. Philippens, L. Kienhorst, J. H. A. M. Kaanders, F. H. M. Corstens, L.-F. de Geus-Oei, and W. J. G. Oyen, "Comparison of tumor volumes derived from glucose metabolic rate maps and SUV maps in dynamic 18F-FDG PET", *J. Nucl. Med.*, vol. 49, no. 6, pp. 892-898, Jun. 2008
- [149] V. J. Cunningham, S. P. Hume, G. R. Price, R. G. Ahier, J. E. Cremer and A. K. P. Jones, "Compartmental analysis of diprenorphine binding to opiate receptors in the rat in vivo and its comparison with equilibrium data in vitro", *J Cereb Blood Flow Metab.* vol. 11, no. 1, pp. 1-9, Jan. 1991
- [150] R. N. Gunn, A. A. Lammertsma, S. P. Hume and V. J. Cunningham "Parametric imaging of ligand-receptor binding in PET using a simplified reference region model", *Neuroimage*, vol. 6, no. 4, pp. 279-287, Nov. 1997
- [151] H. Watabe, Y. Ikoma, Y. Kimura, M. Naganawa, and M. Shidahara, "PET kinetic analysis - compartmental model", *Ann. Nucl. Med.*, vol. 20, no. 9, pp. 583-588, Nov. 2006

- [152] R. E. Carson, "Tracer Kinetic Modelling in PET" in *Positron Emission Tomography: Basic Sciences*, D. L. Bailey, D. W. Townsend, P. E. Valk and M. N. Maisey (Eds.), London, UK, Springer Ltd., pp. 127–160, 2004
- [153] M. D. Silva, C. Glaus, J. Y. Hesterman, J. Hoppin, G. H. Della Puppa, T. Kazules, K. M. Orcutt, M. Germino, D. Immke, and S. Miller, "Regional, kinetic [(18)F]FDG PET imaging of a unilateral Parkinsonian animal model", *Am. J. Nucl. Med. Mol. Imaging*, vol. 3, no. 2, pp. 129-141, Jan. 2013
- [154] C. S. Patlak, R. G. Blasberg, and J. D. Fenstermacher, "Graphical evaluation of blood-to-brain transfer constants from multiple-time uptake data", *J. Cereb. Blood Flow Metab.*, vol. 3, no. 1, pp. 1-7, Mar. 1983
- [155] M. Muzi, F. OSullivan, D. A. Mankoff, R. K. Doot, L. A. Pierce, B. F. Kurland, H. M. Linden, and P. E. Kinahan, "Quantitative assessment of dynamic PET imaging data in cancer imaging", *J. Magn. Reson. Imaging*, vol. 30, no. 9, pp. 1203-1215, Nov. 2012
- [156] P. Zanotti-Fregonara, E. M. Fadaili, R. Maroy, C. Comtat, A. Souloumiac, S. Jan, M.-J. Ribeiro, V. Gaura, A. Bar-Hen, and R. Trébossen, "Comparison of eight methods for the estimation of the image-derived input function in dynamic [(18)F]-FDG PET human brain studies", *J. Cereb. Blood Flow Metab.*, vol. 29, no. 11, pp. 1825–1835, Nov. 2009
- [157] K. Shimoji, L. Ravasi, K. Schmidt, M. L. Soto-montenegro, T. Esaki, J. Seidel, E. Jagoda, L. Sokoloff, M. V Green, and W. C. Eckelman, "Measurement of cerebral glucose metabolic rates in the anesthetized rat by dynamic scanning with 18F-FDG, the ATLAS small animal PET scanner and arterial blood sampling", *J. Nucl. Med.*, vol. 45, pp. 665-672, Dec. 2003
- [158] B. Weber, C. Burger, P. Biro and A. Buck, "A femoral arteriovenous shunt facilitates arterial whole blood sampling in animals", *Eur. J. Nucl. Med. Mol. Imaging*, vol. 29, no. 3, pp. 319–323, Mar. 2002
- [159] A. C. Riches, J. G. Sharp, D. B. Thomas, and S. V Smith, "Blood volume determination in the mouse", *J. Physiol.*, vol. 228, no. 2, pp. 279-284, Jan. 1973
- [160] K.-P. Wong, W. Sha, X. Zhang, and S.-C. Huang, "Effects of administration route, dietary condition, and blood glucose level on kinetics and uptake of 18F-FDG in mice", *J. Nucl. Med.*, vol. 52, no. 5, pp. 800-807, May 2011
- [161] T. Ose, H. Watabe, T. Hayashi, N. Kudomi, M. Hikake, H. Fukuda, N. Teramoto, Y. Watanabe, H. Onoe, and H. Iida, "Quantification of regional cerebral blood flow in rats using an arteriovenous shunt and micro-PET", *Nucl. Med. Biol.*, vol. 39, no. 5, pp. 730–741, Jan. 2012

- [162] G. Warnock, M.-A. Bahri, D. Goblet, F. Giacomelli, C. Lemaire, J. Aerts, A. Seret, X. Langlois, A. Luxen, and A. Plenevaux, "Use of a beta microprobe system to measure arterial input function in PET via an arteriovenous shunt in rats", *EJNMMI Res.*, vol. 1, no. 13, pp. 1–11, Aug. 2011
- [163] N. Kudomi, H. Sipilä, A. Autio, V. Oikonen, H. Liljenbäck, M. Tarkia, J. Laivola, J. Johansson, M. Teräs, and A. Roivainen, "Cross-validation of input functions obtained by H₂15O PET imaging of rat heart and a blood flow-through detector", *Mol. Imaging Biol.*, vol. 14, no. 4, pp. 509-516, Aug. 2012
- [164] F. Roehrbacher, J. P. Bankstahl, M. Bankstahl, T. Wanek, J. Stanek, M. Sauberer, J. Muellauer, T. Schroettner, O. Langer and C. Kuntner, "Development and performance test of an online blood sampling system for determination of the arterial input function in rats", *EJNMMI Physics*, vol. 2, no. 1, pp. 1–19, Jan. 2015
- [165] F. Pain, P. Lanièce, R. Mastrippolito, P. Gervais, P. Hantraye and L. Besret "Arterial input function measurement without blood sampling using a beta-microprobe in rats", *J. Nucl. Med.*, vol. 45, no. 9, pp. 1577-1582, Apr. 2004
- [166] S. Maramraju, S. Stoll, C. Woody, D. Schlyer, W. Schiffer, D. Lee, S. Dewey, and P. Vaska, "A LSO Beta Microprobe for Measuring Input Functions for Quantitative Small Animal PET", *Nucl. Instrum. Meth. A*, vol. 571, no. 12, pp. 407-410, Feb. 2007
- [167] P. T. Meyer, V. Circiumaru, C. A. Cardi, D. H. Thomas, H. Bal, and P. D. Acton, "Simplified quantification of small animal [18F]FDG PET studies using a standard arterial input function", *Eur. J. Nucl. Med. Mol. Imaging*, vol. 33, no. 8, pp. 948-954, Aug. 2006
- [168] K-P. Wong, X. Zhang and S-C Huang, "Improved Derivation of Input Function in Dynamic Mouse [18F] FDG PET Using Bladder Radioactivity Kinetics", *Mol. Imaging Biol.*, vol. 15, no. 4, pp. 486–496, Aug. 2013
- [169] S. D. Rani, S. T. Nemanich, N. Fettig, and K. I. Shoghi, "Kinetic analysis of FDG in rat liver: Effect of dietary intervention on arterial and portal vein input", *Nucl. Med. Biol.*, vol. 40, no. 4, pp. 537–546, Feb. 2013
- [170] P. Zanotti-Fregonara, K. Chen, J.-S. Liow, M. Fujita, and R. B. Innis, "Image-derived input function for brain PET studies: many challenges and few opportunities", *J. Cereb. Blood Flow Metab.*, vol. 31, no. 10, pp. 1986–1998, Oct. 2011
- [171] G. Xiong, C. Paul, A. Todica, M. Hacker, P. Bartenstein, and G. Böning, "Noninvasive image derived heart input function for CMRglc measurements in small animal slow infusion FDG PET studies", *Phys. Med. Biol.*, vol. 57, no. 23, pp. 8041-8059, Dec. 2012

- [172] K. I. Shoghi and M. J. Welch, "Hybrid image and blood sampling (HIBS) input function for quantification of microPET data", *Nucl. Med. Biol.*, vol. 34, no. 8, pp. 989-994, Nov. 2007
- [173] R. Mabrouk, F. Dubeau, M. Bentourkia, and L. Bentabet, "Extraction of time activity curves from gated FDG-PET images for small animals heart studies", *Comput. Med. Imaging Graph.*, vol. 36, no. 6, pp. 484-491, Sep. 2012
- [174] L. W. Locke, M. B. Williams, K. D. Fairchild, M. Zhong, B. K. Kundu, and S. S. Berr, "FDG-PET Quantification of Lung Inflammation with Image-Derived Blood Input Function in Mice", *Int. J. Mol. Imaging*, vol. 2011, no. 356730, pp. 1-6, Jan. 2011
- [175] D. Schulz, A. Tapfer, A. Buck, S. Reeder, M. Miederer, E. Weidl, S. I. Ziegler, and M. Schwaiger, "Non-Negative Matrix Factorization Based Input Function Extraction for Mouse Imaging in Small Animal PET Comparison with Arterial Blood Sampling and Factor Analysis", *J. Mol. Imaging Dynam.*, vol. 2, no. 2, pp. 1-6, Apr. 2012
- [176] J. Kim, P. Herrero, T. Sharp, R. Laforest, D. J. Rowland, Y.-C. Tai, J. S. Lewis, and M. J. Welch, "Minimally invasive method of determining blood input function from PET images in rodents", *J. Nucl. Med.*, vol. 47, no. 2, pp. 330-336, Feb. 2006
- [177] E. J. Hoffman, S. C. Huang and M. E. Phelps, "Quantitation in positron emission computed tomography: Effect of object size," *J. Comput. Assist. Tomogr.*, vol. 3, no. 3, pp. 299-308, Jun. 1979
- [178] L. A. Green, S. S. Gambhir, A. Srinivasan, P. K. Banerjee, C. K. Hoh, S. R. Cherry, S. Sharfstein, J. R. Barrio, H. R. Herschman, and M. E. Phelps, "Noninvasive methods for quantitating blood time-activity curves from mouse PET images obtained with fluorine-18-fluorodeoxyglucose", *J. Nucl. Med.*, vol. 39, no. 4, pp. 729-734, Apr. 1998
- [179] L. A. Green, K. Nguyen, B. Berenji, M. Iyer, E. Bauer, J. R. Barrio, M. Namavari, N. Satyamurthy, and S. S. Gambhir, "A tracer kinetic model for 18F-FHBG for quantitating herpes simplex virus type 1 thymidine kinase reporter gene expression in living animals using PET", *J. Nucl. Med.*, vol. 45, no. 9, pp. 1560-1570, Sep. 2004
- [180] T. Dumouchel, S. Thorn, M. Kordos, J. DaSilva, R. S. B. Beanlands, and R. A. deKemp, "A three-dimensional model-based partial volume correction strategy for gated cardiac mouse PET imaging", *Phys. Med. Biol.*, vol. 57, no. 13, pp. 4309-4334, Jul. 2012
- [181] Y.-H. D. Fang and R. F. Muzic Jr, "Spillover and partial-volume correction for image-derived input functions for small-animal 18F-FDG PET studies", *J. Nucl. Med.*, vol. 49, no. 4, pp. 606-614, Apr. 2008

- [182] G. Z. Ferl, X. Zhang, H.-M. Wu, M. C. Kreissl, and S.-C. Huang, "Estimation of the 18F-FDG input function in mice by use of dynamic small-animal PET and minimal blood sample data", *J. Nucl. Med.*, vol. 48, no. 12, pp. 2037-2045, Dec. 2007
- [183] F. Vlachos, Y.-S. Tung, and E. Konofagou, "Permeability dependence study of the focused ultrasound-induced blood-brain barrier opening at distinct pressures and microbubble diameters using DCE-MRI", *Magn. Reson. Med.*, vol. 66, no. 3, pp. 821-830, Sep. 2011
- [184] J. P. B. O'Connor, A. Jackson, G. J. M. Parker, and G. C. Jayson, "DCE-MRI biomarkers in the clinical evaluation of antiangiogenic and vascular disrupting agents", *Br. J. Cancer*, vol. 96, no. 2, pp. 189-195, Jan. 2007
- [185] R. J. Maxwell, J. Wilson, V. E. Prise, B. Vojnovic, G. J. Rustin, M. A. Lodge, and G. M. Tozer, "Evaluation of the anti-vascular effects of combretastatin in rodent tumours by dynamic contrast enhanced MRI", *NMR Biomed.*, vol. 15, no. 2, pp. 89-98, Apr. 2002.
- [186] M. M. Pike, C. N. Stoops, C. P. Langford, N. S. Akella, L. B. Nabors, and G. Y. Gillespie, "High-resolution Longitudinal Assessment of Flow and Permeability in Mouse Glioma Vasculature: Sequential Small Molecule and SPIO Dynamic Contrast Agent MRI", *Magn. Reson. Med.*, vol. 61, no. 3, pp. 615-625, Mar. 2009
- [187] D. M. McGrath, D. P. Bradley, J. L. Tessier, T. Lacey, C. J. Taylor, and G. J. M. Parker, "Comparison of model-based arterial input functions for dynamic contrast-enhanced MRI in tumor bearing rats", *Magn. Reson. Med.*, vol. 61, no. 5, pp. 1173-1184, May 2009
- [188] H.-L. M. Cheng, "Investigation and optimization of parameter accuracy in dynamic contrast-enhanced MRI", *J. Magn. Reson. Imaging*, vol. 28, no. 3, pp. 736-743, Sep. 2008
- [189] S. L. Barnes, J. G. Whisenant, M. E. Loveless, G. D. Ayers, and T. E. Yankeelov, "Assessing the reproducibility of dynamic contrast enhanced magnetic resonance imaging in a murine model of breast cancer", *Magn. Reson. Med.*, vol. 69, no. 6, pp. 1721-1734, Jun. 2013
- [190] J. Sedlacik, A. Myers, R. B. Loeffler, R. F. Williams, A. M. Davidoff, and C. M. Hillenbrand, "A dedicated automated injection system for dynamic contrast-enhanced MRI experiments in mice", *J. Magn. Reson. Imaging*, vol. 37, no. 3, pp. 746-751, Mar. 2013
- [191] R. Zhou, S. Pickup, T. E. Yankeelov, C. S. Springer, and J. D. Glickson, "Simultaneous measurement of arterial input function and tumor pharmacokinetics in mice by dynamic contrast enhanced imaging: effects of transcytolemmal water exchange", *Magn. Reson. Med.*, vol. 52, no. 2, pp. 248-257, Aug. 2004

- [192] I. C. Benjaminsen, B. A. Graff, K. G. Brurberg, and E. K. Rofstad, "Assessment of tumor blood perfusion by high-resolution dynamic contrast-enhanced MRI: a preclinical study of human melanoma xenografts", *Magn. Reson. Med.*, vol. 52, no. 2, pp. 269-276, Aug. 2004
- [193] M. Heilmann, C. Walczak, J. Vautier, J.-L. Dimicoli, C. D. Thomas, M. Lupu, J. Mispelter, and A. Volk, "Simultaneous dynamic T1 and T2* measurement for AIF assessment combined with DCE MRI in a mouse tumor model", *MAGMA*, vol. 20, no. 4, pp. 193-203, Oct. 2007
- [194] S. Pickup, R. Zhou and J. Glickson, "MRI Estimation of the arterial input function in mice", *Acad. Radiol.*, vol. 10, no. 9, pp. 963-968, Sep. 2003
- [195] M. E. Loveless, J. Halliday, C. Liess, L. Xu, R. D. Dortch, J. Whisenant, J. C. Waterton, J. C. Gore, and T. E. Yankeelov, "A quantitative comparison of the influence of individual versus population-derived vascular input functions on dynamic contrast enhanced-MRI in small animals", *Magn. Reson. Med.*, vol. 67, no. 1, pp. 226-236, Jan. 2012
- [196] D. A. Hormuth 2nd, J. T. Skinner, M. D. Does, and T. E. Yankeelov, "A comparison of individual and population-derived vascular input functions for quantitative DCE-MRI in rats", *J. Magn. Reson. Imaging*, vol. 32, no. 4, pp. 397-401, May 2014
- [197] J. T. Skinner, T. E. Yankeelov, T. E. Peterson and M. D. Does, "Comparison of Dynamic Contrast Enhanced MRI and Quantitative SPECT in a Rat Glioma Model", *Contrast Media Mol. Imaging*, vol. 7, no. 6, pp. 494-500, Nov.-Dec. 2012
- [198] Y. Tanaka, T. Nagaoka, G. Nair, K. Ohno, and T. Q. Duong, "Arterial spin labeling and dynamic susceptibility contrast CBF MRI in postischemic hyperperfusion, hypercapnia, and after mannitol injection", *J. Cereb. Blood Flow Metab.*, vol. 31, no. 6, pp. 1403-1411, Jun. 2011
- [199] K. Mouridsen, S. Christensen, L. Gyldensted, and L. Ostergaard, "Automatic selection of arterial input function using cluster analysis", *Magn. Reson. Med.*, vol. 55, no. 3, pp. 524-531, Mar. 2006
- [200] F. Calamante, D. G. Gadian, and A. Connelly, "Quantification of bolus-tracking MRI: Improved characterization of the tissue residue function using Tikhonov regularization", *Magn. Reson. Med.*, vol. 50, no. 6, pp. 1237-1247, Dec. 2003
- [201] H. K. Thompson, C. F. Starmer, R. E. Whalen, and H. D. McIntosh, "Indicator Transit Time Considered As a Gamma Variate", *Circ. Res.*, vol. 14, no. 6, pp. 502-515, Jun. 1964
- [202] T. Benner, S. Heiland, G. Erb, M. Forsting, and K. Sartor, "Accuracy of gamma-variate fits to concentration-time curves from dynamic susceptibility-contrast enhanced MRI: influence of time

- resolution, maximal signal drop and signal-to-noise”, *J. Magn. Reson. Imaging*, vol. 15, no. 3, pp. 307–317, Jan. 1997
- [203] M. Rausch, K. Scheffler, M. Rudin and E. W. Radü, “Analysis of input functions from different arterial branches with gamma variate functions and cluster analysis for quantitative blood volume measurements”, *J. Magn. Reson. Imaging*, vol. 18, no. 10, pp. 1235–1243, Dec. 2000
- [204] A. Bjørnerud and K. E. Emblem, “A fully automated method for quantitative cerebral hemodynamic analysis using DSC-MRI”, *J. Cereb. Blood Flow Metab.*, vol. 30, no. 5, pp. 1066–1078, May 2010
- [205] P. Vakil, J. J. Lee, J. J. Mouannes-Srour, C. P. Derdeyn, and T. J. Carroll, “Cerebrovascular Occlusive Disease: Quantitative Cerebral Blood Flow Using Dynamic Susceptibility Contrast MR Imaging Correlates with Quantitative H₂[15O] PET”, *Radiology*, vol. 266, no. 3, pp. 879–886, Mar. 2013
- [206] D. E. Crane, M. J. Donahue, M. A. Chappell, E. Sideso, A. Handa, J. Kennedy, P. Jezzard, and B. J. MacIntosh, “Evaluating quantitative approaches to dynamic susceptibility contrast MRI among carotid endarterectomy patients”, *J. Magn. Reson. Imaging*, vol. 37, no. 4, pp. 936-943, Apr. 2013
- [207] L. Knutsson, D. van Westen, E. T. Petersen, K. M. Bloch, S. Holtås, F. Ståhlberg, and R. Wirestam, “Absolute quantification of cerebral blood flow: correlation between dynamic susceptibility contrast MRI and model-free arterial spin labelling”, *J. Magn. Reson. Imaging*, vol. 28, no. 1, pp. 1-7, Jan. 2010
- [208] L. Knutsson, F. Ståhlberg, R. Wirestam, and M. J. van Osch, “Effects of blood ΔR_2^* non-linearity on absolute perfusion quantification using DSC-MRI: Comparison with Xe-133 SPECT”, *J. Magn. Reson. Imaging*, vol. 31, no. 5, pp. 651–655, Jun. 2013
- [209] A. J. de Langen, V. E. M. van den Boogaart, J. T. Marcus, and M. Lubberink, “Use of H₂(15)O-PET and DCE-MRI to measure tumor blood flow”, *Oncologist*, vol. 13, no. 6, pp. 631–644, Jun. 2008
- [210] C. C. Quarles and K. M. Schmainda, “Assessment of the morphological and functional effects of the anti-angiogenic agent SU11657 on 9L gliosarcoma vasculature using dynamic susceptibility contrast MRI”, *Magn. Reson. Med.*, vol. 57, no. 4, pp. 680-687, Apr. 2007
- [211] A. Yamamoto, H. Sato, J. Enmi, K. Ishida, T. Ose, A. Kimura, H. Fujiwara, H. Watabe, T. Hayashi, and H. Iida, “Use of a clinical MRI scanner for preclinical research on rats”, *Radiol. Phys. Technol.*, vol. 2, no. 1, pp. 13-21, Jan. 2009

- [212] D. Peruzzo, A. Bertoldo, F. Zanderigo, and C. Cobelli, "Automatic selection of arterial input function on dynamic contrast-enhanced MR images", *Comput. Methods Programs Biomed.*, vol. 104, no. 3, pp. e148–e157, Dec. 2011
- [213] E. J. W. Bleeker, M. J. P. van Osch, A. Connelly, M. A. van Buchem, A. G. Webb, and F. Calamante, "New criterion to aid manual and automatic selection of the arterial input function in dynamic susceptibility contrast MRI", *Magn. Reson. Med.*, vol. 65, no. 2, pp. 448–456, Feb. 2011
- [214] M.-Y. Yeh, T.-H. Lee, S.-T. Yang, H.-H. Kuo, T.-K. Chyi, and H.-L. Liu, "Automated detection of arterial input function in DSC perfusion MRI in a stroke rat model" *J. Instrum.*, vol. 4, no. P05021, pp. 1–6, May 2009
- [215] G. O. Cron, J. C. Wallace, W. D. Stevens, T. Fortin, B. A. Pappas, R. C. Wilkins, F. Kelcz, and G. E. Santyr, "A comparison of T2*-weighted magnitude and phase imaging for measuring the arterial input function in the rat aorta following intravenous injection of gadolinium contrast agent", *Magn. Reson. Imaging*, vol. 23, no. 5, pp. 619–627, Jun. 2005
- [216] E. Kellner, I. Mader, M. Mix, D. N. Splitthoff, M. Reiser, K. Foerster, T. Nguyen-Thanh, P. Gall, and V. G. Kiselev, "Arterial input function measurements for bolus tracking perfusion imaging in the brain", *Magn. Reson. Med.*, vol. 69, no. 3, pp. 771–780, Mar. 2013
- [217] T. E. Conturo, P. B. Barker, V. P. Matthews, L. H. Monsein, R. N. Bryan, "MR imaging of cerebral perfusion by phase angle reconstruction of bolus paramagnetic-induced frequency shifts", *Magn. Reson. Med.*, vol. 27, pp. 375–390, 1992
- [218] F. Calamante, "Arterial input function in perfusion MRI: A comprehensive review", *Prog. Nucl. Magn. Reson. Spectrosc.*, vol. 74, pp. 1–32, Oct 2013
- [219] E. Akbudak and T. E. Conturo, "Arterial input functions from MR phase imaging", *Magn. Reson. Med.*, vol. 36, pp. 809–815, 1996
- [220] M. S. Koyts, E. Akbudak, J. Markham and T. E. Conturo, "Precision, signal-to-noise ratio and dose optimization of magnitude and phase arterial input functions in dynamic susceptibility contrast MRI", *J. Magn. Reson. Imaging*, vol. 25, pp. 598–611, 2007
- [221] D. Izquierdo-Garcia, J. R. Davies, M. J. Graves, J. H. F. Rudd, J. H. Gillard, P. L. Weissberg, T. D. Fryer, and E. a Warburton, "Comparison of methods for magnetic resonance-guided [18-F]fluorodeoxyglucose positron emission tomography in human carotid arteries: reproducibility, partial volume correction, and correlation between methods", *Stroke*, vol. 40, no. 1, pp. 86–93, Jan. 2009

- [222] M. Soret, S. L. Bacharach, and I. Buvat, “Partial-volume effect in PET tumor imaging”, *J. Nucl. Med.*, vol. 48, no. 6, pp. 932-945, Jun. 2007
- [223] M. S. Judenhofer, S. Wiehr, D. Kukuk, K. Fischer and B. J. Pichler, “Guidelines for Nuclear Image Analysis”, in *Small Animal Imaging: Basics and Practical Guide*, F. Kiessling and B. J. Pichler (Eds.), Springer-Verlag, Berlin Heidelberg, Germany, pp. 379–386, 2011
- [224] O. G. Rousset, Y. Ma, and A. C. Evans, “Correction for partial volume effects in PET: Principle and Validation”, *J. Nucl. Med.*, vol. 39, no. 5, pp. 904–911, May 1998
- [225] S. L. Hackett, D. Liu, A. Chalkidou, P. Marsden, D. Landau, and J. D. Fenwick, “Estimation of input functions from dynamic [^{18}F] FLT PET studies of the head and neck with correction for partial volume effects”, *EJNMMI Res.*, vol. 3, no. 84, pp. 1-9, Dec. 2013
- [226] W. Lehnert, M.-C. Gregoire, A. Reilhac, and S. R. Meikle, “Characterisation of partial volume effect and region-based correction in small animal positron emission tomography (PET) of the rat brain”, *Neuroimage*, vol. 60, no. 4, pp. 2144-2157, May 2012
- [227] M. Sattarivand, J. Armstrong, G. M. Szilagyi, M. Kusano, I. Poon and C. Caldwell, “Region-Based Partial Volume Correction Techniques for PET Imaging: Sinogram Implementation and Robustness”, *Int. J. Mol. Imaging* vol. 2013, no. 435959, pp. 1–12, Oct. 2013
- [228] G. Buonincontri, C. Methner, T. Krieg, R. C. Hawkes, T. A. Carpenter, and S. J. Sawiak, “PET/MRI assessment of the infarcted mouse heart,” *Nucl. Instrum. Meth. A*, vol. 734, part B, pp. 152-155, Jan. 2014.
- [229] R. C. Hawkes, S. J. Sawiak, R. E. Ansorge, G. Buonincontri, E. Evans, and T. A. Carpenter, “NEMA Test Results for the Cambridge Split Magnet Scanner”, *Poster Presentation at PSMR 2013*, May 2013
- [230] J. Breuer, R. Grazioso, N. Zhang, M. Schmand, and K. Wienhard, “Evaluation of an MR-compatible blood sampler for PET”, *Phys. Med. Biol.*, vol. 55, no. 19, pp. 5883-5893, Oct. 2010
- [231] G. M. Blake, M. Siddique, M. L. Frost, A. E. B. Moore and I. Fogelman, “Quantitative PET Imaging Using ^{18}F Sodium Fluoride in the Assessment of Metabolic Bone Diseases and the Monitoring of Their Response to Therapy”, in *Clinical Utility of ^{18}F NaF PET/CT in Benign and Malignant Bone Disorders*, M. Beheshti (Ed.), Elsevier, New York, USA, PET Clinics, vol. 7, no. 3, pp. 275–292, Jul. 2012
- [232] S. Basu, M. Beheshti, A. Alavi, “Value of ^{18}F NaF PET/CT in the Detection and Global Quantification of Cardiovascular Molecular Calcification as Part of the Atherosclerotic Process”, in

- Clinical Utility of ^{18}F NaF PET/CT in Benign and Malignant Bone Disorders*, M. Beheshti, (Ed.), Elsevier, New York, USA, PET Clinics, vol. 7, no. 3, pp. 329–340, Jul. 2012
- [233] J. Czernin, N. Satyamurthy, and C. Schiepers, “Molecular mechanisms of bone ^{18}F -NaF deposition”, *J. Nucl. Med.*, vol. 51, no. 12, pp. 1826-1829, Dec. 2010
- [234] F. Berger, Y.-P. Lee, A. M. Loening, A. Chatziioannou, S. J. Freedland, R. Leahy, J. R. Lieberman, A. S. Belldegrun, C. L. Sawyers, and S. S. Gambhir, “Whole-body skeletal imaging in mice utilizing microPET: optimization of reproducibility and applications in animal models of bone disease”, *Eur. J. Nucl. Med. Mol. Imaging*, vol. 29, no. 9, pp. 1225-1236, Jul. 2002
- [235] L. Wen, S. Eberl, D. D. Feng, P. Stalley, G. Huang, and M. J. Fulham, “Parametric Images in Assessing Bone Grafts Using Dynamic F-Fluoride PET”, *Int. J. Mol. Imaging*, vol. 2011, no. 189830, pp. 1–8, Jan. 2011
- [236] R. S. Ripa and A. Kjær, “Imaging Atherosclerosis with Hybrid Positron Emission Tomography/Magnetic Resonance Imaging”, *BioMed Research International*, vol. 2015, no. 914516, pp. 1–8, Sep. 2014
- [237] U. Schnöckel, S. Reuter, L. Stegger, E. Schlatter, K. P. Schfers, S. Hermann, O. Schober, G. Gabrils, and M. Schfers, “Dynamic ^{18}F -fluoride small animal PET to noninvasively assess renal function in rats”, *Eur. J. Nucl. Med. Mol. Imaging*, vol. 35, no. 12, pp. 2267-2274, Dec. 2008
- [238] M. J. Silva, B. A. Uthgenannt, J. R. Rutlin, G. R. Wohl, J. S. Lewis, and M. J. Welch, “In vivo skeletal imaging of ^{18}F -fluoride with positron emission tomography reveals damage- and time-dependent responses to fatigue loading in the rat ulna”, *Bone*, vol. 39, no. 2, pp. 229-236, Aug. 2006
- [239] J.-C. Richard, Z. Zhou, D. L. Chen, M. a Mintun, D. Piwnica-Worms, P. Factor, D. E. Ponde, and D. P. Schuster, “Quantitation of pulmonary transgene expression with PET imaging”, *J. Nucl. Med.*, vol. 45, no. 4, pp. 644-654, Apr. 2004
- [240] R. Rhoades and D. R. Bell, “Blood Components”, in *Medical Physiology: Principles for Clinical Medicine*, Third edition, Philadelphia, PA, USA, Lippincott, Williams and Wilkins, p. 171, 2008
- [241] G. J. R. Cook, M. A. Lodge, P. K. Marsden, A. Dynes and I. Fogelman, “Non-invasive assessment of skeletal kinetics using fluorine-18 fluoride positron emission tomography: evaluation of image and population-derived arterial input functions”, *Eur. J. Nucl. Med.*, vol. 26, no. 11, pp. 1424–1429, Nov. 1999

- [242] G. J. R. Cook, G. M. Blake, P. K. Marsden, B. Cronin and I. Fogelman, "Quantification of skeletal kinetic indices in Paget's disease using dynamic F-18-Fluoride positron emission tomography", *J. Bone Miner. Res.*, vol. 17, no. 5, pp. 854–859, May 2002
- [243] M. Piert, T. T. Zittel, R. Machulla, G. A. Becker, M. Jahn, G. Maier, R. Bares, and H. D. Becker, "Blood Flow Measurements with [(15)O]H₂O and [18F] Fluoride Ion PET in Porcine Vertebrae", *J. Bone Miner. Res.* vol. 13, no. 8, pp. 1328-1336, Aug. 1998
- [244] G. M. Blake, M. Siddique, M. L. Frost, A. E. B. Moore, and I. Fogelman, "Imaging of site specific bone turnover in osteoporosis using positron emission tomography", *Curr. Osteoporos. Rep.*, vol. 12, no. 4, pp. 475-485, Dec. 2014
- [245] M. Sakoh, L. Rohl, C. Gyldensted, A. Gjedde, L. Østergaard, and R. A. Knight, "Cerebral Blood Flow and Blood Volume Measured by Magnetic Resonance Imaging Bolus Tracking After Acute Stroke in Pigs: Comparison With [¹⁵O]H₂O Positron Emission Tomography", *Stroke*, vol. 31, no. 8, pp. 1958–1964, Aug. 2000
- [246] A. G. Sorensen, W. A. Copen, L. Østergaard, F. S. Buonanno, R. G. Gonzalez, G. Rordorf, B. R. Rosen, L. H. Schwamm, R. M. Weisskoff, and W. J. Koroshetz, "Hyperacute stroke: simultaneous measurement of relative cerebral blood volume, relative cerebral blood flow, and mean tissue transit time", *Radiology*, vol. 210, no. 2, pp. 519–527, Feb. 1999
- [247] J. Kucharczyk, Z. S. Vexler, T. P. Roberts, H. S. Asgari, J. Mintorovitch, N. Derugin, A. D. Watson, and M. E. Moseley, "Echo-planar perfusion-sensitive MR imaging of acute cerebral ischemia", *Radiology*, vol. 188, no. 3, pp. 711–717, Sept. 1993
- [248] M. L. Forbes, K. S. Hendrich, P. M. Kochanek, D. S. Williams, J. K. Schiding, S. R. Wisniewski, S. F. Kelsey, S. T. DeKosky, S. H. Graham, D. W. Marion, and C. Ho, "Assessment of cerebral blood flow and CO₂ reactivity after controlled cortical impact by perfusion magnetic resonance imaging using arterial spin-labeling in rats", *J. Cereb. Blood Flow Metab.*, vol. 17, no. 8, pp. 865–874, Aug. 1997
- [249] G. J. Harris, R. F. Lewis, A. Satlin, C. D. English, T. M. Scott, D. A. Yurgelun-Todd, and P. F. Renshaw, "Dynamic susceptibility contrast MR imaging of regional cerebral blood volume in Alzheimer disease: a promising alternative to nuclear medicine", *Am. J. Neuroradiol.*, vol. 19, no. 9, pp. 1727–1732, Oct. 1998
- [250] B. Hakyemez, C. Erdogan, N. Bolca, N. Yildirim, G. Gokalp, and M. Parlak, "Evaluation of different cerebral mass lesions by perfusion-weighted MR imaging", *J. Magn. Reson. Imaging*, vol. 24, no. 4, pp. 817–824, Oct. 2006

- [251] A. E. Hansen, H. Pedersen, E. Rostrup, and H. B. W. Larsson, "Partial volume effect (PVE) on the arterial input function (AIF) in T1-weighted perfusion imaging and limitations of the multiplicative rescaling approach", *Magn. Reson. Med.*, vol. 62, no. 4, pp. 1055–1059, Oct. 2009
- [252] M. J. P. van Osch, E.-J. P. A. Vonken, M. A. Viergever, J. van der Grond, and C. J. G. Bakker, "Measuring the arterial input function with gradient echo sequences", *Magn. Reson. Med.*, vol. 49, no. 6, pp. 1067–1076, Jun. 2003
- [253] A. Dorr, J. G. Sled, and N. Kabani, "Three-dimensional cerebral vasculature of the CBA mouse brain: a magnetic resonance imaging and micro computed tomography study", *NeuroImage*, vol. 35, no. 4, pp. 1409–1423, May 2007
- [254] E. Bullitt, S. R. Aylward, T. Van Dyke and W. Lin, "Computer-Assisted Measurement of Vessel Shape from 3T Magnetic Resonance Angiography of Mouse Brain", *Methods*, vol. 43, no. 1, pp. 29–34, Sep. 2007
- [255] W. L. Nowinski, B. C. Chua, Y. Marchenko, F. Puspitsari, I. Volkau, and M. V Knopp, "Three-dimensional reference and stereotactic atlas of human cerebrovasculature from 7 Tesla", *Neuroimage*, vol. 55, no. 3, pp. 986-998, Apr. 2011
- [256] J. R. Rangarajan, K. Van Kuyck, U. Himmelreich, B. Nuttin, F. Maes, and P. Suetens, "Assessment of variability in cerebral vasculature for neuro-anatomical surgery planning in rodent brain", *Proc. SPIE*, vol. 7965, no. 79650Q, pp. 1–9, Mar. 2011
- [257] O. U. Scremin, "Cerebral Vascular System," in *The Rat Nervous System*, G. Paxinos (Ed.), Third edition, London, UK, Gulf Professional Publishing, pp. 1165–1202, 2004
- [258] D. J. Williamson, S. Ejaz, S. Sitnikov, T. D. Fryer, S. J. Sawiak, P. Burke, J.-C. Baron, and F. I. Aigbirhio, "A comparison of four PET tracers for brain hypoxia mapping in a rodent model of stroke", *Nucl. Med. Biol.*, vol. 40, no. 3, pp. 338-344, Apr. 2013
- [259] S. Ejaz, D. J. Williamson, T. Ahmed, S. Sitnikov, Y. T. Hong, S. J. Sawiak, T. D. Fryer, F. I. Aigbirhio, and J.-C. Baron, "Characterizing infarction and selective neuronal loss following temporary focal cerebral ischemia in the rat: a multi-modality imaging study", *Neurobiol. Dis.*, vol. 51, pp. 120-132, Mar. 2013
- [260] A. Singh, R. K. S. Rathore, M. Haris, S. K. Verma, N. Husain, and R. K. Gupta, "Improved bolus arrival time and arterial input function estimation for tracer kinetic analysis in DCE-MRI", *J. Magn. Reson. Imaging*, vol. 29, no. 1, pp. 166–176, Jan. 2009

- [261] O. Wu, L. Østergaard, R. M. Weisskoff, T. Benner, B. R. Rosen, and A. G. Sorensen, “Tracer arrival timing-insensitive technique for estimating flow in MR perfusion-weighted imaging using singular value decomposition with a block-circulant deconvolution matrix”, *Magn. Reson. Med.*, vol. 50, no. 1, pp. 164–174, July 2003
- [262] S. Ulmer, M. Reeh, J. Krause, T. Herdegen, J. Heldt-Feindt, O. Jansen, and A. Rohr, “Dynamic contrast-enhanced susceptibility-weighted perfusion MRI (DSC-MRI) in a glioma model of the rat brain using a conventional receive-only surface coil with a inner diameter of 47 mm at a clinical 1.5 T scanner”, *J. Neurosci. Methods*, vol. 172, no. 2, pp. 168-172, Jul. 2008
- [263] A. M. Stokes, J. T. Skinner, and C. C. Quarles, “Assessment of a combined spin- and gradient-echo (SAGE) DSC-MRI method for preclinical neuroimaging”, *J. Magn. Reson. Imaging*, vol. 32, no. 10, pp. 1181-1190, Dec. 2014
- [264] R. Liu, R. He, K. H. Bockhorst, V. K. Magatadakala, P.A. Narayana, “Quantitative Cerebral Perfusion in Rodents Assisted by Susceptibility Weighted Imaging”, *Proc. Intl. Mag. Res. Med.* 17, p. 1476, May 2009
- [265] E. R. Muir, Q. Shen and T. Q. Duong, “Cerebral Blood Flow MRI in Mice using the Cardiac Spin Labelling Technique”, *Magn. Reson. Med.*, vol. 60, no. 3, pp. 744–748, Sep. 2008
- [266] C. Leithner, K. Gertz, H. Schrck, J. Priller, K. Prass, J. Steinbrink, a Villringer, M. Endres, U. Lindauer, U. Dirnagl, and G. Roysl, “A flow sensitive alternating inversion recovery (FAIR)-MRI protocol to measure hemispheric cerebral blood flow in a mouse stroke model”, *Exp. Neurol.*, vol. 210, no. 1, pp. 118-127, Mar. 2008.
- [267] J. Hofmeijer, J. Schepers, H. B. van der Worp, L. J. Kappelle, and K. Nicolay, “Comparison of perfusion MRI by flow-sensitive alternating inversion recovery and dynamic susceptibility contrast in rats with permanent middle cerebral artery occlusion”, *NMR Biomed.*, vol. 18, no. 6, pp. 390-394, Oct. 2005
- [268] L. Røhl, L. Østergaard, C. Z. Simonsen, P. Vestergaard-Poulsen, G. Andersen, M. Sakoh, D. Le Bihan, and C. Gyldensted, “Viability Thresholds of Ischemic Penumbra of Hyperacute Stroke Defined by Perfusion-Weighted MRI and Apparent Diffusion Coefficient”, *Stroke*, vol. 32, no. 5, pp. 1140-1146, May 2001
- [269] J.-H. Kim, G. H. Im, J. Yang, D. Choi, W. J. Lee, and J. H. Lee, “Quantitative dynamic contrast-enhanced MRI for mouse models using automatic detection of the arterial input function”, *NMR Biomed.*, vol. 25, no. 4, pp. 674–684, Apr. 2012

- [270] M. J. P. van Osch, J. van der Grond, and C. J. G. Bakker, "Partial volume effects on arterial input functions: shape and amplitude distortions and their correction", *J. Magn. Reson. Imaging.*, vol. 22, no. 6, pp. 704–709, Dec. 2005
- [271] L. Knutsson, E. Lindgren, A. Ahlgren, M. J. P. van Osch, K. Markenroth Bloch, Y. Surova, F. Sthlberg, D. van Westen, and R. Wirestam, "Reduction of arterial partial volume effects for improved absolute quantification of DSC-MRI perfusion estimates: Comparison between tail scaling and prebolus administration", *J. Magn. Reson. Imaging*, vol. 41, no. 4, pp. 903–908, Apr. 2015
- [272] E. Poulin, R. Lebel, E. Croteau, M. Blanchette, L. Tremblay, R. Lecomte, M. Bentourkia, and M. Lepage, "Optimization of the reference region method for dual pharmacokinetic modeling using Gd-DTPA/MRI and (18) F-FDG/PET", *Magn. Reson. Med.*, vol. 73, no. 2, pp. 740–748, Feb. 2015
- [273] C. Lois, I. Bezrukov, H. Schmidt, N. Schwenzer, M. K. Werner, J. Kupferschlger, and T. Beyer, "Effect of MR contrast agents on quantitative accuracy of PET in combined whole-body PET/MR imaging", *Eur. J. Nucl. Med. Mol. Imaging*, vol. 39, no. 11, pp. 1756-1766, Nov. 2012
- [274] T. E. Yankeelov, G. O. Cron, C. L. Addison, J. C. Wallace, R. C. Wilkins, B. A. Pappas, G. E. Santyr, and J. C. Gore, "Comparison of a reference region model with direct measurement of an AIF in the analysis of DCE-MRI data", *Magn. Reson. Med.*, vol. 57, no. 2, pp. 353–361, Feb. 2007
- [275] A. Steingoetter, J. Svensson, Y. Kosanke, R. M. Botnar, M. Schwaiger, E. Rummeny, and R. Braren, "Reference region-based pharmacokinetic modeling in quantitative dynamic contrast-enhanced MRI allows robust treatment monitoring in a rat liver tumor model despite cardiovascular changes", *Magn. Reson. Med.*, vol. 65, no. 1, pp. 229–238, Jan. 2011
- [276] S. L. Bacharach and R. E. Carson, "In hot blood: quantifying the arterial input function", *JACC. Cardiovasc. Imaging*, vol. 6, no. 5, pp. 569-573, May 2013
- [277] T. Matsuzawa, N. Morita, Y. Hayashi, M. Nomura, T. Unno, T. Igarashi, T. Furuya, K. Sekita, A. Ono, Y. Kurokawa and Y. Hayashi, "A Survey of the Results of Haematological Parameters, Using a Common Rat Blood Sample in Japanese Laboratories", *Comp. Haematol. Int.*, vol. 6, no. 3, pp. 125–133, 1996.
- [278] R. Davenport, "The derivation of the gamma variate relationship for tracer dilution curves", *J. Nucl. Med.*, vol. 24, no. 10, pp. 945-949, Oct. 1983
- [279] K. Chen, D. Bandy, E. Reiman, S. C. Huang, M. Lawson, D. Feng, L. S. Yun, and A. Palant, "Noninvasive quantification of the cerebral metabolic rate for glucose using positron emission tomography, 18F-fluoro-2-deoxyglucose, the Patlak method, and an image-derived input function", *J. Cereb. Blood Flow Metab.*, vol. 18, no. 7, pp. 716-723, Jul. 1998

- [280] T. Fritz-Hansen, E. Rostrup, H. B. Larsson, L. Søndergaard, P. Ring, and O. Henriksen, "Measurement of the arterial concentration of Gd-DTPA using MRI: a step toward quantitative perfusion imaging", *Magn. Reson. Med.*, vol. 36, no. 2, pp. 225–231, Aug. 1996
- [281] O. L. Munk, S. Keiding, and L. Bass, "A method to estimate dispersion in sampling catheters and to calculate dispersion-free blood time-activity curves", *Med. Phys.*, vol. 35, no. 8, pp. 3471-3481, Aug. 2008
- [282] E. K. Fung and R. E. Carson, "Cerebral blood flow with [15O] water PET studies using an image-derived input function and MR-defined carotid centerlines", *Phys. Med. Biol.*, vol. 58, no. 6, pp. 1903-1923, Mar. 2013
- [283] J. Moroz, C. L. Wong, A. C. Yung, P. Kozlowski, and S. A. Reinsberg, "Rapid measurement of arterial input function in mouse tail from projection phases", *Magn. Reson. Med.*, vol. 71, no. 1, pp. 238–245, Jan. 2014
- [284] A-C. Fruytier, J. Magat, F. Colliez, B. Jordan, G. Cron, and B. Gallez, "Dynamic contrast-enhanced MRI in mice at high field: Estimation of the arterial input function can be achieved by phase imaging", *Magn. Reson. Med.*, vol. 71, no. 2, pp. 544–550, Feb. 2014
- [285] N. A. Mullani, R. S. Herbst, R. G. O'Neil, K. L. Gould, B. J. Barron, and J. L. Abbruzzese, "Tumor blood flow measured by PET dynamic imaging of first-pass 18F-FDG uptake: a comparison with 15O-labeled water-measured blood flow", *J. Nucl. Med.*, vol. 49, no. 4, pp. 517–523, Apr. 2008
- [286] A. J. de Langen, V. van den Boogaart, M. Lubberink, W. H. Backes, J. T. Marcus, H. van Tinteren, J. Pruijm, B. Brans, P. Leffers, A.-M. C. Dingemans, E. F. Smit, H. J. M. Groen, and O. S. Hoekstra, "Monitoring response to antiangiogenic therapy in non-small cell lung cancer using imaging markers derived from PET and dynamic contrast-enhanced MRI", *J. Nucl. Med.*, vol. 52, no. 1, pp. 48–55, Jan. 2011
- [287] J. G. Mannheim, M. S. Judenhofer, A. Schmid, J. Tillmanns, D. Stiller, V. Sossi, and B. J. Pichler, "Quantification accuracy and partial volume effect in dependence of the attenuation correction of a state-of-the-art small animal PET scanner", *Phys. Med. Biol.*, vol. 57, no. 12, pp. 3981-3993, Jun. 2012
- [288] T. E. Cheng, K. K. Yoder, M. D. Normandin, S. L. Risacher, A. K. Converse, J. A. Hampel, M. A. Miller, and E. D. Morris, "A rat head holder for simultaneous scanning of two rats in small animal PET scanners: design, construction, feasibility testing and kinetic validation", *J. Neurosci. Methods*, vol. 176, no. 1, pp. 24-33, Jan. 2009

- [289] P. E. Kinahan, B. H. Hasegawa, and T. Beyer, "X-ray-based attenuation correction for positron emission tomography/computed tomography scanners", *Semin. Nucl. Med.*, vol. 33, no. 3, pp. 166-179, Jul. 2003
- [290] V. Keereman, Y. Fierens, C. Vanhove, T. Lahoutte, and S. Vandenberghe, "Magnetic resonance-based attenuation correction for micro-single-photon emission computed tomography", *Mol. Imaging*, vol. 11, no. 2, pp. 155-165, Apr. 2012
- [291] H. Sari, K. Erlandsson, A. Barnes, D. Atkinson, S. Arridge, S. Ourselin, and B. Hutton, "Modelling the impact of injection time on the bolus shapes in PET-MRI AIF Conversion", *EJNMMI Phys.*, vol. 1, no. Suppl 1, p. A54, May 2014
- [292] L. Caldeira, S. D. Yun, N. A. da Silva, C. Filss and N. J. Shah, "Estimation of the arterial input function using accelerated dual-contrast EPIK: a multi-modality MR-PET study", *Proc. Intl. Mag. Res. Med.* 22, p. 1500, May 2014
- [293] M. Poole, R. Bowtell, D. Green, S. Pittard, A. Lucas, R. Hawkes, and T. A. Carpenter, "Split gradient coils for simultaneous PET-MRI", *Magn. Reson. Med.*, vol. 62, no. 5, pp. 1106-1111, Nov. 2009
- [294] M. D. Robson, P. D. Gatehouse, M. Bydder and G. M. Bydder, "Magnetic resonance: an introduction to ultrashort TE (UTE) imaging," *J. Comput. Assist. Tomogr.*, vol. 27, no. 6, pp. 825-846, Nov. 2003
- [295] C. F. Chan, N. G. Keenan, S. Nielles-Vallespin, P. Gatehouse, M. N. Sheppard, J. J. Boyle, D. J. Pennell and D.N. Firmin, "Ultra-short echo time cardiovascular magnetic resonance of atherosclerotic carotid plaque," *J. Cardiovasc. Magn. Reson.*, vol. 12, no. 17, pp. 1-8, Mar. 2010
- [296] M. C. Schabel and G. R. Morrell, "Uncertainty in T1 mapping using the variable flip angle method with two flip angles", *Phys. Med. Biol.*, vol. 54, no. 1, pp. N1-N8, Jan. 2009
- [297] K.-H. Chuang and A. Koretsky, "Improved neuronal tract tracing using manganese enhanced magnetic resonance imaging with fast T(1) mapping", *Magn. Reson. Med.*, vol. 55, no. 3, pp. 604-611, Mar. 2006
- [298] S. Pickup, A. K. W. Wood, and H. L. Kundel, "Gadodiamide T1 relaxivity in brain tissue in vivo is lower than in saline", *Magn. Reson. Med.*, vol. 53, no. 1, pp. 35-40, Jan. 2005
- [299] D. N. Guilfoyle, V. V. Dyakin, J. O'Shea, G. S. Pell, and J. A. Helpert, "Quantitative measurements of proton spin-lattice (T1) and spin-spin (T2) relaxation times in the mouse brain at 7.0 T", *Magn. Reson. Med.*, vol. 49, no. 3, pp. 576-580, Mar. 2003

- [300] M. Pedersen, J. Mørkenborg, F. T. Jensen, H. Stødkilde Jørgensen, J. C. Djurhuus, and J. Frokiaer, “In vivo measurements of relaxivities in the rat kidney cortex”, *J. Magn. Reson. Imaging*, vol. 12, no. 2, pp. 289–296, Aug. 2000
- [301] A. F. Stalder, D. V. Elverfeldt, D. Paul, J. Hennig, and M. Markl, “Variable echo time imaging: signal characteristics of 1-M gadobutrol contrast agent at 1.5 and 3T”, *Magn. Reson. Med.*, vol. 59, no. 1, pp. 113–123, Jan. 2008
- [302] M. Rijpkema, J. H. Kaanders, F. B. Joosten, A. J. van der Kogel, and A. Heerschap, “Method for quantitative mapping of dynamic MRI contrast agent uptake in human tumors”, *J. Magn. Reson. Imaging*, vol. 14, no. 4, pp. 457–463, Oct. 2001
- [303] E. Ashton, D. Raunig, C. Ng, F. Kelcz, T. McShane, and J. Evelhoch, “Scan-rescan variability in perfusion assessment of tumors in MRI using both model and data-derived arterial input functions”, *J. Magn. Reson. Imaging*, vol. 28, no. 3, pp. 791–796, Sep. 2008
- [304] A. Fedorov, J. Fluckiger, G. D. Ayers, X. Li, S. N. Gupta, C. Tempany, R. Mulkern, T. E. Yankeelov, and F. M. Fennessy, “A comparison of two methods for estimating DCE-MRI parameters via individual and cohort based AIFs in prostate cancer: A step towards practical implementation”, *J. Magn. Reson. Imaging*, vol. 32, no. 4, pp. 321–329, May 2014
- [305] L. Shi, D. Wang, W. Liu, K. Fang, Y.-X. J. Wang, W. Huang, A. D. King, P. A. Heng, and A. T. Ahuja, “Automatic detection of arterial input function in dynamic contrast enhanced MRI based on affinity propagation clustering”, *J. Magn. Reson. Imaging*, vol. 39, no. 5, pp. 1327–1337, May 2014
- [306] R. E. Port, M. V. Knopp, and G. Brix, “Dynamic contrast-enhanced MRI using Gd-DTPA: interindividual variability of the arterial input function and consequences for the assessment of kinetics in tumors”, *Magn. Reson. Med.*, vol. 45, no. 6, pp. 1030–1038, Jun. 2001
- [307] B. J. van Nierop, B. F. Coolen, W. J. R. Dijk, A. D. Hendriks, L. de Graaf, K. Nicolay, and G. J. Strijkers, “Quantitative first-pass perfusion MRI of the mouse myocardium”, *Magn. Reson. Med.*, vol. 69, no. 6, pp. 1735–1744, Jun. 2013